Tethering surface tension to organic synthesis: a quest for chemoselectivity

GIULIA FRANCESCA GRELLI

Tethering surface tension to organic synthesis: a quest for chemoselectivity

Giulia Francesca Grelli, BChem, MChem

University of Durham

Department of Chemistry

St Hild and St Bede College

A thesis presented in fulfilment of the requirements

For the degree of *Doctor of Philosophy*

March 2024

Ne cherchez pas midi à quatorze heures.
(Do not make things more complicated than they are).

- *Luigi Carlo Giuseppe Marangoni*
(On the spreading of liquid droplets).

Tethering surface tension to organic synthesis: a quest for chemoselectivity

Giulia Francesca Grelli

Submitted for the degree of Doctor of Philosophy

Primary supervisor: Dr. Matthew O. Kitching

Abstract

The development of chemoselective processes is of utmost importance for the future of synthetic organic chemistry and has been described as 'one of the greatest obstacles to complex molecule synthesis.' This dissertation was written with this main objective in mind, which was pursued from two perspectives.

Development of surface-tension driven droplet devices towards parallel and chemoselective synthesis of substituted 2H-chromen-2-ones was at first investigated on a sub-millimolar scale (Chapters 1-3). Multi-droplet sorting devices were manufactured and key parameters such as droplet composition, substrate temperature and orientation were optimised. Test reactions in aqueous propylene glycol (PG) were conducted in batch conditions, affording 3,6-disubstituted coumarins references *via* Knoevenagel condensation of 5-substituted salicyladehydes with activated methylene compounds and acid-promoted intramolecular cyclisation. Reactivity transposition onto droplets was thoroughly investigated, leading to a three-pair reagent (3x3) chemical sorter. Product quantification method by ^{1}H-NMR spectroscopy was successfully implemented in micro-liter sized droplets, proving how chemoselectivity can be achieved following such unconventional, synthetic methodology.

The second project studied chemoselective formation of 2-alkenyl tertiary anilines and 1,1,2-trimethylindolinium hexafluorophosphates *via* charged aza-Claisen rearrangement and thermal cyclisation of quaternary *N*-allylated ammonium salts (Chapter 4-6). In the latter case, early attempts of the reaction were unsuccessful due to decomposition catalysed by the bromide anion, but a switch to a non-nucleophilic anion (PF_6^-) allowed the ring closure to occur. Compound library synthesis was carried out to assess the synthetic methodology robustness. Key strengths and limitations were identified and ammonium substrate regiochemical effects were examined and discussed. Finally, interesting research avenues were suggested to broaden substrate scope studies and, most importantly, to link structural connectivity analysis of ammonium salts with modulation of their surface properties.

Declaration

I declare that;

This submission is entirely my own work and is based on research carried out within the Kitching group at Durham University. I confirm that I have read and understood the Department and University regulations on plagiarism. No part of this thesis has been submitted elsewhere for any other degree or qualification. Each contribution to, and quotation in this submission which is taken from the work or works of other people, has been cited correctly.

Signed: 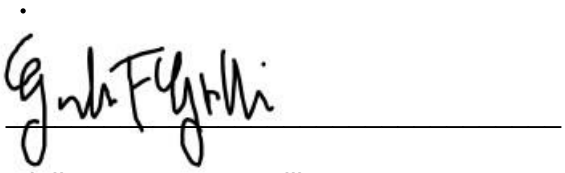

Giulia Francesca Grelli

Acknowledgements

The results reported in this manuscript were obtained during my postgraduate studies under supervision of Dr. Matthew O. Kitching. I would like to express my deepest gratitude to him for his guidance and for this opportunity, which enabled my growth from an academic and, most importantly, from a personal standpoint.

I also thank Dr. Michael John Hall from the School of Natural and Environmental Sciences of Newcastle University as well as Dr. Richard Thompson from the Department of Chemistry of the University of Durham, for accepting to judge this thesis work. I express to them also my gratitude for all the remarks they will make to improve this manuscript.

A deep, heart-felt acknowledgement goes for two of my past fellow colleagues, who first investigated the research projects herein discussed. So, I would like to thank Mr. Thomas H. Fox and Dr. Mark P. Walsh for their painstaking research focused on multi-droplet motion and aza-Claisen rearrangement of bromide arylammonium salts, respectively. I am also grateful to Dr. Alexander J. Nicholls and Dr. James A. Barclay who participated in the correction of this manuscript and, more in general, I warmly thank all past members of the group who allowed me to work in a relaxed and enthusiastic atmosphere, despite of the COVID-19 disruption.

Last but not the least, I deeply thank my mother and my siblings for their emotional support in the most challenging times.

Contents

Abbreviations

^{1}H-NMR	Proton nuclear magnetic resonance spectroscopy
^{19}F-NMR	Fluorine nuclear magnetic resonance spectroscopy
^{31}P-NMR	Phosphorus nuclear magnetic resonance spectroscopy
1,2-BD	1,2-butanediol
1,2-PeD	1,2-pentanediol
1,2-HD	1,2-hexanediol
2-ClC_6H_4	2-chlorophenyl
4-$MeOC_6H_4$	4-methoxyphenyl
(2x2)	Two pair droplet sorter
(3x3)	Three pair droplet sorter
(6DT)	Six pair droplet reactor
(aq)	Aqueous solution
(eq)	Equivalents
$[BPh_4]^-$	Tetraphenylborate
$\%_{(v/v)}$	Volume percentage
AcCl	Acetyl chloride
Anth	9-anthracenyl
Ar	Aryl
BF_3•OEt_2	Boron trifluoride diethyl etherate
BF_4^-	Tetrafluoroborate
Bn	Benzyl
Br	Bromo
Br^-	Bromide
Cl^-	Chloride
CH_2Cl_2	Dichloromethane
C_6H_5Br	Bromobenzene
CD_3CN	Deuterated acetonitrile
$CDCl_3$	Deuterated chloroform
C_nTAB	Aryltrimethylammonium bromide surfactant
CuAAC	Copper-catalysed azide-alkyne cycloaddition
Cy	Cyclohexyl
DABCO	1,4-diazabicyclo[2.2.2]octane
DMF	*N,N*-dimethyl formamide
DMSO	Dimethyl sulfoxide
DMSO-d_6	Deuterated dimethyl sulfoxide

DSS	sodium 3-(trimethylsilyl)-1-propanesulfonate
dw	Infinitesimal gradient of work
dσ	Infinitesimal gradient of surface area
ee	Enantiomeric excess
eq	Equivalents
EDG	Electron donating group
EG	Ethylene glycol
Et	Ethyl
EtOH	Ethanol
EWG	Electron withdrawing group
fps	frames per second
GC-MS	Gas chromatography-mass spectrometry
GUV	Giant unilamellar vesicle
h	Height
$HAuCl_4$	Chloroauric acid
HPLC	High performance liquid chromatography
hr	Hour
HMPA	Hexamethylphosphoramide
I^-	Iodide
^{i}Pr	Isopropyl
^{i}PrOH	Propan-2-ol
$iPrNEt_2$	*N,N*-diisopropylethylamine
ITO	Indium tin oxide
k_R	First rate order constant
l	Wire length
LA	Lewis acid
LUV	Large unilamellar vesicle
m-CPBA	*meta*-chloroperoxybenzoic acid
m/z	Mass-to-charge ratio
$M(OTf)_x$	Metal triflate salt
MALDI-MS	Matrix assisted laser desorption/ionization mass spectrometry
MBO	3-methoxy-2-butanol
Me	Methyl
MeCN	Acetonitrile
MeOH	Methanol
Ms	Mesyl
MW	Microwave irradiation

MUA	11-mercaptoundecanoic acid
ND	Not determined
NMe_2	*N,N*-dimethylamino
NP	Nanoparticle
OA	Oleic acid
OMe	Methoxy
OEt	Ethoxy
OTf	Triflate
P	Vapour pressure
PDMS	Poly(dimethylsiloxane)
PET	Polyethylene terephthalate
PG	1,2-propanediol (propylene glycol)
Ph	Phenyl
$PPh_3P=O$	Triphenylphosphine oxide
PMP	Paramagnetic particle
$PhNMe_2$	*N,N*-dimethylaniline
PhMe	Toluene
PPA	Polyphosphoric acid
PTSA	*para*-toluensulfonic acid
R	Droplet radius
r.t.	Room temperature
RH	Relative humidity
s	Seconds
S	Initial spreading coefficient
SAMs	Self-assembled monolayers
SLIPS	Slippery liquid-infused porous substrate
SUV	Small unilamellar vesicle
^tBu	*tert*-butyl
TFA	Trifluoroacetic acid
THF	Tetrahydrofuran
TMS	Trimethylsilyl
T_R	Reaction temperature
t_R	Reaction time
t_W	Experimental time interval
t_C	Experimental critical time
V	Droplet volume
x_S	Distance between localised vapour source and binary mixture droplet

x_E	Equilibrium distance between localised vapour source and binary mixture drop
α	Solid substrate tilt angle
Δ	Heat
$\Delta E^{\ddagger}$	Activation energy
$\Delta S^{\ddagger}$	Activation entropy
Δγ	Surface tension difference
γ	Surface tension
γ_{CW}	Predicted Connors-Wright surface tension
γ_{LG}	Surface tension at liquid-gas interface
γ_{SL}	Surface tension at solid-liquid interface
γ_{SG}	Surface tension at solid-gas interface
θ_{EQ}	Equilibrium contact angle
θ	Experimental contact angle
Φ	Molar fraction
σ	Liquid surface area

Chapter 1

Introduction

Chemical encapsulation within fluid compartments has become one of the most investigated strategies for the programmed release of active pharmaceutical ingredients and agrochemicals. This strategy pursues the long-discussed idea of the "magic bullet": being able to transport and deliver biologically active compounds to target locations. Indeed, painstaking efforts have been made in this context by “mimicking” the high degree of compartmentalisation found within living cells. Unlike biologically occurring systems however, other factors must come in consideration to achieve chemical and physical stabilisation of bioactive molecules, which can be understood by introducing fundamental concepts of interfacial and colloidal chemistry.

Compartmentalisation of chemical species has been investigated on a range of length scales. For instance, a size-dependent classification can be easily traced between micelles and unilamellar vesicles such as SUVs and LUVs within colloidal dispersions (Figure 1).[1] On the other hand, less clear-cut definitions are associated to bigger fluid compartments, such as drops and droplets (blurred dotted line, Figure 1). Liquid compartments visible by the naked eye can be classified either as microscopic or macroscopic drops, depending on the shape they would assume upon deposition on a flat solid surface.[2] Centimetre-sized droplets known as macrodrops feature a flattened, “pancake-like” shape whereas millimetre-sized droplets, also called microdrops, usually retain a spherical, “lens-like” droplet profile. This observation is linked to the balance between gravity and surface tension within such liquid compartments; microscopic droplet behaviour is dominantly governed by surface tension whereas a balance between both forces takes place within macroscopic drops.[2]

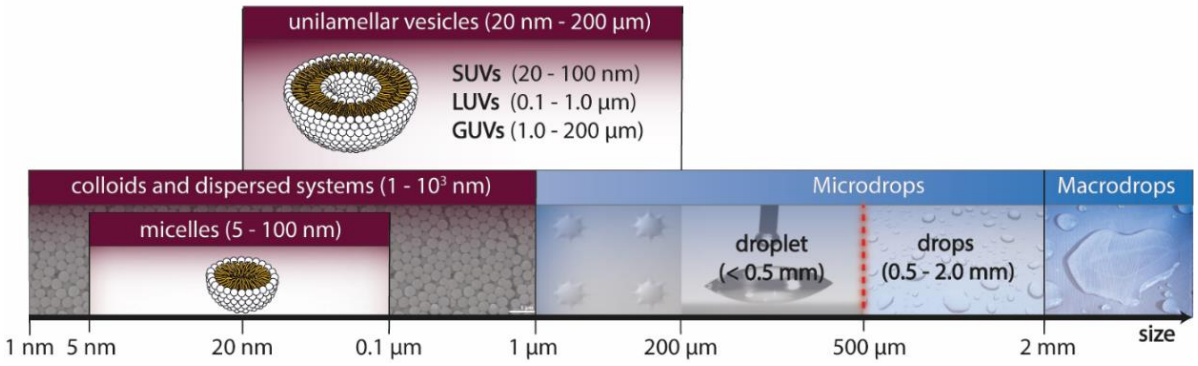

Figure 1. Size-dependent classification of commonplace liquid compartments.

The terms “drop” and “droplet” are often used synonymously in literature (e.g., Langmuir, Soft Matter, J. Phys. Chem. B), therefore making their distinction quite challenging. It is important for the reader to understand that all droplet literature and research studies described within the following three chapters are associated to “naked eye visible” microdroplets. The terms “droplets” and “drops” will be used interchangeably from this moment onwards in association to microdroplets, which formation is governed solely by surface tension effects.[3]

1.1 Surface Tension

Surface tension is a phenomenon arising from the imbalance in molecular cohesive forces at the surface of the liquid and is an essential parameter used to explain droplets formation as well as wetting behaviour of solid substrates.

Differently from bulk-liquid phases, description of non-moving droplets (also known as sessile droplets)[3] is more complex, since two fundamentally distinct regions can be defined in the latter case. Either in single- or multi-component droplets, molecules are free to change their positions and may migrate from the inner region, displaying bulk liquid features, to the outer layer, responsible for surface properties. Each molecule (white circles, Figure 2) in the interior layer experiences an intramolecular force from the surrounding ones resulting in an average net force with no preferential direction (yellow arrows, Figure 2). On the other hand, each surface molecule experiences an imbalance in cohesive forces towards the interior bulk molecules, resulting in a net inward directional force that minimises the droplet surface area (red arrows, Figure 2).[4,5]

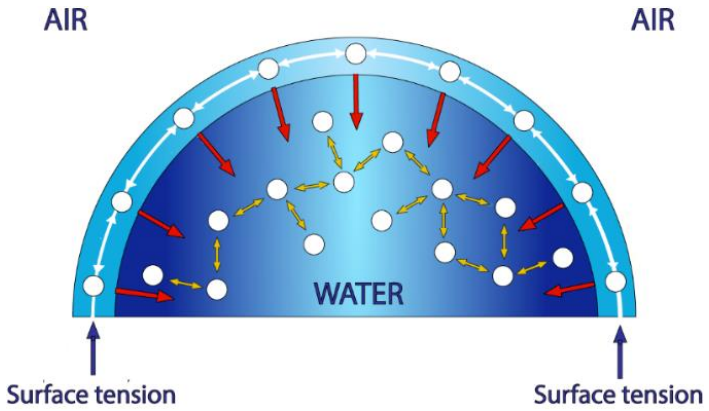

Figure 2. Molecular definition of surface tension.

This phenomenon, known as surface tension, plays a crucial role in the context of droplets stability and motion. Provided that surface tension values of liquids are reported in literature either in mN/m or dyne/cm, it would be reasonable to further interpret this parameter as the amount of work required to increase a liquid film’s surface area by one unit (Figure 3).

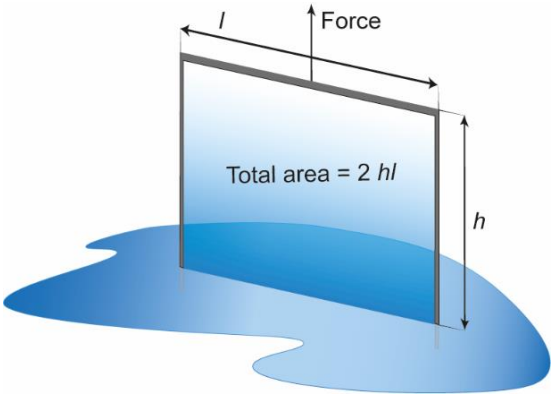

Figure 3. Mechanical definition of surface tension.[4]

When the wire of length *l* is raised through a height *h* it increases the area σ of the liquid by twice the area of the rectangle, since there is a liquid-vapour interface on each side of the liquid film. The total area increase is therefore given by 2*lh* and the work *dw* needed to change the surface area σ by an infinitesimal amount *dσ* can be expressed as follows (Equation 1),

$$\mathrm{d}w = \gamma \cdot \mathrm{d}\sigma = \gamma \cdot 2l\,\mathrm{d}h \qquad (1)$$

where the constant of proportionality γ is called the surface tension.[4] The expression $\gamma \cdot 2l\,\mathrm{d}h$ can be expressed as force x distance by writing it as $2\gamma l \cdot h$, where the γl factor can be regarded as the opposing force on the wire of length *l*. This interpretation is why γ is called a tension and why its units are often chosen to be millinewtons per metre (or dyne per centimetre, following the cgs system).

As previously mentioned, the surface tension of liquids plays a determining role in the formation of curved surfaces, occurring for instance when a raindrop falls from the sky and collides with a surface below. A solid–gas interface and a liquid–gas interface can be identified, which are associated with surface tensions values γ_{SG} and γ_{LG}, respectively (Figure 4A).[5] As the droplet impacts the surface a third interface is also formed: a solid–liquid interface characterised by surface tension γ_{SL}. The spreading of the droplet on the solid surface is determined by the fact that each of these three surface tensions pulls on the droplet's contact line (black dashed line) to minimise the area of their respective interface (Figure 4B).

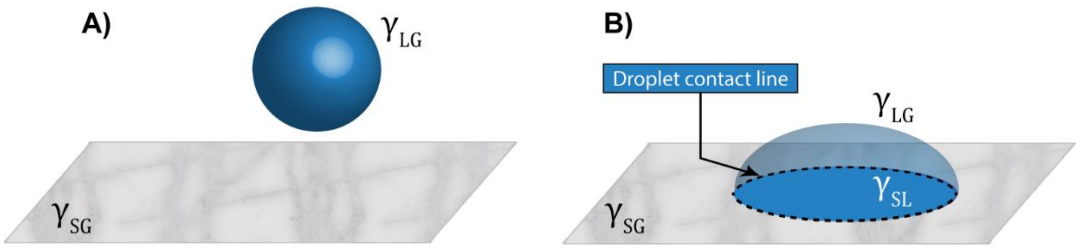

Figure 4. Number and type of interfaces found in liquid drops associated to: A) a droplet yet to impact the solid surface below; B) Droplet spreading onto the solid substrate and identification of the droplet contact line.[5]

Small-sized, water-based droplets at rest on a surface have their shape defined by the balance of three surface tensions, which are associated to the solid-gas interface (γ_{SG}), liquid-vapour interface (γ_{LG}), and solid-vapor interface (γ_{SL}). Provided that surface tension effects are the predominant forces influencing their shape, sessile droplets feature an equilibrium contact angle θ_{EQ}, which can be defined as the angle formed between the solid surface and the plane tangent to the liquid surface at the point of contact. This balance of surface tension is described by the Young equation (Equation 2).[6]

$$\gamma_{SG} = \gamma_{SL} + \gamma_{LG} \cdot \cos\theta_{EQ} \quad (2)$$

Depending on the θ_{EQ} value featured by aqueous droplets, solid substrates are classified as hydrophilic when $\theta_{EQ} < 90^{o}$ and hydrophobic in the opposite case. In a similar way, high and low energy surfaces are defined in function of the degree by which they interact at the droplet contact line (Figure 5).

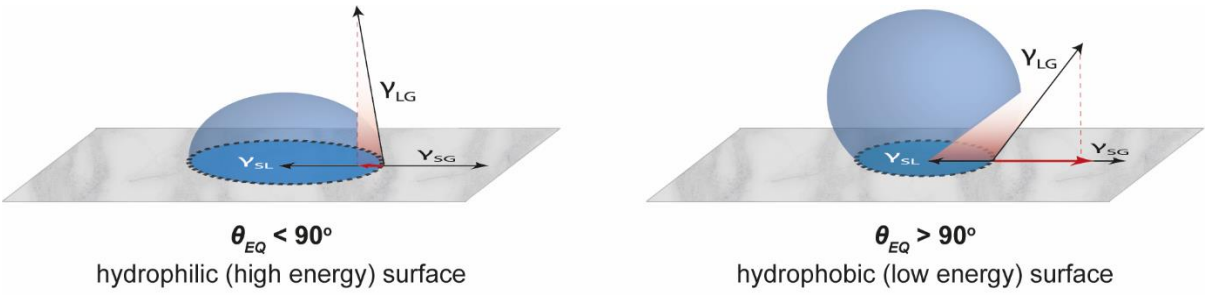

Figure 5. Partial surface wetting of solid substrates after deposition of a sessile droplet, expressed in function of equilibrium contact angle θ_{EQ}.[5]

Another useful concept in defining droplet's behaviour on a substrate is the initial spreading coefficient *S*, which is a parameter associated to wetting regimes exhibited by solid substrates and can be expressed as described below (Equation 3).[5,7]

$$S = \gamma_{SG} - \gamma_{SL} - \gamma_{LG} \quad (3)$$

Moreover, initial spreading coefficient *S* can be expressed in function of the droplet's θ_{EQ} upon combination of Equation 2 and 3:

$$\begin{gathered} S = \gamma_{SG} - \gamma_{SL} - \gamma_{LG} \rightarrow \gamma_{SG} = S + \gamma_{SL} + \gamma_{LG} \\ \gamma_{SG} = (S + \gamma_{SL} + \gamma_{LG}) = \gamma_{SL} + \gamma_{LG} \cdot \cos\theta_{EQ} \\ S = \gamma_{LG} \cdot \cos\theta_{EQ} - \gamma_{LG} \\ S = \gamma_{LG} \cdot (\cos\theta_{EQ} - 1) \end{gathered} \quad (4)$$

Complete droplet spreading takes place when $S \geq 0$ ($\cos\theta_{EQ} = 1$, Equation 4) whereas partial wetting of the solid surface is predicted when $S < 0$ (Table 1).[5,7,8] The liquid drop would feature a characteristic equilibrium shape only in the latter case and the solid substrate area wetted by the resting droplet is delimited by its contact line (Figure 6).

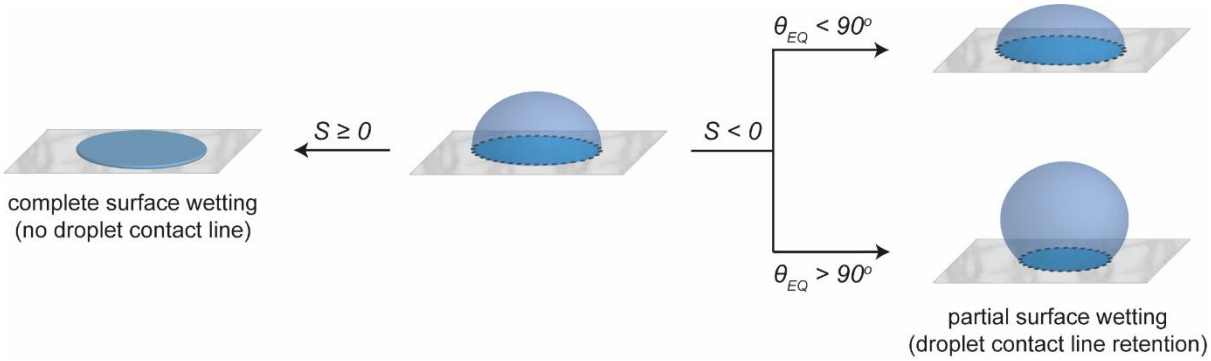

Figure 6. Wetting regimes exhibited by solid substrates after deposition of a sessile aqueous droplet, described by initial spreading coefficient S.

Table 1. Wetting regime comparison with varying equilibrium contact angle θ_{EQ} and spreading coefficient S.

$\theta_{EQ} = 0°$	$\cos \theta_{EQ} = 1$	$S = 0$	complete surface wetting
$0° < \theta_{EQ} < 90°$	$0 < \cos \theta_{EQ} < 1$	$S < 0$	partial surface wetting
$90° < \theta_{EQ} < 180°$	$-1 < \cos \theta_{EQ} < 0$	$S < 0$	partial surface wetting

1.2 Marangoni Effect

1.2.1 Historical perspective

Surface wetting phenomena were extensively studied since the beginning of the 19th century, as documented by eminent physicists such as Young, Laplace, Dupré as well as Marangoni.[9]

Back in 1865, 25-year-old Italian graduate named Luigi *Carlo* Giuseppe Marangoni (1840-1925) defended his doctoral dissertation, which was centred *on the spreading behaviour displayed by droplets onto dispersing liquid films ("*Sull'espansione delle goccie d'un liquido galleggianti sulla superficie d'un altro liquido*")*.[10] Marangoni investigated the spreading behaviour exhibited by pendant oil droplets, which were allowed to collide with an immiscible liquid surface. More specifically, deposition of a first oil droplet on water lead to colourful patterns and grooves, such as concentric rings, which were detected on the liquid surface. However, lack of reproducibility was described in these experiments since this curious phenomenon would not occur when additional oil drops were introduced onto the same water surface. On the contrary, they retained a lens-like shape at first and, depending on the deposited volumes, they would spread and then contract on the dispersing liquid film, forming smaller oil drops with defined contact angles.

Prior to Marangoni's pioneering studies, both gravity and formation of gases within spreading droplets were thought to be the main driving forces leading to these peculiar yet irreproducible behaviours. Furthermore, a pre-existing droplet theory, previously suggested by fellow colleague Ambrogio Fusinieri in 1833, reasoned droplets spreading behaviour with *repulsive*

forces within attenuated matter (“forze repulsive della materia attenuata”) and *presence of unknown forces* (“forze ignote”) somehow generated nearby them. The resultant of these counteracting forces would explain not only how droplets spread but also the formation of lenticular drops on liquid surfaces.[11]

Carlo Marangoni sought to provide a more substantial explanation of such phenomena and disputed all previously given hypotheses. He conducted his preliminary studies in the *Jardins des Tuileries*, where he located the widest flat-water surface available in Central Paris. An oil-soaked bath sponge was prepared and thrown by himself in the 70 metre-wide *Grand Bassin Octogonal* pond and the gathered experimental evidence was found in accordance with previous qualitative observations. To gain further insight, droplet spreading was next studied on a smaller droplet setup manufactured by Marangoni himself. Differently from the *Grand Bassin Octogonal* pond, a thin water film was produced over a flat crystalline surface, which was then vertically oriented. As the single oil drop was introduced on the top edge, it spread in all directions, rather than trickling down the surface, forming star-shaped patterns beginning from the drop deposition point, proving that droplet spreading is independent of gravity. In addition, he observed olive oil droplets displaying one of the highest degrees of spreading, despite being a viscous liquid with low volatility. Such observation was not consistent with his initial assumptions, by which volatile drops were expected to quickly spread onto a liquid surface due to the nearby atmosphere, saturated with droplet vapours. Consequently, Marangoni discredited formation of either gases or vapours on droplet surfaces as key factors in droplet spreading behaviour. For sake of comparison, a second oil droplet was then introduced onto the same water surface and featured uneven widths along its perimeter, forming what he called a *climbing edge* (“bordo sagliente”). Although he did not thoroughly reason why a liquid transfer took place from the droplet centre, Marangoni had suspected that the phenomenon was governed by surface tension effects, which could be accounted for these uneven widths.

Upon comparison between the scientific efforts made by Marangoni and fellow colleague Fusinieri, the studies carried out by the former had a more solid foundation, developed in stronger accordance with pre-existing reports on surface tension-driven capillary action, published for instance by Young, Poisson and Mossotti. Needless to mention, Marangoni starkly argued why Fusinieri’s experimental approach was *neither valid nor thoroughly explained* (“non è nè vera, nè soddisfacente”) as it grossly approximated all droplet behaviours arising from a single, generic factor – *unknown* and *repulsive forces* counteracting *in attenuated matter* – without providing any quantitative measurements! Overall, his thorough investigation led to a better understanding of droplet spreading and these preliminary studies

represent the first milestone towards the formal definition of the Marangoni effect – namely, the mass transfer occurring at fluid interfaces due to surface tension gradients.[12]

1.2.2 Marangoni effect: definition

The Marangoni effect is the spontaneous mass transfer from a low surface tension region to a high surface tension area within a droplet, caused either by composition inhomogeneity or temperature.[12,13]

Marangoni flow has been reported in papers investigating the "coffee-ring" effect which is commonly observed when droplets containing solids in suspension are left to dry, leaving ring-like stains on clean solid surfaces. In this context, differing evaporation rates across the droplet induce liquid capillary flow within the drying droplet: consequently, liquid evaporating from the edge is replenished by liquid from the interior. Simultaneously, particle movement towards the edge occurs, leading to the formation of such deposits (Figure 7A).[14] Evaporation can also induce a Marangoni flow within the droplet which reverses the coffee-ring phenomenon and produces solid deposition at the droplet centre rather than the edge. Thus, outward Marangoni effect within the drying droplet must be suppressed, either with surfactants or starting from liquids displaying weak Marangoni flow, like water (Figure 7B).[15,16]

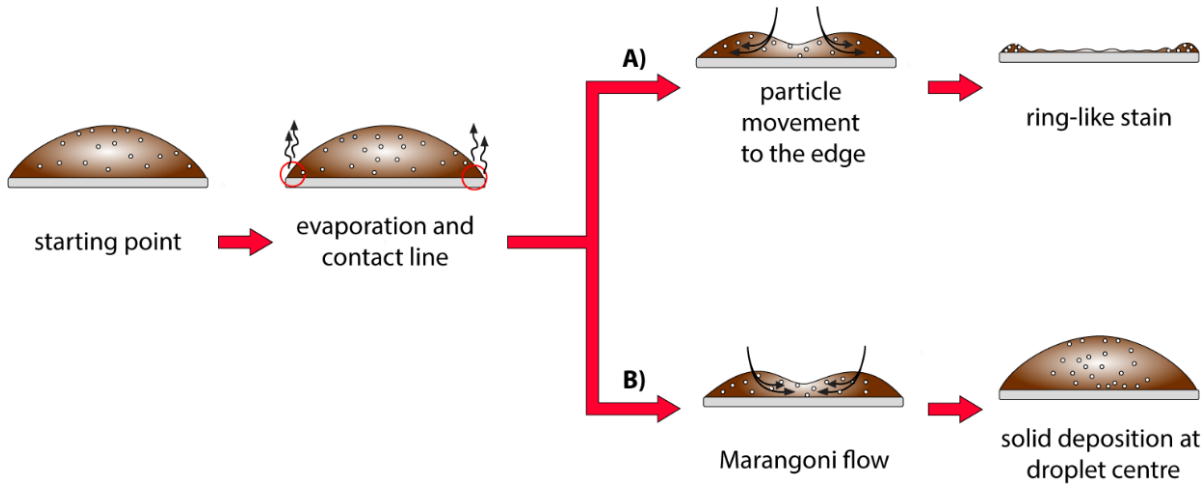

Figure 7. "Coffee-ring" effect displayed by a drying droplet: a) evaporation-induced particle motion and deposition towards the droplet edge; b) Marangoni-driven particle deposition at droplet centre.

In a similar fashion, the "tears of wine" phenomenon heavily relies on the Marangoni effect, which was first described in separate instances by Thomson in 1855 and Loewenthal in 1931.[17,18] Wine is a mixture of water and ethanol with the latter featuring a lower surface tension than the former (72.80 mN/m and 22.10 mN/m respectively).[19] When poured into a glass, generation of a surface tension gradient occurs as ethanol evaporates faster at the thinner region of the meniscus, resulting in the water enrichment in this area. A Marangoni flow is observed as the liquid attempts to climb up the glass walls and such motion is

maintained by the evaporation of the alcohol from the resulting film. After continuous evaporation of alcohol, the relative quantity of water in this area increases, and because of its high surface tension, the liquid now tends to accumulate in the form of drops. When the drops become heavy enough, they roll back down the glass due to gravity, resembling the aforementioned “tears” (Figure 8).[20]

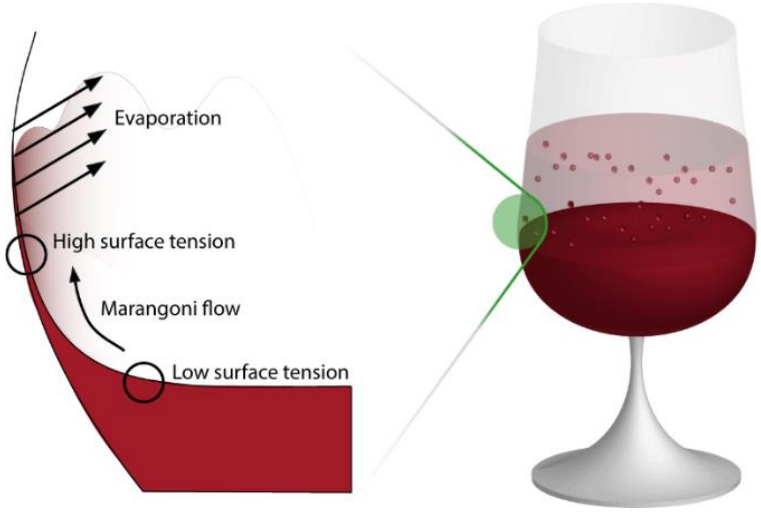

Figure 8. “Tears of wine” effect.[21]

Overall, both Thomson and Loewenthal suggested that adhesive forces that ethanol displayed on polar solid surfaces when compared to water were not sufficient to explain why a liquid film of wine is driven upwards on a glass surface.[12] A flow transfer was proposed occurring against gravity along its film on the glass, due to interfacial tension gradients and formation of the tears of wine effect ultimately takes place due to the Marangoni effect, due to a surface tension gradient established by local changes in ethanol-water composition.

1.3 Droplet formation on solid substrates via Marangoni effect

Studies have shown how gradients of surface tensions across a non-moving sessile droplet, triggered in presence of evaporation induced field-gradients, can stabilise droplets (or slow the spreading process of the liquid compartment) *via* Marangoni effect, therefore causing retention of a finite contact angle.

For instance, prevention of liquid spreading was studied by Bernett and Zisman for the development of military-grade lubricants and was achieved by following either one of the following approaches.[22] Besides using non-spreading liquids and modification of the solid substrate properties, an array of additives can be added to lubricants to inhibit complete surface wetting. For instance, control of oil spreading was achieved by Cottington and co-workers upon addition of silicone solutes, which were capable of adsorbing on high energy-

surfaces, therefore forming a monolayer with lower critical surface tension than the one given by the spreading liquid.[23]

Following this study, a systematic report was reported by Pesach and Marmur which investigated the composition-dependent spreading of various binary mixtures on Pyrex glass.[24] Given two liquid components A and B, two hypothetical case scenarios were investigated with reference to the Marangoni effect. If $P_A < P_B$, where P_i is the vapour pressure of component i, and $\gamma_A > \gamma_B$, where γ_i is the surface tension of component i, then the relatively higher evaporation of component B at the droplet's edge tends to increase the surface tension in that area. Such a combination of volatilities and surface tensions leads to a Marangoni flow within hexane/decane droplets to occur in the same direction as the spreading, i.e., away from the centre of the drop (Figure 9A, A = decane (23.83 mN/m)[20], B = *n*-hexane (18.43 mN/m)[20]). In the opposite situation, namely, $P_A < P_B$ and $\gamma_A < \gamma_B$, the Marangoni flow will be induced from the droplet edge inwards and will counteract the spreading process. Consequently, the spreading phenomenon exhibited by an acetone/octane binary droplet, for instance, may be delayed or even arrested until enough of the more volatile component had evaporated (Figure 9B, A = octane (21.62 mN/m)[20], B = acetone (25.20 mN/m)[20]).

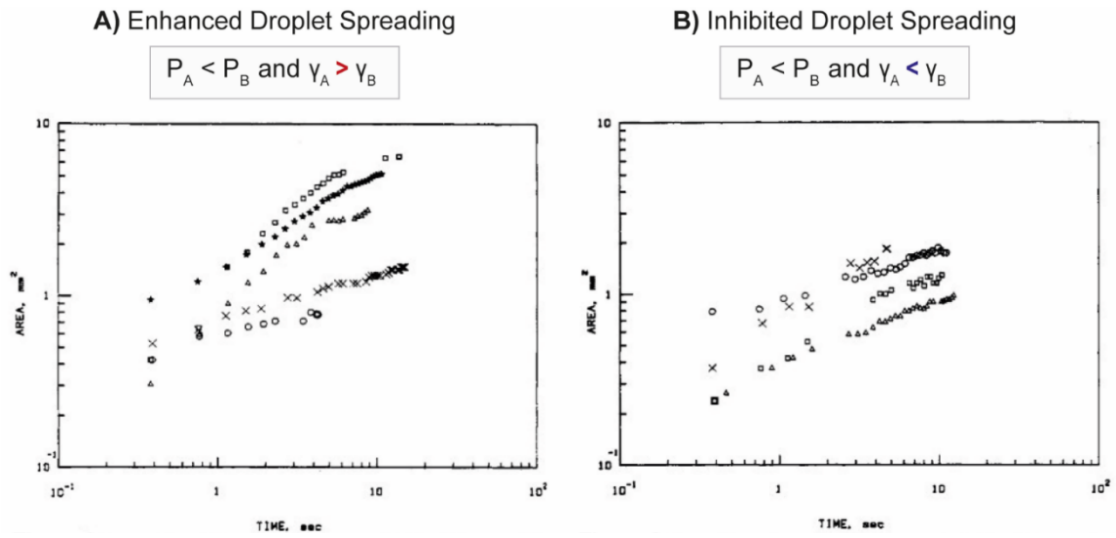

Figure 9A (left). Spreading of hexane, decane and their mixtures: (○) 0% decane; (△) 10% decane by volume; (□) 50% decane; (☆) 90% decane; (×) 100% decane. Figure 9B (right). Spreading of acetone, octane and their mixtures: (○) 0% acetone; (□) 10% acetone by volume; (△) 50% acetone; (×) 100% acetone. Adapted with permission from *Langmuir 1987, 3, 4, 519–524*. *Copyright © 1987 American Chemical Society.*

In separate efforts, research groups led by Karpitshka and Cira confirmed how the interplay between capillary and Marangoni-induced flows within binary mixtures can lead to a quasi-stationary droplet profile, even if both liquid components displayed complete surface wetting ($S > 0$).[25,26] For example, the wetting properties exhibited by aqueous 1,2-propanediol (PG) droplets were investigated and non-zero contact angles were measured when $0\% < PG_{(aq)}\ \%_{(v/v)} < 100\%$. In addition, experimental contact angle values θ were measured from droplets

with fixed PG/H_2O composition and varied depending on the relative humidity RH associated to their surroundings (Figure 10).[27]

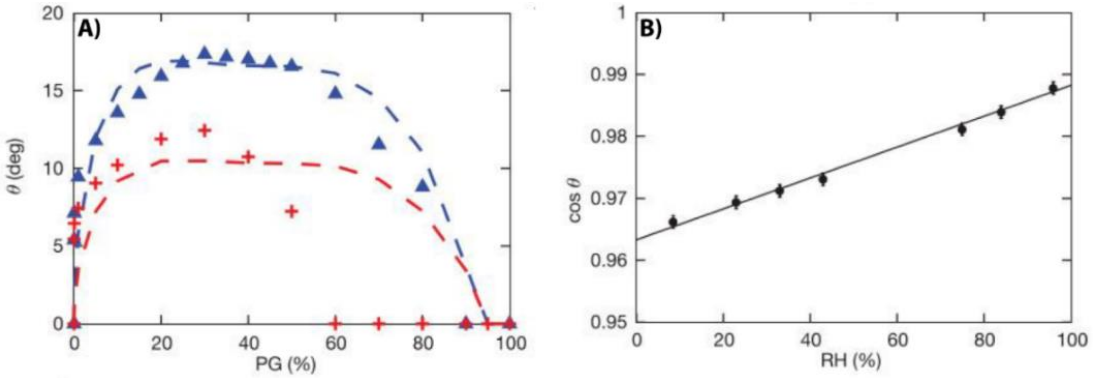

Figure 10. Contact angle measurements of PG/H_2O droplet mixtures.[26] *A) Isolated droplets (0.5 mL) on a clean glass surface featured a non-zero contact angle as a function of PG percentage. Data recorded at 75% RH and 40% RH (crosses and triangle, respectively); B) Starting from 10%$_{(v/v)}$ PG$_{(aq)}$ droplets (0.5 mL), the cosine of the contact angle linear dependence to external humidity (RH). Adapted with permission from Nature volume 519, pages 446–450 (2015). Copyright © 2015 Springer Nature.*

Vapour fields surrounding binary mixture droplets were suspected to play a pivotal role in their contact angle retention since θ measurements significantly varied in function of the external humidity percentage.[26] Convective flows within isolated droplets were visualised with tracer beads and an inward flow was observed from the droplet edge towards the centre (Figure 11A). Upon microscope observation, significant differences between PG/H_2O droplets deposited on high- and low-energy solid substrates were also highlighted. Droplet stabilisation took place only in the former case and was associated with tracer beads migration at the liquid/vapour interface and formation of a thin liquid film extending from the droplet edge (Figure 11B).

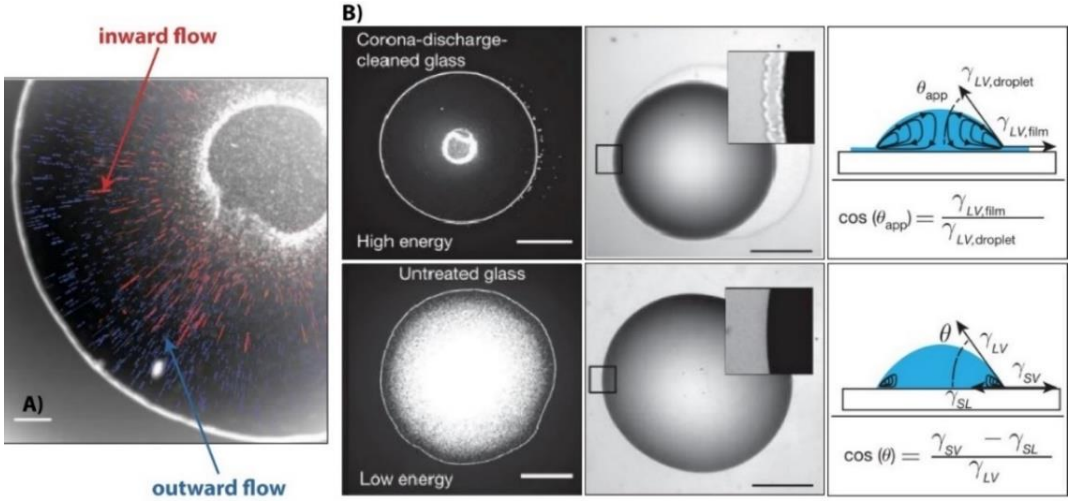

Figure 11. Microscope observation of isolated PG/H_2O droplets on bare glass slides.[26] *A) Time-lapse trajectories of tracer beads in the droplet (scale bar, 200 mm); B) Data comparison between droplets deposited on high and low energy surfaces, from left to right: tracer beads migration across the droplet, thin film visualisation away from droplet bulk (scale bars, 1 mm), flow representation (diagram), and force equilibrium (equation). Adapted with permission from Nature volume 519, pages 446–450 (2015). Copyright © 2015 Springer Nature.*

Provided that water is more volatile than PG, different water evaporation rates would be found across the sessile droplet with enhanced rates occurring near the droplet's edge.[27] Consequently, a lower surface tension area would form at the liquid-vapour interface compared to the droplet bulk, due to the higher surface tension exhibited by water compared to propylene glycol. Vapour fields generated by asymmetric water evaporation across the droplet would concur in a surface tension gradient established within the liquid compartment. Therefore, a Marangoni flow was identified from the droplet edge towards its apex, leading to droplet contraction and contact angle retention on high-energy substrates.

1,2-propanediol however is not the only co-solvent capable of imparting Marangoni-driven droplet stabilisation on high energy surfaces. Other 1,2-alkane diols were later investigated by Snoeijer *et al.*, who reported binary mixture droplet stabilisation due to concurrent Marangoni and autophobing effects.[28] Unusually high contact angle values were measured from 1,2-hexanediol (1,2-HD)/H_2O droplets as 1,2-HD molar fraction Φ increased (Figure 12A). Similarly to PG/H_2O droplets, the experimental θ values were initially attributed to the Marangoni effect, since 1,2-HD was the least volatile liquid featuring the lowest surface tension within the two-component mixture. Interestingly, the contact angle of 1,2-HD/H_2O droplets continuously increased with higher molar fractions Φ in contrast to the PG/H_2O counterparts, which completely wetted the solid substrate ($\Phi \approx 1$, Figure 12B).

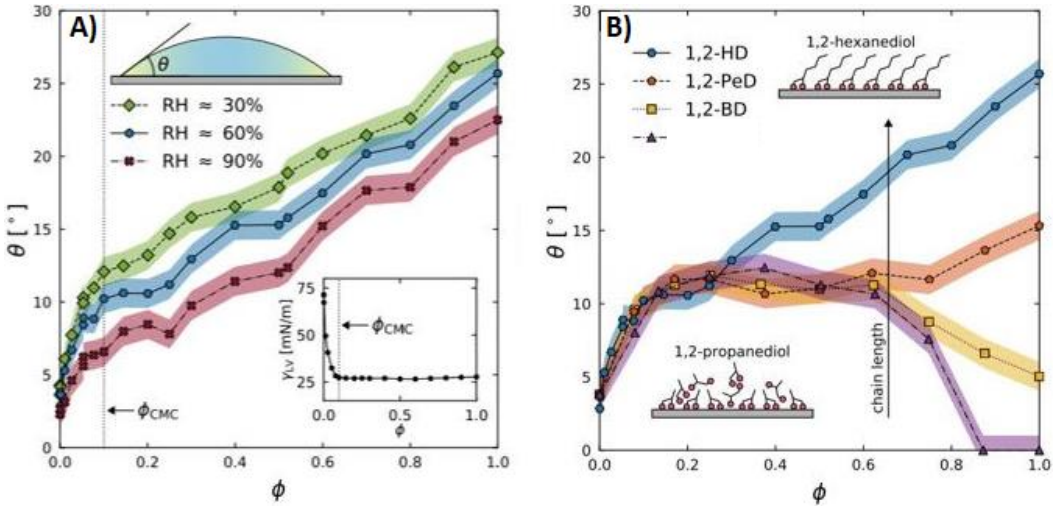

Figure 12. Synergistic Marangoni and autophobing effect-driven stabilisation of 1,2-alkanediols/H_2O droplets on hydrophilic surfaces.[28] A) Experimental contact angles plotted against 1,2-HD (1,2-hexanediol) molar fraction, at specific RH values; B) Experimental contact angles plotted against molar fraction of 1,2-HD, 1,2-PeD (1,2-pentanediol), 1,2-BD (1,2-butanediol) and PG, in RH = 60%. Adapted with permission from Langmuir 2021, 37, 12, 3605–3611. Copyright © 2021 The Authors.

A second mechanism was deemed responsible since alkane diols not only promoted the Marangoni-dependent droplet stabilisation at lower Φ but were also known to behave as autophobes within liquid drops – namely surface active solutes inhibiting droplet spreading upon its own adsorbed oriented monolayer.[29] Various degrees of autophobic character were exhibited by 1,2-alkane diols, depending on the size of their hydrophobic chain. Following this

consideration, the alkyl chain length featured by the autophobic droplet constituent determined which mechanism prevailed at high Φ and for less autophobic co-solvents such as PG, the Marangoni effect was the predominant effect leading to contact angle retention (Figure 12B).

Many instances in literature reported how binary and single-component droplet spreading behaviour can be tuned by exposure to saturated vapour fields of a separate, volatile component.[30,31] For example, spreading acceleration of non-volatile polydimethylsiloxane (PDMS) droplets exposed to *trans*-decaline vapours was described by Carles and Cazabat, proving how the Marangoni effect can promote surface wetting. More in detail, PDMS droplets were initially found to spread on glass in absence of volatile *trans*-decaline, which featured a higher surface tension value compared to PDMS (γ_{PDMS} = 20.0 mN/m; $\gamma_{trans\text{-decaline}}$ = 26.3 mN/m). Since $\gamma_{trans\text{-decaline}} > \gamma_{\text{PDMS}}$, spreading rate acceleration of silicone oil droplets on glass took place upon exposure to saturated *trans*-decaline vapours, which evaporated and penetrated the oil drop, causing a local increase of surface tension at the droplet edge. Marangoni flow would be established outwards, inducing a mass transfer of liquid from the droplet bulk, thus promoting its spreading onto glass (Figure 13).[32]

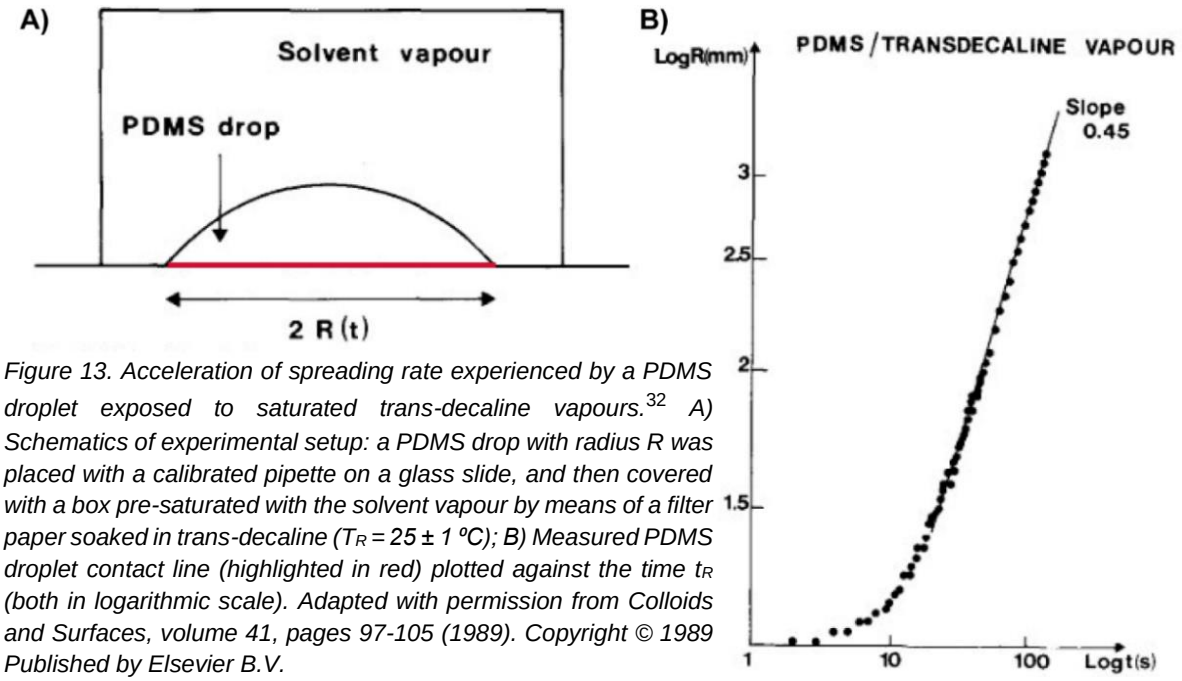

Figure 13. Acceleration of spreading rate experienced by a PDMS droplet exposed to saturated trans-decaline vapours.[32] *A) Schematics of experimental setup: a PDMS drop with radius R was placed with a calibrated pipette on a glass slide, and then covered with a box pre-saturated with the solvent vapour by means of a filter paper soaked in trans-decaline (T_R = 25 ± 1 ºC); B) Measured PDMS droplet contact line (highlighted in red) plotted against the time t_R (both in logarithmic scale). Adapted with permission from Colloids and Surfaces, volume 41, pages 97-105 (1989). Copyright © 1989 Published by Elsevier B.V.*

Conversely, vapour-mediated current flows within droplets can be modified to inhibit their spreading. For instance, starkly different results were reported by Majumder *et al.* whenever nanoparticle (NP)-laden water droplets were left to dry under ambient atmosphere or in presence of a surrounding EtOH vapour field (Figure 14).[34] In the former case, unequal evaporation rates were established across the drying drop, therefore explaining $HAuCl_4$ particles migration towards the droplet edges and coffee-stain formation (Figure 14A). On the opposite, a Marangoni flow was established across droplets dried under saturated EtOH

vapours, which caused the nanoparticles migration from the droplet edge. $HAuCl_4$ particles recirculation driven by Marangoni effect ultimately led to deposition of a homogeneous NP film on solid substrates, such as Teflon, glass, silicon, mica and PDMS (Figure 14B).

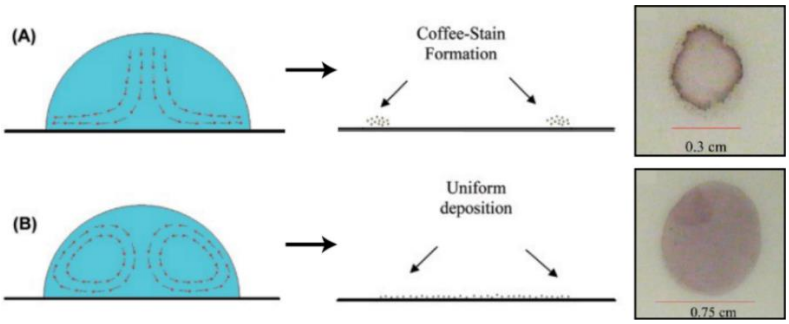

Figure 14. Sideview schematics and front view photographs of dried $HAuCl_4$-laden water droplets on Teflon, from top.[34] A) conventional coffee-stain formation upon droplet exposure to standard ambient atmosphere; B) NP film homogeneous deposition achieved via Marangoni-assisted drying of a drop under saturated EtOH vapours. Adapted with permission from J. Phys. Chem. B, 116, 22, 6536–6542, (2012). Copyright © 2012, American Chemical Society.

1.4 Strategies for motion of liquid drops on solids: an overview

The presence of surface tension gradients, established across either pure or binary mixture droplets exposed to newly generated or pre-existing vapour fields, was crucial not only within Marangoni-contracted droplets but also during their motion on solid substrates. Alongside the Marangoni-promoted droplet motion, two other main strategies (or combinations thereof) have been established in literature to promote droplet motion on solids, which will be briefly mentioned for sake of comparison.

First, solid substrate *pre*-modification is a commonplace technique where permanent wettability gradients are generated either *via* chemical or morphological surface patterning. For instance, Chaudhury and Whitesides explained in their landmark study how water droplets moved across a surface with varying hydrophobicity, which was produced by partially exposing a silicon wafer to decyltrichlorosilane vapours (Figure 15A).[33] On-demand wettability gradient can be imparted on solid substrates coated with photosensitive self-assembly monolayers (SAMs) such as azobenzene moieties, which become more hydrophilic when irradiated with UV light, and return to a more hydrophobic state when illuminated with blue light (Figure 15B).[34,35] In contrast with the chemical patterning of surfaces, surface-morphological gradients were produced by manufacturing of synthetic materials – e.g. slippery liquid-infused porous substrates (SLIPS),[36–39] micro-textured composite surfaces[40–43] – which featured reduced pinning spots formation on their surfaces (Figure 15C). Alternatively, liquid droplets can move on solid substrates by means of “reactive flow”. First described by Bain *et al.,* this key concept is centred on the chemistry occurring at the liquid-solid interface, with formation of temporary surface tension gradients imparted by moving drops onto the solid surface.[44]

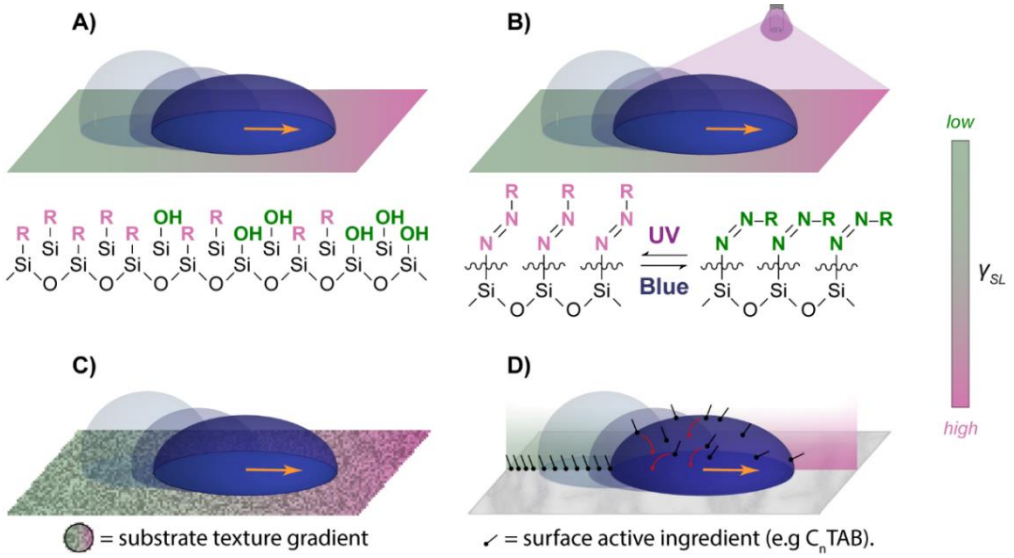

Figure 15. Simplified schematics of droplet transport driven by surface tension gradients, from top left: A) permanent chemical surface patterning; B) on-demand wettability gradient generated on the solid substrate coated with photosensitive SAMs; C) permanent morphological surface patterning; D) transient surface tension gradients generated by surface active ingredients within liquid droplets.

For instance, self-propelled motion of water drops containing *n*-alkyltrimethylammonium bromide (CnTAB) surfactants was recently described on bare glass substrates by Baigl *et al.*, which reasoned droplet actuation with electrostatic adsorption of the cationic surfactant beneath the moving drop. Anisotropic wettability of the substrate was proposed to occur due to CnTAB solutes, whose dynamic adsorption behaviour was found to either promote or inhibit droplet motion depending on the degree of hydrophobicity featured by the cation surfactant as well as its concentration within the water drop.[48] Moreover, other examples can be found in literature, where surface reactive ingredients including *n*-alkylamines[45] and perfluoro-alkylated species[46,47] were embedded in liquid droplets, acting as “chemical fuel”, allowing droplet motion on solid substrates until complete reagent depletion (Figure 15D).

1.4.1 Marangoni-induced droplet coalescence and actuation on solid substrates

Differently from the other two methods, a third and final strategy has been recently explored, where self-sustained droplet motion was achieved without external stimuli, manufacturing of functionalised solid substrates and addition of surface-active solutes. In this case, the driving force was induced *via* Marangoni effect by direct action of moving droplets, which displayed surface tension imbalances at their liquid-air interface.

Many droplet studies harnessed the Marangoni effect to initiate their coalescence and motion on solid substrates. Back in 1919, Hardy observed the spreading behaviour of fluids on glass and briefly described how droplets of acetic acid were prone to attract one another, when placed apart on a glass slide.[31] In a similar way, Bangham and Saweris also described the delayed fusion behaviour of droplets of miscible liquids on mica, such as water/acetic acid and

benzene/hexane.[30] However, their observations were not specifically targeted towards the study of droplet coalescence and were made without accounting for the concept of mass transfers driven by surface tension gradients. Starting from unfunctionalised solid substrates, the pivotal role played by the Marangoni effect within droplet pairs was determined upon repetition of Hardy's historical experiments with millimetre-sized drops of water and acetic acid by Riegler and Lazar.[48] A delay by many seconds was observed prior to their coalescence, followed by formation of a shallow conduit connecting the main bodies of the droplets, which remain separated at first. Droplet bulks began to merge as a Marangoni-induced mass transfer – directed from low to high surface tension areas – took place through the connecting liquid film (Figure 16).[48]

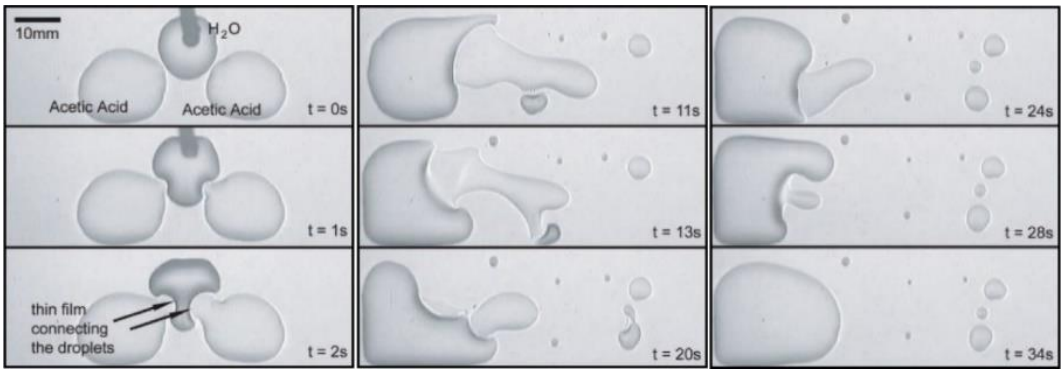

Figure 16. Timelapse of the delayed coalescence between water and neighbouring acetic acid droplets on a single glass microscope slide. Adapted with permission from Langmuir, 24, 13, 6395–6398 (2008). Copyright © 2008, American Chemical Society.

In a similar fashion, delayed droplet coalescence behaviour was observed by Karpitschka and Riegler within two-components droplet mixtures of miscible liquids – e.g. aqueous solutions of different non-volatile diols, such as 1,2-butanediol (1,2-BD).[49,50] A series of experiments was undertaken to better outline the transition between the fast and delayed coalescence regimes (Figure 17A and 17B, respectively) knowing that the latter case scenario was expected to occur when the surface tension difference within merging drops was higher than ≈3 mN/m.[49]

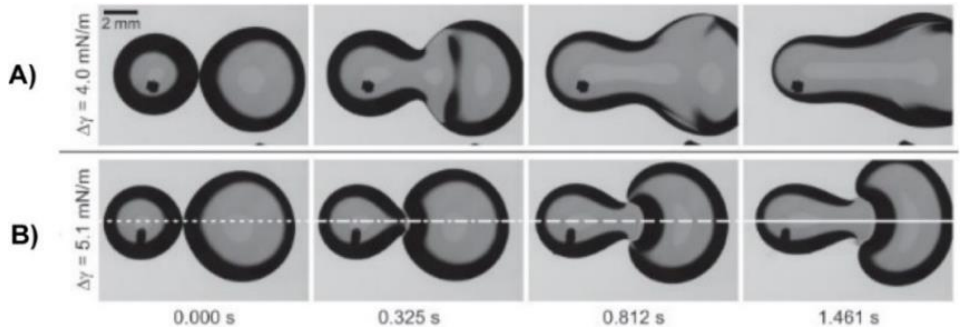

Figure 17. Timelapse of rapid and delayed coalescence within 1,2-BD/H_2O droplet pairs, front view. From top: A) Rapid droplet coalescence between 45%$_{(v/v)}$ 1,2-BD$_{(aq)}$ and 28.4%$_{(v/v)}$ 1,2-BD$_{(aq)}$ droplet; B) Delayed coalescence between 45%$_{(v/v)}$ 1,2-BD$_{(aq)}$ and 25.9%$_{(v/v)}$ 1,2-BD$_{(aq)}$ droplet. Adapted with permission from Langmuir, 26, 14, 11823–11829 (2010). Copyright © 2010, American Chemical Society.

In addition to previous computational studies,[51,52] a ground-breaking publication from Prakash and co-workers further validated the pre-existing experimental evidence gathered from coalescing droplet pairs.[26,53] Marangoni-driven motion of PG/H_2O droplet pairs was investigated on high energy solid substrates; droplets having the same concentration immediately coalesced into a single entity (Figure 18A) whereas droplets featuring sufficiently different composition behaved differently. In the latter case, as the two droplets approached and came in contact, the droplet with the overall lower surface tension (higher PG content) propelled the droplet with higher surface tension away (lower PG content) until the difference in surface tension was reduced sufficiently to induce coalescence (Figure 18B).

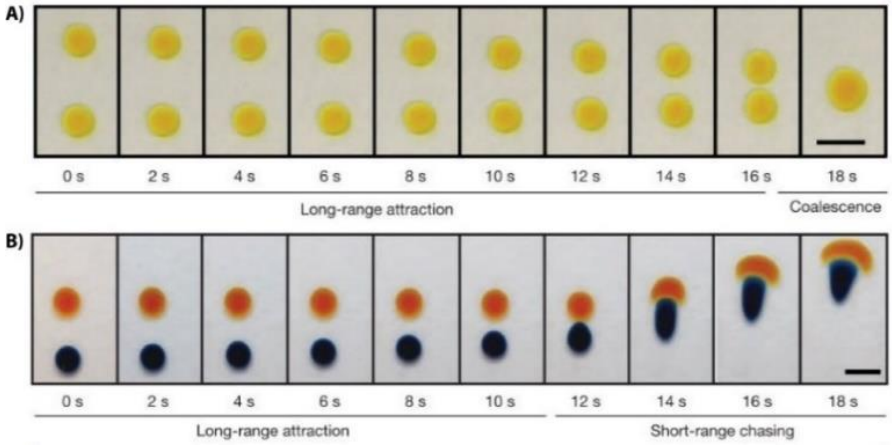

Figure 18. Long-range and short-range interactions in two-component droplets by Prakash et al, front view.[27] A) Two 0.5 mL droplets of 25%$_{(v/v)}$ PG$_{(aq)}$ (blue) and 1%$_{(v/v)}$ PG$_{(aq)}$ (orange) interacting (scale bar, 3 mm); B) Two 0.5 mL of 10%$_{(v/v)}$ PG$_{(aq)}$ interacting (scale bar, 5 mm). Adapted with permission from Nature volume 519, pages 446–450 (2015). Copyright 2015 © Springer Nature.

PG/H_2O droplet actuation was further investigated on unfunctionalized solid surfaces placed on an incline.[54] Interestingly, PG/H_2O drops featured reduced contact line pinning upon deposition – i.e. droplets were able to roll down tilted glass slides without sticking to the solid substrate. Although these unusual properties were attributed to the presence of a thin film generated by the moving PG/H_2O drop onto the inclined surface, the selective directionality exhibited by interacting binary mixture droplet pairs cannot be fully explained by taking in consideration the droplet film precursors alone. An initial symmetry breaking event was suggested taking place as neighbouring droplets explored their surroundings and started sensing each other through their vapour fields. More specifically, each PG/H_2O droplet evaporated producing a vapour field that was largely composed of water. Water evaporation rate decreased as a droplet's vapour field was exposed to a second neighbouring droplet, leading to an increased water fraction between adjacent droplets. Provided that water also displayed a higher surface tension then the other component, a surface tension gradient was established in this area, causing the neighbouring droplets to move towards each other.

Evaporation-induced attraction, chasing, and repulsion between a water droplet and a second PG/H_2O binary mixture droplet was investigated by Majhy and Sen on flat, plasma-treated polydimethylsiloxane (PDMS).[55] Different droplet pair interactions were observed by varying the time interval t_W by which both droplets were dispensed. Once the PG/H_2O droplet was deposited on the hydrophilic surface (t_W = 0 s), long-range attraction followed by short-range chasing took place when the second H_2O droplet was introduced within four minutes ($t_W < t_C$, Figure 19A). On the contrary, repulsive forces prevailed within the droplet pair when the water drop was deposited beyond the experimental critical time t_C ($t_W > t_C$, Figure 19B).[55]

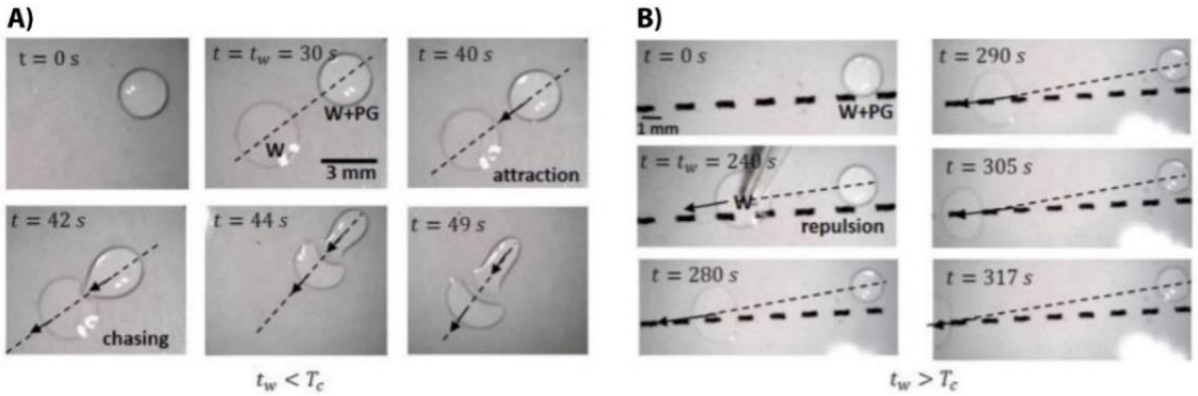

Figure 19. Timelapse of evaporation-induced interactions between a 20%$_{(v/v)}$ PG$_{(aq)}$ and pure water droplets ($V_{W+PG} = V_W$ = 0.5 µL, RH = 40%), front view. A) Attractive/chasing behaviour ($t_W < t_C$); B) Droplet pair repulsion ($t_W > t_C$). Adapted with permission from Nature volume 519, pages 446–450 (2015). Adapted with permission from Physics of Fluids 32, 032003 (2020). *Copyright © 2015 AIP Publishing.*

Although the microscopic process leading to reduced droplet pinning is yet to be fully defined, Cira *et al.* suggested that the droplet-derived PG/H_2O film layer played a significant role for its motion, which was generated not only in presence of neighbouring droplets but also under external humidity gradients.[54] Further evidence to support the latter observation was gathered by Malinowski and co-workers, who demonstrated contactless long-range manipulation of a single 17%$_{(v/v)}$ PG$_{(aq)}$ droplet by means of localised water vapour sources.[56] Starting from a pristine solid substrate, no droplet motion was recorded in absence of the vapour source. Conversely, an attractive force was experienced by the PG/H_2O droplet towards the localised vapour field when deposited away from it by a distance x_S (Figure 20A). The long-range attraction experienced by the droplet towards the localised vapour field was consistent with a relative larger local increase in humidity at the droplet's edge nearest to the source. Droplet motion was initiated by slowing down evaporation and comparatively increasing the value of surface tension at that edge with respect to the opposite side. Although a stable equilibrium position was initially pinpointed at the vapour source's centre (x_S = 0), an off-centred, equilibrium distance x_E was observed, which the PG/H_2O droplet consistently reached regardless of its deposition point – i.e., either away or underneath the localised vapour source (Figure 20B and 20C, respectively).

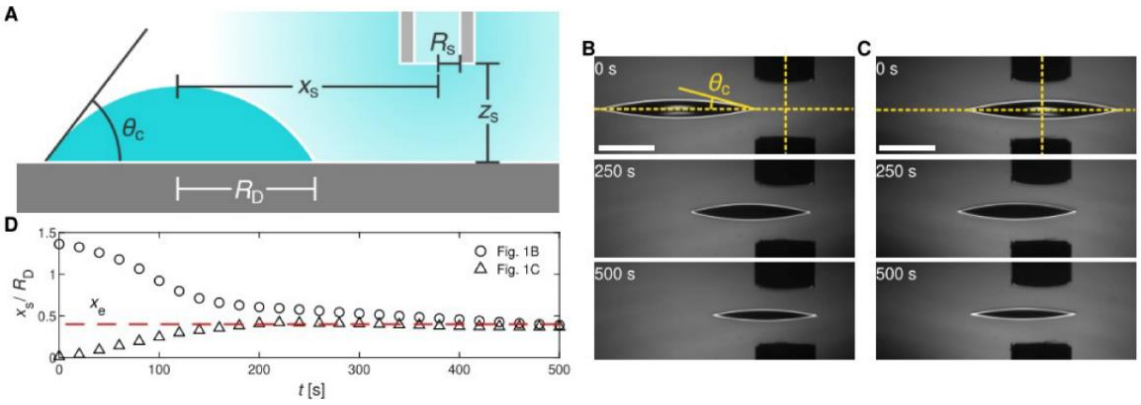

Figure 20. Contactless manipulation of a single PG/H_2O droplet via sensing of localised vapour sources, from top: A) Schematics of the experimental setup (T = 21 ± 0.5 ºC, RH = 50 ± 5%) B) Timelapse showing a 0.5 µL 17%$_{(v/v)}$ PG$_{(aq)}$ droplet migration towards the vapour source (x_S = 2 mm); C) Timelapse showing a 0.5 µL 17%$_{(v/v)}$ PG$_{(aq)}$ droplet repulsion from the vapour source (x_S = 0 mm); (D) Droplet trajectories observed in B (circles) and C (triangles) plotted against time for off-set distance x_E quantification. Adapted with permission from Science Advances, 6, 40, 1-8 (2020). Copyright © 2020 The Authors.

Alongside vapor-mediated droplet motion, a mechanism of rapid and focused solvent depletion using vapor-mediated interactions was described by Basu and co-workers.[57] In this case, a pendant droplet of ethanol (highlighted in black, Figure 21) was placed nearby a second, sessile water droplet (highlighted in pink, Figure 21), which was previously deposited on a clean microscope glass slide. A surface tension gradient was generated this time across the water droplet, as EtOH evaporated from the pendant drop and was adsorbed on the surface of former. Areas with higher EtOH adsorption featured lower surface tension compared to the less exposed sections within the sessile drop. Consequently, a Marangoni-driven mass transfer took place therein, which was called “Moses Effect” and resulted in a variety of droplet behaviours, such as droplet splitting and side shifting (Figure 21).

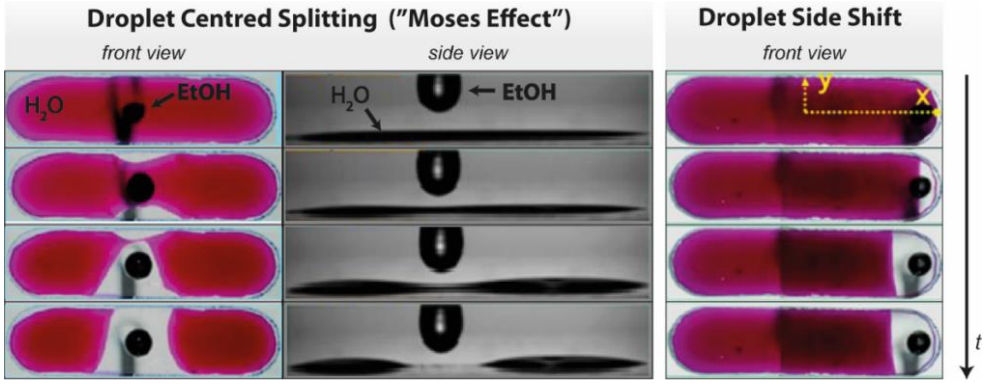

Figure 21. Vapor-mediated solvent depletion experienced by a single water droplet, exposed to a pendant drop of EtOH, from left: Overview and sideview timelapses associated to symmetric droplet splitting known as “Moses Effect”; Overview timelapse associated to droplet splitting known as “Moses Effect”; Front-view timelapse of a side-shifting water droplet triggered by localised EtOH vapour fields. Adapted with permission from Langmuir, 36, 5, 1279–1287 (2020). Copyright © 2020 American Chemical Society.

Focused solvent depletion demonstrated how the “Moses Effect” concept can be extended to liquid actuation in open digital microfluidics as well as surface patterning tailored *via* nanoparticle deposition.[57]

1.5 Application scope of droplet transport

Liquid motility is not the only outcome of vapour-mediated – or more broadly, Marangoni induced – interactions between droplets on solid surfaces. As discussed in depth in a recent review on this topic,[5] controlled self-propelling of droplets was also capitalised for the development of practically important devices, whose applications encompassed water and fog harvesting, heat transfer, electrical energy generation as well as surface coating and patterning with nanoparticles.

For instance, droplet-based devices were manufactured by following these principles. Droplet self-alignment from vertically offset starting positions, sustained chasing along circular paths or uphill gradients were achieved as well as surface-tension driven sorting of Marangoni-contracted droplets.[26] In the latter case, the required sorting device was created on a tilted corona-discharged microscope slide featuring “hydrophobic tracks”, which were drawn on the glass with a permanent marker. Droplets with decreasing PG/H_2O composition were introduced in the sorting area prior to sampling droplet deposition. A Marangoni flow was established between each well and the newly dispensed droplet, with the latter ultimately reaching its target destination only when its surface tension closely resembled the one given by a well's content (Figure 22).[26]

Figure 22. Time-lapse of droplet trajectories in a surface tension sorter, front view. Droplets within the sorting area featured decreasing PG/H_2O composition which varied as follows: 30%$_{(v/v)}$ PG$_{(aq)}$ (red), 25%$_{(v/v)}$ PG$_{(aq)}$ (orange), 20%$_{(v/v)}$ PG$_{(aq)}$ (yellow), 15%$_{(v/v)}$ PG$_{(aq}$, 10%$_{(v/v)}$ (green), PG$_{(aq}$ (blue) and 5%$_{(v/v)}$ PG$_{(aq)}$ (indigo). Adapted with permission from Nature volume 519, pages 446–450 (2015). Copyright © 2015 Springer Nature..

Tracing of hydrophobic tracks onto unfunctionalized high energy surfaces was proven not mandatory for the development of droplet-based devices. A follow-up study led by Prakash *et al.* featured manufacturing of additional PG/H_2O droplet devices, where various degrees of droplet confinement were investigated.[58] Higher levels of constraints – e.g. vertical obstacles, parallel horizontal plates – corresponded to inhibited droplet evaporation and generation of stronger vapour fields. Consequently, prolonged droplet lifespan and enhanced long-range attractive interactions within droplet pairs were achieved in constrained droplet-based devices (Figure 23).[58]

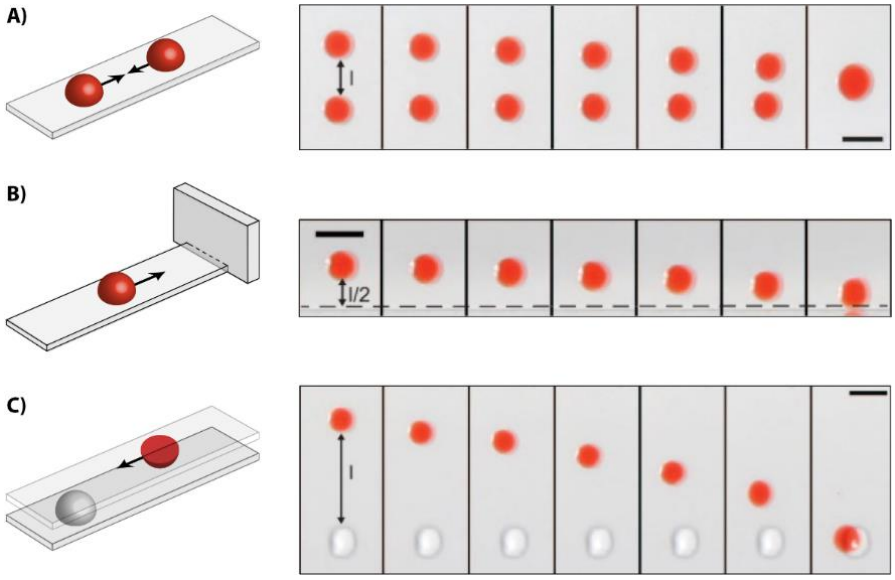

Figure 23. Timelapse *and droplet device schematics investigated by Prakash et al. featuring increasing degrees of droplet confinement*, *from top:*[58] *A) 10%$_{(v/v)}$ PG$_{(aq)}$ droplet pair coalescence on a generic glass slide; B) 10 %$_{(v/v)}$ PG$_{(aq)}$ droplet motion towards a vertical wall (position is highlighted by a dashed line); C) Long-range attraction between a 10%$_{(v/v)}$ PG$_{(aq)}$ droplet and a pure water droplet, resulting in their vertical alignment. Adapted with permission from arXiv:1711.06404 [cond-mat.soft]. Copyright © 2017 The Authors.*

Moreover, several examples can be found in literature where droplets acted as self-contained liquid compartments, which enabled the handling, collection and transport of chemical and biological material.[59,60] In this context however, the use of droplets as micro-reactors is starkly different compared to the analogues utilised in droplet microfluidics. Motion of liquid drops is restricted to prefabricated channels in the latter case, causing droplets to lose their ability to "decide" on their motion. Secondly, limited reaction and solvent scopes are commonplace, due to their incompatibility with mainstream construction materials, which in turn are usually expensive and laborious to work with. For these reasons, the potential that droplets inherently possess as micro-reactors may be hindered following conventional microfluidic strategies whereas a dynamic, constraint-free droplet reactor would offer many advantages.

1.5.1 Development of self-contained droplet reactors

At present there have been few examples on the use of droplets as micro-reactors outside the field of digital microfluidics.

For example, formation of inorganic salts within water droplets was documented by Dai *et al.*, where the reacting droplets were dispensed onto a microtextured, superhydrophobic surface and forced to coalesce by electrostatic means.[61] Alongside laser and UV light irradiation, applied electric and magnetic fields were required for the synthesis of zeolite microcrystals within multi-responsive droplets, starting from $CoCl_2$ and 2-methylimidazole.[62] Room temperature polymerisation of adipoyl chloride with hexamethyl diamine was successfully carried out by Agrawal and co-workers *via* magnetic actuation of droplets.[36] Synthesis of Nylon

6,6 was undertaken on SLIPS, starting from water and organic droplets loaded with paramagnetic particles (PMP). At first, droplet pair coalescence was conducted *via* magnetic actuation between an aqueous diamine droplet and a second $NaOH_{(aq)}$ drop, with the latter featuring PMPs in suspension. Following this the water coalesced droplet was guided towards a heptane drop of adipoyl chloride, resulting in formation of a thin film between the reactive droplet pair constituents. The bi-phasic reaction took place at the H_2O/heptane interface, from which the droplet film was removed and analysed *via* MALDI-MS for reaction monitoring. Successful synthesis of Nylon 6,6 was demonstrated upon inspection of the MALDI-MS mass spectrometry data, which featured characteristic mass peaks associated to Nylon 6,6-derived oligomers.

Controlled motion of droplet reactors was also demonstrated between aqueous drops of HCl and NaOH. pH-sensitive reactions are by far the most reported ones in literature as their monitoring can be visually carried out with water-soluble pH indicators. For instance, the neutralization reaction between NaOH and HCl was investigated by Malinowski *et al.* where PG/H_2O droplets moved under the influence of localised vapour sources (Figure 24).[56] A pH universal indicator was used in this case, which was added to 0.1 M NaOH and 0.1 M HCl PG/H_2O droplets, prior to their deposition. Upon visual inspection, it was noted that the reaction began as the vapour-mediated droplets coalescence took place (t = 0 s). Colour changes were initially detected at the interface (t = 100 s) and became more evident as the reaction progressed towards completion (t = 950 s). After thirty minutes, the coalesced droplet pair turned light blue indicating complete consumption of the reactive species (t = 1800 s).

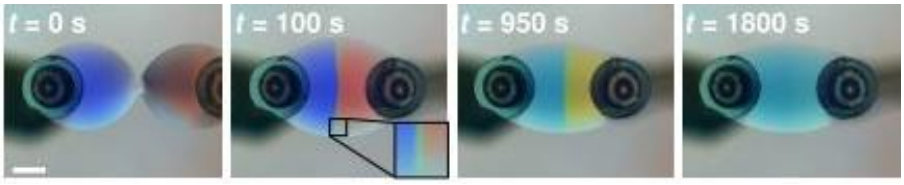

Figure 24. pH variations within a two-component droplet reactor by Malinowski et al., front view timelapse (scale bar size: 1 mm). Adapted with permission from Science Advances, 6, 40, 1-8 (2020). Copyright © 2020 The Authors.

The same exact reaction was carried out in Milli-Q water droplets by Dai and co-workers, which moved across a flat superhydrophobic substrate exposed to a vertically oriented electric field.[61] In this case, droplet motion was triggered by electrostatic repulsion between a positively charged glass rod and an HCl aqueous drop, which travelled across the solid substrate towards a second droplet of NaOH (t = 0 s, Figure 25). Thus, the applied electric field not only allowed for the rearrangement of positive charges within aqueous droplets but also governed their motion and coalescence. Two additional key differences can be found upon comparison against the vapour-field mediated approach investigated by Malinowski *et al*. Firstly, a rapid, rightward motion was detected as soon as the droplet pair coalescence

occurred, which was imparted by the positively charged electrode across the solid substrate. Furthermore, infrared imaging was used as an alternative to pH indicators. Thermal changes were detected throughout the experiment, as the exothermic reaction took place immediately after droplet pair merging. Droplet pair coalescence was accompanied by a temperature increase of 0.8 °C, hence confirming that the droplet-sized acid/base reaction had occurred between 0.39 and 0.78 seconds (Figure 25).

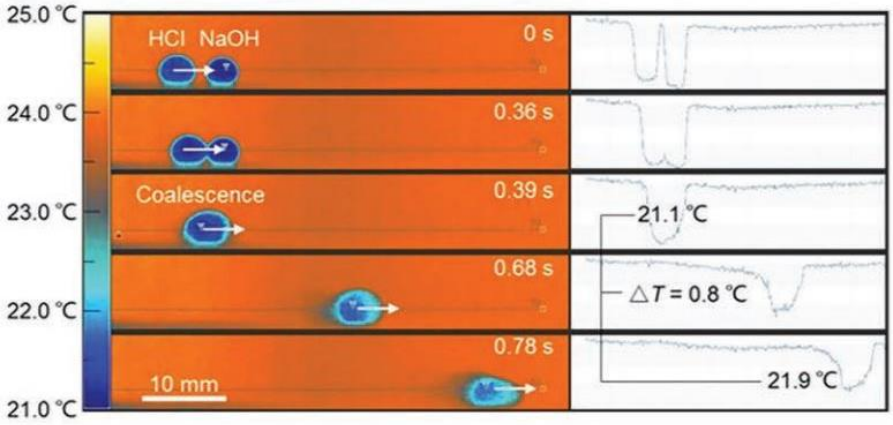

Figure 25. Electrostatic manipulation of an aqueous droplet pair investigated on superhydrophobic surfaces by Dai et al. Reused with permission from Advanced Materials, 31, 43, 1905449 (2019). Copyright © 2019 WILEY-VCH Verlag GmbH & Co. KGaA Wienheim.

Finally, painstaking efforts were made by Yang and co-workers, who performed a variety of chemical transformations within reactive droplets powered by multi-responsive surfactants.[62] Their most comprehensive example featured a redox sequence, which was carried out in dumbbell-shaped droplet reactors as follows:

$$2Cu^{2+} + 4I^- \rightarrow 2CuI + I_2 \textbf{ (a)} \quad \text{and} \quad CuI + EDTA^{4-} \rightarrow EDTA^{3-} + I^- \textbf{ (b)}$$

Combinations of multiple stimuli (electric, magnetic fields and laser light) were used to initiate and control the redox process within $1{:}1_{(v/v)}$ ethylene glycol (EG)-H_2O droplets, coated with nanoparticle-based magnetic surfactants. Fe_3O_4 with oleic acid (Fe_3O_4-OA) as well as gold with 11-mercaptoundecanoid acid (MUA-Au) were considered, conferring both hydrophobicity and hydrophilicity to the droplets. The reactors contained three differing reagents: 1 μmol $CuSO_4$ (R_1), 2 μmol KI (R_2) and 1 μmol Na_4EDTA (R_3). Owing to their dumbbell shape, the reactors oriented along an external magnetic field which was applied throughout the redox sequence (Figure 26). At first, reactor R_1 and R_2 were electrostatically welded: a 200 μm wide channel was generated between the two-dumbbell shaped reactors, through which reactants diffused very slowly (step 1, Figure 26). In a similar way, reactor R_3 was also linked to the newly formed reactor by imparting short bursts of an electric field (step 2, Figure 26). The narrow linking channel between reactors R_1 and R_2 was broadened *via* 660 nm laser beam irradiation (step 3, Figure 26), allowing reaction **(a)** to occur with formation of elemental iodine

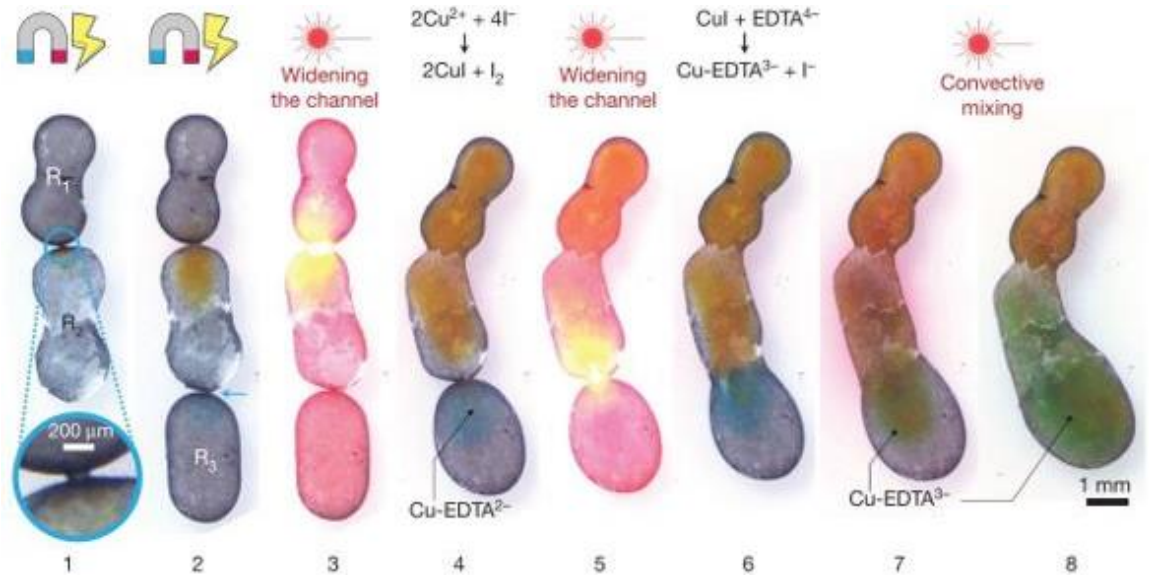

Figure 26. Droplet reactor developed by Yang and co-workers. Reused with permission from Nature, volume 553, pages 313–318 (2018). Copyright © 2018, Macmillan Publishers Limited, part of Springer Nature.

(step 4, Figure 26). Subsequently, the R_2–R_3 junction was widened (step 5, Figure 26), allowing CuI to react with $EDTA^{4-}$, affording the final product expected from reaction **(b)**, Cu-$EDTA^{3-}$ (Step 6, Figure 26). Further light irradiation was carried out for additional convective mixing throughout the merged droplet reactors. Previously synthesised I_2 mixed with the Cu-$EDTA^{3-}$ complex produced in the second reaction and ultimately imparted a green colour to the manipulated droplet reactors (Step 7, Figure 26).

As seen with the literature findings herein discussed, droplet motion application scope relied on the use of highly functionalised solid substrates and external stimuli (or a combination thereof). Besides chemical reactors, water-harvesting and self-cleaning/anti-fouling technologies were also developed by harnessing droplet actuation on textured, superhydrophobic substrates.[63–66] Likewise, electrostatically-driven motion of droplets was also utilised to deposit trails of colloidal or polymeric material embedded within them, thus offering alternative approaches towards patterning of planar and curved surfaces.[63,67,68] Although many literature examples can be found where digital microfluidics principles were applied for the development of bioassay tools,[59,69] few instances can be found where mere droplet evaporation by means of Marangoni effect was harnessed to manufacture devices destined for biomarker detection of M13K07 bacteriophage and tubercolosis pathogen.[70–72] Thus, an untapped research area can be identified by programming droplet actuation (rather than exclusive, yet controlled, Marangoni-induced evaporation) in presence of asymmetric vapour fields and surface tension gradients within neighbours drops.

1.6 Aims and objectives

As previously described, Gryzbowski and co-workers investigated how chemical reactivity can be implemented within multi-responsive droplets powered by manipulation of external energy sources – i.e magnetic and electric field, light irradiation.[62] On the other hand, instances of Marangoni-driven droplets motion were recently described in literature, where no external stimuli were required to initiate and sustain droplet actuation.[73] For example, controlled motion of aqueous drops on hydrophilic surfaces was demonstrated in separate efforts by Galy[73] and Prakash,[27] which occurred due to dynamic adsorption of cationic surfactants onto bare glass substrates and generation of asymmetric vapour fields, respectively.

Following these ground-breaking studies, a simpler experimental setup, solely based on surface tension gradients between self-propelling droplets, has been developed for parallel and selective organic synthesis within PG/H_2O droplet pair reactors. Programmed 3,6-disubstituted coumarin synthesis took place without external stimuli and evaporation-induced surface tension gradients were the driving forces causing reacting droplet pairs to move across bare solid substrates. Temporal and spatial patterning of chemical reactivity was achieved starting from a population of droplets and high degree of product selectivity was observed in microliter-sized droplets *via* commonplace analytical techniques, therefore proving that surface tension-driven droplet devices can become viable synthetic alternatives to conventional "static" chemical methodologies.

A series of objectives was set to achieve parallel and selective organic synthesis within PG/H_2O droplet reactors, which comprised:

- Preliminary screening of factors influencing droplet motion on solid substrates – i.e., PG/H_2O droplet pairs composition, substrate properties (activation method, temperature, tilt angle);
- Development of more complex droplet-based devices where a population of droplets would correctly sort after simultaneous deposition on the solid surface;
- Identification of suitable chemistry to be carried out in droplets – i.e., compatible with aqueous reaction media, good yielding at mild reaction conditions, rapid starting material conversion;
- Programmed synthesis of target compounds by means of surface tension-driven droplet chemistry, analysis of droplet reactors content and experimental outcome comparison against batch experiments carried out in conventional round bottom flasks.

Chapter 2

Research work and discussion

A vast array of high-energy surfaces was reported in literature enabling droplet actuation on solid substrates, such as clean silicon wafers,[74] graphene,[75] freshly scraped steel[76] and plasma-oven-treated indium tin oxide (ITO)-coated polyethylene terephthalate (PET).[27] However, the use of equipment fabricated from glass has proceeded relatively unchanged in the history of synthetic chemistry. Glass is an inert substrate that is resistant to chemical corrosion, inexpensive, readily available and easily cleaned. This made it an ideal starting substrate to investigate droplet coalescence and motion.[26,73] In addition to the solid hydrophilic surface, other factors were investigated and standardised for the development of droplet reactors, such as the liquid droplets composition.

Droplet motion of a single pair of binary mixture droplets will be discussed, followed by a brief description of solid substrate activation methods – namely flame-drying and corona-discharge treatments. Next, the role of the solid substrate temperature alongside its tilt angle will be introduced in the context of droplet motion within multiple binary mixture pairs. Finally, surface tension-driven droplet sorters, developed for parallel and autonomous organic synthesis, will be described.

2.1 Mechanics development for the droplet reactor

2.1.1 Motion of a single droplet pair on hydrophilic surfaces: surface tension effects

Following the studies carried out by Prakash *et al.* on the motion of binary mixture droplets,[27,56,61] preliminary experiments were centred on PG/H_2O binary mixture droplet behaviour on flat, high-energy surfaces. Droplet motion basics were studied on clean, flame dried glass slides and three PG/H_2O solutions were prepared with different solvent ratios, being $10\%_{(v/v)}$, $30\%_{(v/v)}$ and $70\%_{(v/v)}$ $PG_{(aq)}$. Droplet motions were captured using a camera (Nikon D5300 50 fps, 50 mm lens) placed at a 90° angle for post-experimental analysis (Figure 27).

Droplets did not spread on the glass slide unlike its separate components, regardless of their PG/H_2O composition. Pure liquids, such as propylene glycol and water, exhibit complete wetting on hydrophilic surfaces when their spreading parameter $S > 0$ and therefore spread onto high-energy surfaces ($\theta = 0$).[77] Conversely, PG/H_2O binary mixtures featured a non-zero contact angle θ despite $S > 0$ because of the balance between capillary and Marangoni fluxes

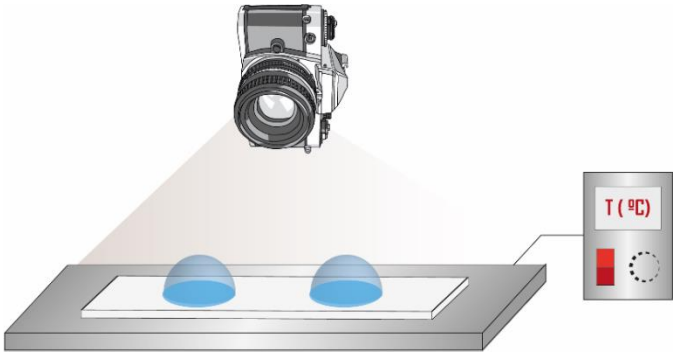

Figure 27. Motion of a single PG/H_2O droplet pair on hydrophilic surfaces, schematics of experimental setup, side view.

within each droplet. Surface wetting was prevented on high-energy substrates and lenticular shaped droplets formed as long as the evaporation process took place at their vapour/liquid interface. Moreover, the surface energy associated to the solid must be higher than that of the liquid mixture.

When introduced in pairs, droplets having same solvent composition featured delayed coalescence whereas drops featuring different PG/H_2O ratio behaved differently (Supplementary Video S1, Section 3.7). A short-range chase occurred between the pair, with the higher PG concentrated droplet chasing the lower PG concentrated away. In both cases, the short-range interactions were preceded by a long-range attraction between neighbouring droplets (Figure 28).

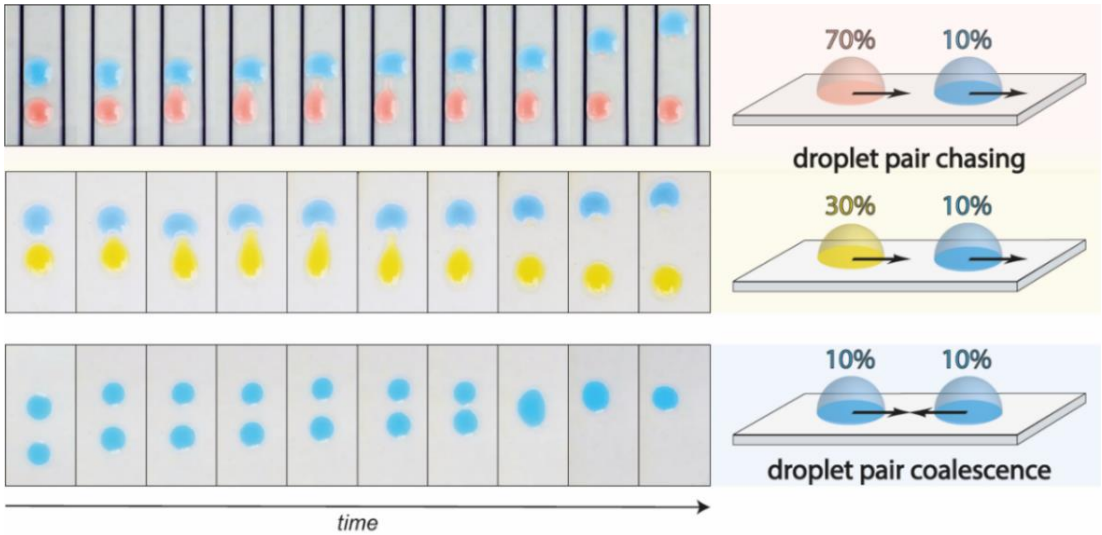

Figure 28. PG/H_2O droplet pair motion depending on solvent composition: timelapse, front view (left), schematics of observed short-range interaction within each pair (right). Utilised PG/H_2O compositions noted as follows: 10%$_{(v/v)}$ PG$_{(aq)}$ (blue), 30%$_{(v/v)}$ PG$_{(aq)}$ (yellow), 70%$_{(v/v)}$ PG$_{(aq)}$ (red).

The interactions observed within PG/H_2O droplets were determined by surface tension effects, which in turn were dependent from temperature and droplet composition. In the latter case, surface tension values of aqueous binary mixtures can be estimated using the Connors-Wright mathematical model (Equation 5),[78–80]

$$\gamma_{CW} = \gamma_A - \left(1 + \frac{b\Phi_A}{1 - a\Phi_A}\right) \cdot \chi_B(\gamma_A - \gamma_B) \quad (5)$$

where γ_{CW} is the predicted surface tension, γ_A and γ_B are the surface tensions of the pure aqueous and non-aqueous component respectively,[19,79] Φ_A and Φ_B are the molar fractions of the aqueous and non-aqueous components respectively, a and b are fitting parameters which are temperature and co-solvent dependent (a = 0.9495, b = 0.7885 for 1,2-propanediol).[78] Conversion of mole fractions to volume fractions yielded the surface tension as a function of volume percentage (grey and black curve respectively, Figure 29).

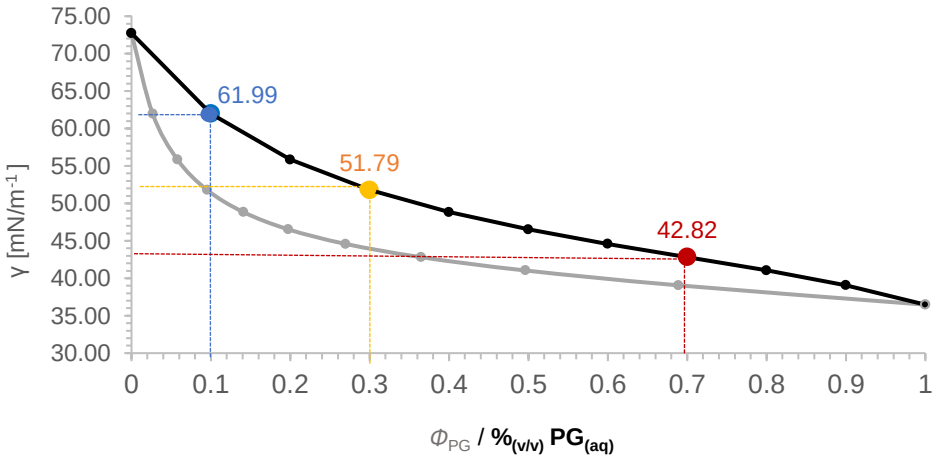

Figure 29. Calculated surface tension values of various PG/H_2O binary mixtures, determined via Connors-Wright equation in function of PG molar fraction (grey curve) and PG volume percentage (black curve). Data points associated to PG/H_2O compositions used in droplet motion studies: 10%$_{(v/v)}$ PG$_{(aq)}$ (blue), 30%$_{(v/v)}$ PG$_{(aq)}$ (yellow), 70%$_{(v/v)}$ PG$_{(aq)}$ (red).

A surface tension difference Δγ between droplet pairs was empirically determined, which allowed prediction of the interaction expected to occur. Short-range attraction or chasing took place depending on each droplet PG/H_2O composition, hence on the surface tension difference generated between them, being lower and higher than 5 mN/m, respectively. This preliminary assumption was crucial for the development of more complex droplet-based devices and the calculated Δγ threshold value was found in accordance with pre-existing literature studies.[49,81]

2.1.2 Motion of a single droplet pair on hydrophilic surfaces: solid substrate properties

Glass substrates activation is generally achieved by altering their surface wettability – i.e. coating with zwitterionic or quasi-superamphiphobic monolayers.[82,83] In this context however, high-energy surface generating techniques which involved chemicals were avoided as the objective was to demonstrate active droplet motion on an inert, unfunctionalized substrate.

Two non-chemical methods were compared for solid substrates activation which were flame-drying and corona-discharge treatment. In the flame-dried glass method, the slides were

passed through the tip of a blue flame for ~10 seconds and cooled at room temperature for 30 seconds before droplet deposition. Although PG/H_2O droplet pairs were mobile on flame-dried glass slides, this activation method not only increased the solid surface energy but also uncontrollably increased their temperature. In turn, the substrate temperature was no longer likely to be constant between each iteration and consequently generated droplet experiments of non-consistent temperature. This is the major reason why corona-discharge treated glass would offer superior properties, since high-energy surfaces would be generated without the extra heat.[84] Glass slides were treated for 60 s using a handheld corona-discharge apparatus. Droplet mixtures of PG/H_2O were placed onto the surface and exhibited higher mobility with more consistent coalescing behaviours, compared to flame-dried glass substrates. Therefore, corona-discharge became the activation method of choice for the generation of high-energy glass substrates.

Another solid substrate property required fine-tuning however, which was investigated in collaboration with Mr. Thomas H. Fox (MChem graduate in Durham University, 2018).[85] Substrate temperature played an important role in droplets evaporation rate and therefore in the asymmetric generation of aqueous vapour fields. Optimum droplet velocities were achieved when the corona-discharged glass slide was constantly heated by a thermostat plate, initially set at 37 °C, prior to their deposition.[85]

2.1.3 Two-by-two droplet pairs orientation studies

As droplet pair coalescence and chasing took place due to evaporation gradients established between neighbouring drops, more complex vapour fields were next investigated by Mr. Thomas H. Fox (MChem graduate in Durham University, 2018).[85] A brief outline of Fox's results is now described, whose objective was to determine whether two droplet pairs were able to coalesce into the correct respective pairings upon simultaneous deposition on a corona-discharged glass slide.

A hydrophobic, square-shaped perimeter featuring round edges was traced with a Sharpie™ ink pen on the solid substrate, prior to droplet pairs deposition. The corona-discharged-glass slide was positioned either on a flat or tilted thermostat plate and heated at a constant temperature of 37 °C. Four 8 µL droplets consisting of two $10\%_{(v/v)}$ and $30\%_{(v/v)}$ $PG_{(aq)}$ droplets (dyed blue and red respectively) were placed within the hydrophobic perimeter drawn on the solid surface. Six possible orientations were investigated with respect to the *xy* plane (Figure 30), and any undesired visual contamination was monitored by observing the change in hue between the droplet pairs. In this context, it is important to emphasise that an iteration was classified as successful if both droplets coalesced into the correct pairings with no visual contamination of opposing dyes (Table 2).[85]

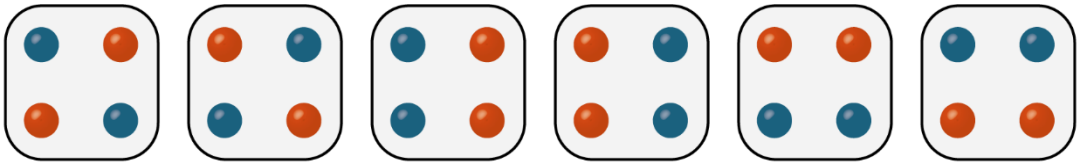

Figure 30. Orientations study of two droplet pairs with observed success rates depending on solid substrates tilt angle. PG/H_2O droplet compositions highlighted as follows: 10%$_{(v/v)}$ PG$_{(aq)}$ (blue), 30%$_{(v/v)}$ PG$_{(aq)}$ (red) – with permission from Mr. Thomas H. Fox, MChem graduate in Durham University, 2018.[76]

Table 2. Orientations study of two droplet pairs: experimental outcome.

α°	Orientation **1**	Orientation **2**	Orientation **3**	Orientation **4**	Orientation **5**	Orientation **6**
0°	**0%**	**0%**	100%	90%	100%	87%
4°	**50%**	**59%**	86%	78%	86%	59%

At a 0° incline, droplets in orientations **1** and **2** experienced a drastic reduction in the success rate compared to the other orientations (Table 2, α = 0°). As shown in case study **2**, the 10%$_{(v/v)}$ PG$_{(aq)}$ droplet would sense the mismatched 30%$_{(v/v)}$ PG$_{(aq)}$ drop because of its closer proximity, compared to the second 10%$_{(v/v)}$ PG$_{(aq)}$ of the original pair. As a result, the correct pairs remained separated since the droplets were too far apart to experience the "correct" vapour field. No Marangoni flow was therefore generated as such to move the matching droplets together in a controlled manner (Figure 31).[85]

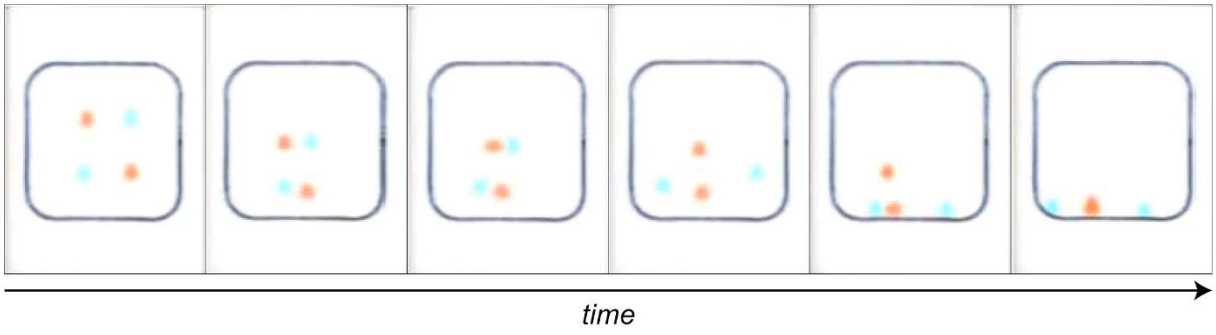

*Figure 31. Time lapse images of unsuccessful sorting of orientation **2** on flat glass slides (α = 0°) – with permission from Mr. Thomas H. Fox, MChem graduate in Durham University, 2018.*[85]

Knowing that past literature studies emphasised the key role played by asymmetric vapour fields within droplet pairs,[53,56] it was hypothesised that a higher success rate in orientations **1** and **2** can be achieved if the droplets were placed on an incline (α ≠ 0°) because the initial vapour field would no longer be static. Success rates for orientations **1** and **2** improved by positioning the glass slide on an incline (α = 4°) and increased up to 50% and 59%, respectively (Table 2, α = 4°). The role played by the round-edged perimeter became evident in the latter case, as 10%$_{(v/v)}$ PG$_{(aq)}$ droplets were no longer "cornered" and forced to coalesce with pursuing 30%$_{(v/v)}$ PG$_{(aq)}$ drops. On the contrary, incorrect droplet fusion was prevented since the pursued 10%$_{(v/v)}$ PG$_{(aq)}$ drops were capable of self-propelling along the curved corner and over the chasing 30%$_{(v/v)}$ PG$_{(aq)}$ pair (Figure 32).[85]

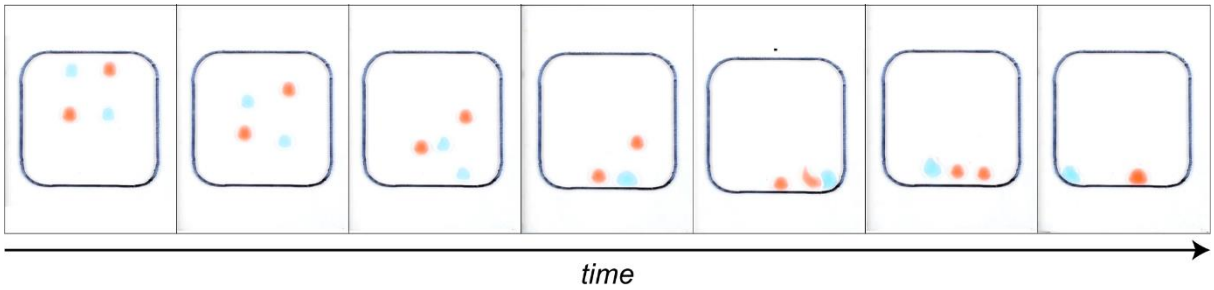

Figure 32. Time lapse images showing prevention of incorrect droplet pair coalescence by adopting a rounded corner shape – with permission from Mr. Thomas H. Fox, MChem graduate in Durham University, 2018.[85]

The important conclusion drawn by Mr. Thomas H. Fox from these experiments was that the autonomous sorting behaviour of two droplet pairs did not occur sporadically, provided that an appropriately shaped hydrophobic track was drawn onto a tilted high-energy solid surface, prior to droplet pair deposition. Starting from a single orientation, experimentally determined success rates were found independent from droplet pairs initial deposition points. Most importantly, drop coalescence within matching pairs was observed upon simultaneous dispensing of all four PG/H_2O droplets, which self-propelled and correctly sorted on the glass slide without external intervention.

2.1.4 Development of Marangoni-driven droplet devices

Surface tension-driven sorters were developed in which multiple droplet pairs would simultaneously coalesce in a controlled manner and reach their target destinations on a heated high energy surface. The solid substrate consisted of a corona-discharged glass slide (6.50 cm x 8.00 cm), which was placed on an inclined, thermostatic hot plate (Figure 33). Underlying gravity effects played a minor role in this context, by assisting the downward motion featured by droplets after correct pair merging. Following this consideration, it is important to clarify that the substrate tilt angle was orthogonal to the starting orientation of the individual droplets, therefore proving that both droplet pair coalescence and sorting events did not occur by gravitational means. Water-soluble dyes were added to differing PG/H_2O compositions to monitor droplet pairs motion and for clear-cut detection of undesired interactions between neighbouring drops.

Two key areas can be identified within the surface tension-driven sorter, depending on the type of droplet behaviour expected to occur. As shown in the two-by-two droplet pair (2x2) device (Supplementary Video S2, Section 3.7), the first area is where droplet pairs would fuse into their correct pairings (green square, Figure 33A). Following this each coalesced drop was expected to reach a target destination within the sorting area (purple square, Figure 33A). A hydrophobic track (black lines, Figure 33A) was drawn with a Sharpie™ marker on the activated solid substrate to convey droplet motion, which can be described occurring through three phases being droplet pair coalescence, transportation and sorting (Figure 33B).

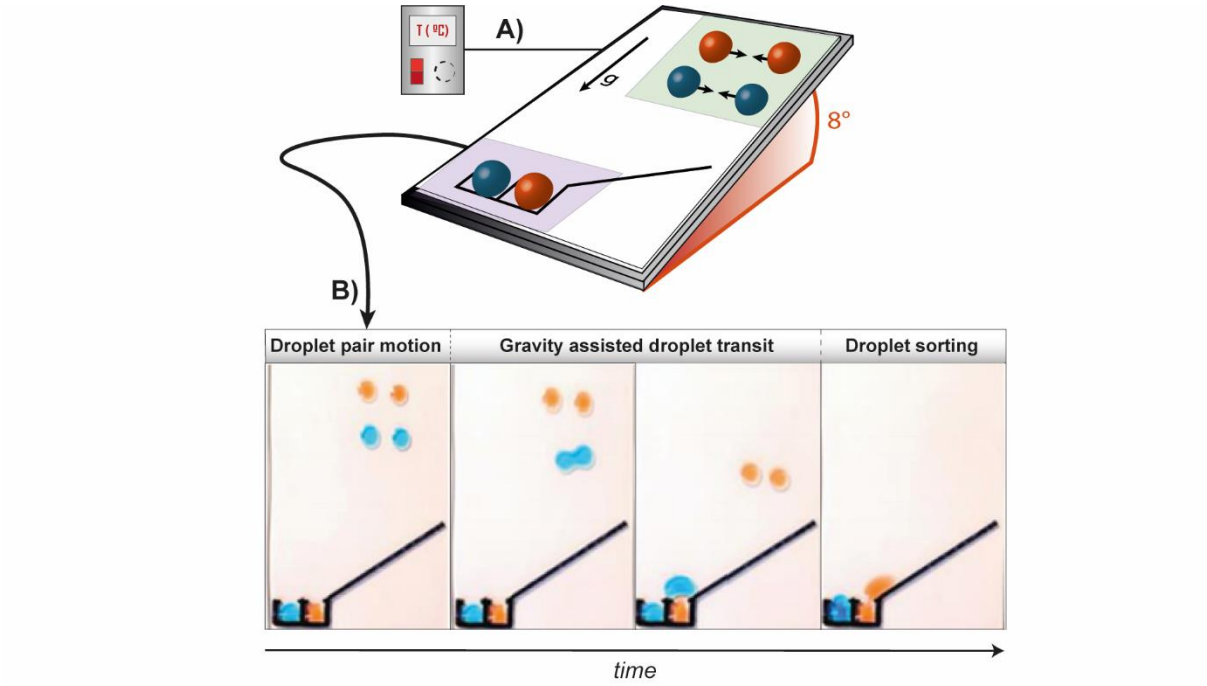

Figure 33. Surface tension-driven droplet reactor, from top: A) Overall droplet-based device setup – side-angle sketch; B) Successful droplet experiment – timelapse, front view (T = 42 ºC, α = 8º, V ≈ 5 µL). PG/H_2O droplets dyed as follows: 10%$_{(v/v)}$ PG$_{(aq)}$ (Acid Blue), 35%$_{(v/v)}$ PG$_{(aq)}$ (Congo red).

The order by which droplet pairs were simultaneously dispensed onto the hydrophilic surface was also investigated. Given that increasing PG volume percentage corresponded to higher droplet viscosities, undesirable interactions within 10%$_{(v/v)}$ and 35%$_{(v/v)}$ PG$_{(aq)}$ droplet pairs for instance were minimised by careful deposition with decreasing PG percentage, starting from the top right corner of the (2x2) sorting device.

Similarly to the (2x2) droplet sorter, a three-by-three droplet pair (3x3) device was next manufactured in which 60%$_{(v/v)}$, 30%$_{(v/v)}$ and 10%$_{(v/v)}$ PG$_{(aq)}$ droplet pair motion was investigated (Supplementary Video S3, Section 3.7). Further optimisation was required for the (3x3) droplet sorter however, due to its increased complexity. More specifically, (2x2) sorting devices were initially produced by drawing a hydrophobic track by hand with custom-made cardboard templates. Despite of its simplicity, droplet sorting reproducibility was negatively affected by the stencil material, which quickly worn out after repeated use. The (2x2) droplet sorter was therefore regarded as a “prototype model”, proving that Marangoni-driven droplets can be utilised to partake organic synthesis. The negative impact that casual error provided in this step was minimised in the (3x3) droplet device by implementing a drawing apparatus (*AxiDraw*™ V3 robotic arm), which was programmed to yield the same track over time.

As previously described for the (2x2) sorter, a hydrophobic track was traced onto a corona-discharged glass slide which was then positioned on a tilted thermostat plate (Figure 34A). Droplet pairs were dispensed on the heated solid substrate and initiated their gravity-assisted

motion towards the sorting area (Figure 34B). Correct droplet pair coalescence took place prior to the 10%$_{(v/v)}$ PG$_{(aq)}$ droplet sorting, which occurred when its surface tension closely resembled the one associated to its target destination (Figure 34C). In a similar fashion, the more viscous 35%$_{(v/v)}$ and 60%$_{(v/v)}$ PG$_{(aq)}$ coalesced drops transited towards the sorting area and reached their respective target location (Figure 34D and 34E, respectively). Overall, droplet runs were classified as successful whenever *all* droplet pairs fused into the correct pairings *and* reached their respective target locations within the sorting area (Figure 34F).

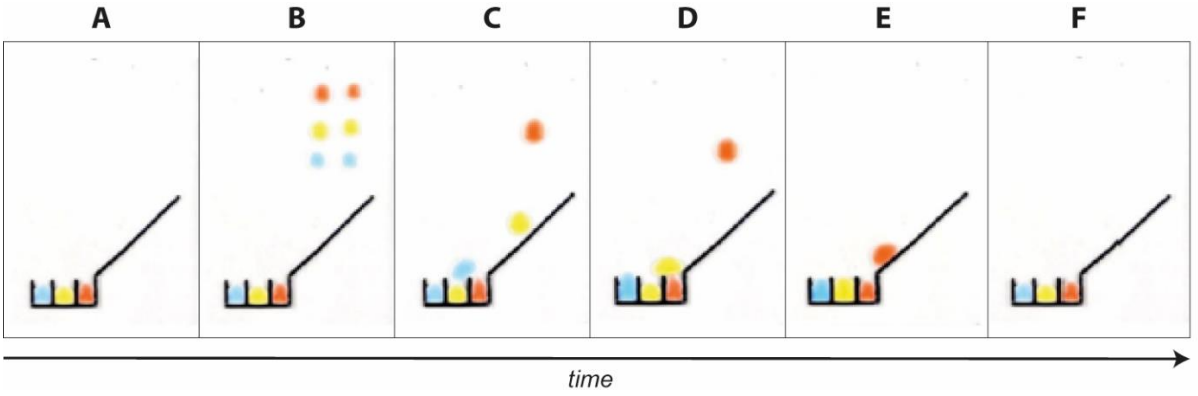

Figure 34. Timelapse of a successful run in a multi-droplet sorter, front view, still images. A) Droplet device manufacturing; B) Deposition of PG/H_2O droplet pairs; C) Droplet pair coalescence and 10%$_{(v/v)}$ PG$_{(aq)}$ merged drop transit towards the sorting area; D) 30%$_{(v/v)}$ PG$_{(aq)}$ merged drop sorting; E) 30%$_{(v/v)}$ PG$_{(aq)}$ drop coalescence in target well and 60%$_{(v/v)}$ PG$_{(aq)}$ droplet transit; F) 60%$_{(v/v)}$ PG$_{(aq)}$ drop coalescence in target well. PG/H_2O droplets dyed as follows: 10%$_{(v/v)}$ PG$_{(aq)}$ (acid blue), 35%$_{(v/v)}$ PG$_{(aq)}$ (methyl orange), 60%$_{(v/v)}$ PG$_{(aq)}$ (methyl orange). (T = 42 ºC, *α* = 8º, V ≈ 5 µL)

2.2 Chemistry implemented in Marangoni-driven droplet reactors

2.2.1 Droplet chemistry in DMSO/H_2O solvent media: "click" chemistry attempts

According to pre-existing studies,[27] surface tension-driven attractive/repulsive behaviour can be achieved not only with PG/H_2O binary mixtures but also with aqueous solutions featuring organic, water-miscible co-solvents such as DMSO, which is a commonplace reaction medium within the biorthogonal and "click" chemistry literature. According to Sharpless *et al.,*[86] a chemical process must meet a list of strict criteria to be classified as a "click" reaction, among which simple reaction conditions, minimal workup and short reaction times – all features that are desirable in droplet chemistry. For this reasons, synthetic protocols belonging to this reaction pool were initially considered for droplet chemistry.

Huisgen 1,3-dipolar cycloadditions and the copper-catalysed azide–alkyne 1,3-dipolar cycloaddition (CuAAC) were considered, with the latter being recognised as the quintessential click reaction.[87] Separate studies independently undertaken by Fokin and Meldal reported the use of copper(I) catalysts to further enhance 1,3-dipolar cycloaddition of azides with terminal alkynes to produce 1,4-disubstituted 1,2,3-triazoles.[88,89] The azide moiety reacts as a 1,3-dipole with a second molecule bearing a terminal alkyne, known as dipolarophile, giving rise

to 1,4-disubstituted 1,2,3-triazoles. In presence of a copper(I) catalyst however, CuAAC proceeds approximately seven times faster than the uncatalyzed cycloaddition, due to the formation of a dinuclear copper intermediate, which activates terminal alkynes towards the reaction with azides (Scheme 1).[90,91]

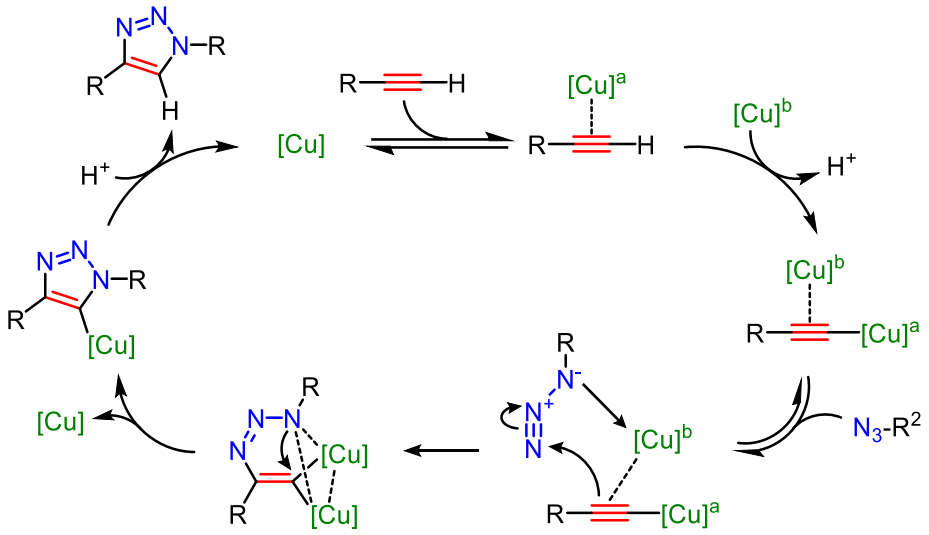

Scheme 1. Copper catalyzed azide–alkyne cycloaddition (CuAAC) reaction mechanism.[91]

Moreover, significant rate enhancement of CuAAC cycloadditions was also documented when reactions were carried out in aqueous media, making CuAAC a perfect candidate for droplet chemistry.[92,93]

DMSO/H_2O binary mixture droplet behaviour was assessed in a (2x2) sorter before embedding any reagents required for CuAAC. Although droplet coalescence took place between the $10\%_{(v/v)}$ and $60\%_{(v/v)}$ $DMSO_{(aq)}$ pairs as predicted, DMSO-based droplets dissolved the hydrophobic track whilst transiting towards the sorting area. A series of changes, centred on the hydrophobic track material, was attempted to overcome this issue and was investigated in collaboration with Mr. Thomas H. Fox (MChem graduate in Durham University, 2018).[85]

At first, a silicone-based track was drawn by manual pipetting on an activated glass slide. The dispensed pairs coalesced in a controlled manner after droplet deposition. The resulting fused drops did not suffer from contact line pinning and, most importantly, did not dissolve the hydrophobic track. On the other hand, they completely spread on the silicone track and often flowed under the hydrophobic barrier, with the latter behaviour occurring due to poor adhesion displayed by the pipetted silicone track towards the activated glass surface. Composite solid substrates were next examined. Polydimethylsiloxane (PDMS) coated glass slides as well as double-layered glass wafers were fabricated and activated *via* corona discharge before droplet pairs deposition. Droplet spreading was again observed after correct pair coalescence and no droplet sorting took place onto both composite, high-energy solids (Figure 35).[85]

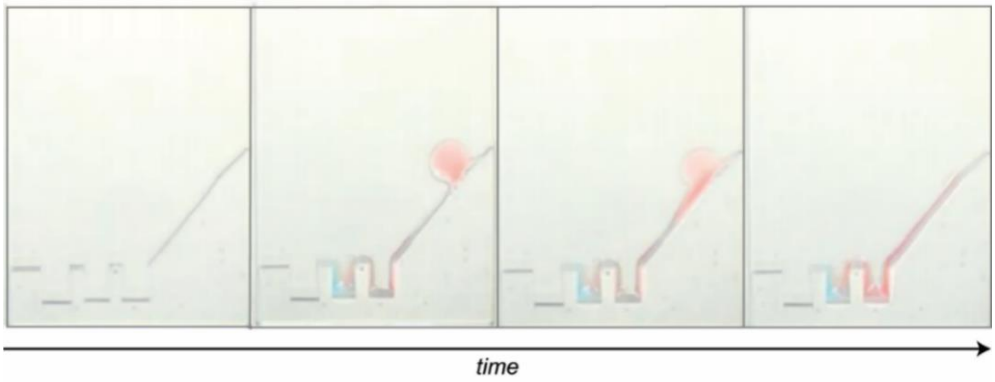

Figure 35. Time lapse showing the spreading of DMSO/H_2O droplets on a PDMS-glass composite substrate – with permission from Mr. Thomas H. Fox, MChem graduate in Durham University, 2018.[85]

Contact angle retention and droplet motion on composite, high-energy solid substrates may be more convoluted in these circumstances as droplets would be in contact with a surface in two planes as opposed to one. In addition to the undesired spreading behaviour displayed by DMSO/H_2O droplets, presence of dimethyl sulfoxide in analytical samples destined for mass spectrometry and chromatographic separation would be detrimental. Moreover, CuAAC precursors exhibited poor solubility in $10\%_{(v/v)}$ and $60\%_{(v/v)}$ DMSO/H_2O mixtures, which limited the cycloaddition optimisation scope to be carried out in droplets.

It was therefore concluded that CuAAC reactions were not compatible with the newly developed droplet sorting devices and alternative synthetic protocols were next investigated.

2.2.2 Droplet chemistry in PG/H_2O solvent media

The Knoevenagel condensation was initially investigated as a model reaction to be implemented in droplet reactors. Encouraged by the research work carried out by Jalalakshmi *et al.*, in which arylidenemalononitriles were synthesised in PG/H_2O media,[94] preliminary studies were undertaken for the synthesis of benzilidenemalononitrile **3** (Scheme 2).

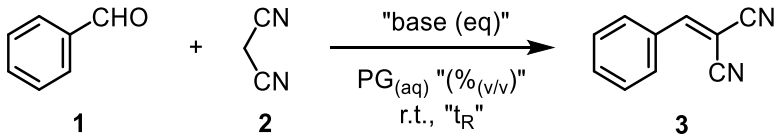

*Scheme 2. Compound **3** synthesis via Knoevenagel condensation.*

Table 3. Benzilidenemalononitrile 3 synthesis in PG/H_2O: experimental outcome.

Entry	"base (eq)"	"(% (v/v))"	"t_R"	Isolated yield
1	-	60%	8'	84%
2	-	10%	30'	33%
3	NaOH (1.5 eq)	10%	5'	ND
4	DABCO (0.1 eq)	10%	<5'	75%

Benzilidenemalononitrile **3** was isolated in 84% yield following the procedure described in literature, which featured 60%$_{(v/v)}$ PG$_{(aq)}$ as reaction medium (Table 3, Entry 1). In a similar fashion, 10%$_{(v/v)}$ PG$_{(aq)}$ was next investigated for the synthesis of **3** at room temperature, however conversion of starting material into the desired product did not immediately occur as previously observed and reaction yield decreased to 33% (Table 3, Entry 2). Unlike malononitrile **2**, benzaldehyde **1** was found immiscible in aqueous mixtures featuring less than 45%$_{(v/v)}$ PG$_{(aq)}$ and this evidence could account for the lower yield observed in 10%$_{(v/v)}$ PG$_{(aq)}$. Consequently, base screening was next carried out to resolve both reactivity and solubility issues displayed by aromatic aldehyde **1** in 10%$_{(v/v)}$ PG$_{(aq)}$. Isolation of target compound **3** proved challenging during NaOH-mediated Knoevenagel condensation since no solid material was found in suspension as the reaction progressed towards completion (Table 3, Entry 3). On the opposite, solid precipitation took place in 10%$_{(v/v)}$ PG$_{(aq)}$ as soon as sub-stoichiometric amounts of DABCO were added to the reaction mixture and benzylidenemalononitrile **3** was successfully isolated by simple vacuum filtration with 75% yield (Table 3, Entry 4).

Overall, benzaldehyde **1** solubility in 10%$_{(v/v)}$ PG$_{(aq)}$ did not improve upon base addition and better suited carbonyl precursors were required to carry out the DABCO-promoted Knoevenagel condensation in aqueous media. Thus, different aldehydes and activated methylene compounds were screened for their solubility in 10%$_{(v/v)}$ PG$_{(aq)}$, the latter being the binary solvent composition in which starting materials were the least likely to dissolve in (Figure 36).

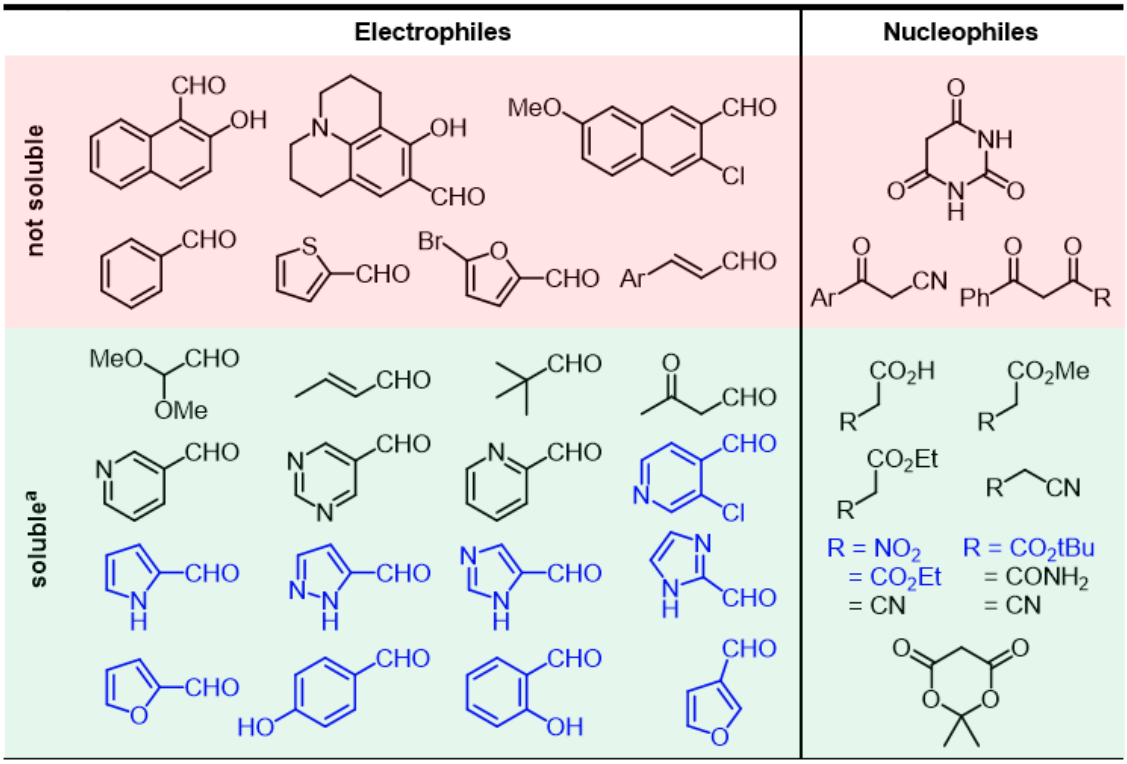

Figure 36. Solubility screening of aldehydes and activated methylene compounds. [a.] Entry compounds dissolving only upon base addition highlighted in blue.

0.306 mmol of reagent were introduced in 2 mL of solvent mixture (0.153 M): several electrophilic and nucleophilic reagents were found either as solids or suspended in the solvent media even when sodium hydroxide was added in stoichiometric amounts (Figure 36, highlighted in red). Conversely, a trend was observed amongst the array of starting materials dissolving in $10\%_{(v/v)}$ $PG_{(aq)}$ (Figure 36, highlighted in green). More specifically, aldehydes bearing hydroxyl groups became soluble in PG/H_2O binary mixtures only after addition of NaOH in stoichiometric amounts (Figure 36, chemical structures highlighted in blue). Their improved solubility can be rationalised by considering the base-promoted deprotonation of the hydroxyl moieties and aldehydes reversible conversion into hydrates, with the latter species generally being more soluble than the former in aqueous media.

PG/H_2O-soluble arylaldehydes **4-6** were next screened in batch conditions and electrophiles reactivity was monitored under the operative parameters later used in the optimised multi-droplet systems, such as concentration and reaction temperature (Scheme 3).

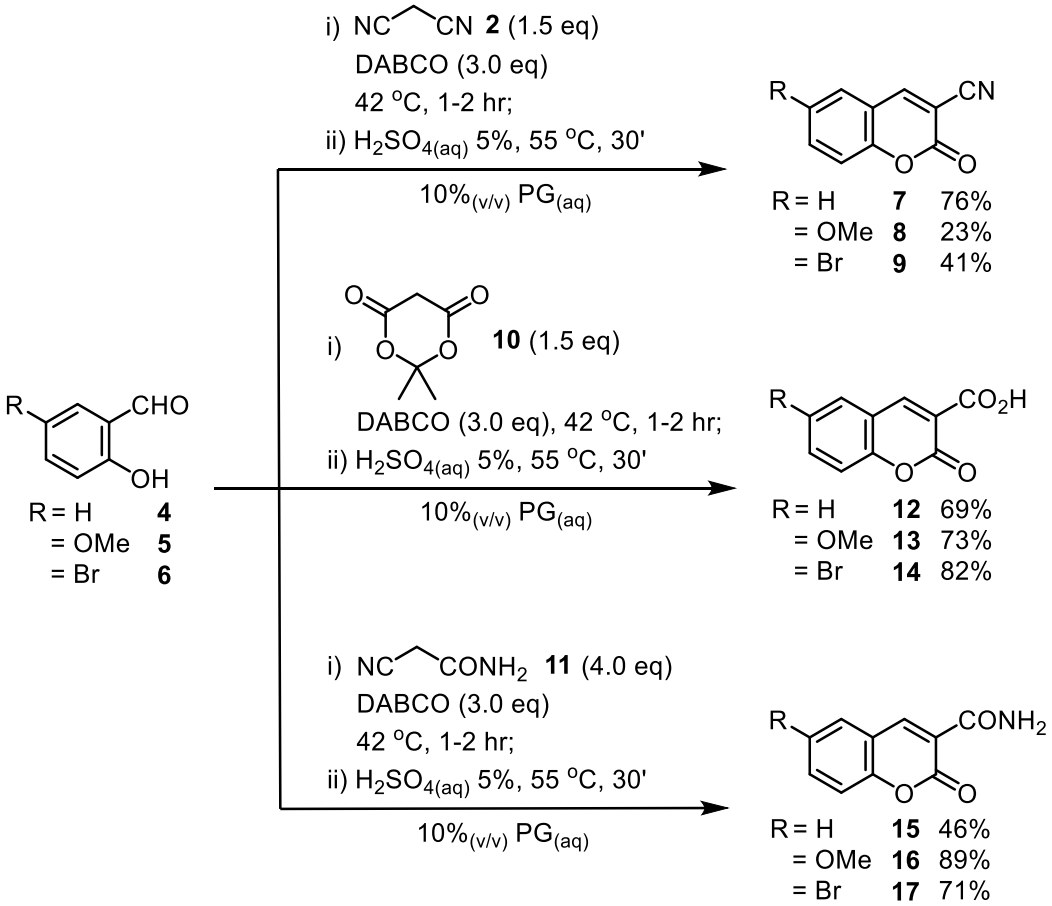

Scheme 3. 3,6-disubstituted coumarin derivatives synthesis and isolated yields

Synthesis of 6-substituted-3-cyanocoumarins **7-9** in presence of malononitrile **2** was undertaken *via* a two-step synthetic protocol featuring initial Knoevenagel condensation (step *i,* Scheme 3), followed by acid-promoted intramolecular cyclisation and hydrolysis (step *ii,* Scheme 3). The library of compounds required for micro-scale synthetic chemistry in droplets

was completed upon identification of two additional nucleophilic species alongside malononitrile, being cyanoacetamide **10** and Meldrum's acid (2,2-dimethyl-1,3-dioxane-4,6-dione) **11**. Isolation of 6-substituted coumarin-3-carboxylic acid **12-14** and coumarin-3-carboxamides derivatives **15-17** was achieved following the reaction conditions previously utilised for the synthesis of coumarins **7-9**, with isolated yields ranging between 23% and 89% (Scheme 3).

Following the same principle, *N*-benzyl cyanoacetamide **18** was initially considered as an alternative to primary amide **11**. Although *N*-benzyl coumarin derivatives **19-21** were successfully isolated in batch conditions (Scheme 4), nucleophile **18** was later discarded for droplet chemistry purposes, due to solubility issues displayed not only by *N*-benzyl cyanoacetamide in PG/H_2O mixtures but also by target products **19-21** in commonplace NMR solvents – e.g., $CDCl_3$, DMSO-d_6, acetone-d_6.

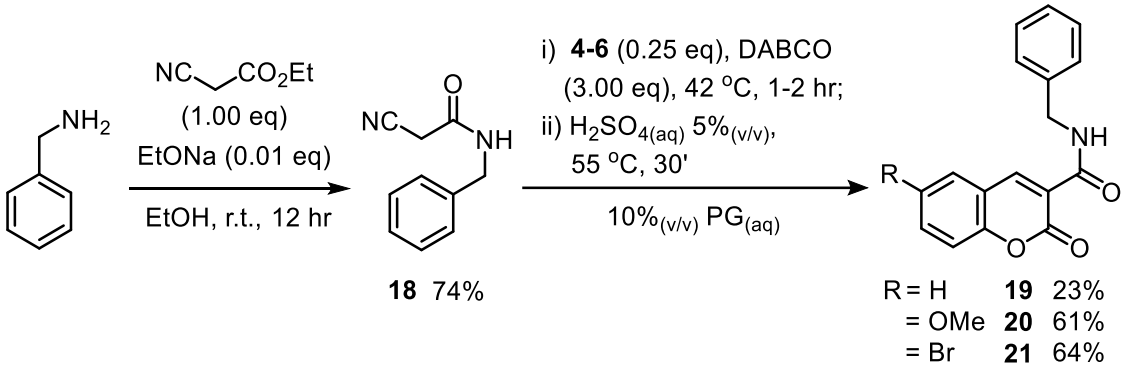

*Scheme 4. N-benzyl-6-disubstituted-3-coumarin carboxamides **19-21** synthesis and isolated yields*

Overall, juxtaposition between conventional synthetic methodologies (e.g., borosilicate round bottom flasks) and droplet chemistry was undertaken by carrying out the DABCO-promoted Knoevenagel condensation in microliter-sized droplets. Following this, formation of new C-C bonds selectively took place in autonomously moving drops after simultaneous deposition of all reagent pairs. Synthesis of variously substituted *ortho*-hydroxy intermediates would occur in microlitre-sized reaction mixtures and the subsequent cyclisation step, required for the synthesis of coumarins **7-17**, was carried out after complete consumption of salicylaldehydes **4-6** within each droplet reactor.

2.3 Two-by-two droplet pair (2x2) chemical sorter

A two-by-two droplet pair (2x2) sorter was developed for programmed and parallel synthesis of coumarins **13** and **7** starting from reagent pairs **5, 10** and **4, 2**, which were dissolved in 35%$_{(v/v)}$ and 10%$_{(v/v)}$ PG$_{(aq)}$, respectively (Scheme 5). Fabrication of the droplet reactor was undertaken by tracing a hydrophobic track onto a clean, corona-discharged glass slide and deposition of blank 35%$_{(v/v)}$ and 10%$_{(v/v)}$ PG$_{(aq)}$ droplets in the sorting area (bottom left corner, orange and blue circles respectively, Figure 37). Coumarin synthesis took place as soon as the droplet pairs coalesced and carried on whilst the merged droplets approached their target destination. Once all droplet reactors reached their pre-defined locations, they were left on the heated energy surface for thirty minutes (step *i*, Figure 37). Finally, droplet reactors were transferred in separate compartments, where they were quenched with diluted hydrochloric acid and heated (step *ii*, Figure 37).

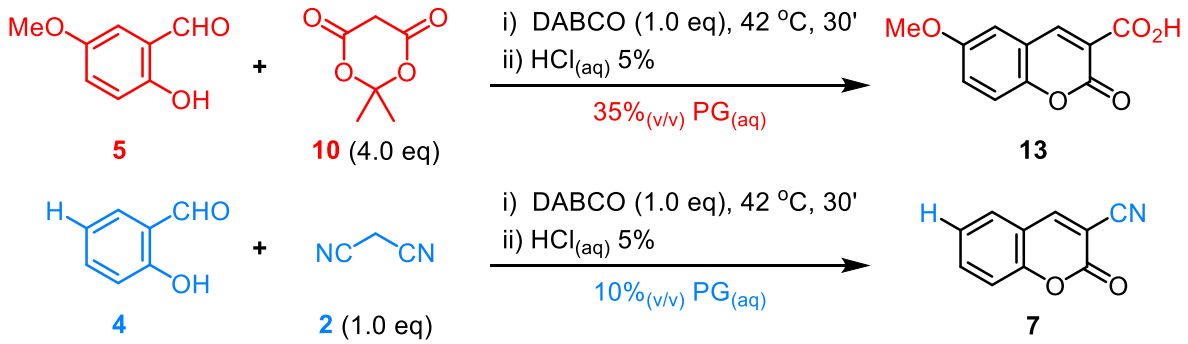

*Scheme 5. 3,6-disubstituted coumarins **7, 13** synthesis in a (2x2) chemical sorter*

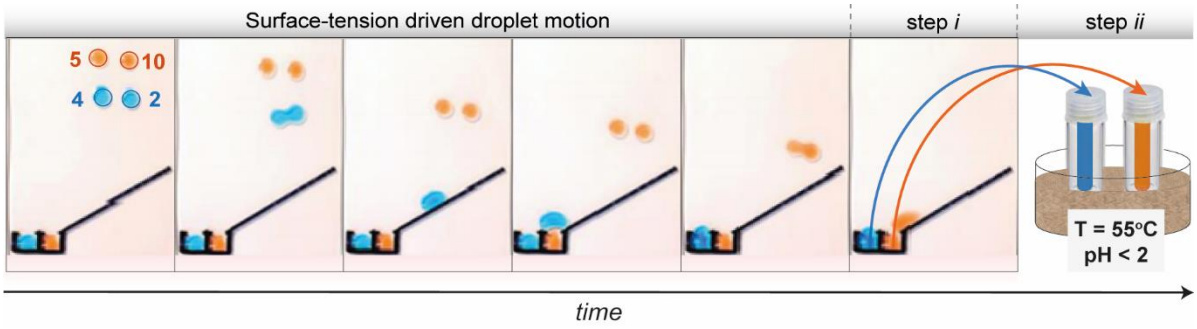

*Figure 37. Timelapse of a successful run in a (2x2) chemical sorter for parallel synthesis of coumarins **13** and **7**, front view, still images.*

Unlike malononitrile, a large excess of Meldrum's acid **10** (4.00 eq) was required to promote coumarin **13** formation in the 35%$_{(v/v)}$ PG$_{(aq)}$ droplet reactor. Propylene acetal derivative of arylaldehyde **5** was observed upon GC-MS analysis instead of target compound **13** when stoichiometric amounts of nucleophile **10** were utilised in the (2x2) droplet sorter. Focus was placed on solving the newly encountered reactivity issue and the acid-promoted side reaction occurring between precursor **5** and PG was minimised by increasing the excess of nucleophilic reagent **10.** Target molecules **7** and **13** were observed *via* GC-MS in the 10%$_{(v/v)}$ and 35%$_{(v/v)}$

$PG_{(aq)}$ droplet reactor, respectively. High product chemoselectivity was achieved *via* droplet chemistry (chromatogram *i* and *ii* respectively, Figure 38A) whereas simultaneous addition of the two reagent pairs in a round bottom flask resulted in formation of cross-products (6-methoxy-3-cyanocoumarin **8** and coumarin-3-carboxylic acid **12**) alongside 3-cyanocoumarin **7** and 6-methoxycoumarin-3-carboxylic acid **13** (chromatogram *iii*, Figure 38A). Minor baseline impurities (e.g., triphenylphosphine oxide) were detected in all chromatograms, which arose from the communal, walk-up mass spectrometer available in Durham university. Nonetheless, the molecular ion peaks and *m/z* ratios associated to each chromatogram peaks further consolidated the potential held by the droplet chemistry approach towards the chemoselective synthesis of target coumarins **7** and **13** (Figure 38B, Spectra *i* and *ii*).

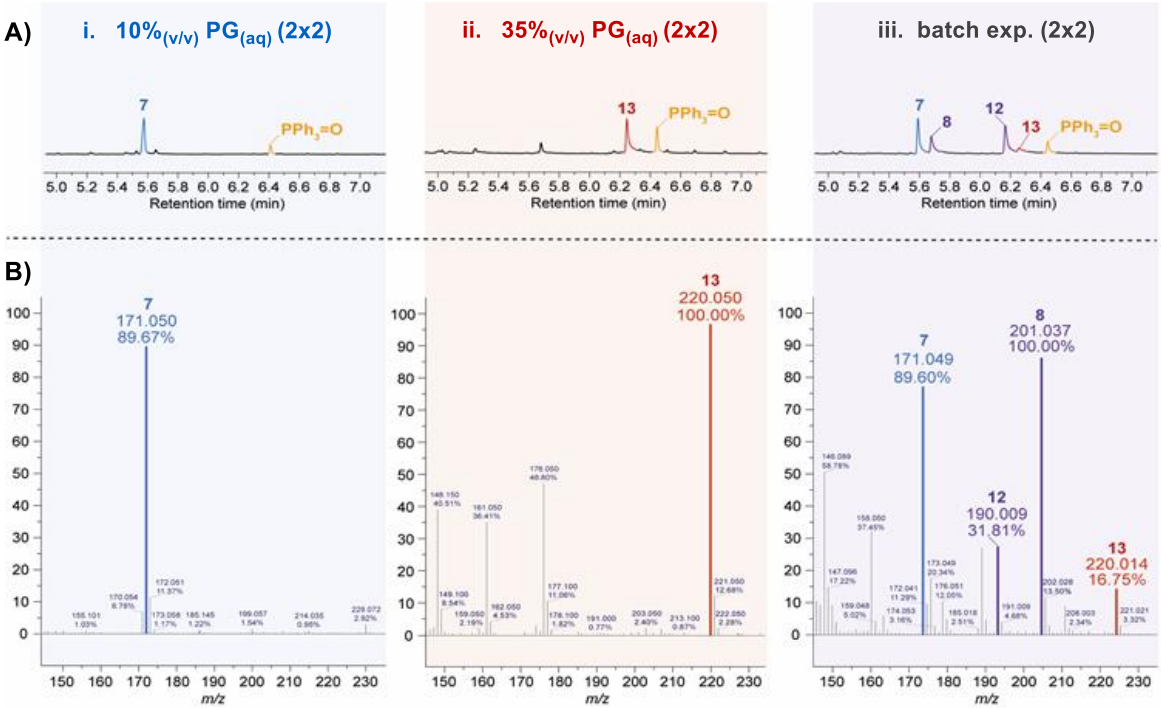

Figure 38. Qualitative analysis via GC-MS of 10%$_{(v/v)}$ and 35%$_{(v/v)}$ $PG_{(aq)}$ (2x2) droplet reactors (column i and ii, respectively) as well as the (2x2) batch experiment (column iii), from top: A) GC chromatographs data comparison; B) Mass spectra comparison.

Alongside GC-MS analysis, ^{1}H-NMR spectra (recorded in DMSO-d_6) were acquired from droplet reactors: 10%$_{(v/v)}$ and 35%$_{(v/v)}$ $PG_{(aq)}$ spectroscopic evidence were recorded alongside their batch counterpart (Figure 39, Spectra *i-iii*). In addition, reference compound samples for target molecules and cross-products were prepared following droplet chemistry operating conditions (Figure 39, Spectra *iv-v* and *vi-vii* respectively). ^{1}H-NMR spectra were compared within the aromatic chemical shift region (6.9-9.2 ppm), highlighting the matching signal patterns observed between the 10%$_{(v/v)}$ $PG_{(aq)}$ droplet reactor and product of interest **7** (Figure 39, Spectra *i* and *iv*). In a similar fashion, ^{1}H-NMR signal pattern arising from the 35%$_{(v/v)}$ $PG_{(aq)}$ sample closely matched target compound **13** (Figure 39, Spectra *ii* and *v*). No cross products

12 and **8** (Figure 39, Spectra *vi*, *vii*) were detected in droplet reactors upon ^{1}H-NMR spectra comparison.

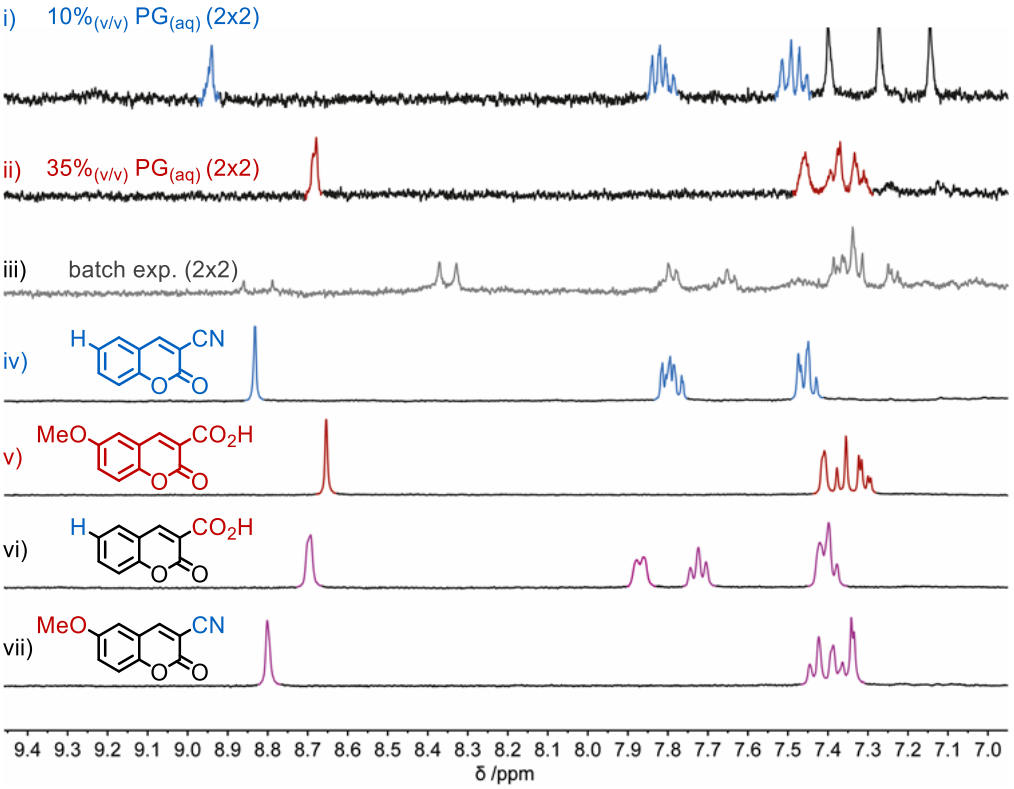

*Figure 39. (2x2) droplet reactor ^{1}H-NMR spectra comparison, recorded in DMSO-d_6, from top: (2x2) droplet reactors i) 10%$_{(v/v)}$ PG$_{(aq)}$, ii) 35%$_{(v/v)}$ PG$_{(aq)}$, iii) (2x2) batch experiment; reference compounds iv) 3-cyanocoumarin **7**, v) 6-methoxycoumarin-3-carboxylic acid **13**, vi) coumarin-3-carboxylic acid **12**, vii) 6-methoxy-3-cyanocoumarin **8**.*

2.4 Optimisation of batch reactions for (3x3) droplet chemistry

A six-droplet pair (6DT) reactor was developed to screen the synthesis of 3,6-disubstituted coumarins **13**, **7** and **17** in micro-litre sized droplets (Supplementary Video S4, Section 3.7). The sorting device utilised for these assessments was manufactured on a corona-discharged glass slide where six square-shaped hydrophobic tracks were drawn on its hydrophilic surface (black lines, Figure 40A). Once the glass slide was positioned on a tilted thermostatic hot plate set at 42 °C, six blank PG/H_2O droplets were deposited within each confining area (white circles, Figure 40A) and the solvent ratio in which blank droplets were prepared matched the ones in both aldehyde and nucleophilic reagents were dissolved in. Six droplets, containing one of the three electrophilic reagents and DABCO (yellow circles, Figure 40B), were next introduced and allowed to merge with the blank droplets. Similarly, six droplets, containing only a single nucleophilic reagent (grey circles, Figure 40C) were deposited onto the glass slide and were observed coalescing with the pre-existing droplets. Consequently, six droplet reactors have formed (brown circles, Figure 40D), which were left on the heated high energy surface for thirty minutes. Prior to ^{1}H-NMR sample preparation and data acquisition, the droplets were collected in a separate compartment (Figure 40E), quenched with diluted sulfuric acid and heated at 55 °C for 35 minutes (step *ii,* Figure 40).

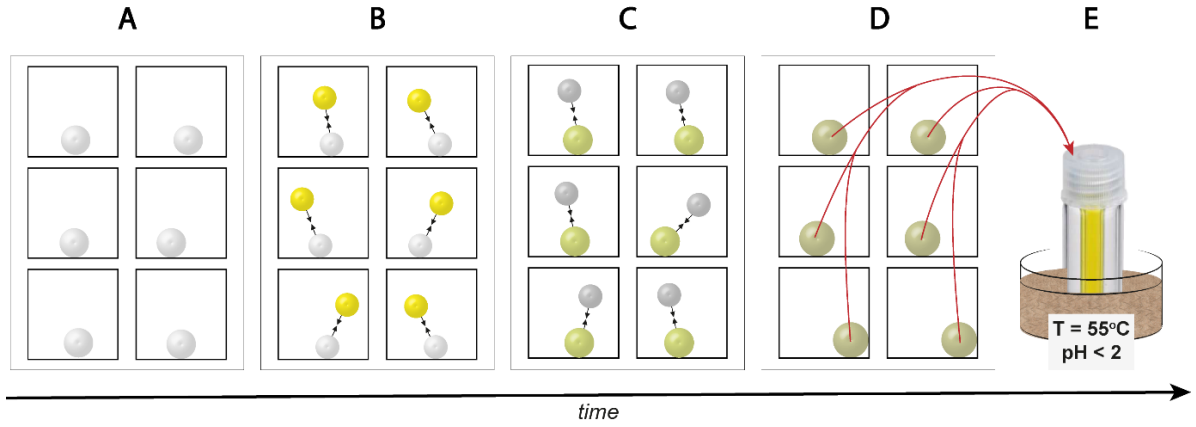

Figure 40. (6DT) device timelapse, sketched front view. A) Sorting device manufacturing and blank PG/water droplets deposition; B) Introduction of droplets containing electrophilic reagent + DABCO mixture; C) Nucleophile-containing droplets deposition and coalescence with pre-existing merged droplets; D) Droplet microreactors formation (step i); E) Droplet transfer to a separate compartment, where both acid quenching and additional heating (step ii) were carried out.

Differently from the (2x2) droplet sorter, no studies related to autonomous droplet motion were undertaken at this stage as the main objective was to assess the reagent pairs reactivity. Each *o*-hydroxyl 5-substituted salicylaldehyde was combined with the respective activated methylene compound and all (6DT) droplet reactions were carried out in the corresponding PG/H_2O solvent composition. Starting from the reaction set successfully carried out in the (2x2) chemical sorter, compound identification in *unquenched* (6DT) experiments was of paramount importance since direct coumarin synthesis was achieved in the 35%$_{(v/v)}$ PG$_{(aq)}$

(6DT) test run, which afforded 6-methoxycoumarin-3-carboxylic acid **13**. Conversely, salicylaldehyde **4** condensation with malononitrile **2** in 10%$_{(v/v)}$ PG$_{(aq)}$ did not yield 3-cyanocoumarin **7** as expected, since intermediate compounds of a different chemical nature were detected before reaction quenching. Consequently, arylaldehydes reactivity in droplets was further investigated to confirm complete consumption of starting materials **4-6** as well as to identify the reacting species involved in the synthesis of coumarins **13**, **7** and **17** in 10%$_{(v/v)}$, 35%$_{(v/v)}$, and 60%$_{(v/v)}$ PG$_{(aq)}$ droplet reactors.

2.4.1 6-bromocoumarin-3-carboxamide 17 synthesis in 60%$_{(v/v)}$ PG$_{(aq)}$ (6DT) experiments

Reaction conditions previously optimised in batch conditions towards the synthesis of coumarin **17** were adopted in preliminary (6DT) experiments (Scheme 6). Complete conversion of 6-bromosalicylaldehyde **6** was achieved in (6DT) droplet reactors when a large excess of cyanoacetamide **11** was used and formation of 6-bromocoumarin-3-carboxamide **17** in droplets was confirmed *via* ^{1}H-NMR spectroscopy (Figure 41, Spectrum *iii*).

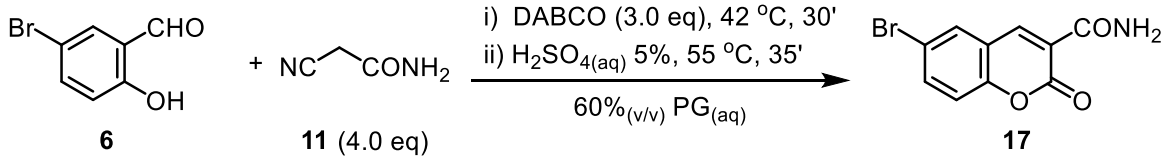

*Scheme 6. 6-bromocoumarin-3-carboxamide **17** synthesis in (6DT) microreactor.*

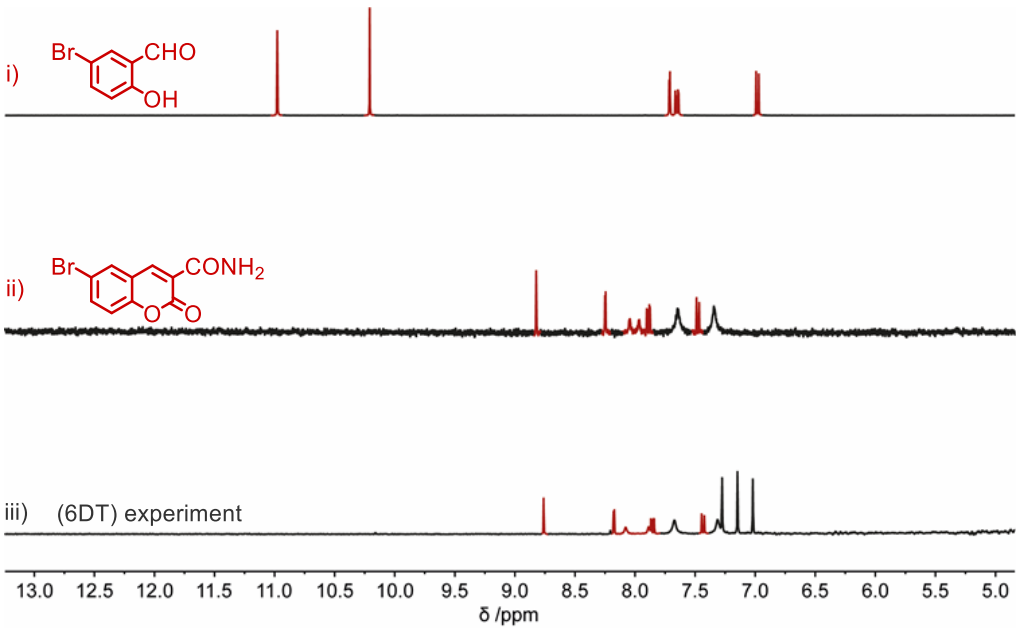

*Figure 41. ^{1}H-NMR stackplot comparison related to compound **17** synthesis in 60%$_{(v/v)}$ PG$_{(aq)}$, from top: i) (6DT) reference precursor **6**; ii) (6DT) reference compound **17;** iii) (6DT) experiment*

Additional (6DT) experiments were run to further investigate starting materials' reactivity in droplet reactors and their quenching with diluted aqueous sulfuric acid was discovered essential for the synthesis of target compound **17**. Interestingly, ^{1}H-NMR spectra recorded

from unquenched (6DT) runs again featured complete consumption of aldehyde precursor **6,** but no bromo-substituted coumarin **17** was observed upon data comparison (Figure 42). Formation of Knoevenagel condensation product **17a** in absence of $H_2SO_{4(aq)}$ was initially hypothesised as the ^{1}H-NMR signal patterns associated to unquenched (6DT) experiments (Figure 42, Spectra *iii*, *iv*) did not align with the ones provided by coumarin **17** (Figure 42, Spectrum *i*) and were consistent with formation of intermediate **17a** (Figure 42, Spectrum *v*).

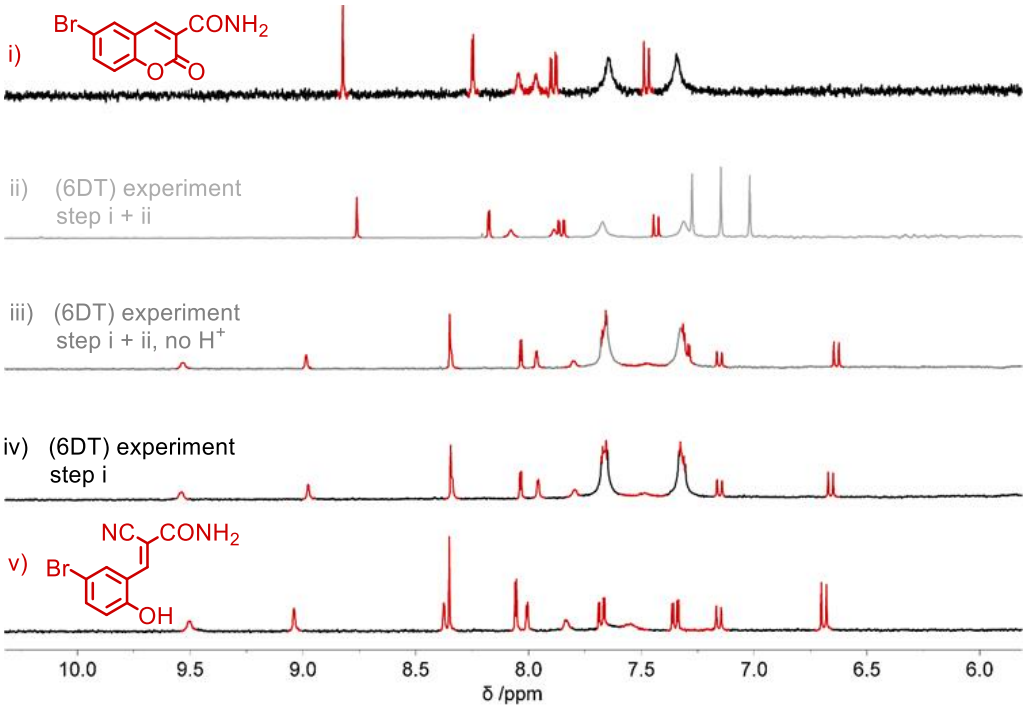

*Figure 42. ^{1}H-NMR stackplot comparison related to compound **17** synthesis in 60%$_{(v/v)}$ PG$_{(aq)}$, from top: i) (6DT) reference compound **17**; (6DT) experiments: ii) step i + ii, iii) step i + ii, no acid quenching, iv) step i only, v) (6DT) reference compound **17a***

Reaction conditions adopted towards acquisition of spectrum *iv* were replicated in a separate batch experiment to isolate and characterise Knoevenagel intermediate **17a**. No diagnostic peak was found around 2243 cm^{-1} upon IR analysis however, therefore ruling out the presence of a nitrile functional group in the isolated material. This experimental evidence suggested that no Knoevenagel product **17a** was isolated in droplet-sized reaction mixtures as it underwent rapid intramolecular cyclisation to provide its more stable aromatic derivative **17b** (Scheme 7).

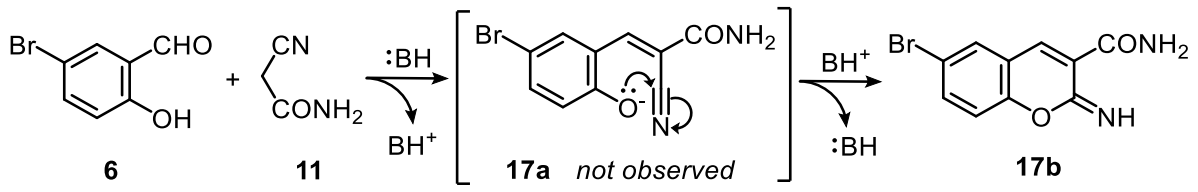

*Scheme 7. Proposed reaction mechanism towards 6-bromo-benzopyran-2-imine coumarin **17b** via Knoevenagel intermediate **17a***

Provided that all spectra acquired during these studies were recorded in DMSO-d_6, iminocoumarin **17b** detection *via* ^{1}H-NMR was more convoluted than expected, due to the presence of not only of benzopyran derivative **17b** but also of uncyclized analogue **17a**. A thorough spectroscopic study published by O'Callaghan *et al*. described how substituted benzopyran-2-imine derivatives underwent ring-opening at room temperature upon dissolution in DMSO-d_6.[95] Isomerisation of iminocoumarins into their respective ring-opened form in DMSO-d_6 was proven reversible and temperature dependent, further suggesting an equilibrium taking place upon sample preparation in DMSO-d_6.[95]

6-Bromobenzopyran-2-imine **17b,** previously isolated in batch conditions (Scheme 8), was fully characterised and (6DT) reference samples were prepared from the same batch and acquired in DMSO-d_6 and acetone-d_6 (Figure 43, Spectrum *ii*$_a$ and *ii*$_b$ respectively). Exclusive formation of 6-bromobenzopyran-2-imine **17b** in unquenched (6DT) runs was at last confirmed upon ^{1}H-NMR analysis in both deuterated solvents (Figure 43, Spectrum *i*$_a$ and *i*$_b$ respectively).

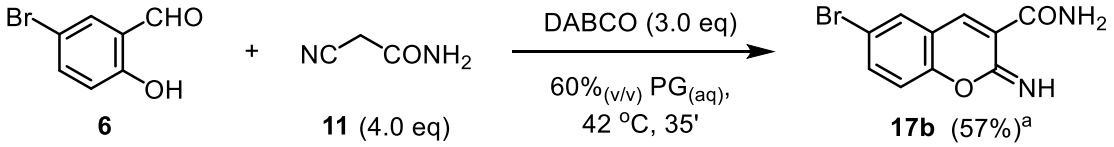

*Scheme 8. 6-bromobenzopyran-2-imine **17b** synthesis in (6DT) microreactor. [a.] Isolated yield in batch conditions*

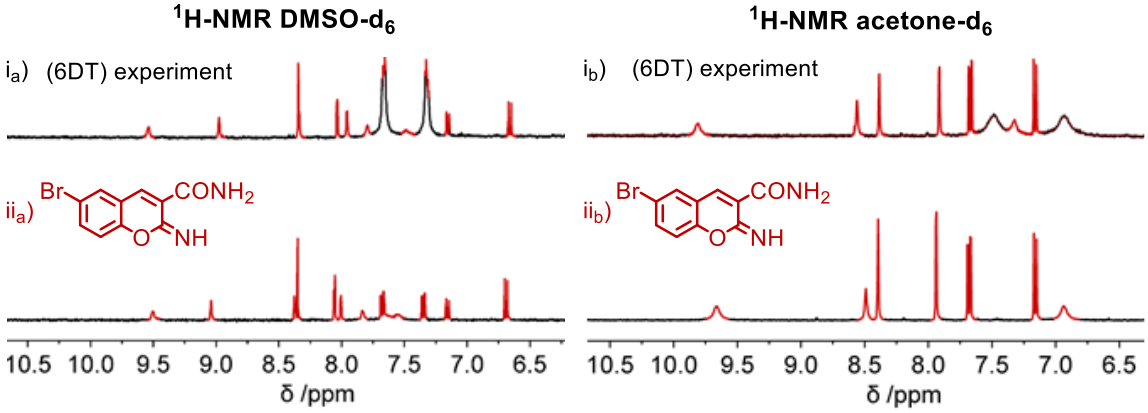

*Figure 43. ^{1}H-NMR spectra comparison for the identification of iminocoumarin **17b**, recorded in DMSO-d_6 (left) and acetone-d_6 (right), from top: i_a), i_b): (6DT) experiment; ii_a), ii_b) (6DT) reference compound **17b.***

2.4.2 3-cyanocoumarin 7 synthesis in 35%$_{(v/v)}$ PG$_{(aq)}$ (6DT) experiments

Starting from 4.0 equivalents of malononitrile **2**, synthesis of coumarin **7** was investigated in droplet chemistry conditions (Scheme 9). Although complete conversion of starting material **4** was achieved and desired product **7** was observed upon ^{1}H-NMR analysis, an unexpected signal pattern was detected whenever no diluted sulfuric acid was added (Figure 44, Spectra *iii* and *iv*).

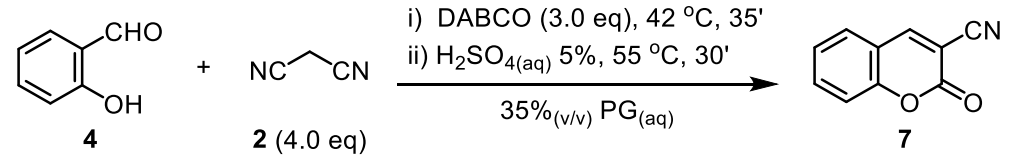

*Scheme 9. 3-cyano coumarin **7** synthesis in (6DT) microreactor.*

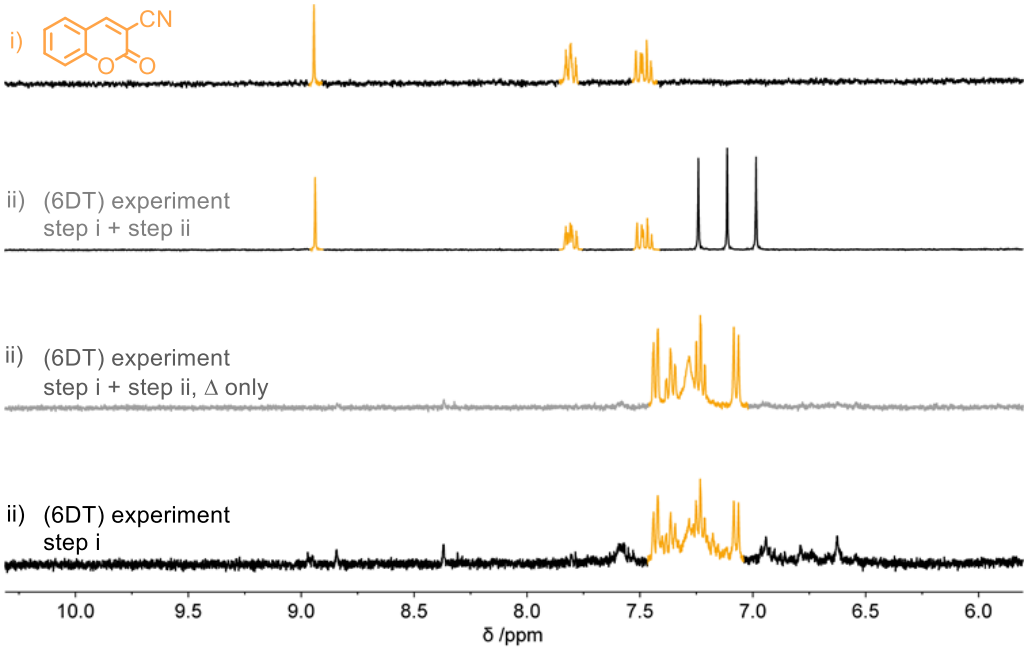

*Figure 44. ^{1}H-NMR stackplot comparison related to compound **7** synthesis in 35%$_{(v/v)}$ PG$_{(aq)}$, from top: i) (6DT) reference compound **7**; ii) (6DT) experiment (both step i and ii carried out); iii) (6DT) experiment (no acid addition was performed during step ii); iv) (6DT) (step i only).*

A thorough investigation for the identification of the newly formed intermediate began from the assumption that excess amounts of nucleophilic reagent can further react to provide Michael addition product **7b**, since iminocoumarin intermediate **7a** can be further attacked by deprotonated malononitrile **2,** the latter acting as a Michael donor (Scheme 10).

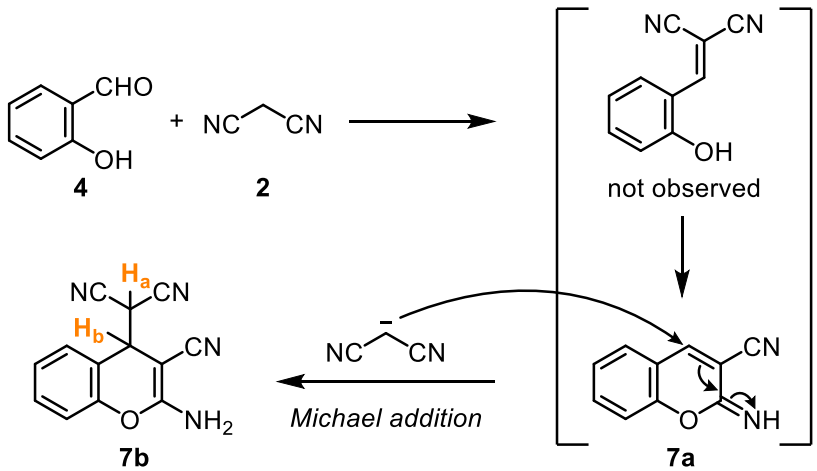

*Scheme 10. Proposed reaction mechanism towards Michael adduct **7b** synthesis*

Michael addition product **7b** was synthesised in a separate batch experiment in 7% yield (Scheme 11) and its related ^{1}H-NMR reference in (6DT) conditions was recorded in DMSO-d_6 (Figure 45, Spectrum *i*). Additional peaks can be identified in the aliphatic region and their detection was consistent with the presence of vicinal protons H_a and H_b (highlighted in orange, Scheme 10). Collected experimental evidence was compared against a second NMR sample where 3 equivalents of DABCO were introduced alongside compound **7b** (Figure 45, Spectrum *ii*) and a previously acquired (6DT) experiment in which no acid quenching and additional heating were carried out (Figure 45, Spectrum *iii*). Differences between spectra *i* and *ii* (Figure 45) were observed, with the ^{1}H-NMR signal pattern observed in the latter spectrum closely matching the one provided by the (6DT) experiment (Figure 45, Spectrum *iii*). These observations were consistent with formation of Michael adduct **7b** in unquenched droplets whenever a large excess of malononitrile **2** was utilised to promote complete consumption of salicyladehyde **4** in droplet reactors.

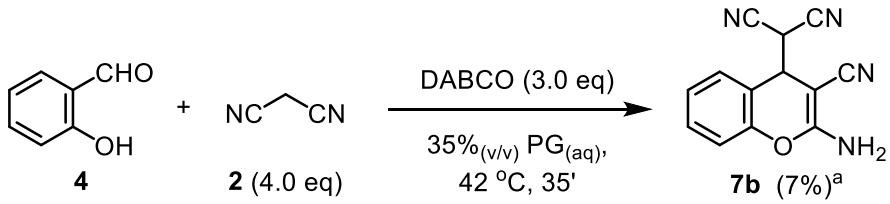

*Scheme 11. 6-bromobenzopyran-2-imine **7b** synthesis in (6DT) microreactor. [a] Isolated yield in batch conditions*

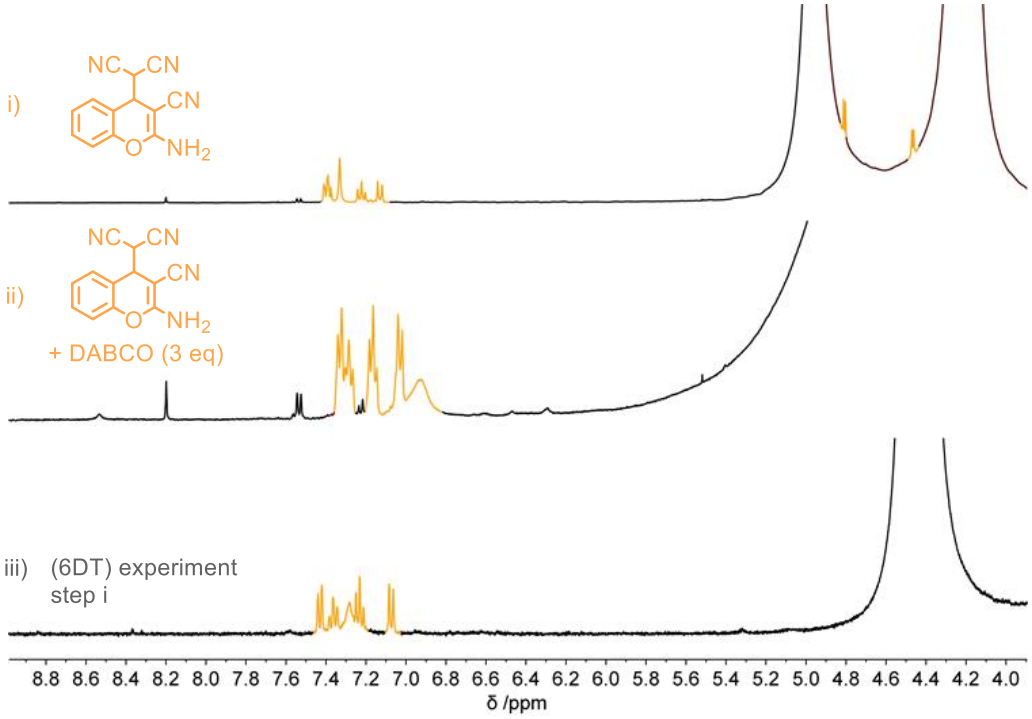

*Figure 45. ^{1}H-NMR stackplot comparison related to compound **7b** synthesis in (6DT) experiments, from top: i) (6DT) reference compound **7b** only ii) (6DT) reference compound **7b** spiked with excess of DABCO (3 eq.); iii) (6DT) experiment where both acid addition and additional heating were not carried out.*

2.4.3 6-methoxycoumarin-3-carboxylic acid 13 synthesis in 10%$_{(v/v)}$ PG$_{(aq)}$ (6DT) experiments

At first, optimised reaction conditions to observe complete starting material conversion into product **13** featured a large excess of nucleophilic reagent (Scheme 12). Detection of 6-methoxycoumarin-3-carboxylic acid **13** was observed upon comparison between ^{1}H-NMR spectra arising from the (6DT) test run and a previously prepared reference of the desired product (Figure 46, Spectra *ii* and *i* respectively).

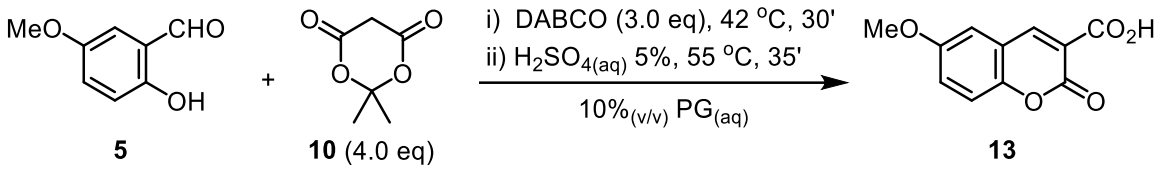

*Scheme 12. 3-methoxycoumarin-6-carboxylic acid **13** synthesis in (6DT) microreactor*

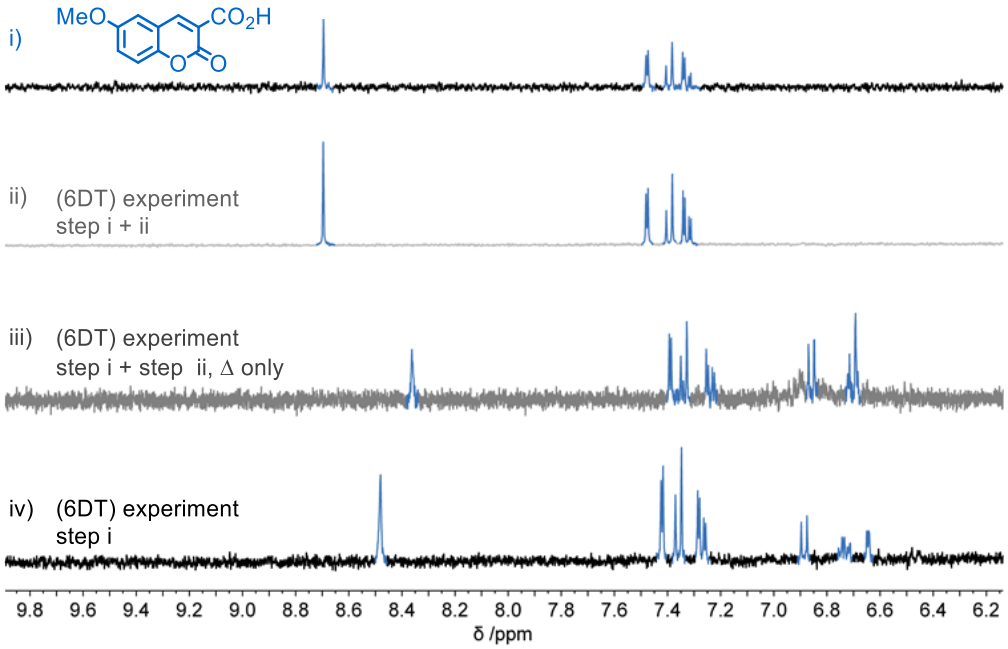

*Figure 46. ^{1}H-NMR stackplot comparison related to compound **13** synthesis in 10%$_{(v/v)}$ PG$_{(aq)}$, from top i) (6DT) reference compound **13**; ii) (6DT) experiment (both step i and ii carried out); iii) (6DT) experiment (no acid addition was performed during step ii); iv) (6DT) (step i only).*

The signal pattern observed in the ^{1}H-NMR spectra within 7.2-8.8 ppm was consistent with product **13** being produced in all (6DT) experiments, regardless of whether acid addition and/or additional heating were carried out after droplets collection. Nevertheless, undesired peaks were detected in 6.5-6.8 ppm range when no quenching agent was added to the coalesced droplets (Figure 46, Spectra *iii*, *iv*).

Provided that this set of (6DT) experiments were run with large excess of both base and Meldrum's acid **10**, the additional peaks detected upon ^{1}H-NMR analysis can be associated with the formation of dimer side-product **13a** (Scheme 13). A reaction mechanism leading to byproduct **13a** was proposed, which comprised initial deprotonation of excess nucleophile **10**

and Michael addition occurring between the newly generated carbanion and coumarin **13.** Ester hydrolysis of the resulting Michael adduct, and further deprotonation would occur as the single proton in alpha position between the carboxylic groups is acidic (highlighted in red, Scheme 13). The newly formed deprotonated adduct would react as a Michael donor towards a second molecule of coumarin **13**, which in turn behaves as a Michael acceptor. Formation of dimer **13a** would take place *via* decarboxylation of the second Michael addition product and detection of the intruding aromatic peaks found in ^{1}H-NMR spectra *iii* and *iv* (Figure 46) was consistent with the presence of additional aromatic protons found in side-product **13a** (highlighted in blue, Scheme 13).

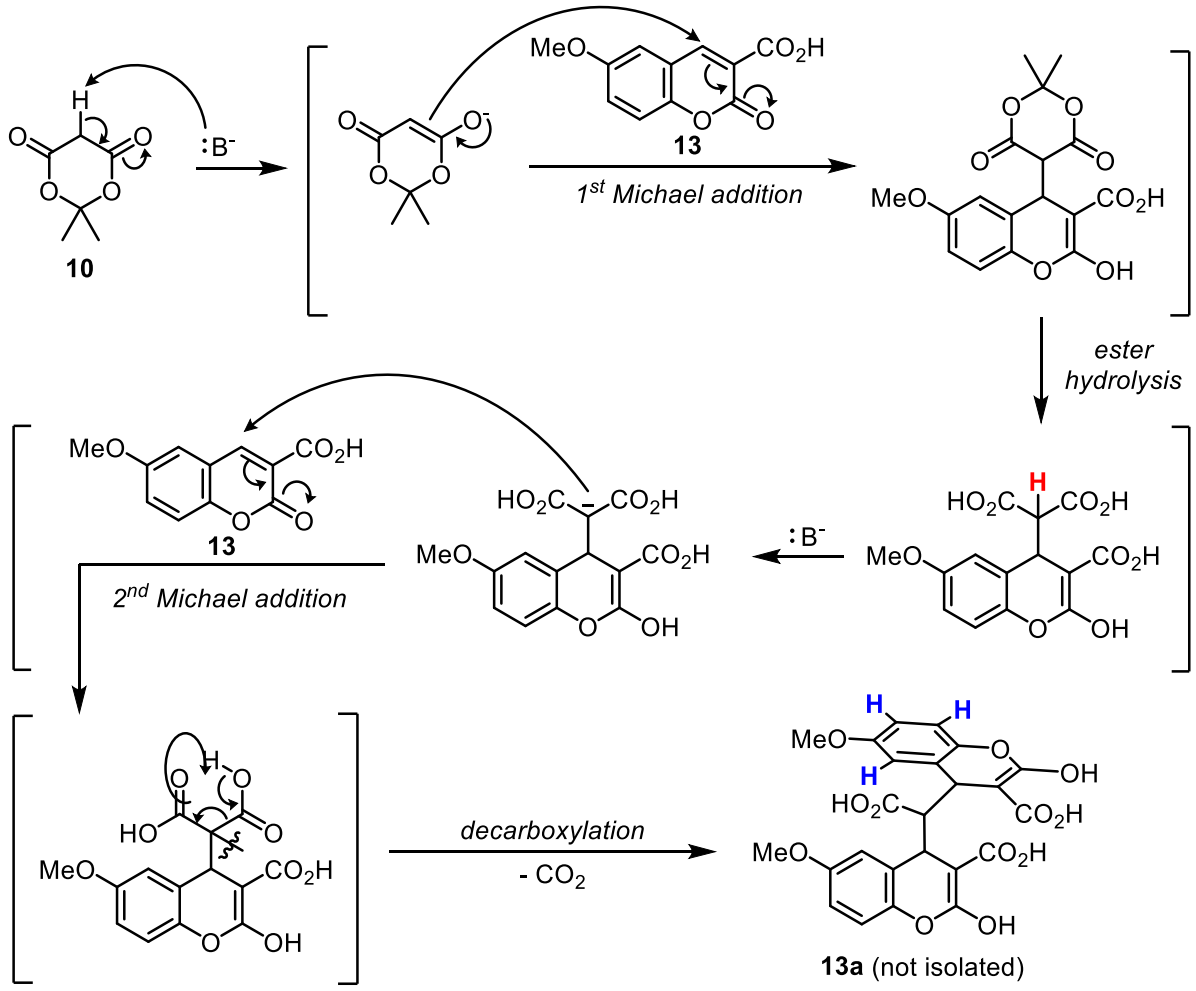

*Scheme 13. Proposed reaction mechanism leading to dimer byproduct **13a**.*

Decreasing amounts of nucleophile **10** were screened in additional (6DT) experiments while keeping the other reaction conditions unmodified (Scheme 14). Complete conversion of aldehyde precursor **5** into coumarin **13** with minimised dimer formation was achieved when 1.5 equivalents of Meldrum's acid **10** were used (Figure 47, Spectrum *ii*). Although synthesis of target compound **13** was successfully achieved with limited formation of dimer **13a**, it was noted that all aromatic peaks found in spectrum *ii* were not precisely aligning with the ^{1}H-NMR signal pattern recorded from the reference sample (Figure 47, Spectrum *i*).

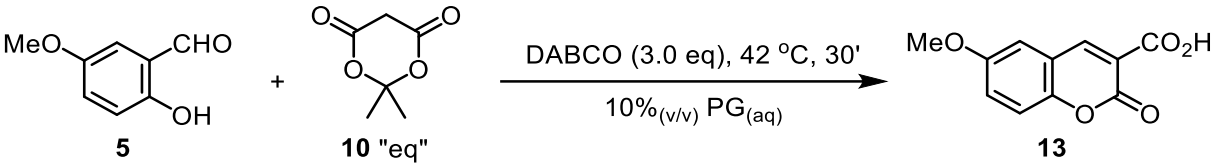

*Scheme 14. Coumarin **13** synthesis optimisation in (6DT) experiments.*

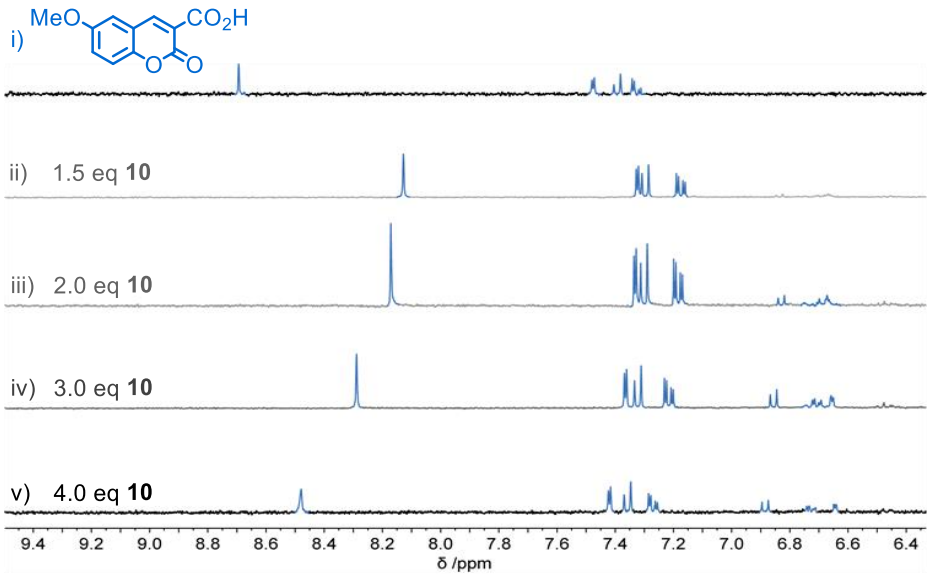

*Figure 47. ^{1}H-NMR stackplot comparison related to compound **13** synthesis in 10%$_{(v/v)}$ PG$_{(aq)}$, from top: i) (6DT) reference compound **13**; (6DT) experiments with increasing amounts of Meldrum's acid **10**: ii) 1.5 eq; iii) 2.0 eq, iv) 3.0 eq; v) 4.0 eq.*

Upon dilution of the sample that initially provided spectrum *ii*, ^{1}H-NMR signal pattern of coumarin **13** was found concentration dependent since the aromatic protons' chemical shifts were strongly affected by repeated dilutions. Once the pre-existing sample was sufficiently diluted, it was confirmed that no intermediate products were formed in this reaction, which directly yielded the desired coumarin 3-carboxylic acid **13** (Figure 48).

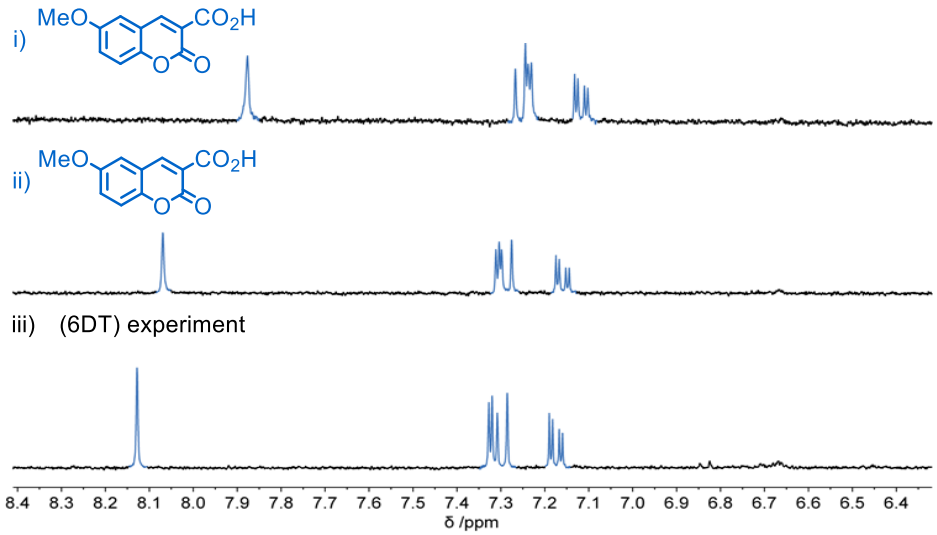

*Figure 48. ^{1}H-NMR stackplot comparison related to compound **13** synthesis in 10%$_{(v/v)}$ PG$_{(aq)}$, from top: (6DT) reference compound **13**: i) concentrated sample (0.744 mg/mL) ii) diluted sample (0.019 mg/mL); iii) (6DT) droplet run in which neither acid quenching and additional heating were carried out.*

2.5 Three-by-three droplet pair (3x3) chemical sorter

Following the reaction conditions optimised for droplet chemistry in (6DT) experiments, a three-by-three pair (3x3) droplet sorter was developed to prove the multi-droplet system feasibility for programmed and parallel synthesis of coumarins **13, 7** and **17** (Scheme 15, Supplementary Video S5, Section 3.7).

Fabrication of the droplet reactor was undertaken by tracing a hydrophobic track onto a clean, corona-discharged glass slide and deposition of blank 60%$_{(v/v)}$, 35%$_{(v/v)}$ and 10%$_{(v/v)}$ PG$_{(aq)}$ droplets in the sorting area (bottom left corner, red, yellow and blue circles respectively, Figure 49). Synthesis of coumarins **13**, **7** and **17** took place as soon the droplet pairs coalesced and carried on whilst the merged droplets approached their target destination. Once all droplet reactors reached their target locations, they were left on the heated surface for thirty minutes (Figure 49, step *i*). The droplet reactors were next transferred in three separate compartments and the overall process was repeated six times to achieve droplet chemistry samples suitable for analysis. Once all required droplet reactors were collected, they were treated with diluted acid and heated to promote the hydrolysis of intermediates into coumarins (Figure 49, step *ii*).

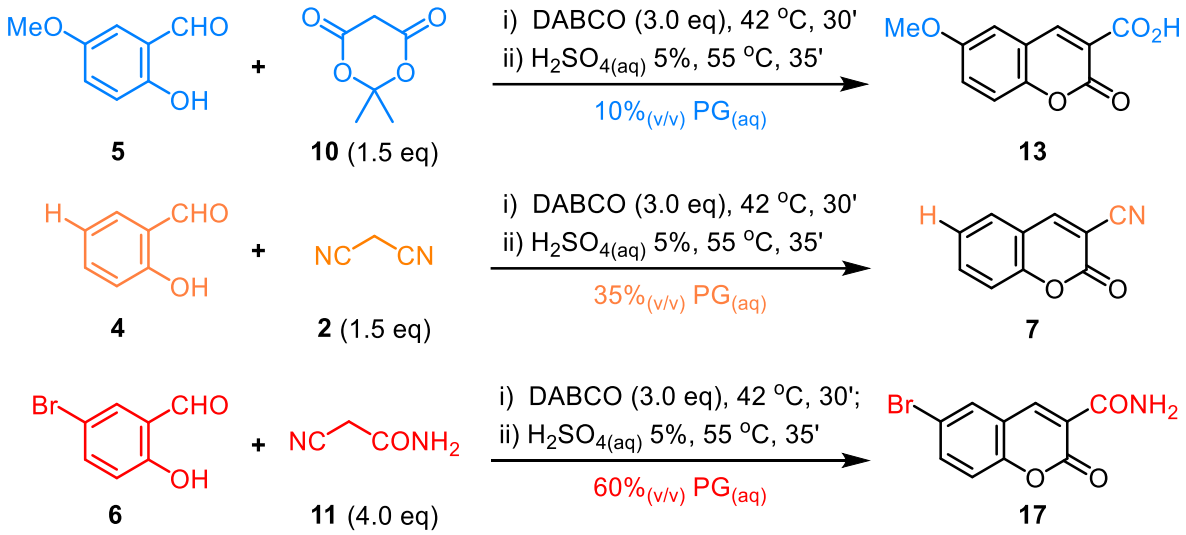

Scheme 15. 3,6-disubstituted coumarins synthesis in (3x3) droplet experiments.

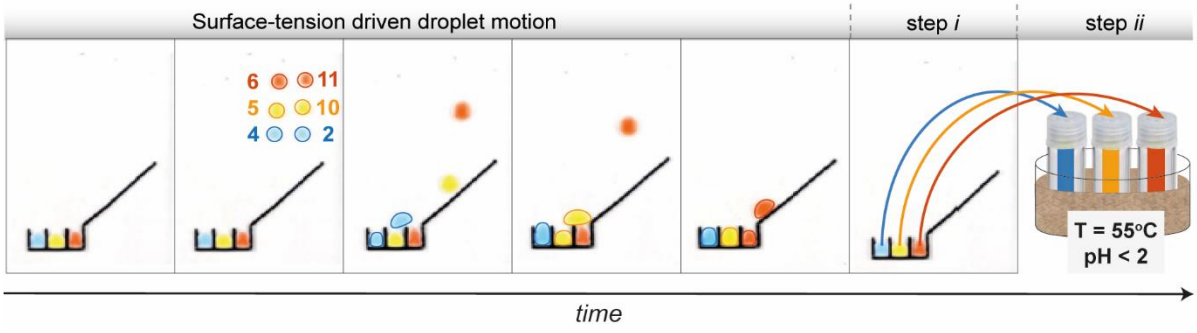

*Figure 49. Timelapse of a successful run in a (3x3) chemical sorter for parallel synthesis of coumarins **13**, **7** and **17**, front view, still images*

Several test runs were carried out to retrieve ^{1}H-NMR analytical evidence which were recorded in DMSO-d_6. ^{1}H-NMR spectra were obtained from isolated 10%$_{(v/v)}$, 35%$_{(v/v)}$ and 60%$_{(v/v)}$ PG$_{(aq)}$ (3x3) droplet reactors (Figure 50, Spectra *i-iii* respectively) and from an additional batch reaction in which all reagents were simultaneously introduced in a round bottom flask, mimicking the exact operating conditions used in the multi-droplet system (Figure 50, Spectrum *iv*). In addition, ^{1}H-NMR references of coumarins **13**, **7** and **17** were prepared replicating the droplet chemistry operating conditions (Figure 50, Spectra *v-vii*) and the ^{1}H-NMR spectra were compared within the aromatic chemical shift region (6.9-9.4 ppm). The ^{1}H-NMR signal pattern observed in the 10%$_{(v/v)}$ PG$_{(aq)}$ (3x3) sample (Figure 50, Spectrum *i*) matched the one given by reference compound **13** (Figure 50, Spectrum *v*) whereas the ^{1}H-NMR signal pattern provided by the 35%$_{(v/v)}$ PG$_{(aq)}$ (3x3) droplet microreactor (Figure 50, Spectrum *ii*) aligned with the ^{1}H-NMR reference spectrum of coumarin **7** (Figure 50, Spectrum *vi*). Matching signal patterns were also detected upon comparison between spectra arising from the 60%$_{(v/v)}$ PG$_{(aq)}$ (3x3) sample (Figure 50, Spectrum *iii*) and compound **9** ^{1}H-NMR reference (Figure 50, Spectrum *vii*).

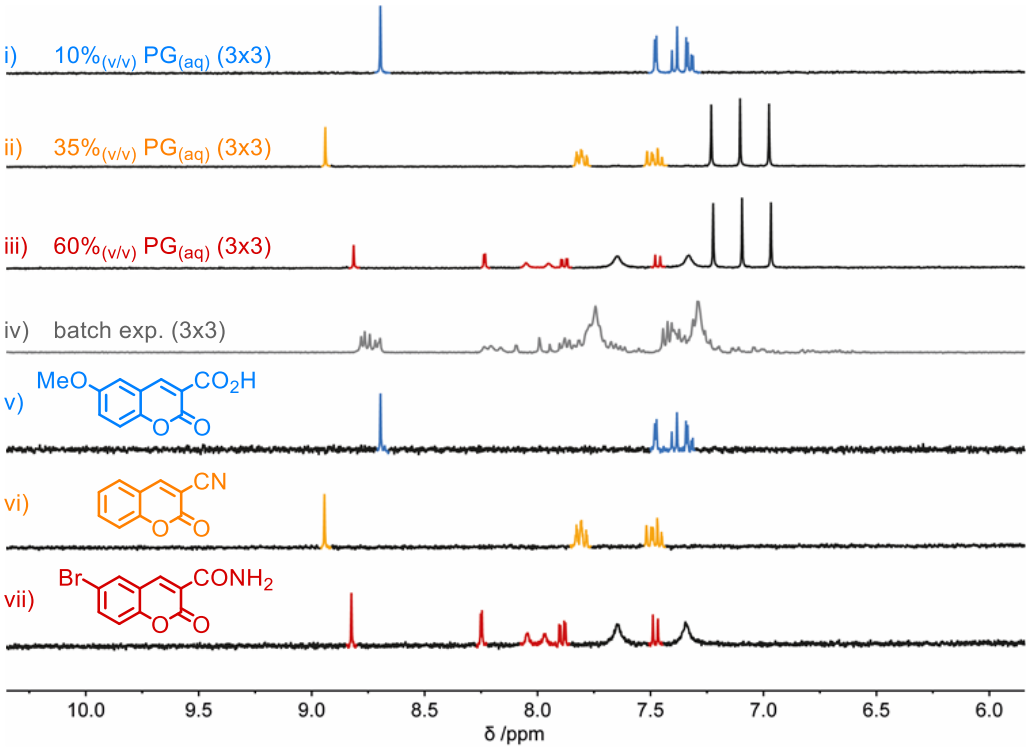

Figure 50. (3x3) droplet reactor ^{1}H-NMR spectra comparison, recorded in DMSO-d_6; from top: (3x3) droplet reactors: i) 10%$_{(v/v)}$ PG$_{(aq)}$, ii) 35%$_{(v/v)}$ PG$_{(aq)}$, iii) 60%$_{(v/v)}$ PG$_{(aq)}$, iv) (3x3) batch experiment; (3x3) reference compounds: v) 5-methoxycoumarin-3-carboxylic acid **13**, vi) 3-cyanocoumarin **7**, vii), 6-bromocoumarin-3-carboxamide **17**.

A relatively sharp 1:1:1 triplet is observed in ^{1}H-NMR spectra associated to both 35%$_{(v/v)}$ and 60%$_{(v/v)}$ PG$_{(aq)}$ (3x3) droplet runs (Figure 50, Spectra *ii* and *iii*). This particular multiplicity was associated to quadrupolar nucleus ^{14}N (having I = 1) coupling with neighbouring protons:

presence of inorganic ammonium species, which were produced *in situ* whilst coumarin formation occurred in droplets, was confirmed upon chemical shift and coupling constant measurements (~7 ppm, with $^{1}J_{1H\text{-}14N}$ = 51 Hz), which matched values previously reported in literature.[96]

^{1}H-NMR internal standards were next implemented in the (3x3) sorting device to determine reaction yields upon ^{1}H-NMR analysis of droplets. Provided that a vast array of compounds could be utilised for this purpose, the list of palatable compounds was at first focused on those which provided distinctive signals in the aromatic region. However, both fumaric acid and 3,5-dinitrobenzene were found to disrupt chemical reactivity in droplets. Conversely, DSS (sodium 3-(trimethylsilyl)-1-propanesulfonate) was found suitable for ^{1}H-NMR quantitation in droplet chemistry since it did not interact with any reacting species embedded in the droplets. Unlike the minor ^{1}H-NMR DSS signals observable within 0.8-3.1 ppm, a sharp singlet at 0.00 ppm, arising from the -$SiMe_3$ moiety, was easily identified despite of the redundant presence of PG and water, arising from the droplet reaction medium. Thus, ^{1}H-NMR yields were expressed as DSS-to-product ratios and were quantified in both (6DT) and (3x3) droplet sorter experiments (Table 4).

*Table 4. Salicylaldehydes **4-6** conversion rate determination via ^{1}H-NMR spectroscopy.*

Entry	$PG\%_{(aq)}$	Product	^{1}H-NMR Conversion rate[a]	
			(6DT)	(3X3)
1	$10\%_{(v/v)}$	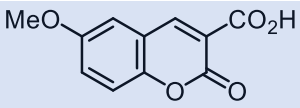	1:1	0.9:1
2	$35\%_{(v/v)}$	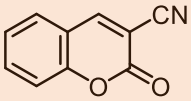	2.1:1	3:1
3	$60\%_{(v/v)}$	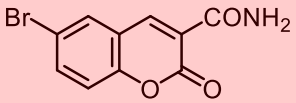	1:1	1.1:1

[a] *^{1}H-NMR Spectroscopy conversion rate expressed as DSS-to-product ratio*

Although the observed DSS-to-product ratios did not vary significantly in $10\%_{(v/v)}$ and $60\%_{(v/v)}$ $PG_{(aq)}$ droplet microreactors in experimental setups (Table 4, Entries 1 and 3 respectively), ^{1}H-NMR spectra arising from both (6DT) and (3x3) experiments carried out in $35\%_{(v/v)}$ $PG_{(aq)}$ droplets yielded lower conversion rates (Table 4, Entry 2). As complete conversion of aldehyde precursor **4** was observed in both cases, the inherent volatility that salicylaldehyde **4** displayed in both droplet reactors can explain the lower conversion rates observed in $35\%_{(v/v)}$ $PG_{(aq)}$. To prove this hypothesis, ^{1}H-NMR spectra were acquired from droplets containing only compound **4** and excess of DABCO, which were allowed to stand on the heated glass surface. Suspicions arising from the volatility exhibited by salicyladehyde **4** were confirmed upon ^{1}H-NMR analysis

as peaks related to the arylaldehyde **4** were observed having lower intensity when compared to the other screened aldehydes **5** and **6**. Selectivity was not observed when all reactant pairs were simultaneously added in a round bottom flask, since production of undesired cross-products took place in batch conditions. A convoluted signal pattern was detected (Figure 51, Spectrum *xiii*) upon comparison against the (3x3) ^{1}H-NMR references associated to each unwanted coumarin that may have formed (Figure 51, Spectra *vii-xii*).

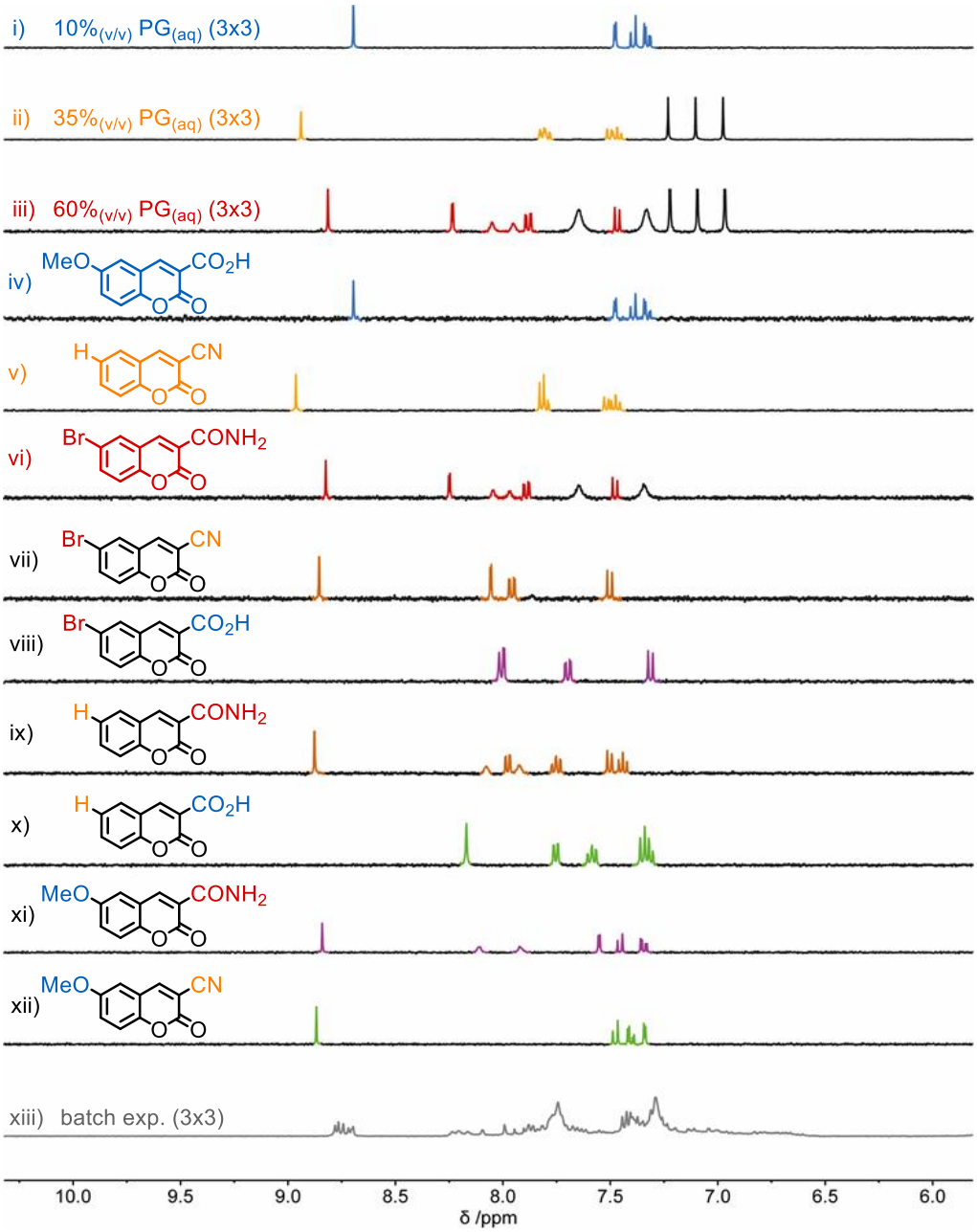

*Figure 51. (3x3) droplet reactor ^{1}H-NMR spectra comparison, recorded in DMSO-d_6; from top: (3x3) droplet reactors i) 10%$_{(v/v)}$ PG$_{(aq)}$, ii) 35%$_{(v/v)}$ PG$_{(aq)}$, iii) 60%$_{(v/v)}$ PG$_{(aq)}$; (3x3) reference compounds: iv) 3-cyanocoumarin **7**, v) 6-methoxycoumarin-3 carboxylic acid **13**, vi) 6-bromocoumarin-3-carboxamide **17**, vii) 6-bromo-3-cyanocoumarin **9**, viii) 6-bromocoumarin-3-carboxylic acid **14**, ix) coumarin-3-carboxamide **15**, x) coumarin-3-carboxylic acid **12**, xi) 6-methoxycoumarin-3-carboxamide **16**, (xii) 6-methoxy-3-cyanocoumarin **8**; xiii) (3x3) batch experiment.*

Overall, high degree of product selectivity was achieved only in single (3x3) droplet microreactors (Figure 51, Spectra *i-iii*): no unwanted aromatic cross-products were detected by ^{1}H-NMR, unlike the experimental result arising from synthetic conventional methodologies.

2.6 Conclusions and future outlook

Production of 3,6-disubstituted coumarins selectively took place as neighbouring droplets were simultaneously introduced in a sorting device, which only relied on differing surface tensions that droplets displayed and their consequent Marangoni-driven motion. No manipulation of external energy sources and additional human intervention were required to observe product selectivity in the developed droplet microreactors. Although further investigation would be required to optimise the measured ^{1}H-NMR yields observed in autonomously sorting $35\%_{(v/v)}$ $PG_{(aq)}$ droplets, a product quantification method was successfully implemented in the (3x3) droplet sorter, which featured in all cases complete conversion of starting materials, no undesired by-product formation and proven parallel and selective synthesis of the target compounds. Additional evidence can be gathered to support the research study herein discussed such as development of qualitative and quantitative HPLC methods for microlitre-sized droplet analysis.

Last but not least, it is pivotal to emphasise that repeated attempts were needed to gather the results herein discussed. Setup of six successful droplet reactions was required to achieve this experimental outcome, which was strongly affected by external operative parameters such as relative humidity (RH) of the area surrounding the droplet sorter. Instances by which the hydrophobic track partially dissolved upon prolonged contact with reactant-embedded droplets were also observed due to water evaporation, since PG/H_2O droplet reactors were left standing on heated glass slides over thirty minutes. Moreover, contact line pinning often occurred either after droplet pairs deposition or whilst droplet sorting was taking place, therefore making droplet coalescence and sorting less reliable. Thus, subsequent studies (e.g. statistical studies in better controlled RH surroundings, computation of recorded droplet runs) would be required to improve the multi-droplet systems' reliability and robustness towards chemical synthesis.

Overall, a wider application scope can be envisioned for droplet chemistry, therefore expanding the operations enabled by PG/H_2O droplets beyond reactions and controlled transport of fine chemicals - i.e., digital microfluidics, droplet logic computation, surface patterning, chemical and biological analysis.

Chapter 3

Experimental section

3.1 General methods

Reagents and solvents were purchased from Fisher Scientific, Sigma Aldrich or Alfa Aesar, and were used as received, unless specified. Column chromatography refers to purification of the mixture on 60 Å silica gel (70-230 µm mesh size) from Sigma Aldrich.[97] TLC was conducted using 2.00 cm x 5.00 cm aluminium backed plates coated with silica matrix (0.20 mm) and fluorescent indicator (254 nm). Visualisation of TLC was carried out using a UV lamp and iodine chamber staining.

NMR spectra were recorded in specified deuterated solvents purchased from Apollo Scientific™, at room temperature. Either a *Bruker*™ Avance IIII-HD-400 (400.07 MHz for ^{1}H; 100.60 MHz for ^{13}C), *Varian*™ VNMRS-600 (599.42 MHz for ^{1}H; 150.72 MHz for ^{13}C) or *Varian*™ VNMRS-700 (699.73 MHz for ^{1}H; 175.95 MHz for ^{13}C) spectrometer was utilised for ^{1}H and proton-decoupled ^{13}C NMR spectra acquisition. Chemical shifts were referenced to residual solvent peaks in the NMR solvent; $CDCl_3$ (δ_H = 7.26 ppm, δ_C = 77.00 ppm), DMSO-d_6 (δ_H = 2.50 ppm, δ_C = 39.52 ppm), acetone-d_6 (δ_H = 2.05 ppm, δ_C = 29.92 ppm).[98] Spectra were processed using *MestreNova* (V 11.0.1) and are reported as follows: chemical shift δ (ppm) (number of protons, multiplicity, coupling constant J (Hz)). Multiplicities are reported using the following abbreviations: s (singlet), d (doublet), dd (doublet of doublets), t (triplet) and m (unresolved multiplet). Product identification and peak assignments were completed using 2D spectra (COSY, HSQC, HMBC) where appropriate.

High-resolution mass spectra were obtained with an *LCT Premier XE* mass spectrometer (Waters Ltd., UK); all were obtained by Durham University Mass Spectrometry service. ASAP mass spectra were obtained using a *Waters*™ Synapt G2s apparatus, by Durham University Mass Spectrometry Service. ESI–LC MeCN (TQD) spectra were acquired using tandem Acquity UPLC (Waters Ltd, UK) and a TQD with ESI mass spectrometer. The UPLC was equipped with a Acquity UPLC BEH C18 1.7 µm (2.1 mm x 50 mm) column, and mobile phase composition of H_2O containing formic acid (0.1% v/v): Acetonitrile mobile phase (gradient elution; t = 0 min, 95%: 0%, t = 4 min, 5%: 95%), set at 0.6mL/min.

Infrared spectra were recorded on a *Perkin-Elmer*™ 1000 FT-IR spectrometer fitted with a Diamond attenuated total reflection (ATR) accessory (Golden Gate). Spectra were recorded from a range of 4000 – 380 cm^{-1} and assigned peaks are reported in wavenumbers (cm^{-1}), with the following abbreviations used to describe the appearance: s (strong, signal > 70% of

strongest signal), m (moderate, signal between 40-70% of the strongest signal), w (weak, signal < 40% of strongest signal), br (broad).

All XRD experiments were carried out by a crystallography experimental officer (Dr. Andrei S. Batsanov), using a *Bruker*™ *D8 Venture* equipped with Mo/Cu Dual IμS2 sources and an *Oxford Cryosystems*™ *HELIX* open flow helium cryostat (Temp. range: 25 – 300 K).

Melting points of solid crystalline products were recorded on a *Griffin*™ variable heater equipped with a 300 °C mercury thermometer. Solvents of crystallisation are listed along with the observed melting point range where appropriate.

3.1.1 Materials and Methods for droplet microscale synthesis

Glass slides (65.0 mm x 80.0 mm), were custom made by the glassblowing workshop service in Durham University and were thoroughly cleaned with detergent, washed with cold water and dried with acetone to minimise surface contamination. High energy surface was generated on the glass slide using an *Electro-Technic*™ laboratory corona treater (BD-20ACV) for twenty seconds. Hydrophobic tracks were traced with an *AxiDraw*™ V3 robotic arm onto the surface with a Sharpie™ marker. Water-propylene glycol droplets were placed onto a corona-discharged glass slide, placed onto a hot plate and heated at a constant temperature (42 °C), *via Gilson*™ pipette or syringes equipped with blunt needles. PG/H_2O droplet retrieval from the tilted glass slides was carried out *via Gilson*™ pipette. Micro-litre sized reactor transfer from the heated solid substrate was carefully undertaken to avoid unwanted cross contamination between droplet receptacles.

Droplet motions were captured using a camera *(Nikon*™ D5300 50 fps, 50 mm lens) placed at a 45° angle for post-experimental analysis. 5.00 mL stock solutions of water and propylene glycol (Sigma Aldrich, purity ≥ 99%) were prepared by pipetting the required volumes into a vial. Each stock solution was prepared as a volume percentage of propylene glycol (volume fraction.

^{1}H-NMR spectra were recorded in DMSO-d_6, which was purchased from Apollo Scientific™, at room temperature. A *Bruker*™ Avance IIII-HD-400 (400.07 MHz for ^{1}H) spectrometer was utilised for spectra acquisition and *MestreNova* software (V 11.0.1) was employed for data processing. Individual spectra and stackplots were referenced to the residual solvent peak found in DMSO-d_6 (δ_H = 2.50 ppm).[98] EI GC-MS spectra were obtained using a Shimadzu™ QP2010-Ultra apparatus.

3.2 Synthesis of benzilidenemalononitrile 3

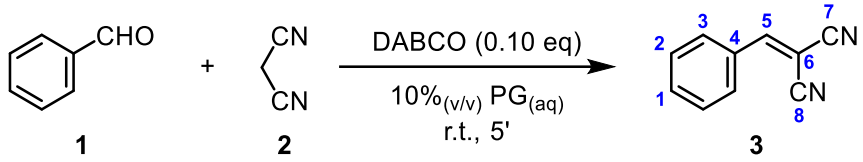

Experimental procedure was based on publications reported in literature.[94] Benzaldehyde **1** (0.102 mL, 1.00 mmol, 1.00 eq) and DABCO (0.02 M, 0.10 eq, 5.00 mL) were stirred in a mixture of water (4.50 mL) and propylene glycol (0.50 mL). Malononitrile **2** (0.07 g, 1.00 mmol, 1.00 eq) was added to the reaction mixture and instantaneous solid precipitation was observed. After five minutes, benzilidenemalononitrile **3** was isolated after filtration from the reaction mixture and re-crystallised in EtOH, to give pink needles (128 mg, 0.75 mmol, 75% yield). ^{1}H NMR (700 MHz, $CDCl_3$) δ 7.90 (2H, d, *J* = 7.5 Hz, H^3), 7.77 (1H, s, H^5), 7.63 (1H, t, *J* = 7.5 Hz, H^1), 7.54 (2H, t, *J* = 7.5 Hz, H^2);[99,100] ^{13}C NMR (101 MHz, $CDCl_3$) δ 159.9 (C^5), 134.6 (C^1), 130.9 (C^4), 130.7 (C^3), 129.7 (C^2), 113.6 (C^7), 112.5 (C^8), 82.9 (C^6);[99] LCMS (ASAP) *m/z*: $[M+H]^+$ 155.059 (100); HRMS (ASAP) m/z*:* calculated for $C_{10}H_7N_2^+$: 155.0609, found 155.0602 (-0.7 mDa, -4.5 ppm); IR (max/cm^{-1}): 3034w, 2223m, 1590m, 1567m, 1450m, 1100m, 958m, 754s, 677s, 616s; mp: 78-80 °C [EtOH];[101] XRD: Title compound was crystallised in EtOH, resulting in pink-coloured needles. Crystal data for $C_{10}H_6N_2$ (m = 154.17 g/mol): monoclinic, space group $P2_1/c$ (no. 14).

3.3 Synthesis of N-benzylcyanoacetamide 18

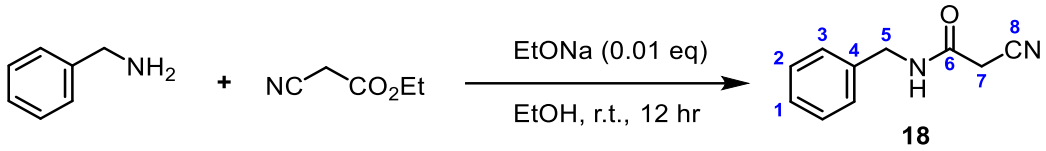

Title compound **18** was synthesised according to experimental procedure reported in literature.[102] Benzylamine (1.09 mL, 100 mmol, 1.00 eq) and ethyl cyanoacetate (1.06 mL, 100 mmol, 1.00 eq) were added to a sodium ethoxide solution (0.03 M, 0.01 eq) in ethanol (30.0 mL). The reaction mixture was stirred at room temperature for 12 hours and was monitored *via* TLC (hexanes:EtOAc, 1:1). A white precipitate was observed, which was separated by filtration and washed with Et_2O (100 mL). *N*-benzylcyanoacetamide **18** was isolated as a white solid without further purification (12.9 g, 74.1 mmol, 74% yield). ^{1}H NMR (600 MHz, $CDCl_3$) δ 7.38 – 7.24 (5H, m, $H^{1,2,3}$), 6.49 (1H, bs, NH), 4.44 (2H, d, *J* = 5.7 Hz, H^5), 3.36 (2H, s, H^7);[103] ^{13}C NMR (151 MHz, $CDCl_3$) δ 160.8 (C^6), 136.8 (C^4), 128.9 (C^2), 128.0 (C^1), 127.9 (C^3), 114.6 (C^8), 44.4 (C^5), 25.8 (C^7);[103] LRMS (ESI-TOF) *m/z*: $[M+H]^+$ 175.271 (53); $[M+Na]^+$ 197.254 (100); HRMS (ESI-TOF) *m/z*: calculated for $C_{10}H_{11}N_2O^+$: 175.0871, found 175.0865 (-0.6 mDa,

-3.4 ppm);[103] IR (max/cm^{-1}): 3307w, 2223m, 1644s, 1542s, 1455m, 1368m, 1231m, 1062w, 751m;[103] mp: 131-132 °C;[103] XRD: A portion of isolated product was crystallised in EtOH/H_2O, resulting in colourless needles. Crystal data for $C_{10}H_{10}N_2O$ (m = 174.20 g/mol): monoclinic, space group $P2_1/c$ (no. 14).

3.4 Coumarins reference synthesis in batch conditions

3.4.1` General procedure for the synthesis of 6-substituted-2-oxo-2H-chromene-3-carbonitriles 7-9

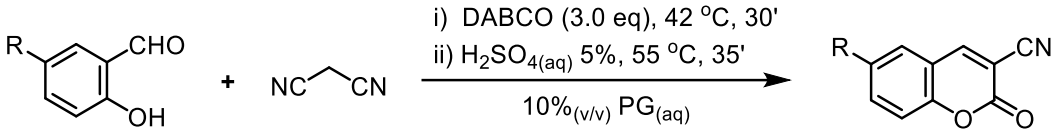

4-6 **2** **7-9**

5-substituted salicylaldehyde **4-6** (1.00 eq) was added to a heated solution of DABCO (0.013 M, 3.00 eq) in 10%$_{(v/v)}$ PG$_{(aq)}$. Malononitrile **2** (1.50 eq) was added, and the reaction mixture was stirred at 42 °C for thirty minutes (step *i*). 5%$_{(v/v)}$ $H_2SO_{4(aq)}$ was added after complete consumption of starting materials **4-6** and the acidified reaction mixture was stirred at 55 °C for thirty-five minutes (step *ii*). A solid was observed in suspension which was separated by vacuum filtration. The filtrate was next extracted with CH_2Cl_2 (40 mL x 3). The organic phase was dried ($MgSO_4$) and concentrated *in vacuo,* yielding 6-substituted-2-oxo-2H-chromene-3-carbonitriles **7-9.** Further purification of both residue and filtered solid was carried out where appropriate by crystallisation.

2-oxo-2H-chromene-3-carbonitrile 7

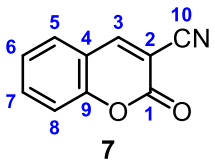

7

Following the general procedure described in **3.4.1**, using salicylaldehyde **4** (52.0 µl, 0.50 mmol), title compound **7** was isolated *via* crystallisation in EtOH (65.0 mg, 0.38 mmol, 76% yield). ^{1}H NMR (600 MHz, DMSO-d_6) δ 8.94 (1H, s, H^3), 7.83 – 7.76 (2H, m, $H^{5,7}$), 7.49 (1H, d, *J* = 7.9 Hz, H^8), 7.46 (1H, t, *J* = 8.1 Hz, H^6);[104] ^{13}C NMR (151 MHz, DMSO-d_6) δ 156.9 (C^1), 154.1 (C^9), 153.5 (C^3), 135.5 (C^7), 130.0 (C^5), 125.5 (C^6), 117.5 (C^4), 116.8 (C^8), 114.6 (C^{10}), 102.1 (C^2);[104] LCMS (ASAP) *m/z*: $[M+H]^+$ 172.000 (65), $[M]^+$ 171.1 (100);[104] HRMS (ASAP) *m/z*: $[M+H]^+$ calculated for $C_{10}H_6NO_2^+$: 172.0399, found 172.0405 (0.6 mDa, 3.5 ppm); IR (max/cm^{-1}): 3043w, 2230m, 1723s, 1604s, 1186m, 971m, 758s; mp: 175-176 °C [PhMe/$CHCl_3$];[105] XRD: Title compound was crystallised in PhMe/$CHCl_3$, yielding yellow crystals. Crystal data for $C_{10}H_5NO_2$ (m = 171.15 g/mol): monoclinic, space group $P2_1/c$ (no. 14).

6-methoxy-2-oxo-2H-chromene-3-carbonitrile 8

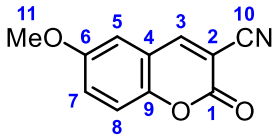

8

Following the general procedure described in **3.4.1**, using 5-methoxysalicylaldehyde **5** (0.31 g, 2.00 mmol), title compound **8** was isolated *via* crystallisation in EtOH (0.11 g, 0.55 mmol, 23% yield). ^{1}H NMR (700 MHz, DMSO-d_6) δ 8.82 (1H, s, H^3), 7.43 (1H, d, *J* = 9.2 Hz, H^8), 7.37 (1H, dd, *J* = 9.2, 2.8 Hz, H^7), 7.30 (1H, d, *J* = 2.8 Hz, H^5), 3.80 (3H, s, H^{11});[106] ^{13}C NMR (176 MHz, DMSO-d_6) δ 157.4 (C^1), 156.5 (C^6), 153.6 (C^3), 149.0 (C^9), 123.6 (C^7), 118.4 (C^8), 118.33 (C^4), 115.1 (C^2), 111.9 (C^5), 102.8 (C^{10}), 56.3 (C^{11});[106] LCMS (ASAP) *m/z*: $[M+H]^+$ 202.0529 (73), $[M]^+$ 201.0662 (100); HRMS (ASAP) *m/z*: $[M+H]^+$ calculated for $C_{11}H_8NO_3^+$: 202.0504, found 202.0508 (0.4 mDa, 2.0 ppm); IR (max/cm^{-1}): 3094w, 2233m, 1752s, 1568s, 1279s, 1191m, 1022s, 873m, 759s; mp: 224-225 °C [PhMe/EtOH];[107] XRD: Portion of title compound was crystallised in PhMe, resulting in yellow plates. Crystal data for $C_{10}H_7NO_3$ (m = 201.18 g/mol): triclinic, space group P_1 (no. 2).

6-bromo-2-oxo-2H-chromene-3-carbonitrile 9

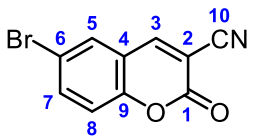

9

Following the general procedure described in **3.4.1**, using 5-bromosalicylaldehyde **6** (0.40 g, 2.00 mmol), title compound **9** was isolated *via* crystallisation in EtOH (0.20 g, 0.81 mmol, 41% yield). ^{1}H NMR (600 MHz, DMSO-d_6) δ 8.84 (1H, s, H^3), 8.06 – 8.01 (1H, m, H^5), 7.96 – 7.90 (1H, m, H^7), 7.48 (1H, d, *J* = 8.9 Hz, H^8);[108] ^{13}C NMR (151 MHz, DMSO-d_6) δ 156.4 (C^1), 153.1 (C^9), 152.0 (C^3), 137.5 (C^7), 131.7 (C^5), 119.2 (C^4), 119.1 (C^8), 116.9 (C^6), 114.3 (C^{10}), 103.4 (C^2);[108,109] LRMS (ASAP) *m/z*: $[^{79}BrM+H]^+$ 249.945 (100), $[^{81}BrM+H]^+$ 251.944 (100); HRMS (ASAP) *m/z*: $[M+H]^+$ calculated for $C_{10}H_5NO_2{}^{79}Br^+$: 249.9504, found 249.9513 (0.9 mDa, 3.6 ppm); IR (max/cm^{-1}): 3094w, 2239m, 1732s, 1354m, 1185s, 1053m, 833s, 761s; mp: 196-197 °C [PhMe];[108] XRD: A portion of title compound was crystallised in PhMe, resulting in colourless plates. Crystal data for $C_{10}H_4BrNO_2$ (m = 250.05 g/mol): monoclinic, space group $P2_1/c$ (no. 14).

3.4.2 General procedure for the synthesis of 6-substituted-2-oxo-2H-chromene-3-carboxylic acids 12-14

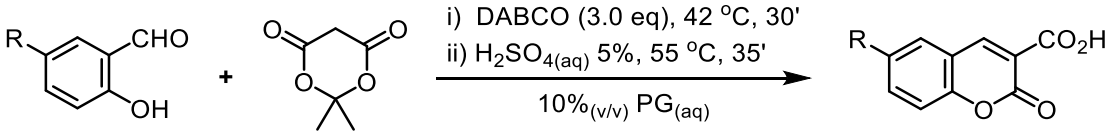

4-6 **10** **12-14**

5-substituted salicylaldehyde **4-6** (1.00 eq) was added to a heated solution of DABCO (0.013 M, 3.00 eq) in 10%$_{(v/v)}$ PG$_{(aq)}$. 2,2-dimethyl-1,3-dioxane-4,6-dione **10** (1.50 eq) was added and the reaction mixture was stirred at 42 °C for thirty minutes (step *i*). 5%$_{(v/v)}$ $H_2SO_{4(aq)}$ was added

after complete consumption of starting materials **4-6** and the acidified reaction mixture was stirred at 55 °C for thirty-five minutes (step *ii*). A solid was observed in suspension which was separated by vacuum filtration. The filtered reaction mixture was next extracted with CH_2Cl_2 (40 mL x 3). The organic phase was dried ($MgSO_4$) and concentrated *in vacuo,* yielding 6-substituted-2-oxo-2H-chromene-3-carboxylic acids **12-14.**

2-oxo-2H-chromene-3-carboxylic acid 12

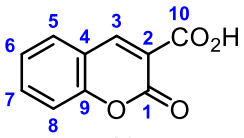

12

Following the general procedure outlined in **3.4.2** using salicylaldehyde **4** (0.26 mL, 2.50 mmol, 1.00 eq), the reaction mixture was directly extracted with CH_2Cl_2 (50 mL x 3) after H_2SO_4 addition and heating (step *ii*). Title compound **12** was obtained as a white solid after reaction workup and residue trituration with water (0.33 g, 1.72 mmol, 69% yield). ^{1}H NMR (600 MHz, DMSO-d_6) δ 13.20 (1H, bs, -OH), 8.72 (1H, s, H^3), 7.89 (1H, d, *J* = 7.6 Hz, H^5), 7.71 (1H, t, *J* = 8.3 Hz, H^7), 7.41 (1H, d, *J* = 8.3 Hz, H^8), 7.39 (1H, t, *J* = 7.5 Hz, H^6);[110] ^{13}C NMR (151 MHz, DMSO-d_6) δ 164.4 (C^{10}), 156.8 (C^1), 154.5 (C^9), 148.4 (C^3), 134.3 (C^7), 130.2 (C^5), 124.8 (C^6), 118.4 (C^2), 118.0 (C^4), 116.1 (C^8);[110] LRMS (ESI-TOF) *m/z:* $[M+H]^+$ 191.108 (100); HRMS (ESI-TOF) ***m/z*:** $[M+H]^+$ Calculated $C_{10}H_7O_4^+$: 191.0344, found 191.0347 (0.3 mDa, 1.6 ppm); IR (max/cm^{-1}): 2931w, 1737s, 1672s, 1607m, 1567m, 1415s, 1373m, 1226m, 1040m, 800s, 766s, 646s, 468s; mp: 186-187 °C [EtOH];[110] XRD: A portion of isolated product was crystallised in $CHCl_3$, yielding colourless crystals. Crystal data for $C_{10}H_6O_4$ (m = 190.15 g/mol): monoclinic, space group $P2_1/n$ (no.14).

6-methoxy-2-oxo-2H-chromene-3-carboxylic acid 13

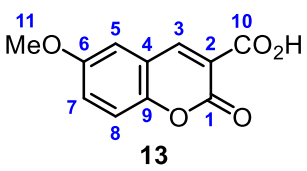

13

Following the general procedure outlined in **3.4.2** using 5-methoxysalicylaldehyde **5** (0.31 mL, 2.50 mmol, 1.00 eq), 6-methoxycoumarin-3-carboxylic acid **13** was isolated as a yellow solid without further purification (0.40 g, 1.82 mmol, 73% yield). ^{1}H NMR (600 MHz, DMSO-d_6) δ 13.22 (bs, 1H, -OH), 8.64 (1H, s, H^3), 7.46 (1H, d, *J* = 3.0 Hz, H^5), 7.37 (1H, d, *J* = 9.0 Hz, H^8), 7.31 (1H, dd, *J* = 9.0, 3.0 Hz, H^7), 3.81 (3H, s, H^{11});[110] ^{13}C NMR (151 MHz, DMSO-d_6) δ 164.0 (C^{10}), 157.0 (C^1), 155.7 (C^6), 148.9 (C^9), 148.1 (C^3), 122.0 (C^7), 118.5 (C^2), 118.4 (C^4), 117.2 (C^8), 111.8 (C^5), 55.8 (C^{11});[110] LRMS (ESI-TOF) *m/z*: $[M+H]^+$ 221.121 (100); HRMS (ESI-TOF) *m/z*: $[M+H]^+$ Calculated for $C_{11}H_9O_5^+$: 221.0450, found 221.0450 (0.0 mDa, 0.0 ppm); IR (max/cm^{-1}): 3054w, 1750s, 1677m, 1571s, 1352m, 1243m, 1197m, 1019s, 797s, 628m, 564m; mp: 200-201 °C [PhMe/EtOH];[110] XRD: A portion of isolated product was crystallised in THF, resulting in yellow triangular plates. Crystal data for $C_{11}H_8O_5$ (m = 220.17 g/mol): monoclinic, space group $P2_1$ (no. 4).

6-bromo-2-oxo-2H-chromene-3-carboxylic acid 14

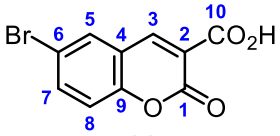

14

Following the general procedure outlined in **3.4.2** using 5-bromosalicylaldehyde **6** (0.40 g, 2.00 mmol, 1.00 eq), 6-bromocoumarin-3-carboxylic acid **14** was isolated as a white solid without further purification (0.44 g, 1.64 mmol, 82% yield). ^{1}H NMR (700 MHz, DMSO-d_6) δ 13.38 (1H, bs, OH), 8.68 (1H, s, H^3), 8.15 (1H, d, *J* = 2.4 Hz, H^5), 7.85 (1H, dd, *J* = 8.8, 2.4 Hz, H^7), 7.40 (1H, d, *J* = 8.8 Hz, H^8);[110] ^{13}C NMR (176 MHz, DMSO-d_6) δ 163.7 (C^{10}), 156.1 (C^1), 153.5 (C^9), 146.9 (C^3), 136.4 (C^7), 132.0 (C^5), 119.9 (C^4), 119.5 (C^2), 118.4 (C^8), 116.2 (C^6);[110] LRMS (ASAP) *m/z*: [^{79}BrM+H]$^+$ 268.946 (99), [^{81}BrM+H]$^+$ 270.944 (100); HRMS (ASAP) *m/z*: [M+H]$^+$ Calculated for $C_{11}H_6O_4{}^{79}Br^+$: 268.9449, found 268.9461 (1.2 mDa, 4.5 ppm); IR (max/cm^{-1}): 3027w, 2980w, 1740m, 1673m, 1557s, 1363s, 1206s, 1031s, 820s, 666s, 518m; mp: 193-195 °C [EtOH];[110] XRD: A portion of isolated product was crystallised in EtOH, yielding colourless, block-shaped crystals. Crystal data for $C_{10}H_5BrO_4$ (m = 269.05 g/mol): monoclinic, space group $P2_1/c$ (no. 14).

3.4.3 General procedure for the synthesis of 6-substituted 2-oxo-2H-chromene-3-carboxamides 15-17

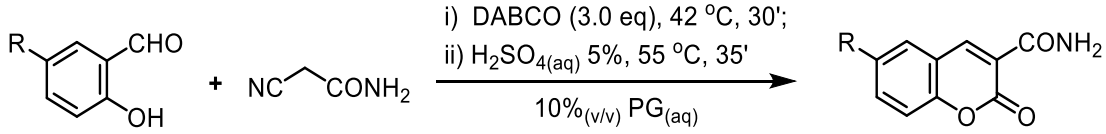

4-6 **11** **15-17**

5-substituted salicylaldehyde **4-6** (1.00 eq) was added to a heated solution of DABCO (0.013 M, 3.00 eq) in 10%$_{(v/v)}$ PG$_{(aq)}$. Cyanoacetamide **11** (4.00 eq) was added, and the reaction mixture was stirred at 42 °C (step *i*). 5%$_{(v/v)}$ $H_2SO_{4(aq)}$ was added after complete consumption of starting materials **4-6** and the acidified reaction mixture was stirred at 55 °C (step *ii*). A solid was observed in suspension which was separated by vacuum filtration. The filtered reaction mixture was next extracted with CH_2Cl_2 (40 mL x 3). The organic phase was dried ($MgSO_4$) and concentrated *in vacuo,* yielding 6-substituted 2-oxo-2H-chromene-3-carboxamides **15-17.** Further purification of both residue and filtered solid was carried out by crystallisation in EtOH or MeOH.

2-oxo-2H-chromene-3-carboxamide 15

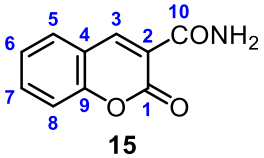

15

Following the general procedure outlined in **3.4.3** using salicylaldehyde **4** (0.42 mL, 4.05 mmol, 1.00 eq), title compound **15** was isolated as a white solid *via* crystallisation in EtOH (0.35 g, 1.86 mmol, 46% yield). ^{1}H NMR (700 MHz, DMSO-d_6) δ 8.87 (1H, s, H^3), 8.07 (1H, bs, -NH), 7.97 (1H, dd, *J* = 7.8, 1.7 Hz, H^5), 7.91 (1H, bs, -NH), 7.75 (1H, td, *J* = 7.9, 1.6 Hz, H^7), 7.50

(1H, d, *J* = 8.1 Hz, H^8), 7.44 (1H, t, *J* = 7.3 Hz, H^6);[111] ^{13}C NMR (176 MHz, DMSO-d_6) δ 162.5 (C^{10}), 160.3 (C^1), 154.0 (C^9), 147.8 (C^3), 134.1 (C^5), 130.3 (C^7), 125.1 (C^6), 119.3 (C^2), 118.5 (C^4), 116.1 (C^8); LRMS (ASAP) *m/z*: $[M+H]^+$ 190.052 (100);[111] HRMS (ASAP) *m/z:* $[M+H]^+$ Calculated $C_{10}H_8NO_3^+$: 190.0504, found 190.0502 (-0.2 mDa, -1.1 ppm); IR (max/cm^{-1}): 3384m, 3132w, 1709s, 1589m, 1561s, 1387m, 1160m, 1007m, 768s, 614s, 579s; mp: 264-265 °C [EtOH/H_2O];[111] XRD: Title compound was re-crystallised in EtOH/H_2O, resulting in clear colourless plates. Crystal data for $C_{10}H_7NO_3$ (m = 189.17 g/mol): monoclinic, space group $P2_1/c$ (no. 14).

6-methoxy-2-oxo-2H-chromene-3-carboxamide 16

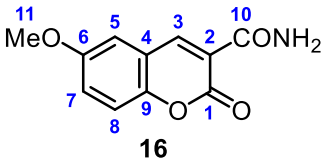

16

Following the general procedure outlined in **3.4.3** using 5-methoxysalicylaldehyde **5** (0.32 mL, 2.56 mmol, 1.00 eq), 6-methoxy-2-oxo-2H-chromene-3-carboxamide **15** was isolated as a yellow powder *via* crystallisation in EtOH (0.50 g, 2.28 mmol, 89% yield). ^{1}H NMR (700 MHz, DMSO-d_6) δ 8.82 (1H, s, H^3), 8.10 (bs, 1H, NH), 7.90 (bs, 1H, NH), 7.52 (1H, d, *J* = 3.0 Hz, H^5), 7.43 (1H, d, *J* = 8.9 Hz, H^8), 7.32 (1H, dd, *J* = 8.9, 3.0 Hz, H^7), 3.79 (3H, s, H^{11}); ^{13}C NMR (176 MHz, DMSO-d_6) δ 162.5 (C^{10}), 160.4 (C^1), 155.9 (C^6), 148.5 (C^9), 147.7 (C^3), 121.9 (C^7), 119.3 (C^2), 118.9 (C^4), 117.2 (C^8), 111.8 (C^5), 55.8 (C^{11}); LRMS (ASAP) *m/z*: $[M+H]^+$ 220.060 (100); HRMS (ASAP) *m/z*: $[M+H]^+$ Calculated for $C_{11}H_{10}O_4^+$: 220.0610, found 220.0611 (0.1 mDa, 0.5 ppm); IR (max/cm^{-1}) 3421m, 3134m, 1698s, 1490s, 1260s, 1018s, 826s, 800s, 613s, 582s; mp: 200-201 °C [EtOH/H_2O]; XRD: Title compound was crystallised in EtOH/H_2O, resulting in colourless crystals. Crystal data for $C_{10}H_9NO_4$ (m = 219.19 g/mol): monoclinic, space group $P2_1/n$ (no. 14).

6-bromo-2-oxo-2H-chromene-3-carboxamide 17

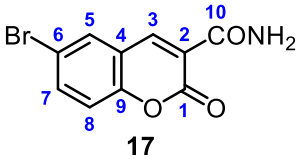

17

Following the general procedure outlined in **3.4.3** using 5-bromosalicylaldehyde **6** (0.64 g, 3.18 mmol, 1.00 eq), 6-bromo-2-oxo-2H-chromene-3-carboxamide **17** was isolated as white needles *via* crystallisation in MeOH (0.61 g, 2.28 mmol, 71% yield). ^{1}H NMR (700 MHz, DMSO-d_6) δ 8.81 (1H, s, H^3), 8.22 (1H, d, *J* = 2.6 Hz, H^5), 8.03 (1H, bs, NH), 7.95 (1H, bs, NH), 7.86 (1H, dd, *J* = 8.8, 2.6 Hz, H^7), 7.45 (1H, d, *J* = 8.8 Hz, H^8);[111] ^{13}C NMR (176 MHz, DMSO-d_6) δ 162.2 (C^{10}), 159.8 (C^1), 153.0 (C^9), 146.4 (C^3), 136.2 (C^7), 132.1 (C^5), 120.4 (C^2), 120.3 (C^4), 118.4 (C^8), 116.7 (C^6);[111] LRMS (ASAP) *m/z*: $[^{79}BrM+H]^+$ 267.969 (99), $[^{81}BrM+H]^+$ 269.958 (100); HRMS (ASAP) *m/z*: $[M+H]^+$ calculated for $C_{10}H_7NO_3{}^{79}Br^+$: 267.9609 found: 267.9608 (-0.1 mDa, -0.4 ppm); IR (max/cm^{-1}): 3424m, 3037m, 1709s, 1692s, 1555s, 1379m, 830s, 793s, 595s; mp: 238-239 °C (product decomposed);[111] XRD: Title compound

was crystallised in MeOH/CH_2Cl_2, resulting in colourless prisms. Crystal data for $C_{10}H_6BrNO_3$ (m = 268.07 g/mol): triclinic, space group P_1 (no. 2).

3.4.4 General procedure for the synthesis of 6-substituted *N*-benzyl-2-oxo-2H-chromene-3-carboxamides 19-21

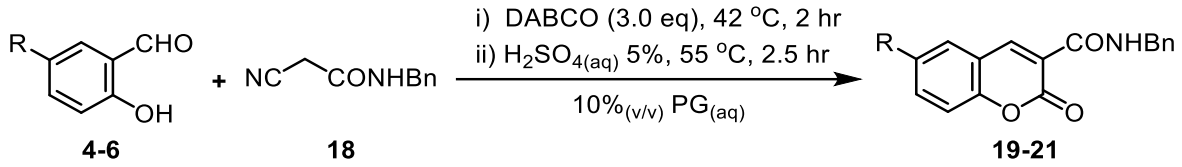

4-6 **18** **19-21**

5-substituted salicylaldehyde **4-6** (1.00 eq) was added to a heated solution of DABCO (0.013 M, 3.00 eq) in 10%$_{(v/v)}$ PG$_{(aq)}$. *N*-benzylcyanoacetamide **18** (4.00 eq) was added and the reaction mixture was stirred at 42 °C for two hours (step *i*). 5%$_{(v/v)}$ $H_2SO_{4(aq)}$ was added after complete consumption of starting materials **4-6** and the acidified reaction mixture was stirred at 55 °C (step *ii*). A solid was observed in suspension which was separated by vacuum filtration, yielding coumarins **19-21.** Further purification of both residue and filtered solid was carried out by crystallisation in EtOH.

N-benzyl-2-oxo-2H-chromene-3-carboxamide 19

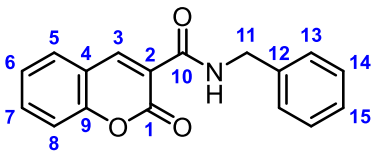

19

Following the general procedure outlined in **3.4.4** using salicylaldehyde **4** (117 µL, 1.00 mmol, 1.00 eq), a white solid residue was isolated after reaction mixture filtration which was crystallised in ethanol. Title compound **19** was obtained as a white crystalline solid (65.0 mg, 0.23 mmol, 23% yield). ^{1}H NMR (700 MHz, DMSO-d_6) δ 9.12 (1H, t, *J* = 6.0 Hz, NH), 8.85 (1H, s, H^3), 7.98 (1H, dd, *J* = 7.8, 1.7 Hz, H^8), 7.74 (1H, td, *J* = 7.8, 1.7 Hz, H^6), 7.50 (1H, d, *J* = 8.3 Hz, H^5), 7.41 (1H, td, *J* = 7.5, 1.1 Hz, H^7), 7.38 – 7.29 (4H, m, $H^{13,14}$), 7.26 (1H, tt, *J* = 6.6, 1.8 Hz, H^{15}), 4.55 (2H, d, *J* = 5.9 Hz, H^{11}); ^{13}C NMR (176 MHz, DMSO-d_6) δ 161.2 (C^{10}), 160.3 (C^1), 153.9 (C^9), 147.5 (C^3), 138.9 (C^{12}), 134.1 (C^6), 130.2 (C^8), 128.4 (C^{14}), 127.4 (C^{13}), 127.0 (C^{15}), 125.1 (C^5), 119.1 (C^2), 118.5 (C^4), 116.1 (C^7), 42.7 (C^{11}); LRMS (ASAP) *m/z*: $[M+H]^+$ 280.088 (100); HRMS (ASAP) *m/z:* $[M+H]^+$ Calculated $C_{17}H_{14}NO_3^+$: 280.0974, found 280.0980 (0.6 mDa, 2.1 ppm); IR (max/cm^{-1}): 3338w, 3060w, 1703s, 1654s, 1612s, 1566s, 1531s, 1245m, 749s, 698s; mp: 164-165 °C (decomposed); XRD: Title compound was crystallised in MeOH/CH_2Cl_2, resulting in clear colourless plates. Crystal data for $C_{17}H_{13}NO_3$ (m = 279.28 g/mol): triclinic, space group P-1 (no. 2).

***N*-benzyl-6-methoxy-2-oxo-2H-chromene-3-carboxamide 20**

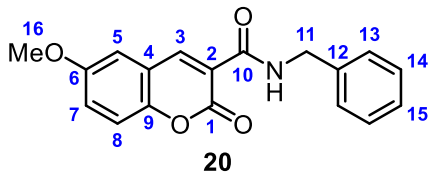

20

Following the general procedure outlined in **3.4.4** using 5-methoxysalicylaldehyde **5** (117 µl, 1.00 mmol, 1.00 eq), a white solid residue was isolated after reaction mixture filtration which was crystallised in ethanol. Title compound **20** was obtained as a white crystalline solid (188 mg, 0.61 mmol, 61% yield). ^{1}H NMR (700 MHz, DMSO-d_6) δ 9.15 (1H, t, *J* = 6.0 Hz, -NH), 8.85 (1H, s, H^{3}), 7.56 (1H, d, *J* = 3.1 Hz, H^{5}), 7.46 (1H, d, *J* = 9.2 Hz, H^{8}), 7.38 – 7.31 (5H, m, $H^{7,13,14}$), 7.29 – 7.23 (1H, m, H^{15}), 4.55 (2H, d, *J* = 6.0 Hz, H^{11}), 3.82 (3H, s, H^{16}); ^{13}C NMR (176 MHz, DMSO-d_6) δ 161.3 (C^{10}), 160.5 (C^{1}), 156.0 (C^{6}), 148.4 (C^{9}), 147.4 (C^{3}), 138.9 (C^{12}), 128.4 (C^{13}), 127.4 (C^{14}), 127.0 (C^{15}), 122.0 (C^{7}), 119.2 (C^{2}), 118.9 (C^{4}), 117.3 (C^{8}), 111.9 (C^{5}), 55.8 (C^{16}), 42.7 (C^{11}); LRMS (ASAP) *m/z*: $[M+H]^{+}$ 310.093 (100); HRMS (ASAP) *m/z*: $[M+H]^{+}$ Calculated for $C_{18}H_{16}NO_4^{+}$: 310.1079, found 310.1076 (-0.3 mDa, 1.0 ppm); IR (max/cm^{-1}): 3326w, 3037s, 1699s, 1571s, 1529s, 1365s, 1258s, 1243s, 1031m, 797s, 705s; mp: 138-139 °C [MeOH/CH_2Cl_2]; XRD: Title compound was re-crystallised in MeOH/CH_2Cl_2, resulting in colourless crystals. Crystal data for $C_{18}H_{15}NO_4$ (m = 309.31 g/mol): triclinic, space group P-1 (no. 2).

***N*-benzyl-6-bromo-2-oxo-2H-chromene-3-carboxamide 21**

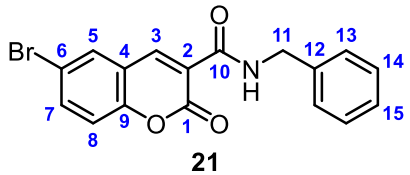

21

Following the general procedure outlined in **3.4.4** using 6-5-bromosalicylaldehyde **6** (117 µL, 1.00 mmol, 1.00 eq), a white solid residue was isolated after reaction mixture filtration which was crystallised in ethanol. Title compound **21** was obtained as a white crystalline solid (230 mg, 0.64 mmol, 64% yield). Incomplete ^{1}H/^{13}C NMR assignment was given due to poor solubility displayed by **21** in deuterated solvents. ^{1}H NMR (400 MHz, DMSO-d_6) δ 9.11 (1H, t, *J* = 6.0 Hz, -NH), 8.83 (1H, s, H^{3}), 8.26 (1H. d, *J* = 2.4 Hz, H^{5}), 7.89 (1H, dd, *J* = 8.9, 2.4 Hz, H^{7}), 7.49 (1H, d, *J* = 8.8 Hz, H^{8}), 7.41 – 7.30 (1H m, $H^{13,14}$), 7.28 – 7.19 (1H, m, H^{15}), 4.54 (2H, d, *J* = 6.0 Hz, H^{11}); ^{13}C NMR (101 MHz, DMSO-d_6) δ 161.0, 159.8, 153.0, 146.2 (C^{3}), 138.9, 136.3 (C^{7}), 132.1 (C^{5}), 128.4 ($C^{13/14}$), 127.4 ($C^{14/13}$), 127.0 (C^{15}), 120.42, 120.35, 118.5 (C^{8}), 116.7, 42.8 (C^{11}); LRMS (ASAP) *m/z*: $[^{79}BrM+H]^{+}$ 358.001 (100), $[^{81}BrM+H]^{+}$ 360.002 (96); HRMS (ASAP) *m/z*: $[M+H]^{+}$ calculated for $C_{17}H_{13}NO_3{}^{79}Br^{+}$: 358.0079 found: 358.0070 (-0.9 mDa, -2.5 ppm); IR (max/cm^{-1}): 3341w, 3043w, 1715m, 1653s, 1535m, 1420m, 1353m, 831s, 720s, 664s; mp: 236-237 °C (decomposed).

3.5 Reference compound synthesis (no acid) in batch conditions

3.5.1 Synthesis of 2-imino-2H-1-benzopyran-3-carboxamide 17b

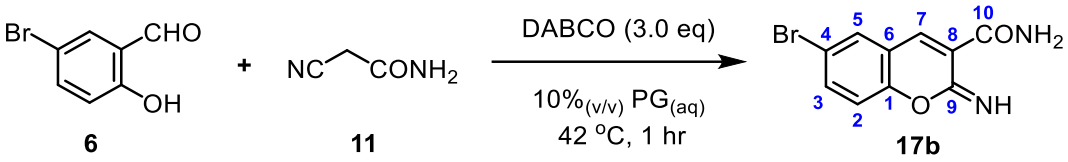

5-bromosalicylaldehyde **6** (260 µl, 2.50 mmol, 1.00 eq) was added to a heated solution of DABCO (0.013 M, 3.00 eq, 190 mL) in PG (19.0 mL) and water (171 mL). Cyanoacetamide **11** (841 mg, 10.0 mmol, 4.00 eq) was added and the reaction mixture was stirred at 42 °C for one hour. A solid was observed in suspension and was filtered from the reaction mixture and crystallised in ethanol: title compound **17b** was isolated as thin white needles (383 mg, 1.43 mmol, 57% yield). ^{1}H NMR (600 MHz, $CDCl_3$) δ 9.91 (1H, bs, =NH), 8.38 (1H, d, *J* = 1.1 Hz, H^7), 7.66 (1H, bs, -NH), 7.60 (1H, d, *J* = 2.4 Hz, H^5), 7.56 (1H, dd, *J* = 8.6, 2.4 Hz, H^3), 7.02 (1H, d, *J* = 8.6 Hz, H^2), 5.83 (1H, bs, -NH); ^{13}C NMR (151 MHz, $CDCl_3$) δ 163.6 (C^9), 156.9 (C^{10}), 153.1 (C^1), 141.1 (C^7), 135.6 (C^3), 131.8 (C^5), 121.7 (C^8), 120.6 (C^4), 117.2 (C^2), 116.7 (C^6); LRMS (ESI-TOF) *m/z*: 265.103 [^{79}BrM-H]$^+$ (100), 267.107 [^{81}BrM-H]$^+$ (87); HRMS (ESI-TOF) *m/z*: [M+H]$^+$ calculated for $C_{10}H_6N_2O_2{}^{79}Br^+$: 264.9613 found: 264.9611 (-0.2 mDa, -0.8 ppm); IR (max/cm^{-1}): 3275m, 2980w, 1679m, 1611m, 1563m,1389m, 1181s, 1087m, 851s, 810s, 643s, 513s; mp: 238-239 °C [EtOH].

3.5.2 Synthesis of 2(-2-amino-3-cyano-4H-chromen-4-yl)malononitrile 7b

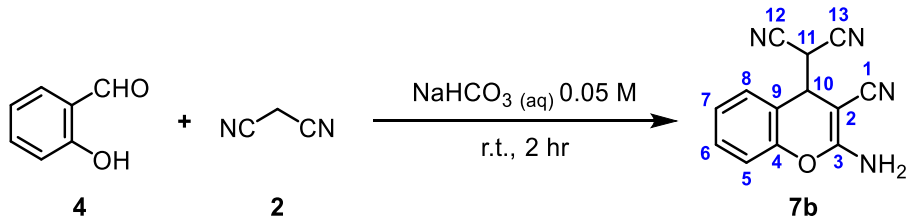

Known literature procedure was followed.[108] Salicylaldehyde **4** (1.17 mL, 10.0 mmol, 1.00 eq) was added to a 0.05 M solution of $NaHCO_3$ water (50.0 mL), followed by malononitrile **2** (825 mg, 12.5 mmol, 1.25 eq). The reaction mixture was stirred at room temperature for two hours. A solid was observed in suspension and was filtered from the reaction mixture and crystallised in CH_2Cl_2: title compound was isolated as thin white needles (163 mg, 0.69 mmol, 7% yield). ^{1}H NMR (600 MHz, DMSO-d_6) δ 7.52 (2H, s, -NH_2), 7.47 (1H, dd, *J* = 7.7, 1.6 Hz, H^8), 7.43 (1H, dt, *J* = 7.8, 1.6 Hz, H^6), 7.27 (1H, dt, *J* = 7.5, 1.2 Hz, H^7), 7.14 (1H, d, *J* = 8.3 Hz, H^5), 5.07 (1H, d, *J* = 4.0 Hz, H^{10}), 4.59 (1H, d, *J* = 4.0 Hz, H^{11});[99,108] ^{13}C NMR (101 MHz, DMSO-d_6) δ 163.5 (C^2), 149.8 (C^4), 130.2 (C^6), 128.9 (C^8), 125.1 (C^7), 119.4 (C^1), 118.0 (C^9), 116.4 (C^5), 113.1 (C^{12}), 113.0 (C^{13}), 84.8 (C^3), 37.1 (C^{10}), 32.5 (C^{11});[99] LRMS (ESI-TOF) *m/z*: 267.176 [M+H]$^+$ (100); 237.228 [M+H]$^+$ (24); [M-C_3HN_2]$^+$ 171.061 (93); HRMS (ESI-TOF) *m/z*: [M+H]$^+$

calculated for $C_{13}H_9N_4O^+$: 237.0776 found: 237.0794 (1.8 mDa, 7.6 ppm); IR (max/cm^{-1}): 3462w, 3336w, 2190m, 1643m, 1577m, 1426m, 1261m, 1182m, 1057m, 761s; mp: 143-145 °C [CH_2Cl_2];[99] XRD: Title compound was crystallised in CH_2Cl_2, resulting in clear platelets. Crystal data for $C_{13}H_8N_4O$ (m = 236.23 g/mol): triclinic, space group P-1 (no. 2).

3.6 General procedure for coumarin synthesis in surface tension-driven droplet devices

3.6.1 General procedure for coumarin synthesis in a (2x2) chemical sorter

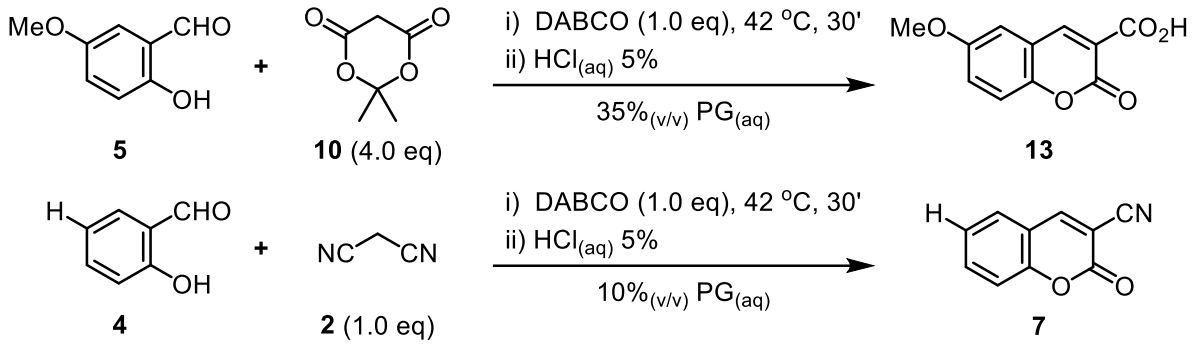

(2x2) chemical sorter manufacturing and setup: PG/H_2O solutions of the reactants were prepared as follows: aldehydes **4** (0.02 mL, 0.20 mmol, 1.00 eq) and **5** (0.02 mL, 0.20 mmol, 1.00 eq) were introduced in two different vials, containing 5 mL of PG/H_2O mixtures ($10\%_{(v/v)}$ and $35\%_{(v/v)}$ $PG_{(aq)}$, respectively). In a similar way, malononitrile **2** (13.2 mg, 0.20 mmol, 1.00 eq) was dissolved in $10\%_{(v/v)}$ $PG_{(aq)}$ (5.00 mL) whereas Meldrum's acid **10** (115 mg, 0.80 mmol, 4.00 eq) was added to a $35\%_{(v/v)}$ $PG_{(aq)}$ solution (5.00 mL). DABCO (22.4 mg, 0.20 mmol, 1.00 eq) was then added to each solution containing the aldehydic reagents to allow their solubilization in the binary mixture. A high-energy surface was created onto a clean glass slide and an ink-based hydrophobic track was traced onto the surface with a cardboard template. The marked glass slide was placed on a hot plate (42 °C), which was tilted with a goniometer (8°). $10\%_{(v/v)}$ and $35\%_{(v/v)}$ $PG_{(aq)}$ blank droplets (7.5 µL for each composition) were deposited in respective wells on the corona-discharged clean glass slide. The first set of reagent pairs was introduced by simultaneous dispensing of all stock solutions and allowed to autonomously sort in wells. For each introduced droplet pair, the droplet carrying the nucleophilic reagent was deposited approximately 0.5 - 0.7 cm away from the other containing aldehyde and DABCO.

(2x2) chemical sorter GCMS sample preparation: After 30 minutes, the samples were prepared by firstly pipetting the confined droplet reactor into two separate mass spec vials. Three drops of $5\%_{(v/v)}$ $HCl_{(aq)}$ were added and finally 50.0 µL of MeOH were introduced to dissolve and dilute the reaction mixture. Reference compound samples were prepared in

droplet chemistry conditions. Solutions of coumarins **7**, **8**, **12** and **13** (0.013 M, 0.13 mmol, 10.0 mL) were prepared in 10 mL volumetric flasks containing 5.00 mL MeOH, 3.50 mL PG/H_2O mixture (10%$_{(v/v)}$ PG$_{(aq)}$ for **7** and 35%$_{(v/v)}$ PG$_{(aq)}$ for **8**, **12** and **13**) and 1.50 mL 5%$_{(v/v)}$ HCl$_{(aq)}$. DABCO (14.6 mg, 1.00 mmol, 1.00 eq) was then added to each sample. 100 µL of each solution were then transferred into four separate mass spec vials and analysed *via* GCMS.

(2x2) chemical sorter ^{1}H-NMR sample preparation: After 30 minutes, each droplet reactor was transferred in separate NMR tubes and the droplet deposition process was repeated another three times. Three drops of 5%$_{(v/v)}$ HCl$_{(aq)}$ were then added to both NMR samples, followed by 0.50 mL of DMSO-d_6. Reference compound samples were prepared circumventing coumarin solubility issues encountered in PG/H_2O mixtures. 35.0 µL of PG/H_2O mixture were added (10%$_{(v/v)}$ PG$_{(aq)}$ for **7** and 35%$_{(v/v)}$ PG$_{(aq)}$ for **8**, **12** and **13**) to a DMSO-d_6 solution of coumarins **7**, **8**, **12** and **13** (0.013 M, 0.07 mmol, 0.5 mL). DABCO (1.45 mg, 1.00 mmol, 1.00 eq) was next added to each sample, followed by three drops of 5%$_{(v/v)}$ HCl$_{(aq)}$, prior to sample submission.

(2x2) sorter experiment in batch conditions: Aldehydes **4** (13.5 µL, 0.13 mmol, 1 eq) and **5** (16.2 µL, 0.13 mmol, 1.00 eq) were introduced in a 22.5%$_{(v/v)}$ PG$_{(aq)}$ solution of DABCO (0.03 M, 0.26 mmol, 10.0 mL). Nucleophiles **2** (8.60 mg, 0.13 mmol, 1.00 eq) and **10** (75.0 mg, 0.52 mmol, 4.00 eq) were next added to the reaction mixture, which was left to stir for thirty minutes. ^{1}H-NMR sample were prepared and analysed in DMSO-d_6 as previously described whereas GCMS samples were diluted with 0.15 mL of MeOH, prior to submission.

3.6.2 General procedure for coumarin synthesis in a (6DT) droplet reactor

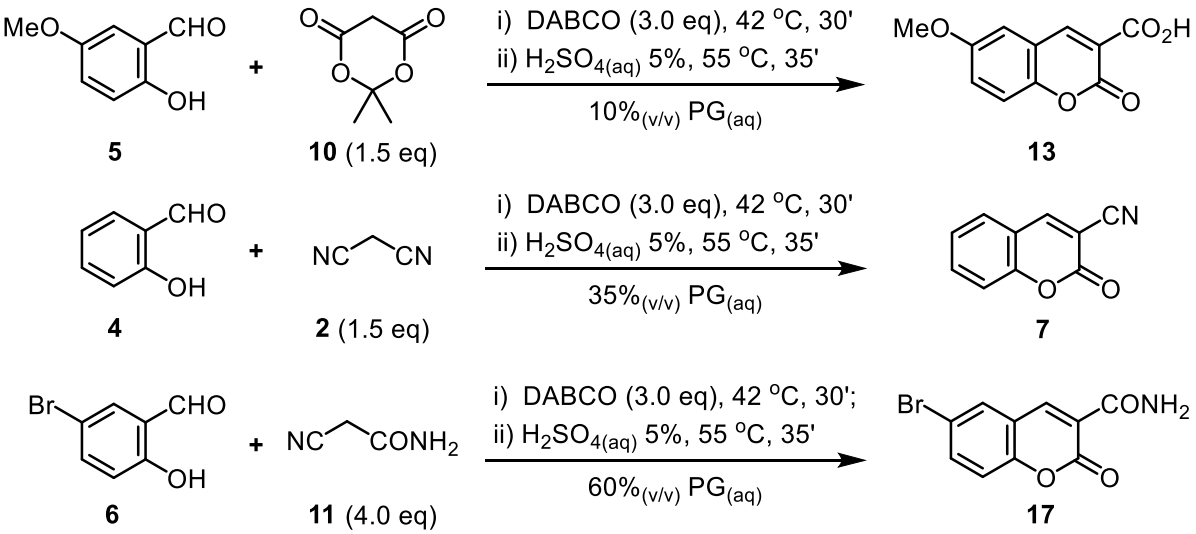

Reactions shown in the above scheme were separately investigated in (6DT) experiments. Droplet-scale synthetic procedure of coumarin **13** is herein described, which was also followed for the synthesis of target compounds **7** and **17**.

(6DT) droplet reactor manufacturing and setup: 5-methoxysalicylaldehyde **5** (47.0 µL, 0.38 mmol, 1.00 eq) was introduced in a vial, containing a solution of DABCO (0.075 M, 1.13 mmol, 3.00 eq) in PG (0.50 mL) and water (4.50 mL). Similarly, Meldrum's acid **11** (81.1 mg, 0.56 mmol, 1.50 eq) was dissolved in a second $10\%_{(v/v)}$ $PG_{(aq)}$ stock solution (5.00 mL). A high-energy surface was created onto a clean glass slide and six square-shaped hydrophobic tracks were traced onto the surface with an *AxiDraw*™ V3 robotic arm onto the surface (Figure 52). The activated glass slide was placed on a hot plate (set at 42 °C), which was tilted with a goniometer (8°). Six 5.00 µL blank $10\%_{(v/v)}$ $PG_{(aq)}$ droplets were deposited with a *Gilson*™ pipette, one in each square-shaped track, followed by introduction of six 5.00 µL droplets containing electrophilic reagent **5** and DABCO. After droplet pair coalescence, six 5.00 µL droplets of nucleophilic stock solution were deposited onto the glass slide. As a result, six 15.0 µL sized-droplet reactors were generated and left on the heated high energy surface for thirty minutes.

(6DT) droplet reactor ^{1}H-NMR sample preparation: Droplets confined in the well were collected and transferred in a vial: diluted sulfuric acid (5%, 9.00 µL) was added, and the quenched droplets were further heated at 55 °C for thirty minutes. Following this, the vial content was diluted with 0.50 mL of DMSO-d_6 prior to sample submission.

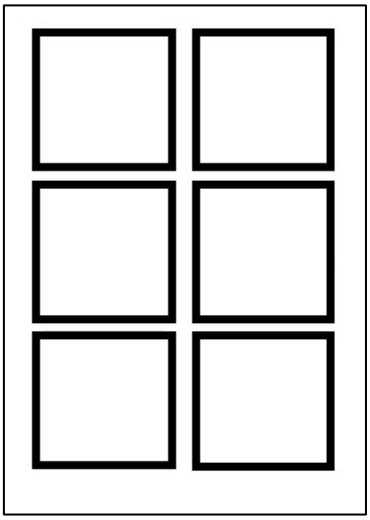

Figure 52. 1:1 scale (6DT) reactor template used during droplet device manufacturing.

3.6.3 General procedure for coumarin synthesis in a (3x3) chemical sorter

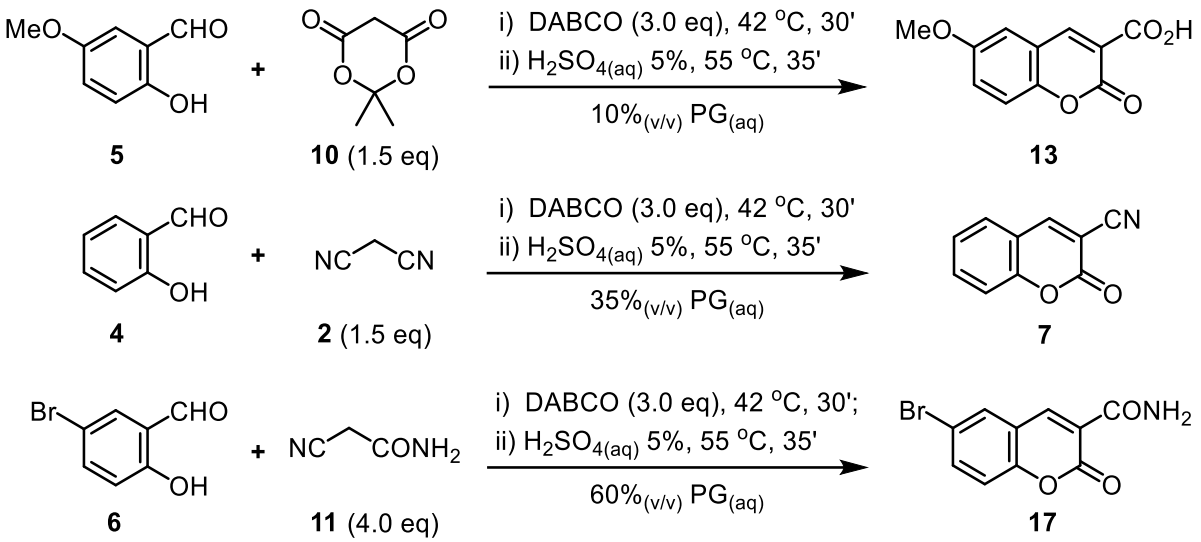

(3x3) chemical sorter manufacturing and setup: PG/H_2O solutions of the reactants were prepared as follows: 5-substituted salicylaldehydes **5** (47.0 µL, 0.38 mmol, 1.00 eq), **4** (39.0 µL, 0.38 mmol, 1.00 eq) and **6** (75.0 mg, 0.38 mmol, 1.00 eq) were introduced in three different vials, containing 5.00 mL of $10\%_{(v/v)}$, $35\%_{(v/v)}$ and $60\%_{(v/v)}$ $PG_{(aq)}$, respectively. In a similar way, Meldrum's acid **10** (81.2 mg, 0.56 mmol, 1.50 eq) was dissolved in $10\%_{(v/v)}$ $PG_{(aq)}$ solution (5.00 mL) whereas cyanoacetamide **11** (126 mg, 1.50 mmol, 4.00 eq) and malononitrile **2** (37.2 mg, 0.56 mmol, 1.50 eq) were added to 5.00 mL of $35\%_{(v/v)}$ and $60\%_{(v/v)}$ $PG_{(aq)}$ solution, respectively. DABCO (126 mg, 1.13 mmol, 3.00 eq) was next added to each aldehyde stock solution, followed by DSS (9.10 mg, 0.04 mmol, 0.11 eq). A high-energy surface was created onto a clean glass slide and a hydrophobic track was traced onto the surface with an *AxiDraw*™ V3 robotic arm onto the surface (Figure 53). The marked glass slide was placed on a hot plate (set at 42 °C), which was tilted with a goniometer (8°). 5.00 µL droplets of $10\%_{(v/v)}$, $35\%_{(v/v)}$ and $60\%_{(v/v)}$ $PG_{(aq)}$ blank droplets were deposited in respective wells on the corona-discharged clean glass slide with a *Gilson*™ pipette. All reagents (approximately 5.00 µL x 6) were simultaneously dropped on the heated glass slide with a syringe apparatus equipped with blunt needles and allowed to autonomously sort in wells. For each introduced droplet pair, the droplet carrying the nucleophilic reagent was deposited approximately 0.50 - 0.70 cm away from the other containing aldehyde, DABCO and DSS. Three 15.0 µL sized-droplet reactors were generated and left on the heated high energy surface for thirty minutes.

(3x3) droplet sorter ^{1}H-NMR sample preparation: After 30 minutes, each droplet reactor was transferred in a different vial and the droplet deposition process was repeated another five times, achieving an approximate volume of 75.0 µL of reaction mixture in each vial. $35\%_{(v/v)}$ and $60\%_{(v/v)}$ $PG_{(aq)}$ droplet reactors sample preparation was carried out by following the

procedure herein described for 10%$_{(v/v)}$ PG$_{(aq)}$ droplets, which were quenched with 5%$_{(v/v)}$ $H_2SO_{4(aq)}$ (12.0 µL) and further heated at 55 °C for thirty-five minutes. Following this, vial content was diluted with 0.50 mL of DMSO-d_6 prior to sample submission. ^{1}H-NMR sample reference was prepared by dissolving coumarin **13** (5.50 mg, 0.03 mmol, 1 eq.) in DMSO-d_6 (0.62 mL). PG (0.39 mL) was added to the DMSO-d_6 solution, followed by DABCO (8.46 mg, 0.08 mmol, 3.00 eq) and 5%$_{(v/v)}$ $H_2SO_{4(aq)}$ (12.0 µL). 0.50 mL of reference **13** stock solution were transferred in a second NMR tube and repeatedly diluted to match the DMSO-d_6-to-PG concentration ratio previously observed in the (3x3) experiment.

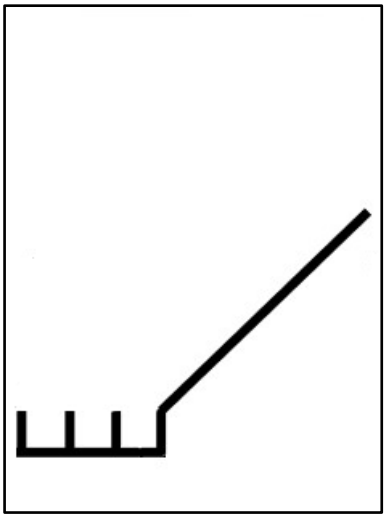

Figure 53. 1:1 scale (3x3) chemical sorter template used during droplet device manufacturing.

(3x3) sorter experiment in batch conditions: 0.15 M reagents stock solutions were prepared in 35%$_{(v/v)}$ PG$_{(aq)}$ (1.75 mL of PG and 3.25 mL of water), each one containing a different 5-substituted salicylaldehyde **6** (151 mg, 0.75 mmol, 1.00 eq), **4** (78.0 µL, 0.75 mmol, 1.00 eq) and **5** (93.0 µL, 0.75 mmol, 1.00 eq). In a similar way, malononitrile **2** (74.3 mg, 1.13 mmol, 1.50 eq), Meldrum's acid **10** (162 mg, 1.13 mmol, 1.50 eq) and cyanoacetamide **11** (252 mg, 3.00 mmol, 4.00 eq) were added to separate 5.00 mL 35%$_{(v/v)}$ PG$_{(aq)}$ stock solutions. DABCO (252 mg, 2.25 mmol, 3.00 eq) was next introduced to each solution containing the aldehydic reagent, to allow their solubilisation in the binary mixture. 0.05 mL of each aldehyde and nucleophile stock solution were transferred in two separate vials (0.15 mL each, 0.05 M) and quickly combined in a 5.00 mL reaction vessel, heated at 42 °C and equipped with a stirring bar. The resulting reaction mixture (0.30 mL, 0.03 M) was stirred for thirty minutes, followed by addition of 5%$_{(v/v)}$ $H_2SO_{4(aq)}$ (0.03 mL) and heating at 55 °C for thirty-five minutes. ^{1}H NMR sample was prepared by transferring 0.15 mL of quenched reaction mixture into a NMR tube, in which 0.50 mL of DMSO-d_6 were added.

3.7 Droplet Chemistry – Supplementary videos

S1. Droplet Pair Behaviour – Motion basics, front view.

A corona-discharged microscope slide was placed on a horizontal hot plate set at 37 °C, before deposition of blank PG/H_2O droplets (V = 5.00 µL). Water-soluble chemical dyes were utilised to monitor droplet pair interactions as follows: $10\%_{(v/v)}$ $PG_{(aq)}$ (Acid Blue), $30\%_{(v/v)}$ $PG_{(aq)}$ (methyl orange), $70\%_{(v/v)}$ $PG_{(aq)}$ (Congo Red).

S2. (2x2) Droplet Sorter with Dyes, front view.

A corona-discharged glass slide was placed on a hot plate set at 37 °C, which was tilted with a goniometer (8°) before droplet deposition (V ≈ 5.00 µL). Water-soluble chemical dyes were utilised to monitor droplet pair interactions as follows: $10\%_{(v/v)}$ $PG_{(aq)}$ (Acid Blue), $35\%_{(v/v)}$ $PG_{(aq)}$ (methyl orange). Droplet pair coalescence took place and the resulting droplet reactors were allowed to explore their surroundings and reach their target destination.

S3. (3x3) Droplet Sorter with Dyes, front view.

A corona-discharged glass slide was placed on a hot plate (42 °C), which was tilted with a goniometer (8°) before deposition of blank $PG_{(aq)}$ droplets in the sorting area. Droplets containing electrophilic reagent and DABCO were next introduced alongside droplets of nucleophilic stock solution. Water-soluble chemical dyes were utilised to monitor droplet pair interactions as follows: $10\%_{(v/v)}$ $PG_{(aq)}$ (Acid Blue), $35\%_{(v/v)}$ $PG_{(aq)}$ (methyl orange), $60\%_{(v/v)}$ $PG_{(aq)}$ (Congo Red). Droplet pair coalescence took place and the resulting droplet reactors were allowed to explore their surroundings and reach their target destination.

S4. (6DT) Droplet reactor: system setup, front view.

A corona-discharged glass slide was placed on a hot plate (42 °C), which was tilted with a goniometer (8°) before deposition of blank $10\%_{(v/v)}$ $PG_{(aq)}$ droplets. Droplets containing electrophilic reagent and DABCO were next introduced followed by droplets of nucleophilic stock solution. Droplet pairs were allowed to sequentially coalesce within each square-shaped perimeter.

S5. (3x3) Chemical Sorter with Chemicals, front view.

A corona-discharged glass slide was placed on a hot plate (42 °C), which was tilted with a goniometer (8°) before deposition of blank $PG_{(aq)}$ droplets in the sorting area. Droplets containing electrophilic reagent and DABCO were next introduced alongside droplets of nucleophilic stock solution. Droplet pair coalescence took place and the resulting droplet reactors were allowed to explore their surroundings and reach their target destination.

Chapter 4

Introduction

[3,3] sigmatropic rearrangements are a class of pericyclic reactions wherein the transition state of the molecule has a cyclic geometry, and the reaction progresses in a concerted fashion. From a synthetic standpoint, this reaction category occupies a distinctive position as a reliable method for the stereospecific construction of carbon–carbon or carbon–heteroatom bonds. First described in 1940, the Cope rearrangement of substituted 1,5-hexadienes can be considered as the basic type of such a process, where C-C single bonds undergo sigmatropic shift alongside relocation of π-bonding electrons. Likewise, aromatic allyl vinyl ethers are known to rearrange into *o*-allyl phenols at high temperatures, following a process known as the Claisen rearrangement. Overall, [3,3] sigmatropic reactions within systems displaying a nitrogen atom in position 3 are described in literature as hetero-Claisen (or 3-hetero-Cope) rearrangements but most frequently as 3-aza-Cope, amino-Claisen and aza-Claisen rearrangement (Scheme 16).[112]

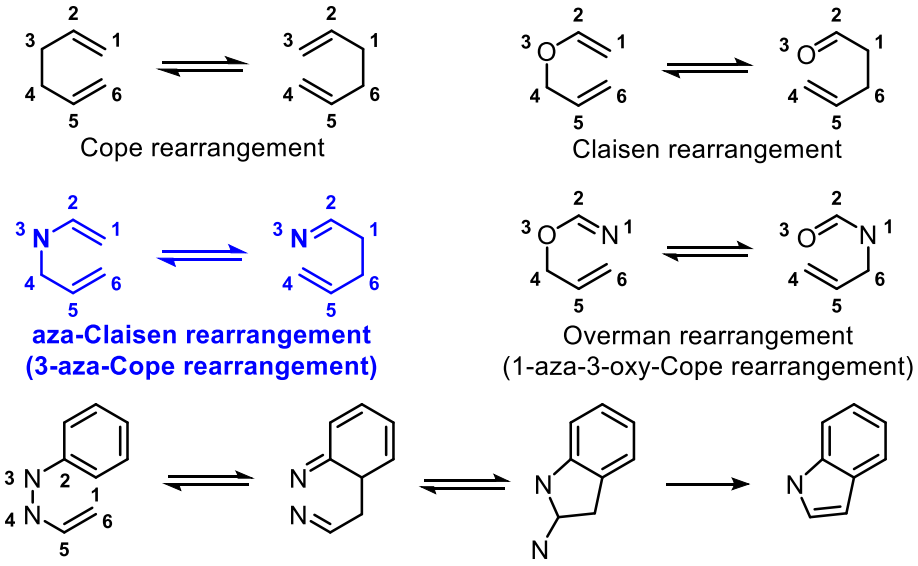

Scheme 16. [3,3]-σ sigmatropic rearrangements.[151]

Provided that the term aza-Claisen rearrangement is widely used in literature to indicate *any* [3,3] sigmatropic reaction involving nitrogen-containing substrates, the following introduction focuses exclusively on [3,3]-σ systems featuring a N heteroatom in position 3, where the nitrogen plays an active role in the reaction mechanism alongside neighbouring aromatic rings.

4.1 Thermal aza-Claisen rearrangement of aromatic amines

For a long period, aromatic aza-Claisen rearrangements were overlooked by the scientific community. Differently from aryl allyl ethers, rearrangement of *N*-allylanilines required higher reaction temperatures and were accompanied by undesired side-reactions such as secondary (or tertiary) anilines degradation and loss of the *N*-alkenyl moiety. Initial observations regarding the latter topic were documented by Dains and co-workers as early as 1922, who briefly described how *N*-allylaniline **22** underwent partial decomposition when purified *via* atmospheric distillation at 250 °C.[113]

Formation of *o*-allylaniline **23** was initially suggested since model substrate **22** shared structural analogies with allyloxybenzene, which was known to undergo Claisen rearrangement at high temperatures. Subsequent studies undertaken by Carnahan and Hurd disproved this hypothesis since no rearrangement product was detected upon pyrolysis of **22** (Scheme 17).[114] Thermal amino-Claisen rearrangement of *N*-allylaniline **22** was next attempted at higher temperatures and, to their dismay, secondary aromatic amine degradation occurred in all cases (Table 5). Interestingly, small amounts of quinoline were observed upon *N*-allylaniline pyrolysis at 700 °C, suggesting that ring closure of either **22** or *o*-allylaniline **23** took place albeit to a limited extent (Table 5, Entry 3).

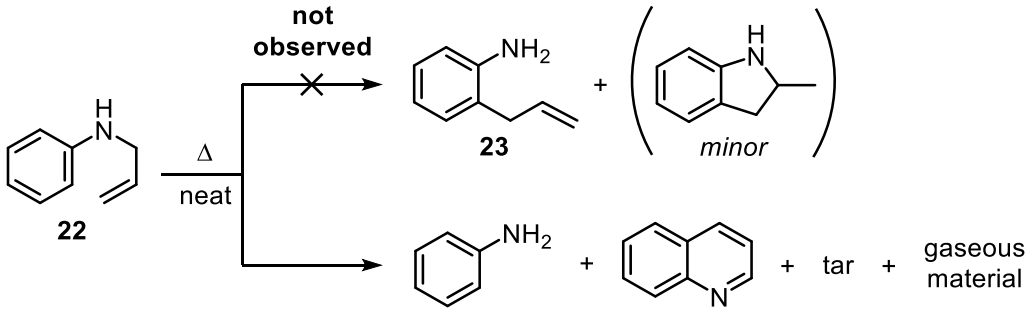

*Scheme 17. Thermal aza-Claisen rearrangement of N-allylaniline **22**.*

*Table 5. Pyrolysis of N-allylaniline **22** at increasing T_R: experimental outcome.*

Entry	T_R	t_R	mmol 22	mmol aniline	mmol quinoline	mmol converted to tar
1	275 °C	48 hr	44	11	nil	29
2	600 °C	2.5 min	105	54	nil	17
3	700 °C	39 s	376	204	15	60

A pyrolysis mechanism was proposed to account for the thermal degradation of *N*-allylaniline **22**, which was thought to occur at high temperatures *via* homolytic cleavage of the N-$C_{(allyl)}$ bond. Generation of radical species ensued, followed by their disproportionation and recombination, triggering aromatic amine **22** decomposition into aniline, propylene gas and tar-like material – i.e., polymerised *N*-phenyl-1-azabutadiene **24** (Scheme 18).

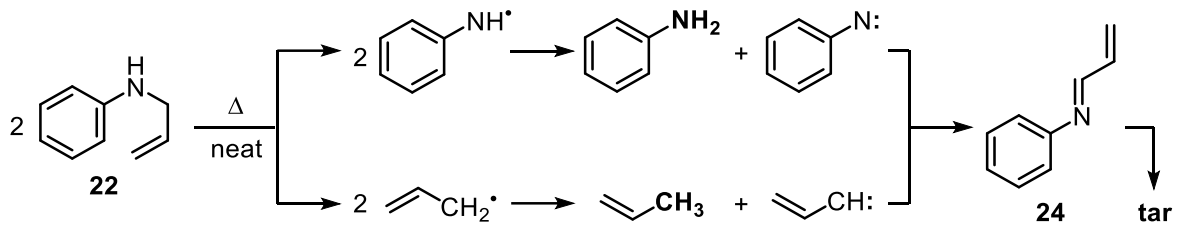

*Scheme 18. Proposed mechanism for N-allylaniline **22** thermal decomposition.*

The first successful example of a thermal aza-Claisen rearrangement was demonstrated by Marcinkiewicz *et al.* (Scheme 19), where *N*-allyl-1-naphthylamine **25a** conversion into 2-allyl-1-aminonaphtalene **26a** was achieved at 280 °C with excellent yield (Table 6, Entry 1).[115] Nonetheless, these reaction conditions were more drastic than the ones required for allyloxy counterpart **25b**, which in turn provided satisfactory amounts of 2-allyl-1-naphtol **26b** in less than an hour (Table 6, Entry 2). Moreover, detailed kinetic studies were undertaken for both rearrangements, therefore explaining why higher reaction temperatures and longer reaction times were required during [3,3]-σ rearrangement of precursor **25a**.[115]

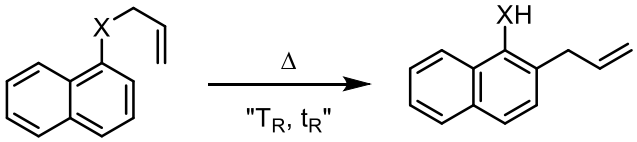

*Scheme 19. Thermal aza-Claisen rearrangement of N-allyl-1-naphthylamine **25a** and oxy-counterpart **25b***

*Table 6. Oxy- and aza-Claisen rearrangement of allyl aryl precursors **25a** and **25b**: kinetic study comparison.*

Entry	X		T_R	t_R	yield[a]	$\Delta E^{\ddagger}$[b]	$\Delta S^{\ddagger}$[c]	k_R[b]
1	NH	**25a**	280 °C	3 hr	90 %	32.4 kcal	-17 e.u.	$3.28 \cdot 10^{-4}$ s^{-1}
2	O	**25b**	194 °C	0.75 hr	84 %	26.0 kcal	-15.9 e.u.	$2.05 \cdot 10^{-3}$ s^{-1}

[a] Isolated yield. [b] First order rate constants and $\Delta E^{\ddagger}$ calculated with the Arrhenius equation. [c] $\Delta S^{\ddagger}$ determined via Eyring equation, assuming that transmission coefficient k = 1

Differently from 2-allyloxynaphtalene **25b**, greater activation energy $\Delta E^{\ddagger}$ and larger negative activation entropy $\Delta S^{\ddagger}$ were associated to the [3,3]-σ rearrangement of amine **25a**. Two major reasons were accounted for the higher reaction temperature needed for the synthesis **26a**. Firstly, more energy would be required to bring coplanarity in aromatic allylamines than in allyl ethers, which in the former case was hindered by the sp^3-hybridised nitrogen atom. Furthermore, inhibited rotation around the amino-hydrogen bond would result in a more rigid, cyclic transitional state featuring more negative entropy of activation $\Delta S^{\ddagger}$.

Interestingly, competition studies between oxy- and amino-Claisen reactive sites within 3-*N*-propargylaminocoumarin **27** were reported by Majumdar *et al*, which demonstrated otherwise. Thermal rearrangement of precursor **27** was attempted in refluxing chlorobenzene, *o*-

dichlorobenzene and *N,N*-dimethylaniline, with only the latter solvent allowing coumarin **27** conversion into pyrrolocoumarin **28** with 91% yield. Neither oxy-Claisen rearranged material or pyridocoumarin side-products were detected after reflux, suggesting that exclusive formation of pyrrolocoumarin **28** occurred *via* regioselective [3,3]-σ rearrangement of the propargylamine moiety. According to their proposed reaction mechanism, allene intermediate would form, which would undergo imine/enamine tautomerism to give intermediate **27a**. Following this, pyrrolocoumarin derivative **28** formation was suggested taking place *via 5-exo-trig* cyclization of enamine intermediate **27a** (Scheme 20).[116]

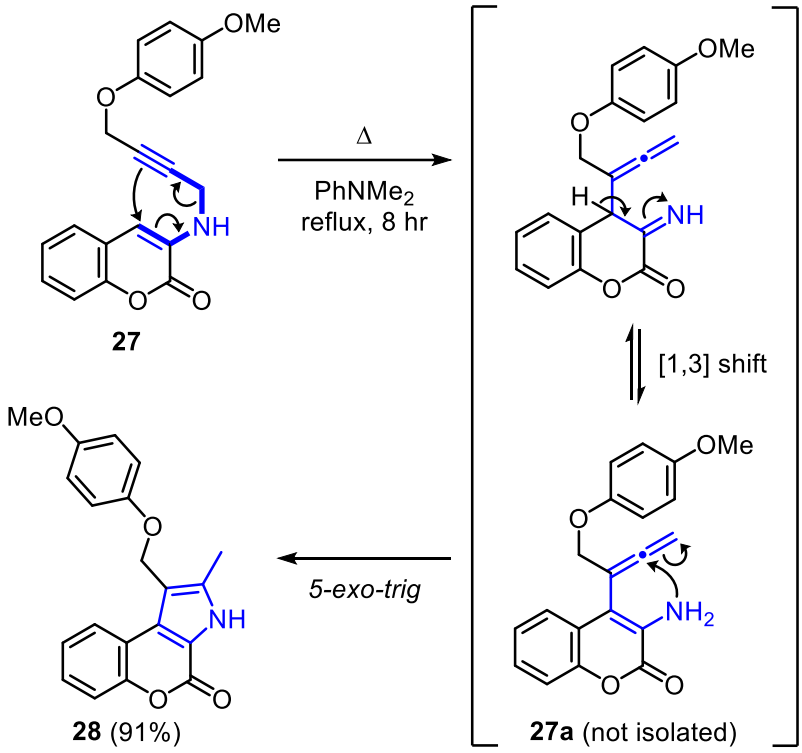

Scheme 20. Competitive oxy- and aza-Claisen study within 3-N-propargylaminocoumarin ***27****.*

Water-accelerated aza-Claisen rearrangement of *N*-(1,1-dimethylallyl)naphthylamines and anilines was reported by Beare and McErlean, which took place upon vigorous stirring of aqueous emulsions at 80 °C.[117] Self-sustained, “on-water” catalysis was proposed since rearrangement of *N*-alkenyl arylamine **29** occurred faster in presence of additional target product **30**. Water-mediated protonation of the latter compound was invoked due to the basic nature featured by the primary amino group, leading to proton transfer and further activation of unreacted starting material (Scheme 21).

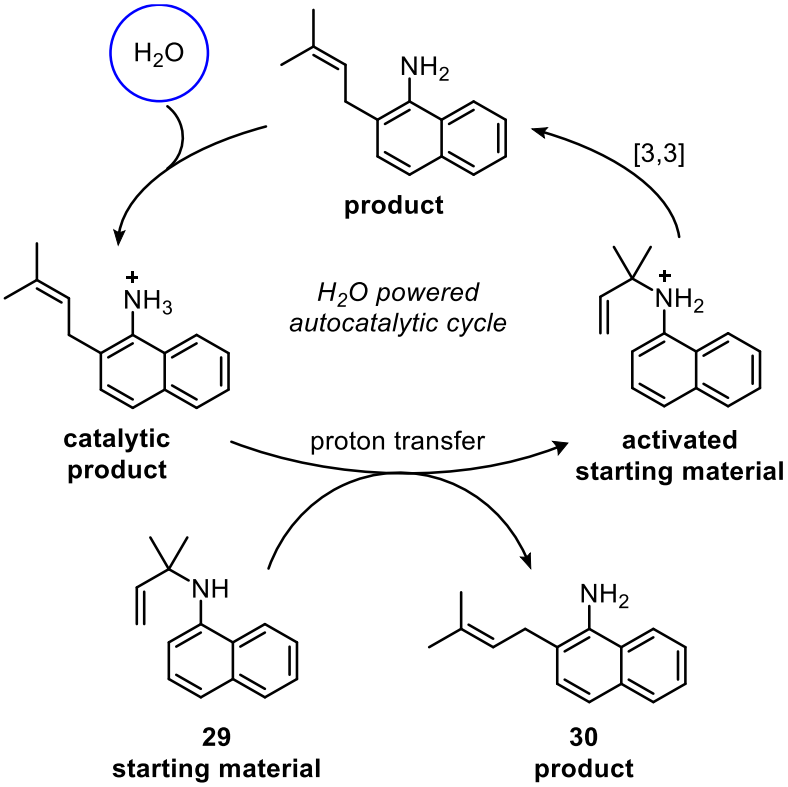

Scheme 21. Autocatalytic, "on-water" reaction mechanism proposed by Beare and McErlean.

Moreover, development of “on-water” catalysis in thermal conditions enabled rearrangement of *N*-(1,1-dimethylallyl)naphthylamine **29** followed by *m*-CPBA-mediated ring closure of *o*-prenyl intermediate **30,** yielding fused N-heterocycles such as **31** (Scheme 22).[117]

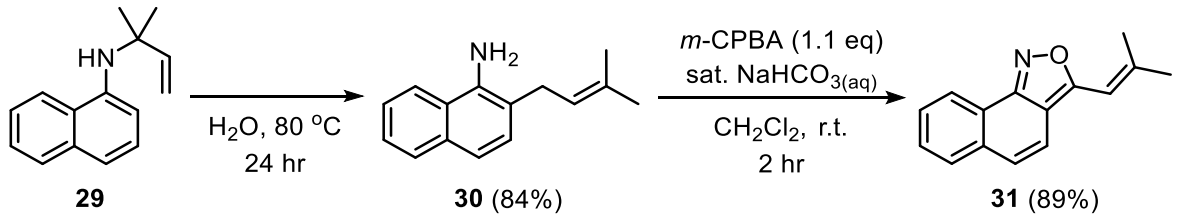

*Scheme 22. Synthesis of naphtho[c]isoxasole **31** via "on-water" catalysed amino-Claisen rearrangement.*

This system perfectly illustrated how the synthetic challenges associated to the thermal aza-Claisen rearrangement such as drastic reaction temperatures and thermal degradation of *N*-alkenyl precursors, may be circumvented through correct use of catalysis.

4.2 Charge-accelerated aza-Claisen rearrangement of aromatic amines

4.2.1 Brønsted acid-mediated aza-Claisen rearrangement of aromatic amines

As early as 1957, Bader and Hyre were among the first to describe a "proton-catalysed Claisen-type" rearrangement of *N*-(2-butenyl)aniline derivative into 2,3-dimethyl indoline, which took place at reflux conditions in polyphosphoric acid (PPA). Their reasoning for the formation of the cyclic product was that the aniline proceeded *via* initial charged aza-Claisen reaction, followed by acid-catalysed cyclisation through the resulting terminal alkene (Scheme 23).[118]

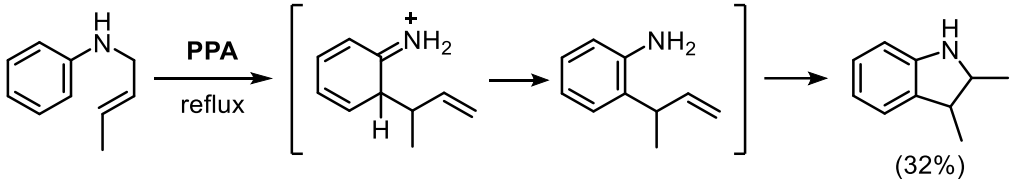

Scheme 23. PPA-catalysed aza-Claisen rearrangement by Bader et al.

Commonplace issues affecting aromatic anilines reactivity in thermal conditions could be overcome *via* Brønsted acid catalysis, therefore promoting aza-Claisen rearrangements at lower reaction temperatures. Besides PPA, other proton sources were investigated such as H_2SO_4, HCl and heteropoly acids – e.g., phosphomolybdic acid. Although the latter catalysts were demonstrated in separate efforts by Chaskar[119] and Xie[120] to be efficient, greener alternatives to mineral acids, use of more conventional protic acids still prevails to this day to promote the amino-Claisen rearrangement of *N*-alkenyl substrates.

Jolidon and co-workers were among the first to investigate acid-promoted [3,3]-σ rearrangement of *N*-alkylated secondary and tertiary anilines (Scheme 24).[121] Upon comparison between the experimental outcomes arising from thermal and H_2SO_4-mediated rearrangements, the latter methodology proved without doubt to be more effective for this purpose. Thermal decomposition of *N*-alkenylanilines **22, 32** and **33** into by-products **36-37** was minimised only when their rearrangement was undertaken in acidic environment, therefore explaining the improved yields isolated in H_2SO_4 2N at lower reaction temperatures (Table 7).[121]

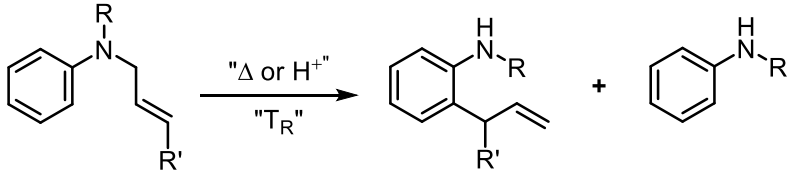

22, 32-33 **23, 34-35** **36-37**

*Scheme 24. Thermal (Δ) and acid-mediated (H^+) aza-Claisen rearrangement of N-alkenylanilines **22**, **32** and **33**. Thermal and acid-mediated [3,3]-σ reactions carried out in 3-methoxy-2-butanol (MBO) and H_2SO_4 2N, respectively.*

Table 7. Thermal and acid-promoted aza-Claisen rearrangement of N-alkenyl anilines: experimental outcome.

Entry	Starting material	[3-3]-σ product	Dissociation by-product		"T_R"	Yield [3-3]-σ	Yield Diss.
1	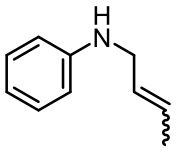	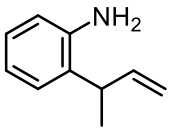	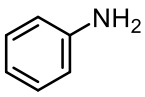	Δ	335 °C	5-12%	60%
				H^+	160 °C	71-72%	<2%
	***(E/Z)*-32**	**34**	**36**				
2	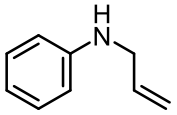	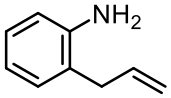	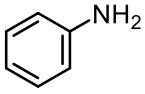	Δ	310 °C	26%	31%
				H^+	170 °C	47%	<1%
	22	**23**	**36**				
3	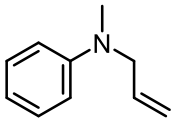	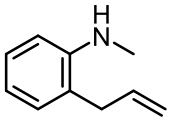	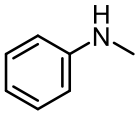	Δ	320 °C	19%	59%
				H^+	170 °C	38%	<2%
	33	**35**	**37**				

Lattes and Majumdar demonstrated how *N*-alkylanilines bearing either a *N*-(1'-methylallyl) or *N*-(cyclohex-2'-enyl) moiety successfully rearranged in presence of hydrochloric acid, which promoted starting materials conversion into *o*-allylic compounds upon reflux in EtOH/H_2O mixtures.[122,123] Likewise, milder reaction conditions were required for the conversion of saturated indole precursors into its *o*-allyl derivatives, which was achieved by Abdrakhmanov and co-workers at room temperature in presence of diluted HCl.[124]

[3,3] sigmatropic rearrangement of *N*-(1',1'-disubstituted-allyl)anilines was achieved in aqueous acetonitrile, which allowed hindered aromatic amines conversion at lower reaction temperatures in presence of catalytic amounts of *p*-toluenesulfonic acid (PTSA).[125] Moreover, use of PTSA as reaction promoter was recently highlighted by Liang and Wang, who successfully isolated 7-prenylisatin *via* a five-step procedure. Two key steps were described in their total synthesis, with the first one being the protic acid-catalysed aza-Claisen rearrangement of intermediate **38** and into *o*-prenyl substituted aniline **39** (Scheme 25).[126]

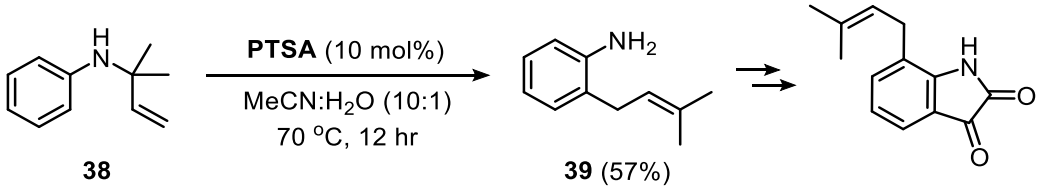

*Scheme 25. Total synthesis of 7-prenylisatin via PTSA-catalysed amino-Claisen rearrangement of N-(1,1-dimethylallyl)aniline **38.***

Danishefsky and Ganesan also demonstrated how aza-Claisen rearrangements can be implemented in natural product synthesis, provided that protic acids were employed in this context.[127] Indole alkaloid (+)-okaramine J was isolated following a 12-step synthetic

procedure, with one key reaction being the TFA-promoted, room-temperature aza-Claisen rearrangement of *N*-prenylhexahydro[2,3-b]pyrroloindole intermediate **40** to its *C*-prenylated derivative **41** with 84% yield (Scheme 26).[128]

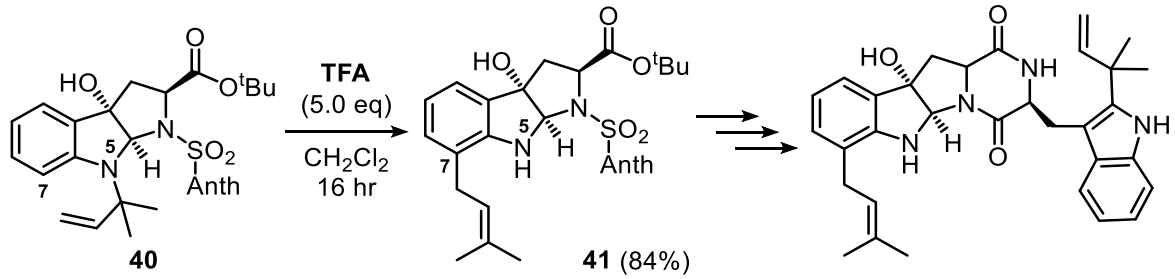

*Scheme 26. Total synthesis of (+)-okaramine J via TFA-promoted aza-Claisen rearrangement of N-prenyl intermediate **40.***

One major shortfall of the use of Brønsted acid catalysis is the lack of chiral information, so any observed diastereoselectivity was due to the concerted pericyclic nature of the reaction, and classically there was no means to externally control the enantioselectivity. However, Tambar *et al.* recently revolutionised the use of Brønsted acid catalysis by using chiral phosphoric acid **42** to mediate an enantioselective aza-Claisen rearrangement.[129] The phosphoric acid-derived catalyst bonded to the substrate with a 2-point interaction, which allowed for the observed stereo-induction in the final product. The chiral Brønsted acid **42** also allowed for high yields (81-96%) and *ee* (86-96%) for a variety of aryl substituents tested in the scope (Scheme 27).[129]

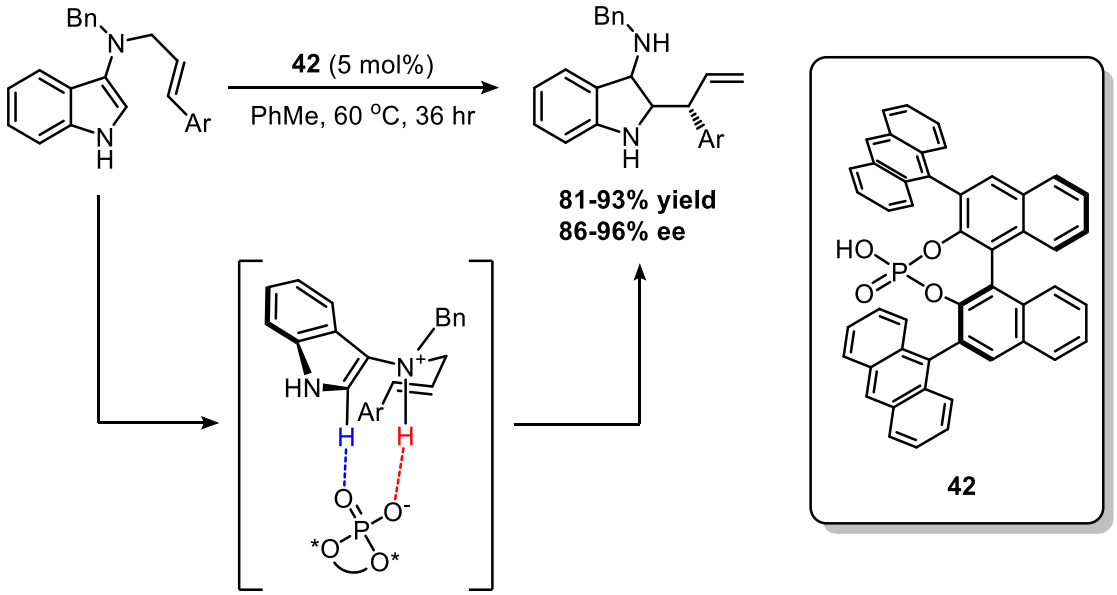

*Scheme 27. Enantioselective aza-Claisen rearrangement promoted by chiral Brønsted acid **42.***

4.2.2 Lewis acid-mediated aza-Claisen rearrangement of aromatic amines

Contemporary to Bader and Hyre's studies on PPA-mediated aza-Claisen reactions, Hurd and Jenkins achieved rearrangement of unsubstituted *N*-allylaniline into 2-allylaniline with 42% yield, by introducing stoichiometric amounts of zinc chloride in refluxing xylene.[130] Although the scope of this transformation was previously explored by Schmidt *et al.*,[131] a systematic study was carried out by Beholz and Stille in the early 1990s, where several reaction variables were optimised for secondary and tertiary *N*-allylanilines conversion into their *o*-allyl derivatives. High yielding synthesis of rearranged 2-allyl-*N*-methylaniline **33** was achieved upon addition of aluminium chloride in slight excess. Moreover, formation of undesired side-products, such as cyclised and *de*-allylated derivatives of precursor **35,** was minimised following these reaction conditions (Scheme 28).[132]

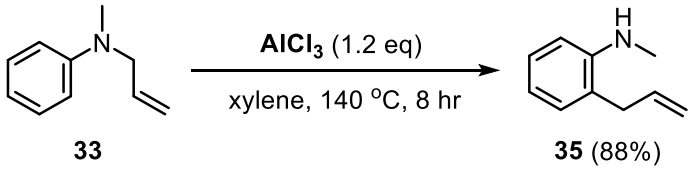

*Scheme 28. Lewis acid promoted aza-Claisen rearrangement of N-allyl-N-methylaniline **33***

Later, Cruces *et al.* developed conditions to carry out the same reaction, but in a fraction of the time, due to the use of a microwave reactor.[133] Using BF_3•OEt_2 as Lewis acid reagent, it has been observed that the use of microwave heating may lead to vastly reduced reaction times, as well as cleaner conversion of rearranging N-alkenyl aromatic amines.[133] On the other hand, cyclisation of secondary and tertiary *N*-allylanilines was efficiently carried out under microwave heating by Yadav *et al.* in presence of Zn^{2+} montmorillonite. A range of substituted indolines were isolated following this method, which led to complete starting material conversion within 3-5 minutes in solventless conditions (Scheme 29).[134]

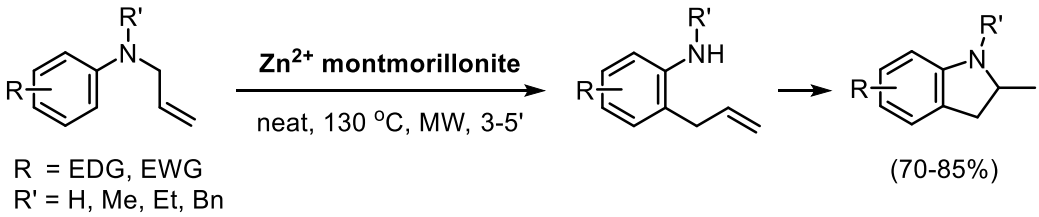

Scheme 29. Tandem aza-Claisen and cyclisation of N-allylanilines under microwave condition.

In addition to Zn^{2+} montmorillonite, catalytic properties of a range of zeolites were investigated by Padmakumar and co-workers for the aza-Claisen rearrangement of *N*-allyl-*N*-methylaniline **33**. Use of different Lewis acid impacted the final products acquired, since HY-Zeolite produced cyclised indoline **43** after a 2 hour reaction at 80 °C (Scheme 30).[135]

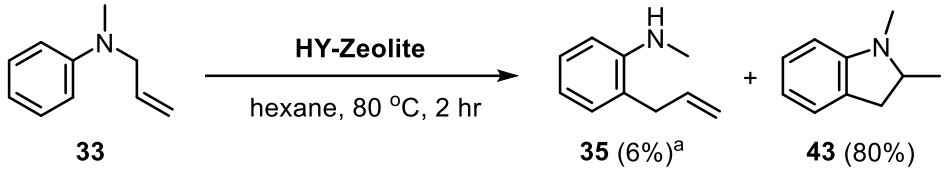

*Scheme 30. Tandem aza-Claisen and cyclisation of N-allylaniline **33** mediated by zeolite catalysis.*

To this day, BF_3•OEt_2 has become the most well-established Lewis acid reagent used for the [3,3] sigmatropic rearrangement of aromatic amines, which are regularly applied for the synthesis of biologically active compounds.[136–139] For instance, Anderson and Lai achieved conversion of *N*-allyl-1,2-phenylenediamine **44** into *o*-allyl derivative **45** upon BF_3•OEt_2 catalysis with 53% yield, with the latter being a key intermediate required in the total synthesis of mycophenolic acid benzimidazole analogue **46** (Scheme 31).[140] The method therein developed was further investigated on a broader substrate scope, which comprised variously substituted *N*-allyl-1,2-phenylenediamines and 6-substituted-*N*-allyl indolines.[141]

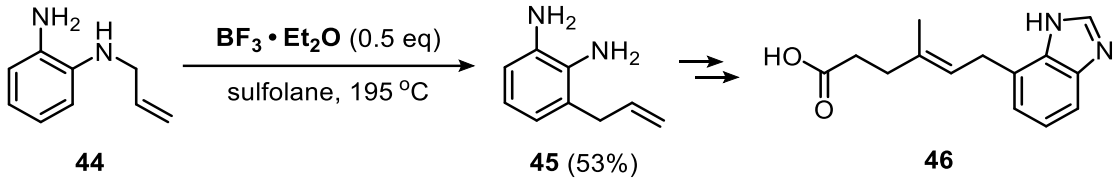

*Scheme 31. Total synthesis of mycophenolic acid benzimidazole analogue **46.***

Interestingly, total synthesis of indole alkaloids has been revisited less than two years ago by Chan and co-workers, further proving that aza-Claisen rearrangements have become a powerful synthetic tool in natural product synthesis. A successful and convenient synthetic strategy was developed, which featured [3,3]-σ rearrangement of *N*-(1',1'-dimethylallyl) substituted intermediates such as **47**. Nonetheless, different reaction conditions were required compared to the ones previously described by Ganesan *et al*. for (+)-okaramine J (Scheme 32, top).[142] Use of either TFA or PTSA as promoting agents was found detrimental during reverse-prenyl group migration from N-5 to C-7 position whereas Lewis acid catalysis proved more effective for this purpose, therefore providing an alternative synthetic route towards the target compound (Scheme 32, bottom).[128]

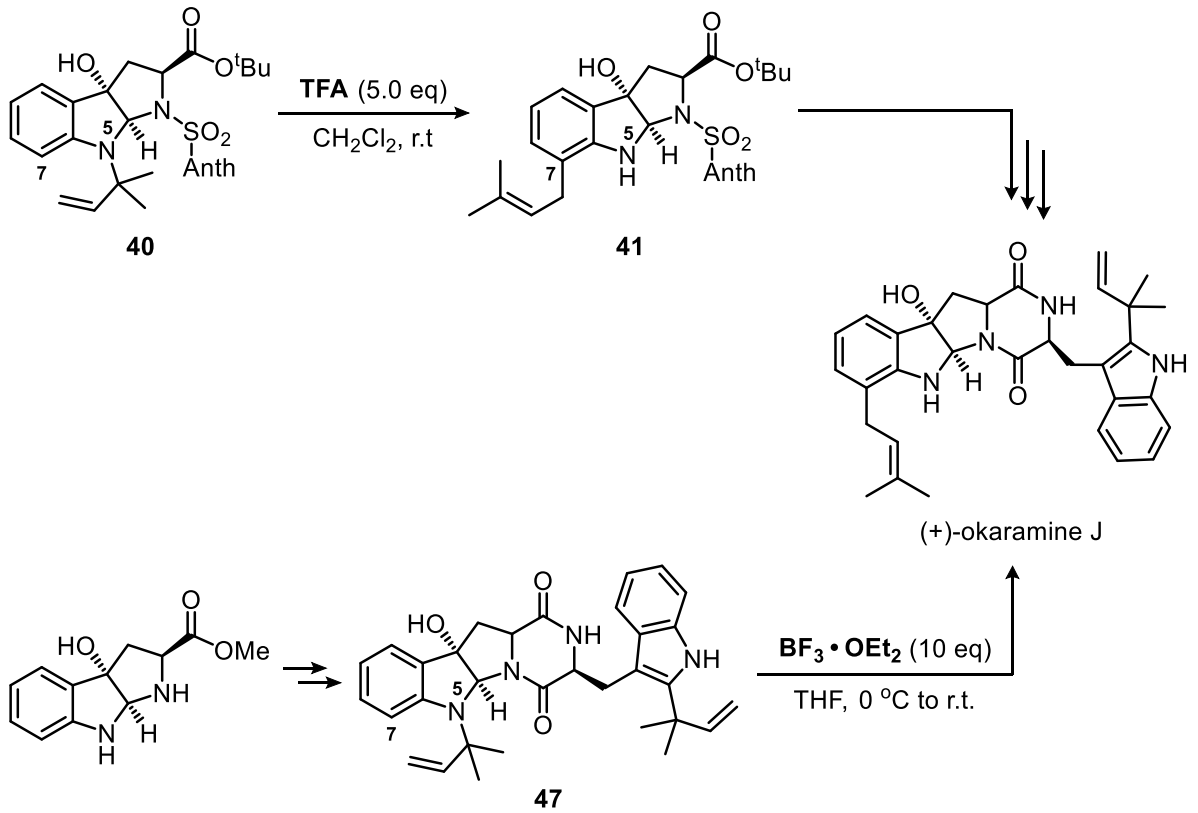

Scheme 32. Comparison between synthetic strategies developed during total synthesis of (+)-okaramine J.

Synthesis of (-)-indolactam-V derivative **50** was reported by Wender *et al.* who investigated the biological activity displayed by tumour-promoting indole alkaloids – namely teleocidins and their monoterpenoid analogues.[143] Allylation of (-)-N^{13}-desmethylindolactam-V **48** afforded *N*-allyl derivative **49** which was then refluxed in xylene for twenty minutes in presence of various Lewis acids (Scheme 33). H_2SO_4 mediated [3,3]-σ rearrangement of **49** proved ineffective whereas the Lewis acid-catalysed reaction with either $AlCl_3$ or $ZnCl_2$ was more efficient, with the former becoming the reagent of choice (Table 8).

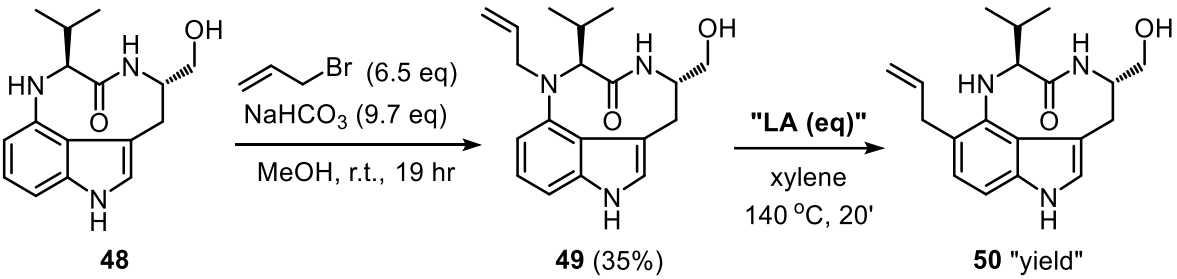

*Scheme 33. Lewis acid-catalysed aza-Claisen rearrangement of (-)-N^{13}-allyl-N^{13}-desmethylindolactam-V **49**.*

Equivalency fine-tuning of aluminium chloride was required however, since reactions carried out with 0.7 equivalents of $AlCl_3$ led to decomposition of the nine-membered lactam backbone (Table 8, Entry 3). Conversely, aza-Claisen rearrangement of **49** with 0.45 equivalents of $AlCl_3$ afforded *o*-allyl compound **50** with 36% yield alongside a mixture of *o*-cyclised indolactams (Table 8, Entry 2).[143]

*Table 8. aza-Claisen rearrangement of (-)-N^{13}-allyl-N^{13}-desmethylindolactam-V **49**: Lewis Acid screening*

Entry	"Lewis Acid (eq)"	50 Yield[a]	Entry	"Lewis Acid (eq)"	50 Yield[a]
1	$AlCl_3$ (0.35)	23%	4	$ZnCl_2$ (0.70)	26%
2	$AlCl_3$ (0.45)	36%	5	$ZnCl_2$ (0.90)	22%
3	$AlCl_3$ (0.70)	0%	6	2N H_2SO_4 (1.20)	0%

[a] *Isolated yield.*

Metal triflate salts also proved to be effective catalysts for the aza-Claisen rearrangement of *N*-allyanilines. For instance, Tomilov and co-workers described $M(OTf)_3$-catalysed rearrangement of *N*-Allyl-*N*-methylanilines in presence of either methyl diazoacetate or diazoacetone to give the corresponding methyl *N*-(2-allylaryl)-*N*-methylglycinates or 2-allyl-*N*-methyl-*N*-(2-oxopropyl)anilines (M = Y, Sc, Sm).[144]

Likewise, $In(OTf)_3$-catalysed synthesis of (*Z*)-alkylidene oxindoles *via* aza-Claisen rearrangement of α-amino acid derived α,β-unsaturated esters was recently described by Panda *et al*. Mechanistic insight was provided in this instance, explaining the crucial role played by indium triflate, which allowed initial rearrangement of *N*-α,β-unsaturated ester substituted aniline **51** and synthesis of (*Z*)-alkylidene oxindole **52** in presence of coordinating $[In(OTf)_2]^+$ (Scheme 34).[145]

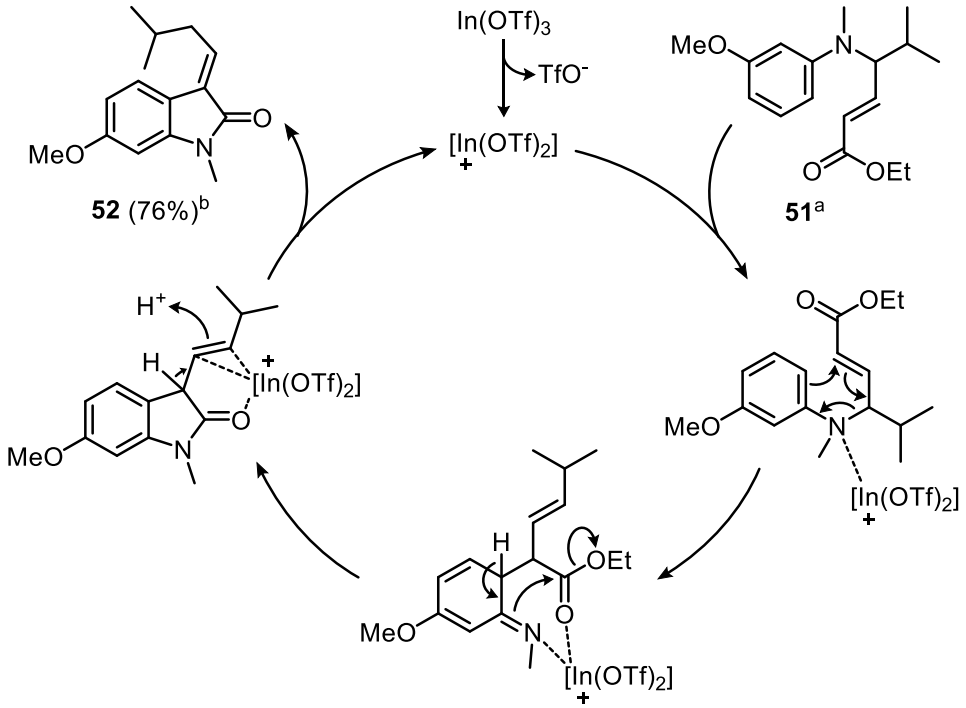

*Scheme 34. Proposed mechanism for $In(OTf)_3$-catalysed aza-Claisen rearrangement of N-aryl-α,β-unsaturated ester **51**. [a]·Reaction conditions: $In(OTf)_3$ 10% mol, 1,4-Dioxane, 80 °C· 16 h, [b]·Isolated yield.*

4.2.3 Generation of rearranging quaternary ammonium salts *in situ*

An unconventional amino-Claisen rearrangement methodology was published by Munoz *et al.*, which used SelectFluor to doubly fluorinate *N*-allenyl substituted indoles such as **53**, thus generating a quaternary ammonium centre within activated iminium **54**.[146] Catalytic amounts of iron triflate were utilised to better promote *in situ* aza-Claisen rearrangement of **54,** which in turn afforded 2-allenyl-3,3-difluoro derivative **55** with 83% yield (Scheme 35).[146] Although merely speculative, the reaction mechanism therein proposed did not feature formation of the quaternary ammonium centre assisted by $Fe(OTf)_3$, which in turn coordinated to the rearranging allenyl moiety rather than the nitrogen atom.

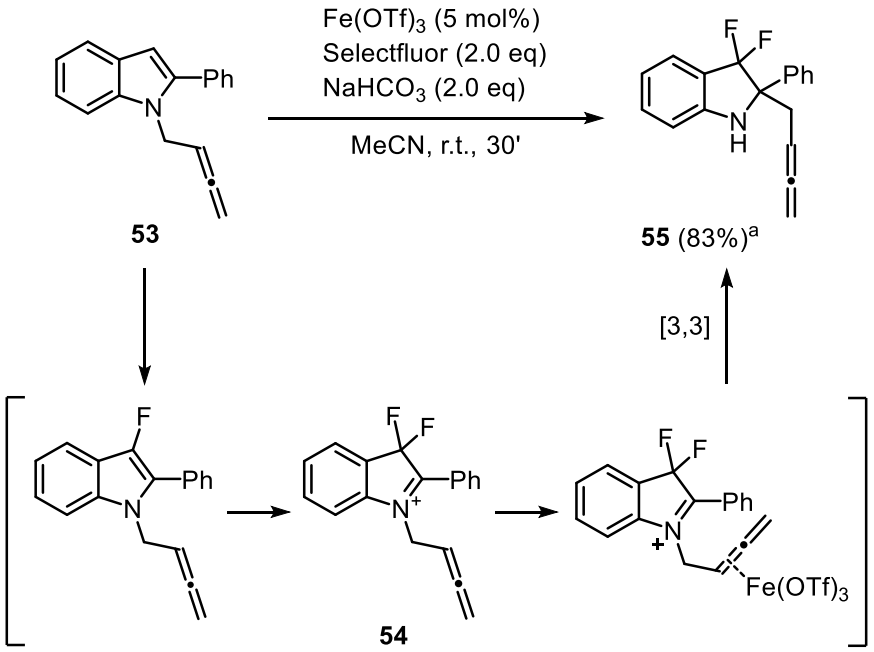

*Scheme 35. $Fe(OTf)_3$-catalysed tandem indole fluorination/allenic aza-Claisen rearrangement of precursor **53**. [a] Isolated yield.*

As early as 1988, many literature studies can be found where formation of a charged ammonium species took place within reaction cascades, where tertiary amines bearing either *N*-allyl or *N*-propargyl substituents underwent tandem Michael addition/aza-Claisen rearrangement in presence of π-electrophiles.[147–155] For instance, Tian and co-workers investigated nucleophilic addition of enantioenriched α-chiral-*N*-alkenyl amines **56-64** to allenone **65**. The resulting Michael adducts underwent room temperature aza-Claisen rearrangement in absence of catalysts and additives, yielding δ-chiral β-diketones **66-74** upon hydrolysis of the rearranged intermediate (Scheme 36). Enantiopurity retention was observed between starting materials and final products, proving that N-C chirality transfer occurred during amino-Claisen rearrangement of precursor **56-64** (Table 9).[156]

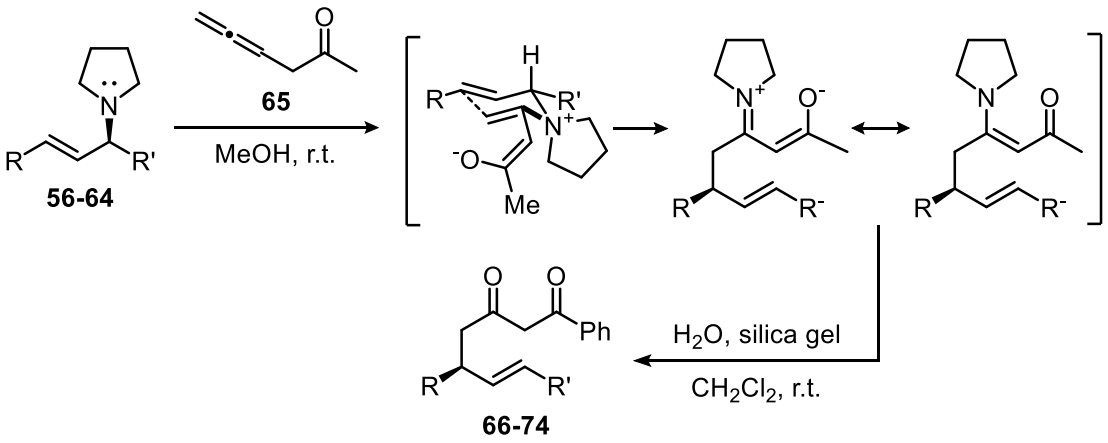

*Scheme 36.Tandem MIchael addition/aza-Claisen rearrangement of enantioenriched α-chiral-N-alkenylamines **56-64.***

*Table 9. Tandem Michael addition/aza-Claisen rearrangement of precursors **56-64**: substrate scope studies.*

Entry	R	R'	Starting Material (ee)[b]	Product yield[a] (ee)[b]
1	Ph	Me	**56** (97% ee)	**66** 95% (97% ee)
2	Ph	Et	**57** (97% ee)	**67** 83% (97% ee)
3	Ph	$(CH_2)_2Ph$	**58** (96% ee)	**68** 90% (96% ee)
4	Ph	^{i}Pr	**59** (98% ee)	**69** 90% (98% ee)
5	Ph	Ph	**60** (96% ee)	**70** 78% (96% ee)
6	2-ClC_6H_4	Me	**61** (99% ee)	**71** 90% (99% ee)
7	4-$MeOC_6H_4$	Et	**62** (80% ee)	**72** 90% (80% ee)
8	*(E)*-styryl	Me	**63** (99% ee)	**73** 89% (99% ee)
9	Cy	Me	**64** (97% ee)	**74** 88% (97% ee)

[a] Isolated yield. [b] ee values determined by HPLC analysis on a chiral stationary phase.

Regioselective functionalisation of *N*-protected indoles such as **75** was achieved by Wang *et al.,* who developed a synthetic protocol featuring initial *N*-alkylation of the starting material with a large excess of enamine **76**.The resulting *N*-benzyl-*N,N*-dimethylammonium salt **77** rapidly underwent aza-Claisen rearrangement followed by microwave-assisted hydrolysis in $^{i}PrOH/H_2O$ at 100 ^{o}C, yielding indoline derivative **78** with insertion of a reverse-prenyl moiety in C^2 position (Scheme 37).[157]

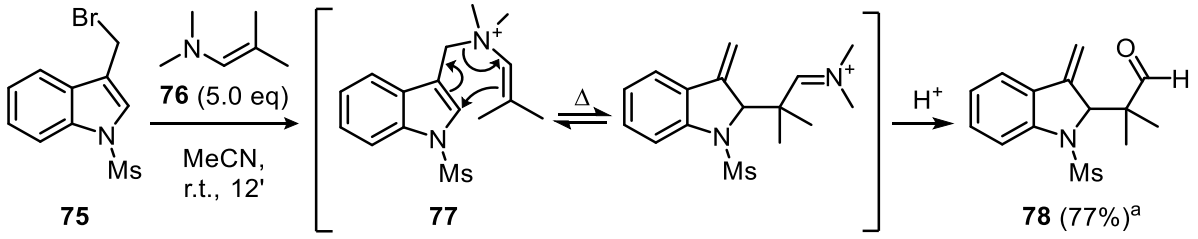

*Scheme 37. Microwave-assisted, tandem N-alkylation/aza-Claisen rearrangement of N-protected-3-(1-bromoethyl)indole **75**. [a] Isolated yield over two steps.*

More recently, a novel synthetic strategy was envisaged to promote the amino-Claisen rearrangement of tertiary cycloamines, which revolved around aryne chemistry. The first successful example of a benzyne aza-Claisen rearrangement was demonstrated by Greaney and co-workers, who investigated conversion of a series of tertiary amines including *N*-allylpiperidine **79** in presence of benzyne precursor **80** and caesium fluoride. Provided that optimised reaction conditions comprised a mixture of toluene and acetonitrile as reaction medium, mechanistic insight was provided as starting materials conversion took place either *via* [3,3]-σ or 6-endo S_N2' reaction. Deuterium labelling of the latter co-solvent provided a clear-cut answer to this conundrum as ^2H atom transfer took place between CD_3CN and the zwitterionic adduct resulting from **79** and *o*-trimethylsilylphenyl triflate **80**. This key intermediate underwent solvent-mediated protonation affording ammonium salt **81** with 71% yield, which rearranged *via* charge-accelerated aza-Claisen pathway to produce 2-allyl substituted aniline **82** (Scheme 38).[158]

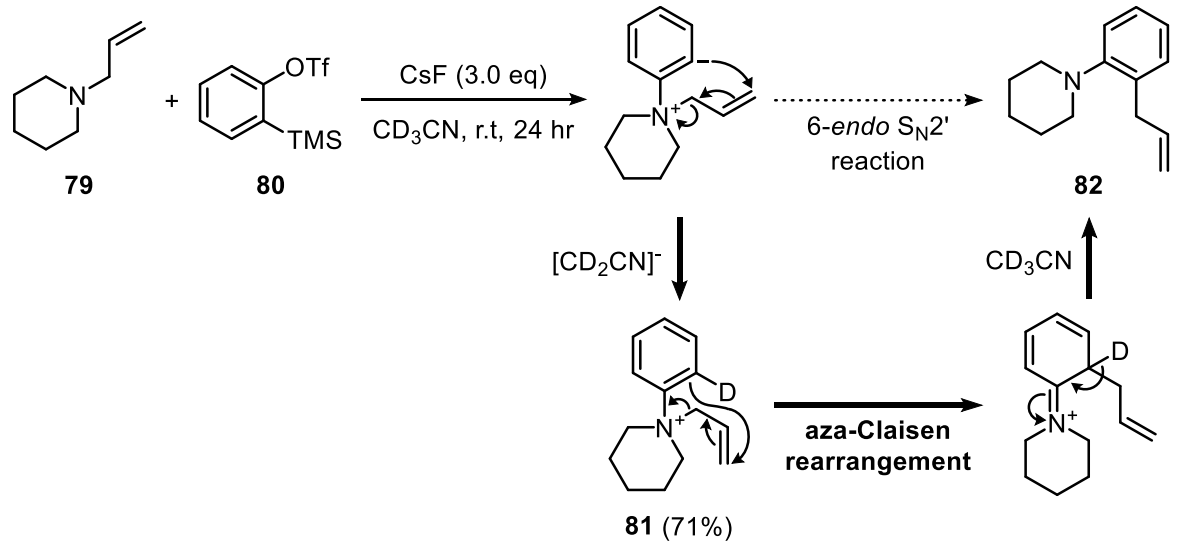

*Scheme 38. Benzyne aza-Claisen rerrangement of N-allylpiperidine **79**, deuterium labelling studies.*

Similar reaction conditions were required for the benzyne aza-Claisen rearrangement of substituted *N,N*-diallylanilines[159] as well as ring-strained *N*-allylamines such as 2-vinylaziridines.[160] Particular mention goes for the cycloaddition reaction of 2-vinylazetidines studies undertaken by Saito and co-workers, who investigated both acid and benzyne-mediated aza-Claisen rearrangement procedures.[161,162] Unlike the latter variant, amino-Claisen rearrangement/ring opening of *N*-(*p*-methoxyphenyl)-2-vinylazetidine **83** took place in presence of protic acids at room temperature.[161] Further *N*-acetylation was required in order to isolate fused macrolactam **84** whereas no derivatisation was required when the ring-expansion reaction was promoted by arynes, yielding 1-benzazocine derivative **85** (Scheme 39).[162]

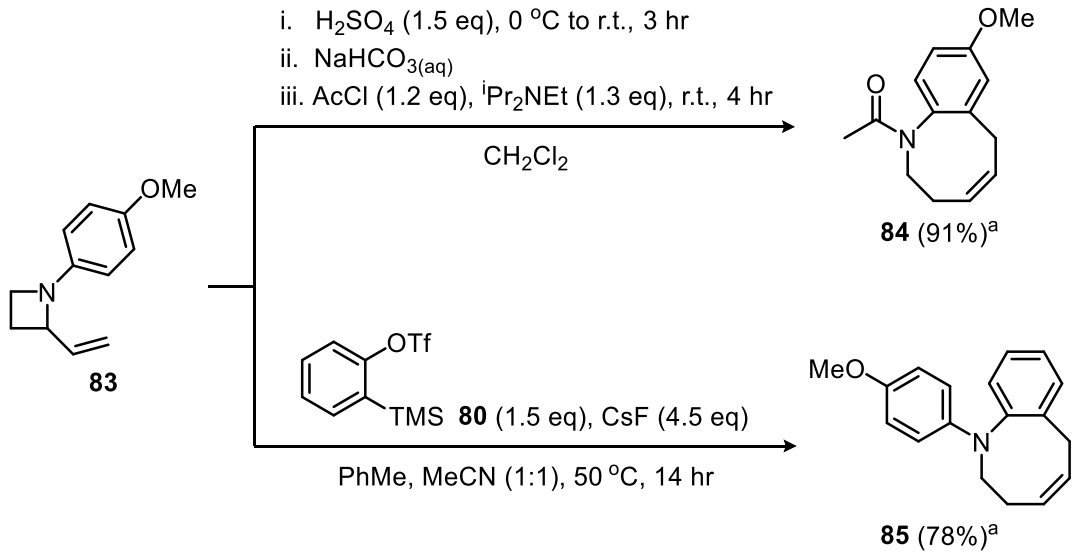

*Scheme 39. Ring expansion of 2-vinylazetidine precursor **83** via aza-Claisen rearrangement promoted by protic acid and aryne precursor **80.** [a.] Isolated yield.*

Experimental evidence gathered during rearrangement of *N*-benzyl-2-vinylazetidine **86** in CD_3CN were in accordance with pre-existing mechanistic studies described by Greaney *et al.*[162] Benzyne precursor activation followed by nucleophilic attack of the nitrogen atom within **86** afforded zwitterionic species **87**, which underwent rapid protonation (Scheme 40). Although the resulting deuterated azetidinium salt was not isolated, the S_N2' reaction pathway was again disfavoured as equimolar amounts of 1-benzoacines **88-H** and **88-D** were isolated in 43% combined yield.[162]

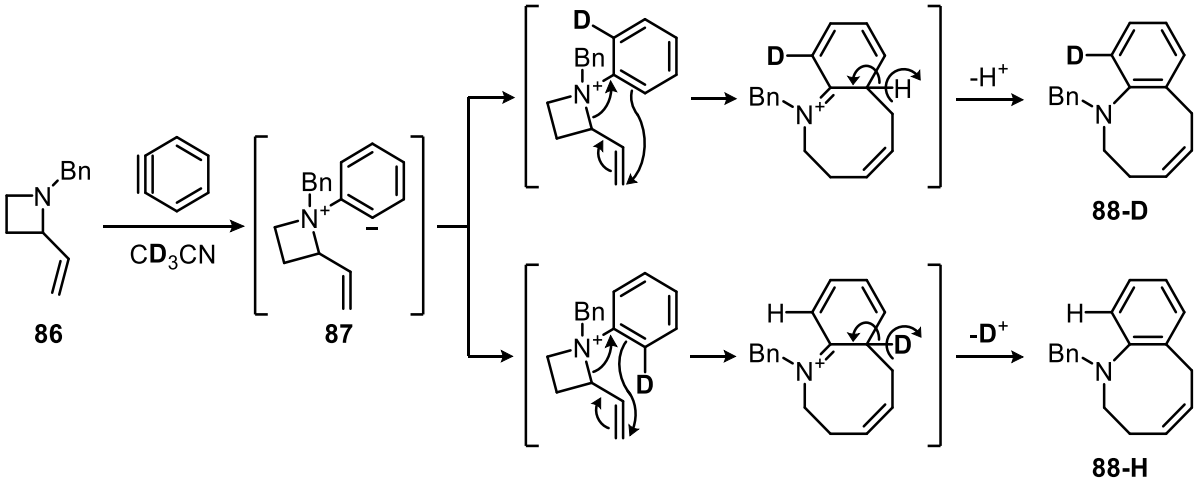

*Scheme 40. Benzyne-mediated synthesis of 1-benzoazocine derivatives **88-D** and **88-H**. Reaction pathways investigated via ^2H-labelling of reaction medium. [a.] 43% combined yield determined via crude ^1H-NMR analysis* (**88-H : 88-D** = 1:1)

In a similar fashion, Tian *et al.* demonstrated how arylpropargylammonium salts, generated *in situ* from arynes and tertiary propargylamines, underwent aromatic aza-Claisen rearrangement and allenyl-to-propargyl isomerization to afford 2-propargylanilines with good to excellent yields (Scheme 41).[163]

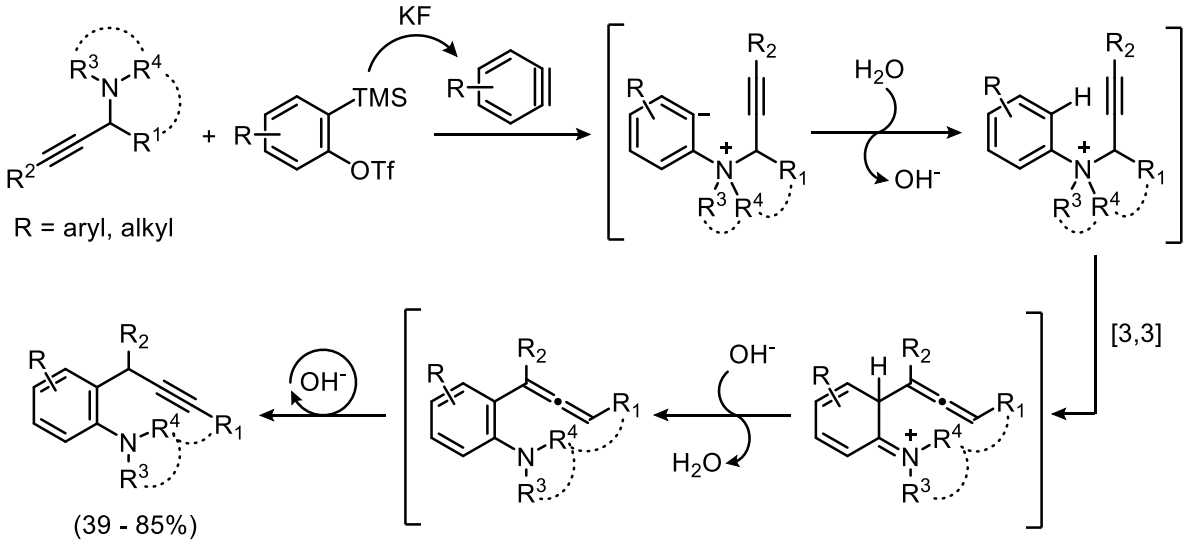

Scheme 41. Proposed reaction pathway for the synthesis of 2-propargylanilines from arynes and tertiary N-propargylamines.

Moreover, cyclisation of 2-propargylaniline intermediates was optimised, yielding substituted indoles in presence of stoichiometric amounts of $AlCl_3$ in refluxing ethanol (Scheme 42).[163]

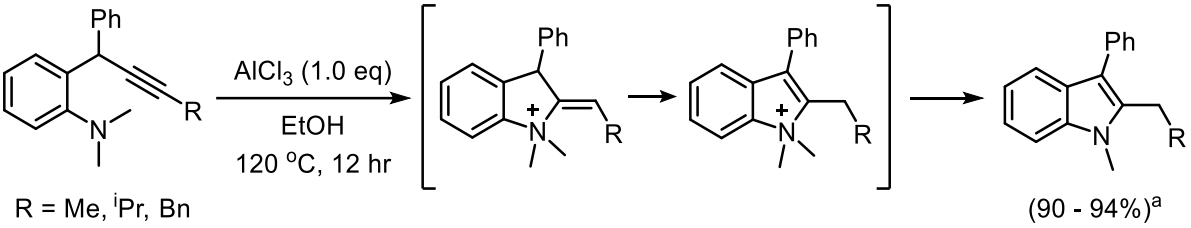

Scheme 42. Aluminium chloride-mediated transformation of 2-propargylanilines into indoles.

4.3 Aromatic aza-Claisen rearrangement of ammonium salts

Following the amount of literature studies reporting in *situ* aza-Claisen rearrangement of tertiary arylamines, sigmatropic reactions starting from an already charged substrate have been documented, albeit to a limited extent by Katayama and co-workers (Scheme 43). Thermal rearrangement of *N*-allyl-*N,N*-dimethylanilinium halide salts **89-92** into *o*-allylsubstituted products **93-94** took place with yields ranging between 2% and 81%, depending on the polarity of the solvent, nucleophilic character featured by ammonium salt's counterion as well as addition of $NaHCO_3$ in stoichiometric amounts (Table 10).[164]

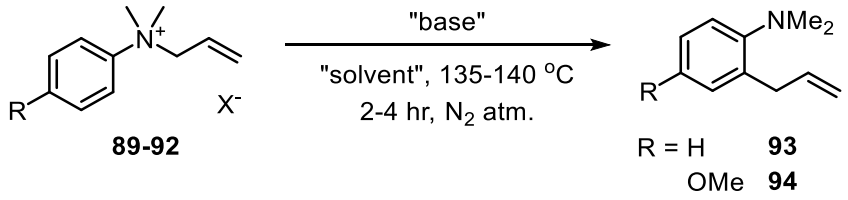

*Scheme 43. Thermal rearrangement of N-allyl-N,N-dimethylanilinium halides **89-92**.*

*Table 10. aza-Claisen rearrangement of halide arylammonium salts **89-92**: solvent, base and counterion screening*

Entry	R	X^-		"Solvent"	"Base"	Yield[a]
1	H	Br^-	**89**	DMF	-	2%
2	H	Br^-	"	EG	-	34%
3	H	Br^-	"	EG, H_2O (2:1)	-	53%
4	H	Br^-	"	EG, H_2O (2:1)	$NaHCO_3$ (1.10 eq)	81%
5	OMe	Cl^-	**90**	EG, H_2O (2:1)	$NaHCO_3$ (1.10 eq)	61%
6	OMe	Br^-	**91**	EG, H_2O (2:1)	$NaHCO_3$ (1.10 eq)	60%
7	OMe	I^-	**92**	EG, H_2O (2:1)	$NaHCO_3$ (1.10 eq)	43%

[a] Yield determined by GC analysis.

Use of polar aprotic solvents proved detrimental towards formation of aniline **93** *via* rearrangement of bromide ammonium salt **89** (Table 10, Entry 1). Conversely, increased yields were achieved when the same reaction was carried out in pure and aqueous ethylene glycol (Table 10, Entry 2 and 3 respectively). Moreover, starting material **89** conversion into 2-allyl-*N,N*-dimethylaniline **93** further improved upon addition of $NaHCO_3$, which neutralised the $HBr_{(aq)}$ generated *in situ* during rearrangement (Table 10, Entry 4). Reaction yields were also influenced by counterion effects. As exemplified by a series of *p*-methoxy-*N,N*-dimethylanilinium salts, similar reaction yields were isolated starting from either chloride or bromide salts **90-91** whereas counterion switch from Br^- to I^- adversely affected conversion of **92** into desired product **94** (Table 10, Entry 5-7). Following the latter experimental results, Katayama *et al.* proposed that increased counterion nucleophilicity corresponded to poorer reaction yields. Thus, additional rearrangement studies were carried out starting from non-nucleophilic counterions, such as the ones featured by *N,N*-dimethylanilinium salts **95** and **96,** further consolidating the explanation provided for this reactivity trend (Scheme 44).

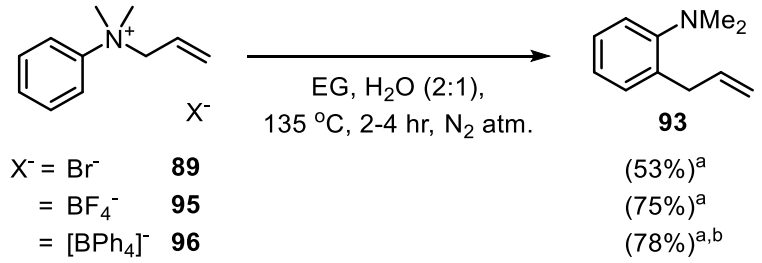

*Scheme 44. Thermal aza-Claisen rearrangement of N-allyl-N,N-dimethylanilinium salts **89, 95** and **96**.*
*[a] Yields determined upon GC analysis; [b] Ammonium salt **96** dissolved in DMF, heated at 145 °C for 5.5 hr.*

Effects of *ortho*-substituents on the phenyl ring were next investigated upon rearrangement of *N*-allyl-*N,N*-dimethylanilinium salts either bearing either a freely rotating or locked substituent on the anilinium ring.[165] In the former case, *o*-methyl and *o*-methoxy substituted *N*-allyl-*N,N*,-

dimethylanilinium salts suffered a high degree of de-allylation, suggesting that rearrangement was halted due to steric hindrance between the ammonium moiety and the phenyl ring substituent. As a result, the so-called "*ortho*-effect" was invoked to explain this sluggish reactivity, which became noticeable starting from the bulkier, *o*-methoxy substituted ammonium salt.[165] Conversely, further insight was achieved by comparing the reactivity displayed by chiral tetrahydroquinolinium salt **97** and tertiary aniline counterpart **98**, which underwent thermal and conventional Lewis-acid promoted aza-Claisen rearrangement, respectively (Scheme 45).[165,166]

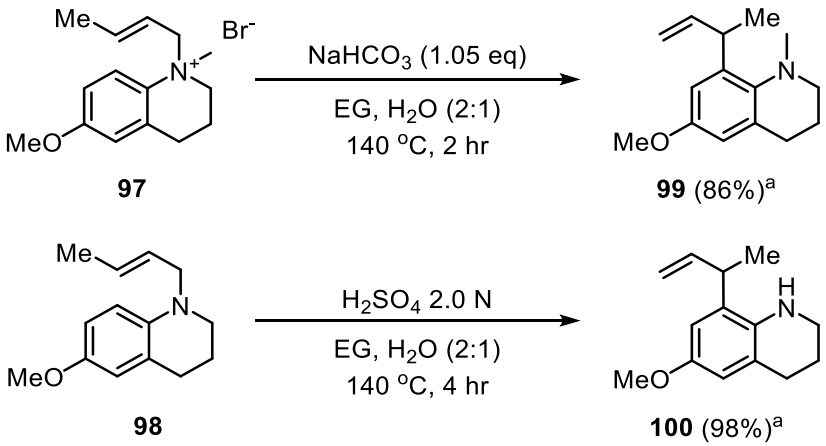

*Scheme 45. Charged aza-Claisen rearrangement of bromide salt **97**: reactivity comparison against Bronsted acid-catalysed rearrangement of aniline **98**, [a] Crude reaction yield determined upon GC analysis.*

Both reactions were conducted under relatively mild temperatures without jeopardising the reaction yields; 98% for the protic acid catalysed reaction and 86% for the charged, uncatalysed reaction. Thus, it was confirmed that the rearrangement of quaternary ammonium salt **97** was possible without external catalysis whilst maintaining similar reaction conditions employed during rearrangement of **98**. Allyl group inversion was observed in both cases, therefore suggesting that thermal rearrangement of ammonium salt **97** took place in a concerted manner, as previously noted for *N*-(2-butenyl)-*N,N*-dimethylanilinium bromide.

Follow-up studies were undertaken to better understand the effect exerted by differing alkenyl groups bound to the ammonium centre.[166] *N*-allyl, *N-(E)*-2-butenyl and *N*-(2-methyl-2-butenyl) substituted tertiary anilines **101-103** and quaternary ammonium salt precursors **104-106** were prepared prior to rearrangement, starting from either 1,2,3,4-tetrahydroquinoline or its *N*-methyl substituted analogue. In all cases, aromatic aza-Claisen rearrangement of substrates featuring *N*-allyl or *N*-crotyl side chains seemed effective whereas *N*-prenyl group migration proved more convoluted (Scheme 46). Although faster reaction rates were observed during conversion of *(E)*-2-butenyl aniline **102** compared to the *N*-allyl substituted analogue **101**, aza-Claisen rearrangement of both anilines resulted in formation of *o*-rearranged product **107o** and **108o** in satisfactory amounts (Table 11, Entries 1 and 2). Conversely, no *ortho*-substituted

aza-Claisen compound **109o** was detected starting from aniline **103,** which in turn afforded a complex mixture of products (Table 11, Entry 3).

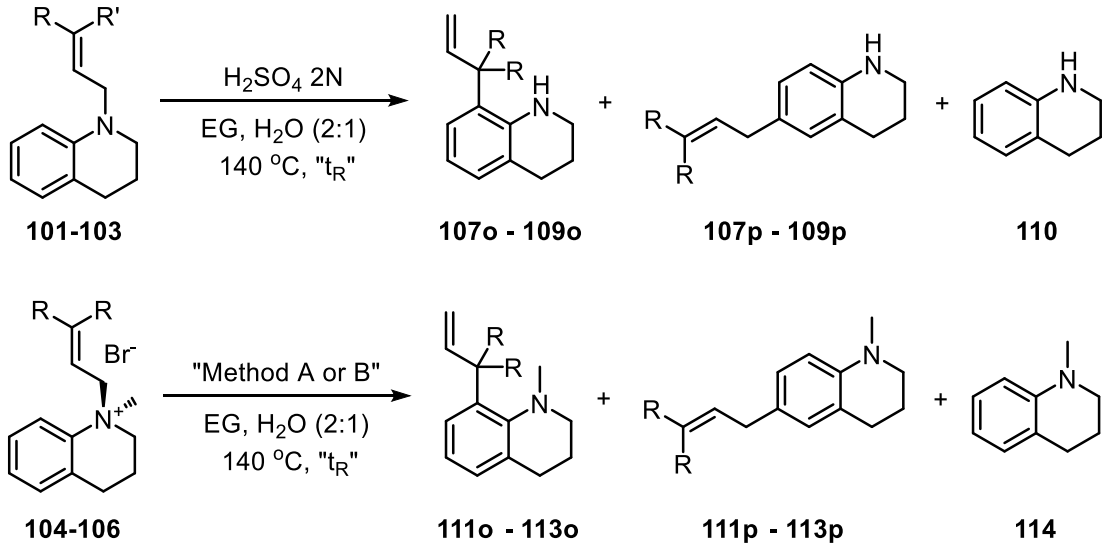

*Scheme 46. Charged aza-Claisen rearrangement of ammonium salts **104-106**: reactivity comparison against acid-catalysed rearrangement of tertiary anilines **101-103**.*

*Table 11. Crude material analysis after rearrangement of N-alkenyl substituted anilines **101-103** and bromide ammonium salts **104-106.***

Entry	R	R'	t_R		Method[b]	Products (Yield %)[a]	By-products[a]
1	H	H	8 hr	**101**	-	**107o** 81% **107p** 1% **110** <1%	12%
2	Me	H	4 hr	**102**	-	**108o** 89% **108p** 2% **110** -	9%
3	Me	Me	2 hr	**103**	-	**109o** - **109p** 9% **110** 30%	56%
4	H	H	2 hr	**104**	A	**111o** 90% **111p** 4% **114** 6%	-
					B	**111o** 92% **111p** 4% **114** 3%	-
5	Me	H	2 hr	**105**	A	**112o** 46% **112p** 53% **114** 2%	*E/Z* = 91:9
					B	**112o** 88% **112p** 4% **114** 8%	*E/Z* = 91:9
6	Me	Me	2 hr	**106**	A	**113o** 5% **113p** 4% **114** 81%	9%
					B	**113o** 5% **113p** 38% **114** 47%	9%

[a] Yield determined by GC analysis; [b] Method A: EG, H_2O (2:1, 8 mL), 140 °C, 2h; Method B: EG, H_2O (2:1, 8 mL), $NaHCO_3$ (2.10 eq), 140 °C, 2h.

A similar outcome was observed during thermal rearrangement of bromide ammonium salts **104-106,** which was carried out either with or without stoichiometric amounts of $NaHCO_3$ (Scheme 46, Method A and B, respectively). Overall, addition of sodium bicarbonate proved beneficial for the regioselective synthesis of *ortho*-substituted derivatives **111o** and **112o** as well as **113o**, albeit to limited extent in the latter case (Table 11, Entries 4-6). Introduction of a single γ-methyl onto the allyl group affected the reaction pattern only in absence of $NaHCO_3$, yielding *para*-substituted rearranged product **112p** in greater amounts (Table 11, Entry 5A). The selectivity shift imparted by $NaHCO_3$ was consistent with both [3,3]-σ rearrangement and deprotonation of **105‡** taking place, with the latter process occurring faster only under weakly basic conditions (Table 11, Entry 5B). Nonetheless, retention of (*E*)-configuration exhibited by **112p** was observed in both cases, suggesting that inversion of the migrating alkenyl moiety leading to **112o** mostly proceeded *via* chair-like conformation (Scheme 47).

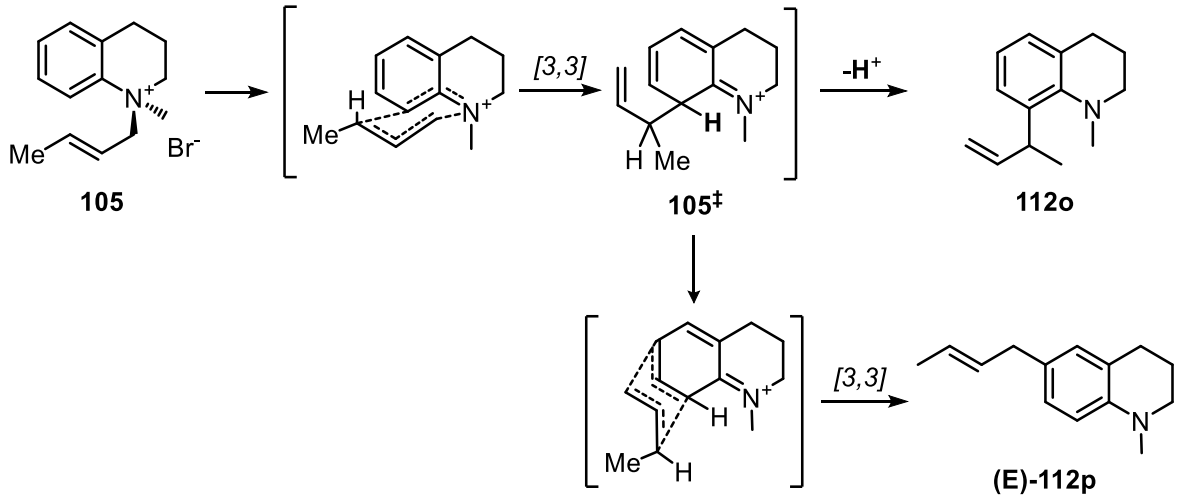

*Scheme 47. Reaction pathways proposed during charged aza-Claisen rearrangement of ammonium salt **105***

Similarly to tertiary aniline **103**, *N*-prenyl group rearrangement of tetrahydroquinolium salt **106** proved challenging since large amounts of *de*-prenylated material **114** were detected in the reaction mixture (Table 11, Entry 6). Moreover, an additional compound was identified alongside both *ortho*- and *para*-rearranged minor products, being 8-prenyl-*N*-methyltetrahydroquinoline **115** (Scheme 48). Differently from the former compounds, conversion of ammonium salt **106** into aniline **115** did not proceed *via* [3,3]-σ sigmatropic rearrangement but through a dissociative mechanism, which was suggested occurring through formation of stabilised benzylic and allylic radicals.

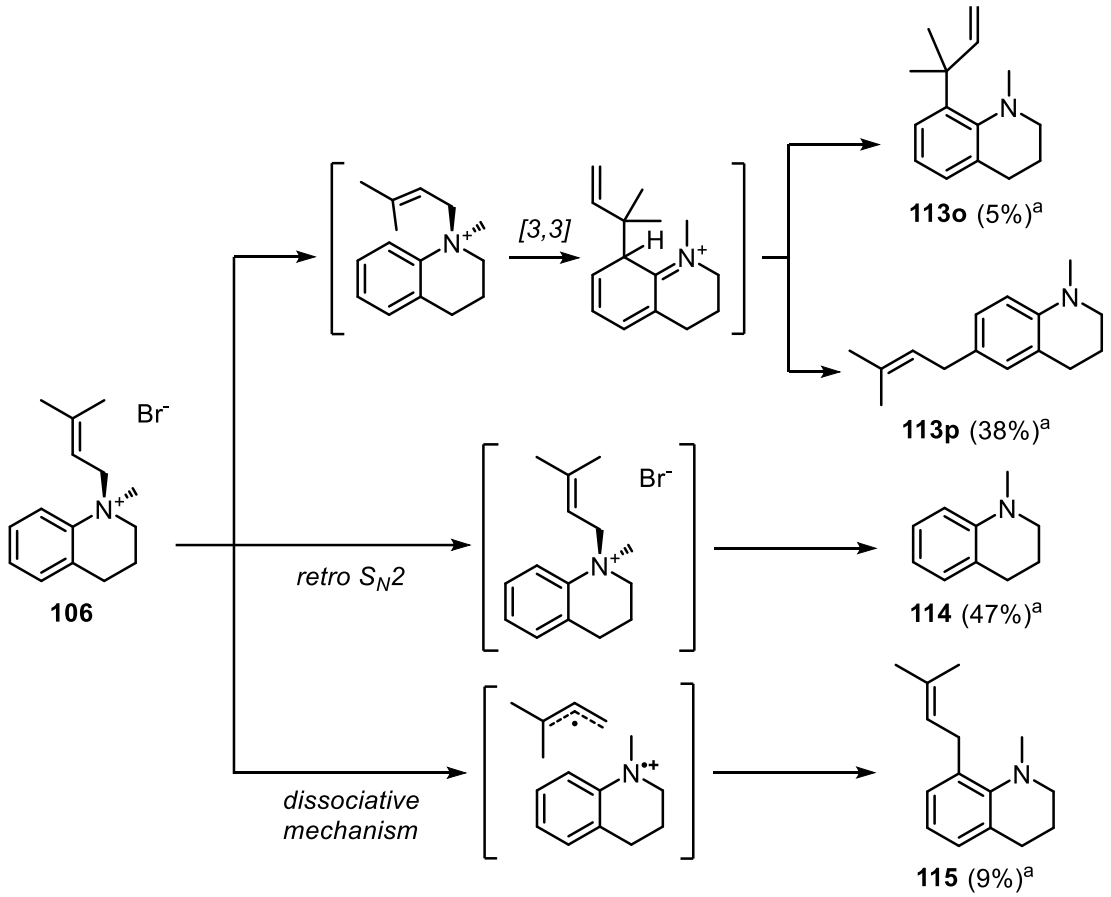

*Scheme 48. Competitive reaction pathways during aza-Claisen rearrangement of N-prenyl-N-methyl-tetrahydroquinolium salt **106**. [a] Crude yield determined via GCMS*

4.3.1 Aromatic aza-Claisen rearrangement of ammonium salts: a mechanistic debate

Despite of the thorough research undertaken by Katayama *et al.*,[164–166] earlier literature studies provided evidence by which two competing reaction mechanisms took place during rearrangement of *N*-alkenyl anilines and ammonium salts. Hurd and Jenkins first reported a $ZnCl_2$-promoted aza-Claisen rearrangement of *N*-allylaniline as well as *N*-cinnamylaniline **116**.[130] Concerning the latter substrate, conversion of **116** proved more challenging, since rearrangement of the latter arylamine yielded *o*-cinnamylaniline **117** rather than 2-(3-phenylallyl)aniline **118.** To justify this unexpected result, a "bimolecular mechanism" was proposed for formation of compound **93a**, or in other words, a dissociative mechanism mediated by $ZnCl_2$ at high temperatures (Scheme 49).

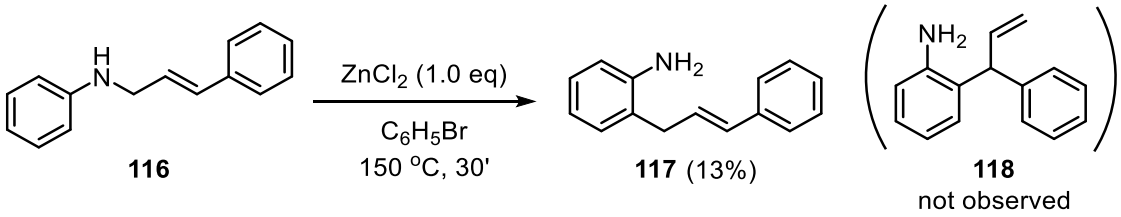

*Scheme 49. Zinc chloride-mediated aza-Claisen rearrangement of N-cinnamylaniline **116***

Nonetheless, the results by them reported prompted Kishi *et al.* not only to successfully replicate their research work but also to attempt rearrangement of *N,N-(*2-methyl-2-butenyl)aniline **119** into intermediate **120**.[167] Upon closer inspection of the product isolated *via* $ZnCl_2$-assisted rearrangement of **119** however, the product they sought for did not originate from a sigmatropic process but rather from a dissociative mechanism (Scheme 50).

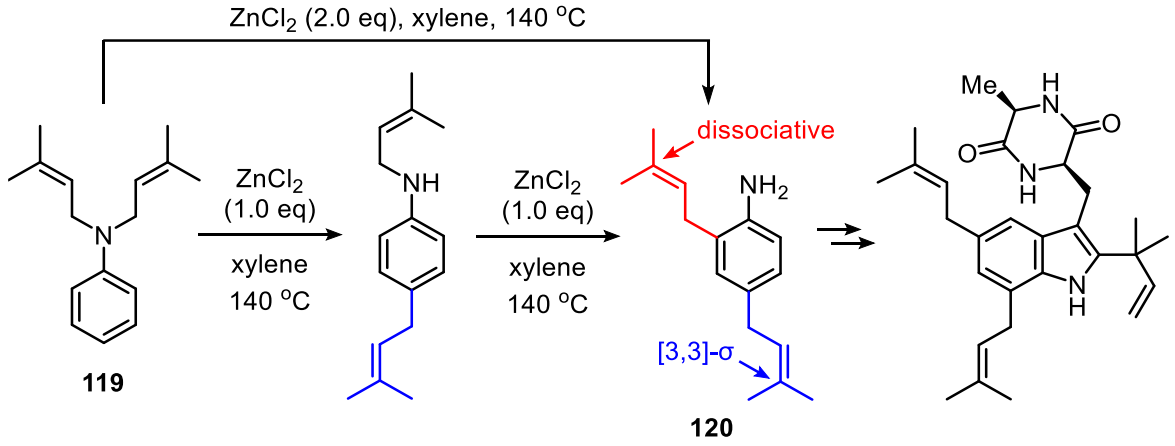

*Scheme 50. Total synthesis of echinulin by Kishi et al. via $ZnCl_2$-promoted conversion of N,N-diallylaniline **119** into intermediate **120**.*

On the other hand, rearrangement of *N*-alkenyl-*N,N*-dimethylanilinium tetraphenylborates was investigated by Schmidt *et al.* in hexamethylphosphoramide (HMPA).[131] Although clean conversion of *N*-crotyl and *N*-allyl precursors into 2-(1-methylallyl) and 2-allyl-*N,N*-dimethyl aniline took place with moderate yields, poor conversion was observed starting from N-cinnamyl-*N,N*-dimethylanilinium tetraphenyl borate **121.** A mixture of products was isolated in the latter case, which comprised the expected [3,3]-σ product **122** as well as 2-cinnamyl-*N,N*-dimethylaniline **123** and thermal degradation byproduct *N,N*-dimethylaniline **124** (Scheme 51).

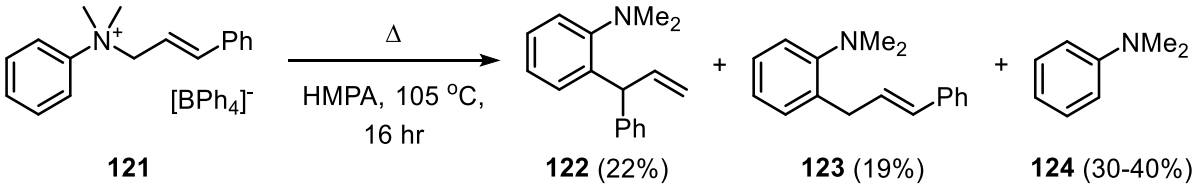

*Scheme 51. Thermal rearrangement of N-cinnamyl-N,N-dimethylanilinium tetraphenylborate **121** in HMPA.*

Finally, work by McComsey and Maryanoff demonstrated that rearrangement of enantiopure benzo[a]quinolizine ammonium salt **125** and pyrrolo-[2,1-a]isoquinoline analogue **126** resulted in an excellent chirality transfer from the nitrogen centre to the resulting quaternary carbon centre.[168] Stereospecific synthesis of iminium **127-*trans*** took place *via* intramolecular rearrangement of the allylic moiety from N^5 to C^7 and absolute lack of the *cis* isomer suggested that conversion of ammonium salt **125** into **127-*trans*** proceeded through a concerted suprafacial rearrangement (Scheme 52, top). On the opposite, stereoselective formation of

128-*trans* was observed since small amounts of **128-*cis*** isomer were detected upon ^{1}H-NMR analysis (Scheme 52, bottom).

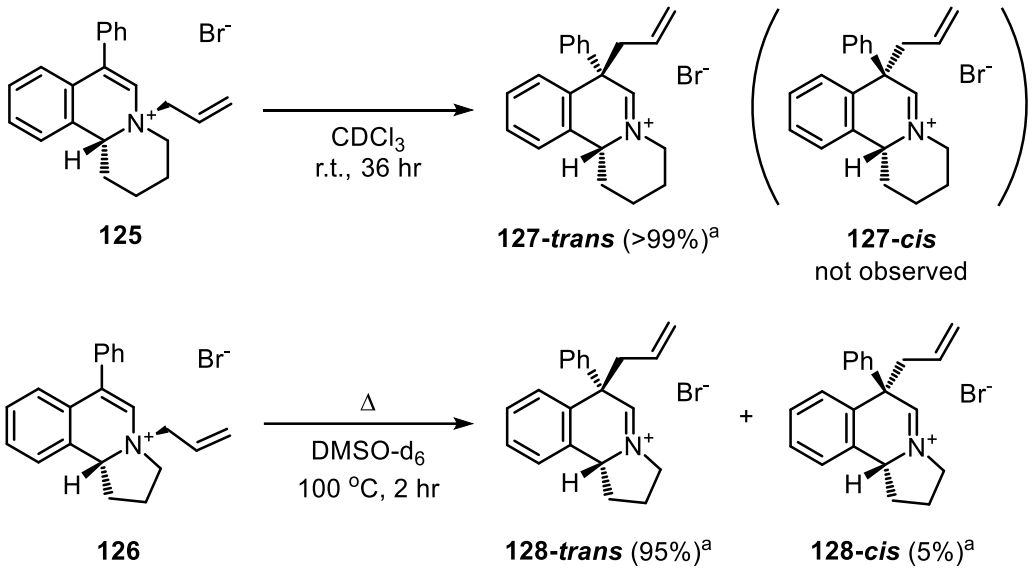

*Scheme 52. Stereoselective aza-Claisen rearrangement of bromide ammonium salts **125** and **126**.*
[a] Diastereomeric ratio determined via crude product ^{1}H NMR

This experimental result was consistent with the allyl group dissociation occurring alongside the [3,3]-σ rearrangement of **126**, probably due to the harsher reaction conditions required in such instance. Although this research publication seemed one of very few definitive examples of N-C chiral transfer occurring *via* aza-Claisen rearrangement, both examples were conducted on a 5 mg scale and the presence of an additional chiral centre in α position to the ammonium group may have influenced on the chiral transfer and overall experimental outcome.

4.4 Aims and objectives

As previously shown, much of the existing literature focused either on using Lewis acid or Brønsted acid catalysis or generation of arylammonium salts *in situ* to achieve reasonable conditions for the aza-Claisen arrangement. Use of catalysis, electrophilic π species and aryne precursors can be circumvented *via* direct rearrangement of isolated ammonium species since the proposed quaternary ammonium substrates already contain a sufficiently electron deficient nitrogen centre. Furthermore, proof of concept was provided throughout the years that charge-accelerated aza-Claisen rearrangement of ammonium salts can be synthetically viable, and that further investigation would be required to better understand which reaction mechanism, namely sigmatropic or dissociative, was preferred during substrates rearrangement.

This charged aza-Claisen variant was therefore hypothesized to allow for easier rearrangement of ammonium salts, with selective formation of either [3,3]-σ rearranged or cyclised material in a single synthetic step. A series of objectives was therefore set for the development of such synthetic methodology, which comprised:

- Development of a facile synthetic protocol for synthesis of the substrate scope library – i.e., ammonium salts precursors;
- Screening and optimisation of reaction conditions for aza-Claisen rearrangement and cyclisation of quaternary ammonium salts;
- Substrate scope broadening and identification of limiting factors impacting the investigated synthetic methodology.

Chapter 5

Research work and discussion

The research work herein discussed focused on the development of a simple, convenient route for the chemoselective synthesis of indolinium salts and substituted *o*-allylanilines.

In the former case, targeted production of quaternary ammonium salts has been documented in literature as early as the 1930s, due to their medicinal and surface active properties.[169] Besides commonplace species such as C_nTAB cationic surfactants, synthesis of charged *N*-heterocyclic core structures was investigated due to their presence within biologically active compounds - e.g. flavopereirine, coralyne chloride and 9-amino-benzo[c]cinnoliniums salts.[170–172] Isolation of positively charged ammonium scaffolds proved challenging however since it generally took place starting from tailored synthetic precursors and by means of metal-catalysed C-H activation/annulations with internal alkynes.[173,174] On the other hand, synthesis of *ortho*-alkenyl substituted arylamines was explored since they can be regarded as useful precursors to indole and quinoline compounds. Among the various synthetic strategies developed for this purpose, Denmark and Chi recently reported three routes to accomplish the preparation of *o*-alkenylanilines. Besides Pd(II)-catalysed amination of aryl chlorides and olefinic cross-metathesis of *N*-tosyl aromatic compounds, a two-step procedure was described for the synthesis of tethered *o*-allylanilines which featured initial $ZnCl_2$-promoted Grignard addition to aldimines and $BF_3 \bullet Et_2O$/PTSA-mediated aza-Claisen rearrangement at high temperatures.[175]

Given these painstaking efforts to access both compound categories with starkly different synthetic protocols, no alternative reaction conditions have been reported thus far for the synthesis of either quaternary *N*-heterocyclic salts or substituted *o*-allylanilines starting from a communal precursor. Therefore, a metal-free, tandem *ortho*-allylation and cyclisation of arylammonium salts was investigated, which occurred *via* charged aza-Claisen rearrangement of quaternary ammonium species. Mild and easily tuneable reaction conditions were optimised for the development of this synthetic methodology, which was probed to identify its key strengths and limitations.

5.1 Thermal cyclisation of arylammonium salts *via* charged aza-Claisen rearrangement: optimisation studies

Following Katayama *et al*. pioneering studies on the charged aza-Claisen rearrangement of ammonium species,[164–166] fellow colleague Dr. Mark P. Walsh spearheaded this research topic by identifying the limiting factors associated to rearranging *N,N*-dimethylanilinum bromide salts. A brief overview of his work will be covered in Sections 5.1.1 and 5.1.2 (where specified), to better describe which key parameters were later optimised to achieve chemoselective synthesis of quaternary indolinium salts and *ortho*-allyl substituted anilines.[176]

5.1.1 Thermal cyclisation of bromide arylammonium salt 89

Model substrate *N*-allyl-*N,N*-dimethylanilinium bromide **89** was at first synthesised for this purpose, which was obtained *via* alkylation of *N,N*-dimethylaniline **124** in 98% yield (Scheme 53). A range of reaction conditions were adapted by Dr. Mark P. Walsh from synthetic procedures originally developed for the aza-Claisen rearrangement of tertiary arylamines and screened to evaluate their effectiveness for bromide salt **89** conversion into *N*-heterocyclic ammonium product **129** (Table 12).

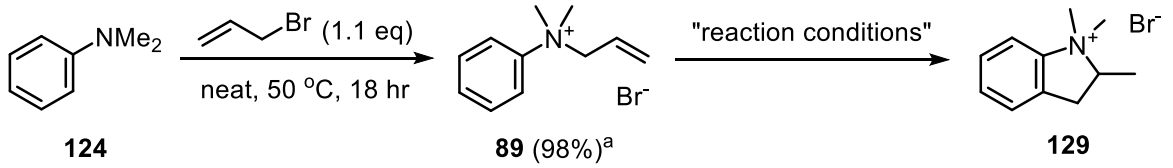

124 **89** (98%)[a] **129**

*Scheme 53. Reaction conditions screening for the aza-Claisen rearrangement/thermal cyclisation of ammonium bromide salt **89***

*Table 12. aza-Claisen rearrangement of N-allyl-N,N-dimethylanilinium bromide **89**: solvent screening.[c]*

Entry[ref.]	Solvent	T_R	t_R	Starting material conversion rate[b]
1[155]	EG, H_2O (9:1)	140 °C	16 hr	decomposed
2	DMSO	155 °C	16 hr	decomposed
3[107]	H_2O	80 °C	48 hr	0%
4[149]	PhMe, MeCN (3:1)	80 °C	48 hr	22%
5[149]	PhMe, MeCN (3:1)	110 °C	48 hr	100%

[a] Isolated yield (provided by GFG); [b] Based on analysis of crude mixture using ^{1}H NMR spectroscopy. [c] Experimental results gathered by Dr. Mark P. Walsh.

Starting material decomposition was observed when precursor **89** was exposed to highly polar reaction media at temperatures equal or greater than 140 °C (Table 12, Entries 1 and 2). For this reason, lower temperatures were next screened in water and toluene/acetonitrile mixtures, which afforded 0% and 22% starting material conversion, respectively (Table 12, Entries 3 and 4). Although complete consumption of bromide salt **89** was achieved upon reflux in a (3:1)

toluene/acetonitrile mixture (Table 12, Entry 5), no cyclised product was observed upon crude ^{1}H-NMR analysis, which revealed ammonium salt degradation back to tertiary anilines *via* bromide-initiated *retro* S_N2. Side products isolation carried out by Dr. Mark P. Walsh by means of flash chromatography confirmed this hypothesis, since the experimental results by him gathered were consistent with unwanted *de*-allylation and *de*-methylation processes taking place starting from *N*-allyl-*N,N*-dimethylanilinium bromide **89** (Scheme 54, pathway *i* and *ii* respectively).

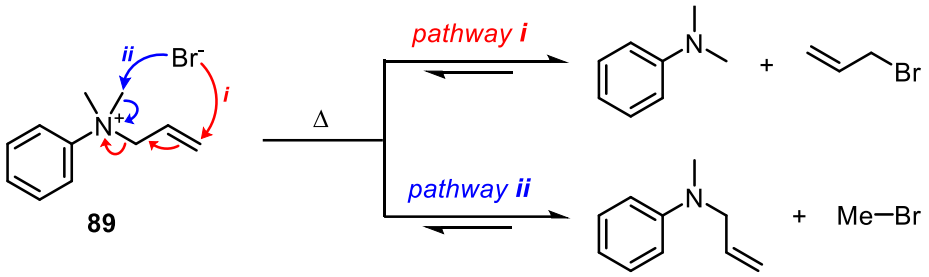

*Scheme 54. Proposed bromide-mediated degradation of arylammonium salt **89**.*

This experimental outcome was found in accordance with pre-existing research work by Lehn *et al.*, who investigated the dynamic exchange rate displayed by halide ammonium salts into their respective tertiary anilines. Higher degrees of nucleophilicity displayed by the counterion corresponded to greater exchange rates ($I^- > Br^- > Cl^-$) whereas non-nucleophilic anions, such as hexafluorophosphate (PF_6^-), greatly hindered the thermal degradation exhibited by quaternary ammonium salts.[177]

As such, it was decided that the bromide anion would be exchanged for PF_6^- and synthesis of an alternative model substrate was pursued to optimise this synthetic methodology.

5.1.2 Thermal cyclisation of hexafluorophosphate arylammonium salt 130

N-allyl-*N,N*-dimethylanilinium hexafluorophosphate **130** was isolated following a two-step procedure, starting from *N,N*-dimethylaniline **124**. More specifically, tertiary arylamine *N*-alkylation was required before KPF_6-promoted counterion exchange of ammonium salt **89**, which was carried out at room temperature in aqueous environment (Scheme 55).

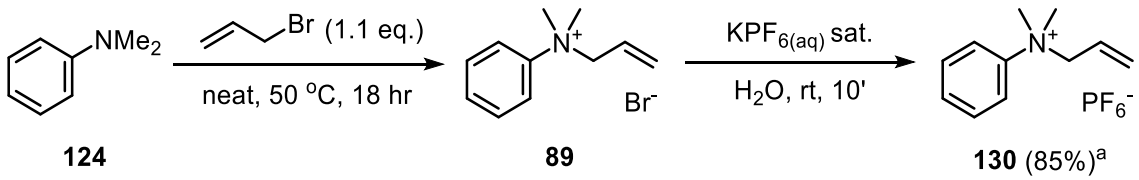

*Scheme 55. Two-step synthesis of hexafluorophosphate model substrate **130** starting from commercially available N,N-dimethylaniline **124**. [a] Isolated yield over two steps.*

Starting from hexafluorophosphate precursor **130**, further optimisation studies were conducted in PhMe/MeCN (3:1) mixtures to investigate the reaction times required for PF_6^- substrate conversion into indolinium **131**, with limited formation of aza-Claisen product **93** (Scheme 56).

Moreover, two alternative reaction setups were initially probed (microwave irradiation and solvent mixture reflux) and further insight was sought on whether such chemical transformation could benefit from inert reaction conditions (Table 13).

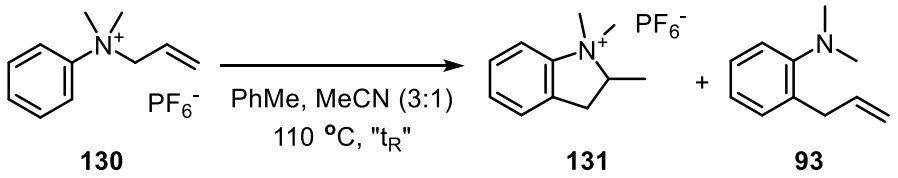

130 **131** **93**

*Scheme 56. Reaction condition screening for the aza-Claisen rearrangement /thermal cyclisation of PF_6^- salt **130** into indolinium **131.***

*Table 13. aza-Claisen rearrangement of N-allyl-N,N-dimethylanilinium hexafluorophosphate **131** in PhMe/MeCN mixtures: reaction condition screening.*

Entry	Reaction conditions	"t_R"	Yield %[b]	130[a]	131[a]	93[a]
1[c]	MW (200 W), Ar	1 hr	-	83%	1%	17%
2[c]	MW (200 W), Ar	4 hr	-	49%	14%	37%
3[c]	MW (200 W), Ar	8 hr	88%	15%	73%	12%
4	reflux, Ar	48 hr	69%	0%	100%	0%
5	reflux	48 hr	82%	41%	57%	2%
6	reflux	54 hr	-	8%	92%	0%
7	reflux	72 hr	87%	0%	100%	0%

[a] Crude mixture composition determined via ^{1}H-NMR spectroscopy; [b] Crude yield; [c] Experimental results provided by Dr. Mark P. Walsh

Preliminary studies carried out by Dr. Mark P. Walsh were undertaken in a sealed microwave vial and several timestamps were acquired during rearrangement of **130** under inert atmosphere (Table 13, Entries 1-3).[176] Longer reaction times were required to achieve complete starting material conversion into cyclised compound **131**, since both model substrate **130** and aza-Claisen product **93** were observed in comparable amounts upon ^{1}H-NMR inspection of the crude mixture (Table 13, Entry 3). Use of conventional reaction vessels was next explored and complete conversion of ammonium salt **130** into cyclised product **131** was observed when t_R = 48 hr, provided that the reaction mixture was left to reflux under argon flow (Table 13, Entry 4). As similarly described for the microwave irradiation experiments, longer reaction times were next examined to monitor the timeframe required for complete starting material consumption in “open air” reflux conditions (Table 13, Entries 5-7). Incomplete starting material conversion into **131** was observed after 48 hours whereas decreasing amounts of PF_6^- precursor **130** were detected when t_R = 54 hr (Table 13, Entry 5 and 6 respectively). Complete consumption of hexafluorophosphate salt **130** was achieved upon “open air” reflux for 72 hours, affording 1,1,2-trimethylindolin-1-ium hexafluorophosphate **131** with 87% crude yield (Table 13, Entry 7).

Overall, bromide counterion replacement with non-nucleophilic hexafluorophosphate proved beneficial towards the synthesis of target compound **131** since no starting material decomposition into *retro* S_N2 by-products took place in all experimental entries. Although shorter reaction times were required under inert conditions for the selective synthesis of indolinium salt **131** (Figure 54, Spectrum *a*), improved reaction yields were attained when the same reaction was carried in open atmosphere, albeit at a slower rate. Prolonged reaction times did not jeopardise the reaction selectivity and emergence of cyclised ammonium salt **131** was demonstrated upon comparison of ^{1}H-NMR spectra associated to reactions mixtures refluxed for 48, 54 and 72 hours (Figure 54, Spectra *b-d* respectively).

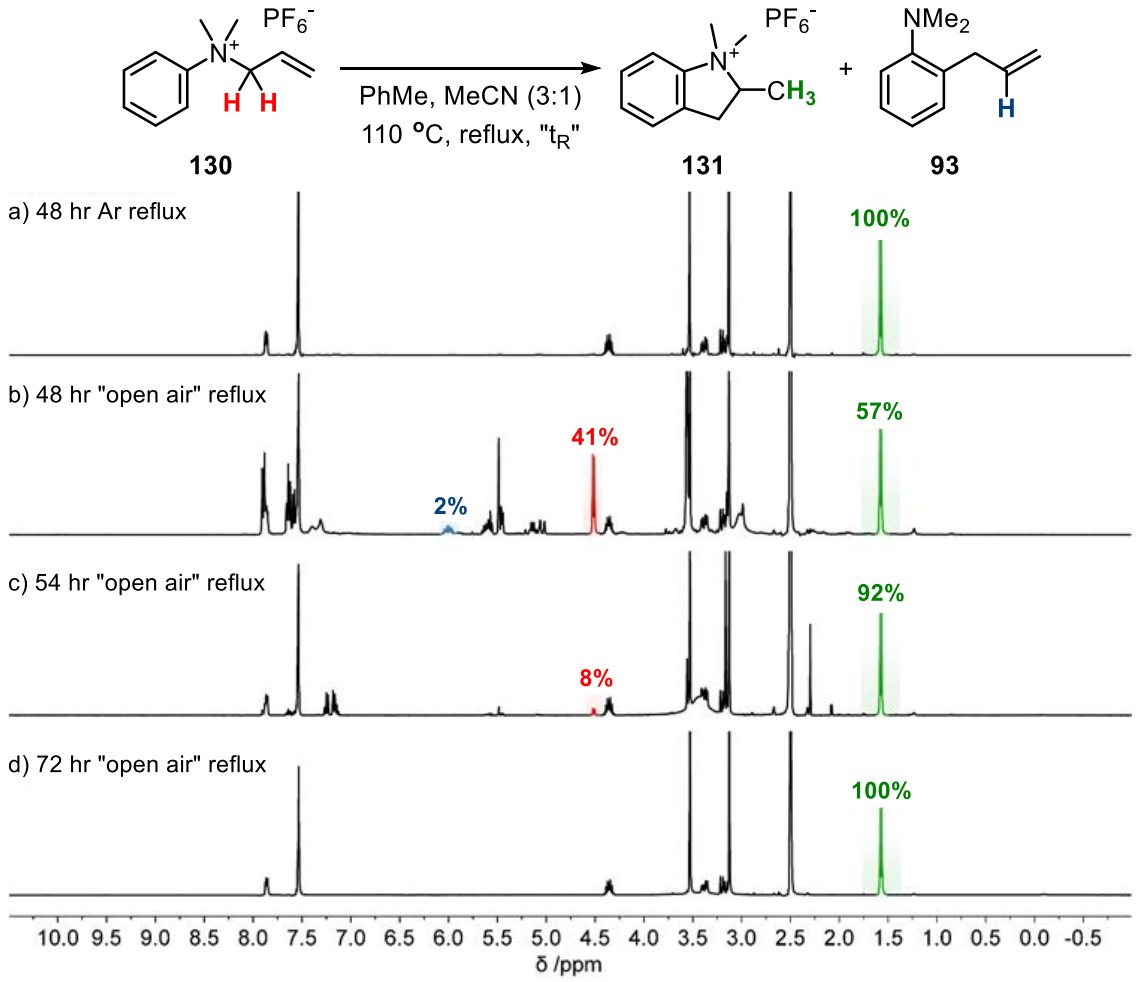

*Figure 54. aza-Claisen rearrangement/thermal cyclisation of hexafluorophosphate salt **130.** ^{1}H-NMR spectra comparison of crude reaction mixtures (recorded in DMSO-d_6), from top: a) t_R = 48 hr, inert atmosphere (Table 13, Entry 4)**;** b) t_R = 48 hr, open air (Table 13, Entry 5); c) t_R = 54 hr, open air (Table 13, Entry 6); d) t_R = 72 hr, open air (Table 13, Entry 7).*

Crude product analysis at t_R = 72 hr was also carried out *via* heteronuclear spectroscopy, to assess whether any side-reactions took place starting from the hexafluorophosphate counterion. Minor impurities were detected alongside PF_6^- suggesting that partial anion decomposition had occurred during thermal cyclisation of arylammonium salt **130** (Figure 55).

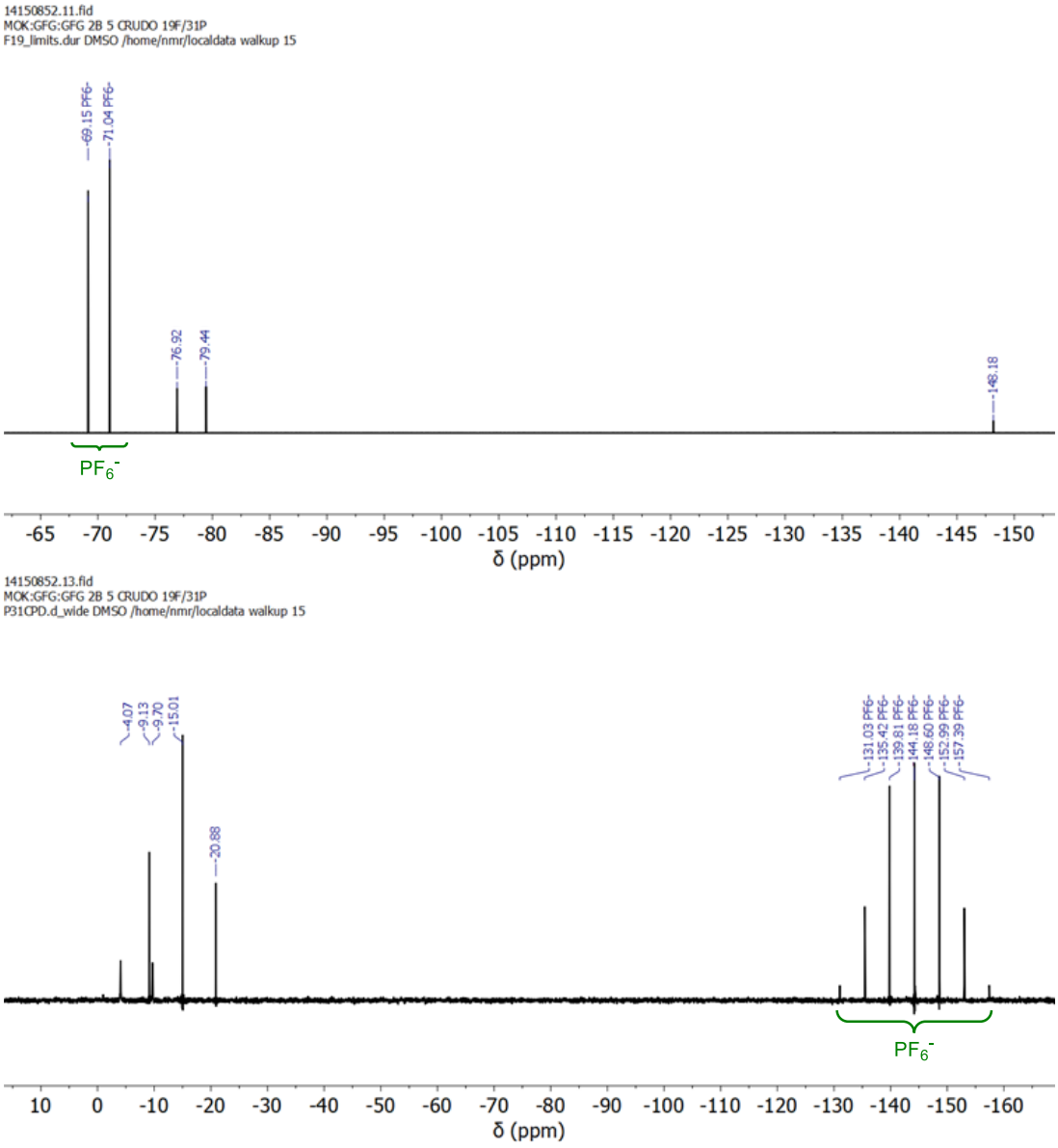

Figure 55. Crude material analysis by heteronuclear spectroscopy, recorded in DMSO-d_6: top) ^{19}F-NMR (376 MHz); bottom) ^{31}P-NMR (243 MHz). Hexafluorophosphate anion peaks are highlighted in green

Thorough investigation aimed towards by-product isolation and characterisation was not carried out at this stage, since further insight on this matter would have fallen outside the research scope set during optimisation studies.

In view of the above findings, counterion decomposition was suggested to take place in “open air” reflux conditions due to the synergistic contributions provided by elevated reaction temperature and presence of water in trace amounts. Corroborating evidence was found in literature reports examining the thermal stability displayed by hexafluorophosphate-based electrolytes.[178–180] For instance, temperature-dependent anion decomposition was assessed by Nowak and co-workers *via* quantitative ^{19}F-NMR measurements conducted on dry and water-containing $LiPF_6$ samples, which were prepared in carbonate-based solvents and stored at 60 °C before analysis.[180] Degradation by-products (e.g. HF and $OPF_2(OH)$) were found in

higher concentration in the latter case, thus suggesting how lithium hexafluorophosphate underwent faster PF_6^- hydrolysis due to “thermal aging” of water-contaminated analytes.[180]

A work-up procedure was developed to achieve counterion restoration as well as removal of heteronuclear impurities. Target molecule **131** was isolated from the cooled reaction mixture, which was at first concentrated to dryness under reduced pressure. A wax-like residue was obtained after solvent removal, which was re-dissolved in dichloromethane and stirred at room temperature, before addition of saturated $KPF_{6(aq)}$. Biphasic mixture separation *via* liquid-liquid extraction (CH_2Cl_2/H_2O) proved effective and successful by-product removal was demonstrated upon ^{19}F and ^{31}P-NMR spectroscopic analysis of the “counterion restored” material (Figure 56).

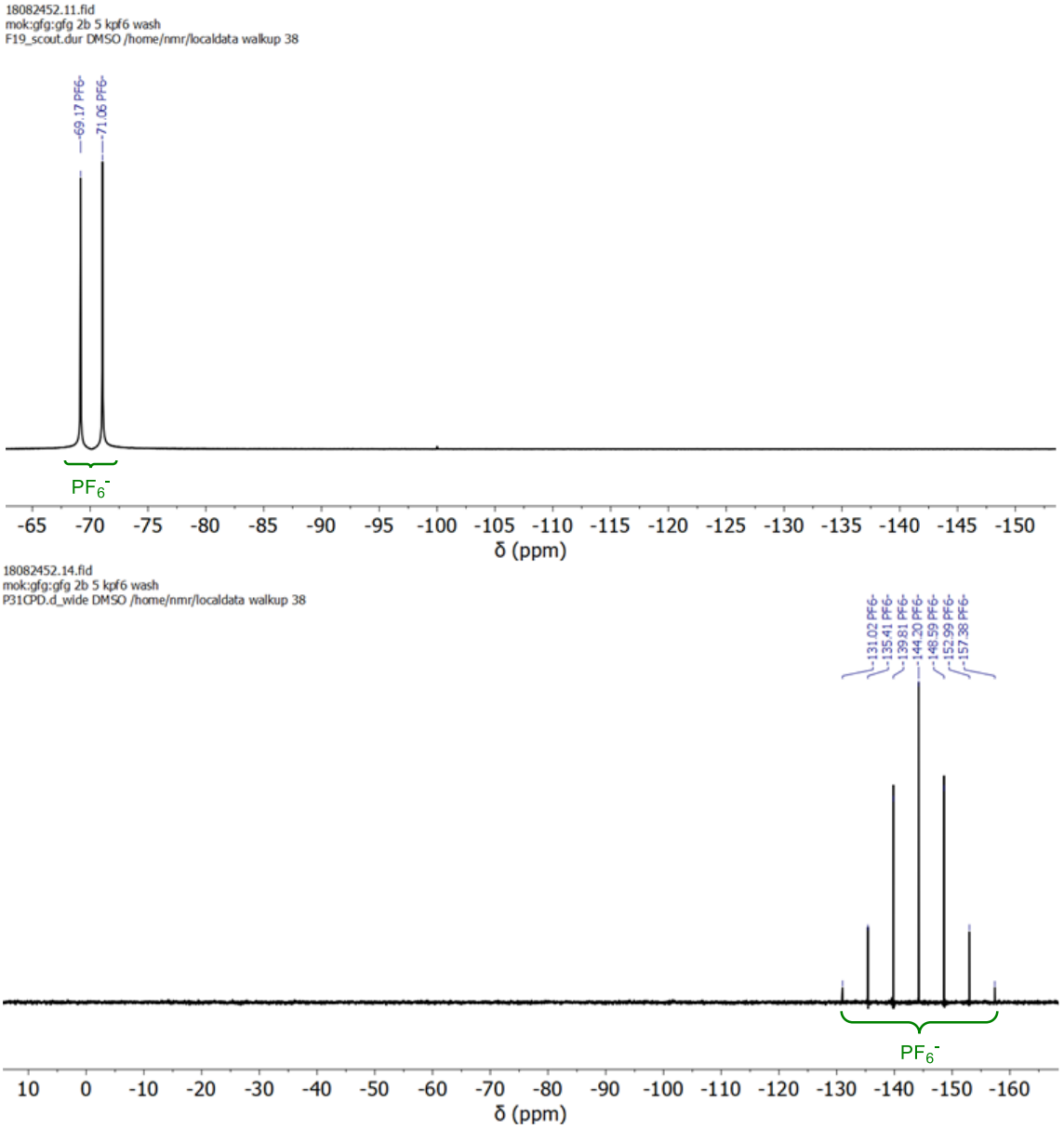

Figure 56. Heteronuclear NMR spectroscopic analysis of "counterion restored" material (recorded in DMSO-d_6): top) ^{19}F-NMR (376 MHz); bottom) ^{31}P-NMR (243 MHz).

Target ammonium salt synthesis was achieved in satisfactory yield. Formation of the charged five-membered ring moiety was confirmed by structural connectivity analysis of the isolated material *via* XRD crystallography (Scheme 57).

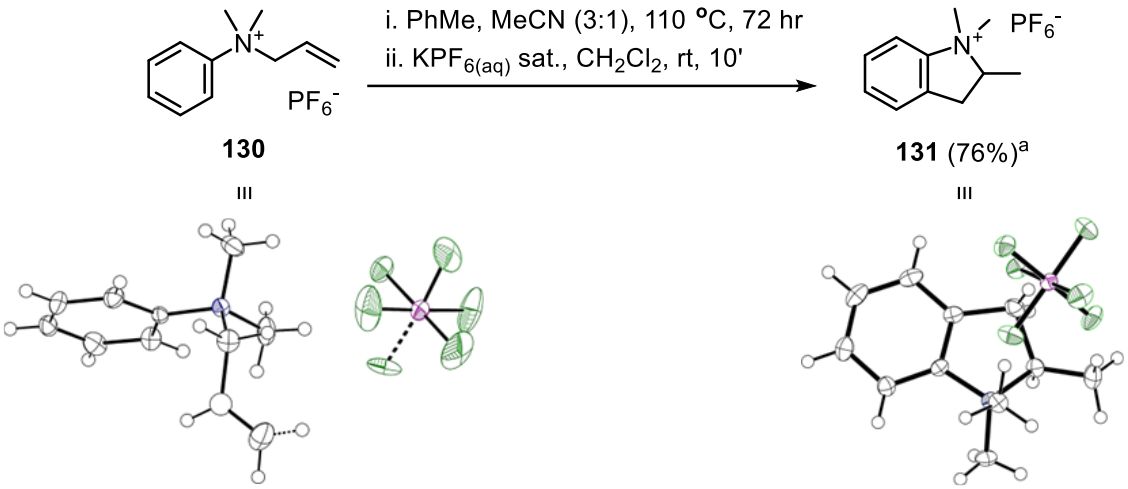

*Scheme 57. Synthesis of indolinium salt **131** via hexafluorophosphate counterion restoration. [a.] Isolated yield.*

5.1.3 Charged aza-Claisen rearrangement of hexafluorophosphate arylammonium salt 130

Moving from the synthetic challenges tackled to achieve chemoselective formation of indolinium salt **131**, mechanistic insight was sought after to better understand how synthesis of the latter compound was favoured over aza-Claisen product **93**.

Charged sigmatropic rearrangement of *N*-allyl-*N,N*-dimethylanilinium hexafluorophosphate **130** was suggested to occur in thermal conditions, giving rise to tertiary arylamine **93** after re-aromatisation (Scheme 58).

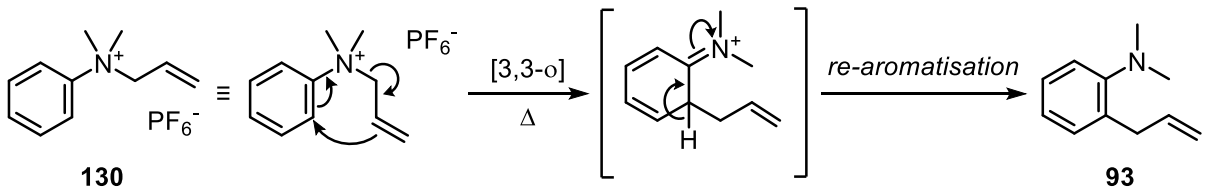

*Scheme 58. aza-Claisen rearrangement of arylammonium salt **130** into tertiary arylamine **93**.*

Intermediate deprotonation would take place in presence of newly formed 2-allyl-*N,N*-dimethylaniline **93**, due to the presence of the allyl side chain π-system and lone pair of the dimethylamino group. Conversely, protonation of hexafluorophosphate anion would be unlikely, given the low pKa featured by HPF_6 (pKa= -20).[181,182]

Regarding the cyclisation step, it can be argued that ammonium salt intermediates would form at first instead of carbocations, which would then result from proton addition to the terminal carbon-carbon double bond.[183] However, the experimental results herein discussed may be

reasoned with protonation of the terminal double bond and formation of a secondary carbocation, which would be favoured over the primary carbenium ion. Intramolecular trap of the former would be promoted by the adjacent dimethylamino group, affording *N*-heterocyclic ammonium salt **131.** Such mechanistic reasoning was found in accordance with the experimental evidence gathered thus far, since six-membered ring side-product **132** was not observed during thermal cyclisation studies (Scheme 59).

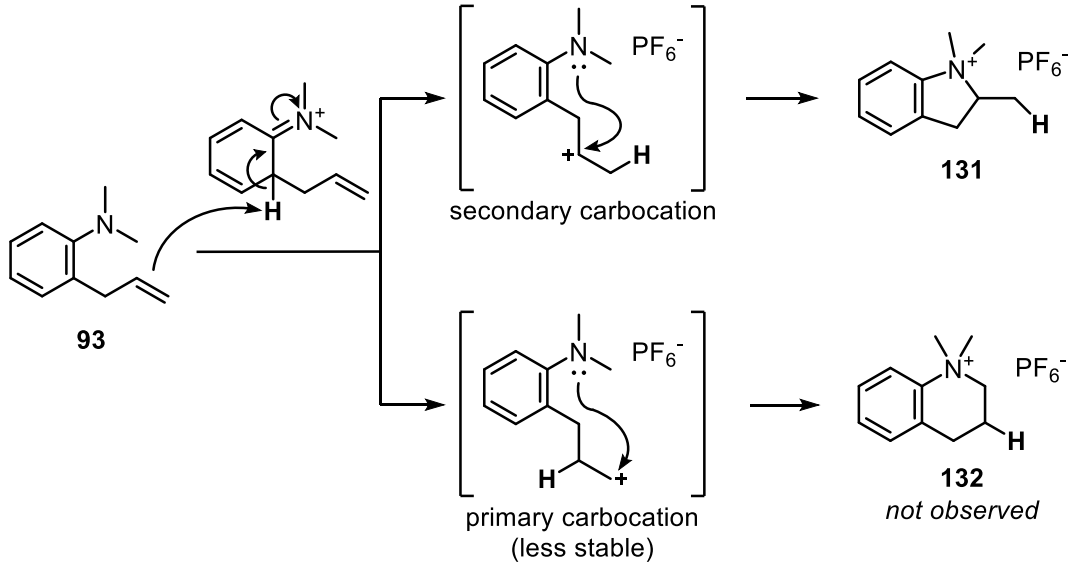

Scheme 59. Proposed reaction mechanism leading to ring closure selectivity.

Regardless of which intermediate would first form to promote thermal ring closure, another observation can be drawn from the reaction mechanism herein proposed, which stems from pre-existing studies conducted by Katayama *et al*.[164–166] Use of $NaHCO_3$ as base to promote aza-Claisen rearrangement of bromide arylammonium salts was reported as it would neutralise HBr forming *in situ* during sigmatropic rearrangement.[164] In a similar fashion, it was thought that cyclisation should only occur if there is an acid present in the reaction mixture whereas presence of a base would hinder *N*-heterocyclic salt synthesis, therefore favouring conversion of hexafluorophosphate salt **130** into aza-Claisen product **93**. Use of an inorganic base such as K_2CO_3 was deemed ideal due to its ubiquity, low cost and toxicity and was trialled to validate the hypothesis above discussed. Reaction conditions previously optimised towards synthesis of cyclised indolinium salt **130** were revisited. Use of potassium carbonate in slight excess was confirmed to halt the ring closure step and rearrangement product **93** was easily accessed after reaction work-up and crude material purification (Scheme 60).

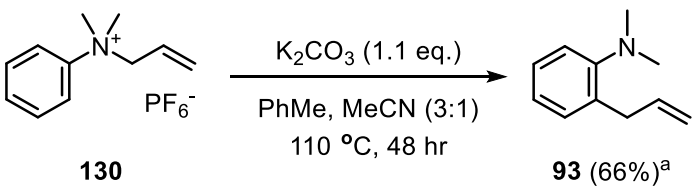

*Scheme 60. Base-mediated synthesis of aza-Claisen product **93.** [a.] Isolated yield.*

5.2 Synthesis of hexafluorophosphate ammonium salt precursors

Following the encouraging results achieved starting from PF_6^- model substrate **130**, synthesis of substituted *N*,*N*-dimethylanilinium hexafluorophosphate salts was undertaken to test the synthetic methodology's robustness. A three-step synthetic protocol was envisaged, featuring reductive amination of commercially available primary or secondary arylamines (Scheme 61, Step *a*). Next, tertiary aniline intermediates were converted into their bromide salt derivatives *via* S_N2 reaction with allyl bromide (Scheme 61, Step *b*). Lastly, quaternary ammonium species underwent counterion swap, yielding an array of substituted hexafluorophosphate salts (Scheme 61, Step *c*).

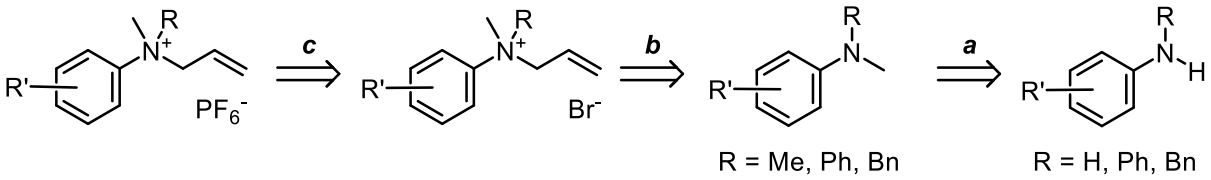

Scheme 61. Synthesis of hexafluorophosphate ammonium salts bearing polysubstituted aromatic motifs.

Given that ammonium salts reactivity was expected to vary depending on the substitution pattern pre-installed on the phenyl ring, aza-Claisen rearrangement and thermal cyclisation of *N*-allylated heterocyclic salts was also investigated. Synthesis of hexafluorophosphate indolinium and 1,2,3,4-tetrahydroquinolinium salts was therefore pursued, to assess whether presence of *ortho*-substituents locked in rings would hinder synthesis and cyclisation of their corresponding [3,3-σ]-rearrangement products (Scheme 62).

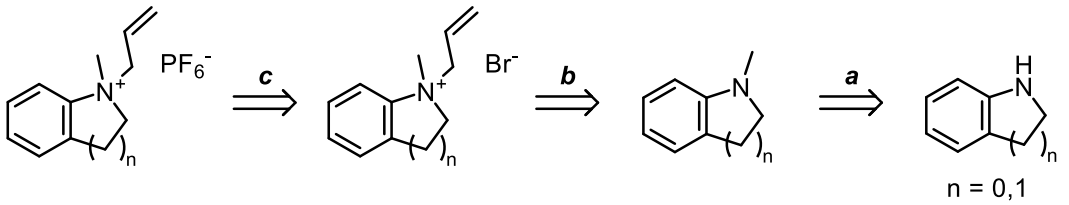

Scheme 62. Synthesis of N-allylated indolinium and 1,2,3,4-tetrahydroquinolinium PF_6^- salts.

5.2.1 *Step a*: Reductive amination of primary and secondary arylamines

The procedure described by Giumanini *et al*. was adapted for the permethylation of primary and secondary anilines.[184] Being a strongly exothermal reaction, the sodium borohydride-formaldehyde-acid promoted methylation was initially carried out at 0 °C, where a $NaBH_4$/aniline suspension was added portion-wise to a cooled $CH_2O_{(aq)}/H_2SO_4$ solution in tetrahydrofuran.

The number of equivalents used in this synthetic step varied, depending on the number of methyl groups to be installed on the starting material. Method A was followed for the reductive amination of primary anilines whereas Method B was applied when secondary arylamines were utilised instead (Scheme 63, Table 14).

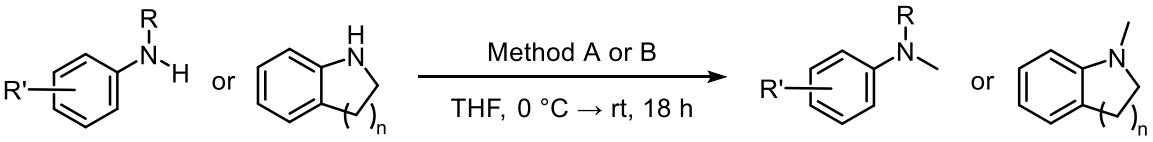

Scheme 63. Reductive amination of primary (R = H) and secondary (R ≠ H) anilines. Method A) $NaBH_4$ (11.7 eq.), $CH_2O_{(aq)}$ 37%$_{(v/v)}$ (8.12 eq.), $H_2SO_{4(aq)}$ 3.0 M (3.08 eq.); Method B) $NaBH_4$ (5.85 eq.), $CH_2O_{(aq)}$ 37%$_{(v/v)}$ (4.06 eq.), $H_2SO_{4(aq)}$ 3.0 M (1.56 eq.).

Table 14. Permethylation of primary and secondary aniline precursors: substrate scope.

Method A – Product (Yield)[a]

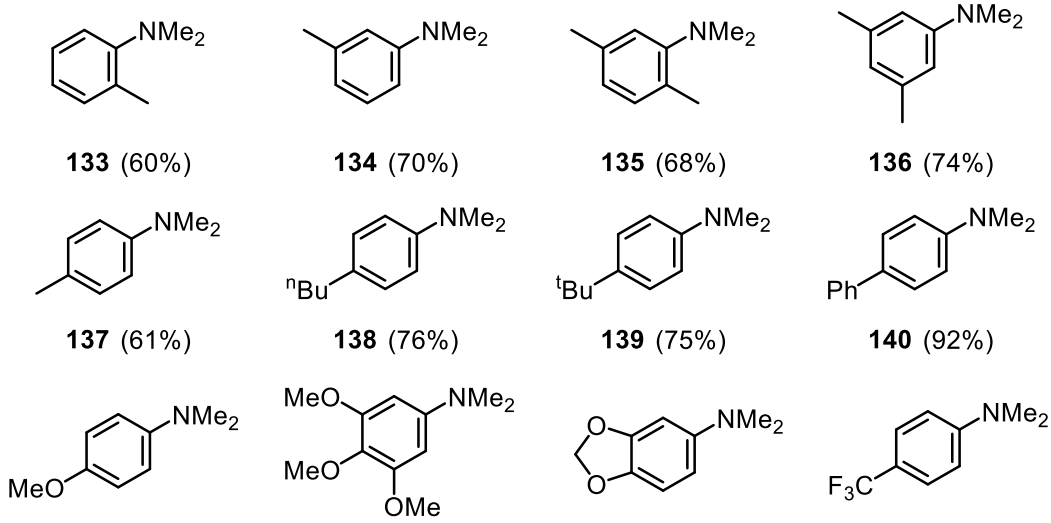

133 (60%) **134** (70%) **135** (68%) **136** (74%)

137 (61%) **138** (76%) **139** (75%) **140** (92%)

141 (81%) **142** (86%) **143** (90%) **144** (49%)

145 (51%) **146** (47%) **147** (76%) **148** (89%)

149 (91%) **150** (90%) **151** (75%) **152** (90%)

Method B – Product (Yield)[a]

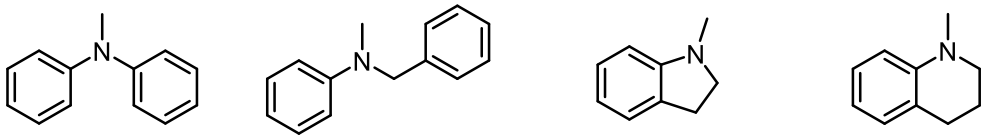

153 (45%) **154** (99%) **155** (97%) **114** (79%)

[a] *Isolated yield*

Despite of the satisfactory yields associated to isolated tertiary anilines **114** and **133-155**, it is incontrovertible that a large excess of reagents was required in both methods. This observation however can be reasoned by considering its reaction mechanism (Scheme 64).

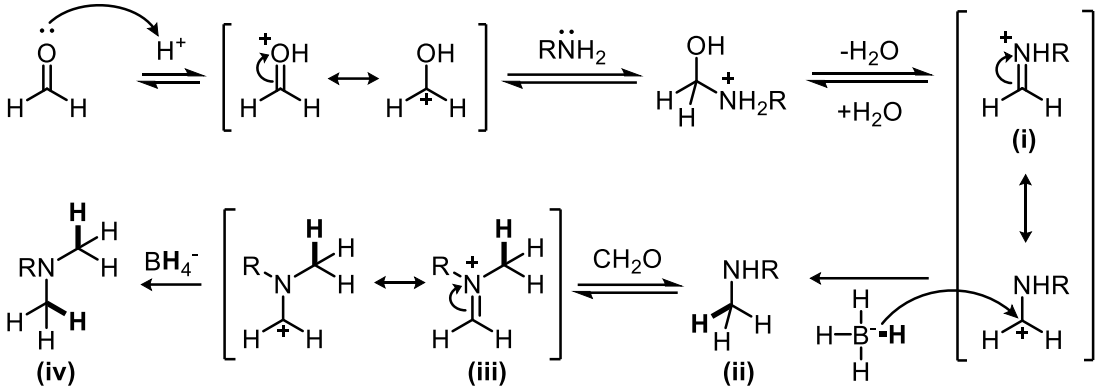

Scheme 64. Proposed reaction mechanism for the methylation of primary and secondary anilines.

The role of the acid in the borohydride-formaldehyde-mediated amination was rapidly noticed. Firstly, it activated the formaldehyde towards the aniline nucleophilic addition, yielding iminium ion **(i)**. The borohydride acted as a hydride donor: as the protonated form of imine **(i)** was reduced, the monomethylated product **(ii)** was formed. These two key steps reiterated, with the latter being the reduction of the protonated formaldehyde-monomethylated adduct **(iii)**. Depending on the number of protons available for iminium formation, up to two methyl groups can be added to the arylamine yielding permethylated product **(iv)**.[185]

In light of such reaction mechanism, it would be expected for the acid to be neutralised as reductive amination took place. Indeed, additional equivalents of H_2SO_4 were often added throughout dropwise addition of the $NaBH_4$/aniline slurry to readjust the reaction mixture pH below 2. On the other hand, conspicuous amounts of both $NaBH_4$ and CH_2O were necessary as the former would not only react with the starting material but also with the excess formaldehyde found in solution.

5.2.2 *Step b*: Bromide ammonium salt synthesis *via* tertiary anilines S_N2 alkylation

Following the isolation of tertiary anilines **114** and **133-155**, synthesis of arylammonium bromide salts was pursued either in solventless conditions or in acetonitrile, depending on the arylamine's aggregation state. In general, S_N2 alkylation step with allyl bromide proceeded smoothly, affording *N*-allylated quaternary aniline derivatives after reaction mixture trituration with diethyl ether. Successful reaction outcome was determined upon visual inspection since bromide salt intermediates **91**, **104** and **156-172** were expected to precipitate as *N*-alkylation progressed towards completion (Scheme 65, Table 15).

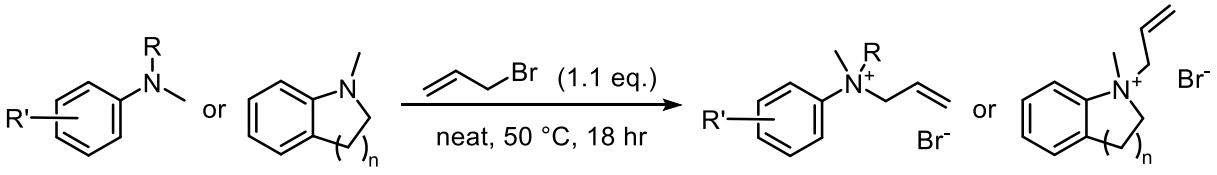

Scheme 65. Synthesis of arylammonium bromide salts via N-alkylation of permethylated anilines.

Table 15. Synthesis of N-allyl substituted arylammonium bromide salts: substrate scope.

Product (Yield)[a]

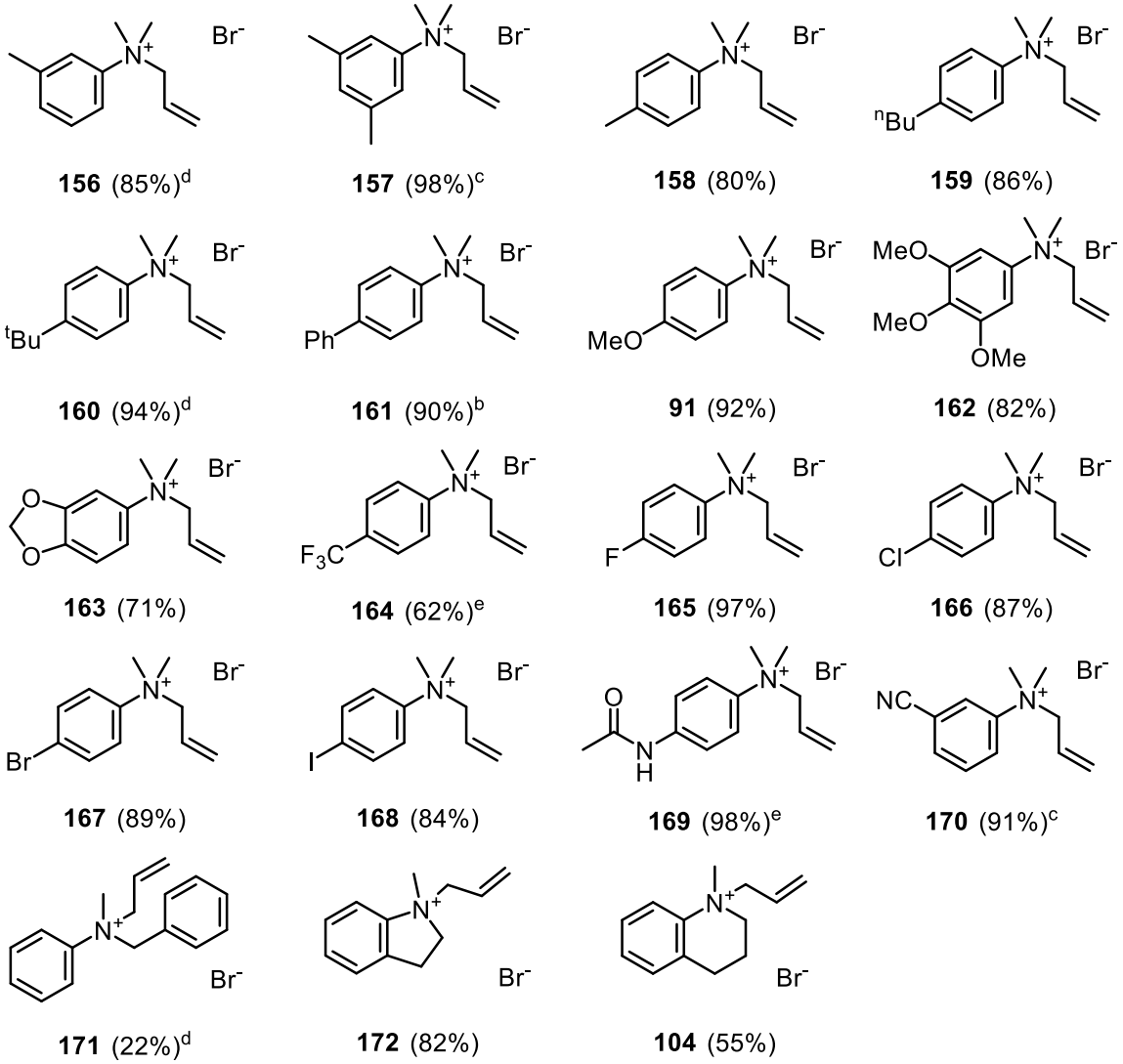

156 (85%)[d] **157** (98%)[c] **158** (80%) **159** (86%)

160 (94%)[d] **161** (90%)[b] **91** (92%) **162** (82%)

163 (71%) **164** (62%)[e] **165** (97%) **166** (87%)

167 (89%) **168** (84%) **169** (98%)[e] **170** (91%)[c]

171 (22%)[d] **172** (82%) **104** (55%)

[a] *Isolated yield;* [b] t_R= 24 hr; [c] t_R= 48 hr; [d] t_R= 72 hr; [e] t_R= 7 days.

Isolation of *N*-allyl-*N,N*-dimethylanilinium bromide salts proved challenging in a number of cases and two main reasons can be invoked to justify the sluggish reactivity (or lack thereof) exhibited by aniline precursors (Figure 57).

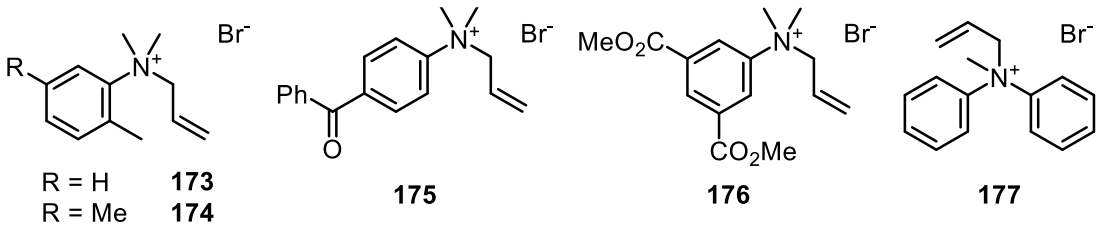

R = H **173**
R = Me **174**

175 **176** **177**

*Figure 57. Unsuccessful synthesis of bromide ammonium salts **173-177.***

Steric hindrance caused by bulky substituents linked to the protonated nitrogen (such as **177**) or *ortho*-substituted methyl groups on the aromatic ring (**173** and **174**) would hinder the S_N2 reaction. Secondly, the poor reactivity featured by anilines can be reasoned upon

consideration of the electronic properties exerted by substituents attached to the aromatic ring, which in case of compounds **175** and **176** have negatively impacted the dimethylamino lone pair availability towards nucleophilic substitution. Synthesis of these ammonium salts was not further pursued, since further insight on this matter would have fallen outside the research scope set during compound library synthesis.

5.2.3 *Step c*: Hexafluorophosphate ammonium salts synthesis via counterion swap

Rapid bromide-to-PF_6^- ion exchange was carried out in aqueous environment in presence of potassium hexafluorophosphate (Scheme 66).

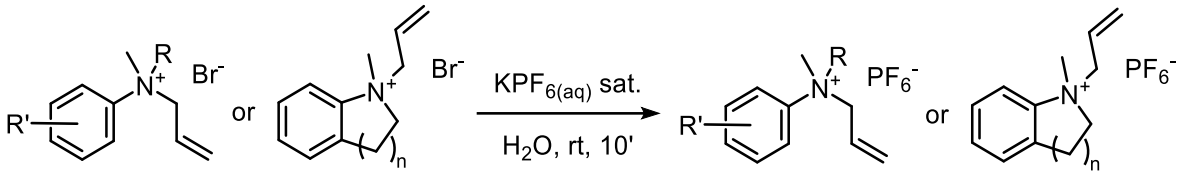

Scheme 66. Synthesis of arylammonium hexafluorophosphate salts via bromide-to-PF_6^- counterion swap.

KPF_6 was chosen as counterion source, since it is less expensive than its $M^+PF_6^-$ analogues (M^+= -Li^+, -Na^+, -Ag^+) and safer to handle than aqueous solutions of hexafluorophosphoric acid. The reaction was quickly driven to completion as soon as potassium hexafluorophosphate was added, since PF_6^- salts precipitated out of the reaction mixture. In virtue of their different solubility trends, unreacted Br^- and newly formed PF_6^- salts could be easily separated *via* L/L extraction with CH_2Cl_2. Differently from the alkylation step, neither the type nor number of aromatic substituents played influencing roles, affording compounds **178-196** after crude material re-crystallisation in polar protic solvents (Table 16).

Table 16. Synthesis of N-allyl arylammonium hexafluorophosphate salts: substrate scope.

Product (Yield)[a]			
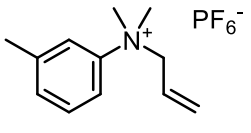	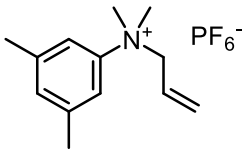	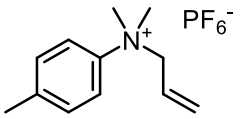	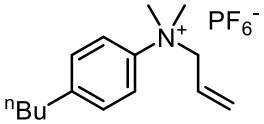
178 (80%)	**179** (96%)	**180** (72%)	**181** (76%)
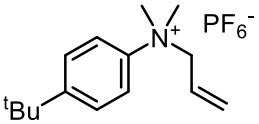	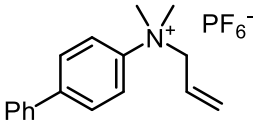	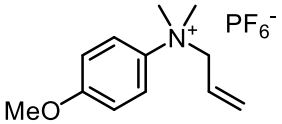	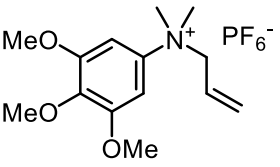
182 (71%)	**183** (94%)	**184** (90%)	**185** (86%)
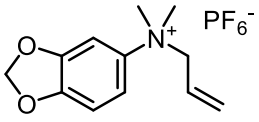	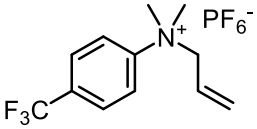	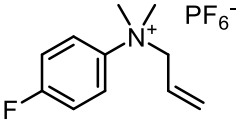	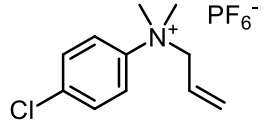
186 (70%)	**187** (67%)	**188** (61%)	**189** (84%)

[a] *Isolated yield.*

Table 16 (cont.) Synthesis of N-allyl arylammonium hexafluorophosphate salts: substrate scope.

Product (Yield)[a]			
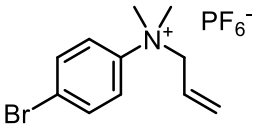	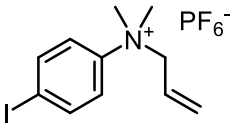	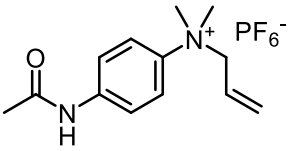	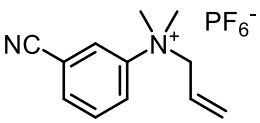
190 (62%)	**191** (92%)	**192** (54%)	**193** (57%)
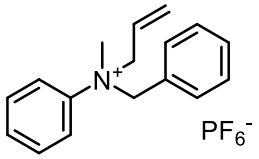	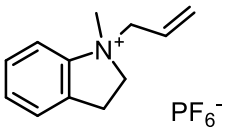	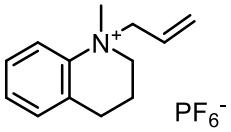	
194 (45%)	**195** (96%)	**196** (26%)	

[a] *Isolated yield.*

Isolated yield discrepancy can be noticed between *Step b* and *Step c* however, which can be reasoned upon consideration of two factors: a) deliquescent behaviour featured by air-sensitive bromide ammonium salts; b) likelihood of PF_6^- salts for poor repartition within biphasic mixture components, due to their surface-active properties. Moreover, solubility issues displayed by newly formed PF_6^- salts were observed during reaction work-up – i.e., aqueous reaction mixture extraction with CH_2Cl_2. For instance, *m*-cyano substituted compound **193** was found not soluble in chlorinated solvents and hexafluorophosphate salt retrieval was therefore undertaken from the reaction mixture by vacuum filtration.

5.3 Thermal cyclisation of arylammonium salts *via* charged aza-Claisen rearrangement: substrate scope studies

Synthetic methodology previously developed for aza-Claisen rearrangement and thermal cyclisation of model substrate **130** was screened against newly prepared hexafluorophosphate ammonium salts. Results and discussion associated to substrates **178-196** will be elucidated in function of the type and number of substituents pre-installed on the phenyl ring.

Formation of a single product was expected in both cases, starting from *p*-substituted hexafluorophosphate ammonium salts. Such hypothesis was corroborated by the presence of the two equivalent rearrangement positions in *ortho* with respect to the ammonium moiety. Indeed, straightforward synthesis of aza-Claisen products **94, 197-206** and indolinium salts **207-217** was confirmed to take place following previously optimised reaction conditions (Scheme 67, Table 17).

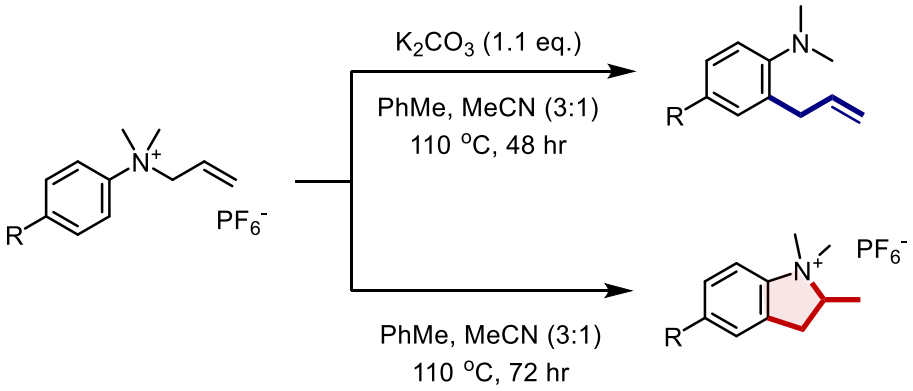

Scheme 67. aza-Claisen rearrangement and thermal cyclisation of para-substituted PF_6^- ammonium salts.

Table 17. Synthesis of para-substituted ortho-allylanilines and N,N-dimethylindolinium hexafluorophosphates.

Entry	Starting material	Aza-Claisen Product (Yield)[a,b]	PF_6^- Indolinium salt (Yield)[a,c]
1	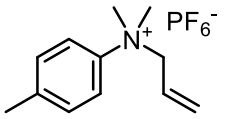 **180**	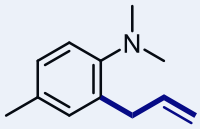 **197** (53%)	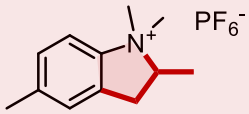 **207** (75%)
2	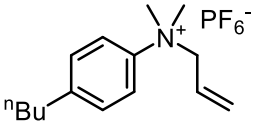 **181**	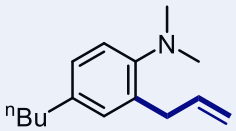 **198** (58%)	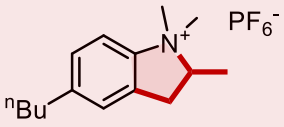 **208** (56%)
3	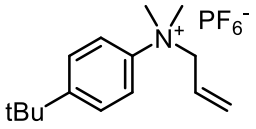 **182**	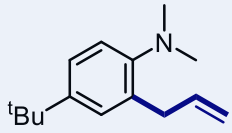 **199** (92%)	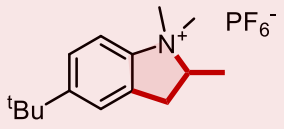 **209** (82%)

[a] Isolated yield. [b] Reaction conditions: K_2CO_3 (1.1 eq.), PhMe, MeCN (3:1), 110 °C, 48 hr; [c] Reaction conditions: PhMe, MeCN (3:1), 110 °C, 72 hr.

Table 17 (cont.) Synthesis of para-substituted ortho-allylanilines and N,N-dimethylindolinium PF_6^- salts.

Entry	Starting material	Aza-Claisen Product (Yield)[a,b]	PF_6^- Indolinium salt (Yield)[a,c]
4	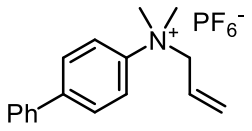	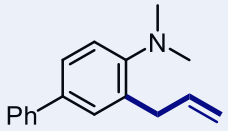	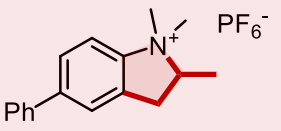
	183	**200** (80%)	**210** (81%)
5	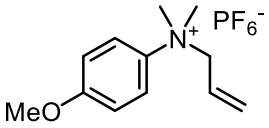	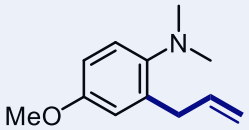	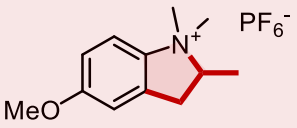
	184	**94** (77%)	**211** (42%)
6	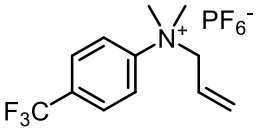	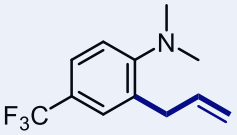	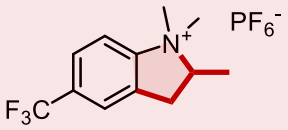
	187	**201** (44%)	**212** (85%)
7	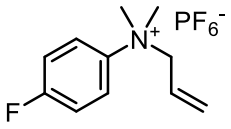	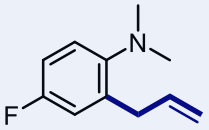	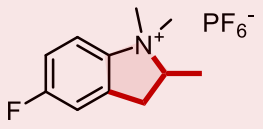
	188	**202** (16%)	**213** (55%)
8	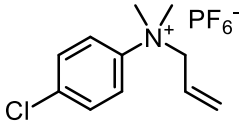	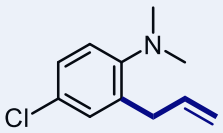	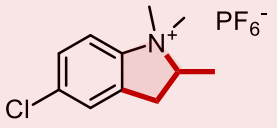
	189	**203** (81%)	**214** (65%)
9	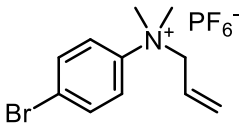	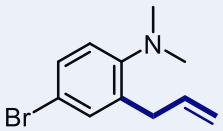	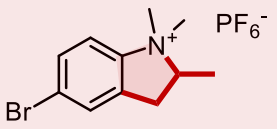
	190	**204** (63%)	**215** (42%)
10	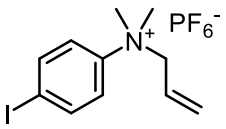	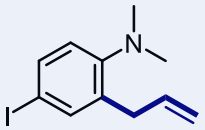	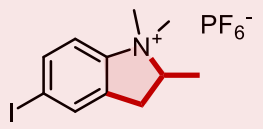
	191	**205** (96%)	**216** (83%)
11	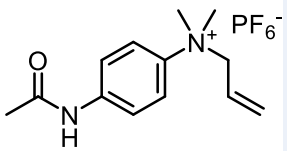	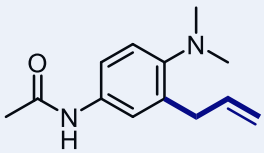	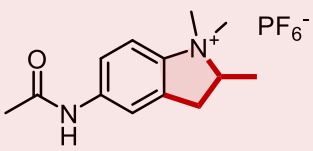
	192	**206** (28%)	**217** (73%)

[a] Isolated yield; [b] Reaction conditions: K_2CO_3 (1.1 eq.), PhMe, MeCN (3:1), 110 °C, 48 hr; [c] Reaction conditions: PhMe, MeCN (3:1), 110 °C, 72 hr.

In general, no side-products were observed during rearrangement, despite of prolonged reaction heating. An exception (proving the rule!) can be found however amongst the *p*ara-substituted ammonium salts herein discussed.

Sigmatropic rearrangement of hexafluorophosphate salt **192** afforded its corresponding *o*-allyl-*N*,*N*-dimethylaniline **206** as well as *N*-allyl-*N*-(4-(dimethylamino)phenyl)acetamide **218** (Scheme 68). Isolation of latter dimethylamino derivatives was challenging due to poor chromatographic separation. Nonetheless, ^{1}H-NMR spectroscopic analysis of purified compound **218** was consistent with presence of a *para*-substituted aromatic moiety (Figure 58).

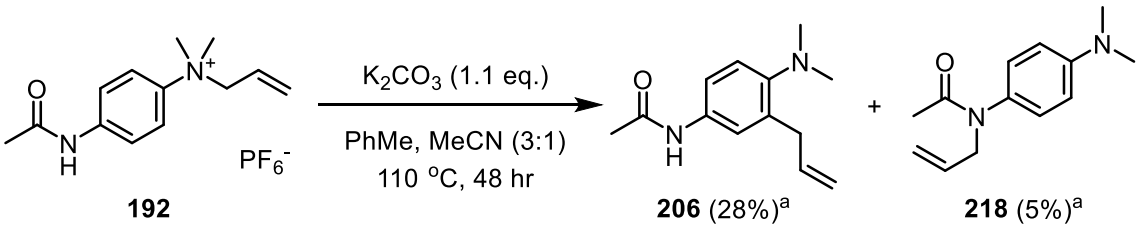

*Scheme 68. N-allylated side-product **218** formation via aza-Claisen rearrangement of hexafluorophosphate ammonium salt **192**. [a] Isolated yield.*

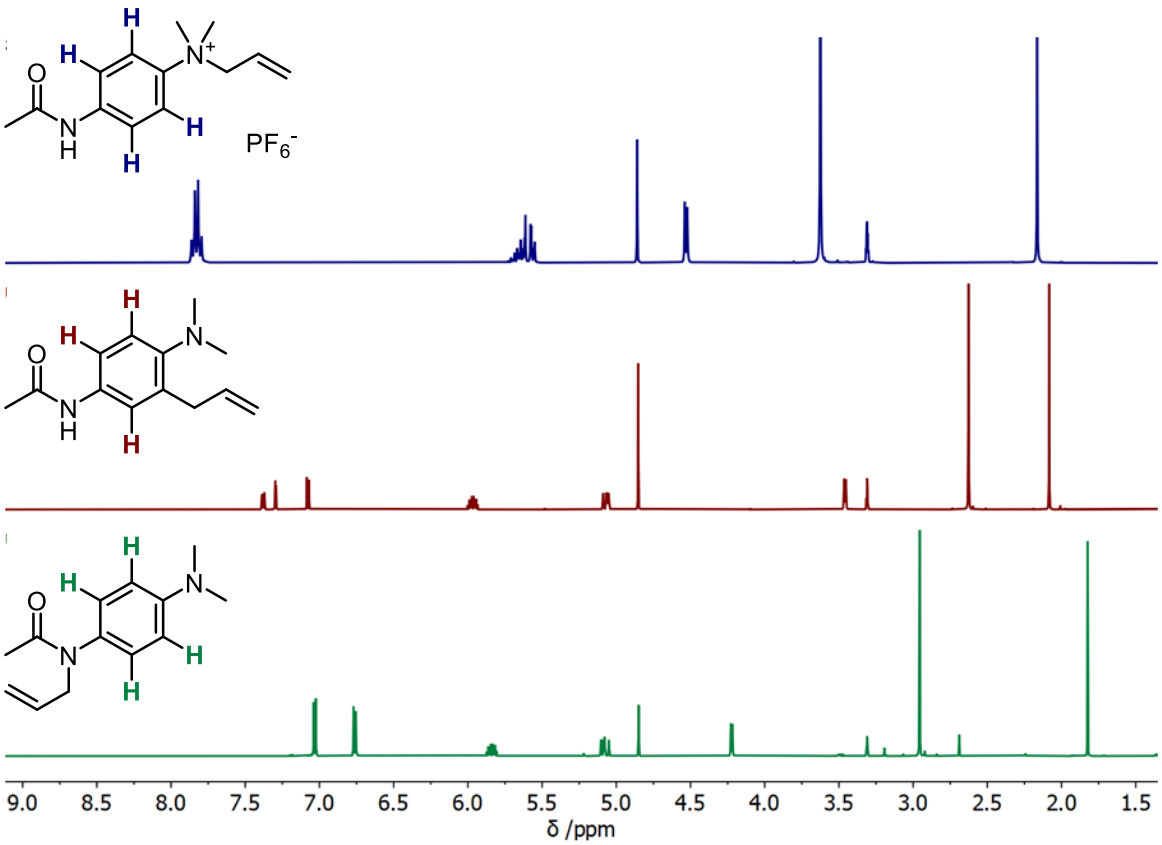

*Figure 58. ^{1}H-NMR spectra comparison, recorded in MeOD-d_4 (600 MHz), from top: 4-acetamido-N-allyl-N,N-dimethylbenzenaminium hexafluorophosphate **192** (blue), N-(3-allyl-4-(dimethylamino)phenyl)acetamide **206** (maroon), N-allyl-N-(4-(dimethylamino)phenyl)acetamide **218** (green).*

More complex substitution patterns were explored within the developed substrate scope such as di- and tri- substituted PF_6^- ammonium precursors **179**, **185** and **186** (Scheme 69). As similarly described for the *para*-substituted hexafluorophosphate salts, compounds featuring symmetrical substitution patterns such as **179** and **185** were expected to yield a single product. Such hypothesis was confirmed upon rearrangement and thermal cyclisation of both substrates (Table 18, Entry 1 and 2, respectively).

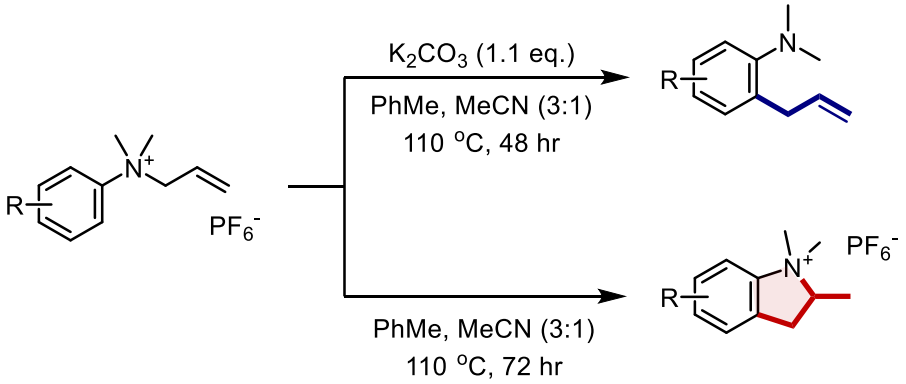

Scheme 69. aza-Claisen rearrangement and thermal cyclisation of poly-substitutent PF_6^- ammonium salts.

Table 18. Synthesis of poly-substituted ortho-allylanilines and N,N-dimethylindolinium hexafluorophosphates.

Entry	Starting material	Aza-Claisen Product (Yield)[a]	PF_6^- Indolinium salt (Yield)[a]
1	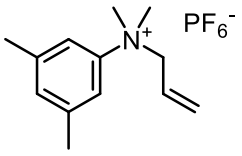	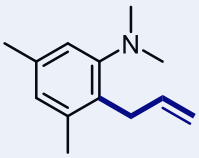	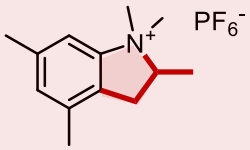
	179	**219** (78%)	**222** (91%)
2	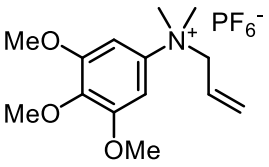		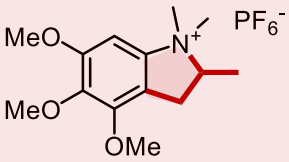
	185	**220** (68%)	**223** (75%)
3	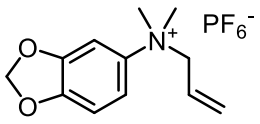	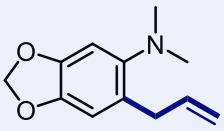	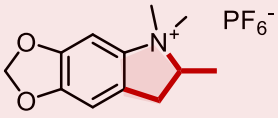
	186	**221** (74%)	**224** (66%)

[a] *Isolated yield.*

On the other hand, rearrangement of *N*-allyl-*N*,*N*-dimethylbenzo[d][1,3]dioxol-5-aminium hexafluorophosphate **186** unexpectedly took place in a regioselective fashion (Table 18, Entry 3). Provided that a mixture of *ortho*-allyl substituted arylamines was expected to be found, intruding sets of doublets were not found alongside two singlet peaks arising from **221** by ^{1}H-NMR spectroscopy. Therefore, formation of sterically demanding compound **225** was ruled out after crude material analysis (Scheme 70, Figure 59).

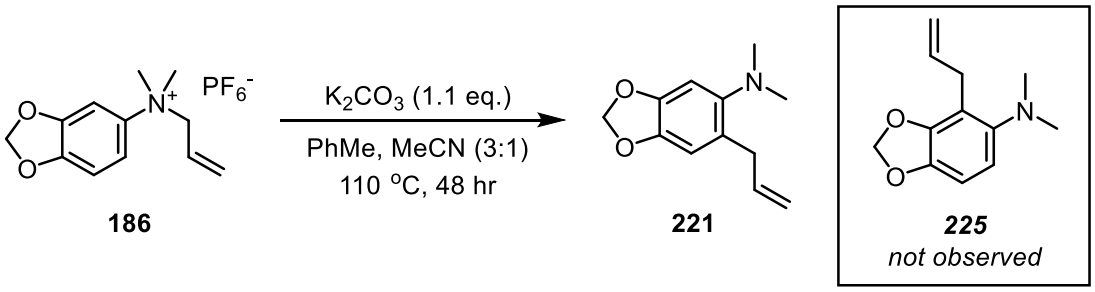

*Scheme 70. Regioselective synthesis of aza-Claisen rearrangement product **221**.*

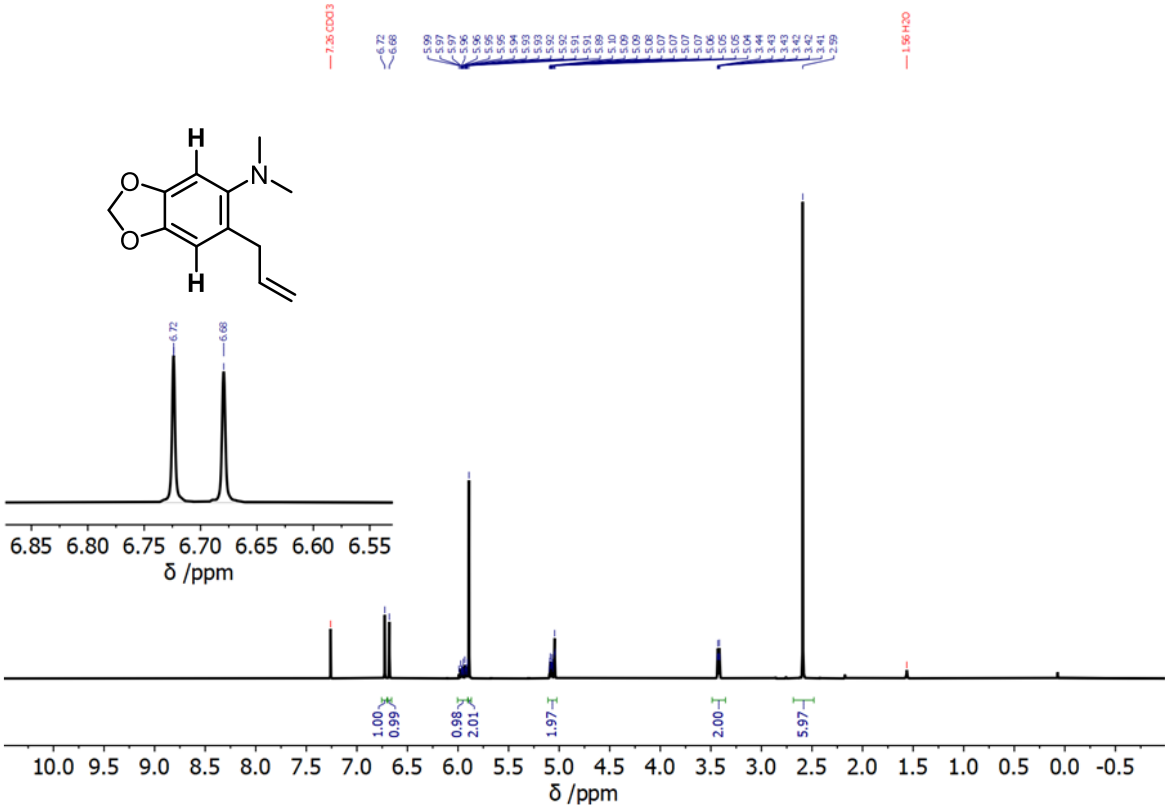

Figure 59. Crude material analysis by ^{1}H-NMR spectroscopy. Data recorded in MeOD-d_4 (600 MHz).

Although steric hindrance could be invoked as the key factor leading to regioselective synthesis of aza-Claisen product **221**, such experimental outcome can also be reasoned upon consideration of the electronic properties exerted by the oxygen atoms of the methylenedioxy bridge. Resonance forms associated to the oxygen atom positioned in *para* with respect to the charged nitrogen afforded either unavailable or unfavourable reaction sites. On the opposite, the oxygen atom positioned in *meta* with respect to the *N*-allylated moiety would promote rearrangement both in *ortho*- and *para*- positions (Scheme 71).

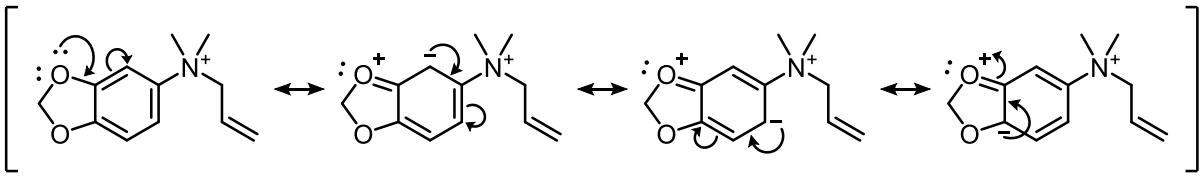

*Scheme 71. Resonance forms associated to PF_6^- ammonium salt **186**.*

Unlike ammonium salt **186**, hexafluorophosphate substrates bearing either methyl or cyano groups in *meta* position afforded an equimolar mixture of two rearranged and cyclised products (Scheme 72). More in detail, *N*-allyl-*N*,*N*-dimethyl-3-methylanilinium precursor **178** gave rise to aza-Claisen products **226a** and **226b** whereas formation of 1,1,2-trimethylindolinium salts **228a** and **228b** took place after thermal ring closure (Table 19, Entry 1). Electronic effects exerted by *meta*-positioned aromatic substituents may have influenced the reaction yield, since rearrangement products **227a** and **227b** were isolated after crude material purification in lower amounts. Likewise situation occurred during thermal cyclisation of 3-cyanosubstituted precursor **193** (Table 19, Entry 2).

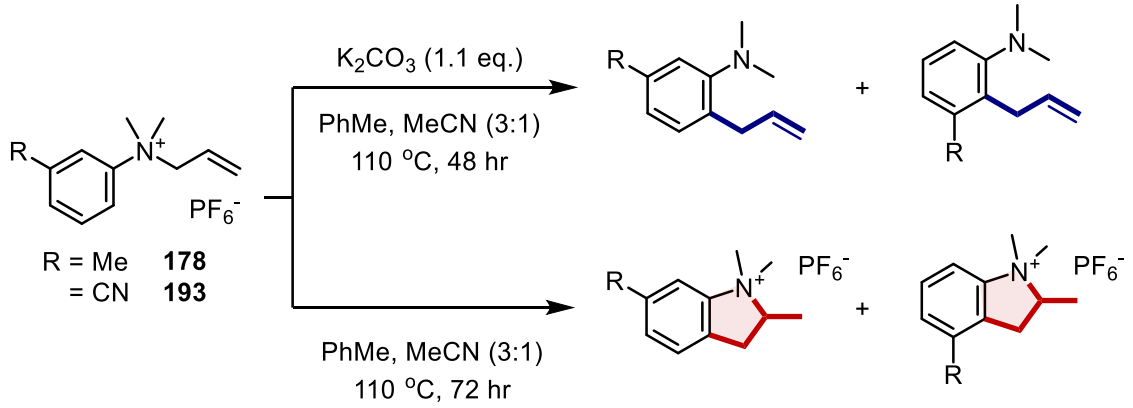

Scheme 72. aza-Claisen rearrangement and thermal cyclisation of meta-substituted PF_6^- ammonium salts.

Table 19. Synthesis of meta-substituted ortho-allylanilines and N,N-dimethylindolinium hexafluorophosphates.

Entry	R	Aza-Claisen Product (Yield)[a]	PF_6^- Indolinium Product (Yield)[a]
1	Me	**226a, 226b** (63%)[b]	**228a, 228b** (85%)[b]
2	CN	**227a, 227b** (23%)[b]	**229a, 229b** (36%)[b]

[a] *Isolated yield;* [b] *(1:1) regioisomers ratio determined via ^{1}H-NMR spectroscopy.*

Equimolar amounts of 1,2,3- and 1,2,5-trisubstituted regioisomers were isolated after crude material purification, regardless of which type of *meta*-substituent was pre-installed in the aromatic ring. The reason why poorly regioselective synthesis took place in these cases requires further investigation. Unlike the methylenedioxy moiety, no lone pairs would be available from the carbon atom within the *m*-methyl and *m*-cyano group, which can also be regarded as sterically less demanding. Therefore, reasoning of such experimental results

goes beyond consideration of electronic properties and steric hindrance exerted by both substituents, since comparable reaction outcomes were observed from a regioselective standpoint, starting from hexafluorophosphate ammonium salts **178** and **193**.

Following Katayama *et al.* pre-existing studies on rearrangement of *N*-allylated heterocyclic salts,[165] reactivity of hexafluorophosphate substrates **195** and **196** was investigated (Scheme 73). As expected, aza-Claisen rearrangement afforded the corresponding 7-allyl substituted products **230** and **114** with good yields. On the other hand, crude material analysis after thermal cyclisation of *N*-allyl substituted indolinium salt **195** revealed absence of tricyclic PF_6^- salt **231** (Table 20, Entry 1). ^{1}H-NMR signals consistent with presence of *N*-allyl moiety were observed, suggesting that ring closure starting from **230** did not take place, possibly due to ring strain exerted by the pre-existing five membered ring. Conversely, thermal cyclisation was successful only starting from *N*-allyl-*N*-methyl-1,2,3,4-tetrahydroquinoline compound **196**, affording **232** in modest amounts (Table 20, Entry 2).

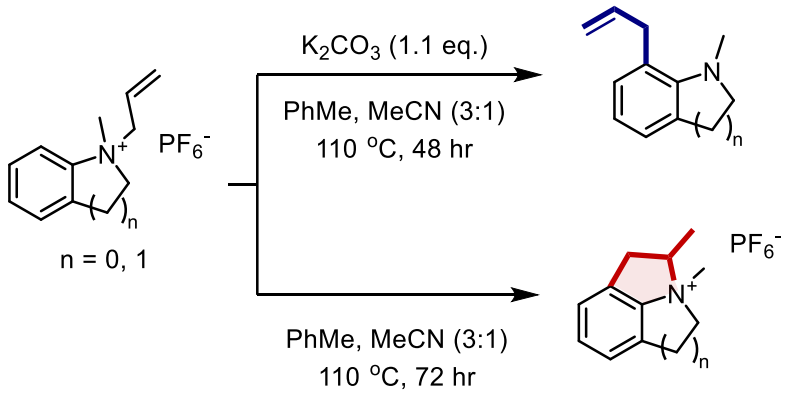

Scheme 73. aza-Claisen rearrangement and thermal cyclisation of N-heterocyclic hexafluorophosphate salts.

Table 20. Synthesis of allyl substituted N-heterocycles and tricyclic ammonium hexafluorophosphates.

Entry	Starting material	Aza-Claisen Product (Yield)[a]	PF_6^- Indolinium Product (Yield)[a]
1	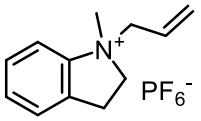 **195**	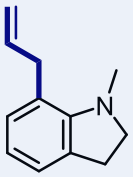 **230** (74%)	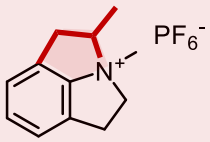 **231** *(not observed)*
2	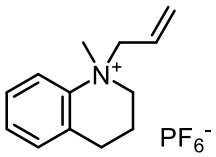 **196**	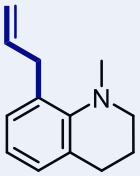 **114** (79%)	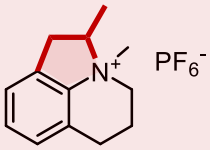 **232** (33%)

[a] *Isolated yield.*

Two observations can be drawn following reactivity assessment of quaternary ammonium salt **194**. *N*-allyl-*2*-benzyl substituted side-product was not observed after [3,3-σ] sigmatropic rearrangement, which afforded *N*-benzyl substituted arylamine **233** in a chemoselective fashion (71% yield). Conversely, thermal cyclisation of **194** gave rise to a (85:15) diastereoisomeric mixture of indolinium salts **234a** and **234b** (Scheme 74).

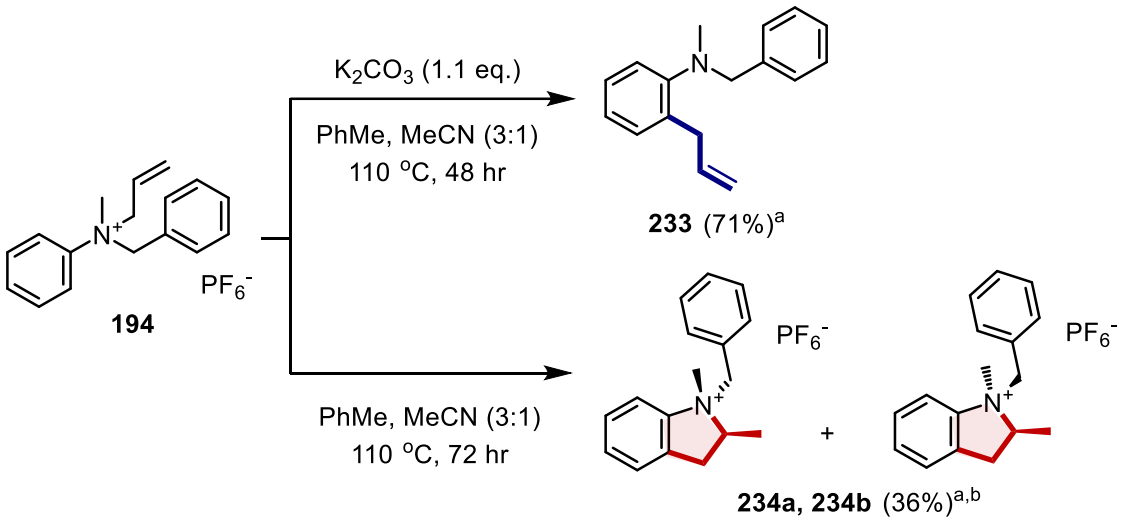

*Scheme 74. aza-Claisen rearrangement and thermal cyclisation of N-allyl-N-benzyl-N,N-dimethylanilinium hexafluorophosphate **194**. [a] Isolated yield. [b] (85:15) Diastereomer ratio determined by ^{1}H-NMR spectroscopy on crude material, after counterion restoration.*

Regarding compounds **234a** and **234b,** experimental evidence gathered after crude material analysis were consistent with complete starting material consumption, moderate diastereoselective control and formation of one major by-product, likely to be *de*-benzylated derivative of ammonium salt **234a.** Isolation of the diastereomer mixture components was convoluted and poor chromatographic resolution was observed after attempted purification. Thus, full characterisation of both compounds was not carried out and further studies could be undertaken to confirm whether the (1R,2S)-diastereomer **234a** formed in greater amounts, due to steric effects exerted by the *N*-benzyl group.

5.4 Final remarks and future outlook

The goal of conducting synthesis of quaternary 1,1,2-trimethylindolinium salts and tertiary *ortho*-allylanilines starting from a communal precursor was achieved. This was possible by tuning the reaction conditions (e.g., reaction time, presence of base) to allow for tandem aza-Claisen rearrangement and thermal ring closure to occur, as well as halting the overall process to the [3,3-σ] sigmatropic step.

Important key points can be drawn by the results herein discussed, since different experimental outcomes were observed depending on the aromatic substitution pattern featured by hexafluorophosphate ammonium salts. Newly developed synthetic methodology was effective in the rearrangement of *para*-substituted substrates as well as ammonium salts bearing polysubstituted yet symmetrical motifs. Limitations were spotted whenever *meta*-substituted PF_6^- salts underwent rearrangement and thermal cyclisation. Concerning the latter kind of reaction, poor experimental outcome was also observed starting from *N*-heterocyclic substrates bearing strained *ortho*-substituents locked in rings. Moreover, lack of stereochemical control was evident during thermal ring closure of chiral *N*-allyl-*N*-benzyl-*N*-methylanilinium hexafluorophosphate.

Further investigation could be undertaken to improve thermal ring closure of these challenging substrates, which still afforded their corresponding *ortho*-allyl substituted anilines with good yield and purity. Moreover, additional candidate substrates could be assessed towards rearrangement including (but not limited to): *N*-alkenyl substituted hexafluorophosphate salts, quaternary ammonium species bearing fused, aromatic carbocycles and/or multiple *N*-allyl sidechains tethered to either one or two ammonium moieties (Figure 61).

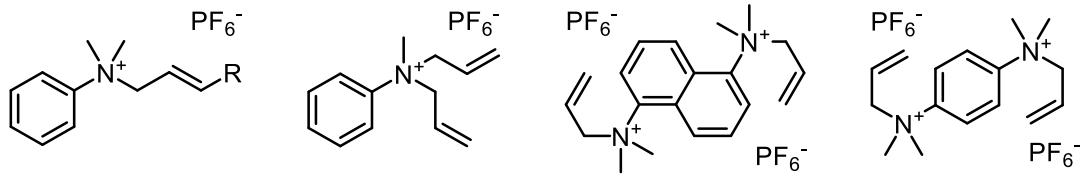

Figure 61. Follow-up substrate scope studies - suggested candidate substrates.

Subsequent research work can be carried out not only to enhance diastereoselective synthesis of *N*-benzyl substituted indolinium salts but also to explore derivatisation of newly formed indolinium substrates and *ortho*-allyl substituted arylamines. Intramolecular cyclisation of the latter compound in presence of $B(C_6F_5)_3$ could be explored, as well as Pd(II)-mediated intramolecular cross-coupling reaction to give 2-dihydro-1-dimethylquinolinium PF_6^- salts.[186–188] Synthesis of conjugated dienones *via* Pd-promoted allylic C-H activation with sulfoxonium ylides and Ni-catalysed coupling of the dimethylamino group with heteroaryl Grignard reagents could also be pursued.[189,190] On the other hand, photochemical synthesis of boron-based compounds could be investigated starting from 1,1,2-trimethylindolinium

hexafluorophosphate.[191] Treatment with base in polar aprotic solvents may lead to methyl group removal or migration *via* Sommelet-Hauser or Stevens rearrangement.[192,193] Functionalisation in benzylic position could also be probed by means of Riley oxidation or Wohl-Ziegler reaction. Finally, instances in literature were found for Birch reduction of quaternary indolinium salts (Scheme 75).[194]

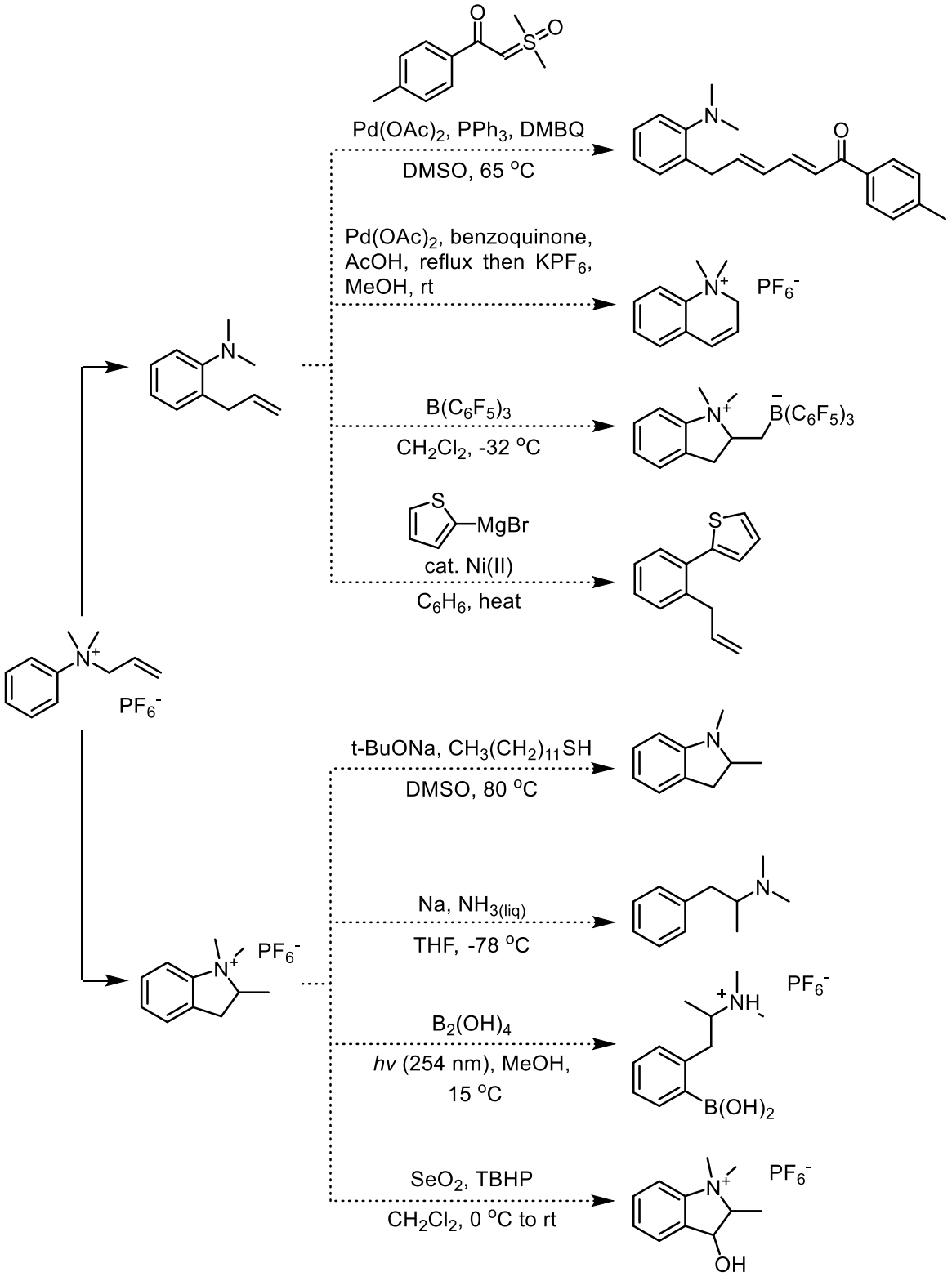

Scheme 75. Suggested application scope studies.

A final, yet crucial, comment can be made regarding the overall research avenues this dissertation could offer. Besides substrate and application scope broadening of the latter synthetic methodology, another comprehensive research topic was envisaged, where structural connectivity analysis of hexafluorophosphate salts could be tethered with modulation of their surface-active properties. Initial assessments would be focused on whether any of the isolated substrates exhibit any surface-active properties and, if so, targeted synthesis of ammonium surfactants could be carried out to further explore this concealed matter of interest.

Chapter 6

Experimental section

6.1 Material and Methods

Reagents and solvents were purchased from *Fisher Scientific*, *Sigma Aldrich* or *Alfa Aesar*, and were used as received, unless specified.[97] Reactions were carried out without drying, open to atmosphere, unless stated otherwise. Room temperature reactions were carried out between 15–25 °C. Column chromatography was typically carried out using 60 Å (70–230 mesh) silica gel from *VWR*.[195] TLC was conducted using 2.00 x 5.00 cm aluminium backed plates coated with silica matrix (0.20 mm) and fluorescent indicator (254 nm). Visualisation of TLC was conducted using a UV lamp and iodine chamber staining.

NMR spectra were recorded in specified deuterated solvents purchased from Apollo Scientific™, at room temperature. NMR spectra were recorded on either a *Bruker* Avance III-HD-400 spectrometer with operating frequencies of 400.07 MHz for ^{1}H, 100.60 MHz for ^{13}C, 376.45 MHz for ^{19}F, 161.95 MHz for ^{31}P or a *Varian* VNMRS-600 spectrometer with operating frequencies of 599.42 MHz for ^{1}H, 150.72 MHz for ^{13}C, 242.65 MHz for ^{31}P. Spectra were processed using *MestReNova* (V 12.0) software. ^{1}H NMR chemical shifts were referenced to residual non-deuterated solvent peaks within the NMR solvent; $CHCl_3$ (δ_H = 7.26 ppm), CH_3CN (δ_H = 1.94 ppm), CH_3OH (δ_H = 3.31 ppm) DMSO (δ_H = 2.50 ppm).[196] The multiplicity of ^{1}H signals are indicated as: s = singlet; d = doublet; t = triplet; q = quartet; quint. = quintet; sex. = sextet; sept. = septet; m = multiplet; br = broad; and combinations thereof. Coupling constants (*J*) are quoted in Hz and reported to the nearest 0.1 Hz. Chemical shifts for ^{13}C NMR spectra were referenced to deuterated solvent peaks in the NMR solvent; $CDCl_3$ (δ_C = 77.16 ppm), CD_3CN (δ_C = 1.32 ppm), CD_3OD (δ_C = 49.00 ppm) DMSO-d_6 (δ_C = 39.52 ppm).[3] All ^{13}C resonances are reported to the nearest 0.1 ppm in general, or to 0.01 ppm to aid in the differentiation of closely resolved signals. Product identification and peak assignments were completed using 2D experiments (COSY, HSQC, HMBC) and pulse experiments (DEPT-135) were appropriate.

All mass spectrometry was carried out using a tandem *Acquity* UPLC (Waters Ltd, UK) and a TQD with ESI mass spectrometer. The UPLC was equipped with a *Acquity* UPLC BEH C18 1.7 mm (2.1 mm x 50 mm) column, and mobile phase composition of H_2O containing formic acid (0.1% v/v): Methanol mobile phase (gradient elution; t = 0 min, 95%: 0%, t = 4 min, 5%: 95%), set at 0.6 mL.min^{-1}.

Infra-red spectra were acquired using a *Perkin Elmer* Spectrum 100 FT-IR spectrometer equipped with a UATR attachment and CsI window. Spectra were recorded from a range of 4,000–380 cm^{-1}. Absorbance shape and intensity are described as w = weak; m = medium; s = strong; sh = sharp; br = broad. Melting points of solid and crystalline products were measured using a *Sanyo* Gallenkamp variable heater equipped with a 300 °C mercury thermometer. Melting points are uncorrected and solvents of crystallisation are listed along with the observed melting point range where appropriate.

XRD experiments were conducted by Dr Dmitry S. Yufit (DSY), using a *Bruker* D8 Venture equipped with Mo/Cu Dual IμS2 sources and an *Oxford Cryosystems* HELIX open flow helium cryostat (temperature range: 25–300 K). The analysed crystals were kept at 120 K during data collection. Using *Olex2* software[197], the collected diffraction data was solved with the *ShelXT* structure solution program using intrinsic phasing and refined with the *ShelXL* refinement package using least squares minimisation.[198,199]

6.2 Tertiary anilines synthesis

6.2.1 General Procedure for Reductive Amination (Method A)

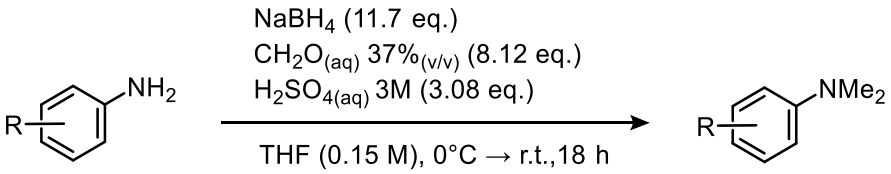

Adapted from Giumanini *et al.* procedure for selective mono-methylation of amines.[184] Powdered $NaBH_4$ (11.7 equiv) was added to a solution of aniline (1.00 equiv) in THF (0.15 M). The aniline/borohydride slurry was added dropwise at 0 °C to a second solution composed of 37% aqueous formaldehyde (8.12 equiv), 3.00 M H_2SO_4 (3.08 equiv) in THF (0.15 M). Reaction mixture pH was checked throughout the slurry addition and further 3 M H_2SO_4 was added accordingly to ensure the reaction mixture featured pH < 2. Once all the aniline was added, the reaction was removed from the ice bath and was left to stir at room temperature overnight. The reaction mixture was diluted with water (100 mL) and quenched using solid NaOH pellets. The basic reaction mixture was then extracted with EtOAc (3 x 100 mL). The combined organic extracts were washed with brine (100 mL), dried with $MgSO_4$ and reduced under pressure to yield the desired crude product which was subsequently purified using flash column chromatography.

_o_-methyl-_N,N_-dimethylaniline 133

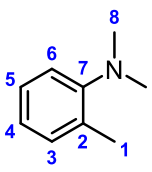

133

Following the method outlined in **6.2.1** using *o*-toluidine (5.00 g, 46.7 mmol) and additional 3 M H_2SO_4 (48.0 mL, 144 mmol, 3.08 equiv.) throughout the slurry portionwise addition, crude permethylated product purification was carried out *via* column chromatography (99:1 hexanes:EtOAc), which afforded the tertiary aniline as a colourless oil (3.77 g, 27.9 mmol, 60% yield). ^{1}H NMR (600 MHz, $CDCl_3$) δ 7.20 – 7.16 (2H, m, $H^{3,4}$), 7.08 – 7.03 (1H, m, H^6), 6.97 (1H, td, J = 7.3, 1.3 Hz, H^5), 2.72 (6H, s, H^8), 2.36 (3H, s, H^1);[200] ^{13}C NMR (151 MHz, $CDCl_3$) δ 152.9 (C^7), 132.3 (C^2), 131.3 (C^3), 126.6 (C^4), 122.7 (C^5), 118.5 (C^6), 44.4 (C^8), 18.5 (C^1);[200] HRMS (ESI-TOF) *m/z*: $[M+H]^+$ Calculated for $C_9H_{14}N^+$: 136.1126, found 136.1121 (-0.5 ppm, -3.7 ppm); IR (max/cm^{-1}): 2947w, 2829w, 2783w, 1500s, 1458m, 1310m, 1158m, 1108m, 1051m, 953s, 770s, 728s.

_m_-methyl-_N,N_-dimethylaniline 134

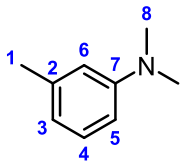

134

Following the method outlined in **6.2.1** using *m*-toluidine (5.00 g, 46.6 mmol) and additional 3 M H_2SO_4 (48 mL, 144 mmol, 3.08 equiv.) throughout the slurry portionwise addition, crude permethylated product purification was carried out *via* silica plug (99:1 hexanes:EtOAc), which afforded the tertiary aniline as a yellow oil (4.39 g, 32.5 mmol, 70% yield). ^{1}H NMR (600 MHz, $CDCl_3$) δ 7.15 (1H, t, *J* = 8.3 Hz, H^4), 6.62 – 6.55 (3H, m, $H^{3,5\text{-}6}$), 2.95 (6H, s, H^8), 2.34 (3H, s, H^1);[200] ^{13}C NMR (151 MHz, $CDCl_3$) δ 151.0 (C^7), 138.8 (C^2), 129.1 (C^4), 117.8 (C^3), 113.6 (C^6), 110.1 (C^5), 40.8 (C^8), 22.0 (C^1);[200] LRMS (ESI-TOF) *m/z*: $[M+H]^+$ 136.096 (100); HRMS (ESI-TOF) *m/z*: $[M+H]^+$ Calculated for $C_9H_{14}N^+$: 136.1126, found 136.1128 (0,2 mDa, 1.5 ppm); IR (max/cm^{-1}): 2918w, 2800w, 1606m, 1496m, 1347m, 1180m, 997m, 762s, 695s.

2,5-dimethyl-_N,N_-dimethylaniline 135

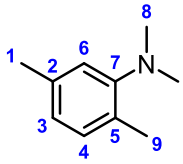

135

Following the method outlined in **6.2.1** using 2,5-dimethylaniline (2.51 g, 20.8 mmol) and additional 3 M H_2SO_4 (21 mL, 63.5 mmol, 3.08 equiv.) throughout the slurry portionwise addition, crude permethylated product purification was carried out *via* column chromatography (95:5 hexanes:Et_2O), which afforded the tertiary aniline as a yellow oil (2.12 g, 14.2 mmol, 68% yield). ^{1}H NMR (600 MHz, $CDCl_3$) δ 7.07 (1H, d, *J* = 7.6 Hz, H^4), 6.87 (1H, s, H^6), 6.79 (1H, d, *J* = 7.5 Hz, H^3), 2.71 (6H, s, H^8), 2.33 (3H, s, H^1), 2.31 (3H, s, H^9); ^{13}C NMR (151 MHz, $CDCl_3$) δ 152.7 (C^7), 136.1 (C^2), 131.1 (C^4), 129.0 (C^5), 123.3 (C^3), 119.3 (C^6), 44.4 (C^8), 21.4 (C^f), 18.1 (C^9); LRMS (ESI-TOF) *m/z*: $[M+H]^+$ 150.272 (100); HRMS (ESI-TOF) *m/z*: $[M+H]^+$ Calculated for $C_{10}H_{16}N^+$: 150.1283, found 150.1280 (-0.3 mDa, -0.2 ppm); IR (max/cm^{-1}): 2943w, 2826w, 2780w, 1609w, 1506s,1307m, 1108s, 997m, 802s.

3,5-dimethyl-_N,N_-dimethylaniline 136

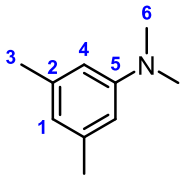

136

Following the method outlined in **6.2.1** using 3,5-dimethylaniline (4.06 g, 33.5 mmol) and additional 3 M H_2SO_4 (33.0 mL, 98.6 mmol, 3.08 equiv.) throughout the slurry portionwise addition, crude permethylated product purification was carried out *via* silica plug (97:3 hexanes:EtOAc), which afforded the tertiary aniline as a yellow oil (3.70 g, 24.8 mmol, 74% yield). ^{1}H NMR (600 MHz, DMSO-d_6) δ 6.33 (2H, s, H^4), 6.29 (1H, s, H^1), 2.84 (6H, s, H^6), 2.19 (6H, s, H^2);[201] ^{13}C NMR (151 MHz, DMSO-d_6) δ 150.6 (C^5), 137.5 (C^3), 118.1 (C^1), 110.4 (C^4), 40.2 (C^6), 21.4 (C^2);[201] LRMS (ESI-TOF) *m/z*: $[M+H]^+$ 150.313 (100); HRMS (ESI-TOF) *m/z*: $[M+H]^+$ Calculated for $C_{10}H_{16}N^+$: 150.1283, found 150.1283 (0.0 mDa, 0.0 ppm); IR (max/cm^{-1}): 2924w, 2803w, 1603s, 1493s, 1359s, 1167w, 1041w, 819s, 693s.

_p_-methyl-_N,N_-dimethylaniline 137

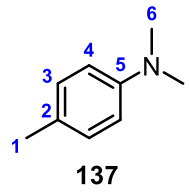

137

Following the method outlined in **6.2.1** using *p*-toluidine (5.00 g, 46.7 mmol) and additional 3 M H_2SO_4 (48.0 mL, 144 mmol, 3.08 equiv.) throughout the slurry portionwise addition, crude permethylated product purification was carried out *via* silica plug (97:3 hexanes:EtOAc), which afforded the tertiary aniline as a yellow oil (3.39 g, 25.1 mmol, 61% yield). ^{1}H NMR (600 MHz, $CDCl_3$) δ 7.08 (2H, d, *J* = 8.4 Hz, H^3), 6.72 (2H, d, *J* = 8.5 Hz, H^4), 2.92 (6H, s, H^6), 2.29 (3H, s, H^1);[202] ^{13}C NMR (151 MHz, $CDCl_3$) δ 149.0 (C^5), 129.7 (C^4), 126.3 (C^2), 113.4 (C^3), 41.3 (C^6), 20.4 (C^1);[202] LRMS (ESI-TOF) *m/z*: $[M+H]^+$ 136.212 (100); HRMS (ESI-TOF) *m/z*: $[M+H]^+$ Calculated for $C_9H_{14}N^+$: 136.1126, found 136.1120 (-0.6 mDa, -4.4 ppm); IR (max/cm^{-1}): 2882w, 1620m, 1522s, 1342m, 944m, 804s.

_p_-butyl-_N,N_-dimethylaniline 138

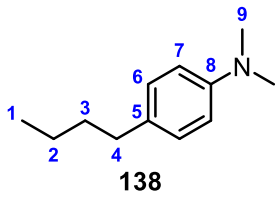

138

Following the method outlined in **6.2.1** using 4-butylaniline (3.86 g, 26.0 mmol) and additional 3 M H_2SO_4 (25.0 mL, 76.4 mmol, 3.08 equiv.) throughout the slurry portionwise addition, crude permethylated product purification was carried out *via* column chromatography (95:5 hexanes:EtOAc), which afforded the tertiary aniline as a light-yellow oil (3.49 g, 19.7 mmol, 76% yield). ^{1}H NMR (600 MHz, DMSO-d_6) δ 6.98 (2H, dt, *J* = 8.5, 3.1 Hz, H^6), 6.98 (2H, dt, *J* = 8.6, 3.0 Hz, H^7), 2.83 (6H, s, H^9), 2.45 (2H, t, *J* = 7.6 Hz, H^4), 1.48 (2H, quint, *J* = 7.7 Hz, H^3), 1.28 (2H, sex, *J* = 7.4 Hz, H^2), 0.88 (3H, t, *J* = 7.4 Hz, H^1); ^{13}C NMR (151 MHz, DMSO-d_6) δ 148.7 (C^8), 129.9 (C^5), 128.6 (C^6), 112.7 (C^7), 40.4 (C^9), 33.8 (C^4), 33.5 (C^3), 21.7 (C^2), 13.8 (C^1); LRMS (ESI-TOF) *m/z*: $[M+H]^+$ 178.323 (100); HRMS (ESI-TOF) *m/z*: $[M+H]^+$ Calculated for $C_{12}H_{20}N^+$: 178.1596, found 178.1597 (0.1 mDa, 0.6 ppm); IR (max/cm^{-1}): 2932m, 2738w, 1622m, 1523s, 1345m, 1165m, 953m, 808s.

_p_-tert-butyl-_N,N_-dimethylaniline 139

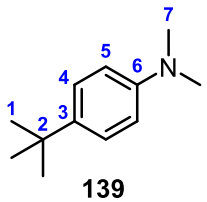

139

Following the method outlined in **6.2.1** using 4-tertbuylaniline (1.18 g, 7.92 mmol) and additional 3 M H_2SO_4 (34.0 mL, 103 mmol, 3.08 equiv.) throughout the slurry portionwise addition, crude permethylated product purification was carried out *via* column chromatography (98:2 hexanes:EtOAc), which afforded the tertiary aniline as an orange oil (1.05 g, 5.93 mmol, 75% yield). ^{1}H NMR (600 MHz, $CDCl_3$) δ 7.30 (2H, dt, *J* = 9.0, 2.5 Hz, H^4), 6.71 (2H, dt, *J* = 9.0, 2.4 Hz, H^5), 2.94 (6H, s, H^7), 1.29 (9H, s, H^1);[203] ^{13}C NMR (151 MHz, $CDCl_3$) δ 148.7 (C^6), 139.6 (C^3), 126.0 (C^4), 112.8 (C^5), 41.0 (C^7), 33.9 (C^2), 31.7 (C^1);[203] LRMS (ESI-TOF) *m/z*: $[M+H]^+$ 178.301 (100); HRMS (ESI-TOF) *m/z*: $[M+H]^+$ Calculated for $C_{12}H_{20}N^+$:

178.1596, found 178.1592 (-0.4 mDa, -2.2 ppm); IR (max/cm^{-1}): 2928m, 2793w, 1619m, 1526s, 1348m, 1204m, 1160m, 815s.

p-phenyl-*N,N*-dimethylaniline 140

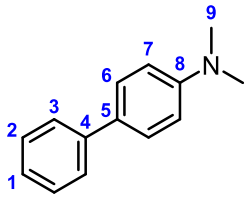

140

Following the method outlined in **6.2.1** using 4-aminobiphenyl (2.50 g, 14.7 mmol) and additional 3 M H_2SO_4 (15.0 mL, 45.4 mmol, 3.08 equiv.) throughout the slurry portionwise addition, the desired permethylated product was isolated as a pink powder without any further purification (2.69 g, 13.7 mmol, 92% yield). ^{1}H NMR (600 MHz, $CDCl_3$) δ 7.59 (2H, d, *J* = 8.1 Hz, H^3), 7.54 (2H, dt, *J* = 8.9, 2.3 Hz, H^6) 7.43 (2H, tt, *J* = 7.5, 1.5 Hz, H^2), 7.29 (1H, tt, *J* = 7.4, 1.2 Hz, H^1), 6.85 (2H, d, *J* = 8.7 Hz, H^7), 3.02 (6H, s, H^9);[204] ^{13}C NMR (151 MHz, $CDCl_3$) 150.1 (C^8), 141.4 (C^4), 129.5 (C^5), 128.7 (C^3), 127.9 (C^6), 126.5 (C^2), 126.2 (C^1), 113.0 (C^7), 40.7 (C^9);[204] LRMS (ESI-TOF) *m/z*: [M+H]$^+$ 198.315 (100); HRMS (ESI-TOF) *m/z*: [M+H]$^+$ Calculated for $C_{14}H_{16}N^+$: 198.1283, found 198.1291 (0.8 mDa, 4.0 ppm); IR (max/cm^{-1}): 3031w, 2792w, 1612m, 1491m, 1345m, 1229m, 1064m, 820s, 757s, 685s; mp: 121-123 °C.[204]

p-methoxy-*N,N*-dimethylaniline 141

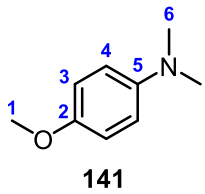

141

Following the method outlined in **6.2.1** using *p*-anisidine (5.00 g, 40.6 mmol) and additional 3 M H_2SO_4 (41.7 mL, 125 mmol, 3.08 equiv.) throughout the slurry portionwise addition, crude permethylated product purification was isolated as a purple powder without any further purification (4.96 g, 32.9 mmol, 81% yield). ^{1}H NMR (600 MHz, $CDCl_3$) δ 6.86 (2H, dt, *J* = 9.1, 2.3 Hz, H^3), 6.77 (2H, dt, *J* = 9.2, 2.3 Hz, H^4), 3.77 (3H, s, H^1), 2.88 (6H, s, H^6);[200] ^{13}C NMR (151 MHz, $CDCl_3$) δ 152.2 (C^2), 145.9 (C^5), 115.1 (C^4), 114.8 (C^3), 55.9 (C^1), 42.0 (C^6);[200] LRMS (ESI-TOF) *m/z*: [M+H]$^+$ 152.107 (100); HRMS (ESI-TOF) *m/z*: [M+H]$^+$ Calculated for $C_9H_{14}NO^+$: 152.1075, found 152.1070 (-0.5 mDa, -3.9 ppm); IR (max/cm^{-1}): 2999w, 2804w, 1517s, 1250s, 1036s, 818s, 687s; mp: 41-43 °C [decomposed].[200]

3,4,5-trimethoxy-*N,N*-dimethylaniline 142

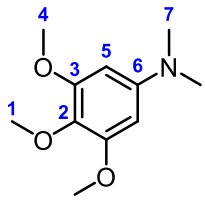

142

Following the method outlined in **6.2.1** using 3,4,5-trimethoxyaniline (3.07 g, 16.8 mmol) and additional 3 M H_2SO_4 (16.8 mL, 50.4 mmol, 3.00 equiv.) throughout the slurry portionwise addition, crude permethylated product purification was carried out *via* silica plug (7:3 hexanes:EtOAc), which afforded the tertiary aniline as a white solid (3.17 g, 15.0 mmol, 86% yield). ^{1}H NMR (600 MHz, DMSO-d_6) δ 5.96 (2H, s, H^5), 3.75 (6H, s, H^4), 3.55 (3H, s, H^1), 2.86 (6H, s, H^7); ^{13}C NMR (151 MHz, DMSO-d_6) δ 153.2 (C^3), 147.5 (C^6), 129.2 (C^2), 90.9 (C^5), 60.1 (C^1), 55.6 (C^4), 40.6 (C^7); LRMS (ESI-TOF) *m/z*: [M+H]$^+$ 212.301 (100); HRMS (ESI-TOF) *m/z*:

[M+H]$^+$ Calculated for $C_{11}H_{18}NO_3^+$: 212.1287, found 212.1290 (0.3 mDa, 1.4 ppm); IR (max/cm^{-1}): 2922w, 2825w, 1592s, 1516s, 1466s, 1252s, 1131s, 1013s, 796s, 770s, 644m; mp: 61-63 °C.

3,4-methylenedioxy-*N,N*-dimethylaniline 143

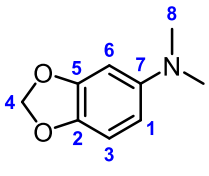

143

Following the method outlined in **6.2.1** using 3,4-(methylenedioxy)aniline (0.98 g, 7.14 mmol) and additional 3 M H_2SO_4 (10.0 mL, 29.8 mmol, 4.17 equiv.) throughout the slurry portionwise addition, crude permethylated product purification was carried out *via* column chromatography (9:1 hexanes:EtOAc), which afforded the tertiary aniline as a brown oil (1.06 g, 6.29 mmol, 90% yield). ^{1}H NMR (600 MHz, $CDCl_3$) δ 6.71 (1H, d, *J* = 8.6 Hz, H^2), 6.43 (1H, d, *J* = 2.5 Hz, H^6), 6.19 (1H, dd, *J* = 8.5, 2.5 Hz, H^1), 5.87 (2H, s, H^4), 2.87 (6H, s, H^8);[205] ^{13}C NMR (151 MHz, $CDCl_3$) δ 148.5 (C^5), 147.3 (C^7), 139.6 (C^3), 108.5 (C^2), 105.4 (C^1), 100.7 (C^4), 96.7 (C^6), 42.0 (C^8); LRMS (ESI-TOF) *m/z*: [M+H]$^+$ 166.275 (100);[205] HRMS (ESI-TOF) *m/z*: [M+H]$^+$ Calculated for $C_9H_{12}NO_2^+$: 166.0868, found 166.0869 (0.1 mDa, 0.6 ppm); IR (max/cm^{-1}): 2882w, 2798w, 1633w, 1508s, 1458m, 1226s, 1176m, 1043s, 937s, 816s.

***p*-(trifluoromethyl)-*N,N*-dimethyl aniline 144**

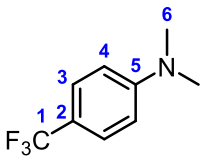

144

Following the method outlined in **6.2.1** using 4-aminobenzotrifluoride (3.60 g, 22.3 mmol) and additional 3 M H_2SO_4 (15.0 mL, 45.2 mmol, 2.02 equiv.) throughout the slurry portionwise addition, crude permethylated product purification was carried out *via* column chromatography (98:2 petroleum ether:EtOAc), which afforded the tertiary aniline as a white solid (2.06 g, 10.9 mmol, 49% yield). ^{1}H NMR (600 MHz, DMSO-d_6) δ 7.45 (2H, d, *J* = 8.3 Hz, H^3), 6.78 (2H, d, *J* = 8.7 Hz, H^4), 2.97 (6H, s, H^6); ^{13}C NMR (151 MHz, DMSO-d_6) δ 152.4 (C^5), 126.0 (1C, q, *J* = 3.8 Hz, C^3), 125.4 (1C, q, *J* = 269 Hz, C^1), 115.3 (1C, q, *J* = 31.8 Hz, C^2); 111.3 (C^4), 39.6 (C^6); ^{19}F NMR (376 MHz, DMSO-d_6) δ -58.6 (3F, s); LRMS (ASAP) *m/z*: [M+H]$^+$ 190.075 (100), [M-^{19}F]$^+$ 170.076 (34); HRMS (ASAP) *m/z*: [M+H]$^+$ Calculated for $C_9H_{11}NF_3^+$: 190.0844, found 190.0831 (-1.3 mDa, - 6.8 ppm); IR (max/cm^{-1}): 2905w, 2829w, 1626m, 1542m, 1329m, 1100s, 1063s, 824s, 585m; mp: 66-68 °C.

***p*-fluoro-*N,N*-dimethylaniline 145**

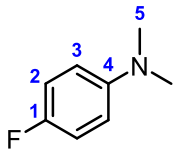

145

Following the method outlined in **6.2.1** using of 4-fluoroaniline (4.03 g, 36.2 mmol) and additional 3 M H_2SO_4 (33.0 mL, 99.7 mmol, 2.75 equiv.) throughout the slurry portionwise addition, crude permethylated product purification was carried out *via* column chromatography (9:1 hexanes:EtOAc), which afforded the tertiary aniline as a white crystalline solid (2.57 g, 18.5 mmol, 51% yield).

^{1}H NMR (600 MHz, DMSO-d_6) δ 7.04 – 6.96 (2H, m, H^2), 6.73 – 6.68 (2H, m, H^3), 2.84 (6H, s, H^5); ^{13}C NMR (151 MHz, DMSO-d_6) δ 154.6 (1C, d, *J* = 231 Hz, C^1), 147.5 (1C, d, *J* = 1.5 Hz, C^4), 115.1 (1C, d, *J* = 22.4 Hz, C^2), 113.6 (1C, d, *J* = 8.0 Hz, C^3), 40.7 (C^5); ^{19}F NMR (376 MHz, DMSO-d_6) δ -129.5 (1F, s); LRMS (ESI-TOF) *m/z*: $[M+H]^+$ 140.088 (100), 125.065 $[M+H\text{-}Me]^+$ (7); HRMS (ESI-TOF) *m/z*: $[M+H]^+$ Calculated for $C_8H_{11}NF^+$: 140.0876, found 140.0878 (0.2 mDa, 1.4 ppm); IR (max/cm^{-1}): 2985w, 2898w, 2810w, 1505m, 1451m, 1223s, 1066m, 812s, 691m; mp: 34-35 °C.

p-chloro-*N,N*-dimethylaniline 146

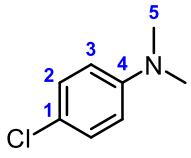

146

Following the method outlined in **6.2.1** using 4-chloroaniline (5.00 g, 39.2 mmol) and additional 3 M H_2SO_4 (40.2 mL, 121 mmol, 3.08 equiv.) throughout the slurry portionwise addition, crude permethylated product purification was carried out *via* column chromatography (100% hexanes), which afforded the tertiary aniline as a yellow solid (2.84 g, 18.3 mmol, 47% yield). ^{1}H NMR (600 MHz, $CDCl_3$) 7.18 (2H, dt, *J* = 9.1, 2.3 Hz, H^2), 6.65 (2H, dt, *J* = 9.0, 2.2 Hz, H^3) 2.93 (6H, s, H^5);[200] ^{13}C NMR (151 MHz, $CDCl_3$) δ: 149.9 (C^4), 128.9 (C^2), 122.0 (C^1), 113.8 (C^3), 40.8 (C^5);[200] LRMS (ESI-TOF) *m/z*: $[^{35}ClM+H]^+$ 156.242 (100), $[^{37}ClM+H]^+$ 158.218 (33); HRMS (ESI-TOF) *m/z*: $[M+H]^+$ Calculated for $C_8H_{11}N^{35}Cl^+$: 156.0580, found 156.0578 (-0.2 mDa, -1.3 ppm); IR (max/cm^{-1}): 2996w, 2808w, 1596m, 1490m, 1226m, 945m, 811s, 765m, 695s; mp: 29-31 °C.[200]

p-bromo-*N,N*-dimethylaniline 147

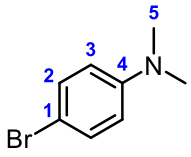

147

Following the method outlined in **6.2.1** using 4-bromoaniline (4.46 g, 25.9 mmol) and additional 3 M H_2SO_4 (25.0 mL, 74.7 mmol, 2.88 equiv.) throughout the slurry portionwise addition, crude permethylated product purification was carried out *via* column chromatography (98:2 hexanes:Et_2O), which afforded the tertiary aniline as an off-white solid (3.94 g, 19.7 mmol, 76% yield). ^{1}H NMR (600 MHz, DMSO-d_6) δ 7.29 (2H, dt, *J* = 9.1, 3.4 Hz, H^2), 6.65 (2H, dt, *J* = 9.0, 3.6 Hz, H^3), 2.87 (6H, s, H^5); ^{13}C NMR (151 MHz, DMSO-d_6) δ 149.5 (C^4), 131.3 (C^2), 114.2 (C^3), 107.1 (C^1), 40.0 (C^5); LRMS (ESI-TOF) *m/z*: $[^{79}BrM+H]^+$ 200.008 (100), $[^{81}BrM+H]^+$ 202.006 (99); HRMS (ESI-TOF) *m/z*: $[M+H]^+$ Calculated for $C_8H_{11}N^{79}Br^+$: 200.0075, found 200.0079 (0.4 mDa, 2.0 ppm); IR (max/cm^{-1}): 2992w, 2806w, 1592m, 1500m, 1226m, 948s, 806s, 755m; mp: 50-52 °C.[206]

_p_-iodo-_N,N_-dimethylaniline 148

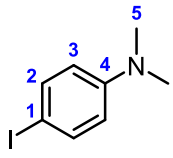

148

Following the method outlined in **6.2.1** using 4-iodoaniline (5.00 g, 22.8 mmol) and additional 3 M H_2SO_4 (23.4 mL, 70.3 mmol, 3.08 equiv.) throughout the slurry portionwise addition, the desired permethylated product was isolated as a green powder without any further purification (5.05 g, 20.4 mmol, 89% yield). ^{1}H NMR (600 MHz, $CDCl_3$) δ 7.47 (2H, dt, J = 9.1, 2.3 Hz, H^2), 6.49 (2H, dt, J = 9.0, 2.1 Hz, H^3), 2.92 (6H, s, H^5);[207] ^{13}C NMR (151 MHz, $CDCl_3$) δ 150.1 (C^4), 137.7 (C^2), 114.9 (C^3), 77.6 (C^1), 40.5 (C^5);[207] LRMS (ESI-TOF) *m/z*: $[M+H]^+$ 248.149 (100); HRMS (ESI-TOF) *m/z*: $[M+H]^+$ Calculated for $C_8H_{11}IN^+$: 247.9936, found 247.9926 (-1.0 mDa, -4.0 ppm); IR (max/cm^{-1}): 2985w, 2802w, 1584m, 1491m, 1226m, 1064s, 801s, 743s; mp: 58-61 °C.[207]

_p_-(dimethylamino)benzophenone 149

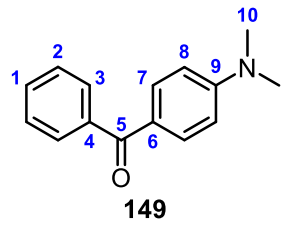

149

Following the method outlined in **6.2.1** using (2.18 g, 11.0 mmol) of precursor aniline, crude permethylated product purification was carried out *via* column chromatography (4:1 hexanes:EtOAc), which afforded the tertiary aniline as a yellow solid (2.27 g, 10.1 mmol, 91% yield). ^{1}H NMR (600 MHz, DMSO-d_6) δ: 7.65 (2H, dt, J = 9.0, 2.1 Hz, H^7), 7.63 – 7.61 (2H, m, H^3), 7.59 (1H, tt, J = 7.3, 1.3 Hz, , H^1), 7.52 (2H, t, J = 7.3 Hz, H^2), 6.77 (2H, dt, J = 9.0, 2.1 Hz, H^8), 3.03 (6H, s, H^{10}); ^{13}C NMR (151 MHz, DMSO-d_6) δ: 193.6 (C^5), 153.2 (C^9), 139.7 (C^4), 138.9 (C^8), 132.1 (C^1), 128.8 (C^3), 128.2 (C^2), 123.6 (C^6), 110.7 (C^7), 39.6 (C^{10}); LRMS (ESI-TOF) *m/z*: 226.287 $[M+H]^+$ (100); 473.505 $[2M+Na]^+$ (15); HRMS (ESI-TOF) *m/z*: $[M+H]^+$ Calculated for $C_{15}H_{16}NO^+$: 226.1232, found 226.1230 (-0.2 mDa, -0.9 ppm); IR (max/cm^{-1}): 2985w, 2905w, 1604s, 1382m, 1318m, 1288m, 1154s, 834s, 701s; mp: 82-83 °C.[208]

dimethyl 5-(_N,N_-dimethylamino)isophthalate 150

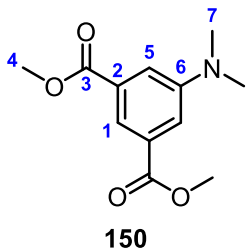

150

Following the method outlined in **6.2.1** using (3.04 g, 14.5 mmol) of precursor aniline, crude permethylated product purification was carried out *via* crystallisation in MeOH, which afforded the tertiary aniline as a pale green solid (3.11 g, 13.1 mmol, 90% yield. ^{1}H NMR (600 MHz, DMSO-d_6) δ: 7.75 (1H, t, J = 1.4 Hz, H^1), 7.41 (2H, d, J = 1.4 Hz, H^5), 3.86 (6H, s, H, H^4), 2.99 (6H, s, H^7); ^{13}C NMR (151 MHz, DMSO-d_6) δ: 166.0 (C^3), 150.2 (C^6), 130.7 (C^2), 116.6 (C^1), 115.9 (C^5), 52.3 (C^4), 39.9 (C^7); LRMS (ESI-TOF) *m/z*: $[M+Na]^+$ 260.341 (100); $[M+H]^+$ 238.336 (11); HRMS (ESI-TOF) *m/z*: $[M+H]^+$ Calculated for $C_{12}H_{16}NO_4^+$: 238.1079, found 238.1074 (-0.5 mDa, -2.1 ppm); IR (max/cm^{-1}): 2956w, 2913w, 2829w, 1717s, 1607m, 1436m, 1375m, 1230s, 1009n, 755s. mp: 119-120 °C [MeOH].

***N*-(4-(dimethylamino)phenyl)acetamide 151**

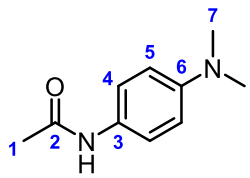

151

Following the method outlined in **6.2.1** using 4'-aminoacetanilide (4.00 g, 26.6 mmol) and additional 3 M H_2SO_4 (25.0 mL, 75.9 mmol, 2.85 equiv.) throughout the slurry portionwise addition, crude permethylated product purification was carried out *via* column chromatography (95:5 CH_2Cl_2:MeOH), which afforded the tertiary aniline as a white solid (3.58 g, 20.1 mmol, 75% yield). ^{1}H NMR (600 MHz, DMSO-d_6) δ 9.60 (1H, s, NH), 7.38 (2H, d, *J* = 9.2 Hz, H^4), 6.67 (2H, d, *J* = 9.3 Hz, H^5), 2.82 (6H, s, H^7), 1.98 (3H, s, H^1);[209] ^{13}C NMR (151 MHz, DMSO-d_6) δ 167.4 (C^2), 146.9 (C^6), 129.3 (C^3), 120.5 (C^4), 112.7 (C^5), 40.5 (C^7), 23.7 (C^1);[209] LRMS (ESI-TOF) *m/z*: $[M+H]^+$ 179.276 (100); HRMS (ESI-TOF) *m/z*: $[M+H]^+$ Calculated for $C_{10}H_{15}N_2O^+$: 179.1184, found 179.1175 (-0.9 mDa, -5.0 ppm); IR (max/cm^{-1}): 3243w, 3050w, 2890w, 2814w, 1644m, 1604m, 1523s, 1325s, 1226s. 1173m, 948m, 816s, 609m, 515s; 121-123 °C.[210]

***m*-cyano-*N,N*-dimethylaniline 152**

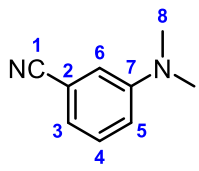

152

Following the method outlined in **6.2.1** using 3-aminobenzonitrile (5.00 g, 42.3 mmol) and additional 3 M H_2SO_4 (43.0 mL, 130 mmol, 3.08 equiv.) throughout the slurry portionwise addition, crude permethylated product purification was carried out *via* silica plug (95:5 hexanes:EtOAc), which afforded the tertiary aniline as a yellow oil (5.58 g, 38.2 mmol, 90% yield). ^{1}H NMR (600 MHz, $CDCl_3$) δ 7.30 – 7.26 (1H, m, H^4), 6.95 (1H, dt, *J* = 7.5, 1.2 Hz, H^3), 6.91 – 6.87 (2H, m, H^{5-6}), 2.98 (6H, s, H^8);[211] ^{13}C NMR (151 MHz, $CDCl_3$) δ 150.3 (C^7), 129.8 (C^4), 119.9 (C^1), 119.6 (C^3), 116.4 (C^5), 115.0 (C^6), 112.9 (C^2), 40.3 (C^8);[211] LRMS (ESI-TOF) *m/z*: $[M+H]^+$ 147.234 (100); HRMS (ESI-TOF) *m/z*: $[M+H]^+$ Calculated for $C_9H_{11}N_2^+$: 147.0922, found 147.0920 (-0.2 mDa, -1.4 ppm); IR (max/cm^{-1}): 2918w, 2816w, 2229m, 1596s, 1496m, 1375m, 1228m, 1001s, 841m, 775s, 678s.

6.2.2 General Procedure for Reductive Amination (Method B)

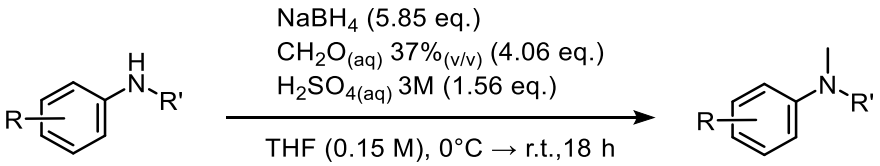

Adapted from Giumanini *et al.* procedure for selective mono-methylation of amines.[184] Powdered $NaBH_4$ (5.85 equiv) was added to a solution of aniline (1.00 equiv) in THF (0.15 M). The aniline/borohydride slurry was added dropwise at 0°C to a second solution composed of 37% aqueous formaldehyde (4.06 equiv), 3 M H_2SO_4 (1.54 equiv) in THF (0.15 M). Reaction

mixture pH was checked throughout the slurry addition and further 3 M H_2SO_4 was added accordingly to ensure the reaction mixture featured pH < 2. Once all the aniline was added, the reaction was removed from the ice bath and was left to stir at room temperature overnight. The reaction mixture was diluted with water (100 mL) and quenched using solid NaOH pellets. The basic reaction mixture was then extracted with EtOAc (3 x 100 mL). The combined organic extracts were washed with brine (100 mL), dried with $MgSO_4$ and reduced under pressure to yield the desired crude product which was subsequently purified using flash column chromatography.

_N_-methyl diphenylamine 153

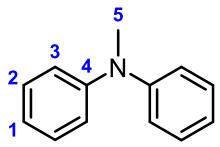

153

Following the method outlined in **6.2.2** using (1.00 g, 5.90 mmol) of precursor aniline, crude permethylated product purification was carried out *via* column chromatography (98:2 hexane:ethyl acetate), which afforded the tertiary aniline (0.49 g, 2.68 mmol, 45% yield) as a light-yellow oil. ^{1}H NMR (600 MHz, $CDCl_3$) δ 7.28 (t, *J* = 8.1 Hz, 4H, H^2), 7.04 (d, *J* = 8.4 Hz, 4H, H^3), 6.97 (tt, *J* = 7.4, 1.2 Hz, 2H, H^1), 3.33 (s, 3H, H^5).[200] ^{13}C NMR (151 MHz, $CDCl_3$) δ 149.2 (C^4), 129.3 (C^2), 121.4 (C^1), 120.6 (C^3), 40.4 (C^5).[200] LRMS (ESI-TOF) *m/z*: 184.328 $[M+H]^+$ (100); HRMS (ESI-TOF) *m/z*: $[M+H]^+$ Calculated for $C_{13}H_{14}N^+$: 184.1126, found 184.1132 (0.6 mDa, 3.3 ppm); IR (max/cm^{-1}): 2924w, 2851w, 1587m, 1496s, 1342m, 1254m, 1131m, 864m, 746s, 691s.

_N_-benzyl-_N_-methyl aniline 154

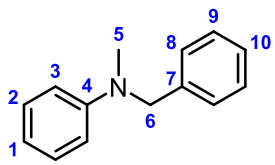

155

Following the method outlined in **6.2.2** using N-benzylaniline (5.00 g, 27.3 mmol) and additional 3 M H_2SO_4 (14 mL, 42.0 mmol, 1.54 equiv.) throughout the slurry portionwise addition, crude permethylated product purification was carried out *via* silica plug (97:3 hexanes:EtOAc), which afforded the tertiary aniline as a colourless oil (5.30 g, 26.9 mmol, 99% yield). ^{1}H NMR (600 MHz, $CDCl_3$) δ 7.33 (2H, t, *J* = 7.9 Hz, H^2), 7.28 – 7.20 (5H, m, H^{8-10}), 6.77 (2H, d, *J* = 8.1 Hz, H^3), 6.73 (1H, t, *J* = 7.9 Hz, H^1), 4.55 (2H, s, H^6), 3.03 (3H, s, H^5);[204] ^{13}C NMR (151 MHz, $CDCl_3$) δ 149.9 (C^4), 139.2 (C^7), 129.3 (C^9), 128.7 (C^2), 127.0 (C^{10}), 126.9 (C^8), 116.7 (C^1), 112.5 (C^3), 56.8 (C^6), 38.6 (C^5);[204] LRMS (ESI-TOF) *m/z*: $[M+H]^+$ 198.187 (100); HRMS (ESI-TOF) *m/z*: $[M+H]^+$ Calculated for $C_{14}H_{16}N^+$: 198.1283, found 198.1293 (1.0 mDa, 5.0 ppm); IR (max/cm^{-1}): 3031w, 2816w, 1599s, 1505s, 1451m, 1354m, 1216m, 948m, 727s, 690s.

***N*-methyl indoline 155**

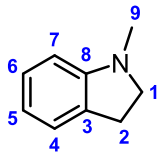

155

Following the method outlined in **6.2.2** using indoline (5.00 g, 41.2 mmol) and additional 3 M H_2SO_4 (21 mL, 63.5 mmol, 1.54 equiv.) throughout the slurry portionwise addition, crude permethylated product purification was carried out *via* column chromatography (98:2 hexanes:EtOAc), which afforded the tertiary aniline as a yellow oil (5.34 g, 40.8 mmol, 97% yield). ^{1}H NMR (600 MHz, $CDCl_3$) δ 7.13 – 7.08 (2H, m, H^{4-6}), 6.70 (1H, t, *J* = 7.5 Hz, H^5), 6.51 (1H, d, *J* = 8.2 Hz, H^7), 3.31 (2H, t, *J* = 8.0 Hz, H^1), 2.97 (2H, t, *J* = 7.8 Hz, H^2), 2.78 (3H, s, H^9);[205] ^{13}C NMR (151 MHz, $CDCl_3$) δ 153.5 (C^8), 130.4 (C^3), 127.4 (C^6), 124.4 (C^4), 117.9 (C^5), 107.4 (C^7), 56.3 (C^1), 36.4 (C^9), 28.9 (C^2);[205] LRMS (ESI-TOF) *m/z*: $[M+H]^+$ 134.165 (100), $[M+H-Me]^+$ 119.153 (23); HRMS (ESI-TOF) *m/z*: $[M+H]^+$ Calculated for $C_9H_{12}N^+$: 134.0970, found 134.0965 (-0.5 mDa, -3.7 ppm); IR (max/cm^{-1}): 2948w, 2804w, 1605m, 1490s, 1390m, 1267m, 1115m, 987m, 743s.

***N*-methyl-(1H,2H,3H,4H)-tetrahydroquinoline 114**

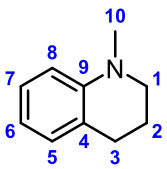

114

Following the method outlined in **6.2.2** using (1H,2H,3H,4H)-tetrahydroquinoline (3.22 g, 24.2 mmol) and additional 3 M H_2SO_4 (11.7 mL, 35.1 mmol, 1.54 equiv.) throughout the slurry portionwise addition, crude permethylated product purification was carried out *via* column chromatography (98:2 petroleum ether:EtOAc), which afforded the tertiary aniline as a yellow oil (2.80 g, 19.0 mmol, 79% yield). ^{1}H NMR (600 MHz, $CDCl_3$) δ 7.11 (1H, t, *J* = 7.1 Hz, H^5), 6.99 (1H, d, *J* = 7.2 Hz, H^7), 6.64 (1H, t, *J* = 7.2 Hz, H^6), 6.63 (1H, d, *J* = 8.1 Hz, H^8), 3.25 (2H, t, J = 5.7 Hz, H^1), 2.92 (3H, s, H^{10}), 2.80 (2H, t, *J* = 6.4 Hz, H^3), 2.02 (2H, quint., *J* = 5.6 Hz, H^2);[211] ^{13}C NMR (151 MHz, $CDCl_3$) δ 146.9 (C^9), 128.9 (C^5), 127.2 (C^7), 123.0 (C^4), 116.3 (C^6), 111.1 (C^8), 51.4 (C^1), 39.2 (C^{10}), 27.9 (C^3), 22.6 (C^2);[211] LRMS (ESI-TOF) *m/z*: $[M+H]^+$ 148.298 (100); HRMS (ESI-TOF) *m/z*: $[M+H]^+$ Calculated for $C_{10}H_{14}N^+$: 148.1126, found 148.1133 (0.7 mDa, 4.7 ppm); IR (max/cm^{-1}): 2935m, 2817w, 1604s, 1508s, 1325s, 1212s, 1097m, 1061m, 1006m, 747m.

6.3 Bromide ammonium salts synthesis

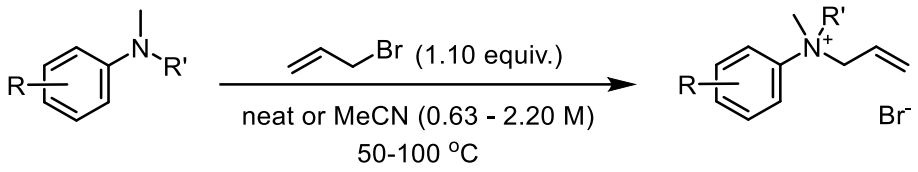

The selected tertiary amine (1.00 equiv.) was charged into a round bottom flask: acetonitrile was added to round bottom flask to allow solid anilines dissolution, when appropriate. With stirring, alkylating agent (1.10 equiv.) was added to the tertiary aniline. The reaction mixture was heated and left to stir at 50 °C, until the desired bromide ammonium salt precipitated from the reaction mixture. The crude solid salt was washed with diethyl ether (x3) to remove excess alkylating agent and unreacted aniline precursor. The salt was recrystallized using a number of solvents (MeOH, EtOH, CH_2Cl_2/Hexane) when necessary, for purification purposes.

N-allyl-*N,N*-dimethylanilinium bromide 89

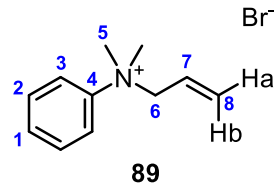

89

Following the method outlined in **6.3** using neat *N,N*-dimethylaniline (2.00 mL, 16.5 mmol) and allyl bromide (1.50 mL, 17.7 mmol), pure bromide ammonium salt was isolated, after leaving the reaction mixture to stir at 50 °C for 18 hours, as a pink powder, without further purification (3.99 g, 16.5 mmol, 90% yield). ^{1}H NMR (700 MHz, $CDCl_3$) δ 7.97 (2H, d, *J* = 8.5 Hz, H^3), 7.61 (2H, t, *J* = 8.1 Hz, H^2), 7.52 (1H, t, *J* = 7.6 Hz, H^1), 5.80 (1H, d, *J* = 16.6 Hz, H^{8a}), 5.50 (1H, d, *J* = 10.3 Hz, H^{8b}), 5.41 (1H, ddt, *J* = 16.5, 10.2, 7.2 Hz, H^7), 5.23 (2H, d, *J* = 7.2 Hz, H^6), 3.99 (6H, s, H^5); ^{13}C NMR (176 MHz, $CDCl_3$) δ 144.7 (C^4), 130.9 (C^2), 130.6 (C^1), 129.8 (C^8), 124.9 (C^7), 121.1 (C^3), 70.9 (C^6), 54.2 (C^5); LRMS (ESI-TOF) *m/z*: $[M]^+$ 162.250 (56), $[M\text{-allyl}]^+$ 121.129 (100); HRMS (ESI-TOF) *m/z*: $[M]^+$ Calculated for $C_{11}H_{16}N^+$: 162.1283, found 162.1290 (0.7 mDa, 4.3 ppm); IR (max/cm^{-1}): 3011w, 2967w, 1487m, 1413s, 1126m, 1001m, 946s, 837s, 690s; mp: 117-120 °C.

N-allyl-*N,N*-dimethyl-3-methylanilinium bromide 156

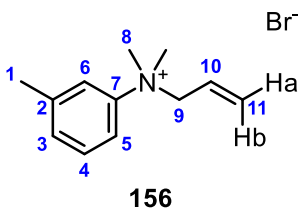

156

Following the method outlined in **6.3**, neat *N,N*-dimethyl-*m*-toluidine **134** (1.45 g, 10.7 mmol) was added into a round bottom flask, followed by allyl bromide (1.00 mL, 11.8 mmol) whilst stirring. The reaction mixture was then heated and stirred at 50 °C for 72 hours, until the desired salt has precipitated from the reaction. Pure bromide ammonium salt was obtained as a pink powder without further purification (2.33 g, 9.09 mmol, 85% yield).^{1}H NMR (600 MHz, $CDCl_3$) δ 7.83 (1H, d, *J* = 3.6 Hz, H^5), 7.67 (1H, dd,

J = 8.5, 2.8 Hz, H^3), 7.45 (1H, t, *J* = 7.9 Hz, H^4), 7.31 (1H, d, *J* = 7.5 Hz, H^6), 5.80 (1H, d, *J* = 16.7 Hz, H^{11a}), 5.49 (1H, d, *J* = 10.1 Hz, H^{11b}), 5.40 (1H, ddt, *J* = 17.2, 10.3, 7.2 Hz, H^{10}), 5.17 (2H, d, *J* = 7.0 Hz, H^9), 3.94 (6H, s, H^8), 2.49 (3H, s, H^1); ^{13}C NMR (151 MHz, $CDCl_3$) δ 144.6 (C^7), 141.6 (C^2), 131.3 (C^6), 130.4 (C^4), 129.5 (C^{11}), 125.0 (C^{10}), 121.5 (C^5), 117.8 (C^3), 70.8 (C^9), 54.2 (C^8), 21.7 (C^1); LRMS (ESI-TOF) *m/z*: $[M]^+$ 176.186 (100); HRMS (ESI-TOF) *m/z*: $[M]^+$ Calculated for $C_{12}H_{18}N^+$: 176.1439, found 176.1445 (0.6 mDa, 3.4 ppm); IR (max/cm^{-1}): 3030w, 2967w, 1615w, 1500m, 1455m, 1380w, 1184w, 1098m, 1001m, 955m, 904m, 788s, 690s; mp: 138-141 °C (decomposed);[212] XRD: sample crystallised in EtOH/Et_2O yielding colourless platelets. Crystal data for $C_{12}H_{18}BrN$ (m = 256.18 g/mol): orthorhombic, $Pca2_1$ (no. 29).

N-allyl-*N,N*-dimethyl-3,5-dimethylanilinium bromide 157

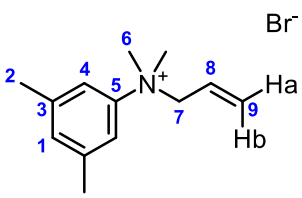

157

Following the method outlined in **6.3** using neat 3,5-dimethyl-*N,N*-dimethylaniline **136** (3.00 g, 20.1 mmol) and allyl bromide (1.90 mL, 22.1 mmol), pure bromide ammonium salt was isolated, after leaving the reaction mixture to stir at 50 °C for 48 hours as a white powder without further purification (5.32 g, 19.7 mmol, 98% yield). ^{1}H NMR (600 MHz, MeOD-d_4) δ 7.50 (2H, s, H^4), 7.24 (1H, s, H^1), 5.70 – 5.52 (3H, m, $H^{8a/b-9}$), 4.52 (2H, d, *J* = 5.9 Hz, H^7), 3.60 (6H, s, H^6), 2.43 (6H, s, H^2);^{13}C NMR (151 MHz, MeOD-d_4) δ 146.1 (C^5), 142.2 (C^3), 132.9 (C^1), 129.0 (C^9), 126.6 (C^8), 119.5 (C^4), 72.5 (C^7), 54.4 (C^6), 21.5 (C^2); LRMS (ESI-TOF) *m/z*: $[M]^+$ 190.333 (100); HRMS (ESI-TOF) *m/z*: $[M]^+$ Calculated for $C_{13}H_{20}N^+$: 190.1596, found 190.1594 (-0.2 mDa, -1.1 ppm); IR (max/cm^{-1}): 2966m, 2909w, 1622m, 1478s, 1379w, 1165m, 1013m, 948s, 891s, 702s; mp: 164-166 °C (decomposed); XRD: sample crystallised in EtOH/Et_2O yielding colourless, block-shaped crystals. Crystal data for $C_{13}H_{20}BrN$ (m = 270.21 g/mol): triclinic, P_{-1} (no. 2).

N-allyl-*N,N*-dimethyl-4-methylanilinium bromide 158

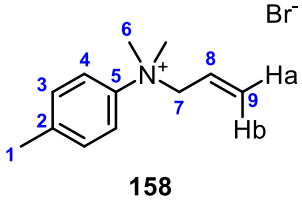

158

Following the method outlined in **6.3** using neat *N,N*-dimethyl-*p*-toluidine **137** (1.00 g, 7.40 mmol) and allyl bromide (0.68 mL, 8.1 mmol), pure bromide ammonium salt was isolated, after leaving the reaction mixture to stir at 50 °C for 18 hours, as a glassy yellow solid after thorough drying (1.52 g, 5.94 mmol, 80% yield). ^{1}H NMR (600 MHz, MeOD-d_4) δ 7.73 (2H, dt, *J* = 8.9, 2.2 Hz, H^3), 7.46 (2H, dt, *J* = 8.4, 2.8 Hz, H^4), 5.65 (1H, ddt, *J* = 17.0, 9.6, 6.4 Hz, H^8), 5.59 (1H, dd, *J* = 17.0, 1.9 Hz, H^{9a}), 5.55 (1H, dd, *J* = 9.6, 1.6 Hz, H^{9b}), 4.53 (2H, d, *J* = 6.5 Hz, H^7), 3.62 (6H, s, H^6), 2.42 (3H, s, H^1); ^{13}C NMR (151 MHz, MeOD-d_4) δ 143.7 (C^5), 142.3 (C^2), 132.0 (C^3), 129.2 (C^9), 126.5 (C^8), 121.9 (C^4), 72.6

(C^7), 54.4 (C^6), 20.8 (C^1); LRMS (ESI-TOF) *m/z*: $[M]^+$ 176.195 (100); 135.111 m/z (80); HRMS (ESI-TOF) *m/z*: $[M]^+$ Calculated for $C_{12}H_{18}N^+$: 176.1439, found 176.1438 (-0.1 mDa, -0.6 ppm); IR (max/cm^{-1}): 2981w, 2842w, 1595m, 1517m, 1468m, 1268m, 1193m, 1028m, 821s, 557s.

N-allyl-*N,N*-dimethyl-4-butylanilinium bromide 159

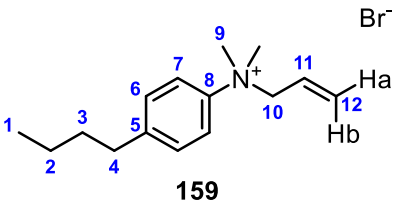

159

Following the method outlined in **6.3** using neat *N,N*-dimethyl-4-butylaniline **138** (3.32 g, 18.8 mmol) and allyl bromide (1.75 mL, 20.6 mmol), pure bromide ammonium salt was isolated, after leaving the reaction mixture to stir at 50 °C for 18 hours, as a glassy brown solid after thorough drying (4.83 g, 16.2 mmol, 86% yield). ^{1}H NMR (600 MHz, MeOD-d_4) δ 7.75 (2H, dt, *J* = 8.9, 2.3 Hz, H^7), 7.47 (2H, dt, *J* = 8.8, 2.2 Hz, H^6), 5.65 (1H, ddt, *J* = 16.4, 9.8, 6.7 Hz, H^{11}), 5.58 (1H, d, *J* = 16.4 Hz, H^{12a}), 5.56 (1H, d, *J* = 9.8 Hz, H^{12b}), 4.51 (2H, d, *J* = 6.7 Hz, H^{10}), 3.61 (6H, s, H^9), 2.71 (2H, t, *J* = 7.7 Hz, H^4), 1.63 (2H, quint, *J* = 7.4 Hz, H^3), 1.37 (2H, sex, *J* = 7.4 Hz, H^2), 0.95 (3H, t, *J* = 7.4 Hz, H^1); ^{13}C NMR (151 MHz, MeOD-d_4) δ 147.2 (C^5), 143.8 (C^8), 131.4 (C^6), 129.2 (C^{12}), 126.5 (C^{11}), 121.9 (C^7), 72.6 (C^{10}), 54.4 (C^9), 35.7 (C^4), 34.5 (C^3), 23.3 (C^2), 14.2 (C^1); LRMS (ESI-TOF) *m/z*: $[M]^+$ 218.356 (100); $[M\text{-allyl}]^+$ 177.350 (34); HRMS (ESI-TOF) *m/z*: $[M]^+$ Calculated for $C_9H_{14}N^+$: 218.1910, found 218.1909 (0.1 mDa, 0.5 ppm); IR (max/cm^{-1}): 2963m, 2935m, 1912w, 1481m, 1440m, 1189m, 1094m, 899s, 884s, 750s.

N-allyl-*N,N*-dimethyl-4-*tert*-butylanilinium bromide 160

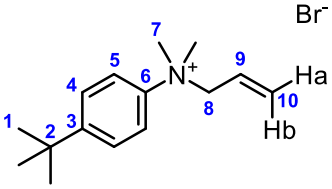

160

Following the method outlined in **6.3** using neat *N,N*-dimethyl-4-tertbutylaniline **139** (0.89 g, 5.03 mmol) and allyl bromide (0.47 mL, 5.53 mmol), pure bromide ammonium salt was isolated, after leaving the reaction mixture to stir at 50 °C for 72 hours, as a hygroscopic white powder without further purification (1.41 g, 4.73 mmol, 94% yield). ^{1}H NMR (600 MHz, MeOD-d_4) δ 7.77 (2H, dt, *J* = 9.2, 2.3 Hz, H^5), 7.68 (2H, dt, *J* = 9.2, 2.4 Hz, H^4), 5.66 (1H, ddt, *J* = 17.0, 9.8, 6.7 Hz, H^9), 5.61 (1H, dd, *J* = 17.2, 2.2 Hz, H^{10a}), 5.57 (1H, dd, *J* = 9.7, 2.2 Hz, H^{10b}), 4.53 (2H, d, *J* = 6.7 Hz, H^8), 3.62 (6H, s, H^7), 1.36 (9H, s, H^1); ^{13}C NMR (151 MHz, MeOD-d_4) ^{13}C NMR (151 MHz, MeOD-d_4) δ 153.2 (C^3), 141.6 (C^6), 127.2 (C^{10}), 126.6 (C^4), 124.5 (C^9), 119.7 (C^5), 70.6 (C^8), 52.4 (C^7), 33.7 (C^2), 29.5 (C^1); LRMS (ESI-TOF) *m/z*: $[M]^+$ 218.268 (100); HRMS (ESI-TOF) *m/z*: $[M]^+$ Calculated for $C_{15}H_{24}N^+$: 218.1909, found 218.1912 (0.3 mDa, 1.4 ppm); IR (max/cm^{-1}): 2967m, 2874w, 1513m, 1468m, 1366w, 1277w, 1140m, 952m, 841s, 580s, 557s; mp: 113-116 °C.

***N*-allyl-*N,N*-dimethyl-4-phenylanilinium bromide 161**

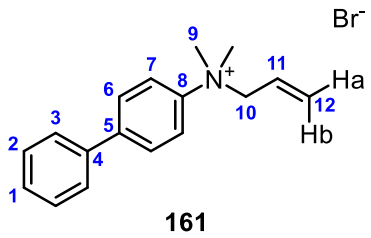

161

Following the method outlined in **6.3** using *p*-phenyl-*N,N*-dimethylaniline **140** dissolved in acetonitrile (1.50 g, 7.61 mmol, 0.63 M) and allyl bromide (0.71 mL, 8.37 mmol), pure bromide ammonium salt was isolated, after leaving the reaction mixture to stir at 50 °C for 24 hours, as a brown powder without further purification (2.19 g, 6.89 mmol, 90% yield). ^{1}H NMR (600 MHz, MeOD-d_4) δ 7.95 (2H, dt, *J* = 9.2, 2.4 Hz, H^{7}), 7.90 (2H, dt, *J* = 9.2, 2.2 Hz, H^{6}), 7.69 (2H, dt, *J* = 7.8, 1.8 Hz, H^{3}), 7.50 (2H, tt, *J* = 7.9, 1.8 Hz, H^{2}), 7.42 (1H, tt, *J* = 7.5, 1.2 Hz, H^{1}), 5.72 (1H, ddt, *J* = 17.1, 10.2, 7.4 Hz, H^{11}), 5.64 (1H, dd, *J* = 17.1, 1.5 Hz, H^{12a}), 5.59 (1H, dd, *J* = 10.2, 1.9 Hz, H^{12b}), 4.60 (2H, d, *J* = 7.3 Hz, H^{10}), 3.69 (6H, s, H^{9}); ^{13}C NMR (151 MHz, MeOD-d_4) δ 143.0 (C^{8}), 142.6 (C^{5}), 137.8 (C^{4}), 128.2 (C^{2}), 127.8 (C^{6}), 127.6 (C^{1}), 127.4 (C^{12}), 126.1 (C^{3}), 124.4 (C^{11}), 120.7 (C^{7}), 70.7 (C^{10}), 52.5 (C^{9}); LRMS (ESI-TOF) *m/z*: $[M]^+$ 238.334 (61), $[M\text{-allyl}]^+$ 197.252 (100); HRMS (ESI-TOF) *m/z*: $[M]^+$ Calculated for $C_{17}H_{20}N^+$: 238.1596, found 238.1592 (-0.4 mDa, -1.7 ppm); IR (max/cm^{-1}): 3011w, 2963w, 1491m, 1416m, 1131w, 1001m, 949m, 838m, 771s, 695s, 562m; mp: 153-154 °C; XRD: sample crystallised in CH_2Cl_2/hexane yielding colourless platelets. Crystal data for $C_{17}H_{20}BrN$ (m = 318.25 g/mol): orthorhombic, Pbca (no. 61).

***N*-allyl-*N,N*-dimethyl-4-methoxyanilinium bromide 91**

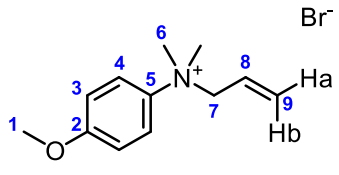

91

Following the method outlined in **6.3** using *N,N*-dimethyl-*p*-anisidine **141** dissolved in acetonitrile (2.00 g, 13.2 mmol, 2.2 M) and allyl bromide (1.22 mL, 14.5 mmol), pure bromide ammonium salt was isolated, after leaving the reaction mixture to stir at 50 °C for 18 hours, as a purple solid without further purification (3.26 g, 12.0 mmol, 92% yield). ^{1}H NMR (600 MHz, $CDCl_3$) δ 7.90 (2H, dt, *J* = 9.2, 2.3 Hz, H^{3}), 7.03 (2H, dt, *J* = 9.4, 2.3 Hz, H^{4}), 5.76 (1H, d, *J* = 16.8 Hz, H^{9a}), 5.47 (1H, dd, *J* = 10.3, 1.7 Hz, H^{9b}), 5.42 (1H, ddt, *J* = 16.6, 10.3, 7.1 Hz, H^{8}), 5.12 (2H, d, *J* = 7.1 Hz, H^{7}), 3.91 (6H, s, H^{6}), 3.81 (3H, s, H^{1}); ^{13}C NMR (151 MHz, $CDCl_3$) δ 160.4 (C^{2}), 137.2 (C^{5}), 129.4 (C^{9}), 125.1 (C^{8}), 122.6 (C^{4}), 115.5 (C^{3}), 71.0 (C^{7}), 55.9 (C^{6}), 54.4 (C^{1}); LRMS (ESI-TOF) *m/z*: $[M]^+$ 192.311 (6), $[M\text{-Me}]^+$ 177.299 (4); HRMS (ESI-TOF) *m/z*: $[M]^+$ Calculated for $C_{12}H_{18}NO^+$: 192.1388, found 192.1382 (-0.6 mDa, -3.1 ppm); IR (max/cm^{-1}): 3007w, 2967w, 1593m, 1487s, 1266m, 1201m, 1024m, 957m, 824s, 687s, 557s; mp: 136-139 °C;[177] XRD: sample crystallised in CH_2Cl_2/hexane to give colourless prism-shaped crystals. Crystal data for $C_{12}H_{18}BrNO$ (m = 272.18 g/mol): orthorhombic, Aea2 (no. 41).

***N*-allyl-*N,N*-dimethyl-3,4,5-trimethoxyanilinium bromide 162**

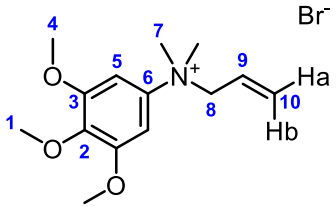

162

Following the method outlined in **6.3** using 3,4,5-trimethoxy-*N,N*-dimethylaniline **142** dissolved in acetonitrile (2.02 g, 9.55 mmol, 2 M) and allyl bromide (0.88 mL, 10.4 mmol)**,** pure bromide ammonium salt was isolated, after leaving the reaction mixture to stir at 50 °C for 18 hours as an off-white solid without further purification (2.60 g, 7.84 mmol, 82% yield). ^{1}H NMR (600 MHz, MeOD-d_4) δ 7.07 (2H, s, H^5), 5.70 (1H, ddt, *J* = 16.5, 9.5, 6.8 Hz, H^9), 5.63 (1H, dd, *J* = 16.6, 1.8 Hz, H^{10a}), 5.59 (1H, dd, *J* = 9.8, 1.8 Hz, H^{10b}), 4.56 (2H, d, *J* = 6.8 Hz, H^8), 3.94 (6H, s, H^3), 3.80 (3H, s, H^1), 3.64 (6H, s, H^7); ^{13}C NMR (151 MHz, $CDCl_3$) δ 155.3 (C^4), 141.6 (C^6), 140.6 (C^2), 129.0 (C^{10}), 126.6 (C^9), 100.6 (C^5), 72.7 (C^8), 61.2 (C^1), 57.5 (C^3), 54.6 (C^7); LRMS (ESI-TOF) *m/z*: $[M]^+$ 252.371 (100); $[M\text{-allyl}]^+$ 211.351 (60); HRMS (ESI-TOF) *m/z*: $[M]^+$ Calculated for $C_{14}H_{22}NO_3^+$: 252.1600, found 252.1592 (-0.8 mDa, -3.2 ppm); IR (max/cm^{-1}): 2989w, 2836w, 1610m, 1474m, 1424m, 1268m, 1127s, 995s, 903m, 580m; mp: 110-112 °C; XRD: sample crystallised in EtOH to give colourless platelets. Crystal data for $C_{14}H_{24}BrNO_4$ (m = 350.25 g/mol): triclinic, P_{-1} (no. 2).

***N*-allyl-*N,N*-dimethyl-(3,4-methylenedioxy)anilinium bromide 163**

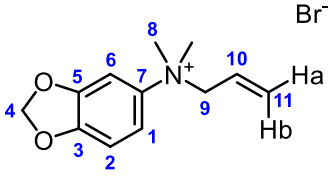

163

Following the method outlined in **6.3** using neat 3,4-methylenedioxy-*N,N*-dimethylaniline **143** (0.875 g, 5.30 mmol) and allyl bromide (0.5 mL, 5.82 mmol), pure bromide ammonium salt was isolated, after leaving the reaction mixture to stir at 50 °C for 18 hours, as a white solid without further purification (1.08 g, 3.77 mmol, 71% yield). ^{1}H NMR (600 MHz, MeOD-d_4) δ 7.48 (1H, d, *J* = 2.8 Hz, H^6), 7.31 (1H, dd, *J* = 8.7, 2.8 Hz, H^1), 6.99 (1H, d, *J* = 8.7 Hz, H^2), 6.13 (2H, s, H^4), 5.69 (ddt, *J* = 16.6, 9.7, 6.9 Hz, H^{10}), 5.61 (1H, dd, *J* = 17.0, 1.6 Hz, H^{11a}), 5.58 (1H, dd, *J* = 9.8, 1.7 Hz, H^{11b}), 4.50 (2H, d, *J* = 6.8 Hz, H^9), 3.60 (6H, s, H^8);^{13}C NMR (151 MHz, MeOD-d_4) δ 150.8 (C^5), 150.5 (C^3), 139.8 (C^7), 129.2 (C^{11}), 126.5 (C^{10}), 116.0 (C^1), 109.2 (C^2), 104.4 (C^4), 103.4 (C^6), 72.8 (C^9), 54.8 (C^8); LRMS (ESI-TOF) *m/z*: $[M]^+$ 206.118 (51), $[M\text{-allyl}]^+$ 165.078 (51), 142.159 (100); HRMS (ESI-TOF) *m/z*: $[M]^+$ Calculated for $C_{12}H_{16}NO_2^+$: 206.1181, found 187.1177 (-0.4 mDa, -1.9 ppm)**;** (max/cm^{-1}): 3011w, 2921w, 1497s, 1252s, 1124w, 1032s, 896s, 838s, 663m; mp: 113-117 °C.

***N*-allyl-*N,N*-dimethyl-4-(trifluoromethyl)anilinium bromide 164**

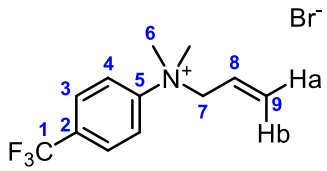

164

Following the method outlined in **6.3** using neat *N,N*-dimethyl-4-(trifluoromethyl)aniline **144** (1.11 g, 5.86 mmol) and allyl bromide (0.55 mL, 6.45 mmol), pure bromide ammonium salt was isolated, after leaving the reaction mixture to stir at 50 °C for 7 days, as an off-white solid without further purification (1.13 g, 3.65 mmol, 62% yield). ^{1}H NMR (600 MHz, MeOD-d$_4$) δ 8.20 – 8.14 (2H, m, H^4), 8.17 (2H, d, *J* = 8.9 Hz, H^3), 5.72 (1H, ddt, *J* = 15.5, 9.9, 7.0 Hz, H^8), 5.63 (1H, d, *J* = 15.6 Hz, H^{9a}), 5.59 (1H, d, *J* = 11.7 Hz, H^{9b}), 4.68 – 4.62 (2H, m, H^7), 3.74 (6H, d, J = 2.9 Hz, H^6); ^{13}C NMR (151 MHz, MeOD-d$_4$) δ 148.9 (C^5), 133.5 (1C, q, *J* = 33.3 Hz, C^2), 130.0 (C^9), 128.8 (1C, q, *J* = 3.8 Hz, C^3), 126.1 (C^8), 124.7 (1C, q, *J* = 274 Hz, C^1), 123.8 (C^4), 72.9 (C^7), 54.6 (C^6); ^{19}F NMR (376 MHz, MeOD-d$_4$) -64.5 (3F, s); LRMS (ESI-TOF) *m/z*: [M]$^+$ 230.295 (100), [M-allyl]$^+$ 189.294 (16); HRMS (ESI-TOF) *m/z*: [M]$^+$ Calculated for $C_{12}H_{15}NF_3^+$: 230.1157, found 230.1151 (-0.6 mDa, -2.6 ppm); IR (max/cm^{-1}): 3061w, 3012m, 1618w, 1429m, 1333s, 1185s, 1128s, 1071s, 899s, 866s, 656m, 614m; mp: 129-130 °C.

***N*-allyl-*N,N*-dimethyl-4-fluoroanilinium bromide 165**

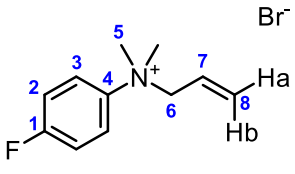

165

Following the method outlined in **6.3** using neat *N,N*-dimethyl-4-fluoroaniline **145** (3.38 g, 24.3 mmol) and allyl bromide (2.3 mL, 26.7 mmol), pure bromide ammonium salt was isolated, after leaving the reaction mixture to stir at 50 °C for 18 hours, as a white powder without further purification (6.13 g, 23.5 mmol, 97% yield). ^{1}H NMR (600 MHz, MeOD-d$_4$) δ 8.03 – 7.91 (2H, m, H^3), 7.43 – 7.38 (2H, m, H^2), 5.70 (1H, ddt, *J* = 17.0, 9.8, 7.1 Hz, H^7), 5.62 (1H, d, *J* = 16.9 Hz, H^{8a}), 5.58 (1H, dd, *J* = 9.8, 1.7 Hz, H^{8b}), 4.58 (2H, d, *J* = 7.1 Hz, H^6), 3.67 (6H, s, H^5); ^{13}C NMR (151 MHz, MeOD-d$_4$) δ 164.2 (1C, d, *J* = 250 Hz, C^1), 142.0 (C^4), 129.6 (C^8) 126.3 (C^7), 125.0 (1C, d, *J* = 9.3 Hz, C^3) 118.2 (1C, d, *J* = 23.4 Hz, C^2), 72.9 (C^6), 54.8 (C^5); ^{19}F NMR (376 MHz, MeOD-d$_4$) δ -112.1 (1F, s); LRMS (ESI-TOF) *m/z*: [M]$^+$ 180.262 (100); [M-allyl]$^+$ 139.245 (100); HRMS (ESI-TOF) *m/z*: [M]$^+$ Calculated for $C_{11}H_{15}NF^+$: 180.1189, found 180.1181 (-0.8 mDa, -4.4 ppm); IR (max/cm^{-1}): 3005w, 2985w, 2925w, 2836w, 1607w, 1517s, 1418m, 1239s, 1179s, 1121m, 1026m, 955s, 845s, 637m, 550s; mp: 110-112 °C.

***N*-allyl-*N,N*-dimethyl-4-chloroanilinium bromide 166**

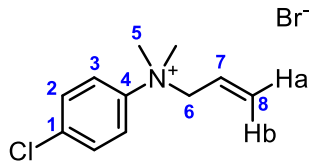

166

Following the method outlined in **6.3** using neat 4-chloro-*N,N*-dimethylaniline **146** (2.00 g, 12.8 mmol) and allyl bromide (1.20 mL, 14.1 mmol), pure bromide ammonium salt was isolated, after leaving the reaction mixture to stir at 50 °C for 18 hours, as a white solid without further purification (3.08 g, 11.2 mmol, 87% yield). ^{1}H NMR (600 MHz, $CDCl_3$) δ 8.03 (2H, dt, *J* = 9.5, 2.2 Hz, H^3), 7.56 (2H, dt, *J* = 9.5, 2.3 Hz, H^2), 5.78 (1H, d, *J* = 16.3 Hz, H^{8a}), 5.51 (1H, dd, *J* = 10.2, 1.3 Hz, H^{8b}), 5.44 (1H, ddt, *J* = 16.2, 10.2, 7.3 Hz, H^7), 5.25 (2H, d, *J* = 7.3 Hz, H^6) 3.98 (6H, s, H^5); ^{13}C NMR (151 MHz, $CDCl_3$) δ 143.0 (C^4), 136.9 (C^1), 130.6 (C^2), 130.1 (C^8), 124.7 (C^7), 123.0 (C^3), 71.0 (C^6), 54.4 (C^5); LRMS (ESI-TOF) *m/z*: [(^{35}Cl)M]$^+$ 196.262 (100), [(^{37}Cl)M]$^+$ 198.239 (30), [(^{35}Cl)M-allyl]$^+$ 155.177 (22), [(^{37}Cl)M-allyl]$^+$ 157.192 (7); HRMS (ESI-TOF) *m/z*: [M]$^+$ Calculated for $C_{11}H_{15}N^{35}Cl^+$: 196.0893, found 196.0894 (0.1 mDa, 0.5 ppm); IR (max/cm^{-1}): 3016w, 2967w, 1490m, 1415m, 1125m, 1098m, 948s, 824s, 659m, 543s; mp: 128-130 °C [EtOH]; XRD: sample crystallised in CH_2Cl_2/hexane yielding colourless platelets. Crystal data for $C_{11}H_{15}BrClN$ (m = 276.60 g/mol): orthorhombic, Pbca (no. 61).

***N*-allyl-*N,N*-dimethyl-4-bromoanilinium bromide 167**

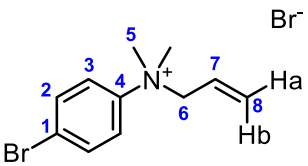

167

Following the method outlined in **6.3** using *N,N*-dimethyl-4-bromoaniline **147** dissolved in acetonitrile (3.00 g, 15.0 mmol, 2 M) and allyl bromide (1.40 mL, 16.5 mmol), pure bromide ammonium salt was isolated, after leaving the reaction mixture to stir at 50 °C for 18 hours, as an off-white solid without further purification (4.29 g, 13.6 mmol, 89% yield). ^{1}H NMR (600 MHz, MeOD-d_4) δ 7.86 – 7.79 (4H, m, H^{2-3}), 5.70 (1H, ddt, *J* = 14.9, 9.7, 7.0 Hz, H^7), 5.61 (1H, dd, *J* = 14.3, 1.3 Hz, H^{8a}), 5.70 (1H, dd, *J* = 9.8, 1.3 Hz, H^{8b}), 4.55 (2H, d, *J* = 7.1 Hz, H^6), 3.65 (6H, s, H^5);^{13}C NMR (151 MHz, MeOD-d_4) δ 143.8 (C^4), 134.6 (C^2), 129.7 (C^8), 126.2 (C^7), 125.6 (C^1), 124.4 (C^3), 72.8 (C^6), 54.5 (C^5); LRMS (ESI-TOF) *m/z*: [^{79}BrM]$^+$ 240.273 m/z (95); [^{81}BrM]$^+$ 242.249 (100); HRMS (ESI-TOF) *m/z*: [M]$^+$ Calculated for $C_{11}H_{15}N^{79}Br^+$: 240.0388, found 240.0400 (1.2 mDa, 5.0 ppm); IR (max/cm^{-1}): 3023w, 2974w, 1489m, 1421m, 1128m, 1013s, 948s, 812s, 709m, 545s; mp: 148-150 °C;[177] XRD: sample crystallised in EtOH/Et_2O yielding colourless crystals. Crystal data for $C_{11}H_{15}Br_2N$ (m = 321.06 g/mol): orthorhombic, Pbca (no. 61).

***N*-allyl-*N,N*-dimethyl-4-iodoanilinium bromide 168**

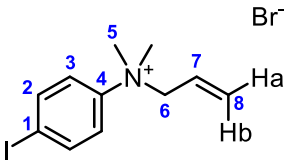

168

Following the method outlined in **6.3** using 4-iodo-*N,N*-dimethylaniline **148** dissolved in acetonitrile (1.03 g, 4.17 mmol, 0.69 M) and allyl bromide (0.38 mL, 4.59 mmol), crude bromide ammonium salt was isolated, after leaving the reaction mixture to stir at 50 °C for 18 hours, as a yellow solid. Further crystallisation in EtOH yielded the desired product as orange needles (1.29 g, 3.52 mmol, 84% yield). ^{1}H NMR (600 MHz, MeOD-d_4) δ 8.01 (2H, dt, *J* = 9.3, 2.2 Hz, H^{2}), 7.67 (2H, dt, *J* = 9.3, 2.3 Hz, H^{3}), 5.69 (1H, ddt, *J* = 16.8, 9.8, 7.0 Hz, H^{7}), 5.60 (1H, d, *J* = 16.8 Hz, H^{8a}), 5.58 (1H, dd, *J* = 9.7, 1.7 Hz, H^{8b}), 4.54 (2H, d, *J* = 6.9 Hz, H^{6}), 3.63 (6H, s, H^{5}); ^{13}C NMR (151 MHz, MeOD-d_4) δ 145.9 (C^{4}), 140.8 (C^{2}), 129.7 (C^{8}), 126.2 (C^{7}), 124.2 (C^{3}), 97.3 (C^{1}), 72.8 (C^{6}), 54.3 (C^{5}); LRMS (ESI-TOF) *m/z*: $[M]^+$ 288.236 (100); $[M\text{-}I]^+$ 161.334 (31); HRMS (ESI-TOF) *m/z*: $[M]^+$ Calculated for $C_{11}H_{15}NI^+$: 288.0249, found 288.0258 (0.9 mDa, 3.1 ppm); IR (max/cm^{-1}): 3011w, 2967w, 1482m, 1415m, 1313w, 1233w, 1122s, 1006s, 952s, 816s, 708m, 548s; mp: 144-146 °C, [EtOH] (decomposed); XRD: sample crystallised in EtOH to give colourless prism-shaped crystals. Crystal data for $C_{11}H_{15}BrIN$ (m = 368.05 g/mol): orthorhombic, Pbca (no. 61).

***N*-allyl-*N,N*-dimethyl-4-acetanilideanilinium bromide 169**

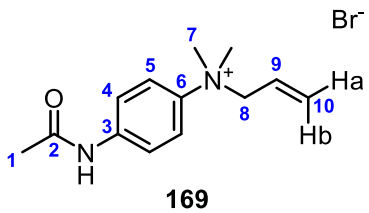

169

Following the method outlined in **6.3** using *N*-(4-(dimethylamino)phenyl)acetamide **151** suspended in acetonitrile (1.22 g, 6.84 mmol, 2.00 M) and allyl bromide (0.64 mL, 7.52 mmol), pure bromide ammonium salt was isolated, after leaving the reaction mixture to stir at 50 °C for 7 days, as a light brown powder without further purification (2.01 g, 6.71 mmol, 98% yield). ^{1}H NMR (600 MHz, MeOD-d_4) δ 7.85 (2H, d, *J* = 9.4 Hz, H^{4}), 7.80 (2H, d, *J* = 9.5 Hz, H^{5}), 5.67 (1H, ddt, *J* = 16.4, 10.7, 7.0 Hz, H^{9}), 5.60 (1H, d, *J* = 16.6 Hz, H^{10a}), 5.57 (1H, d, *J* = 10.3 Hz, H^{10b}), 4.53 (2H, d, *J* = 6.9 Hz, H^{8}), 3.62 (6H, s, H^{7}), 2.16 (3H, s, H^{1}); ^{13}C NMR (151 MHz, MeOD-d_4) δ 172.0 (C^{2}), 141.9 (C^{3}), 140.8 (C^{6}), 129.3 (C^{10}), 126.5 (C^{9}), 122.8 (C^{5}), 121.7 (C^{4}), 72.7 (C^{8}), 54.5 (C^{7}), 24.0 (C^{1}); LRMS (ESI-TOF) *m/z*: $[M]^+$ 219.149 (71); $[M\text{-allyl}]^+$ 178.111 (100); HRMS (ESI-TOF) *m/z*: $[M]^+$ Calculated for $C_{13}H_{19}N_2O^+$: 219.1497, found 219.1489 (-0.8 mDa, -3.8 ppm); IR (max/cm^{-1}): 3251w, 3194m, 3061m, 3012m, 1698s, 1546s, 1333s, 1272s, 1009m, 964m, 854s, 732m, 556s; mp: 154-157 °C [EtOH].

***N*-allyl-*N,N*-dimethyl-3-cyanoanilinium bromide 170**

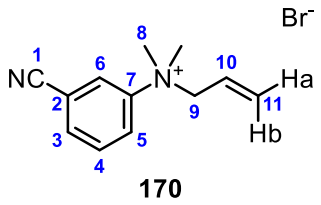

170

Following the method outlined in **6.3** using neat *N,N*-dimethyl-3-cyanoaniline **152** (0.70 g, 4.78 mmol) and allyl bromide (0.45 mL, 5.26 mmol), pure bromide ammonium salt was isolated, after leaving the reaction mixture to stir at 50 °C for 48 hours, as a white crystalline solid without further purification (1.16 g, 4.36 mmol, 91% yield). ^{1}H NMR (600 MHz, MeOD-d_4) δ 8.40 (1H, dd, *J* = 2.8, 1.4 Hz, H^{5}), 8.27 (1H, ddd, *J* = 8.7, 2.9, 0.9 Hz, H^{6}), 8.00 (1H, dt, *J* = 7.7, 1.1 Hz, H^{3}), 7.87 (1H, t, *J* = 8.5 Hz, H^{4}), 5.72 (1H, ddt, *J* = 17.0, 10.2, 7.1 Hz, H^{10}), 5.62 (1H, dd, *J* = 16.8, 1.3 Hz, H^{11a}), 5.62 (1H, dd, *J* = 10.3, 1.5 Hz, H^{11b}), 4.61 (2H, d, *J* = 7.1 Hz, H^{9}), 3.71 (6H, s, H^{8}); ^{13}C NMR (151 MHz, MeOD-d_4) δ 146.6 (C^{7}), 135.5 (C^{3}), 132.9 (C^{4}), 130.1 (C^{11}), 127.3 (C^{6}), 126.7 (C^{5}), 126.0 (C^{10}), 118.1 (C^{1}), 115.8 (C^{2}), 73.1 (C^{9}), 54.5 (C^{8}); LRMS (ESI-TOF) *m/z*: $[M]^+$ 187.293 (100); HRMS (ESI-TOF) *m/z*: $[M]^+$ Calculated for $C_{12}H_{15}N_2^+$: 187.1235, found 187.1232 (-0.3 mDa, -1.6 ppm)**;** IR (max/cm^{-1}): 3025m, 2968m, 2236m, 1582w, 1477m, 1438m, 1205w, 1098m, 955s, 904s, 788s, 690s; mp: 147-151 °C [EtOH]; XRD: sample crystallised in EtOH/Et_2O to give colourless block-shaped crystals. Crystal data for $C_{12}H_{15}BrN_2$ (m = 267.17 g/mol): monoclinic, $P2_1/c$ (no. 14).

***N*-allyl-*N*-benzyl-*N*-methylanilinium bromide 171**

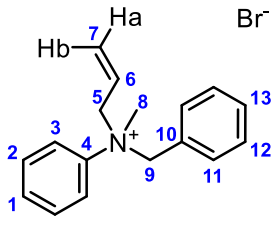

171

Following the method outlined in **6.3** using neat *N*-benzyl-*N*-methylaniline **154** (1.00 g, 5.07 mmol) and allyl bromide (0.47 mL, 5.58 mmol), bromide ammonium salt was isolated, after leaving the reaction mixture to stir at 50 °C for 72 hours as a blue solid *via* crystallisation in EtOH (0.349 g, 1.10 mmol, 22% yield). ^{1}H NMR (600 MHz, MeOD-d_4) δ 7.75 (2H, d, *J* = 7.5, 2.2 Hz, H^{3}), 7.62 – 7.58 (3H, m, H^{1-2}), 7.42 (1H, td, *J* = 7.6, 1.3 Hz, H^{13}), 7.29 (2H, td, *J* = 8.6, 1.7 Hz, H^{12}), 7.07 (2H, dd, *J* = 8.2, 1.7 Hz, H^{11}), 5.71 – 5.61 (2H, m, H^{6-7a}); 5.58 – 5.52 (1H, m, H^{7b}), 5.22 (1H, d, *J* = 12.6 Hz, H^{9}), 5.03 (1H, dd, *J* = 13.5, 3.8 Hz, H^{5}), 5.01 (2H, d, *J* = 12.6 Hz, H^{9}), 4.57 (1H, ddd, *J* = 13.6, 7.2, 2.7 Hz, H^{5}), 3.46 (3H, s, H^{8});[213] ^{13}C NMR (151 MHz, MeOD-d_4) δ 143.0 (C^{4}), 133.9 (C^{11}), 131.9 (C^{13}), 131.8 (C^{1}), 131.3 (C^{2}), 129.9 (C^{12}), 129.1 (C^{7}), 128.7 (C^{10}), 126.3 (C^{6}), 123.7 (C^{3}), 74.0 (C^{9}), 71.0 (C^{5}), 47.1 (C^{8});[213] LRMS (ESI-TOF) *m/z*: $[M]^+$ 238.373 (100), $[M\text{-allyl}]^+$ 197.326 (5); HRMS (ESI-TOF) *m/z*: $[M]^+$ Calculated for $C_{17}H_{20}N^+$: 238.1596, found 238.1602 (0.6 mDa, 2.5 ppm); IR (max/cm^{-1}): 3047m, 2967w, 1487m, 1451m, 1420m, 1349m, 1220m, 1153w, 1033m, 962s, 877s, 752s, 708s, 690s; mp: 143-145 °C [EtOH];[213] XRD: sample crystallised in CH_2Cl_2/hexanes to give colourless block-shaped crystals. Crystal data for $C_{17}H_{20}BrN$ (m = 318.25 g/mol): orthorhombic, $P2_12_12_1$ (no. 19).

***N*-allyl-*N*-methylindolinium bromide 172**

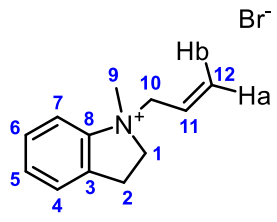

172

Following the method outlined in **6.3** using neat *N*-methylindoline **155** (2.52 g, 18.9 mmol) and allyl bromide (1.76 mL, 20.8 mmol), pure bromide ammonium salt was isolated, after leaving the reaction mixture to stir at 50 °C for 18 hours, as a hygroscopic violet solid without further purification (3.94 g, 15.5 mmol, 82% yield). ^{1}H NMR (600 MHz, $CDCl_3$) δ 8.06 (1H, dd, *J* = 8.0, 1.7 Hz, H^3), 7.49 (1H, td, *J* = 7.7, 1.6 Hz, H^2), 7.47 (1H, td, *J* = 7.6, 1,6 Hz, H^1), 7.40 (1H, d, *J* = 7.2 Hz, H^{12}), 5.85 (1H, d, *J* = 16.7, 1.4 Hz, H^{8b}), 5.65 (1H, dddd, *J* = 16.6, 10.1, 8.2, 6.2 Hz, H^7), 5.55 (1H, dd, *J* = 10.2, 1,4 Hz, H^{8a}), 5.07 (1H, dd, *J* = 12.9, 8.3 Hz, H^6), 4.89 (1H, dd, *J* = 12.8, 6.7 Hz, H^6), 4.70 (1H, ddd, *J* = 12.3, 8.4, 5.6 Hz, H^9), 4.29 (1H, ddd, *J* = 12.2, 8.5, 7.3 Hz, H^9), 3.91 (3H, s, H^5), 3.43 – 3.29 (2H, m, H^{10}); ^{13}C NMR (151 MHz, $CDCl_3$) δ 144.7 (C^4), 133.7 (C^{11}), 131.3 (C^1), 129.9 (C^8), 129.8 (C^2), 126.6 (C^{12}), 125.0 (C^7), 119.1 (C^3), 68.6 (C^6), 64.8 (C^9), 54.6 (C^5), 28.2 (C^{10}); LRMS (ESI-TOF) *m/z*: $[M]^+$ 174.259 (61), $[M\text{-allyl}]^+$ 133.177 (100); HRMS (ESI-TOF) *m/z*: $[M]^+$ Calculated for $C_{12}H_{16}N^+$: 174.1283, found 174.1286 (0.3 mDa, 1.7 ppm); IR (max/cm^{-1}): 3002m, 2886w, 2242w, 1604w, 1477m, 1438m, 1233w, 1095w, 1010m, 962m, 887s, 815s, 685s; mp: 104-107 °C.

***N*-allyl-*N*-methyl-(1H,2H,3H,4H)-tetrahydroquinolinium bromide 104**

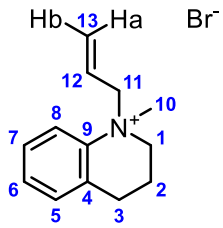

104

Following the method outlined in **6.3** using neat *N*-methyl-(1H,2H,3H,4H)-tetrahydroquinoline **114** (2.04 g, 13.9 mmol) and allyl bromide (1.3 mL, 15.2 mmol), pure bromide ammonium salt was isolated, after leaving the reaction mixture to stir at 50 °C for 18 hours as a pink powder, without further purification (2.03 g, 7.56 mmol, 55% yield). ^{1}H NMR (600 MHz, MeOD-d_4) δ 7.93 – 7.85 (1H, m, H^8), 7.51 – 7.43 (2H, m, $H^{6\text{-}7}$), 7.43 – 7.37 (2H, m, H^5), 5.88 (1H, dddd, *J* = 17.0, 10.1, 7.5, 6.6 Hz, H^{12}), 5.75 (1H, dd, *J* = 17.1, 1.2 Hz, H^{13b}), 5.63 (1H, dd, *J* = 10.2, 1.8 Hz, H^{13a}), 4.70 (1H, dd, *J* = 13.4, 6.7 Hz, H^{11}), 4.48 (1H, dd, *J* = 13.5, 7.6 Hz, H^{11}), 3.98 (1H, ddd, *J* = 12.4, 7.9, 4.2 Hz, H^1), 3.81 (1H, ddd, *J* = 12.8, 6.7, 3.9 Hz, H^1), 3.61 (3H, s, H^{10}), 3.03 (2H, t, *J* = 6.6 Hz, H^3), 2.37 – 2.26 (2H, m, H^2); ^{13}C NMR (151 MHz, MeOD-d_4) δ 142.5 (C^9), 132.9 (C^4), 132.8 (C^5), 131.2 (C^7), 129.55 (C^6), 129.47 (C^{13}), 126.6 (C^{12}), 123.0 (C^8), 71.2 (C^{11}), 61.9 (C^1), 56.0 (C^{10}), 26.7 (C^3), 18.3 (C^2); LRMS (ESI-TOF) *m/z*: $[M]^+$ 188.331 (100), $[M\text{-allyl}]^+$ 147.284 (40); HRMS (ESI-TOF) *m/z*: $[M]^+$ Calculated for $C_{13}H_{18}N^+$: 188,1439, found 188.1433 (-0.6 mDa, -3.2 ppm); IR (max/cm^{-1}): 2976w, 2131w, 1632w, 1460m, 1301w, 1107w, 992m, 898s, 773s, 657s, 593s; mp: 122-123 °C.[165]

6.4 Hexafluorophosphate counter-ion exchange

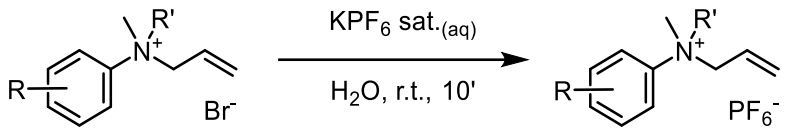

The selected ammonium bromide salt was dissolved in a minimum amount of deionized water. Saturated KPF_6 solution was added (~10 mL) to the aqueous bromide salt, causing a precipitate to form. After leaving the reaction mixture to vigorously stir at room temperature for 10 minutes, the aqueous reaction mixture was transferred to a separatory funnel and was extracted with CH_2Cl_2 (3 x 25 mL). The combined organic layers were dried with $MgSO_4$, filtered and reduced under pressure, yielding the desired hexafluorophosphate ammonium salt.

N-allyl-*N,N*-dimethylanilinium hexafluorophosphate 130

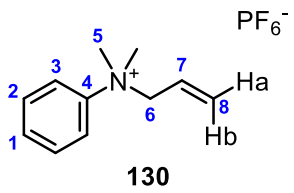

130

Following the method outlined in **6.4** using *N*-allyl-*N,N*-dimethylanilinium bromide **89** (4.93 g, 20.4 mmol), pure title compound was obtained as a pink powder without further purification (4.42 g, 14.4 mmol, 71% yield). ^{1}H NMR (600 MHz, DMSO-d_6) δ 7.89 (2H, dt, *J* = 8.3, 2.1 Hz, H^3), 7.64 (2H, tt, *J* = 8.7, 1.9 Hz, H^2), 7.58 (1H, t, *J* = 7.3 Hz, H^1), 5.61 (1H, ddt, *J* = 18.4, 9.2, 7.2 Hz, H^7), 5.47 (1H, d, *J* = 16.2 Hz, H^{8a}), 5.46 (1H, d, *J* = 9.2 Hz, H^{8b}), 4.51 (2H, d, *J* = 7.2 Hz, H^6), 3.56 (6H, s, H^5); ^{13}C NMR (151 MHz, DMSO-d_6) δ 144.7 (C^4), 130.1 (C^1), 130.1 (C^2), 127.9 (C^8), 125.8 (C^7), 121.2 (C^3), 70.4 (C^6), 53.2 (C^5); ^{31}P NMR (243 MHz, DMSO-d_6) δ -144.2 (1P, sept, *J* = 715 Hz); ^{19}F NMR (376 MHz, DMSO-d_6) δ -65.0 (6F, d, *J* = 715 Hz); LRMS (ESI-TOF) *m/z*: $[M]^+$ 162.250 (73); $[M\text{-allyl}]^+$ 121.129 (100); HRMS (ESI-TOF) *m/z*: $[M]^+$ Calculated for $C_{11}H_{16}N^+$: 162.1283, found 162.1290 (0.7 mDa, 4.3 ppm); IR (max/cm^{-1}): 3140w, 3056w, 1598w, 1487m, 1464m, 1423m, 1122w, 1006w, 967m, 820s, 775s, 695s, 553s; mp: 114-116 °C [MeOH]; XRD: sample crystallised in in EtOH to give colourless crystals. Crystal data for $C_{11}H_{16}F_6NP$ (m = 307.22 g/mol): orthorhombic, Pbca (no. 61).

N-allyl-*N,N*-dimethyl-3-methylanilinium hexafluorophosphate 178

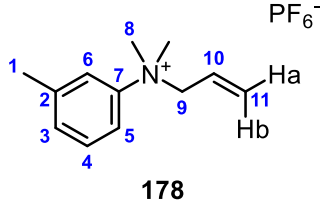

178

Following the method outlined in **6.4** using *N*-allyl-*N,N*-dimethyl-4-fluoroanilinium bromide **156** (0.60 g, 2.32 mmol), pure title compound was obtained *via* crystallisation in EtOH as a pink solid (0.600 g, 1.85 mmol, 80% yield). ^{1}H NMR (600 MHz, DMSO-d_6) δ 7.74 (1H, s, H^6), 7.67 (1H, dd, *J* = 8.4, 2.8 Hz, H^5), 7.51 (1H, t, *J* =

8.0 Hz, H^4), 7.39 (1H, d, *J* = 7.5 Hz, H^3), 5.59 (1H, ddt, *J* = 16.8, 9.7, 7.1 Hz, H^{10}), 5.53 – 5.45 (2H, m, $H^{11a,b}$), 4.49 (2H, d, *J* = 7.0 Hz, H^9), 3.53 (6H, s, H^8), 2.41 (3H, s, H^1); ^{13}C NMR (151 MHz, DMSO-d_6) δ 144.7 (C^7), 140.1 (C^2), 130.6 (C^3), 129.8 (C^4), 127.8 (C^{11}), 125.8 (C^{10}), 121.5 (C^6), 118.2 (C^5), 70.3 (C^9), 53.2 (C^8), 21.0 (C^1); ^{31}P NMR (243 MHz, DMSO-d_6) δ -144.2 (1P, sept, *J* = 716 Hz); ^{19}F NMR (376 MHz, DMSO-d_6) δ -70.1 (6F, d, *J* = 715 Hz); LRMS (ESI-TOF) *m/z*: $[M]^+$ 176.309 (100), $[M\text{-allyl}]^+$ 135.224 (22); HRMS (ESI-TOF) *m/z*: $[M]^+$ Calculated for $C_{12}H_{18}N^+$: 176.1439, found 176.1432 (-0.7 mDa, -4.0 ppm); IR (max/cm^{-1}): 3072w, 2935w, 1591w, 1497m, 1474m, 1432m, 1101w, 1010w, 962m, 818s, 787s, 688s, 553s; mp: 73-75 °C [EtOH]; XRD: sample crystallised in EtOH to give colourless crystals. Crystal data for $C_{12}H_{18}F_6NP$ (m = 321.24 g/mol): monoclinic, $P2_1/n$ (no. 14).

N-allyl-*N,N*-dimethyl-3,5-dimethylanilinium hexafluorophosphate 179

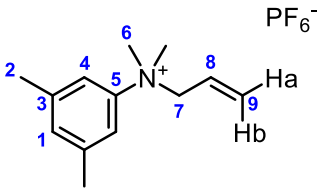

179

Following the method outlined in **6.4** using *N*-allyl-*N,N*-dimethyl-3-methylanilinium bromide **157** (1.24 g, 4.59 mmol), pure title compound was obtained as an off-white solid without further purification (1.47 g, 4.38 mmol, 96% yield). ^{1}H NMR (600 MHz, DMSO-d_6) δ 7.52 (2H, s, H^4), 7.21 (1H, s, H^1), 5.56 (1H, ddt, *J* = 16.6, 9.7, 6.9 Hz, H^8), 5.49 – 5.43 (2H, m, $H^{9a,b}$), 4.44 (2H, d, *J* = 6.9 Hz, H^7), 3.47 (6H, s, H^6), 2.34 (6H, s, H^2);^{13}C NMR (151 MHz, DMSO-d_6) δ 144.7 (C^5), 139.7 (C^3), 131.2 (C^1), 127.7 (C^9), 125.9 (C^8), 118.6 (C^4), 70.2 (C^7), 53.2 (C^6), 21.0 (C^2); ^{31}P NMR (243 MHz, DMSO-d_6) δ -144.2 (1P, sept, *J* = 715 Hz); ^{19}F NMR (376 MHz, DMSO-d_6) δ -70.1 (6F, d, *J* = 713 Hz); LRMS (ESI-TOF) *m/z*: $[M]^+$ 190.343 (100); $[M\text{-allyl}]^+$ 149.322 (45); HRMS (ESI-TOF) *m/z*: $[M]^+$ Calculated for $C_{13}H_{20}N^+$: 190.1596, found 190.1587 (-0.9 mDa, -4.7 ppm); IR (max/cm^{-1}): 2974w, 2932w, 1630m, 1485m, 1451m, 1418w, 995m, 964s, 823s, 693s, 556s; mp: 107-109 °C; XRD: sample crystallised in MeOH yielding colourless, block-shaped crystals. Crystal data for $C_{11}H_{15}F_6INP$ (m = 433.11 g/mol): triclinic, P_{-1} (no. 2).

N-allyl-*N,N*-dimethyl-4-methylanilinium hexafluorophosphate 180

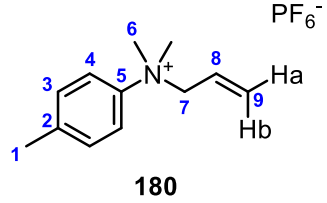

180

Following the method outlined in **6.4** using *N*-allyl-*N,N*-dimethyl-4-methylanilinium bromide **158** (2.05 g, 8.00 mmol), pure title compound was obtained as an orange powder without further purification (1.85 g, 5.75 mmol, 72% yield). ^{1}H NMR (600 MHz, $CDCl_3$) δ 7.50 (2H, dt, *J* = 9.2, 2.1 Hz, H^4), 7.36 (2H, dt, *J* = 9.0, 2.2 Hz, H^3), 5.60 (1H, d, *J* = 16.9 Hz, H^{9a}), 5.50 (1H, d, *J* = 10.2 Hz, H^{9b}), 5.42 (1H, ddt, *J* = 17.0, 10.2, 7.1 Hz, H^8), 4.38 (2H, d, *J* = 6.9 Hz, H^7), 3.52 (6H, s, H^6), 2.37 (3H, s, H^1); ^{13}C NMR (151 MHz, $CDCl_3$) δ 141.70 (C^5), 141.29 (C^2), 131.4 (C^3), 129.7 (C^9), 124.3 (C^8), 120.2 (C^4), 71.7 (C^7), 53.9 (C^6), 20.9 (C^1); ^{31}P NMR (243 MHz, $CDCl_3$) δ -144.2 (1P, sept, *J* = 715 Hz); ^{19}F

NMR (376 MHz, $CDCl_3$) δ -71.2 (6F, d, *J* = 712 Hz); LRMS (ESI-TOF) *m/z*: $[M]^+$ 176.273 (62), $[M\text{-allyl}]^+$ 135.000 (100); HRMS (ESI-TOF) *m/z*: $[M]^+$ Calculated for $C_{12}H_{18}N^+$: 176.1439, found 176.1435 (-0.4 mDa, -2.3 ppm); IR (max/cm^{-1}): 3030w, 2967w, 1615w, 1496m, 1447m, 1429m, 1375w, 1184w, 981m, 873s, 824s, 783s, 755s, 553s; mp: 80-82 °C [MeOH]; XRD: sample crystallised in EtOH to give colourless crystals. Crystal data for $C_{12}H_{18}F_6NP$ (m = 321.24 g/mol): monoclinic, $P2_1/n$ (no. 14).

N-allyl-*N,N*-dimethyl-4-butylanilinium hexafluorophosphate 181

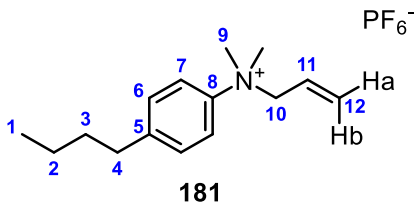

181

Following the method outlined in **6.4** using *N*-allyl-*N,N*-dimethyl-4-butylanilinium bromide **159** (0.70 g, 2.34 mmol), pure title compound was obtained as a glassy yellow solid after thorough drying (0.65 g, 1.78 mmol, 76% yield). ^{1}H NMR (600 MHz, DMSO-d_6) δ 7.78 (2H, dt, *J* = 8.9, 3.2 Hz, H^7), 7.44 (2H, dt, *J* = 8.8, 3.3 Hz, H^6), 5.60 (1H, ddt, *J* = 16.6, 9.5, 7.1 Hz, H^{11}), 5.51 – 5.45 (2H, m, $H^{12a,b}$), 4.50 (2H, d, *J* = 7.0 Hz, H^{10}), 3.44 (6H, s, H^9), 2.65 (2H, t, *J* = 7.3 Hz, H^4), 1.56 (2H, quint, *J* = 7.5 Hz, H^3), 1.30 (2H, sex, *J* = 7.4 Hz, H^2), 0.90 (3H, t, *J* = 7.4 Hz, H^1); ^{13}C NMR (151 MHz, DMSO-d_6) δ 144.6 (C^5), 142.5 (C^8), 129.7 (C^6), 127.7 (C^{12}), 125.9 (C^{11}), 121.0 (C^7), 70.3 (C^{10}), 53.2 (C^9), 33.9 (C^4), 32.7 (C^3), 21.7 (C^2), 13.7 (C^1); ^{31}P NMR (243 MHz, DMSO-d_6) δ -144.2 (1P, sept, *J* = 711 Hz); ^{19}F NMR (376 MHz, DMSO-d_6) δ -70.1 (6F, d, *J* = 710 Hz); LRMS (ESI-TOF) *m/z*: 218.382 (100); $[M\text{-allyl}]^+$ 177.362 (43); HRMS (ESI-TOF) *m/z*: $[M]^+$ Calculated for $C_{15}H_{24}N^+$: 218.1909, found 218.1913 (0.4 mDa, 1.8 ppm); IR (max/cm^{-1}): 2958w, 2930w, 2868w, 1509w, 1470w, 1427w, 1121w, 963w, 823s, 557s.

N-allyl-*N,N*-dimethyl-4-*tert*butylanilinium hexafluorophosphate 182

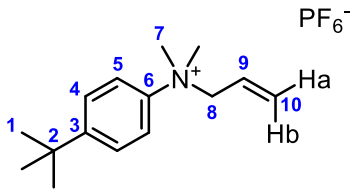

182

Following the method outlined in **6.4** using *N*-allyl-*N,N*-dimethyl-4-*tert*-butylanilinium bromide **160** (0.50 g, 1.68 mmol), pure title compound was obtained *via* crystallisation in EtOH as white needle-shaped crystals (0.46 g, 1.27 mmol, 71% yield).^{1}H NMR (600 MHz, DMSO-d_6) δ 7.79 (2H, d, *J* = 8.9 Hz, H^5), 7.63 (2H, d, *J* = 9.0 Hz, H^4), 5.61 (1H, ddt, *J* = 16.8, 9.6, 6.9 Hz, H^9), 5.54 – 5.47 (2H, m, $H^{10a,b}$), 4.50 (2H, d, *J* = 6.9 Hz, H^8), 3.53 (6H, s, H^7), 1.31 (9H, s, H^1); ^{13}C NMR (151 MHz, DMSO-d_6) δ 152.7 (C^3), 142.4 (C^6), 127.7 (C^{10}), 126.8 (C^4), 125.9 (C^9), 120.8 (C^5), 70.2 (C^8), 53.2 (C^7), 34.5 (C^2), 30.8 (C^1); ^{31}P NMR (243 MHz, DMSO-d_6) δ -144.2 (1P, sept, *J* = 716 Hz); ^{19}F NMR (376 MHz, DMSO-d_6) δ -70.1 (6F, d, *J* = 714 Hz); LRMS (ESI-TOF) *m/z*: $[M]^+$ 218.344 (62), $[M\text{-allyl}]^+$ 177.262 (100); HRMS (ESI-TOF) *m/z*: $[M]^+$ Calculated for $C_{15}H_{24}N^+$: 218.1909, found 218.1912 (0.3 mDa, 1.4 ppm); IR (max/cm^{-1}): 2976w, 2860w, 1584w, 1491m, 1473m, 1420m, 1131w, 989m, 887s, 815s, 553s; mp: 148-150 °C [EtOH]; XRD: sample crystallised in MeOH

yielding colourless, prism-shaped crystals. Crystal data for $C_{15}H_{24}F_6NP$ (m = 363.32 g/mol): monoclinic, $P2_1/c$ (no. 14).

N-allyl-*N,N*-dimethyl-4-phenylanilinium hexafluorophosphate 183

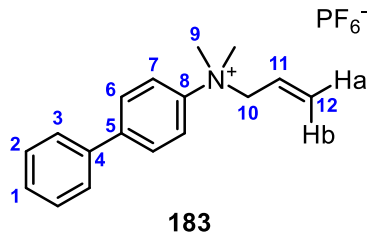

183

Following the method outlined in **6.4** using *N*-allyl-*N,N*-dimethyl-4-phenylanilinium bromide **161** (0.63 g, 1.97 mmol), pure title compound was obtained as a pink, crystalline powder without further purification (0.67 g, 1.86 mmol, 94% yield). ^{1}H NMR (600 MHz, DMSO-d_6) δ 7.98 (2H, dt, *J* = 9.2, 2.5 Hz, H^7), 7.92 (2H, dt, *J* = 9.2, 2.4 Hz, H^6), 7.66 (2H, d, *J* = 7.6 Hz, H^3), 7.51 (2H, tt, *J* = 7.4, 1.8 Hz, H^2), 7.44 (1H, tt, *J* = 7.4, 1.8 Hz, H^1), 5.67 (1H, ddt, *J* = 17.1, 9.9, 7.1 Hz, H^{11}), 5.55 – 5.49 (2H, m, $H^{12a,b}$), 4.56 (2H, d, *J* = 7.1 Hz, H^{10}), 3.60 (6H, s, H^9); ^{13}C NMR (151 MHz, DMSO-d_6) δ 143.9 (C^8), 141.6 (C^4), 137.9 (C^5), 129.1 (C^{12}), 128.4 (C^6), 128.0 (C^2), 127.9 (C^1), 127.0 (C^3), 125.8 (C^{10}), 121.9 (C^7), 70.4 (C^{10}), 53.3 (C^9); ^{31}P NMR (243 MHz, DMSO-d_6) δ -144.2 (1P, sept, *J* = 719 Hz); ^{19}F NMR (376 MHz, DMSO-d_6) δ -70.1 (6F, d, *J* = 711 Hz); LRMS (ESI-TOF) *m/z*: $[M]^+$ 238.259 (100), $[M\text{-allyl}]^+$ 197.212 (69); HRMS (ESI-TOF) *m/z*: $[M]^+$ Calculated for $C_{17}H_{20}N^+$: 238.1596, found 238.1601 (0.5 mDa, 2.1 ppm); IR (max/cm^{-1}): 3072w, 2976w, 1489m, 1466m, 1417m, 1129w, 1015m, 988m, 818s, 772s, 704s, 553s; mp: 122-125 °C [MeOH]; XRD: sample crystallised in EtOH to give colourless crystals. Crystal data for $C_{17}H_{20}F_6NP$ (m = 383.31 g/mol): monoclinic, P21/c (no. 14).

N-allyl-*N,N*-dimethyl-4-methoxyanilinium hexafluorophosphate 184

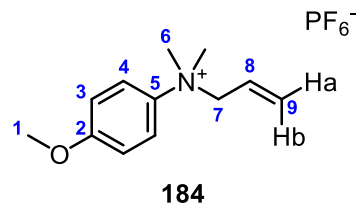

184

Following the method outlined in **6.4** using *N*-allyl-*N,N*-dimethyl-4-methoxylanilinium bromide **91** (0.63 g, 2.31 mmol) of precursor bromide ammonium salt, pure title compound was obtained as a violet hygroscopic solid without further purification (0.70 g, 2.08 mmol, 90% yield). ^{1}H NMR (600 MHz, MeOD-d_4) δ 7.73 (2H, dt, *J* = 9.4, 2.7 Hz, H^4), 7.12 (2H, dt, *J* = 9.4, 2.4 Hz, H^3), 5.64 (1H, ddt, *J* = 16.5, 9.6, 6.8 Hz, H^8), 5.56 (1H, dd, *J* = 14.7, 1.8 Hz, H^{9a}), 5.54 (1H, dd, *J* = 9.5, 1.8 Hz, H^{9b}), 4.44 (2H, d, J = 6.8 Hz, H^7), 3.86 (3H, s, H^1), 3.57 (6H, s, H^6); ^{13}C NMR (151 MHz, MeOD-d_4) δ 162.0 (C^2), 138.5 (C^5), 129.2 (C^9), 126.4 (C^8), 123.4 (C^4), 116.3 (C^3), 72.8 (C^7), 56.3 (C^1), 54.5 (C^6); ^{31}P NMR (243 MHz, MeOD-d_4) -144.5 (1P, sept, *J* = 715 Hz); ^{19}F NMR (376 MHz, MeOD-d_4) δ -74.0 (6F, d, *J* = 716 Hz); LRMS (ESI-TOF) *m/z*: $[M]^+$ 192.196 (100), 151.149 (82); HRMS (ESI-TOF) *m/z*: $[M]^+$ Calculated for $C_{12}H_{18}NO^+$: 192.1388, found 192.1393 (0.5 mDa, 2.6 ppm); IR (max/cm^{-1}): 2984w, 2851w, 1599w, 1516m, 1470m, 1332m, 1262m, 1197m, 988m, 821s, 688m, 553s; mp: 58-61 °C.

***N*-allyl-*N,N*-dimethyl-3,4,5-trimethoxyanilinium hexafluorophosphate 185**

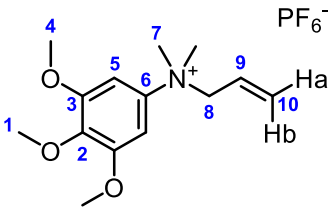

185

Following the method outlined in **6.4** using *N*-allyl-*N,N*-dimethyl-3,4,5-trimethoxyanilinium bromide **162** (1.93 g, 5.81 mmol), pure title compound was obtained as a pink powder without further purification (1.98 g, 5.01 mmol, 86% yield). ^{1}H NMR (600 MHz, DMSO-d_6) δ 7.10 (2H, s, H^5), 5.65 (1H, ddt, *J* = 17.0, 10.0, 7.0 Hz, H^9), 5.53 (1H, d, *J* = 15.1 Hz, H^{10a}), 5.53 (1H, d, *J* = 9.9 Hz, H^{10b}), 4.53 (2H, d, *J* = 7.0 Hz, H^8), 3.88 (6H, s, H^3), 3.70 (3H, s, H^1), 3.55 (6H, s, H^7); ^{13}C NMR (151 MHz, DMSO-d_6) δ 153.1 (C^4), 140.3 (C^6), 138.2 (C^2), 127.5 (C^{10}), 126.0 (C^9), 99.8 (C^5), 70.3 (C^8), 60.2 (C^3), 56.7 (C^1), 53.5 (C^7); ^{31}P NMR (243 MHz, DMSO-d_6) δ -144.2 (1P, sept, *J* = 713 Hz); ^{19}F NMR (376 MHz, DMSO-d_6) δ -70.1 (6F, d, *J* = 711 Hz); LRMS (ESI-TOF) *m/z*: $[M]^+$ 176.309 (100), $[M\text{-allyl}]^+$ 135.224 (22); HRMS (ESI-TOF) *m/z*: $[M]^+$ Calculated for $C_{14}H_{22}NO_3^+$: 252.1600, found 252.1595 (-0.5 mDa, -2.0 ppm); IR (max/cm^{-1}): 2989m, 2891w, 1615m, 1474m, 1265m, 1135m, 1001m, 834s, 561s; mp: 98-100 °C; XRD: sample crystallised in EtOH yielding colourless, block-shaped crystals. Crystal data for $C_{14.4}H_{23.6}F_6NO_{3.4}P$ (m = 410.11 g/mol): triclinic, P_{-1} (no. 2).

***N*-allyl-*N,N*-dimethyl-(3,4-methylenedioxy)anilinium hexafluorophosphate 186**

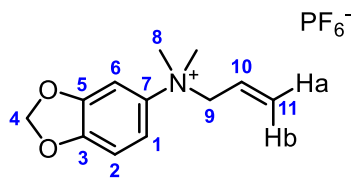

186

Following the method outlined in **6.4** using *N*-allyl-*N,N*-dimethyl-3,4-(methylenedioxy)anilinium bromide **163** (0.98 g, 3.43 mmol), pure title compound was obtained as an orange crystalline powder *via* crystallisation in MeOH (0.84 g, 2.39 mmol, 70% yield). ^{1}H NMR (600 MHz, DMSO-d_6) δ 7.63 (1H, d, *J* = 2.7 Hz, H^a), 7.30 (1H, dd, *J* = 8.7, 2.8 Hz, H^b), 7.09 (1H, d, *J* = 8.7 Hz, H^c), 6.18 (2H, s, H^4), 5.62 (1H, ddt, *J* = 15.5, 11.1, 7.1 Hz, H^{10}), 5.51 – 5.46 (2H, m, H^{11a-b}), 4.45 (2H, d, *J* = 7.0 Hz, H^9), 3.50 (6H, s, H^8); ^{13}C NMR (151 MHz, DMSO-d_6) δ 148.5 (C^q), 148.1 (C^q), 138.5 (C^7), 127.7 (C^{11}), 125.8 (C^{10}), 115.0 (C^b), 107.9 (C^c), 102.80 (C^4), 102.77 (C^a), 70.5 (C^9), 53.7 (C^8); ^{31}P NMR (243 MHz, DMSO-d_6) δ -144.2 (1P, sept, *J* = 713 Hz); ^{19}F NMR (376 MHz, DMSO-d_6) δ; -70.1 (6F, d, *J* = 711 Hz); LRMS (ESI-TOF) *m/z*: $[M]^+$ 206.300 (100); $[M\text{-allyl}]^+$ 165.281 (95); HRMS (ESI-TOF) *m/z*: $[M]^+$ Calculated for $C_{12}H_{16}NO_2^{+:}$ 206.1181, found 206.1183 (0.2 mDa, 1.0 ppm); IR (max/cm^{-1}): 3088m, 2935w, 1516m, 1489m, 1257m, 1043m, 914m, 827s, 561s; mp: 119-120 °C [EtOH]; XRD: sample crystallised in MeOH yielding brown, irregular-shaped crystals. Crystal data for $C_{12}H_{16}F_6NO_2P$ (m = 351.23 g/mol): triclinic, P_{-1} (no. 2).

***N*-allyl-*N,N*-dimethyl-4-(trifluoromethyl)anilinium hexafluorophosphate 187**

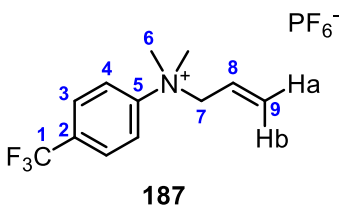

187

Following the method outlined in **6.4** using *N*-allyl-*N,N*-dimethyl-4-(trifluoromethyl)anilinium bromide **164** (1.19 g, 3.60 mmol), pure title compound was obtained *via* crystallisation in EtOH as a white crystalline powder (0.91 g, 2.41 mmol, 67% yield). ^{1}H NMR (600 MHz, CD_3CN) δ 7.96 (2H, d, *J* = 9.1 Hz, H^3), 7.90 (2H, d, *J* = 9.2 Hz, H^4), 5.67 – 5.60 (1H, m, H^8), 5.59 – 5.53 (2H, m, $H^{9a,b}$), 4.37 (2H, d, *J* = 6.8 Hz, H^7), 3.53 (6H, s, H^6); ^{13}C NMR (151 MHz, CD_3CN) δ 148.2 (C^5), 132.9 (1C, q, *J* = 33.3 Hz, C^2), 130.3 (C^8), 128.7 (1C, q, *J* = 3.8 Hz, C^3), 125.5 (C^7), 124.4 (1C, q, *J* = 273 Hz, C^1), 123.4 (C^4), 72.8 (C^7), 54.6 (C^6); ^{31}P NMR (243 MHz, CD_3CN) δ -144.6 (1P, sept, *J* = 709 Hz); ^{19}F NMR (376 MHz, CD_3CN) δ -63.5 (3F, s, CF_3), -72.9 (6F, d, *J* = 706 Hz, PF_6^-); LRMS (ESI-TOF) *m/z*: $[M]^+$ 230.268 (100), $[M\text{-allyl}]^+$ 189.269 (10); HRMS (ESI-TOF) *m/z*: $[M]^+$ Calculated for $C_{12}H_{15}NF_3^+$: 230.1157, found 230.1152 (-0.5 mDa, -2.2 ppm); IR (max/cm^{-1}): 2929w, 2854w, 1622w, 1425w, 1333m, 1190m, 1139m, 1073m, 971m, 822s, 559s; mp: 91-93 °C; XRD: sample crystallised in MeOH to give colourless crystals. Crystal data for $C_{12}H_{15}F_9NP$ (m = 375.22 g/mol): monoclinic, $P2_1/c$ (no. 14).

***N*-allyl-*N,N*-dimethyl-4-fluoroanilinium hexafluorophosphate 188**

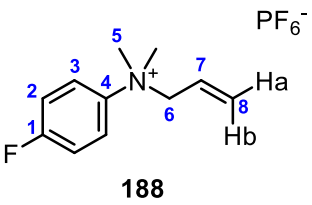

188

Following the method outlined in **6.4** using *N*-allyl-*N,N*-dimethyl-4-fluoroanilinium bromide **165** (1.51 g, 5.81 mmol) pure title compound was obtained *via* crystallisation in EtOH as a white needles (1.16 g, 3.56 mmol, 61% yield). ^{1}H NMR (600 MHz, DMSO-d_6) δ 8.00 – 7.92 (2H, m, H^3), 7.55 – 7.45 (2H, m, H^2), 5.64 (1H, ddt, *J* = 17.1, 10.3, 7.0 Hz, H^7), 5.49 (2H, d, *J* = 9.9 Hz, H^{8b}), 5.47 (2H, d, *J* = 17.3 Hz, H^{8a}), 4.51 (2H, d, *J* = 7.1 Hz, H^6), 3.56 (6H, s, H^5); ^{13}C NMR (151 MHz, DMSO-d_6) δ 162.0 (1C, d, *J* = 249 Hz, C^1), 140.8 (1C, d, *J* = 3.0 Hz, C^4), 128.1 (C^8), 125.7 (C^7), 124.1 (1C, d, *J* = 9.1 Hz, C^3), 116.8 (1C, d, J = 23.3 Hz, C^2), 70.7 (C^6), 53.5 (C^5); ^{31}P NMR (162 MHz, DMSO-d_6) δ -144.2 (1P, sept, *J* = 715 Hz); ^{19}F NMR (376 MHz, DMSO-d_6) δ -70.1 (6F, d, *J* = 707 Hz), -111.3 (1F, s); LRMS (ESI-TOF) *m/z*: $[M]^+$ 180.274 (100), $[M\text{-allyl}]^+$ 139.253 (33); HRMS (ESI-TOF) *m/z*: $[M]^+$ Calculated for $C_{12}H_{15}NF^+$: 180.1189, found 180.1180 (-0.9 mDa, -5.0 ppm); IR (max/cm^{-1}): 2992w, 2893w, 1516m, 1493m, 1257m, 1181m, 956m, 820s, 561s; mp: 110-111 °C [MeOH]; XRD: sample crystallised in MeOH/Et_2O to give colourless crystals. Crystal data for $C_{11}H_{15}F_7NP$ (m = 325.21 g/mol): monoclinic, $P2_1/n$ (no. 14).

***N*-allyl-*N,N*-dimethyl-4-chloroanilinium hexafluorophosphate 189**

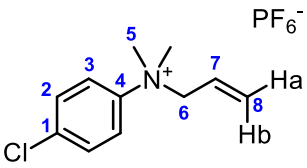

189

Following the method outlined in **6.4** using *N*-allyl-*N,N*-dimethyl-4-chloroanilinium bromide **166** (1.52 g, 5.48 mmol), pure title compound was obtained *via* crystallisation in EtOH (5.00 mL) as white needle-shaped crystals (1.57 g, 4.60 mmol, 84% yield). ^{1}H NMR (600 MHz, DMSO-d$_6$) δ 7.92 (2H, dt, *J* = 9.3, 2.4 Hz, H^{3}), 7.73 (2H, dt, *J* = 9.2, 2.2 Hz, H^{2}), 5.64 (1H, ddt, *J* = 16.5, 9.9, 7.0 Hz, H^{7}), 5.49 (1H, dd, *J* = 10.1, 1.5 Hz, H^{8b}), 5.47 (1H, dd, *J* = 16.8, 1.7 Hz, H^{8a}), 4.51 (2H, d, *J* = 7.1 Hz, H^{6}), 3.56 (6H, s, H^{5}); ^{13}C NMR (151 MHz, DMSO-d$_6$) δ 143.4 (C^{4}), 134.8 (C^{1}), 129.9 (C^{2}), 128.1 (C^{8}), 125.6 (C^{7}), 123.5 (C^{3}), 70.6 (C^{6}), 53.3 (C^{5}); ^{31}P NMR (243 MHz, DMSO-d$_6$) δ -144.2 (1P, sept, *J* = 715 Hz); ^{19}F NMR (376 MHz, DMSO-d$_6$) δ -70.1 (6F, d, *J* = 716 Hz); LRMS (ESI-TOF) *m/z*: [^{35}Cl-M]$^{+}$ 196.230 (100); [^{37}Cl-M]$^{+}$ 198.238 (61); HRMS (ESI-TOF) *m/z*: [M]$^{+}$ Calculated for C$_{11}$H$_{15}$N^{35}Cl^{+}: 196.0893, found 196.0890 (-0.3 mDa, -1.5 ppm); IR (max/cm^{-1}): 3136w, 2927w, 1489m, 1421w, 1189w, 1125w, 1098w, 988m, 825s, 821s, 753m, 553s; mp: 88-90 °C [MeOH]; XRD: sample crystallised in EtOH to give colourless, prism-shaped crystals. Crystal data for C$_{11}$H$_{15}$ClF$_6$NP (m = 341.66 g/mol): monoclinic, P2$_1$/n (no. 14).

***N*-allyl-*N,N*-dimethyl-4-bromoanilinium hexafluorophosphate 190**

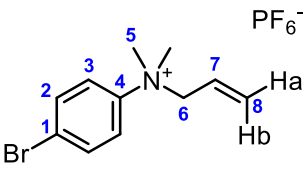

190

Following the method outlined in **6.4** using *N*-allyl-*N,N*-dimethyl-4-bromoanilinium bromide **167** (1.28 g, 4.00 mmol) pure title compound was obtained *via* crystallisation in EtOH as a white crystalline powder (1.09 g, 2.82 mmol, 62% yield). ^{1}H NMR (600 MHz, DMSO-d$_6$) δ 7.89 – 7.83 (4H, m, H^{2,3}), 5.65 (1H, ddt, *J* = 17.2, 10.2, 7.1 Hz, H^{7}), 5.49 (1H, d, *J* = 10.0 Hz, H^{8b}), 5.47 (1H, d, *J* = 17.4 Hz, H^{8a}), 4.50 (2H, d, *J* = 7.1 Hz, H^{6}), 3.55 (6H, s, H^{5}); ^{13}C NMR (151 MHz, DMSO-d$_6$) δ 143.9 (C^{4}), 132.9 (C^{2}), 128.2 (C^{8}), 125.6 (C^{7}), 123.7 (C^{3}), 123.4 (C^{1}), 70.5 (C^{6}), 53.3 (C^{5}); ^{31}P NMR (243 MHz, DMSO-d$_6$) δ -144.2 (1P, sept, *J* = 710 Hz); ^{19}F NMR (376 MHz, DMSO-d$_6$) δ -70.1 (6F, d, *J* = 714 Hz); LRMS (ESI-TOF) *m/z*: [^{79}Br-M]$^{+}$ 240.219 (100), [^{81}Br-M]$^{+}$ 242.227 (99); HRMS (ESI-TOF) *m/z*: [M]$^{+}$ Calculated for C$_{11}$H$_{15}$N^{79}Br^{+}: 240.0388, found 240.0379 (-0.9 mDa, -3.7 ppm); IR (max/cm^{-1}): 3145w, 2989w, 1489m, 1417m, 1125w, 1013m, 964m, 838s, 820s, 667m, 561s; mp: 114-116 °C.

_N_-allyl-_N,N_-dimethy-4-iodoanilinium hexafluorophosphate 191

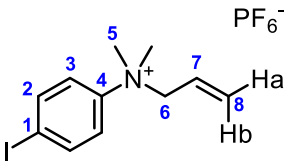

191

Following the method outlined in **6.4** using _N_-allyl-_N,N_-dimethyl-4-iodoanilinium bromide **168** (0.30 g, 0.82 mmol) pure title compound was obtained as a green crystalline solid without further purification (0.33 g, 0.76 mmol, 92% yield). ^{1}H NMR (600 MHz, DMSO-d_6) δ 8.00 (2H, dt, _J_ = 9.3, 2.3 Hz, H^{2}), 7.68 (2H, dt, _J_ = 9.2, 2.2 Hz, H^{3}), 5.64 (1H, ddt, _J_ = 16.1, 9.3, 7.1 Hz, H^{7}), 5.49 (1H, dd, _J_ = 9.2, 1.5 Hz, H^{8b}), 5.46 (1H, dq, _J_ = 15.8, 1.5 Hz, H^{8a}), 4.49 (2H, d, _J_ = 7.1 Hz, H^{6}), 3.53 (6H, s, H^{5}); ^{13}C NMR (151 MHz, DMSO-d_6) δ 144.6 (C^{4}), 138.7 (C^{2}), 128.1 (C^{8}), 125.7 (C^{7}), 123.5 (C^{3}), 97.0 (C^{1}), 70.4 (C^{6}), 53.2 (C^{5}); ^{31}P NMR (243 MHz, DMSO-d_6) δ -144.2 (1P, sept, _J_ = 710 Hz); ^{19}F NMR (376 MHz, DMSO-d_6) δ -70.1 (6F, d, _J_ = 714 Hz); LRMS (ESI-TOF) _m/z_: $[M]^{+}$ 288.048 (100); HRMS (ESI-TOF) _m/z_: $[M]^{+}$ Calculated for $C_{11}H_{15}NI^{+}$: 288.0249, found 288.0240 (-0.9 mDa, -3.1 ppm); IR (max/cm^{-1}): 3004w, 2967m, 1489m, 1417m, 1125w, 1010m, 954m, 821s, 741m, 553s; mp: 135-137 °C [MeOH]; XRD: sample crystallised in CH_2Cl_2/MeOH yielding colourless, block-shaped crystals. Crystal data for $C_{11}H_{15}F_6INP$ (m = 433.11 g/mol): triclinic, P_{-1} (no. 2).

_N_-allyl-_N,N_-dimethyl-4-acetanilideanilinium hexafluorophosphate 192

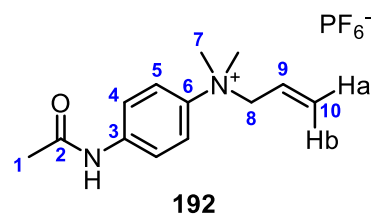

192

Following the method outlined in **6.4** using _N_-allyl-_N,N_-dimethyl-4-acetanilideanilinium bromide **169** (2.04 g, 8.02 mmol), pure title compound was obtained as a brown foamy solid without further purification (1.59 g, 4.37 mmol, 54% yield). ^{1}H NMR (600 MHz, CD_3CN) δ 8.61 (1H, bs, NH), 7.76 (2H, dt, _J_ = 9.3, 3.6 Hz, H^{4}), 7.59 (2H, dt, _J_ = 9.4, 3.6 Hz, H^{5}), 5.66 – 5.57 (1H, m, H^{9}), 5.56 – 5.50 (2H, m, $H^{10a,b}$), 4.29 (2H, d, _J_ = 6.8 Hz, H^{8}), 3.45 (6H, s, H^{7}), 2.09 (3H, s, H^{1}); ^{13}C NMR (151 MHz, CD_3CN) δ 170.2 (C^{2}), 141.8 (C^{3}), 139.9 (C^{6}), 129.6 (C^{10}), 126.0 (C^{9}), 122.6 (C^{5}), 120.9 (C^{4}), 72.5 (C^{8}), 54.6 (C^{7}), 24.4 (C^{1}); ^{31}P NMR (162 MHz, CD_3CN) δ -144.6 (1P, sept, _J_ = 708 Hz); ^{19}F NMR (376 MHz, CD_3CN) δ -72.8 (6F, d, _J_ = 708 Hz); LRMS (ESI-TOF) _m/z_: $[M]^{+}$ 219.303 (100), $[M\text{-allyl}]^{+}$ 178.269 (42); HRMS (ESI-TOF) _m/z_: $[M]^{+}$ Calculated for $C_{13}H_{19}N_2O^{+}$: 219.1497, found: 219.1494 (-0.3 mDa, -1.4 ppm); IR (max/cm^{-1}): 3408w, 2929w, 2860w, 1680m, 1613m, 1552m, 1418m, 1327m, 1201w, 1009w, 967w, 825s, 559s; mp: 125-126 °C.

N-allyl-*N,N*-dimethyl-3-cyanoanilinium hexafluorophosphate 193

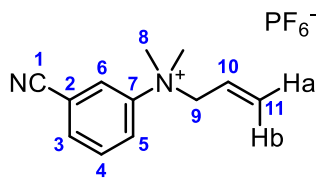

193

Following the method outlined in **6.4** using *N*-allyl-*N,N*-dimethyl-3-cyanoanilinium bromide **170** (0.41 g, 1.61 mmol), pure title compound was isolated *via* vacuum-filtration of the reaction mixture and crystallisation in EtOH as white crystals (0.36 g, 0.93 mmol, 57% yield). ^{1}H NMR (600 MHz, DMSO-d$_6$) δ 8.50 (1H, dd, *J* = 2.7, 1.3 Hz, H^{6}), 8.26 (1H, ddd, *J* = 8.6, 2.7, 1.0 Hz, H^{b}), 8.10 (1H, dt, *J* = 7.8, 1.2 Hz, H^{3}), 7.86 (1H, t, *J* = 8.6, Hz, H^{4}), 5.66 (1H, ddt, *J* = 17.1, 10.1, 7.2 Hz, H^{10}), 5.50 (1H, dd, *J* = 9.9, 1.8 Hz, H^{11b}), 5.48 (1H, dd, *J* = 16.8, 1.7 Hz, H^{11a}), 4.54 (2H, d, *J* = 7.1 Hz, H^{9}), 3.60 (6H, s, H^{8}); ^{13}C NMR (151 MHz, DMSO-d$_6$) δ 145.1 (C^{7}), 134.0 (C^{3}), 131.4 (C^{4}), 128.4 (C^{11}), 126.6 (C^{b}), 125.9 (C^{6}), 125.5 (C^{11}), 117.5 (C^{2}), 113.0 (C^{1}), 70.7 (C^{9}), 53.3 (C^{8}); ^{31}P NMR (243 MHz, DMSO-d$_6$) δ -144.2 (1P, sept, *J* = 719 Hz); ^{19}F NMR (376 MHz, DMSO-d$_6$) δ -70.1 (6F, d, *J* = 711 Hz); LRMS (ESI-TOF) *m/z*: [M]$^{+}$ 187.189 (100), [M-allyl]$^{+}$ 146.170 (28); HRMS (ESI-TOF) *m/z*: [M]$^{+}$ Calculated for $C_{12}H_{15}N_2^{+}$: 187.1235, found 187.1240 (0.5 mDa, 2.7 ppm); IR (max/cm^{-1}): 3132w, 3160w, 2243m, 1594w, 1491m, 1464m, 1166w, 1011m, 962m, 877s, 821s, 685s, 553s; mp: 142-144 °C [EtOH]; XRD: sample crystallised in EtOH to give colourless crystals. Crystal data for $C_{12}H_{15}F_6N_2P$ (m = 332.23 g/mol): monoclinic, P21/n (no. 14).

N-allyl-*N*-benzyl-*N*-methylanilinium hexafluorophosphate 194

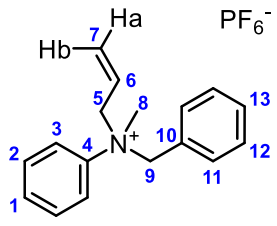

194

Following the method outlined in **6.4** using *N*-allyl-*N*-benzyl-*N*-methylanilinium bromide **171** (1.00 g, 1.57 mmol), pure title compound was isolated *via* crystallisation in EtOH as white crystals (0.57 g, 1.49 mmol, 45% yield). ^{1}H NMR (600 MHz, DMSO-d$_6$) δ 7.80 (2H, d, *J* = 8.7 Hz, H^{3}), 7.65 – 7.53 (3H, m, H^{1,2}), 7.42 (1H, tt, *J* = 7.6, 1.4 Hz, H^{13}), 7.32 (2H, t, *J* = 7.5 Hz, H^{12}), 7.04 (2H, d, *J* = 7.5 Hz, H^{11}), 5.63 (1H, ddt, *J* = 16.8, 10.1, 7.1 Hz, H^{6}), 5.56 (1H, dd, *J* = 17.0, 1.9 Hz, H^{7a}), 5.48 (1H, dd, *J* = 9.9, 1.9 Hz, H^{7b}), 5.14 (1H, d, *J* = 12.8 Hz, H^{9}), 4.98 (1H, d, *J* = 12.8 Hz, H^{9}), 4.94 (1H, dd, *J* = 13.3, 7.0 Hz, H^{5}), 4.48 (1H, dd, *J* = 13.3, 7.1 Hz, H^{5}), 3.38 (3H, s, H^{8}); ^{13}C NMR (151 MHz, DMSO-d$_6$) δ 141.6 (C^{4}), 132.6 (C^{11}), 130.34 (C^{13}), 130.32 (C^{1}), 130.03 (C^{2}), 128.6 (C^{12}), 127.9 (C^{7}), 127.6 (C^{10}), 125.6 (C^{6}), 122.6 (C^{3}), 71.6 (C^{9}), 68.7 (C^{5}), 46.1 (C^{8}); ^{31}P NMR (243 MHz, DMSO-d$_6$) δ -144.2 (1P, sept, *J* = 716 Hz); ^{19}F NMR (376 MHz, DMSO-d$_6$) δ -70.1 (6F, d, *J* = 714 Hz); LRMS (ESI-TOF) *m/z*: [M]$^{+}$ 238.335 (100); HRMS (ESI-TOF) *m/z*: [M]$^{+}$ Calculated for $C_{17}H_{20}N^{+}$: 238.1596, found 238.1607 (1.1 mDa, 4.6 ppm); IR (max/cm^{-1}): 2935w, 2865w, 1598w, 1491m, 1467m, 1420m, 1224w, 957m, 821s, 766s, 685s, 553s; mp: 129-130 °C [MeOH]; XRD: sample crystallised in CH_2Cl_2/Hexanes to give colourless crystals. Crystal data for $C_{17}H_{20}F_6NP$ (m = 383.31 g/mol): triclinic, P-1 (no. 2).

_N_-allyl-_N_-methylindolinium hexafluorophosphate 195

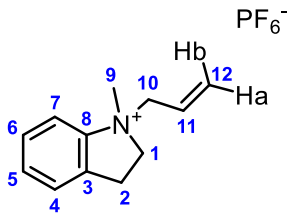

195

Following the method outlined in **6.4** using *N*-allyl-*N*-methylindolinium bromide **172** (1.45 g, 5.70 mmol), pure title compound was obtained as a purple solid without further purification (1.74 g, 5.45 mmol, 96% yield). ^{1}H NMR (600 MHz, DMSO-d_6) δ 7.82 – 7.76 (1H, m, H^{1}), 7.58 – 7.49 (3H, m, H^{2,3,12}), 5.88 (1H, ddt, *J* = 17.5, 10.2, 7.2 Hz, H^{7}), 5.58 (1H, d, *J* = 7.1 Hz, H^{8a}), 5.56 (1H, s, H^{8b}), 4.44 (1H, dd, *J* = 13.0, 7.4 Hz, H^{6}), 4.34 (1H, dd, *J* = 13.0, 7.4 Hz, H^{6}), 4.26 (1H, ddd, *J* = 11.7, 8.0, 5.8 Hz, H^{9}), 4.04 (1H, ddd, *J* = 11.8, 8.3, 7.3 Hz, H^{9}), 3.46 (3H, s, H^{5}), 3.36 – 3.28 (2H, m, H^{10}); ^{13}C NMR (151 MHz, DMSO-d_6) δ 145.1 (C^{4}), 134.4 (C^{11}), 130.8 (C^{2}), 128.7 (C^{8}), 128.1 (C^{3}), 126.5 (C^{7}), 126.0 (C^{12}), 118.3 (C^{1}), 67.5 (C^{7}), 64.1 (C^{9}), 52.3 (C^{5}), 27.1 (C^{10}); ^{31}P NMR (243 MHz, DMSO-d_6) δ -144.2 (1P, sept, *J* = 715 Hz); ^{19}F NMR (376 MHz, DMSO-d_6) δ -70.1 (6F, d, *J* = 714 Hz); LRMS (ESI-TOF) *m/z*: [M]$^{+}$ 174.259 (58); [M-allyl]$^{+}$ 133.139 (100); HRMS (ESI-TOF) *m/z*: [M]$^{+}$ Calculated for $C_{12}H_{16}N^{+}$: 174.1283, found 174.1281 (-0.2 mDa, -1.1 ppm); IR (max/cm^{-1}): 3074w, 2984w, 1487m, 1455m, 1424m, 1304w, 1082w, 966m, 821s, 771s, 553s; mp: 65-68 °C [MeOH]; XRD: sample crystallised in EtOH yielding colourless crystals. Crystal data for $C_{12}H_{16}F_6NP$ (m = 319.23 g/mol): monoclinic, Cc (no. 9).

_N_-allyl-_N_-methyl-(1H,2H,3H,4H)-tetrahydroquinolinium hexafluorophosphate 196

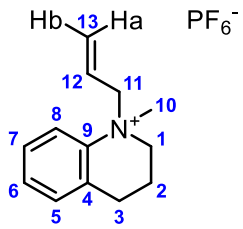

196

Following the method outlined in **6.4** using *N*-allyl-*N*-methyl-(1H,2H,3H,4H)-tetrahydroquinolinium bromide **104** (1.99 g, 7.44 mmol), pure title compound was obtained was isolated *via* crystallisation in MeOH as a red crystalline solid (0.64 g, 1.93 mmol, 26% yield). ^{1}H NMR (600 MHz, DMSO-d_6) δ 7.98 – 7.85 (1H, m, H^{8}), 7.51 – 7.42 (2H, m, H^{6,7}), 7.42 – 7.36 (1H, m, H^{5}), 5.84 (1H, ddt, *J* = 17.1, 10.2, 7.1 Hz, H^{12}), 5.64 (1H, dd, *J* = 17.0, 1.6 Hz, H^{13a}), 5.59 (1H, dd, *J* = 10.2, 1.7 Hz, 1H, H^{13b}), 4.65 (1H, dd, *J* = 13.4, 7.1 Hz, H^{11}), 4.43 (1H, dd, *J* = 13.4, 7.1 Hz, H^{11}), 3.92 – 3.79 (1H, m, H^{1}), 3.79 – 3.67 (1H, m, H^{1}), 3.53 (3H, s, H^{10}), 2.92 (2H, t, *J* = 6.5 Hz, H^{3}), 2.20 (2H, quint, *J* = 6.3 Hz, H^{2}); ^{13}C NMR (151 MHz, DMSO-d_6) δ 141.3 (C^{9}), 131.5 (C^{4}), 131.3 (C^{5}), 129.6 (C^{7}), 128.0 (C^{13}), 127.9 (C^{6}), 125.9 (C^{12}), 122.0 (C^{8}), 69.1 (C^{11}), 60.0 (C^{1}), 54.7 (C^{10}), 25.3 (C^{3}), 16.5 (C^{2}); ^{31}P NMR (162 MHz, DMSO-d_6) δ -144.2 (1P, sept, *J* = 713 Hz); ^{19}F NMR (376 MHz, DMSO-d_6) δ -70.1 (6F, d, *J* = 712 Hz); LRMS (ESI-TOF) *m/z*: [M]$^{+}$ 188.402 (100); [M-allyl]$^{+}$ 147.338 (12); HRMS (ESI-TOF) *m/z*: [M]$^{+}$ Calculated for $C_{13}H_{18}N^{+}$: 188.1439, found 188.1435 (-0.4 mDa, -2.1 ppm); IR (max/cm^{-1}): 2985w, 1505w, 1455m, 964m, 827s, 773s, 728m, 561s; mp: 84-86 °C [EtOH].

6.5 Thermal cyclisation of hexafluorophosphate ammonium salts

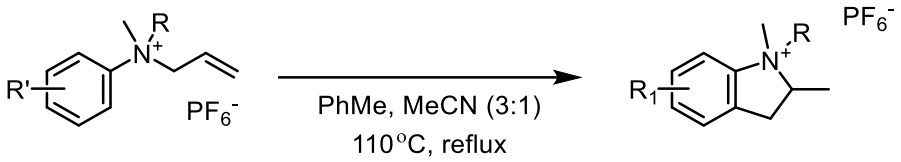

The selected quaternary ammonium salt was dissolved in a 3:1 mixture of toluene and acetonitrile (0.20 M), which was then heated to 110 °C. Once all hexafluorophosphate ammonium salt precursor was consumed, the reaction mixture was cooled down and was reduced under pressure. The solid residue found in the round bottom flask was dissolved in CH_2Cl_2 and stirred at room temperature for 10 minutes in presence of saturated KPF_6 solution (~10 mL). The organic phase was separated from the aqueous layer, which was then extracted with additional CH_2Cl_2 (30 mL x2). The organic fractions were combined, dried with $MgSO_4$, and reduced under pressure, yielding fully exchanged hexafluorophosphate indolinium salt. Title compounds were purified *via* Al_2O_3 flash chromatography or plug, with CH_2Cl_2:MeOH eluents.

1,1,2-trimethylindolin-1-ium hexafluorophosphate 131

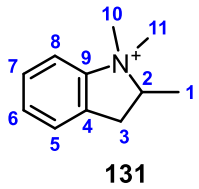

131

Following the method outlined in **6.5** using *N*-allyl-*N,N*-dimethylanilinium hexafluorophosphate **130** (0.49 g, 1.59 mmol), left to reflux for 3 days, pure title compound was obtained as a crystalline white powder *via* Al_2O_3 plug: crude product was eluted with CH_2Cl_2, followed by MeOH (0.35 g, 1.12 mmol, 71% yield). ^{1}H NMR (600 MHz, DMSO-d_6) δ 7.92 – 7.86 (1H, m, H^8), 7.57 – 7.51 (3H, m, $H^{5,6,7}$), 4.37 (1H, dp, *J* = 10.7, 6.7 Hz, H^2), 3.54 (3H, s, H^{10}), 3.38 (1H, dd, *J* = 16.3, 6.9 Hz, H^3), 3.19 (1H, dd, *J* = 16.3, 10.7 Hz, H^3), 3.14 (3H, s, H^{11}), 1.58 (3H, d, *J* = 6.6 Hz, H^1); ^{13}C NMR (151 MHz, DMSO-d_6) δ 147.8 (C^9), 133.3 (C^4), 130.6 (C^6), 128.9 (C^7), 126.3 (C^5), 117.9 (C^8), 75.0 (C^2), 51.0 (C^{10}), 48.5 (C^{11}), 33.5 (C^3), 12.5 (C^1); ^{31}P NMR (243 MHz, DMSO-d_6) δ -144.2 (1P, sept, *J* = 696 Hz); ^{19}F NMR (376 MHz, DMSO-d_6) δ -70.0 (6F, d, *J* = 706 Hz); LRMS (ESI-TOF) *m/z*: $[M]^+$ 162.171 (100); HRMS (ESI-TOF) *m/z*: $[M]^+$ Calculated for $C_{11}H_{16}N^+$: 162.1283, found 162.1279 (-0.4 mDa, -2.5 ppm); IR (max/cm^{-1}): 3048w, 2975w, 1478m, 1450m, 1389m, 1130m, 977m, 865m, 817s, 763s, 715s, 552s; mp: 115-118 °C [EtOH]; XRD: sample crystallised in CH_2Cl_2/MeOH yielding colourless crystals. Crystal data for $C_{11}H_{16}F_6NP$ (m = 307.22 g/mol): orthorombic, Pbca (no. 61).

1,1,2,5(7)-tetramethylindolin-1-ium hexafluorophosphate 228a, 228b

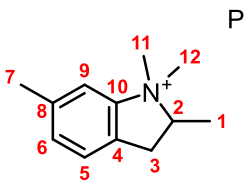

228a

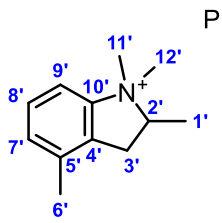

228b

Following the method outlined in **6.5** using *N*-allyl-*N,N*-dimethyl-3-methylanilinium hexafluoro phosphate **178** (0.26 g, 0.80 mmol), left to reflux for 3 days, pure title compound was isolated as a white solid *via* Al_2O_3 plug: crude product was eluted with CH_2Cl_2, followed by MeOH (1:1 mixture of ammonium salt isomers, 0.22 g, 0.67 mmol, 85% yield). ^{1}H NMR (600 MHz, DMSO-d_6) δ 7.78 (1H, s, H^{9}), 7.74 (1H, d, *J* = 8.3 Hz, $H^{9'}$), 7.43 (1H, t, *J* = 8.0 Hz, $H^{8'}$), 7.39 (1H, d, *J* = 7.5 Hz, H^{5}), 7.35 (1H, d, *J* = 7.6 Hz, $H^{7'}$), 7.33 (1H, d, *J* = 8.4 Hz, H^{6}), 4.38 – 4.29 (2H, m, $H^{2,2'}$), 3.53 (3H, s, H^{11}), 3.52 (3H, s, $H^{11'}$), 3.32 (1H, d, *J* = 6.2 Hz, $H^{3'}$), 3.29 (1H, d, *J* = 6.3 Hz, H^{3}), 3.13 (3H, s, H^{12}), 3.12 (3H, s, $H^{12'}$), 3.08 (1H, d, *J* = 9.9 Hz, H^{3}), 3.06 (1H, d, *J* = 10.4 Hz, $H^{3'}$), 2.37 (3H, s, H7), 2.28 (3H, s, $H^{6'}$), 1.57 (3H, d, *J* = 6.7 Hz, $H^{1'}$), 1.55 (3H, d, *J* = 6.7 Hz, H^{1}); ^{13}C NMR (151 MHz, DMSO-d_6) δ 147.9 (C^{10}), 147.7 ($C^{10'}$), 138.8 (C^{8}), 135.8 ($C^{5'}$), 132.2 ($C^{4'}$), 131.2 (C^{6}), 131.0 ($C^{7'}$), 130.2 (C^{4}), 128.8 ($C^{8'}$), 125.8 (C^{5}), 118.2 (C^{9}), 115.2 ($C^{9'}$), 75.2 (C^{2}), 74.6 ($C^{2'}$), 51.2 (C^{11}), 51.1 ($C^{11'}$), 48.7 (C^{12}), 48.5 ($C^{12'}$), 33.6 (C^{3}), 32.9 ($C^{3'}$), 21.0 (C^{7}), 18.2 ($C^{6'}$), 12.63 ($C^{1'}$), 12.58 (C^{1}); ^{31}P NMR (243 MHz, DMSO-d_6) δ -144.7 (1P, sept, *J* = 710 Hz, PF_6^-); ^{19}F NMR (376 MHz, DMSO-d_6) δ -70.1 (6F, d, *J* = 710 Hz); LRMS (ESI-TOF) *m/z*: $[M]^+$ 176.359 (100); HRMS (ESI-TOF) *m/z*: $[M]^+$ Calculated for $C_{12}H_{18}N^+$: 176.1439, found 176.1432 (-0.7 mDa, -4.0 ppm); IR (max/cm^{-1}): 2986w, 1482m, 1459m, 1397m, 1055m, 1033m, 831s, 787s, 716s, 557s; mp: 128-130 °C.

1,1,2,5,7-pentamethylindolin-1-ium hexafluorophosphate 222

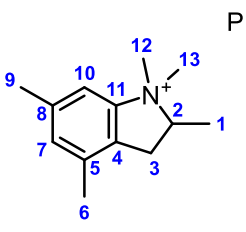

222

Following the method outlined in **6.5** using *N*-allyl-*N,N*-dimethyl-3,5-dimethylanilinium hexafluorophosphate **179** (0.54 g, 1.61 mmol), left to reflux for 3 days, pure title compound was obtained as a light brown solid *via* Al_2O_3 plug: crude product was eluted with CH_2Cl_2, followed by MeOH (0.49 g, 1.47 mmol, 91% yield). ^{1}H NMR (600 MHz, DMSO-d_6) δ 7.52 (1H, s, H^{10}), 7.19 (1H, s, H^{7}), 4.31 (dp, *J* = 10.5, 6.7 Hz, H^{2}), 3.49 (3H, s, H^{12}), 3.29 (1H, dd, *J* = 16.1, 7.0 Hz, H^{3}), 3.09 (3H, s, H^{13}), 3.00 (1H, dd, *J* = 16.2, 10.4 Hz, H^{3}), 2.36 (3H, s, H^{9}), 2.26 (3H, s, H^{6}), 1.57 (3H, d, *J* = 6.6 Hz, H^{1}); ^{13}C NMR (151 MHz, DMSO-d_6) δ 147.7 (C^{11}), 138.8 (C^{8}), 135.4 (C^{5}), 131.8 (C^{7}), 129.1 (C^{4}), 115.2 (C^{10}), 74.8 (C^{2}), 51.1 (C^{12}), 48.5 (C^{13}), 32.0 (C^{3}), 20.9 (C^{9}), 18.2 (C^{6}), 12.6 (C^{1}); ^{31}P NMR (162 MHz, DMSO-d_6) δ -144.2 (1P, sept, *J* = 710 Hz); ^{19}F NMR (376 MHz, DMSO-d_6) δ -70.1 (6F, d, *J* = 710 Hz); LRMS (ESI-TOF) *m/z*: $[M]^+$ 190.371 (100); HRMS (ESI-TOF) *m/z*: $[M]^+$ Calculated for $C_{13}H_{20}N^+$: 190.1596, found 190.1594 (-0.2 mDa, -1.1 ppm); IR (max/cm^{-1}): 2992w, 2874w, 1633w, 1470m, 1447m, 1401w, 1024w, 827s, 717m, 561s; mp: 158-160 °C [EtOH].

1,1,2,6-tetramethylindolin-1-ium hexafluorophosphate 207

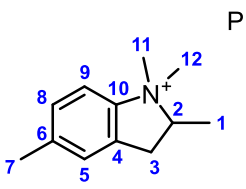

207

Following the method outlined in **6.5** using N-allyl-N,N-dimethyl-4-methylanilinium hexafluorophosphate **180** (0.52 g, 1.61 mmol), left to reflux for 3 days, pure title compound was obtained as a brown solid *via* Al_2O_3 plug: crude product was eluted with CH_2Cl_2, followed by MeOH (0.39 g, 1.21 mmol, 75% yield). ^{1}H NMR (600 MHz, MeOD-d_4) δ 7.60 (1H, d, *J* = 8.3 Hz, H^9), 7.36 – 7.31 (2H, m, $H^{5,8}$), 4.36 (1H, dp, *J* = 10.6, 6.7 Hz, H^2), 3.52 (3H, s, H^{11}), 3.42 (1H, ddd, *J* = 16.4, 6.7, 3.1 Hz, H^3), 3.16 (3H, s, H^{12}), 3.15 (1H, dd, *J* = 16.6, 11.0 Hz, H^3), 2.41 (3H, s, H^7), 1.67 (3H, d, *J* = 6.8 Hz, H^1); ^{13}C NMR (151 MHz, MeOD-d_4) δ 146.9 (t, *J* = 5.6 Hz, C^{10}), 143.1 (C^6), 134.3 (C^4), 131.0 (C^8), 128.0 (C^5), 118.0 (C^9), 77.5 (C^2), 52.3 (C^{11}), 49.4 (C^{12}), 34.9 (C^3), 21.2 (C^7), 13.1 (C^1); ^{31}P NMR (243 MHz, MeOD-d_4) δ -144.6 (1P, sept, *J* = 702 Hz)**;** ^{19}F NMR (376 MHz, MeOD-d_4) δ -74.0 (6F, d, *J* = 706 Hz); LRMS (ESI-TOF) *m/z*: 176.195 $[M]^+$ (100); HRMS (ESI-TOF) *m/z*: $[M]^+$ Calculated for $C_{12}H_{18}N^+$: 176.1439, found 176.1447 (0.8 mDa, 4.5 ppm); IR (max/cm^{-1}): 2981w, 2879w, 1492m, 1469m, 1396w, 1149w, 983w, 877m, 820s, 736m, 552s; mp: 76-78 °C [EtOH].

6-butyl-1,1,2-trimethylindolin-1-ium hexafluorophosphate 208

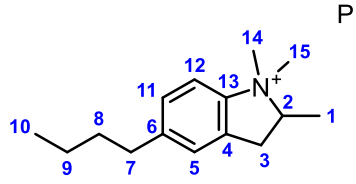

208

Following the method outlined in **6.5** using *N*-allyl-*N,N*-dimethyl-4-butylanilinium hexafluorophosphate **181** (0.59 g, 1.61 mmol), left to reflux for 5 days, pure title compound was obtained as a glassy orange solid *via* Al_2O_3 plug: crude product was eluted with CH_2Cl_2, followed by MeOH (0.33 g, 0.90 mmol, 56% yield). ^{1}H NMR (600 MHz, DMSO-d_6) δ 7.78 (1H, d, *J* = 8.8 Hz, H^{12}), 7.39 – 7.31 (2H, m, $H^{5,11}$), 4.35 (1H, dp, *J* = 10.6, 6.7 Hz, H^2), 3.52 (3H, s, H^{14}), 3.34 – 3.29 (1H, m, H^3), 3.16 (1H, dd, *J* = 15.9, 10.4 Hz, H^3), 3.12 (3H, s, H^{15}), 2.63 (2H, t, *J* = 7.5 Hz, H^7), 1.57 (3H, d, *J* = 6.7 Hz, H^1), 1.55 (2H, pent, *J* = 7.5 Hz, H^8), 1.30 (2H, sex, *J* = 7.4 Hz, H^9), 0.90 (3H, t, *J* = 7.4 Hz, H^{10}); ^{13}C NMR (151 MHz, DMSO-d_6) δ 145.7 (C^{13}), 145.4 (C^6), 133.2 (C^4), 128.7 (C^{11}), 125.8 (C^5), 117.5 (C^{12}), 75.1 (C^2), 51.1 (C^{14}), 48.6 (C^{15}), 34.4 (C^7), 33.5 (C^3), 33.0 (C^8), 21.7 (C^9), 13.7 (C^{10}), 12.5 (C^1); ^{31}P NMR (162 MHz, DMSO-d_6) δ -144.2 (1P, sept, *J* = 720 Hz); ^{19}F NMR (376 MHz, DMSO-d_6) δ -70.2 (6F, d, *J* = 709 Hz); LRMS (ESI-TOF) *m/z*: $[M]^+$ 218.415 (100); HRMS (ESI-TOF) *m/z*: $[M]^+$ Calculated for $C_{15}H_{24}N^+$: 218.1909, found 218.1917 (0.8 mDa, 3.7 ppm); IR (max/cm^{-1}): 2965m, 2940m, 2873w, 1640w, 1468m, 1463m, 1398w, 1150w, 1032w, 987w, 837s, 781m, 560s.

6-*tert*-butyl-1,1,2-trimethylindolin-1-ium hexafluorophosphate 209

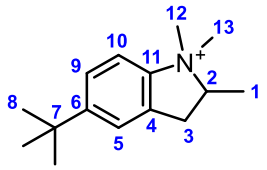

209

Following the method outlined in **6.5** using *N*-allyl-*N,N*-dimethyl-4-*tert*-butylanilinium hexafluorophosphate **182** (0.59 g, 1.61 mmol), left to reflux for 3 days, pure title compound was isolated as a brown solid *via* Al_2O_3 plug: crude product was eluted with CH_2Cl_2, followed by MeOH (0.48 g, 1.33 mmol, 82% yield). ^{1}H NMR (600 MHz, DMSO-d_6) δ 7.76 (1H, d, *J* = 9.2 Hz, H^{10}), 7.59 – 7.52 (2H, m, $H^{5,9}$), 4.35 (1H, dp, *J* = 10.8, 6.7 Hz, H^2), 3.51 (3H, s, H^{12}), 3.35 (1H, dd, *J* = 16.1, 6.9 Hz, H^3), 3.16 (1H, dd, *J* = 16.3, 10.8 Hz, H^3), 3.11 (3H, s, H^{13}), 1.57 (3H, d, *J* = 6.7 Hz, H^1), 1.30 (9H, s, H^8); ^{13}C NMR (151 MHz, DMSO-d_6) δ 153.6 (C^6), 145.4 (C^{11}), 133.0 (C^4), 126.0 (C^9), 123.0 (C^5), 117.2 (C^{10}), 75.2 (C^2), 51.0 (C^{12}), 48.5 (C^{13}), 34.8 (C^7), 33.6 (C^3), 31.0 (C^8), 12.5 (C^1); ^{31}P NMR (243 MHz, DMSO-d_6) δ -144.2 (1P, sept, *J* = 720 Hz); ^{19}F NMR (376 MHz, DMSO-d_6) δ -70.2 (6F, d, *J* = 709 Hz); LRMS (ESI-TOF) *m/z*: $[M]^+$ 218.306 (100); HRMS (ESI-TOF) *m/z*: $[M]^+$ Calculated for $C_{15}H_{24}N^+$: 218.1909, found 218.1913 (0.4 mDa, 1.8 ppm); IR (max/cm^{-1}): 2969m, 2883w, 1492m, 1473m, 1367m, 1162w, 932w, 875m, 821s, 740m, 555s; mp: 115-117 °C [EtOH]; XRD: sample crystallised in EtOH/Et_2O yielding colourless crystals. Crystal data for $C_{15}H_{24}F_6NP$ (m = 363.32 g/mol): monoclinic, $P2_1$ (no. 4).

6-phenyl-1,1,2-trimethylindolin-1-ium hexafluorophosphate 210

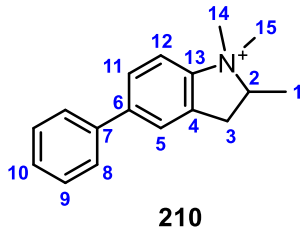

210

Following the method outlined in **6.5** using *N*-allyl-*N,N*-dimethyl-4-phenylanilinium hexafluorophosphate **183** (0.46 g, 1.20 mmol), left to reflux for 3 days, pure title compound was obtained *via* Al_2O_3 flash chromatography (CH_2Cl_2:MeOH, 98:2 → 95:5) as an off-white solid (0.29 g, 0.97 mmol, 81% yield). ^{1}H NMR (600 MHz, DMSO-d_6) δ 7.97 – 7.93 (1H, m, H^{12}), 7.85 – 7.81 (2H, m, H^{5-11}), 7.71 (2H, d, *J* = 7.6 Hz, H^8), 7.51 (2H, t, *J* = 7.7 Hz, H^9), 7.46 – 7.41 (1H, tt, *J* = 7.6, 1.1 Hz, H^{10}), 4.42 (1H, dp, *J* = 10.8, 6.7 Hz, H^2), 3.57 (3H, s, H^{14}), 3.45 (1H, dd, *J* = 16.3, 6.9 Hz, H^3), 3.24 (1H, dd, *J* = 16.2, 10.7 Hz, H^3), 3.18 (3H, s, H^{15}), 1.61 (3H, d, *J* = 6.7 Hz, H^1); ^{13}C NMR (151 MHz, DMSO-d_6) δ 147.0 (C^{13}), 142.8 (C^6), 138.7 (C^7), 134.1 (C^4), 129.1 (C^9), 128.3 (C^{10}), 127.4 (C^{11}), 127.1 (C^8), 124.4 (C^5), 118.3 (C^{12}), 75.3 (C^2), 51.1 (C^{14}), 48.5 (C^{15}), 33.6 (C^3), 12.5 (C^1); ^{31}P NMR (243 MHz, DMSO-d_6) δ -144.2 (1P, sept, *J* = 709 Hz); ^{19}F NMR (376 MHz, DMSO-d_6) δ -70.2 (6F, d, *J* = 709 Hz); LRMS (ESI-TOF) *m/z*: 238.221 $[M]^+$ (100); HRMS (ESI-TOF) *m/z*: $[M]^+$ Calculated for $C_{17}H_{20}N^+$: 238.1596, found 238.1601 (0.5 mDa, 2.1 ppm); IR (max/cm^{-1}): 2978w, 2876w, 1613w, 1478m, 1450m, 1392m, 1146m, 980m, 877m, 824s, 766s, 705s, 551s; mp: 149-152 °C [EtOH]; XRD: sample crystallised in

CH_2Cl_2/MeOH yielding colourless crystals. Crystal data for $C_{17}H_{20}F_6NP$ (m = 383.31 g/mol): monoclinic, $P2_1/c$ (no. 14).

6-methoxy-1,1,2-trimethylindolin-1-ium hexafluorophosphate 211

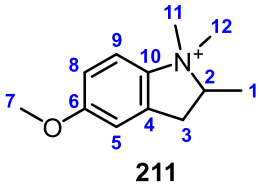

211

Following the method outlined in **6.5** using *N*-allyl-*N,N*-dimethyl-4-methoxyanilinium hexafluorophosphate **184** (0.54 g, 1.60 mmol), left to reflux for 3 days, pure title compound was obtained as a purple solid *via* Al_2O_3 plug: crude product was eluted with CH_2Cl_2, followed by MeOH (0.23 g, 0.68 mmol, 42% yield). ^{1}H NMR (600 MHz, DMSO-d_6) δ 7.83 (1H, dd, *J* = 9.0, 3.0 Hz, H^9), 7.08 (1H, d, *J* = 2.6 Hz, H^5), 7.05 (1H, dd, *J* = 8.9, 2.7 Hz, H^8), 4.35 (1H, dp, *J* = 10.6, 6.7 Hz, H^2), 3.80 (3H, s, H^7), 3.52 (3H, s, H^{11}), 3.33 (1H, dd, *J* = 16.3, 6.9 Hz, H^3), 3.16 (1H, dd, *J* = 16.0, 11.0 Hz, H^3), 3.12 (3H, s, H^{12}), 1.56 (3H, d, *J* = 6.7 Hz, H^1); ^{13}C NMR (151 MHz, DMSO-d_6) δ 160.7 (C^6), 140.7 (C^{10}), 135.0 (C^4), 118.9 (C^9), 114.6 (C^8), 110.7 (C^5), 75.3 (C^2), 55.9 (C^7), 51.4 (C^{11}), 48.7 (C^{12}), 33.6 (C^3), 12.6 (C^1); ^{31}P NMR (243 MHz, DMSO-d_6) δ -144.2 (1P, sept, *J* = 709 Hz); ^{19}F NMR (376 MHz, DMSO-d_6) δ -70.1 (6F, sept, *J* = 711 Hz); LRMS (ESI-TOF) *m/z*: $[M]^+$ 192.287 (100); HRMS (ESI-TOF) *m/z*: $[M]^+$ Calculated for $C_{12}H_{18}NO^+$: 192.1388 found 192.1390 (0.2 mDa, 1.0 ppm); IR (max/cm^{-1}): 2971w, 2841w, 1601w, 1492m, 1456m, 1296w, 1264m, 1158m, 1017m, 828s, 777m, 748m, 553s; mp: 67-70 °C.

5,6,7-trimethoxy-1,1,2-trimethylindolin-1-ium hexafluorophosphate 223

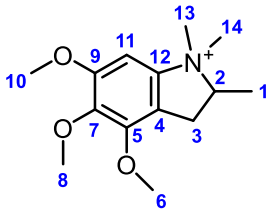

223

Following the method outlined in **6.5** using *N*-allyl-*N,N*-dimethyl-3,4,5-trimethoxyanilinium hexafluorophosphate **185** (0.54 g, 1.36 mmol), left to reflux for 3 days, pure title compound was obtained as a light brown solid *via* Al_2O_3 plug: crude product was eluted with CH_2Cl_2, followed by MeOH (0.40 g, 1.02 mmol, 75% yield). ^{1}H NMR (600 MHz, DMSO-d_6) δ 7.49 (1H, s, H^{11}), 4.38 – 4.28 (1H, m, H^2), 3.89 (3H, d, *J* = 1.5 Hz, H^6), 3.89 (3H, d, *J* = 1.6 Hz, H^8), 3.74 (3H, d, *J* = 1.6 Hz, H^{10}), 3.53 (3H, s, H^{13}), 3.39 – 3.31 (1H, m, H^3), 3.14 (3H, s, H^{14}); 3.10 (1H, dd, *J* = 16.3, 9.9 Hz, H^3), 1.55 (3H, dd, *J* = 6.7 Hz, H^1);^{13}C NMR (151 MHz, DMSO-d^6) δ 154.1 (C^7), 148.9 (C^5), 143.1 (C^{12}), 142.1 (C^9), 117.1 (Cq), 98.1 (C^{11}), 75.2 (C^2), 60.6 (C^6), 60.4 (C^8), 56.8 (C^{10}), 51.2 (C^{13}), 48.5 (C^{14}), 31.2 (C^3), 12.6 (C^1); ^{31}P NMR (243 MHz, DMSO-d_6) δ -144.2 (1P, sept, *J* = 713 Hz); ^{19}F NMR (376 MHz, DMSO-d_6) δ -70.1 (6F, d, *J* = 712 Hz, PF_6^-); LRMS (ESI-TOF) *m/z*: $[M]^+$ 252.381 (100); HRMS (ESI-TOF) *m/z*: $[M]^+$ Calculated for $C_{14}H_{22}NO_3^+$: 252.1600, found 252.1594 (-0.6 mDa, -2.4 ppm); (max/cm^{-1}): 2981m, 2833w, 1630m, 1486s, 1429m, 1345m, 1116s, 1029m, 850s, 561s; mp: 150-152 °C [MeOH].

6,7-(methylenedioxy)-1,1,2-trimethylindolin-1-ium hexafluorophosphate 224

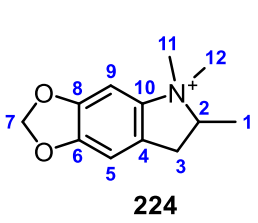

224

Following the method outlined in **6.5** using *N*-allyl-*N,N*-dimethyl-3,4-(methylenedioxy)anilinium hexafluorophosphate **186** (0.57 g, 1.36 mmol), left to reflux for 3 days, pure title compound was obtained as a light brown solid *via* Al_2O_3 plug: crude product was eluted with CH_2Cl_2, followed by MeOH (0.38 g, 1.02 mmol, 66% yield). ^{1}H NMR (600 MHz, DMSO-d_6) δ 7.65 (1H, s, H^9), 7.05 (1H, s, H^5), 6.14 (2H, dd, *J* = 10.7, 1.0 Hz, H^7), 4.35 (1H, dp, *J* = 10.4, 6.7 Hz, H^2), 3.50 (3H, s, H^{11}), 3.11 (3H, s, H^{12}), 3.24 (1H, dd, *J* = 16.0, 6.9 Hz, H^3), 3.05 (1H, ddd, *J* = 16.1, 10.6, 1.0 Hz, H^3), 1.55 (3H, d, *J* = 6.6 Hz, H^1); ^{13}C NMR (151 MHz, DMSO-d_6) δ 149.0 (C^6), 147.6 (C^8), 140.8 (C^{10}), 126.7 (C^4), 105.3 (C^5), 102.6 (C^7), 99.5 (C^9), 75.7 (C^2), 51.5 (C^{11}), 48.5 (C^{12}), 33.5 (C^3), 12.7 (C^1); ^{31}P NMR (162 MHz, DMSO-d_6) δ -144.1 (1P, sept, *J* = 720 Hz); ^{19}F NMR (376 MHz, DMSO-d_6) δ -70.0 (6F, d, *J* = 714 Hz); LRMS (ESI-TOF) *m/z*: $[M]^+$ 206.311 (100); HRMS (ESI-TOF) *m/z*: $[M]^+$ Calculated for $C_{12}H_{16}NO_2^+$: 206.1181, found 206.1180 (-0.1 mDa, -0.5 ppm); IR (max/cm^{-1}): 2981w, 1474m, 1287m, 1118s, 1085s, 817s, 611s, 554s; mp: 169-170 °C [EtOH].

6-(trifluoromethyl)-1,1,2-trimethylindolin-1-ium hexafluorophosphate 212

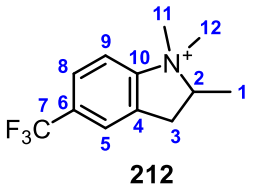

212

Following the method outlined in **6.5** using *N*-allyl-*N,N*-dimethyl-4-(trifluoromethyl)anilinium hexafluorophosphate **187** (0.45 g, 1.21 mmol), left to reflux for 3 days, pure title compound was obtained as a white solid *via* Al_2O_3 plug: crude product was eluted with CH_2Cl_2, followed by MeOH (0.38 g, 1.02 mmol, 85% yield). ^{1}H NMR (600 MHz, DMSO-d_6) δ 8.18 – 8.12 (1H, m, H^9), 8.01 (1H, s, H^5), 7.98 (1H, d, *J* = 8.6 Hz, H^8), 4.50 – 4.40 (1H, m, H^2), 3.49 (1H, dd, *J* = 16.7, 6.9 Hz, H^3), 3.35 (3H, s, H^{11}), 3.27 (1H, dd, *J* = 16.7, 10.7 Hz, H^3), 3.21 (3H, s, H^{12}), 1.60 (3H, d, *J* = 6.7 Hz, H^1); ^{13}C NMR (151 MHz, DMSO-d_6) δ 150.8 (C^{10}), 135.3 (C^4), 131.0 (1C, q, *J* = 32.7 Hz, C^6), 126.4 (1C, q, *J* = 3.9 Hz, C^8), 123.8 (1C, q, *J* = 4.1 Hz, C^5); 123.6 (1C, q, *J* = 274 Hz, C^7), 119.4 (C^9), 75.5 (C^2), 51.1 (C^{11}), 48.4 (C^{12}), 33.5 (C^3), 12.5 (C^1); ^{31}P NMR (243 MHz, DMSO-d_6) δ -144.2 (1P, sept, *J* = 713 Hz); ^{19}F NMR (376 MHz, DMSO-d_6) δ -61.0 (3F, s, $-CF_3$), -70.1 (6F, d, *J* = 712 Hz, PF_6^-); LRMS (ESI-TOF) *m/z*: $[M]^+$ 230.322 (100); HRMS (ESI-TOF) *m/z*: $[M]^+$ Calculated for $C_{12}H_{15}NPF_3^+$: 230.1157, found 230.1156 (-0.1 mDa, -0.4 ppm); IR (max/cm^{-1}): 2981w, 2887w, 1442w, 1335m, 1153m, 1125m, 821s, 776s, 556s; mp: 135-137 °C.

6-fluoro-1,1,2-trimethylindolin-1-ium hexafluorophosphate 213

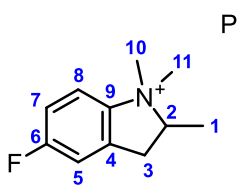

213

Following the method outlined in **6.5** using *N*-allyl-*N,N*-dimethyl-4-fluoroanilinium hexafluorophosphate **188** (0.54 g, 1.65 mmol), left to reflux for 5 days, pure title compound was obtained as a yellow solid *via* Al_2O_3 plug: crude product was eluted with CH_2Cl_2, followed by MeOH (0.29 g, 0.90 mmol, 55% yield). ^{1}H NMR (600 MHz, DMSO-d_6) δ 7.92 (1H, dd, *J* = 9.1, 4.4 Hz, H^8), 7.47 – 7.38 (2H, m, $H^{5,7}$), 4.40 (1H, dp, *J* = 10.7, 6.7 Hz, H^2), 3.52 (3H, s, H^{10}); 3.39 (1H, dd, *J* = 16.6, 6.9 Hz, H^3), 3.19 (1H, dd, *J* = 16.4, 14.3 Hz, H^3), 3.14 (3H, s, H^{11}), 1.57 (3H, d, *J* = 6.7 Hz, H^1); ^{13}C NMR (151 MHz, DMSO-d_6) δ 162.8 (1C, d, *J* = 241 Hz, C^6), 143.9 (C^9), 136.3 (1C, d, *J* = 10.1 Hz, C^4), 120.1 (1C, d, *J* = 9.9 Hz, C^8), 115.9 (1C, d, *J* = 25.1 Hz, C^7), 113.3 (1C, d, *J* = 24.9 Hz, C^5), 75.6 (C^2), 51.3 (C^{10}), 48.7 (C^{11}), 33.5 (C^3), 12.5 (C^1); ^{31}P NMR (162 MHz, DMSO-d_6) δ -144.2 (1P, sept, *J* = 709 Hz); ^{19}F NMR (376 MHz, DMSO-d_6) δ -70.1 (6F, d, *J* = 709 Hz, PF_6^-); -110.6 (1F, s); LRMS (ESI-TOF) *m/z*: $[M]^+$ 180.315 (100); HRMS (ESI-TOF) *m/z*: $[M]^+$ Calculated for $C_{11}H_{15}NF^+$: 180.1189, found 180.1186 (-0.3 mDa, -1.7 ppm); IR (max/cm^{-1}): 2976w, 1490m, 1245m, 1146m, 879m, 829s, 809s, 555s; mp: 165-166 °C.

6-chloro-1,1,2-trimethylindolin-1-ium hexafluorophosphate 214

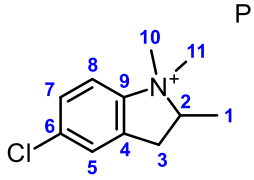

214

Following the method outlined in **6.5** using *N*-allyl-*N,N*-dimethyl-4-chloroanilinium hexafluorophosphate **189** (0.55 g, 1.60 mmol), left to reflux for 3 days, pure title compound was obtained as a light brown solid *via* Al_2O_3 plug: crude product was eluted with CH_2Cl_2, followed by MeOH (0.36 g, 1.06 mmol, 65% yield). ^{1}H NMR (600 MHz, DMSO-d_6) δ 7.96 (1H, d, *J* = 8.7 Hz, H^8), 7.68 (1H, d, *J* = 2.3 Hz, H^5), 7.64 (1H, dd, *J* = 8.7, 2.3 Hz, H^7), 4.40 (1H, dp, *J* = 10.7, 6.7 Hz, H^2), 3.55 (3H, s, H^{10}), 3.39 (1H, dd, *J* = 16.6, 6.9 Hz, H^3), 3.21 (1H, dd, *J* = 16.6, 10.7 Hz, H^3), 3.16 (3H, s, H^{11}), 1.57 (3H, d, *J* = 6.7 Hz, H^1); ^{13}C NMR (151 MHz, DMSO-d_6) δ 146.6 (C^9), 135.9 (C^4), 135.0 (C^6), 128.8 (C^7), 126.3 (C^5), 119.9 (C^8), 75.4 (C^2), 51.2 (C^{10}), 48.5 (C^{11}), 33.4 (C^3), 12.5 (C^1); ^{31}P NMR (243 MHz, DMSO-d_6) δ -144.2 (1P, sept, *J* = 709 Hz); ^{19}F NMR (376 MHz, DMSO-d_6) δ -70.1 (6F, d, *J* = 710 Hz); LRMS (ESI-TOF) *m/z*: $[^{35}ClM]^+$ 196.239 (100); $[^{37}ClM]^+$ 198.277 (34); HRMS (ESI-TOF) *m/z*: $[M]^+$ Calculated for $C_{11}H_{15}N^{35}Cl^+$: 196.0893 found 196.0897 (0.4 mDa, 2.0 ppm); IR (max/cm^{-1}): 3023w, 2946w, 1478m, 1453m, 1420m, 1145m, 1034m, 879m, 828s, 809s, 780s, 709m, 552s; mp: 139-142 °C; XRD: sample crystallised in EtOH yielding colourless, needle-shaped crystals. Crystal data for $C_{11}H_{15}F_6ClNP$ (m = 341.66 g/mol): monoclinic, C2/c (no. 15).

6-bromo-1,1,2-trimethylindolin-1-ium hexafluorophosphate 215

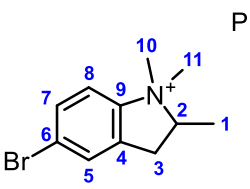

215

Following the method outlined in **6.5** using *N*-allyl-*N,N*-dimethyl-4-bromoanilinium hexafluorophosphate **190** (0.62 g, 1.60 mmol), left to reflux for 5 days, pure title compound was obtained as a brown solid *via* Al_2O_3 plug: crude product was eluted with CH_2Cl_2, followed by MeOH (0.26 g, 0.67 mmol, 42% yield). ^{1}H NMR (600 MHz, DMSO-d_6) δ 7.90 – 7.83 (1H, m, H^8), 7.80 (1H, s, H^5), 7.76 (1H, d, *J* = 9.3 Hz, H^7), 4.42 – 4.33 (1H, m, H^2), 3.54 (3H, d, *J* = 2.8 Hz, H^{10}), 3.38 (1H, dd, *J* = 16.9, 6.9 Hz, H^3), 3.19 (1H, dd, *J* = 16.9, 10.6 Hz, H^3), 3.15 (3H, d, *J* = 2.4 Hz, H^{11}), 1.57 (3H, d, *J* = 6.7 Hz, H^1); ^{13}C NMR (600 MHz, DMSO-d_6) δ 147.0 (C^9), 136.2 (C^4), 131.7 (C^7), 129.3 (C^5), 123.5 (C^6), 120.1 (C^8), 75.3 (C^2), 51.1 (C^{10}), 48.5 (C^{11}), 33.3 (C^3), 12.5 (C^1); ^{31}P NMR (162 MHz, DMSO-d_6) δ -144.2 (1P, sept, *J* = 712 Hz); ^{19}F NMR (376 MHz, DMSO-d_6) δ -71.0 (6F, d, *J* = 715 Hz); LRMS (ESI-TOF) *m/z*: $[^{79}BrM]^+$ 240.272 (100); $[^{81}BrM]^+$ 242.262 m/z (99); HRMS (ESI-TOF) *m/z*: $[M]^+$ Calculated for $C_{11}H_{15}N^{79}Br^+$: 240.0388, found 240.0384 (-0.4 mDa, -1.7 ppm); IR (max/cm^{-1}): 2976w, 2887w, 1471m, 1391m, 1146m, 1088m, 981m, 826s, 808s, 555s; mp: 147-150 °C [EtOH].

6-iodo-1,1,2-trimethylindolin-1-ium hexafluorophosphate 216

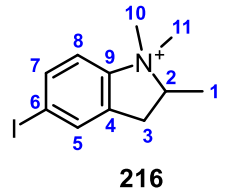

216

Following the method outlined in **6.5** using *N*-allyl-*N,N*-dimethyl-4-iodoanilinium hexafluorophosphate **191** (0.35 g, 0.81 mmol), left to reflux for 3 days, pure title compound was obtained as a light purple solid *via* Al_2O_3 plug: crude product was eluted with CH_2Cl_2, followed by MeOH (0.29 g, 0.67 mmol, 83% yield). ^{1}H NMR (600 MHz, DMSO-d_6) δ 7.96 (1H, d, *J* = 1.8 Hz, H^5), 7.92 (1H, dd, *J* = 8.6, 1.8 Hz, H^7), 7.67 (1H, d, *J* = 8.5 Hz, H^8), 4.34 (1H, dq, *J* = 10.6, 6.8 Hz, H^2), 3.36 (1H, dd, *J* = 16.5, 6.9 Hz, H^3), 3.52 (3H, s, H^{10}), 3.17 (1H, dd, *J* = 16.5, 10.7 Hz, H^3), 3.12 (3H, s, H^{11}), 1.56 (3H, d, *J* = 6.7 Hz, H^1); ^{13}C NMR (151 MHz, DMSO-d_6) δ 147.6 (C^9), 137.5 (C^7), 136.2 (C^4), 135.1 (C^5), 120.0 (C^8), 97.0 (C^6), 75.1 (C^2), 51.0 (C^{10}), 48.4 (C^{11}), 33.2 (C^2), 12.4 (C^1); ^{31}P NMR (162 MHz, DMSO-d_6) δ -144.1 (1P, sept, *J* = 720 Hz); ^{19}F NMR (376 MHz, DMSO-d_6) δ -70.0 (6F, d, *J* = 714 Hz); LRMS (ESI-TOF) *m/z*: 288.160 $[M]^+$ (100); HRMS (ESI-TOF) *m/z*: $[M]^+$ Calculated for $C_{11}H_{15}NI^+$: 288.0249, found 288.0255 (0.6 mDa, 2.1 ppm); IR (max/cm^{-1}): 3106w, 2945w, 1473m, 1443m, 1386m, 1207w, 1082m, 983m, 821s, 801s, 697m, 553s; mp: 170-172 °C [EtOH]; XRD: sample crystallised in EtOH yielding colourless, prism-shaped crystals. Crystal data for $C_{11}H_{15}F_6INP$ (m = 433.11 g/mol): monoclinic, $P2_1/c$ (no. 14).

6-acetanilide-1,1,2-trimethylindolin-1-ium hexafluorophosphate 217

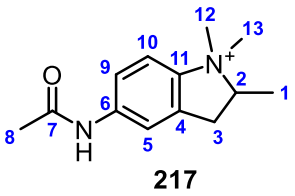

217

Following the method outlined in **5** using *N*-allyl-*N,N*-dimethyl-4-acetanilideanilinium hexafluorophosphate **192** (0.29 g, 0.81 mmol), left to reflux for 3 days, pure title compound was obtained as a light brown solid *via* Al_2O_3 plug: crude product was eluted with CH_2Cl_2, followed by MeOH (0.29 g, 0.67 mmol, 73% yield). ^{1}H NMR (400 MHz, DMSO-d_6) δ 10.60 (1H, s, NH), 7.90 – 7.75 (2H, m, $H^{9,10}$), 7.64 (1H, dd, *J* = 8.9, 2.1 Hz, H^5), 4.35 (1H, dp, *J* = 10.6, 6.7 Hz, H^2), 3.55 (3H, s, $H^{12/13}$), 3.40 – 3.31 (1H, m, overlapping with residual water signal, H^3), 3.20 – 3.15 (1H, m, overlapping with residual MeOH signal, H^3), 3.12 (3H, s, $H^{13/12}$), 2.09 (3H, s, H^8), 1.56 (3H, d, *J* = 6.6 Hz, H^1); ^{31}P NMR (162 MHz, DMSO-d_6) δ -144.1 (1P, sept, *J* = 720 Hz); ^{19}F NMR (376 MHz, DMSO-d_6) δ -70.0 (6F, d, *J* = 714 Hz); LRMS (ESI-TOF) *m/z*: $[M]^+$ 219.361 (100); HRMS (ESI-TOF) *m/z*: $[M]^+$ Calculated for $C_{13}H_{19}N_2O^+$: 219.1497, found 219.1498 (0.1 mDa, 0.5 ppm); IR (max/cm^{-1}): 3422m, 2982w, 1691m, 1540m, 1492m, 1380m, 1281m, 832s, 776s, 551s.

5(7)-cyano-1,1,2-trimethylindolin-1-ium hexafluorophosphate 229a, 229b

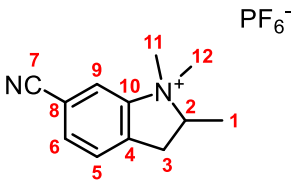

229a

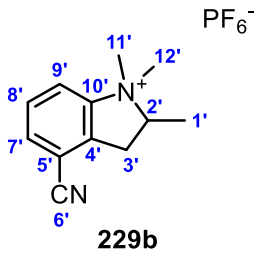

229b

Following the method outlined in **5** using *N*-allyl-*N,N*-dimethyl-3-cyanoanilinium hexafluoro phosphate **193** (0.61 g, 1.60 mmol), pure title compound was obtained *via* Al_2O_3 flash chromatography (CH_2Cl_2:MeOH, 99:1 → 98:2 → 96:4) as an off-white solid (0.22 g, 0.57 mmol, 36% yield). ^{1}H NMR (400 MHz, DMSO-d_6) δ 8.64 (s, 1H), 8.37 (d, *J* = 8.3 Hz, 1H), 8.06 (t, *J* = 8.5 Hz, 2H), 7.78 (t, *J* = 7.3 Hz, 2H), 4.48 (ddt, *J* = 14.0, 10.1, 6.8 Hz, 2H), 3.63 (d, *J* = 3.6 Hz, 6H), 3.59 – 3.15 (m, 10H), 1.62 (d, *J* = 7.0 Hz, 3H), 1.60 (d, *J* = 6.6 Hz, 3H). ^{31}P NMR (162 MHz, DMSO-d_6) δ -144.1 (1P, sept, *J* = 720 Hz); ^{19}F NMR (376 MHz, DMSO-d_6) δ -70.0 (6F, d, *J* = 714 Hz); LRMS (ESI-TOF) *m/z*: $[M]^+$ 187.251 (76), $[M\text{-}CN+H]^+$ 162.206 (100); HRMS (ESI-TOF) *m/z*: $[M]^+$ Calculated for $C_{12}H_{15}N_2^+$: 187.1235, found 187.1236 (0.1 mDa, 0.5 ppm); IR (max/cm^{-1}): 3012w, 2943w, 2229m, 1682w, 1462m, 1393m, 1151w, 1064w, 941m, 828s, 807s, 720s, 560s.

2,3-dimethyl-1,2,5,6-tetrahydro-4H-pyrrolo-[3,2,1-*ij*]-quinolinium hexafluorophosphate 232

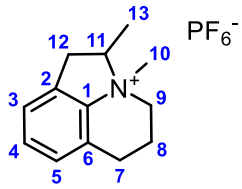

232

Following the method outlined in **6.5** using *N*-allyl-*N*-benzyl-*N,N*-dimethyl-3-cyanoanilinium hexa- fluorophosphate **196** (0.27 g, 0.81 mmol), title compound was obtained *via* Al_2O_3 flash chromatography (100% CH_2Cl_2 then 95:5 CH_2Cl_2:MeOH). Further crystallisation of the columned material in EtOH afforded pure target product as an off-white solid (0.13 g, 0.26 mmol, 32% yield). ^{1}H NMR (600 MHz, DMSO-d_6) δ 7.43 (1H, t, *J* = 7.6 Hz, H^4), 7.33 (1H, d, *J* = 7.5 Hz, H^3), 7.28 (1H, d, *J* = 7.6 Hz, H^5), 4.25 (1H, dp, *J* = 11.2, 6.6 Hz, H^{11}), 4.07 (1H, ddd, *J* = 11.8, 4.5, 2.2 Hz, H^9), 3.41 – 3.34 (1H, m, H^9), 3.33 – 3.28 (1H, m, H^{12}), 3.22 (1H, dd, *J* = 16.3, 6.6 Hz, H^{12}), 3.10 (3H, s, H^{10}), 3.01 (1H, dd, *J* = 18.3, 8.2 Hz, H^8), 2.89 – 2.81 (1H, m, H^8), 2.49 – 2.41 (1H, m, H^7), 2.26 – 2.17 (1H, m, H^7), 1.60 (3H, d, *J* = 6.7 Hz, H^{13}); ^{13}C NMR (151 MHz, DMSO-d_6) δ 143.3 (C^1), 133.1 (C^2), 130.4 (C^4), 128.8 (C^6), 128.1 (C^5), 123.4 (C^3), 76.6 (C^{11}), 57.7 (C^9), 43.9 (C^{10}), 32.6 (C^{12}), 20.6 (C^8), 16.4 (C^7), 12.0 (C^{13}); ^{31}P NMR (243 MHz, DMSO-d_6) δ -144.22 (1P, sept, *J* = 713 Hz) ; ^{19}F NMR (376 MHz, DMSO-d_6) δ -70.0 (6F, d, *J* = 713 Hz); LRMS (ESI-TOF) *m/z*: $[M]^+$ 188.220 (100); HRMS (ESI-TOF) *m/z*: $[M]^+$ Calculated for $C_{13}H_{18}N^+$: 188.1438, found 188.1439 (-0.1 mDa, -0.5 ppm); IR (max/cm^{-1}): 2982w, 1458m, 1428m, 1389m, 1057m, 970m, 880s, 824s, 789m, 556s.

6.6 Charged aza-Claisen rearrangement of PF_6^- ammonium salts to substituted *o*-allylanilines

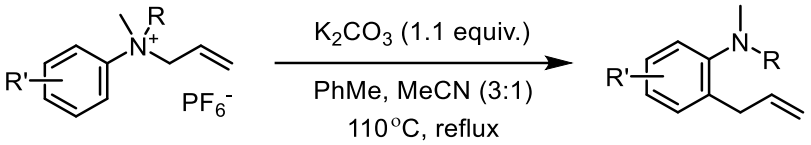

Hexafluorophosphate ammonium salt and K_2CO_3 (1.10 equiv.) were sequentially weighed in a round bottom flask charged with a magnetic stir bar. Following the introduction of the 3:1 mixture of toluene and acetonitrile (0.20 M), the resulting suspension was heated to 110 °C and allowed to reflux for 48 hours. The reaction mixture was then cooled down and reduced under pressure. The isolated residue was extracted with dichloromethane and water (30 mL x3) and the organic phase was dried with $MgSO_4$, vacuum-filtered and concentrated in vacuo. Purification via flash column chromatography (hexanes:EtOAc) yielded the desired *o*-allylanilines.

N,N-dimethyl-2-allylaniline 93

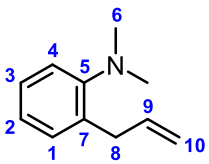

93

Following the method outlined in **6.6** using *N*-allyl-*N,N*-dimethylanilinium hexafluorophosphate **130** (0.24 g, 0.79 mmol), title compound was isolated *via* column chromatography (99:1 hexanes:EtOAc), as a colourless oil (0.09 g, 0.53 mmol, 66% yield). ^{1}H NMR (600 MHz, DMSO-d_6) δ 7.16 (1H, td, *J* = 7.6, 1.7 Hz, H^2), 7.12 (1H, dd, *J* = 7.6, 1.7 Hz, H^4), 7.10 (1H, dd, *J* = 7.9, 1.3 Hz, H^1), 6.99 (1H, td, *J* = 7.5, 1.5 Hz, H^3), 5.97 (1H, ddt, *J* = 16.8, 10.1, 6.6 Hz, H^9), 5.12 – 5.04 (2H, m, H^{10}), 3.43 (2H, d, *J* = 6.6 Hz, H^8), 2.60 (6H, s, H^6); ^{13}C NMR (151 MHz, DMSO-d_6) δ 152.2 (C^5), 137.8 (C^9), 133.7 (C^7), 129.8 (C^4), 126.8 (C^3), 122.9 (C^2), 119.1 (C^1), 115.8 (C^{10}), 44.6 (C^6), 34.4 (C^8); LRMS (ESI-TOF) *m/z*: $[M+H]^+$ 162.247 (100); HRMS (ESI-TOF) *m/z*: $[M+H]^+$ Calculated for $C_{11}H_{16}N^+$: 162.1283, found 162.1289 (0.6 mDa, 3.7 ppm); IR (max/cm^{-1}): 2940w, 2825w, 2784w, 1642w, 1598w, 1496s, 1451s, 1308m, 1050m, 952s, 908s, 762s, 723s, 562m.

N,N-dimethyl-2-allyl-3(5)-methylaniline 226a, 226b

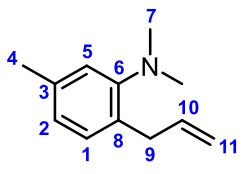

226a

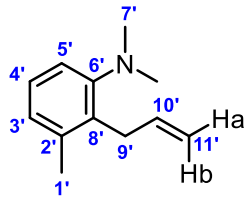

226b

Following the method outlined **6.6** using *N*-allyl-*N,N*-dimethyl-3-dimethylanilinium hexafluoro phosphate **178** (0.26 g, 0.81 mmol), title compound was isolated as a yellow oil without further purification (1:1 regioisomer mixture, 0.09 g, 0.51 mmol, 63% yield). ^{1}H NMR (600 MHz, $CDCl_3$) δ 7.14 (1H, t, *J* = 7.7 Hz, $H^{4'}$), 7.10 (1H, d, *J* = 7.7 Hz, H^1), 7.04 (1H, d, *J* = 7.9 Hz, $H^{5'}$), 6.95 – 6.90 (2H, m, $H^{3'}$, H^5), 6.85 (1H, ddd, *J* = 7.7,

1.8, 0.9 Hz, H^{2}), 6.06 – 5.96 (2H, m, $H^{10,10'}$), 5.15 – 5.06 (2H, m, H^{11}), 5.03 (1H, dq, *J* = 10.2, 1.9 Hz, $H^{11a'}$), 4.92 (1H, dq, *J* = 17.3, 2.0 Hz, $H^{11b'}$), 3.60 (2H, dt, *J* = 5.5, 1.9 Hz, $H^{9'}$), 3.47 (2H, d, *J* = 6.4 Hz, H^{9}), 2.69 (6H, s, H^{7}), 2.67 (6H, s, $H^{7'}$), 2.34 (3H, s, H^{4}), 2.30 (3H, s, $H^{1'}$); ^{13}C NMR (151 MHz, $CDCl_3$) δ 153.5 ($C^{6'}$), 152.5 (C^{6}), 138.6 ($C^{2'}$), 138.3 (C^{10}), 137.2 ($C^{10'}$), 136.5 (C^{3}), 133.4 ($C^{8'}$), 131.4 (C^{8}), 130.2 (C^{1}), 126.7 ($C^{4'}$), 125.8 ($C^{3'}$), 123.9 (C^{2}), 120.0 (C^{5}), 117.7 ($C^{5'}$), 115.6 (C^{11}), 114.7 ($C^{11'}$), 45.9 ($C^{7'}$), 45.1 (C7), 34.8 (C^{9}), 32.1 ($C^{9'}$), 21.6 (C^{4}), 20.0 ($C^{1'}$); LRMS (ESI-TOF) *m/z*: $[M+H]^+$ 176.309 (100); HRMS (ESI-TOF) *m/z*: $[M+H]^+$ Calculated for $C_{12}H_{18}N^+$: 176.1439, found 176.1436 (-0.3 mDa, -1.7 ppm); IR (max/cm^{-1}): 2983m, 2941m, 2864w, 2830m, 2780m, 1634w, 1584w, 1508m, 1477m, 1451m, 1305m, 1185m 1047m, 974s, 908s, 794m, 747m.

N,N-dimethyl-2-allyl-3,5-dimethylaniline 219

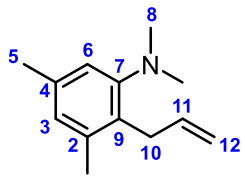

219

Following the method outlined in **6.6** using *N*-allyl-*N,N*-dimethyl-3,5-dimethylanilinium hexafluorophosphate **179** (0.52 g, 1.56 mmol), title compound was isolated *via* column chromatography (99:1 hexanes:Et_2O), as a colourless oil (0.23 g, 1.22 mmol, 78% yield). ^{1}H NMR (600 MHz, $CDCl_3$) δ 6.83 (1H, s, H^{3}), 6.75 (1H, s, H^{6}), 6.08 – 5.88 (1H, m, H^{11}), 5.01 (1H, dqd, *J* = 10.3, 1.9, 1.0 Hz, H^{12b}), 4.91 (1H, dqd, *J* = 17.1, 1.8, 0.7 Hz, H^{12a}), 3.54 (2H, d, *J* = 5.2 Hz, H^{10}), 2.62 (6H, s, H^{8}), 2.30 (3H, s, H^{4}), 2.25 (3H, s, H^{1});^{13}C NMR (151 MHz, $CDCl_3$) δ 153.4 (C^{7}), 138.4 (C^{9}), 137.4 (C^{11}), 136.2 (C^{5}), 130.2 (C^{2}), 126.7 (C^{3}), 118.3 (C^{6}), 114.6 (C^{12}), 45.9 (C^{8}), 31.9 (C^{10}), 21.3 (C^{4}), 20.0 (C^{1}); LRMS (ESI-TOF) *m/z*: $[M+H]^+$ 190.374 (100); HRMS (ESI-TOF) *m/z*: $[M+H]^+$ Calculated for $C_{13}H_{20}N^+$: 190.1596, found 190.1594 (-0.2 mDa, -1.1 ppm); IR (max/cm^{-1}): 2943m, 2833w, 2780m, 1642w, 1585m, 1455s, 1325s, 1189m, 1048s, 979s, 911s, 845s, 606m.

N,N-dimethyl-2-allyl-4-methylaniline 197

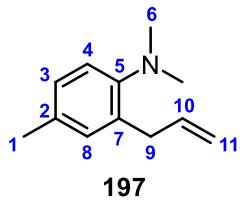

197

Following the method outlined in **6.6** using *N*-allyl-*N,N*-dimethyl-4-methylanilinium hexafluorophosphate **180** (0.26 g, 0.79 mmol), title compound was isolated *via* column chromatography (97:3 hexanes:EtOAc), as a yellow oil (0.07 g, 0.42 mmol, 53% yield). ^{1}H NMR (600 MHz, MeOD-d_4) δ 7.01 (1H, d, *J* = 8.7 Hz, H^{4}), 6.98 – 6.93 (2H, m, $H^{3,8}$), 5.96 (1H, ddt, *J* = 16.8, 10.2, 6.5 Hz, H^{10}), 5.08 – 5.00 (2H, m, H^{11}), 3.43 (2H, d, *J* = 6.5 Hz, H^{9}), 2.61 (6H, s, H^{6}), 2.24 (3H, s, H^{1}); ^{13}C NMR (151 MHz, MeOD-d_4) δ 151.2 (C^{5}), 139.4 (C^{10}), 135.6 (C^{7}), 133.9 (C^{2}), 131.8 (C^{8}), 128.5 (C^{3}), 120.3 (C^{4}), 115.7 (C^{11}), 45.7 (C^{6}), 35.8 (C^{9}), 20.8 (C^{1}); LRMS (ESI-TOF) *m/z*: $[M+H]^+$ 176.189 (100); HRMS (ESI-TOF) *m/z*: $[M+H]^+$ Calculated for $C_{12}H_{18}N^+$: 176.1439, found 176.1445 (0.6 mDa, 3.4 ppm); IR (max/cm^{-1}): 2944w, 2830w, 2780w, 1642w, 1504s, 1455m, 1299m, 1166m, 997m, 913s, 810s, 571m.

***N,N*-dimethyl-2-allyl-4-butylaniline 198**

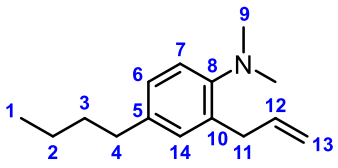

198

Following the method outlined in **6.6** using *N*-allyl-*N,N*-dimethyl-4-butylanilinium hexafluorophosphate **181** (0.57 g, 1.56 mmol), title compound was isolated *via* column chromatography (97:3 hexanes:EtOAc), as a yellow oil (0.20 g, 0.91 mmol, 58% yield). ^{1}H NMR (600 MHz, $CDCl_3$) δ 7.05 – 6.98 (3H, m, $H^{6,7,14}$), 6.02 (1H, ddt, *J* = 16.8, 10.1, 6.6 Hz, H^{12}), 5.15 – 5.07 (2H, m, H^{13}), 3.50 (2H, d, *J* = 6.6, 1.6 Hz, H^{11}), 2.67 (6H, d, *J* = 1.5 Hz, H^{9}), 2.55 (2H, t, *J* = 7.9 Hz, H^{4}), 1.59 (2H, quint, *J* = 7.5 Hz, H^{3}), 1.37 (2H, hex, *J* = 7.3 Hz, H^{2}), 0.94 (3H, t, *J* = 7.3 Hz, H^{1}); ^{13}C NMR (151 MHz, $CDCl_3$) δ: 150.4 (C^{8}), 138.2 (C^{12}), 137.8 (C^{5}), 134.4 (C^{10}), 130.3 (C^{14}), 126.8 (C^{6}), 119.6 (C^{7}), 115.6 (C^{13}), 45.4 (C^{9}), 35.2 (C^{4}), 35.1 (C^{11}), 33.9 (C^{3}), 22.6 (C^{2}), 14.1 (C^{1}); LRMS (ESI-TOF) *m/z*: $[M+H]^+$ 218.393 (100); HRMS (ESI-TOF) *m/z*: $[M+H]^+$ Calculated for $C_{15}H_{24}N^+$: 218.1909, found 218.1918 (0.9 mDa, 4.1 ppm); IR (max/cm^{-1}): 2960m, 2930m, 2867m, 2825m, 2786w, 1642w, 1501s, 1455m, 1309m, 1163m, 1097m, 1043m, 994m, 913s, 825s.

***N,N*-dimethyl-2-allyl-4-*tert*-butylaniline 199**

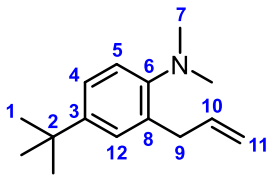

199

Following the method outlined in **6.6** using *N*-allyl-*N,N*-dimethyl-4-*tert*-butylanilinium hexafluorophosphate **182** (0.29 g, 0.80 mmol), title compound was isolated *via* column chromatography (99:1 hexanes:EtOAc), as a colourless oil (0.16 g, 0.73 mmol, 92% yield). ^{1}H NMR (600 MHz, $CDCl_3$) δ 7.23 (1H, d, *J* = 2.5 Hz, H^{12}), 7.21 (1H, dd, *J* = 8.2, 2.5 Hz, H^{4}), 7.05 (1H, d, *J* = 8.2 Hz, H^{5}), 6.04 (1H, ddt, *J* = 16.8, 10.1, 6.5 Hz, H^{10}), 5.11 (1H, dq, *J* = 16.6, 1.6 Hz, H^{11a}); 5.10 (1H, dq, *J* = 10.2, 1.7 Hz, H^{11b}), 3.52 (2H, d, *J* = 6.6 Hz, H^{9}), 2.69 (6H, s, H^{7}), 1.32 (9H, s, H^{1}); ^{13}C NMR (151 MHz, $CDCl_3$) δ 149.7 (C^{6}), 145.9 (C^{3}), 138.3 (C^{10}), 133.9 (C^{8}), 127.4 (C^{12}), 123.7 (C^{4}), 118.7 (C^{5}), 115.6 (C^{11}), 45.3 (C^{7}), 35.3 (C^{9}), 34.4 (C^{2}), 31.6 (C^{1}); LRMS (ESI-TOF) *m/z*: $[M+H]^+$ 218.306 (100); HRMS (ESI-TOF) *m/z*: $[M+H]^+$ Calculated for $C_{18}H_{24}N^+$: 218.1909, found 218.1911 (0.2 mDa, 0.9 ppm); IR (max/cm^{-1}): 2958m, 2825w, 2776w, 1642w, 1504s, 1451m, 1366m, 1175m, 1055m, 914s, 824s, 615m.

***N,N*-dimethyl-2-allyl-4-phenylaniline 200**

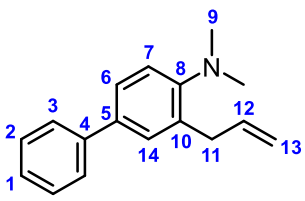

200

Following the method outlined in **6.6** using *N*-allyl-*N,N*-dimethyl-4-phenylanilinium hexafluorophosphate **183** (0.30 g, 0.85 mmol), title compound was isolated *via* column chromatography (97:3 hexanes:EtOAc), as a yellow oil (0.16 g, 0.68 mmol, 80% yield). ^{1}H NMR (600 MHz, $CDCl_3$) δ 7.57 (2H, d, *J* = 8.1 Hz, H^{3}), 7.46 – 7.39 (2H, m, $H^{6,7}$), 7.39 (2H, t, *J* = 7.9 Hz, H^{2}), 7.31 (1H, tt, *J* = 7.4, 1.2 Hz, H^{1}), 7.17 (1H, d, *J* = 8.1 Hz, H^{7}), 6.05 (1H, ddt, *J* = 16.7, 10.0, 6.5 Hz, H^{12}), 5.17 (1H, dq, *J* = 17.1, 1.8 Hz, H^{13b}), 5.13

(1H, dq, J = 10.3, 1.5 Hz, H^{13a}), 3.57 (2H, d, J = 6.5 Hz, H^{11}), 2.74 (6H, s, H^{9}); ^{13}C NMR (151 MHz, $CDCl_3$) δ 152.4 (C^{8}), 141.3 (C^{4}), 137.9 (C^{12}), 135.9 (C^{5}), 134.6 (C^{10}), 129.2 (C^{14}), 128.8 (C^{2}), 127.0 (C^{3}), 126.9 (C^{1}), 125.6 (C^{6}), 119.5 (C^{7}), 116.1 (C^{13}), 45.1 (C^{9}), 35.0 (C^{11}); LRMS (ESI-TOF) *m/z*: $[M+H]^+$ 238.221 (100); HRMS (ESI-TOF) *m/z*: $[M+H]^+$ Calculated for $C_{17}H_{20}N^+$: 238.1596, found 238.1599 (0.3 mDa, 1.3 ppm); IR (max/cm^{-1}): 2940w, 2830w, 2776w, 1642w, 1606w, 1491s, 1447m, 1313m, 1162m, 1046m, 913m, 763s, 695s, 583m.

N,N-dimethyl-2-allyl-4-methoxyaniline 94

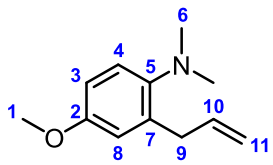

94

Following the method outlined in **6.6** using *N*-allyl-*N,N*-dimethyl-4-methoxyanilinium hexafluorophosphate **184** (0.28 g, 0.82 mmol), title compound was isolated *via* column chromatography (98:2 hexanes:EtOAc), as a colourless oil (0.12 g, 0.62 mmol, 77% yield). ^1H NMR (600 MHz, $CDCl_3$) δ 7.07 (1H, d, J = 8.6 Hz, H^{3}), 6.77 (1H, d, J = 3.0 Hz, H^{8}), 6.73 (1H, dd, J = 8.6, 3.1 Hz, H^{4}), 5.99 (1H, ddt, J = 16.8, 10.1, 6.6 Hz, H^{10}), 5.14 – 5.06 (2H, m, H^{11}), 3.77 (3H, s, H^{1}), 3.49 (2H, d, J = 6.6 Hz, H^{9}), 2.63 (6H, s, H^{6}); ^{13}C NMR (151 MHz, $CDCl_3$) δ 155.9 (C^{2}), 146.1 (C^{5}), 137.8 (C^{10}), 136.6 (C^{7}), 120.6 (C^{3}), 115.9 (C^{11}), 115.7 (C^{8}), 111.8 (C^{4}), 55.5 (C^{1}), 45.7 (C^{6}), 35.1 (C^{9}); LRMS (ESI-TOF) *m/z*: $[M+H]^+$ 192.196 (100); HRMS (ESI-TOF) *m/z*: $[M+H]^+$ Calculated for $C_{12}H_{18}NO^+$: 192.1388, found 192.1395 (0.7 mDa, 3.6 ppm); IR (max/cm^{-1}): 2945w, 2830w, 2776w, 1610w, 1499s, 1451m, 1287m, 1242m, 1162s, 1038s, 913m, 810m, 686m.

N,N-dimethyl-2-allyl-3,4,5-trimethoxyaniline 220

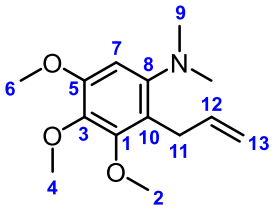

220

Following the method outlined in **6.6** using *N*-allyl-*N,N*-dimethyl-3,4,5-trimethoxyanilinium hexafluorophosphate **185** (0.54 g, 1.36 mmol), title compound was isolated *via* column chromatography (95:5 hexanes:EtOAc), as a brown oil (0.06 g, 0.25 mmol, 68% yield). ^1H NMR (600 MHz, $CDCl_3$) δ 6.49 (1H, s, H^{7}), 6.03 (1H, ddt, J = 16.3, 10.9, 5.8 Hz, H^{12}), 4.96 (1H, dq, J = 19.3, 2.0 Hz, H^{12a}), 4.96 (1H, dq, J = 11.0, 1.9 Hz, H^{12b}), 3.86 (3H, s, H^{2}), 3.85 (3H, s, H^{6}), 3.83 (3H, s, H^{4}), 3.44 (2H, dt, J = 5.9, 1.8 Hz, H^{11}), 2.64 (6H, s, H^{9});^{13}C NMR (151 MHz, $CDCl_3$) δ: 152.9 (C^{1}), 151.9 (C^{5}), 149.0 (C^{8}), 138.8 (C^{3}), 138.6 (C^{12}), 121.4 (C^{10}), 114.2 (C^{13}), 100.0 (C^{7}), 61.0 (C^{2}), 60.8 (C^{4}), 56.1 (C^{6}), 45.7 (C^{9}), 29.7 (C^{11}); LRMS (ESI-TOF) *m/z*: $[M+H]^+$ 252.359 (100); HRMS (ESI-TOF) *m/z*: $[M+H]^+$ Calculated for $C_{14}H_{22}NO_3^+$: 252.1600, found 252.1604 (0.4 mDa, 1.6 ppm); IR (max/cm^{-1}): 2943w, 2829w, 2783w, 1642w, 1581w, 1497s, 1455m, 1409s, 1205m, 1198m, 1120s, 1002s, 906m, 829m.

***N,N*-dimethyl-2-allyl-3,4-(methylenedioxy)aniline 221**

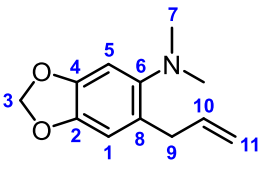

221

Following the method outlined in **6.6** using *N*-allyl-*N,N*-dimethyl-3,4-(methylenedioxy)anilinium hexafluorophosphate **186** (0.57 g, 1.60 mmol), title compound was isolated *via* column chromatography (95:5 hexanes:EtOAc), as a yellow oil (0.25 g, 1.19 mmol, 74% yield). ^{1}H NMR (600 MHz, $CDCl_3$) δ 6.73 (1H, s, H^5), 6.69 (1H, s, H^1), 5.95 (1H, ddt, *J* = 16.7, 10.1, 6.6 Hz, H^{10}), 5.89 (2H, s, H^3), 5.11 – 5.03 (2H, m, $H^{11a\text{-}b}$), 3.43 (2H, d, *J* = 6.5 Hz, H^9), 2.60 (6H, s, H^7); ^{13}C NMR (151 MHz, $CDCl_3$) δ: 146.8 (C^6), 146.2 (C^4), 143.7 (C^2), 138.2 (C^{10}), 128.3 (C^8), 115.6 (C^{11}), 109.7 (C^1), 101.5 (C^5), 101.0 (C^9), 45.8 (C^7), 34.9 (C^9); LRMS (ESI-TOF) *m/z*: $[M+H]^+$ 206.334 (100); HRMS (ESI-TOF) *m/z*: $[M+H]^+$ Calculated for $C_{12}H_{16}NO_2^+$: 206.1181, found 206.1177 (-0.4 mDa, -1.9 ppm); IR (max/cm^{-1}): 2985w, 2943w, 2825w, 2783w, 1645w, 1486s, 1458m, 1234m, 1142s, 1043s, 930s, 846m, 644w.

***N,N*-dimethyl-2-allyl-4-(trifluoromethyl)aniline 201**

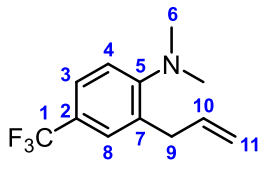

201

Following the method outlined in **6.6** using *N*-allyl-*N,N*-dimethyl-4-(trifluoromethyl)anilinium hexafluorophosphate **187** (0.21 g, 0.55 mmol), title compound was isolated *via* column chromatography (98:2 hexanes:EtOAc), as a colourless oil (0.05 g, 0.21 mmol, 44% yield). ^{1}H NMR (600 MHz, $CDCl_3$) δ 7.45 – 7.40 (2H, m, $H^{3,8}$), 7.13 – 7.08 (1H, m, H^4), 5.98 (1H, ddt, *J* = 16.7, 10.3, 6.5 Hz, H^{10}), 5.22 – 5.11 (2H, m, H^{11}), 3.51 (2H, dt, *J* = 6.5, 1.6 Hz, H^9), 2.74 (6H, s, H^6); ^{13}C NMR (151 MHz, $CDCl_3$) δ 155.7 (C^5), 136.9 (C^{10}), 134.3 (C^7), 127.3 (1C, q, *J* = 3.8 Hz, C^8), 124.7 (1C, q, *J* = 271 Hz, C^1), 124.5 (1C, q, *J* = 32.6 Hz, C^2), 124.0 (1C, q, *J* = 3.8 Hz, C^4), 118.8 (C^3), 116.9 (C^{11}), 44.5 (C^6), 35.3 (C^9); ^{19}F NMR (376 MHz, $CDCl_3$) δ - 61.7 (1F, s); LRMS (ESI-TOF) *m/z*: $[M+H]^+$ 230.227 (100); HRMS (ESI-TOF) *m/z*: $[M+H]^+$ Calculated for $C_{12}H_{15}NF_3^+$: 180.1157, found 230.1160 (0.3 mDa, 1.3 ppm); IR (max/cm^{-1}): 2961w, 2840w, 2793w, 1618m, 1506w, 1332s, 1263m, 1155m, 1108s, 1017m, 801m, 603m.

***N,N*-dimethyl-2-allyl-4-fluoroaniline 202**

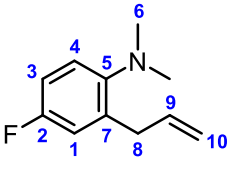

202

Following the method outlined **6.6** using *N*-allyl-*N,N*-dimethyl-4-fluoroanilinium hexafluorophosphate **188** (0.40 g, 1.20 mmol) of precursor hexafluorophosphate salt, title compound was isolated *via* column chromatography (99:1 hexanes:EtOAc), as a colourless oil (0.04 g, 0.16 mmol, 16% yield). ^{1}H NMR (600 MHz, $CDCl_3$) δ 7.06 (1H, dd, *J* = 8.7, 5.3 Hz, H^4), 6.90 (1H, dd, *J* = 9.7, 3.1 Hz, H^1), 6.86 (1H, td, *J* = 8.4, 3.1 Hz, H^3), 5.96 (1H, ddt, *J* = 17.8, 9.1, 6.6 Hz, H^9), 5.15 – 5.08 (2H, m, H^{10}), 3.49 (2H, dt, *J* = 6.6, 1.6 Hz, H^8), 2.64 (6H, s, H^6); ^{13}C NMR (151 MHz, $CDCl_3$) δ 159.2 (1C, d, *J* = 244 Hz, C^2), 148.7 (1C, d, *J* = 2.6 Hz, C^5),

137.3 (1C, d, J = 7.2 Hz, C^7), 137.2 (C^9), 120.4 (1C, d, J = 8.4 Hz, C^4), 116.6 (1C, d, J = 22.2 Hz, C^1), 116.4 (C^{10}), 113.2 (1C, d, J = 21.9 Hz, C^3), 45.5 (C^6), 34.9 (C^8); ^{19}F NMR (376 MHz, $CDCl_3$) δ -120.2 – -120.3 (1F, m); LRMS (ESI-TOF) *m/z*: $[M+H]^+$ 180.356 (100); HRMS (ESI-TOF) *m/z*: $[M+H]^+$ Calculated for $C_{11}H_{15}NF^+$: 180.1189, found 180.1187 (-0.2 mDa, -1.1 ppm); IR (max/cm^{-1}): 2989w, 2949w, 2836w, 2786w, 1645w, 1497s, 1455m, 1269m, 1235m, 1159s, 945s, 872s, 815s, 697s, 587m.

N,N-dimethyl-2-allyl-4-chloroaniline 203

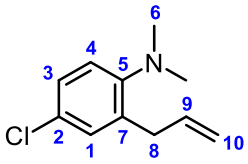

203

Following the method outlined in **6.6** using *N*-allyl-*N,N*-dimethyl-4-chloroanilinium hexafluorophosphate **189** (0.28 g, 0.80 mmol), title compound was isolated *via* column chromatography (99:1 hexanes:EtOAc), as a colourless oil (0.13 g, 0.64 mmol, 81% yield). ^{1}H NMR (600 MHz, $CDCl_3$) δ 7.16 (1H, d, J = 2.5 Hz, H^3), 7.13 (1H, dd, J = 8.5, 2.5 Hz, H^1), 7.00 (1H, d, J = 8.5 Hz, H^4), 5.95 (1H, ddt, J = 16.7, 10.5, 6.9 Hz, H^9), 5.15 – 5.09 (2H, m, H^{10}), 3.45 (2H, d, J = 6.8 Hz, H^8), 2.65 (6H, s, H^6); ^{13}C NMR (151 MHz, $CDCl_3$) δ: 151.3 (C^5), 137.1 (C^9), 136.6 (C^7), 130.1 (C^3), 128.6 (C^2), 126.8 (C^1), 120.6 (C^4), 116.9 (C^{10}), 45.1 (C^6), 34.9 (C^8); LRMS (ESI-TOF) *m/z*: $[^{35}Cl\text{-}M+H]^+$ 196.182 (100), $[^{37}Cl\text{-}M+H]^+$ 198.195 (33); HRMS (ESI-TOF) *m/z*: $[M+H]^+$ Calculated for $C_{11}H_{15}N^{35}Cl^+$: 196.0893, found 196.0901 (0.8 mDa, 4.1 ppm); IR (max/cm^{-1}): 2924w, 2830w, 2784w, 1642w, 1491s, 1455m, 1317m, 1157s, 1117s, 917s, 820s, 629s, 567s.

N,N-dimethyl 2-allyl-4-bromoaniline 204

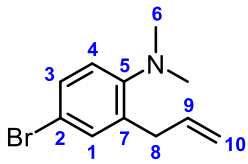

204

Following the method outlined in **6.6** using *N*-allyl-*N,N*-dimethyl-4-bromoanilinium hexafluorophosphate **190** (0.62 g, 1.60 mmol), title compound was isolated *via* column chromatography (97:3 hexanes:EtOAc), as a yellow oil (0.24 g, 1.01 mmol, 63% yield). ^{1}H NMR (600 MHz, $CDCl_3$) δ 7.30 (1H, d, J = 2.5 Hz, H^1), 7.28 (1H, dd, J = 8.5, 2.4 Hz, H^3), 6.95 (1H, d, J = 8.5 Hz, H^4), 5.95 (1H, ddt, J = 17.9, 10.7, 6.5 Hz, H^9), 5.15 – 5.10 (2H, m, H^{10}), 3.46 (2H, d, J = 6.6 Hz, H^8), 2.66 (6H, s, H^6); ^{13}C NMR (151 MHz, $CDCl_3$) δ 151.8 (C^5), 137.1 (C^9), 137.0 (C^7), 133.0 (C^1), 129.8 (C^3), 121.0 (C^4), 116.6 (C^{10}), 116.1 (C^2), 45.0 (C^6), 34.9 (C^8); LRMS (ESI-TOF) *m/z*: $[^{79}BrM+H]^+$ 240.273 (99), $[^{81}BrM+H]^+$ 242.249 (100); HRMS (ESI-TOF) *m/z*: $[M+H]^+$ Calculated for $C_{11}H_{15}N^{79}Br^+$: 240.0388, found 288.0408 (2.0 mDa, 8.3 ppm); IR (max/cm^{-1}): 2947w, 2836w, 2786w, 1644w, 1493s, 1455m, 1322m, 1158s, 1113s, 953m, 919s, 820s, 606s, 568s.

***N,N*-dimethyl-2-allyl-4-iodoaniline 205**

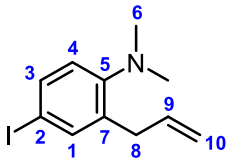

205

Following the method outlined in **6.6** using *N*-allyl-*N,N*-dimethyl-4-iodoanilinium hexafluorophosphate **191** (0.35 g, 0.80 mmol), title compound was isolated *via* column chromatography (99:1 hexanes:EtOAc), as a colourless oil (0.22 g, 0.77 mmol, 96% yield). ^{1}H NMR (600 MHz, $CDCl_3$) δ 7.49 – 7.44 (2H, m, $H^{1,3}$), 6.82 (1H, d, *J* = 8.6 Hz, H^4), 5.99 – 5.89 (1H, m, H^9), 5.15 – 5.08 (2H, m, H^{10}), 3.42 (2H, dt, *J* = 6.4, 1.5 Hz, H^8), 2.66 (6H, s, H^6); ^{13}C NMR (151 MHz, $CDCl_3$) δ 152.6 (C^5), 139.0 (C^1), 137.2 (C^7), 137.1 (C^9), 135.9 (C^3), 121.5 (C^4), 116.6 (C^{10}), 86.8 (C^2), 44.8 (C^6), 34.8 (C^8); LRMS (ESI-TOF) *m/z*: $[M+H]^+$ 228.178 (100); HRMS (ESI-TOF) *m/z*: $[M+H]^+$ Calculated for $C_{11}H_{15}NI^+$: 288.0249, found 288.0261 (1.2 mDa, 4.2 ppm); IR (max/cm^{-1}): 2944w, 2830w, 2780w, 1638w, 1487s, 1451m, 1317m, 1157s, 1104s, 948m, 917s, 815s, 592m, 566s.

***N*-(3-allyl-4-(dimethylamino)phenyl)acetamide 206**

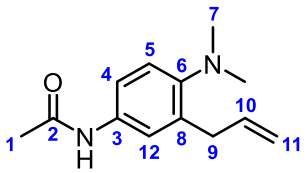

206

Following the method outlined in **6.6** using *N*-allyl-*N,N*-dimethyl-4-acetanilideanilinium hexafluorophosphate **192** (0.58 g, 1.59 mmol), title compound was isolated *via* SiO_2 column chromatography (70:30 hexanes:EtOAc) followed by a second SiO_2 column chromatography (hexanes:Et_2O, 80:20 + 2.5% Et_3N), as a white crystalline solid (0.10 g, 0.44 mmol, 28% yield). ^{1}H NMR (600 MHz, MeOD-d_4) δ 7.38 (1H, dd, *J* = 8.6, 2.6 Hz, H^4), 7.30 (1H, d, *J* = 2.5 Hz, H^{12}), 7.08 (1H, d, *J* = 8.6 Hz, H^5), 5.97 (1H, ddt, *J* = 16.7, 10.1, 6.5 Hz, H^{10}), 5.12 – 5.03 (2H, m, H^{11}), 3.46 (2H, dt, *J* = 6.6, 1.6 Hz, H^9), 2.63 (6H, s, H^7), 2.08 (3H, s, H^1); ^{13}C NMR (151 MHz, MeOD-d_4) δ 171.4 (C^2), 150.2 (C^6), 139.0 (C^{10}), 136.4 (C^8), 135.4 (C^3), 123.3 (C^{12}), 120.7 (C^5), 120.2 (C^4), 116.1 (C^{11}), 45.6 (C^7), 35.9 (C^9), 23.6 (C^1); LRMS (ESI-TOF) *m/z*: $[M+H]^+$ 219.408 (100); HRMS (ESI-TOF) *m/z*: $[M+H]^+$ Calculated for $C_{13}H_{19}N_2O^+$: 219.1497, found 219.1499 (0.2 mDa, 0.9 ppm); IR (max/cm^{-1}): 3290w, 2921w, 2794w, 1658s, 1614s, 1549s, 1503s, 1402m, 1328s, 1185m, 1013m, 885s, 770s, 584s, 541s; mp: 86-88 ^{o}C.

***N,N*-dimethyl-2-allyl-3(5)-cyanoaniline 227a, 227b**

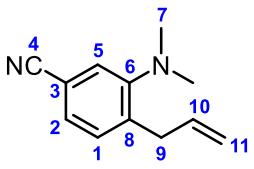

227a

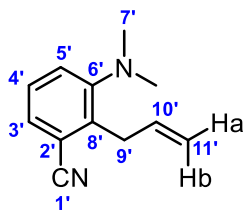

227b

Following the method outlined in **6.6** using *N*-allyl-*N,N*-dimethyl-3-cyanoanilinium hexafluoro phosphate **193** (0.53 g, 1.60 mmol), title compound was isolated *via* SiO_2 column chromatography (98:2 hexanes:EtOAc) followed by neutral Al_2O_3 column chromatography (98:2 hexanes:Et_2O + 2.5% Et_3N), as a yellow oil (1:1 regioisomer mixture, 0.07 g, 0.37 mmol, 23%

yield). ^{1}H NMR (600 MHz, MeOD-d_4) δ 7.47 (1H, dd, *J* = 8.0, 1.4 Hz, $H^{5'}$), 7.39 (1H, s, H^{5}), 7.38 (1H, dd, *J* = 7.7, 1.5 Hz, $H^{3'}$), 7.35 (1H, d, *J* = 7.8 Hz, $H^{4'}$), 7.33 – 7.29 (2H, m, $H^{1,2}$), 6.02 (1H, ddt, *J* = Hz, $H^{10'}$), 5.96 (1H, ddt, *J* = Hz, H^{10}), 5.15 – 5.05 (2H, m, H^{11}), 5.07 (1H, dq, *J* = 10.2, 1.8 Hz, $H^{11'a}$), 4.97 (1H, dq, *J* = 17.2, 1.8 Hz, $H^{11'b}$), 3.70 (2H, dt, *J* = 5.9, 1.8 Hz, $H^{9'}$), 3.53 (2H, dt, *J* = 6.5, 1.6 Hz, H^{9}), 2.70 (6H, s, H^{7}), 2.68 (6H, s, $H^{7'}$); ^{13}C NMR (151 MHz, MeOD-d_4) δ 155.4 ($C^{6'}$), 154.8 (C^{6}), 141.8 (C^{8}), 139.8 ($C^{8'}$), 137.7 (C^{10}), 136.9 ($C^{10'}$), 132.4 (C^{1}), 129.2 ($C^{4'}$), 128.9 ($C^{3'}$), 127.5 (C^{2}), 126.4 ($C^{5'}$), 123.8 (C^{5}), 120.0 (C^{4}), 119.2 ($C^{1'}$), 117.1 (C^{11}), 116.5 ($C^{11'}$), 115.3 ($C^{2'}$), 111.5 (C^{3}), 45.5 ($C^{7'}$), 44.9 (C^{7}), 36.2 (C^{9}), 34.8 ($C^{9'}$); LRMS (ESI-TOF) *m/z*: $[M+H]^+$ 187.298 (100); HRMS (ESI-TOF) *m/z*: $[M+H]^+$ Calculated for $C_{12}H_{15}N_2^+$: 187.1235, found 187.1233 (-0.2 mDa, -1.1 ppm); IR (max/cm^{-1}): 2989w, 2955w, 2840w, 2794w, 2235m, 1644w, 1588m, 1501m, 1455m, 1410m, 1325m, 1189m, 987s, 922s, 804m, 747m.

N-benzyl-*N*-methyl-2-allylaniline 233

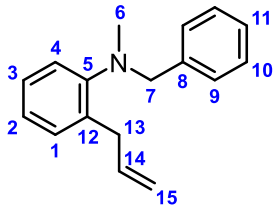

233

Following the method outlined in **6.6** using *N*-allyl-*N*-benzyl-*N*-methylanilinium hexafluorophosphate **194** (0.31 g, 0.80 mmol), title compound was isolated *via* column chromatography (99:1 hexanes:EtOAc), as a colourless oil (0.13 g, 0.56 mmol, 71% yield). ^{1}H NMR (600 MHz, $CDCl_3$) δ 7.39 (2H, d, *J* = 8.1 Hz, H^{9}), 7.35 (2H, t, *J* = 7.5 Hz, H^{10}), 7.28 (1H, tt, *J* = 7.2, 2.3 Hz, H^{8}) 7.25 (1H, dd, *J* = 7.6, 1.8 Hz, H^{1}), 7.22 (1H, td, *J* = 7.4, 2.0 Hz, H^{3}), 7.17 (1H, dd, *J* = 8.0, 1.4 Hz, H^{4}), 7.08 (1H, td, *J* = 7.4, 1.4 Hz, H^{2}), 6.04 (1H, ddt, *J* = 15.8, 11.0, 6.6 Hz, H^{14}), 5.13 – 5.07 (2H, m, H^{15}), 4.03 (2H, s, H^{7}), 3.61 (2H, dt, *J* = 6.6, 1.6 Hz, H^{13}), 2.58 (3H, s, H^{6}); ^{13}C NMR (151 MHz, $CDCl_3$) δ 152.2 (C^{5}), 139.0 (C^{8}), 137.8 (C^{14}), 135.2 (C^{12}), 130.2 (C^{1}), 128.4 (C^{9}), 128.3 (C^{10}), 127.0 (C^{11}), 126.9 (C^{3}), 123.6 (C^{2}), 120.1 (C^{4}), 115.7 (C^{15}), 61.6 (C^{7}), 41.7 (C^{6}), 35.0 (C^{13}); LRMS (ESI-TOF) *m/z*: $[M+H]^+$ 238.221 (100); HRMS (ESI-TOF) *m/z*: $[M+H]^+$ Calculated for $C_{17}H_{20}N^+$: 238.1596, found 238.1604 (0.8 mDa, 3.4 ppm); IR (max/cm^{-1}): 2981w, 2842w, 2799w, 1638m, 1593m, 1496s, 1451m, 1362m, 1175m, 943m, 914m, 726s, 695s, 576s.

N-methyl-7-allylindoline 230

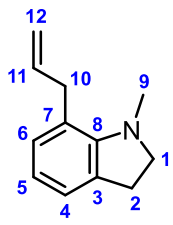

230

Following the method outlined in **6.6** using *N*-allyl-*N*-methylindolinium hexafluorophosphate **195** (0.51 g, 1.61 mmol), title compound was isolated *via* column chromatography (98:2 hexanes:EtOAc), as a yellow oil (0.21 g, 1.18 mmol, 74% yield). ^{1}H NMR (600 MHz, $CDCl_3$) δ 7.00 (1H, d, *J* = 7.4 Hz, H^{4}), 6.89 (1H, d, *J* = 7.4 Hz, H^{7}), 6.72 (1H, t, *J* = 7.4 Hz, H^{6}), 6.04 (1H, ddt, *J* = 17.1, 10.2, 5.9 Hz, H^{12}), 5.12 (1H, dq, *J* = 10.2, 1.7 Hz, H^{13b}), 5.04 (1H, dq, *J* = 17.1, 1.8 Hz, H^{13a}), 3.50 (2H, d, *J* = 5.9 Hz, H^{11}), 3.32 (2H, t, *J* = 8.4 Hz, H^{1}), 2.95 (2H, t, *J* = 8.4 Hz, H^{2}), 2.92 (3H, s, H^{10}); ^{13}C NMR (151 MHz, $CDCl_3$) δ 151.2 (C^{9}), 137.5 (C^{12}), 131.9

(C^3), 130.2 (C^7), 122.9 (C^4), 122.2 (C^8), 119.5 (C^6), 116.0 (C^{13}), 57.6 (C^1), 40.5 (C^{10}), 36.6 (C^{11}), 29.0 (C^2); LRMS (ESI-TOF) *m/z*: $[M+H]^+$ 174.143 (100); HRMS (ESI-TOF) *m/z*: $[M+H]^+$ Calculated for $C_{12}H_{16}N^+$: 174.1283, found 174.1290 (0.7 mDa, 4.0 ppm); IR (max/cm^{-1}): 2965s, 2931s, 2855s, 1664w, 1610w, 1455s, 1417m, 1273s, 1106m, 1061m, 912s, 746s.

_N_-methyl-8-allyl-(1H,2H,3H,4H)-tetrahydroquinoline 114

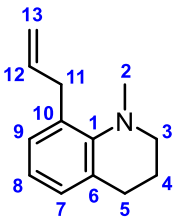

114

Following the method outlined in **6.6** using *N*-allyl-*N*-methyl-(1H,2H,3H,4H)-tetrahydroquinolinium hexafluorophosphate **196** (0.53 g, 1.60 mmol), title compound was isolated *via* column chromatography (95:5 hexanes:Et_2O), as a colourless oil (0.24 g, 1.26 mmol, 79% yield). ^{1}H NMR (600 MHz, $CDCl_3$) δ 7.03 (1H, dd, *J* = 7.4, 2.1 Hz, H^7), 6.96 – 6.86 (2H, m, $H^{9\text{-}8}$), 6.01 (1H, ddt, *J* = 16.6, 10.1, 6.5 Hz, H^{12}), 5.14 (1H, d, *J* = 16.8 Hz, H^{13a}), 5.11 (1H, d, *J* = 10.7 Hz, H^{13b}), 3.46 (2H, d, *J* = 6.5 Hz, 2H, H^{11}), 3.13 – 3.07 (2H, m, H^3), 2.82 (2H, t, *J* = 6.8 Hz, H^5), 2.71 (3H, s, H^2), 1.91 – 1.80 (2H, m, H^4);[165] ^{13}C NMR (151 MHz, $CDCl_3$) δ 147.9 (C^1), 138.1 (C^{12}), 133.4 (C^{10}), 129.3 (C^6), 128.0 (C^7), 127.8 (C^8), 121.9 (C^9), 115.8 (C^{13}), 52.0 (C^3), 44.2 (C^2), 35.2 (C^{11}), 28.0 (C^5), 16.8 (C^4); LRMS (ESI-TOF) *m/z*: $[M+H]^+$ 188.357 (100); HRMS (ESI-TOF) *m/z*: $[M+H]^+$ Calculated for $C_{13}H_{18}N^+$: 188.1439, found 188.1435 (-0.4 mDa, -2.1 ppm); IR (max/cm^{-1}): 2943m, 2810w, 1641w, 1467s, 1333m, 1128m, 998m, 914m, 762s, 561m.

APPENDIX A: Droplet Chemistry Crystallographic Data

Crystal data and structure refinement for 18srv032

Identification code	18srv032
Empirical formula	$C_{10}H_6N_2$
Formula weight	154.17
Temperature/K	120.0
Crystal system	monoclinic
Space group	$P2_1/c$
a/Å	9.3490(9)
b/Å	3.8739(4)
c/Å	21.893(2)
α/°	90
β/°	93.656(4)
γ/°	90
Volume/Å^3	791.29(13)
Z	4
ρ_{calc}g/cm^3	1.294
μ/mm^{-1}	0.080
F(000)	320.0
Crystal size/mm^3	0.370 × 0.130 × 0.020
Radiation	Mo Kα (λ = 0.71073)
2Θ range for data collection/°	4.366 to 55.996
Index ranges	-12 ≤ h ≤ 12, -5 ≤ k ≤ 5, -28 ≤ l ≤ 28
Reflections collected	10295
Independent reflections	1908 [R_{int} = 0.0532, R_{sigma} = 0.0560]
Data/restraints/parameters	1908/0/133
Goodness-of-fit on F^2	1.029
Final R indexes [I>=2σ (I)]	R_1 = 0.0437, wR_2 = 0.0977
Final R indexes [all data]	R_1 = 0.0686, wR_2 = 0.1063
Largest diff. peak/hole / e Å^{-3}	0.17/-0.25

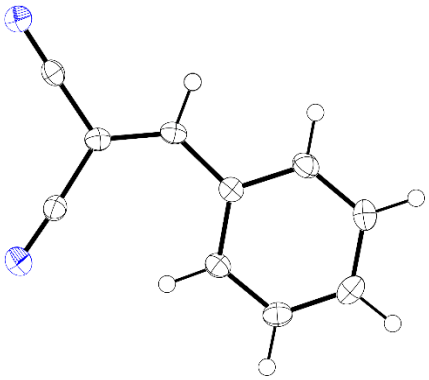

Crystal data and structure refinement for 18srv419

Identification code	18srv419
Empirical formula	$C_{10}H_{10}N_2O$
Formula weight	174.20
Temperature/K	120.0
Crystal system	monoclinic
Space group	$P2_1/c$
a/Å	4.7523(5)
b/Å	15.4067(15)
c/Å	12.1922(12)
α/°	90
β/°	94.393(5)
γ/°	90
Volume/Å^3	890.06(15)
Z	4
ρ_{calc}g/cm^3	1.300
μ/mm^{-1}	0.087
F(000)	368.0
Crystal size/mm^3	0.793 × 0.091 × 0.087
Radiation	Mo Kα (λ = 0.71073)
2Θ range for data collection/°	4.268 to 55.000
Index ranges	-6 ≤ h ≤ 6, -19 ≤ k ≤ 20, -15 ≤ l ≤ 15
Reflections collected	14225
Independent reflections	2041 [R_{int} = 0.0715, R_{sigma} = 0.0488]
Data/restraints/parameters	2041/0/159
Goodness-of-fit on F^2	1.045
Final R indexes [I>=2σ (I)]	R_1 = 0.0412, wR_2 = 0.1015
Final R indexes [all data]	R_1 = 0.0573, wR_2 = 0.1097
Largest diff. peak/hole / e Å^{-3}	0.27/-0.19

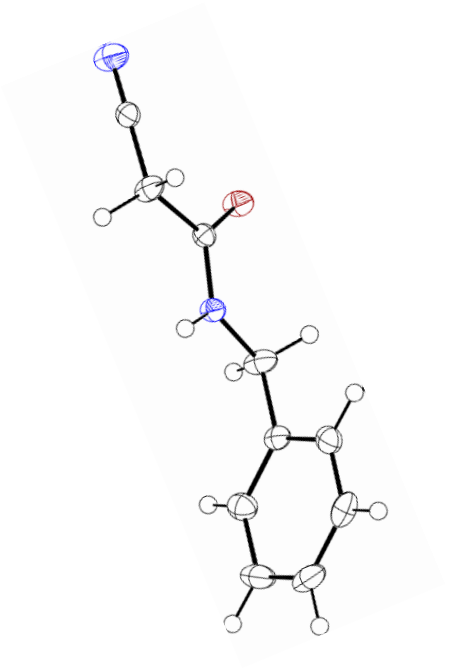

Crystal data and structure refinement for 18srv189

Identification code	18srv189
Empirical formula	$C_{10}H_5NO_2$
Formula weight	171.15
Temperature/K	120.0
Crystal system	monoclinic
Space group	$P2_1/c$
a/Å	11.7037(9)
b/Å	9.2188(7)
c/Å	7.1459(5)
α/°	90
β/°	94.790(3)
γ/°	90
Volume/Å^3	768.31(10)
Z	4
ρ_{calc}g/cm^3	1.480
μ/mm^{-1}	0.106
F(000)	352.0
Crystal size/mm^3	0.401 × 0.203 × 0.068
Radiation	Mo Kα (λ = 0.71073)
2Θ range for data collection/°	5.632 to 60.26
Index ranges	-16 ≤ h ≤ 16, -13 ≤ k ≤ 13, -10 ≤ l ≤ 10
Reflections collected	15308
Independent reflections	2250 [R_{int} = 0.0364, R_{sigma} = 0.0258]
Data/restraints/parameters	2250/0/138
Goodness-of-fit on F^2	1.026
Final R indexes [I>=2σ (I)]	R_1 = 0.0396, wR_2 = 0.1077
Final R indexes [all data]	R_1 = 0.0579, wR_2 = 0.1168
Largest diff. peak/hole / e Å^{-3}	0.43/-0.23

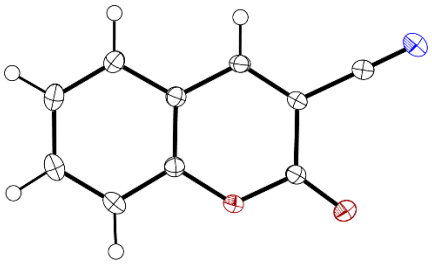

Crystal data and structure refinement for 18srv246

Identification code	18srv246
Empirical formula	$C_{11}H_7NO_3$
Formula weight	201.18
Temperature/K	120.0
Crystal system	triclinic
Space group	P-1
a/Å	6.6110(10)
b/Å	7.2426(11)
c/Å	10.8014(16)
α/°	71.657(6)
β/°	84.232(7)
γ/°	66.775(6)
Volume/Å^3	450.96(12)
Z	2
ρ_{calc}g/cm^3	1.482
μ/mm^{-1}	0.110
F(000)	208.0
Crystal size/mm^3	0.575 × 0.243 × 0.048
Radiation	Mo Kα (λ = 0.71073)
2Θ range for data collection/°	6.418 to 60.176
Index ranges	-9 ≤ h ≤ 9, -10 ≤ k ≤ 10, -15 ≤ l ≤ 15
Reflections collected	9160
Independent reflections	2653 [R_{int} = 0.0300, R_{sigma} = 0.0347]
Data/restraints/parameters	2653/0/164
Goodness-of-fit on F^2	1.036
Final R indexes [I>=2σ (I)]	R_1 = 0.0432, wR_2 = 0.1154
Final R indexes [all data]	R_1 = 0.0690, wR_2 = 0.1276
Largest diff. peak/hole / e Å^{-3}	0.43/-0.25

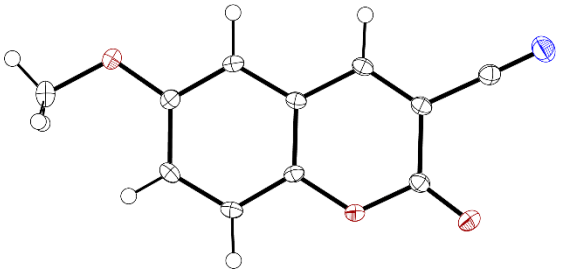

Crystal data and structure refinement for 18srv414

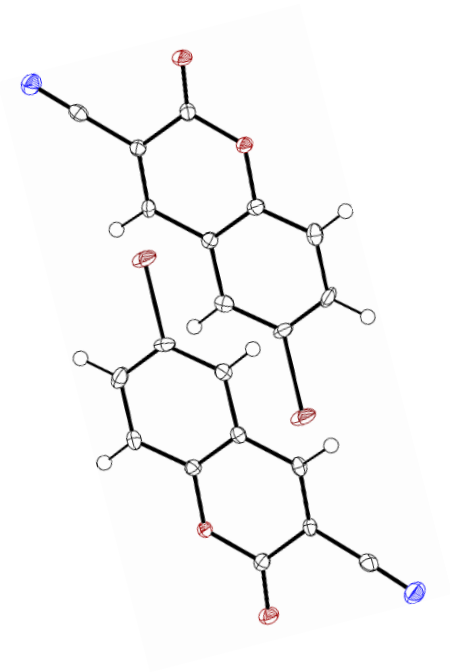

Identification code	18srv414
Empirical formula	$C_{10}H_4BrNO_2$
Formula weight	250.05
Temperature/K	120.0
Crystal system	monoclinic
Space group	$P2_1/c$
a/Å	10.9797(5)
b/Å	12.5503(6)
c/Å	13.1193(6)
α/°	90
β/°	98.065(2)
γ/°	90
Volume/Å^3	1789.94(14)
Z	8
ρ_{calc}g/cm^3	1.856
μ/mm^{-1}	4.560
F(000)	976.0
Crystal size/mm^3	0.207 × 0.163 × 0.124
Radiation	Mo Kα (λ = 0.71073)
2Θ range for data collection/°	4.512 to 54.968
Index ranges	-14 ≤ h ≤ 14, -16 ≤ k ≤ 16, -17 ≤ l ≤ 17
Reflections collected	32916
Independent reflections	4105 [R_{int} = 0.0709, R_{sigma} = 0.0515]
Data/restraints/parameters	4105/0/254
Goodness-of-fit on F^2	1.035
Final R indexes [I>=2σ (I)]	R_1 = 0.0338, wR_2 = 0.0541
Final R indexes [all data]	R_1 = 0.0649, wR_2 = 0.0600
Largest diff. peak/hole / e Å^{-3}	0.57/-0.49

Crystal data and structure refinement for 18srv188

Identification code	18srv188
Empirical formula	$C_{10}H_6O_4$
Formula weight	190.15
Temperature/K	120.0
Crystal system	monoclinic
Space group	$P2_1/n$
a/Å	11.2128(8)
b/Å	5.4642(4)
c/Å	13.7114(9)
α/°	90
β/°	107.239(3)
γ/°	90
Volume/Å^3	802.35(10)
Z	4
ρ_{calc}g/cm^3	1.574
μ/mm^{-1}	0.124
F(000)	392.0
Crystal size/mm^3	0.368 × 0.368 × 0.110
Radiation	Mo Kα (λ = 0.71073)
2Θ range for data collection/°	5.582 to 65.152
Index ranges	-16 ≤ h ≤ 16, -8 ≤ k ≤ 8, -20 ≤ l ≤ 20
Reflections collected	14525
Independent reflections	2921 [R_{int} = 0.0484, R_{sigma} = 0.0426]
Data/restraints/parameters	2921/0/151
Goodness-of-fit on F^2	1.052
Final R indexes [I>=2σ (I)]	R_1 = 0.0461, wR_2 = 0.1210
Final R indexes [all data]	R_1 = 0.0717, wR_2 = 0.1341
Largest diff. peak/hole / e Å^{-3}	0.50/-0.24

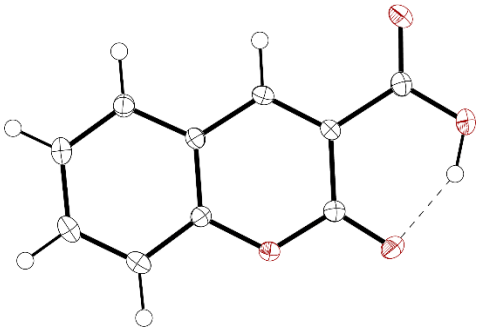

Crystal data and structure refinement for 18srv192

Identification code	18srv192
Empirical formula	$C_{11}H_8O_5$
Formula weight	220.17
Temperature/K	120.0
Crystal system	monoclinic
Space group	$P2_1$
a/Å	3.7519(3)
b/Å	10.8480(7)
c/Å	11.4673(8)
α/°	90
β/°	97.474(3)
γ/°	90
Volume/Å^3	462.76(6)
Z	4
ρ_{calc}g/cm^3	1.580
μ/mm^{-1}	0.127
F(000)	228.0
Crystal size/mm^3	0.305 × 0.259 × 0.084
Radiation	Mo Kα (λ = 0.71073)
2Θ range for data collection/°	5.190 to 65.108
Index ranges	-5 ≤ h ≤ 5, -16 ≤ k ≤ 16, -16 ≤ l ≤ 17
Reflections collected	8825
Independent reflections	3354 [R_{int} = 0.0392, R_{sigma} = 0.0618]
Data/restraints/parameters	3354/1/177
Goodness-of-fit on F^2	0.993
Final R indexes [I>=2σ (I)]	R_1 = 0.0447, wR_2 = 0.0973
Final R indexes [all data]	R_1 = 0.0738, wR_2 = 0.1080
Largest diff. peak/hole / e Å^{-3}	0.38/-0.28
Flack parameter	-0.2(6)

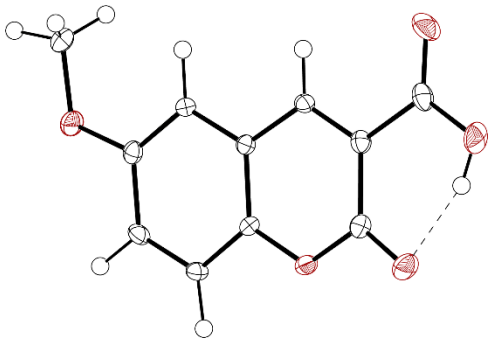

.

Crystal data and structure refinement for 19srv278

Identification code	19srv278
Empirical formula	$C_{10}H_5BrO_4$
Formula weight	269.05
Temperature/K	120.0
Crystal system	monoclinic
Space group	$P2_1/c$
a/Å	12.8408(5)
b/Å	10.9713(4)
c/Å	32.6028(12)
α/°	90
β/°	91.4590(10)
γ/°	90
Volume/Å^3	4591.6(3)
Z	20
ρ_{calc}g/cm^3	1.946
μ/mm^{-1}	4.464
F(000)	2640.0
Crystal size/mm^3	0.267 × 0.129 × 0.129
Radiation	Mo Kα (λ = 0.71073)
2Θ range for data collection/°	3.918 to 59.998
Index ranges	-18 ≤ h ≤ 17, -15 ≤ k ≤ 15, -45 ≤ l ≤ 45
Reflections collected	70167
Independent reflections	13374 [R_{int} = 0.0471, R_{sigma} = 0.0511]
Data/restraints/parameters	13374/0/697
Goodness-of-fit on F^2	1.063
Final R indexes [I>=2σ (I)]	R_1 = 0.0434, wR_2 = 0.0874
Final R indexes [all data]	R_1 = 0.0718, wR_2 = 0.0959
Largest diff. peak/hole / e Å^{-3}	1.05/-0.94

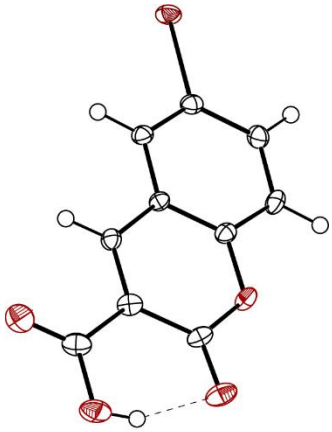

Crystal data and structure refinement for 18srv420

Identification code	18srv420
Empirical formula	$C_{10}H_7NO_3$
Formula weight	189.17
Temperature/K	100.0
Crystal system	monoclinic
Space group	$P2_1/c$
a/Å	4.7623(8)
b/Å	14.184(2)
c/Å	12.220(2)
α/°	90
β/°	96.671(3)
γ/°	90
Volume/Å^3	819.9(2)
Z	4
ρ_{calc}g/cm^3	1.532
μ/mm^{-1}	0.108
F(000)	392.0
Crystal size/mm^3	0.086 × 0.008 × 0.005
Radiation	? (λ = 0.6889)
2Θ range for data collection/°	4.280 to 57.994
Index ranges	-6 ≤ h ≤ 6, -19 ≤ k ≤ 19, -17 ≤ l ≤ 17
Reflections collected	11085
Independent reflections	2383 [R_{int} = 0.0693, R_{sigma} = 0.0691]
Data/restraints/parameters	2383/0/155
Goodness-of-fit on F^2	1.105
Final R indexes [I>=2σ (I)]	R_1 = 0.0576, wR_2 = 0.1619
Final R indexes [all data]	R_1 = 0.0702, wR_2 = 0.1712
Largest diff. peak/hole / e Å^{-3}	0.56/-0.42

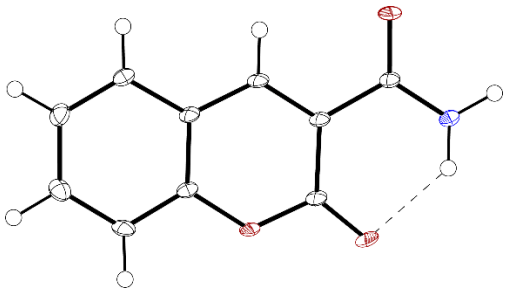

Crystal data and structure refinement for 18srv422

Identification code	18srv422
Empirical formula	$C_{11}H_9NO_4$
Formula weight	219.19
Temperature/K	120.0
Crystal system	monoclinic
Space group	$P2_1/n$
a/Å	7.7638(19)
b/Å	12.316(3)
c/Å	10.322(3)
α/°	90
β/°	111.033(9)
γ/°	90
Volume/Å^3	921.2(4)
Z	4
ρ_{calc}g/cm^3	1.580
μ/mm^{-1}	0.122
F(000)	456.0
Crystal size/mm^3	0.370 × 0.092 × 0.074
Radiation	Mo Kα (λ = 0.71073)
2Θ range for data collection/°	5.368 to 54.992
Index ranges	-10 ≤ h ≤ 10, -16 ≤ k ≤ 16, -13 ≤ l ≤ 13
Reflections collected	17201
Independent reflections	2112 [R_{int} = 0.0452, R_{sigma} = 0.0276]
Data/restraints/parameters	2112/0/182
Goodness-of-fit on F^2	1.043
Final R indexes [I>=2σ (I)]	R_1 = 0.0377, wR_2 = 0.0948
Final R indexes [all data]	R_1 = 0.0560, wR_2 = 0.1027
Largest diff. peak/hole / e Å^{-3}	0.30/-0.20

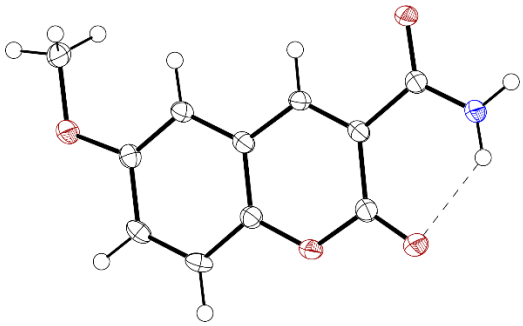

Crystal data and structure refinement for 18srv415

Identification code	18srv415
Empirical formula	$C_{10}H_6BrNO_3$
Formula weight	268.07
Temperature/K	120.0
Crystal system	triclinic
Space group	P-1
a/Å	6.9096(7)
b/Å	11.1186(11)
c/Å	12.5910(13)
α/°	91.032(3)
β/°	100.294(3)
γ/°	102.726(3)
Volume/Å^3	926.69(16)
Z	4
ρ_{calc}g/cm^3	1.921
μ/mm^{-1}	4.418
F(000)	528.0
Crystal size/mm^3	0.073 × 0.069 × 0.052
Radiation	Mo Kα (λ = 0.71073)
2Θ range for data collection/°	4.850 to 50.224
Index ranges	-8 ≤ h ≤ 8, -13 ≤ k ≤ 13, -14 ≤ l ≤ 14
Reflections collected	6532
Independent reflections	3294 [R_{int} = 0.0563, R_{sigma} = 0.0953]
Data/restraints/parameters	3294/4/288
Goodness-of-fit on F^2	0.988
Final R indexes [I>=2σ (I)]	R_1 = 0.0384, wR_2 = 0.0553
Final R indexes [all data]	R_1 = 0.0757, wR_2 = 0.0601
Largest diff. peak/hole / e Å^{-3}	0.47/-0.42

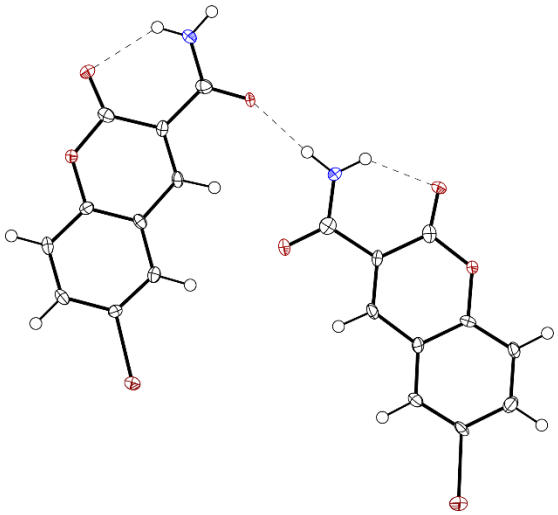

Crystal data and structure refinement for 18srv411

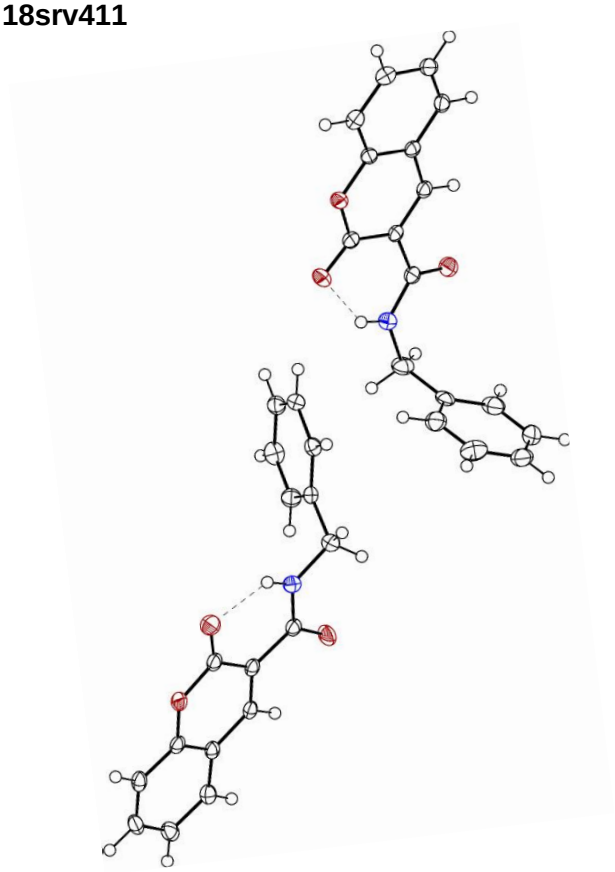

Identification code	18srv411
Empirical formula	$C_{17}H_{13}NO_3$
Formula weight	279.28
Temperature/K	120.0
Crystal system	Triclinic
Space group	P-1
a/Å	5.7909(5)
b/Å	9.5331(7)
c/Å	24.9039(19)
α/°	95.366(3)
β/°	94.317(3)
γ/°	101.253(3)
Volume/Å^3	1336.31(18)
Z	4
ρ_{calc}g/cm^3	1.388
μ/mm^{-1}	0.096
F(000)	584.0
Crystal size/mm^3	0.349 × 0.137 × 0.054
Radiation	Mo Kα (λ = 0.71073)
2Θ range for data collection/°	4.384 to 49.994
Index ranges	-6 ≤ h ≤ 6, -11 ≤ k ≤ 11, -29 ≤ l ≤ 29
Reflections collected	20578
Independent reflections	4688 [R_{int} = 0.0358, R_{sigma} = 0.0339]
Data/restraints/parameters	4688/0/388
Goodness-of-fit on F^2	1.026
Final R indexes [I>=2σ (I)]	R_1 = 0.0349, wR_2 = 0.0812
Final R indexes [all data]	R_1 = 0.0525, wR_2 = 0.0880
Largest diff. peak/hole / e Å^{-3}	0.19/-0.16

Crystal data and structure refinement for 18srv412

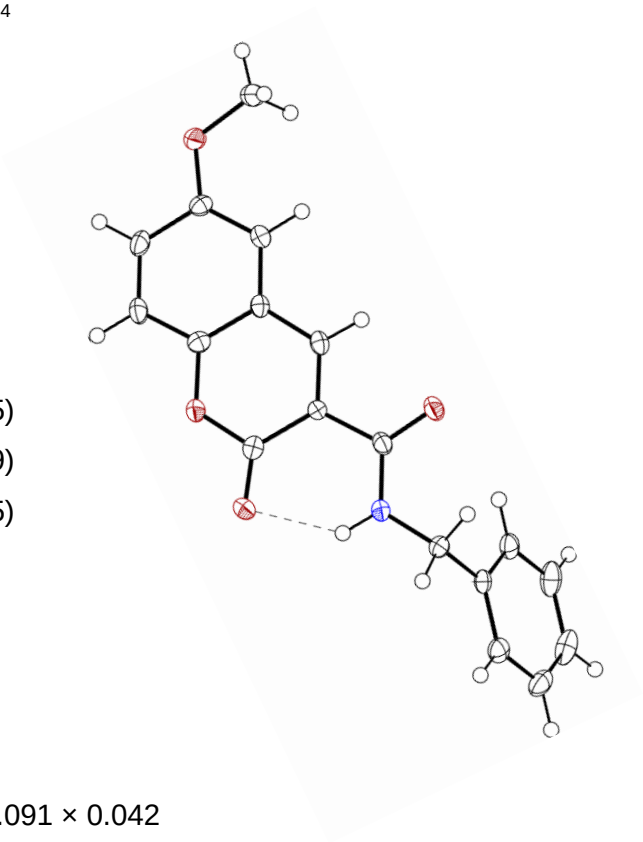

Identification code	18srv412
Empirical formula	$C_{18}H_{15}NO_4$
Formula weight	309.31
Temperature/K	120.0
Crystal system	triclinic
Space group	P-1
a/Å	5.886(3)
b/Å	10.355(4)
c/Å	12.380(6)
α/°	86.707(15)
β/°	83.227(19)
γ/°	89.980(15)
Volume/Å^3	748.1(6)
Z	2
ρ_{calc}g/cm^3	1.373
μ/mm^{-1}	0.098
F(000)	324.0
Crystal size/mm^3	0.653 × 0.091 × 0.042
Radiation	Mo Kα (λ = 0.71073)
2Θ range for data collection/°	5.002 to 50.040
Index ranges	-7 ≤ h ≤ 6, -12 ≤ k ≤ 12, -14 ≤ l ≤ 14
Reflections collected	9573
Independent reflections	2625 [R_{int} = 0.0747, R_{sigma} = 0.1056]
Data/restraints/parameters	2625/0/215
Goodness-of-fit on F^2	0.975
Final R indexes [I>=2σ (I)]	R_1 = 0.0456, wR_2 = 0.0910
Final R indexes [all data]	R_1 = 0.0987, wR_2 = 0.1042
Largest diff. peak/hole / e Å^{-3}	0.21/-0.20

Crystal data and structure refinement for 19srv349

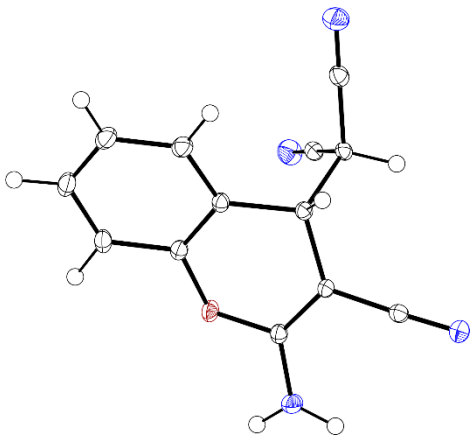

Identification code	19srv349
Empirical formula	$C_{13}H_{14}N_4O$
Formula weight	236.23
Temperature/K	120.0
Crystal system	triclinic
Space group	P-1
a/Å	5.5829(4)
b/Å	8.1140(5)
c/Å	12.3720(8)
α/°	103.753(2)
β/°	90.660(3)
γ/°	96.356(3)
Volume/Å^3	540.62(6)
Z	2
ρ_{calc}g/cm^3	1.451
μ/mm^{-1}	0.098
F(000)	244.0
Crystal size/mm^3	0.450 × 0.335 × 0.144
Radiation	Mo Kα (λ = 0.71073)
2Θ range for data collection/°	5.204 to 66.430
Index ranges	-8 ≤ h ≤ 8, -12 ≤ k ≤ 12, -18 ≤ l ≤ 18
Reflections collected	14155
Independent reflections	4140 [R_{int} = 0.0424, R_{sigma} = 0.0434]
Data/restraints/parameters	4140/0/196
Goodness-of-fit on F^2	1.040
Final R indexes [I>=2σ (I)]	R_1 = 0.0414, wR_2 = 0.1050
Final R indexes [all data]	R_1 = 0.0577, wR_2 = 0.1130
Largest diff. peak/hole / e Å^{-3}	0.53/-0.26

APPENDIX B: aza-Claisen rearrangement crystallographic data

B1. Bromide ammonium salts

Crystal data and structure refinement for 21srv263

Identification code	21srv263
Empirical formula	$C_{12}H_{18}BrN$
Formula weight	256.18
Temperature/K	120.0
Crystal system	orthorhombic
Space group	$Pca2_1$
a/Å	7.7783(4)
b/Å	23.0990(12)
c/Å	13.4665(7)
α/°	90
β/°	90
γ/°	90
Volume/Å^3	2419.5(2)
Z	8
ρ_{calc}g/cm^3	1.407
μ/mm^{-1}	3.362
F(000)	1056.0
Crystal size/mm^3	0.205 × 0.102 × 0.015
Radiation	Mo Kα (λ = 0.71073)
2Θ range for data collection/°	5.290 to 55.058
Index ranges	-10 ≤ h ≤ 10, -30 ≤ k ≤ 30, -17 ≤ l ≤ 17
Reflections collected	33931
Independent reflections	5568 [R_{int} = 0.0743, R_{sigma} = 0.0569]
Data/restraints/parameters	5568/187/266
Goodness-of-fit on F^2	1.097
Final R indexes [I>=2σ (I)]	R_1 = 0.0499, wR_2 = 0.0837
Final R indexes [all data]	R_1 = 0.0643, wR_2 = 0.0877
Largest diff. peak/hole / e Å^{-3}	1.03/-0.83
Flack parameter	0.378(18)

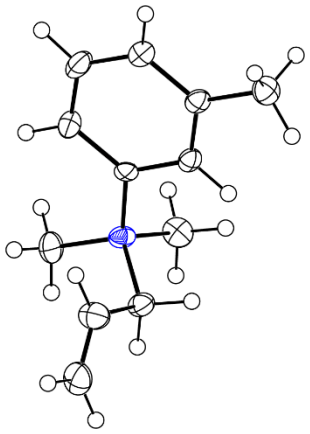

Crystal data and structure refinement for 21srv236

Identification code	21srv236
Empirical formula	$C_{13}H_{20}BrN$
Formula weight	270.21
Temperature/K	120.0
Crystal system	triclinic
Space group	P_{-1}
a/Å	11.3109(6)
b/Å	11.3131(6)
c/Å	11.7426(6)
α/°	101.114(2)
β/°	104.482(2)
γ/°	108.854(2)
Volume/Å^3	1311.98(12)
Z	4
ρ_{calc}g/cm^3	1.368
μ/mm^{-1}	3.104
F(000)	560.0
Crystal size/mm^3	0.174 × 0.114 × 0.084
Radiation	Mo Kα (λ = 0.71073)
2Θ range for data collection/°	3.986 to 62.996
Index ranges	-16 ≤ h ≤ 16, -16 ≤ k ≤ 16, -17 ≤ l ≤ 17
Reflections collected	26485
Independent reflections	8727 [R_{int} = 0.0393, R_{sigma} = 0.0498]
Data/restraints/parameters	8727/0/431
Goodness-of-fit on F^2	1.025
Final R indexes [I>=2σ (I)]	R_1 = 0.0338, wR_2 = 0.0675
Final R indexes [all data]	R_1 = 0.0535, wR_2 = 0.0731
Largest diff. peak/hole / e Å^{-3}	0.49/-0.44

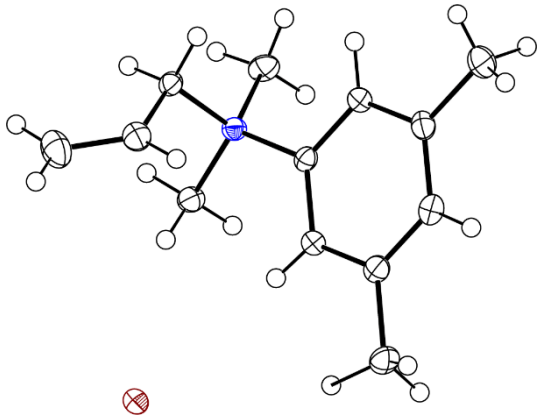

Crystal data and structure refinement for 20srv141

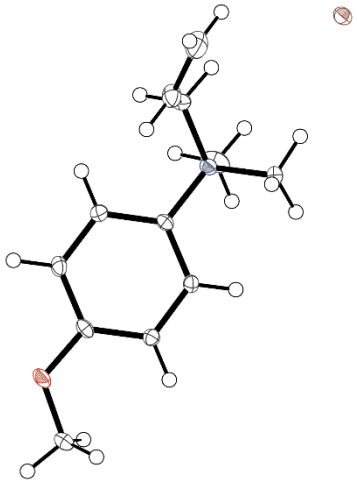

Identification code	20srv141
Empirical formula	$C_{12}H_{18}BrNO$
Formula weight	272.18
Temperature/K	120.0
Crystal system	orthorhombic
Space group	Aea2
a/Å	12.2627(9)
b/Å	17.7610(14)
c/Å	11.4533(9)
α/°	90
β/°	90
γ/°	90
Volume/Å^3	2494.5(3)
Z	8
ρ_{calc}g/cm^3	1.449
μ/mm^{-1}	3.272
F(000)	1120.0
Crystal size/mm^3	0.24 × 0.19 × 0.17
Radiation	Mo Kα (λ = 0.71073)
2Θ range for data collection/°	4.586 to 59.984
Index ranges	-17 ≤ h ≤ 17, -24 ≤ k ≤ 24, -16 ≤ l ≤ 16
Reflections collected	19757
Independent reflections	3639 [R_{int} = 0.0293, R_{sigma} = 0.0207]
Data/restraints/parameters	3639/1/139
Goodness-of-fit on F^2	1.044
Final R indexes [I>=2σ (I)]	R_1 = 0.0170, wR_2 = 0.0394
Final R indexes [all data]	R_1 = 0.0198, wR_2 = 0.0403
Largest diff. peak/hole / e Å^{-3}	0.24/-0.24
Flack parameter	0.083(3)

Crystal data and structure refinement for 21srv229

Identification code	21srv229
Empirical formula	$C_{14}H_{24}BrNO_4$
Formula weight	350.25
Temperature/K	120.0
Crystal system	triclinic
Space group	P_{-1}
a/Å	9.1836(3)
b/Å	9.7411(3)
c/Å	10.1011(3)
α/°	88.8139(12)
β/°	82.4852(12)
γ/°	62.2451(10)
Volume/Å^3	791.96(4)
Z	2
ρ_{calc}g/cm^3	1.469
μ/mm^{-1}	2.608
F(000)	364.0
Crystal size/mm^3	0.311 × 0.234 × 0.08
Radiation	Mo Kα (λ = 0.71073)
2Θ range for data collection/°	4.072 to 66.282
Index ranges	-14 ≤ h ≤ 14, -14 ≤ k ≤ 14, -15 ≤ l ≤ 15
Reflections collected	16227
Independent reflections	5955 [R_{int} = 0.0326, R_{sigma} = 0.0458]
Data/restraints/parameters	5955/0/277
Goodness-of-fit on F^2	1.021
Final R indexes [I>=2σ (I)]	R_1 = 0.0315, wR_2 = 0.0606
Final R indexes [all data]	R_1 = 0.0440, wR_2 = 0.0641
Largest diff. peak/hole / e Å^{-3}	0.46/-0.53

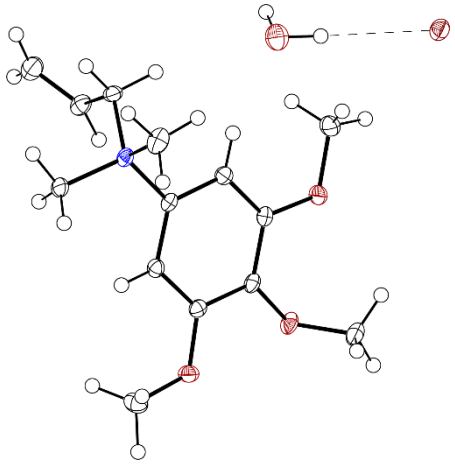

Crystal data and structure refinement for 20srv143

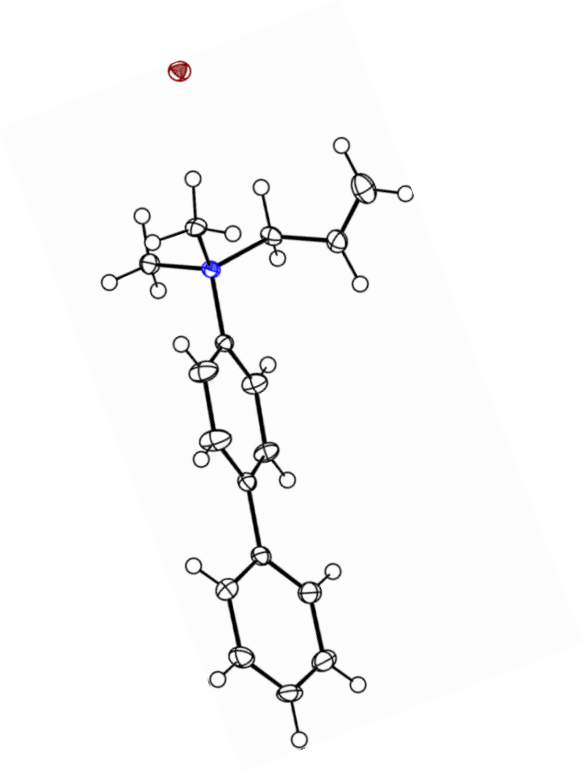

Identification code	20srv143
Empirical formula	$C_{17}H_{20}BrN$
Formula weight	318.25
Temperature/K	120.0
Crystal system	orthorhombic
Space group	Pbca
a/Å	26.866(3)
b/Å	10.9097(11)
c/Å	30.810(3)
α/°	90
β/°	90
γ/°	90
Volume/Å^3	9030.5(15)
Z	24
ρ_{calc}g/cm^3	1.404
μ/mm^{-1}	2.718
F(000)	3936.0
Crystal size/mm^3	0.18 × 0.16 × 0.02
Radiation	Mo Kα (λ = 0.71073)
2Θ range for data collection/°	4.022 to 55.998
Index ranges	-35 ≤ h ≤ 34, -14 ≤ k ≤ 14, -40 ≤ l ≤ 40
Reflections collected	126205
Independent reflections	10902 [R_{int} = 0.0800, R_{sigma} = 0.0416]
Data/restraints/parameters	10902/0/520
Goodness-of-fit on F^2	1.049
Final R indexes [I>=2σ (I)]	R_1 = 0.0344, wR_2 = 0.0590
Final R indexes [all data]	R_1 = 0.0599, wR_2 = 0.0650
Largest diff. peak/hole / e Å^{-3}	0.34/-0.49

Crystal data and structure refinement for 20srv142

Identification code	20srv142
Empirical formula	$C_{11}H_{15}BrClN$
Formula weight	276.60
Temperature/K	120.0
Crystal system	orthorhombic
Space group	Pbca
a/Å	8.8516(19)
b/Å	10.800(3)
c/Å	25.006(6)
α/°	90
β/°	90
γ/°	90
Volume/Å^3	2390.5(9)
Z	8
ρ_{calc}g/cm^3	1.537
μ/mm^{-1}	3.626
F(000)	1120.0
Crystal size/mm^3	0.34 × 0.11 × 0.02
Radiation	Mo Kα (λ = 0.71073)
2Θ range for data collection/°	5.64 to 59.99
Index ranges	-12 ≤ h ≤ 12, -15 ≤ k ≤ 15, -35 ≤ l ≤ 35
Reflections collected	36620
Independent reflections	3488 [R_{int} = 0.0596, R_{sigma} = 0.0302]
Data/restraints/parameters	3488/0/129
Goodness-of-fit on F^2	1.039
Final R indexes [I>=2σ (I)]	R_1 = 0.0244, wR_2 = 0.0534
Final R indexes [all data]	R_1 = 0.0369, wR_2 = 0.0570
Largest diff. peak/hole / e Å^{-3}	0.40/-0.35

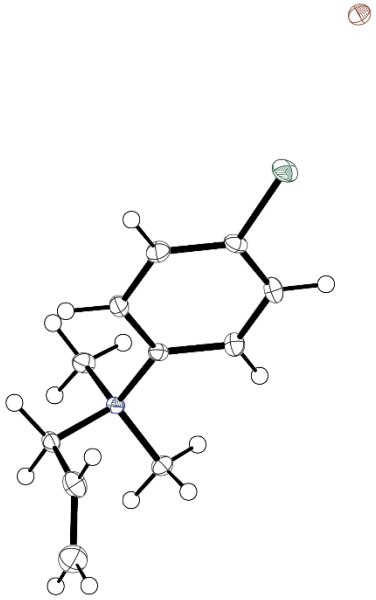

Crystal data and structure refinement for 21srv235

Identification code	21srv235
Empirical formula	$C_{11}H_{15}Br_2N$
Formula weight	321.06
Temperature/K	120.0
Crystal system	orthorhombic
Space group	Pbca
a/Å	8.9455(6)
b/Å	10.8668(6)
c/Å	25.1459(14)
α/°	90
β/°	90
γ/°	90
Volume/Å^3	2444.4(3)
Z	8
ρ_{calc}g/cm^3	1.745
μ/mm^{-1}	6.596
F(000)	1264.0
Crystal size/mm^3	0.182 × 0.142 × 0.139
Radiation	Mo Kα (λ = 0.71073)
2Θ range for data collection/°	5.59 to 69.936
Index ranges	-14 ≤ h ≤ 14, -17 ≤ k ≤ 17, -37 ≤ l ≤ 40
Reflections collected	54961
Independent reflections	5368 [R_{int} = 0.0436, R_{sigma} = 0.0245]
Data/restraints/parameters	5368/0/188
Goodness-of-fit on F^2	1.025
Final R indexes [I>=2σ (I)]	R_1 = 0.0223, wR_2 = 0.0450
Final R indexes [all data]	R_1 = 0.0318, wR_2 = 0.0473
Largest diff. peak/hole / e Å^{-3}	0.53/-0.52

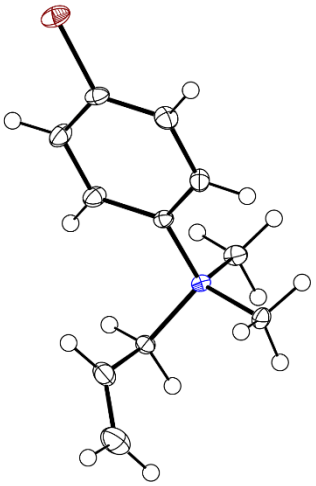

Crystal data and structure refinement for 20srv134

Identification code	20srv134
Empirical formula	$C_{11}H_{15}BrIN$
Formula weight	368.05
Temperature/K	120.0
Crystal system	orthorhombic
Space group	Pbca
a/Å	9.1767(2)
b/Å	10.9809(2)
c/Å	25.5112(5)
α/°	90
β/°	90
γ/°	90
Volume/Å^3	2570.73(10)
Z	8
ρ_{calc}g/cm^3	1.902
μ/mm^{-1}	5.566
F(000)	1408.0
Crystal size/mm^3	0.14 × 0.09 × 0.06
Radiation	Mo-Kα (λ = 0.71073)
2Θ range for data collection/°	5.468 to 58.992
Index ranges	-12 ≤ h ≤ 12, -15 ≤ k ≤ 15, -35 ≤ l ≤ 27
Reflections collected	25607
Independent reflections	3582 [R_{int} = 0.0709, R_{sigma} = 0.0434]
Data/restraints/parameters	3582/0/129
Goodness-of-fit on F^2	1.056
Final R indexes [I>=2σ (I)]	R_1 = 0.0315, wR_2 = 0.0622
Final R indexes [all data]	R_1 = 0.0485, wR_2 = 0.0686
Largest diff. peak/hole / e Å^{-3}	0.78/-0.66

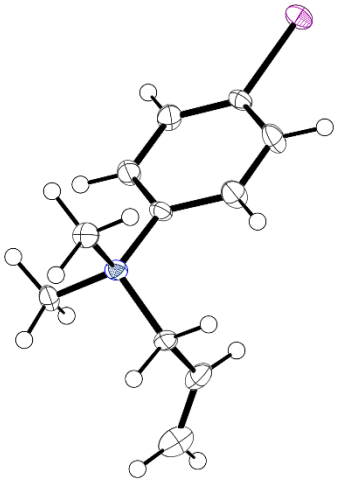

Crystal data and structure refinement for 21srv258

Identification code	21srv258
Empirical formula	$C_{12}H_{15}BrN_2$
Formula weight	267.17
Temperature/K	120.0
Crystal system	monoclinic
Space group	$P2_1/c$
a/Å	19.8787(5)
b/Å	11.5367(3)
c/Å	16.2944(4)
α/°	90
β/°	97.0083(11)
γ/°	90
Volume/Å^3	3708.95(16)
Z	12
ρ_{calc}g/cm^3	1.435
μ/mm^{-1}	3.296
F(000)	1632.0
Crystal size/mm^3	0.347 × 0.287 × 0.102
Radiation	Mo Kα (λ = 0.71073)
2Θ range for data collection/°	4.128 to 64.064
Index ranges	-29 ≤ h ≤ 29, -17 ≤ k ≤ 17, -24 ≤ l ≤ 24
Reflections collected	74083
Independent reflections	12873 [R_{int} = 0.0578, R_{sigma} = 0.0459]
Data/restraints/parameters	12873/5/461
Goodness-of-fit on F^2	1.004
Final R indexes [I>=2σ (I)]	R_1 = 0.0327, wR_2 = 0.0634
Final R indexes [all data]	R_1 = 0.0553, wR_2 = 0.0696
Largest diff. peak/hole / e Å^{-3}	0.51/-0.71

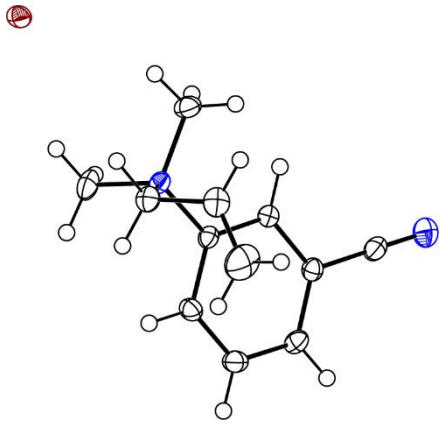

Crystal data and structure refinement for 21srv135

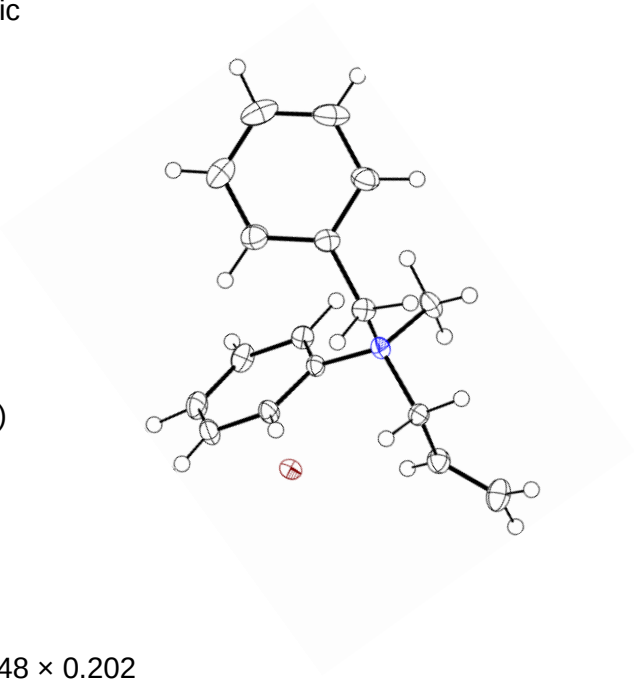

Identification code	21srv135
Empirical formula	$C_{17}H_{20}BrN$
Formula weight	318.25
Temperature/K	120.0
Crystal system	orthorhombic
Space group	$P2_12_12_1$
a/Å	9.1218(4)
b/Å	12.2343(5)
c/Å	13.8372(6)
α/°	90
β/°	90
γ/°	90
Volume/Å^3	1544.22(11)
Z	4
ρ_{calc}g/cm^3	1.369
μ/mm^{-1}	2.649
F(000)	656.0
Crystal size/mm^3	0.308 × 0.248 × 0.202
Radiation	Mo Kα (λ = 0.71073)
2Θ range for data collection/°	4.444 to 68.992
Index ranges	-14 ≤ h ≤ 14, -19 ≤ k ≤ 19, -21 ≤ l ≤ 22
Reflections collected	35691
Independent reflections	6489 [R_{int} = 0.0391, R_{sigma} = 0.0319]
Data/restraints/parameters	6489/0/254
Goodness-of-fit on F^2	1.040
Final R indexes [I>=2σ (I)]	R_1 = 0.0243, wR_2 = 0.0480
Final R indexes [all data]	R_1 = 0.0330, wR_2 = 0.0499
Largest diff. peak/hole / e Å^{-3}	0.30/-0.21
Flack parameter	0.293(8)

B2. Hexafluorophosphate ammonium salts

Crystal data and structure refinement for 20srv131

Identification code	20srv131
Empirical formula	$C_{11}H_{16}F_6NP$
Formula weight	307.22
Temperature/K	120.0
Crystal system	orthorhombic
Space group	Pbca
a/Å	8.467(4)
b/Å	16.221(7)
c/Å	19.264(8)
α/°	90
β/°	90
γ/°	90
Volume/Å^3	2645.7(19)
Z	8
ρ_{calc}g/cm^3	1.543
μ/mm^{-1}	0.265
F(000)	1264.0
Crystal size/mm^3	0.44 × 0.09 × 0.05
Radiation	Mo Kα (λ = 0.71073)
2Θ range for data collection/°	4.228 to 57.998
Index ranges	-11 ≤ h ≤ 11, -22 ≤ k ≤ 22, -26 ≤ l ≤ 26
Reflections collected	36816
Independent reflections	3507 [R_{int} = 0.0942, R_{sigma} = 0.0522]
Data/restraints/parameters	3507/3/211
Goodness-of-fit on F^2	1.028
Final R indexes [I>=2σ (I)]	R_1 = 0.0515, wR_2 = 0.1331
Final R indexes [all data]	R_1 = 0.0764, wR_2 = 0.1487
Largest diff. peak/hole / e Å^{-3}	0.39/-0.46

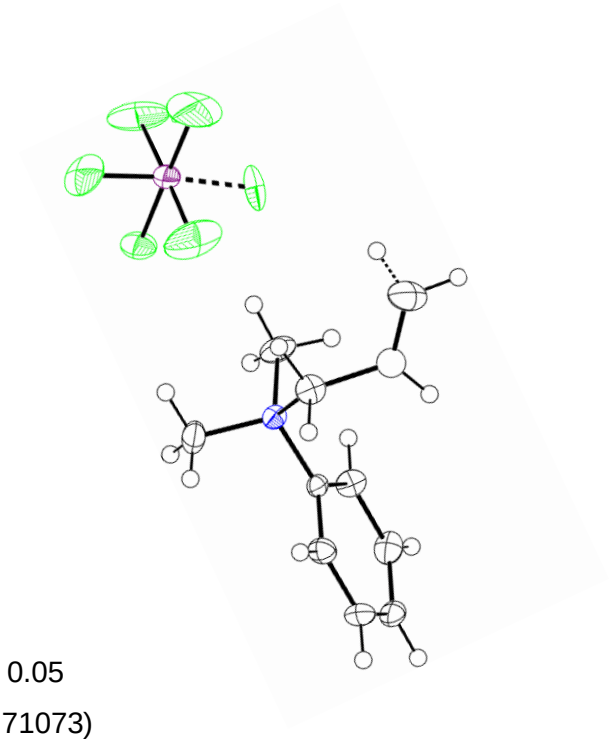

Crystal data and structure refinement for 20srv132

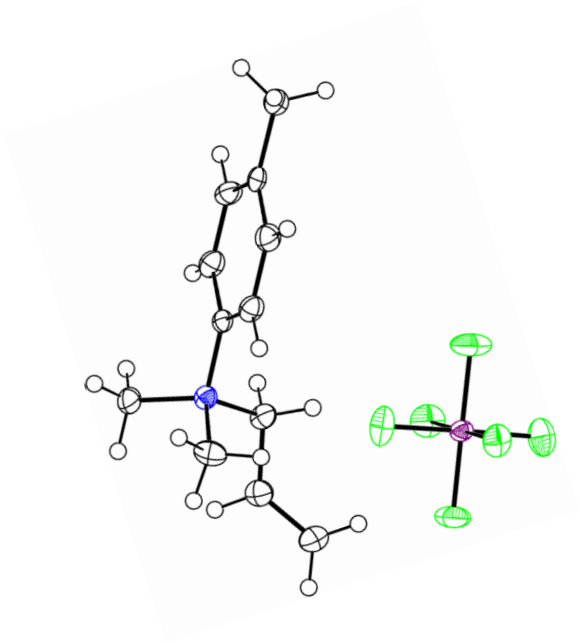

Identification code	20srv132
Empirical formula	$C_{12}H_{18}F_6NP$
Formula weight	321.24
Temperature/K	120.0
Crystal system	monoclinic
Space group	$P2_1/n$
a/Å	13.9408(8)
b/Å	14.7895(8)
c/Å	14.7766(8)
α/°	90
β/°	110.748(2)
γ/°	90
Volume/Å^3	2849.0(3)
Z	8
ρ_{calc}g/cm^3	1.498
μ/mm^{-1}	0.249
F(000)	1328.0
Crystal size/mm^3	0.17 × 0.11 × 0.05
Radiation	Mo Kα (λ = 0.71073)
2Θ range for data collection/°	4.034 to 56.998
Index ranges	-18 ≤ h ≤ 18, -19 ≤ k ≤ 19, -19 ≤ l ≤ 19
Reflections collected	41916
Independent reflections	7217 [R_{int} = 0.0736, R_{sigma} = 0.0793]
Data/restraints/parameters	7217/0/367
Goodness-of-fit on F^2	1.028
Final R indexes [I>=2σ (I)]	R_1 = 0.0552, wR_2 = 0.1206
Final R indexes [all data]	R_1 = 0.0960, wR_2 = 0.1382
Largest diff. peak/hole / e Å^{-3}	0.64/-0.35

Crystal data and structure refinement for 21srv230

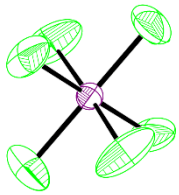

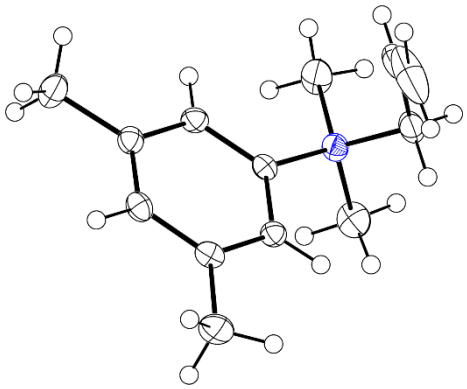

Identification code	21srv230
Empirical formula	$C_{13}H_{20}F_6NP$
Formula weight	335.27
Temperature/K	120.0
Crystal system	monoclinic
Space group	$P2_1/c$
a/Å	8.4320(2)
b/Å	14.3642(4)
c/Å	12.8578(4)
α/°	90
β/°	93.6281(12)
γ/°	90
Volume/Å^3	1554.20(7)
Z	4
ρ_{calc}g/cm^3	1.433
μ/mm^{-1}	0.232
F(000)	696.0
Crystal size/mm^3	0.362 × 0.293 × 0.15
Radiation	Mo Kα (λ = 0.71073)
2Θ range for data collection/°	4.256 to 59.998
Index ranges	-11 ≤ h ≤ 11, -19 ≤ k ≤ 20, -18 ≤ l ≤ 18
Reflections collected	26158
Independent reflections	4520 [R_{int} = 0.0462, R_{sigma} = 0.0360]
Data/restraints/parameters	4520/28/295
Goodness-of-fit on F^2	1.049
Final R indexes [I>=2σ (I)]	R_1 = 0.0458, wR_2 = 0.1097
Final R indexes [all data]	R_1 = 0.0661, wR_2 = 0.1221
Largest diff. peak/hole / e Å^{-3}	0.39/-0.34

Crystal data and structure refinement for 20srv132

Identification code	20srv132
Empirical formula	$C_{12}H_{18}F_6NP$
Formula weight	321.24
Temperature/K	120.0
Crystal system	monoclinic
Space group	$P2_1/n$
a/Å	13.9408(8)
b/Å	14.7895(8)
c/Å	14.7766(8)
α/°	90
β/°	110.748(2)
γ/°	90
Volume/Å^3	2849.0(3)
Z	8
ρ_{calc}g/cm^3	1.498
μ/mm^{-1}	0.249
F(000)	1328.0
Crystal size/mm^3	0.17 × 0.11 × 0.05
Radiation	Mo Kα (λ = 0.71073)
2Θ range for data collection/°	4.034 to 56.998
Index ranges	-18 ≤ h ≤ 18, -19 ≤ k ≤ 19, -19 ≤ l ≤ 19
Reflections collected	41916
Independent reflections	7217 [R_{int} = 0.0736, R_{sigma} = 0.0793]
Data/restraints/parameters	7217/0/367
Goodness-of-fit on F^2	1.028
Final R indexes [I>=2σ (I)]	R_1 = 0.0522, wR_2 = 0.1206
Final R indexes [all data]	R_1 = 0.0960, wR_2 = 0.1382
Largest diff. peak/hole / e Å^{-3}	0.64/-0.35

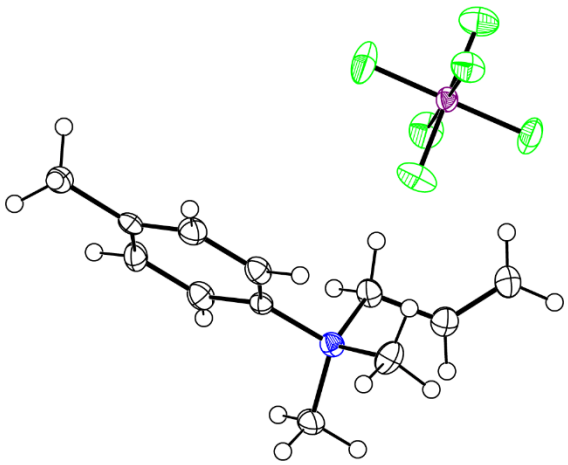

Crystal data and structure refinement for 20srv146

Identification code	20srv146
Empirical formula	$C_{15}H_{24}F_6NP$
Formula weight	363.32
Temperature/K	120.0
Crystal system	monoclinic
Space group	$P2_1/c$
a/Å	13.9604(12)
b/Å	10.4114(9)
c/Å	11.7091(10)
α/°	90
β/°	93.324(3)
γ/°	90
Volume/Å^3	1699.0(3)
Z	4
ρ_{calc}g/cm^3	1.420
μ/mm^{-1}	0.218
F(000)	760.0
Crystal size/mm^3	0.24 × 0.21 × 0.12
Radiation	Mo Kα (λ = 0.71073)
2Θ range for data collection/°	4.884 to 55.988
Index ranges	-18 ≤ h ≤ 18, -13 ≤ k ≤ 13, -15 ≤ l ≤ 15
Reflections collected	23857
Independent reflections	4095 [R_{int} = 0.0339, R_{sigma} = 0.0241]
Data/restraints/parameters	4095/0/225
Goodness-of-fit on F^2	1.051
Final R indexes [I>=2σ (I)]	R_1 = 0.0750, wR_2 = 0.1852
Final R indexes [all data]	R_1 = 0.0881, wR_2 = 0.1952
Largest diff. peak/hole / e Å^{-3}	1.29/-0.84

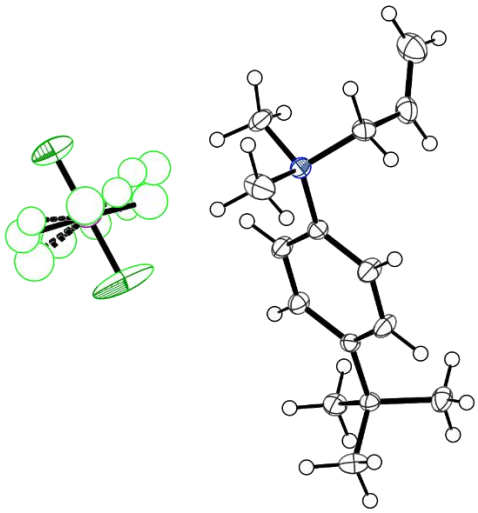

Crystal data and structure refinement for 20srv145

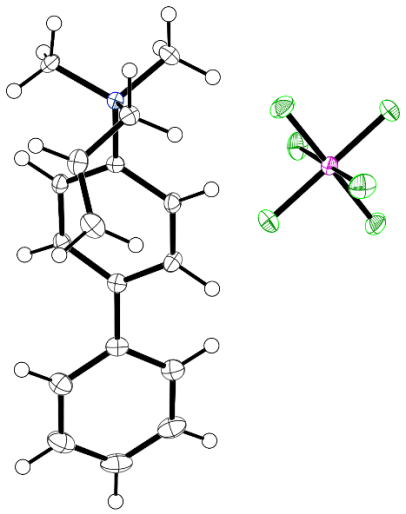

Identification code	20srv145
Empirical formula	$C_{17}H_{20}F_6NP$
Formula weight	383.31
Temperature/K	120.0
Crystal system	monoclinic
Space group	$P2_1/c$
a/Å	6.6043(6)
b/Å	29.045(3)
c/Å	9.1417(8)
α/°	90
β/°	100.416(4)
γ/°	90
Volume/Å^3	1724.7(3)
Z	4
ρ_{calc}g/cm^3	1.476
μ/mm^{-1}	0.220
F(000)	792.0
Crystal size/mm^3	0.28 × 0.23 × 0.02
Radiation	Mo Kα (λ = 0.71073)
2Θ range for data collection/°	4.742 to 59
Index ranges	-9 ≤ h ≤ 9, -40 ≤ k ≤ 40, -12 ≤ l ≤ 12
Reflections collected	27385
Independent reflections	4799 [R_{int} = 0.0390, R_{sigma} = 0.0301]
Data/restraints/parameters	4799/0/306
Goodness-of-fit on F^2	1.031
Final R indexes [I>=2σ (I)]	R_1 = 0.0368, wR_2 = 0.0856
Final R indexes [all data]	R_1 = 0.0522, wR_2 = 0.0915
Largest diff. peak/hole / e Å^{-3}	0.37/-0.44

Crystal data and structure refinement for 21srv227

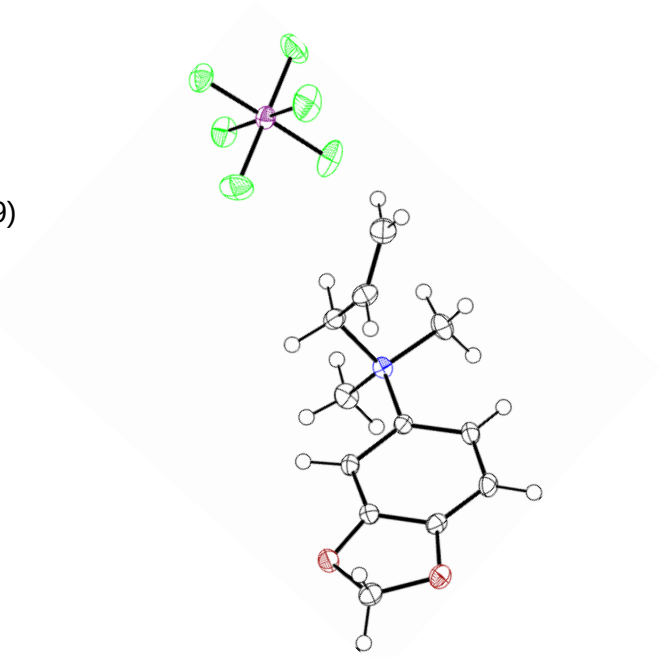

Identification code	21srv227
Empirical formula	$C_{12}H_{16}F_6NO_2P$
Formula weight	351.23
Temperature/K	120.0
Crystal system	triclinic
Space group	P_{-1}
a/Å	6.5677(5)
b/Å	8.5589(6)
c/Å	13.5183(9)
α/°	72.019(3)
β/°	85.669(3)
γ/°	87.381(3)
Volume/Å^3	720.52(9)
Z	2
ρ_{calc}g/cm^3	1.619
μ/mm^{-1}	0.264
F(000)	360.0
Crystal size/mm^3	0.325 × 0.206 × 0.172
Radiation	Mo Kα (λ = 0.71073)
2Θ range for data collection/°	5.006 to 68.812
Index ranges	-10 ≤ h ≤ 10, -13 ≤ k ≤ 13, -21 ≤ l ≤ 21
Reflections collected	22947
Independent reflections	5838 [R_{int} = ?, R_{sigma} = 0.0510]
Data/restraints/parameters	5838/0/259
Goodness-of-fit on F^2	1.129
Final R indexes [I>=2σ (I)]	R_1 = 0.0563, wR_2 = 0.1193
Final R indexes [all data]	R_1 = 0.0772, wR_2 = 0.1248
Largest diff. peak/hole / e Å^{-3}	0.49/-0.37

Crystal data and structure refinement for 21srv233

Identification code	21srv233
Empirical formula	$C_{14.4}H_{23.6}F_6NO_{3.4}P$
Formula weight	410.11
Temperature/K	120.0
Crystal system	triclinic
Space group	P_{-1}
a/Å	9.4285(3)
b/Å	10.1676(4)
c/Å	10.8300(4)
α/°	109.4577(14)
β/°	95.0048(15)
γ/°	102.8451(15)
Volume/Å^3	939.62(6)
Z	2
ρ_{calc}g/cm^3	1.450
μ/mm^{-1}	0.219
F(000)	426.0
Crystal size/mm^3	0.176 × 0.111 × 0.058
Radiation	Mo Kα (λ = 0.71073)
2Θ range for data collection/°	4.052 to 49.998
Index ranges	-11 ≤ h ≤ 11, -11 ≤ k ≤ 12, -12 ≤ l ≤ 12
Reflections collected	12061
Independent reflections	3297 [R_{int} = 0.0489, R_{sigma} = 0.0519]
Data/restraints/parameters	3297/1/328
Goodness-of-fit on F^2	1.033
Final R indexes [I>=2σ (I)]	R_1 = 0.0465, wR_2 = 0.1031
Final R indexes [all data]	R_1 = 0.0682, wR_2 = 0.1131
Largest diff. peak/hole / e Å^{-3}	0.50/-0.35

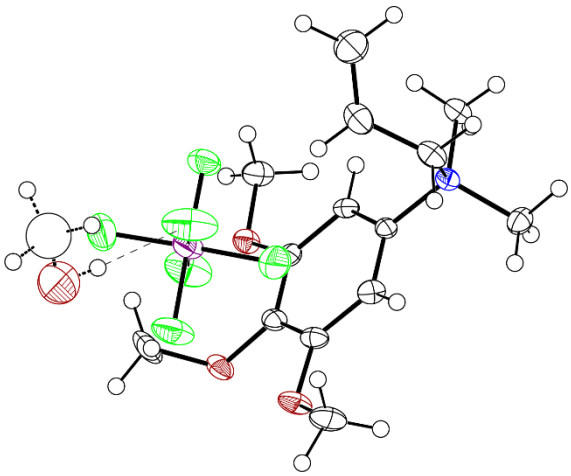

Crystal data and structure refinement for 21srv224

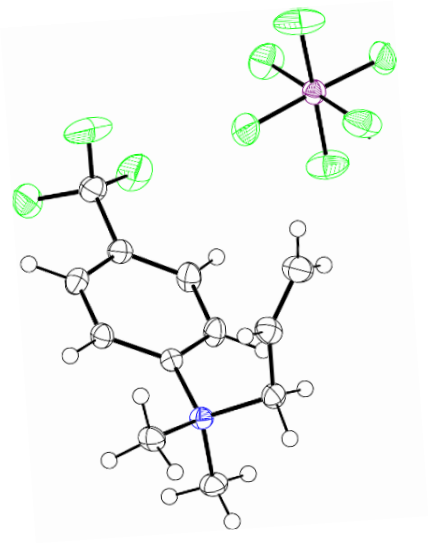

Identification code	21srv224
Empirical formula	$C_{12}H_{15}F_9NP$
Formula weight	375.22
Temperature/K	120.0
Crystal system	Monoclinic
Space group	$P2_1/c$
a/Å	6.4674(2)
b/Å	15.1822(4)
c/Å	15.6334(4)
α/°	90
β/°	95.6738(11)
γ/°	90
Volume/Å^3	1527.51(7)
Z	4
ρ_{calc}g/cm^3	1.632
μ/mm^{-1}	0.272
F(000)	760.0
Crystal size/mm^3	0.576 × 0.557 × 0.186
Radiation	Mo-Kα (λ = 0.71073)
2Θ range for data collection/°	5.238 to 64
Index ranges	-9 ≤ h ≤ 9, -22 ≤ k ≤ 22, -23 ≤ l ≤ 23
Reflections collected	28842
Independent reflections	5312 [R_{int} = 0.0514, R_{sigma} = 0.0386]
Data/restraints/parameters	5312/468/323
Goodness-of-fit on F^2	1.020
Final R indexes [I>=2σ (I)]	R_1 = 0.0445, wR_2 = 0.1024
Final R indexes [all data]	R_1 = 0.0620, wR_2 = 0.1129
Largest diff. peak/hole / e Å^{-3}	0.42/-0.36

Crystal data and structure refinement for 21srv260

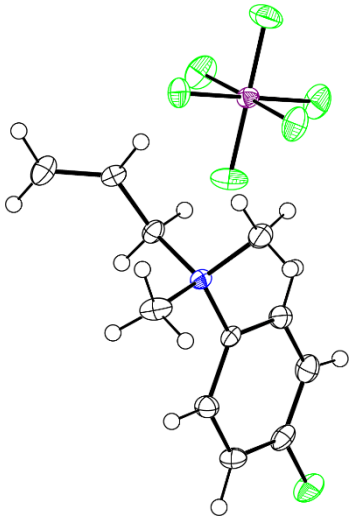

Identification code	21srv260
Empirical formula	$C_{11}H_{15}F_7NP$
Formula weight	325.21
Temperature/K	120.0
Crystal system	monoclinic
Space group	$P2_1/n$
a/Å	13.8263(3)
b/Å	14.9820(4)
c/Å	13.8687(3)
α/°	90
β/°	110.3804(9)
γ/°	90
Volume/Å^3	2693.00(11)
Z	8
ρ_{calc}g/cm^3	1.604
μ/mm^{-1}	0.275
F(000)	1328.0
Crystal size/mm^3	0.341 × 0.125 × 0.088
Radiation	Mo Kα (λ = 0.71073)
2Θ range for data collection/°	4.148 to 61.988
Index ranges	-20 ≤ h ≤ 20, -21 ≤ k ≤ 21, -20 ≤ l ≤ 20
Reflections collected	51735
Independent reflections	8571 [R_{int} = 0.0649, R_{sigma} = 0.0477]
Data/restraints/parameters	8571/0/482
Goodness-of-fit on F^2	1.041
Final R indexes [I>=2σ (I)]	R_1 = 0.0491, wR_2 = 0.0999
Final R indexes [all data]	R_1 = 0.0721, wR_2 = 0.1090
Largest diff. peak/hole / e Å^{-3}	0.42/-0.41

Crystal data and structure refinement for 20srv133

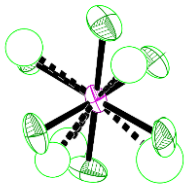

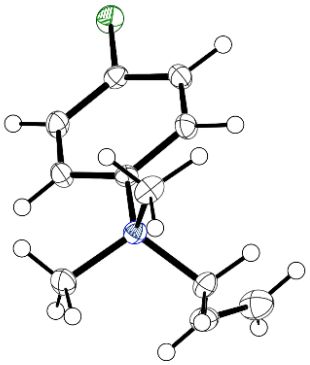

Identification code	20srv133
Empirical formula	$C_{11}H_{15}ClF_6NP$
Formula weight	341.66
Temperature/K	120.0
Crystal system	monoclinic
Space group	$P2_1/n$
a/Å	7.2810(2)
b/Å	18.7449(4)
c/Å	10.5614(2)
α/°	90
β/°	99.580(2)
γ/°	90
Volume/Å^3	1421.34(6)
Z	4
ρ_{calc}g/cm^3	1.597
μ/mm^{-1}	0.437
F(000)	696.0
Crystal size/mm^3	0.46 × 0.38 × 0.21
Radiation	Mo-Kα (λ = 0.71073)
2Θ range for data collection/°	4.346 to 58
Index ranges	-9 ≤ h ≤ 9, -25 ≤ k ≤ 25, -14 ≤ l ≤ 14
Reflections collected	13672
Independent reflections	3778 [R_{int} = 0.0328, R_{sigma} = 0.0307]
Data/restraints/parameters	3778/10/261
Goodness-of-fit on F^2	1.117
Final R indexes [I>=2σ (I)]	R_1 = 0.0354, wR_2 = 0.0913
Final R indexes [all data]	R_1 = 0.0463, wR_2 = 0.1117
Largest diff. peak/hole / e Å^{-3}	0.51/-0.47

Crystal data and structure refinement for 21srv099

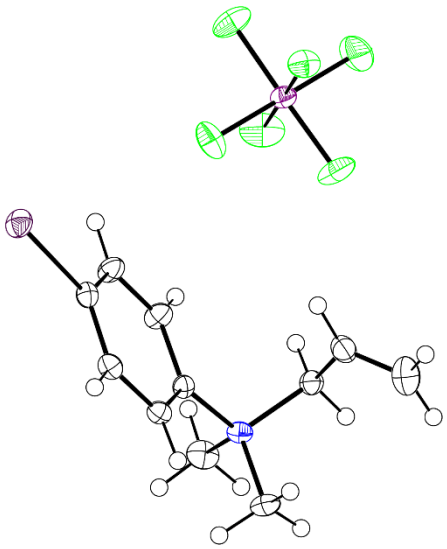

Identification code	21srv099
Empirical formula	$C_{11}H_{15}F_6INP$
Formula weight	433.11
Temperature/K	120.0
Crystal system	triclinic
Space group	P_{-1}
a/Å	6.6573(2)
b/Å	8.4164(2)
c/Å	13.7075(3)
α/°	77.7698(10)
β/°	87.3973(10)
γ/°	85.5631(10)
Volume/Å^3	748.03(3)
Z	2
ρ_{calc}g/cm^3	1.923
μ/mm^{-1}	2.301
F(000)	420.0
Crystal size/mm^3	0.14 × 0.09 × 0.044
Radiation	Mo-Kα (λ = 0.71073)
2Θ range for data collection/°	4.964 to 68.668
Index ranges	-10 ≤ h ≤ 10, -13 ≤ k ≤ 13, -21 ≤ l ≤ 21
Reflections collected	17254
Independent reflections	6201 [R_{int} = 0.0289, R_{sigma} = 0.0383]
Data/restraints/parameters	6201/0/242
Goodness-of-fit on F^2	1.050
Final R indexes [I>=2σ (I)]	R_1 = 0.0283, wR_2 = 0.0556
Final R indexes [all data]	R_1 = 0.0363, wR_2 = 0.0581
Largest diff. peak/hole / e Å^{-3}	0.57/-0.54

Crystal data and structure refinement for 20srv290

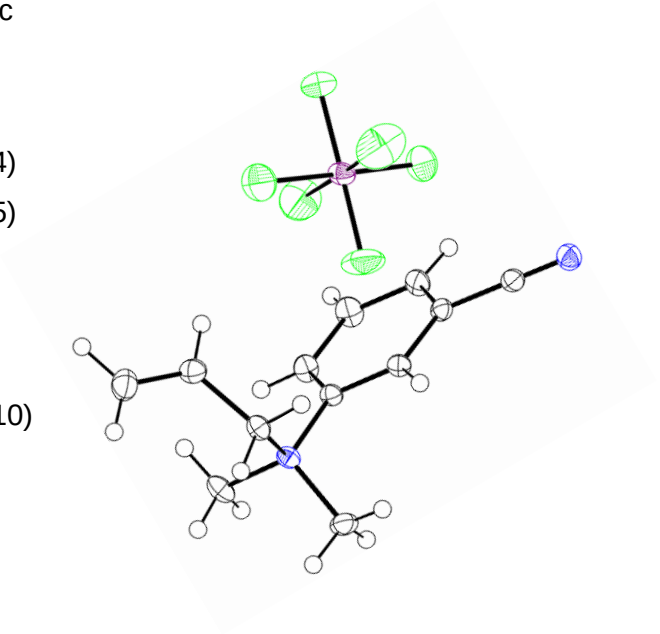

Identification code	20srv290
Empirical formula	$C_{12}H_{15}F_6N_2P$
Formula weight	332.23
Temperature/K	120.0
Crystal system	monoclinic
Space group	$P2_1/n$
a/Å	9.5509(4)
b/Å	11.4185(4)
c/Å	13.4321(5)
α/°	90
β/°	99.052(2)
γ/°	90
Volume/Å^3	1446.62(10)
Z	4
ρ_{calc}g/cm^3	1.525
μ/mm^{-1}	0.250
F(000)	680.0
Crystal size/mm^3	0.26 × 0.17 × 0.08
Radiation	Mo Kα (λ = 0.71073)
2Θ range for data collection/°	4.706 to 59.994
Index ranges	-13 ≤ h ≤ 13, -16 ≤ k ≤ 16, -18 ≤ l ≤ 18
Reflections collected	25670
Independent reflections	4202 [R_{int} = 0.0317, R_{sigma} = 0.0230]
Data/restraints/parameters	4202/0/250
Goodness-of-fit on F^2	1.057
Final R indexes [I>=2σ (I)]	R_1 = 0.0529, wR_2 = 0.1412
Final R indexes [all data]	R_1 = 0.0594, wR_2 = 0.1460
Largest diff. peak/hole / e Å^{-3}	1.02/-0.64

Crystal data and structure refinement for 21srv136

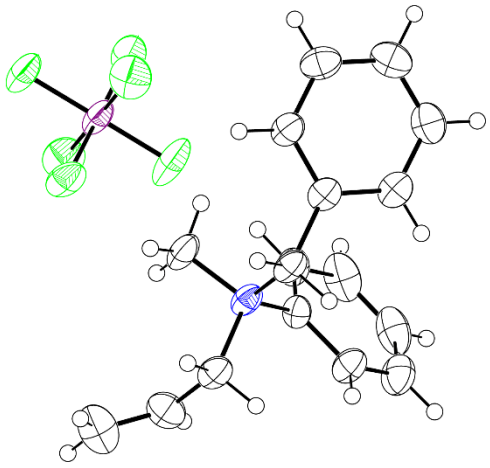

Identification code	21srv136
Empirical formula	$C_{17}H_{20}F_6NP$
Formula weight	383.31
Temperature/K	120.0
Crystal system	triclinic
Space group	P_{-1}
a/Å	8.2815(4)
b/Å	10.2787(5)
c/Å	10.9358(5)
α/°	93.0495(18)
β/°	95.7766(19)
γ/°	105.1298(18)
Volume/Å^3	890.99(7)
Z	2
ρ_{calc}g/cm^3	1.429
μ/mm^{-1}	0.212
F(000)	396.0
Crystal size/mm^3	0.203 × 0.11 × 0.029
Radiation	Mo Kα (λ = 0.71073)
2Θ range for data collection/°	3.756 to 49.994
Index ranges	-9 ≤ h ≤ 9, -12 ≤ k ≤ 12, -12 ≤ l ≤ 12
Reflections collected	11234
Independent reflections	3126 [R_{int} = 0.0327, R_{sigma} = 0.0333]
Data/restraints/parameters	3126/0/227
Goodness-of-fit on F^2	1.060
Final R indexes [I>=2σ (I)]	R_1 = 0.0617, wR_2 = 0.1402
Final R indexes [all data]	R_1 = 0.0752, wR_2 = 0.1467
Largest diff. peak/hole / e Å^{-3}	0.45/-0.26

Crystal data and structure refinement for 20srv288

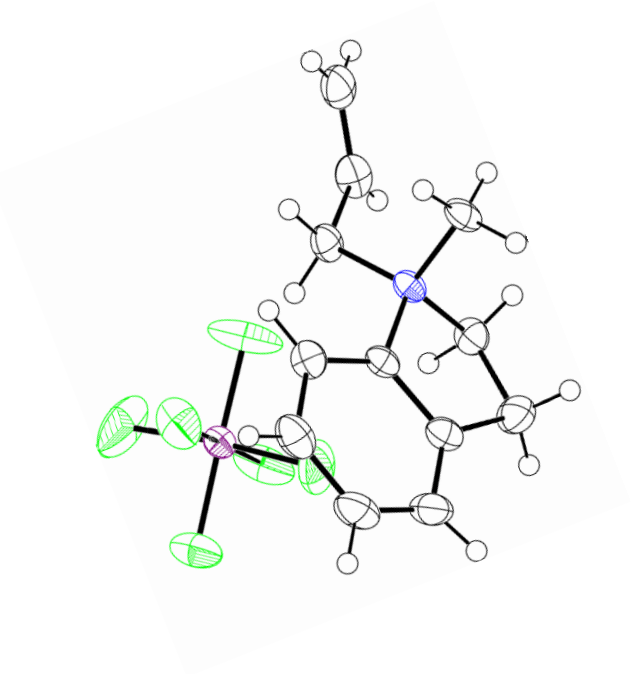

Identification code	20srv288
Empirical formula	$C_{12}H_{16}F_6NP$
Formula weight	319.23
Temperature/K	120.0
Crystal system	monoclinic
Space group	Cc
a/Å	8.4607(3)
b/Å	18.6854(7)
c/Å	8.8633(3)
α/°	90
β/°	95.548(2)
γ/°	90
Volume/Å^3	1394.65(9)
Z	4
ρ_{calc}g/cm^3	1.520
μ/mm^{-1}	0.254
F(000)	656.0
Crystal size/mm^3	0.19 × 0.14 × 0.08
Radiation	Mo Kα (λ = 0.71073)
2Θ range for data collection/°	6.352 to 59.996
Index ranges	-11 ≤ h ≤ 11, -26 ≤ k ≤ 26, -12 ≤ l ≤ 12
Reflections collected	12373
Independent reflections	4034 [R_{int} = 0.0280, R_{sigma} = 0.0324]
Data/restraints/parameters	4034/30/261
Goodness-of-fit on F^2	1.039
Final R indexes [I>=2σ (I)]	R_1 = 0.0377, wR_2 = 0.0914
Final R indexes [all data]	R_1 = 0.0405, wR_2 = 0.0933
Largest diff. peak/hole / e Å^{-3}	0.26/-0.28
Flack parameter	0.02(3)

B3. Hexafluorophosphate indolinium salts

Crystal data and structure refinement for 21srv098

Identification code	21srv098
Empirical formula	$C_{11}H_{16}F_6NP$
Formula weight	307.22
Temperature/K	120.0
Crystal system	orthorhombic
Space group	Pbca
a/Å	8.0056(2)
b/Å	13.9253(3)
c/Å	23.6159(5)
α/°	90
β/°	90
γ/°	90
Volume/Å^3	2632.71(10)
Z	8
ρ_{calc}g/cm^3	1.550
μ/mm^{-1}	0.266
F(000)	1264.0
Crystal size/mm^3	0.299 × 0.16 × 0.156
Radiation	Mo Kα (λ = 0.71073)
2Θ range for data collection/°	5.852 to 64.056
Index ranges	-11 ≤ h ≤ 11, -20 ≤ k ≤ 20, -35 ≤ l ≤ 35
Reflections collected	51200
Independent reflections	4569 [R_{int} = 0.0545, R_{sigma} = 0.0273]
Data/restraints/parameters	4569/5/249
Goodness-of-fit on F^2	1.053
Final R indexes [I>=2σ (I)]	R_1 = 0.0409, wR_2 = 0.0936
Final R indexes [all data]	R_1 = 0.0537, wR_2 = 0.0990
Largest diff. peak/hole / e Å^{-3}	0.45/-0.40

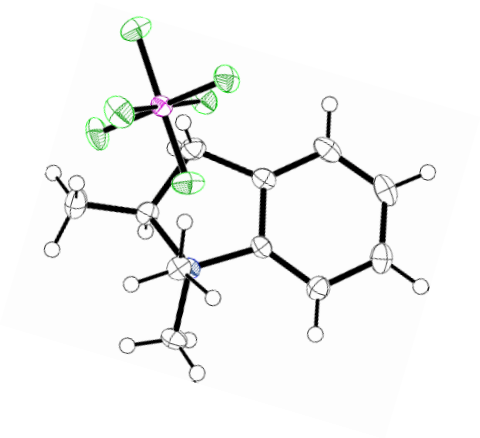

Crystal data and structure refinement for 21srv060

Identification code	21srv060
Empirical formula	$C_{15}H_{24}F_6NP$
Formula weight	363.32
Temperature/K	120.0
Crystal system	monoclinic
Space group	$P2_1$
a/Å	6.2281(3)
b/Å	10.2497(6)
c/Å	13.2430(7)
α/°	90
β/°	98.991(2)
γ/°	90
Volume/Å^3	835.00(8)
Z	2
ρ_{calc}g/cm^3	1.445
μ/mm^{-1}	0.222
F(000)	380.0
Crystal size/mm^3	0.188 × 0.054 × 0.033
Radiation	Mo Kα (λ = 0.71073)
2Θ range for data collection/°	5.050 to 54.986
Index ranges	-8 ≤ h ≤ 8, -13 ≤ k ≤ 13, -17 ≤ l ≤ 17
Reflections collected	12457
Independent reflections	3811 [R_{int} = 0.0351, R_{sigma} = 0.0419]
Data/restraints/parameters	3811/122/278
Goodness-of-fit on F^2	1.101
Final R indexes [I>=2σ (I)]	R_1 = 0.0704, wR_2 = 0.1733
Final R indexes [all data]	R_1 = 0.0814, wR_2 = 0.1802
Largest diff. peak/hole / e Å^{-3}	0.44/-0.28
Flack parameter	0.4(3)

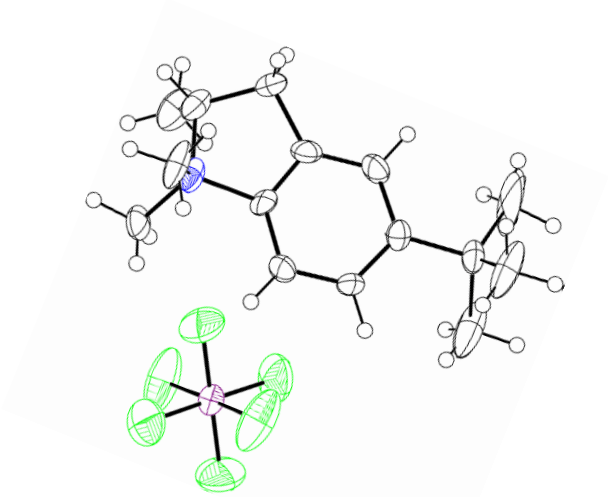

Crystal data and structure refinement for 21srv087

Identification code	21srv087
Empirical formula	$C_{17}H_{20}F_6NP$
Formula weight	383.31
Temperature/K	120.0
Crystal system	monoclinic
Space group	$P2_1/c$
a/Å	10.1458(4)
b/Å	11.9012(5)
c/Å	14.4476(6)
α/°	90
β/°	92.186(2)
γ/°	90
Volume/Å^3	1743.24(12)
Z	4
ρ_{calc}g/cm^3	1.460
μ/mm^{-1}	0.217
F(000)	792.0
Crystal size/mm^3	0.374 × 0.287 × 0.124
Radiation	Mo Kα (λ = 0.71073)
2Θ range for data collection/°	4.436 to 61.996
Index ranges	-14 ≤ h ≤ 14, -17 ≤ k ≤ 17, -20 ≤ l ≤ 20
Reflections collected	33127
Independent reflections	5549 [R_{int} = 0.0507, R_{sigma} = 0.0356]
Data/restraints/parameters	5549/24/314
Goodness-of-fit on F^2	1.017
Final R indexes [I>=2σ (I)]	R_1 = 0.0450, wR_2 = 0.1095
Final R indexes [all data]	R_1 = 0.0573, wR_2 = 0.1070
Largest diff. peak/hole / e Å^{-3}	0.57/-0.35

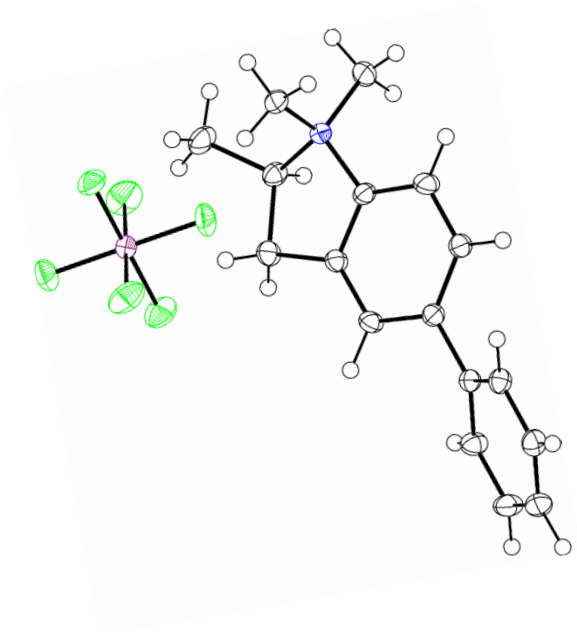

Crystal data and structure refinement for 21srv088

Identification code	21srv088
Empirical formula	$C_{11}H_{15}ClF_6NP$
Formula weight	341.66
Temperature/K	120.0
Crystal system	monoclinic
Space group	C2/c
a/Å	24.6220(12)
b/Å	16.8569(8)
c/Å	13.6806(7)
α/°	90
β/°	94.676(2)
γ/°	90
Volume/Å^3	5659.2(5)
Z	16
ρ_{calc}g/cm^3	1.604
μ/mm^{-1}	0.439
F(000)	2784.0
Crystal size/mm^3	0.547 × 0.108 × 0.102
Radiation	Mo Kα (λ = 0.71073)
2Θ range for data collection/°	4.088 to 60.104
Index ranges	-34 ≤ h ≤ 34, -23 ≤ k ≤ 23, -19 ≤ l ≤ 19
Reflections collected	47354
Independent reflections	8289 [R_{int} = 0.0765, R_{sigma} = 0.0525]
Data/restraints/parameters	8289/5/388
Goodness-of-fit on F^2	1.081
Final R indexes [I>=2σ (I)]	R_1 = 0.0555, wR_2 = 0.1188
Final R indexes [all data]	R_1 = 0.0720, wR_2 = 0.1261
Largest diff. peak/hole / e Å^{-3}	0.59/-0.52

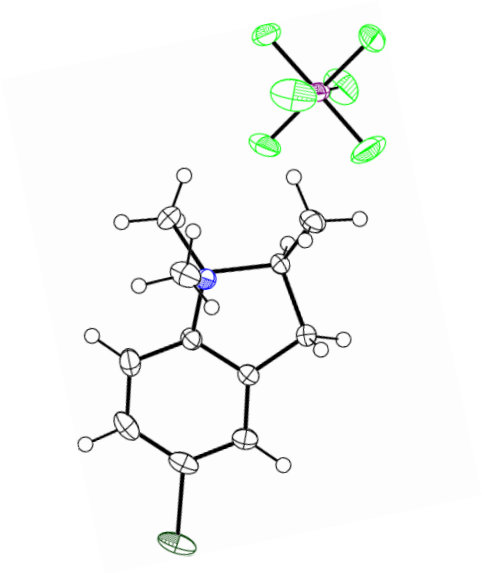

Crystal data and structure refinement for 21srv061

Identification code	21srv061
Empirical formula	$C_{11}H_{15}F_6INP$
Formula weight	433.11
Temperature/K	120.0
Crystal system	monoclinic
Space group	$P2_1/c$
a/Å	6.3304(9)
b/Å	17.950(2)
c/Å	13.3139(19)
α/°	90
β/°	100.757(6)
γ/°	90
Volume/Å^3	1486.3(4)
Z	4
ρ_{calc}g/cm^3	1.936
μ/mm^{-1}	2.316
F(000)	840.0
Crystal size/mm^3	0.18 × 0.08 × 0.05
Radiation	Mo Kα (λ = 0.71073)
2Θ range for data collection/°	4.538 to 55.998
Index ranges	-8 ≤ h ≤ 8, -23 ≤ k ≤ 23, -17 ≤ l ≤ 17
Reflections collected	21192
Independent reflections	3585 [R_{int} = 0.0754, R_{sigma} = 0.0518]
Data/restraints/parameters	3585/28/214
Goodness-of-fit on F^2	1.038
Final R indexes [I>=2σ (I)]	R_1 = 0.0476, wR_2 = 0.0957
Final R indexes [all data]	R_1 = 0.0744, wR_2 = 0.1067
Largest diff. peak/hole / e Å^{-3}	1.58/-1.25

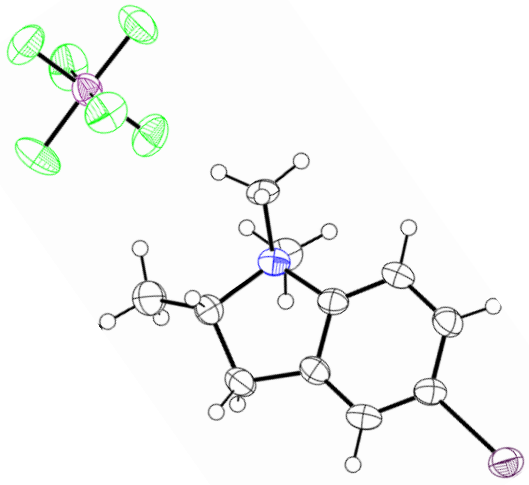

Bibliographic Section

1. Butt, H., Graf, K. & Kappl, M. *Physics and Chemistry of Interfaces*. *Physics and Chemistry of Interfaces* (Wiley, 2003).
2. Berthier, J. & Silberzan, P. Shape of Microdrops. in *Microfluidics for Biotechnology* 105–106 (Artech House, 2010).
3. Garcia-Cordero, J. L. & Fan, Z. H. Sessile droplets for chemical and biological assays. *Lab Chip* **17**, 2150–2166 (2017).
4. Butt, H., Graf, K. & Kappl, M. *Physics and Chemistry of Interfaces*. *Physics and Chemistry of Interfaces* (Wiley, 2003). doi:10.1002/3527602313.
5. Malinowski, R., Parkin, I. P. & Volpe, G. Advances towards programmable droplet transport on solid surfaces and its applications. *Chem. Soc. Rev.* **49**, 7879–7892 (2020).
6. Young, T. An Essay on the Cohesion of Fluids. *Philos. Trans. R. Soc.* **95**, 65–87 (1805).
7. De Gennes, P. G. Wetting: Statics and dynamics. *Rev. Mod. Phys.* **57**, 827–863 (1985).
8. Bonn, D., Eggers, J., Indekeu, J., Meunier, J. & Rolley, E. Wetting and spreading. *Rev. Mod. Phys.* **81**, 739–805 (2009).
9. Extrand, C. W. Origins of Wetting. *Langmuir* **32**, 7697–7706 (2016).
10. Marangoni, C. Sull'espansione delle goccie d'un liquido galleggianti sulla superficie di altro liquido. (Parigi, 1865).
11. Fusinieri, A. *Memorie sperimentali di mecanica molecolare e d'una forza repulsive novamente scoperta nella materia attenuata*. (Tipi di Angelo Sicca, 1844).
12. Scriven, L. E. & Sterling, C. V. The Marangoni Effects. *Nature* **187**, 186–188 (1960).
13. Chen, P., Harmand, S., Ouenzerfi, S. & Schiffler, J. Marangoni Flow Induced Evaporation Enhancement on Binary Sessile Drops. *J. Phys. Chem. B* **121**, 5824–5834 (2017).
14. Deegan, R. D., Bakajin, O., Dupont, T.F., Huber, G., Nagel, S.R., & Witten, T.A. Capillary flow as the cause of ring stains from dried liquid drops. *Nature* **389**, 827–829 (1997).
15. Sempels, W., De Dier, R., Mizuno, H., Hofkens, J. & Vermant, J. Auto-production of biosurfactants reverses the coffee ring effect in a bacterial system. *Nat. Commun.* **4**, 1757 (2013).
16. Hu, H. & Larson, R. G. Marangoni Effect Reverses Coffee-Ring Depositions. *J. Phys. Chem. B* **110**, 7090–7094 (2006).
17. Thomson, J. On certain curious Motions observable at the Surfaces of Wine and other Alcoholic Liquors. *London, Edinburgh, Dublin Philos. Mag. J. Sci.* **10**, 330–333 (1855).
18. Loewenthal, M. XL. Tears of strong wine. *London, Edinburgh, Dublin Philos. Mag. J. Sci.* **12**, 462–472 (1931).
19. Surface tension values of some common test liquids for surface energy analysis. *http://www.surface-tension.de/* 1–4 http://www.surface-tension.de/ (2017).
20. Gugliotti, M. & Todd Silverstein. Tears of Wine. *J. Chem. Educ.* **81**, 67–68 (2004).
21. Krechetnikov, R. Thermodynamics of chemical Marangoni-driven engines. *Soft Matter*

13, 4931–4950 (2017).

22. Bernett, M. K. & Zisman, W. A. Prevention of Liquid Spreading or Creeping. in *Adv. Chem. Ser.* vol. 43 332–340 (1964).

23. Cottington, R. L., Murphy, C. M. & Singleterry, C. R. Effect of Polar-Nonpolar Additives on Oil Spreading on Solids, with Applications to Nonspreading Oils. *Adv. Chem. Ser.* **43**, 341–354 (1964).

24. Pesach, D. & Marmur, A. Marangoni effects in the spreading of liquid mixtures on a solid. *Langmuir* **3**, 519–524 (1987).

25. Karpitschka, S., Liebig, F. & Riegler, H. Marangoni Contraction of Evaporating Sessile Droplets of Binary Mixtures. *Langmuir* **33**, 4682–4687 (2017).

26. Cira, N. J., Benusiglio, A. & Prakash, M. Vapour-mediated sensing and motility in two-component droplets. *Nature* **519**, 446–450 (2015).

27. Hu, H. & Larson, R. G. Evaporation of a sessile droplet on a substrate. *J. Phys. Chem. B* **106**, 1334–1344 (2002).

28. Hack, M. A. *et al.* Wetting of Two-Component Drops: Marangoni Contraction Versus Autophobing. *Langmuir* **37**, 3605–3611 (2021).

29. Zisman, W. A. Relation of the Equilibrium Contact Angle to Liquid and Solid Constitution. in *Contact Angle, Wettability, and Adhesion* 1–51 (Americal Chemical Society, 1964).

30. Bangham, D. H. & Saweris, Z. The behaviour of liquid drops and adsorbed films at cleavage surfaces of mica. *Trans. Faraday Soc.* **34**, 554 (1938).

31. Hardy, W. B. III. The spreading of fluids on glass. *London, Edinburgh, Dublin Philos. Mag. J. Sci.* **38**, 49–55 (1919).

32. Carles, P. & Cazabat, A. M. Spreading involving the marangoni effect: Some preliminary results. *Colloids and Surfaces* **41**, 97–105 (1989).

33. Chaudhury, M. K. & Whitesides, G. M. How to Make Water Run Uphill. *Science (80-.).* **256**, 1539–1541 (1992).

34. Oh, S.-K., Nakagawa, M. & Ichimura, K. Photocontrol of liquid motion on an azobenzene monolayer. *J. Mater. Chem.* **12**, 2262–2269 (2002).

35. Ichimura, K., Oh, S.-K. & Nakagawa, M. Light-Driven Motion of Liquids on a Photoresponsive Surface. *Science (80-.).* **288**, 1624–1626 (2000).

36. Agrawal, P., Salomons, T. T., Chiriac, D. S., Ross, A. C. & Oleschuk, R. D. Facile Actuation of Organic and Aqueous Droplets on Slippery Liquid-Infused Porous Surfaces for the Application of On-Chip Polymer Synthesis and Liquid–Liquid Extraction. *ACS Appl. Mater. Interfaces* **11**, 28327–28335 (2019).

37. Wong, T.-S., Kang, S-H., Tang, S.K.Y., Smythe, E.J., Hatton, B.D., Grinthal, A. & Aizenberg, J. Bioinspired self-repairing slippery surfaces with pressure-stable omniphobicity. *Nature* **477**, 443–447 (2011).

38. Chang, C.-C., Wu, C.-J., Sheng, Y.-J. & Tsao, H.-K. Anti-smudge behavior of facilely fabricated liquid-infused surfaces with extremely low contact angle hysteresis property. *RSC Adv.* **6**, 19214–19222 (2016).

39. Epstein, A. K., Wong, T.-S., Belisle, R. A., Boggs, E. M. & Aizenberg, J. Liquid-infused structured surfaces with exceptional anti-biofouling performance. *Proc. Natl. Acad. Sci.*

109, 13182–13187 (2012).

40. Movafaghi, S., Wang, W., Metzger, A., Williams, D.D., Williams, J.D. & Kota, A.K. Tunable superomniphobic surfaces for sorting droplets by surface tension. *Lab Chip* **16**, 3204–3209 (2016).

41. Liu, J., Guo, H., Zhang, B., Qiao, S., Shao, M., Zhang, X., Feng, X-Q., Li, Q., Song, Y., Jiang L. & Wang, J. Guided Self-Propelled Leaping of Droplets on a Micro-Anisotropic Superhydrophobic Surface. *Angew. Chemie Int. Ed.* **55**, 4265–4269 (2016).

42. Li, J., Tian, X., Perros, A. P., Franssila, S. & Jokinen, V. Self-Propelling and Positioning of Droplets Using Continuous Topography Gradient Surface. *Adv. Mater. Interfaces* **1**, 1–6 (2014).

43. Tang, X., Zhu, P., Tian, Y., Zhou, X., Kong, T. & Wang, L. Mechano-regulated surface for manipulating liquid droplets. *Nat. Commun.* **8**, 14831 (2017).

44. Bain, C. D. Motion of Liquids on Surfaces. *ChemPhysChem* **2**, 580–582 (2001).

45. Lee, S.-W., Kwok, D. Y. & Laibinis, P. E. Chemical influences on adsorption-mediated self-propelled drop movement. *Phys. Rev. E* **65**, 051602 (2002).

46. Bain, C. D., Burnett-Hall, G. D. & Montgomerie, R. R. Rapid motion of liquid drops. *Nature* **372**, 414–415 (1994).

47. Dos Santos, F. D. & Ondarcuhu, T. Free-Running Droplets. *Phys. Rev. Lett.* **75**, 2972–2975 (1995).

48. Riegler, H. & Lazar, P. Delayed coalescence behavior of droplets with completely miscible liquids. *Langmuir* **24**, 6395–6398 (2008).

49. Karpitschka, S. & Riegler, H. Quantitative experimental study on the transition between fast and delayed coalescence of sessile droplets with different but completely miscible liquids. *Langmuir* **26**, 11823–11829 (2010).

50. Karpitschka, S., Hanske, C., Fery, A. & Riegler, H. Coalescence and noncoalescence of sessile drops: Impact of surface forces. *Langmuir* **30**, 6826–6830 (2014).

51. Borcia, R., Menzel, S., Bestehorn, M., Karpitschka, S. & Riegler, H. Delayed coalescence of droplets with miscible liquids: Lubrication and phase field theories. *Eur. Phys. J. E* **34**, 1–9 (2011).

52. Borcia, R. & Bestehorn, M. Different behaviors of delayed fusion between drops with miscible liquids. *Phys. Rev. E - Stat. Nonlinear, Soft Matter Phys.* **82**, 1–5 (2010).

53. Cira, N. J., Benusiglio, A. & Prakash, M. Dancing droplets: Autonomous surface tension-driven droplet motion. *Phys. Fluids* **26**, 1–3 (2014).

54. Benusiglio, A., Cira, N. J. & Prakash, M. Two-component marangoni-contracted droplets: friction and shape. *Soft Matter* **14**, 7724–7730 (2018).

55. Majhy, B. & Sen, A. K. Evaporation-induced transport of a pure aqueous droplet by an aqueous mixture droplet. *Phys. Fluids* **32**, 032003 (2020).

56. Malinowski, R., Parkin, I. P. & Volpe, G. Nonmonotonic contactless manipulation of binary droplets via sensing of localized vapor sources on pristine substrates. *Sci. Adv.* **6**, 1–8 (2020).

57. Kabi, P., Pal, R. & Basu, S. Moses Effect: Splitting a Sessile Droplet Using a Vapor-Mediated Marangoni Effect Leading to Designer Surface Patterns. *Langmuir* **36**, 1279–1287 (2020).

58. Benusiglio, A., Cira, N., Lai, A. W. & Prakash, M. Two-component self-contracted droplets: long-range attraction and confinement effects. *arXiv Soft Condens. Matter* (2017).

59. Samiei, E., Tabrizian, M. & Hoorfar, M. A review of digital microfluidics as portable platforms for lab-on a-chip applications. *Lab Chip* **16**, 2376–2396 (2016).

60. Cejkova, J., Banno, T., Hanczyc, M. M. & Stepanek, F. Droplets as Liquid Robots. *Artif. Life* **23**, 528–549 (2017).

61. Dai, H., Gao, C., Sun, J., Li, C., Li, N., Wu, L., Dong, Z. & Jiang, L. Controllable High-Speed Electrostatic Manipulation of Water Droplets on a Superhydrophobic Surface. *Adv. Mater.* **31**, 1905449 (2019).

62. Yang, Z., Wei, J., Sobolev, Y. I. & Grzybowski, B. A. Systems of mechanized and reactive droplets powered by multi-responsive surfactants. *Nature* **553**, 313–318 (2018).

63. Malinowski, R., Parkin, I. P. & Volpe, G. Advances towards programmable droplet transport on solid surfaces and its applications. *Chem. Soc. Rev.* **49**, 7879–7892 (2020).

64. Sun, D. & Böhringer, K. F. Self-cleaning: From bio-inspired surface modification to MEMS/microfluidics system integration. *Micromachines* **10**, (2019).

65. Huang, K.-T., Yeh, S.-B. & Huang, C.-J. Surface Modification for Superhydrophilicity and Underwater Superoleophobicity: Applications in Antifog, Underwater Self-Cleaning, and Oil−Water Separation. *ACS. Appl. Mater. Interfaces* **7**, 21021–21029 (2015).

66. Xu, C. *et al.* Continuous and controlled directional water transportation on a hydrophobic/superhydrophobic patterned surface. *Chem. Eng. J.* **352**, 722–729 (2018).

67. Kuang, M., Wang, L. & Song, Y. Controllable Printing Droplets for High-Resolution Patterns. *Adv. Mater.* **26**, 6950–6958 (2014).

68. Homede, E., Abo-jabal, M., Ionescu, R. & Haick, H. Printing Ultrasensitive Artificially Intelligent Sensors Array with a Single Self-Propelled Droplet Containing Nanoparticles. (2016) doi:10.1002/adfm.201602326.

69. Mashaghi, S., Abbaspourrad, A., Weitz, D. A. & van Oijen, A. M. Droplet microfluidics: A tool for biology, chemistry and nanotechnology. *TrAC Trends Anal. Chem.* **82**, 118–125 (2016).

70. Tang, E. M., Tao, Y. K. & Haselton, F. R. Controlling Droplet Marangoni Flows to Improve Microscopy-Based TB Diagnosis. *Diagnostics* **11**, 2155 (2021).

71. J. Trantum, M. Baglia, Z. Eagleton, R. M. & F. H. Biosensor design based on Marangoni flow in an evaporating drop. *Lab Chip* **14**, 315–324 (2014).

72. Hernandez-Perez, R., Fan, Z. H. & Garcia-Cordero, J. L. Evaporation-Driven Bioassays in Suspended Droplets. *Anal. Chem.* **88**, 7312–7317 (2016).

73. Galy, P. E., Rudiuk, S., Morel, M. & Baigl, D. Self-Propelled Water Drops on Bare Glass Substrates in Air: Fast, Controllable, and Easy Transport Powered by Surfactants. *Langmuir* **36**, 6916–6923 (2020).

74. Collinson, M. M. & Higgins, D. A. Organosilane Chemical Gradients: Progress, Properties, and Promise. *Langmuir* **33**, 13719–13732 (2017).

75. Hernández, S. C. *et al.* Chemical Gradients on Graphene To Drive Droplet Motion. *ACS Nano* **7**, 4746–4755 (2013).

76. Sin, M.-C., Sun, Y.-M. & Chang, Y. Zwitterionic-Based Stainless Steel with Well-Defined Polysulfobetaine Brushes for General Bioadhesive Control. *ACS Appl. Mater. Interfaces* **6**, 861–873 (2014).

77. de Gennes, P.-G., Brochard-Wyart, F. & Quéré, D. Deformable Interfaces. in *Capillarity and Wetting Phenomena* 16–17 (Springer New York, 2004). doi:10.1007/978-0-387-21656-0_9.

78. Shardt, N. & Elliott, J. A. W. Model for the Surface Tension of Dilute and Concentrated Binary Aqueous Mixtures as a Function of Composition and Temperature. *Langmuir* **33**, 11077–11085 (2017).

79. Hoke, B. C. & Patton, E. F. Surface tensions of propylene glycol + water. *J. Chem. Eng. Data* **37**, 331–333 (1992).

80. Connors, K. A. & Wright, J. L. Dependence of Surface Tension on Composition of Binary Aqueous-Organic Solutions. *Anal. Chem.* **61**, 194–198 (1989).

81. Karpitschka, S. & Riegler, H. Noncoalescence of Sessile Drops from Different but Miscible Liquids: Hydrodynamic Analysis of the Twin Drop Contour as a Self-Stabilizing Traveling Wave. *Phys. Rev. Lett.* **109**, 066103 (2012).

82. Singh, V., Wu, C.-J., Sheng, Y.-J. & Tsao, H.-K. Self-Propulsion and Shape Restoration of Aqueous Drops on Sulfobetaine Silane Surfaces. *Langmuir* **33**, 6182–6191 (2017).

83. Zhang, Y-P., Fan, D., Bai, X-Z., Cui, C-X., Chen, J., Li, R-L., Liu, P-F. & Qu, L-B. Sorting Liquid Droplets by Surface Tension Using Devices with Quasi-Superamphiphobic Coatings. *Polymers,* **12**, 820 (2020).

84. Yamamoto, T., Okubo, M., Imai, N. & Mori, Y. Improvement on Hydrophilic and Hydrophobic Properties of Glass Surface Treated by Nonthermal Plasma Induced by Silent Corona Discharge. *Plasma Chem. Plasma Process.* **24**, 1–12 (2004).

85. Fox, T. H. Master Degree Report. (University of Durham, 2018).

86. Kolb, H. C., Finn, M. G. & Sharpless, K. B. Click Chemistry: Diverse Chemical Function from a Few Good Reactions. *Angew. Chemie Int. Ed.* **40**, 2004–2021 (2001).

87. Fokin, V.V. & Matyjaszewski, K. *CuAAC: The Quintessential Click Reaction* in *Organic Chemistry – Breakthroughs and Perspectives,* 247–277 (Wiley, 2012).

88. Rostovtsev, V. V, Green, L. G., Fokin, V. V & Sharpless, K. B. A Stepwise Huisgen Cycloaddition Process: Copper(I)-Catalyzed Regioselective “Ligation” of Azides and Terminal Alkynes. *Angew. Chemie Int. Ed.* **41**, 2596–2599 (2002).

89. Tornøe, C. W., Christensen, C. & Meldal, M. Peptidotriazoles on Solid Phase: [1,2,3]-Triazoles by Regiospecific Copper(I)-Catalyzed 1,3-Dipolar Cycloadditions of Terminal Alkynes to Azides. *J. Org. Chem.* **67**, 3057–3064 (2002).

90. Sletten, E. M. & Bertozzi, C. R. Bioorthogonal Chemistry: Fishing for Selectivity in a Sea of Functionality. *Angew. Chemie Int. Ed.* **48**, 6974–6998 (2009).

91. Worrell, B. T., Malik, J. A. & Fokin, V. V. Direct Evidence of a Dinuclear Copper Intermediate in Cu(I)-Catalyzed Azide-Alkyne Cycloadditions. *Science (80-.).* **340**, 457–460 (2013).

92. ouj, N., Chakchouk-Mtibaa, A., Mansour, L., Harrath, A.H., Al-Tamimi, J.H., Ozdemir, I., Mellouli, L., Yasar, S. & Hamdi N. Copper-catalyzed azide–alkyne cycloaddition (CuAAC) under mild condition in water: Synthesis, catalytic application and biological activities. *J. Organomet. Chem.* **853**, 49–63 (2017).

93. Butler, R. N., Cunningham, W. J., Coyne, A. G. & Burke, L. A. The Influence of Water on the Rates of 1,3-Dipolar Cycloaddition Reactions: Trigger Points for Exponential Rate Increases in Water−Organic Solvent Mixtures. Water-Super versus Water-Normal Dipolarophiles. *J. Am. Chem. Soc.* **126**, 11923–11929 (2004).

94. Jayalakshmi, L.N., Karuppasamy, A., Stalindurai, K., Sivaramakarthikeyan, R., Devadoss, V. & Ramalingan, C. Straightforward syntheses of nitriles, acrylates, and acrylamides in aqueous propan-1,2-diol: A catalyst free and waste free methodology. *Tetrahedron Lett.* **56**, 4207–4210 (2015).

95. O'Callaghan, C. N., McMurry, T. B. H. & O'Brien, J. E. Isomerisation of benzopyran-2-imines in [2H6]dimethyl sulfoxide. *J. Chem. Soc. Perkin Trans. 2* **1**, 425–430 (1998).

96. Mooney, E. F. & Winson, P. H. Nitrogen Magnetic Resonance Spectroscopy. in *Annual Reports on NMR Spectroscopy* vol. 2 125–152 (1969).

97. Still, W. C., Kahn, M. & Mitra, A. Rapid chromatographic technique for preparative separations with moderate resolution. *J. Org. Chem.* **43**, 2923–2925 (1978).

98. Fulmer, G.R., Miller, A.J.M., Sherden, N.H., Gottlieb, E.H., Nudelman, A., Stoltz, B.M., Bercaw, J.E. & Goldberg, K.I. NMR Chemical Shifts of Trace Impurities: Common Laboratory Solvents, Organics, and Gases in Deuterated Solvents Relevant to the Organometallic Chemist. *Organometallics* **29**, 2176–2179 (2010).

99. Panja, S. K., Dwivedi, N. & Saha, S. First Report of Application of Simple Molecular Complexes as Organo-Catalyst for Knoevenagel Condensation. *RSC Adv.* **5**, 65526–65531 (2015).

100. Xiao, R., Tobin, J.M., Zha, M., Hou, Y-L., He, J., Vilela, F. & Xu, Z. A nanoporous graphene analog for superfast heavy metal removal and continuous-flow visible-light photoredox catalysis. *J. Mater. Chem. A* **5**, 20180–20187 (2017).

101. Gupta, M., Gupta, R. & Anand, M. Hydroxyapatite supported caesium carbonate as a new recyclable solid base catalyst for the Knoevenagel condensation in water. *Beilstein J. Org. Chem* **5**, 1–7 (2009).

102. Cheikh, N., Bar, N., Choukchou-Braham, N., Mostefa-Kara, B., Lohier, J-F., Sopkova, J. & Villemin, D. Efficient synthesis of new butenolides by subsequent reactions: Application for the synthesis of original iminolactones, bis-iminolactones and bis-lactones. *Tetrahedron* **67**, 1540–1551 (2011).

103. Morimoto, H., Fujiwara, R., Shimizu, Y., Morisaki, K. & Ohshima, T. Lanthanum(III) Triflate Catalyzed Direct Amidation of Esters. *Org. Lett.* **16**, 2018–2021 (2014).

104. Wei, L., Wang, J., i Zhang, X., Wang, P., Zhao, Y., Li, J., Hou, T., Qu, L., Shi, L., Liang, X. & Fang, Y. Discovery of 2H-Chromen-2-one Derivatives as G Protein-Coupled Receptor-35 Agonists. *J. Med. Chem.,* **60**, 362–372 (2017).

105. He, X., Yan, Z., Hu, X., Zuo, Y., Jiang, C., Jin, L. & Shang, Y. $FeCl_3$-Catalyzed Cascade Reaction: An Efficient Approach to Functionalized Coumarin Derivatives. *Synth. Commun.,* **44**, 1507–1514 (2014).

106. Yuan, H. J., Wang, M., Liu, Y. J. & Liu, Q. Copper(II)-catalyzed C-C bond-forming reactions of α-electron-withdrawing group-substituted ketene S,S-acetals with carbonyl compounds and a facile synthesis of coumarins. *Adv. Synth. Catal.* **351**, 112–116 (2009).

107. Nemeryuk, M.P., Dimitrova, V.D., Anisimova, O.S., Sedov, A.L., Solov'eva, N.P. & Traven, V.F. Conversion of Coumarins Accompanied by Opening and Recyclization of the Lactone Ring. 1. Study of the Reaction of 3-Ethoxycarbonyl(3-acyl)coumarins with

Cyanoacetylhydrazine and Its Derivatives. *Chem. Heterocycl. Compd.* **39**, 1454–1465 (2003).

108. Costa, M., Areias, F., Abrunhosa, L., Venâncio, A. & Proença, F. The condensation of salicylaldehydes and malononitrile revisited: Synthesis of new dimeric chromene derivatives. *J. Org. Chem.* **73**, 1954–1962 (2008).

109. Augustine, J. K., Bombrun, A., Ramappa, B. & Boodappa, C. An efficient one-pot synthesis of coumarins mediated by propylphosphonic anhydride (T3P) via the Perkin condensation. *Tetrahedron Lett.* **53**, 4422–4425 (2012).

110. Brahmachari, G. Room Temperature One-Pot Green Synthesis of Coumarin-3-carboxylic Acids in Water: A Practical Method for the Large-Scale Synthesis. *ACS Sustain. Chem. Eng.* **3**, 2350–2358 (2015).

111. Chernov, N. M., Filippova, P. V, Yakovlev, I. P., Zakhs, V. E. & Belyakov, A. V. Synthesis and Reactivity of 4-Hydroxy-5-methyl-2-(2-oxo-2H-chromen-3-yl)-6H-1,3-oxazin-6-ones. *Russ. J. Gen. Chem* **86**, 1292–1299 (2016).

112. Nubbemeyer, U. Recent Advances in Charge-Accelerated Aza-Claisen Rearrangements. in *Topics in Current Chemistry* vol. 244 149–213 (2005).

113. Dains, F. B., Brewster, R. Q., Blair, J. S. & Thompson, W. C. The substituted thio-ureas III. The synthesis of thiazolidine and thiazane derivatives. *J. Am. Chem. Soc.* **44**, 2637–2643 (1922).

114. Carnahan, F. L. & Hurd, C. D. Pyrolysis of allylanilines. *J. Am. Chem. Soc.* **52**, 4586–4595 (1930).

115. Marcinkiewicz, S., Green, J. & Mamalis, P. The relation between the Claisen rearrangement of allyl ethers and their electronic structure. *Tetrahedron* **14**, 208–222 (1961).

116. Majumdar, K. & Chattopadhyay, B. Amino-Claisen versus Oxy-Claisen Rearrangement: Regioselective Synthesis of Pyrrolocoumarin Derivatives. *Synthesis (Stuttg).* **2008**, 921–924 (2008).

117. Beare, K. D. & McErlean, C. S. P. Revitalizing the aromatic aza-Claisen rearrangement: implications for the mechanism of 'on-water' catalysis. *Org. Biomol. Chem.* **11**, 2452 (2013).

118. Hyre, J. E. & Bader, A. R. Unsaturated Aromatic Amines; a Novel Synthesis of Indoles. *J. Am. Chem. Soc.* **80**, 437–439 (1958).

119. Chaskar, A., Padalkar, V., Phatangare, K., Patil, K., Bodkhe, A. & Langi, B. Heteropoly acids as useful recyclable heterogeneous catalysts for the facile and highly efficient aza-Cope rearrangement of N-allylanilines. *Appl. Catal. A Gen.* **359**, 84–87 (2009).

120. Hui, Z., Jiang, S., Qi, X., Ye, X.-Y. & Xie, T. Investigating the microwave-accelerated Claisen rearrangement of allyl aryl ethers: Scope of the catalysts, solvents, temperatures, and substrates. *Tetrahedron Lett.* **61**, 151995 (2020).

121. Jolidon, S. & Hansen, H. Untersuchungen über aromatische Amino-Claisen - Umlagerungen. *Helv. Chim. Acta* **60**, 978–1032 (1977).

122. Krowicki, K., Paillous, N., Rivière, M. & Lattes, A. Synthesis of indolines from N-allylarylamines. *Journal of Heterocyclic Chemistry* vol. 13 555–560 (1976).

123. Majumdar, K. C. & Das, U. Synthesis of 1-alkoxy-1,2,3,4-tetra-hydrocarbazoles by mercury(II) mediated heterocyclization of 2-cyclohex-2′-enyl- N -alkylanilines. *Can. J. Chem.* **74**, 1592–1596 (1996).

124. Abdrakhmanov, I. B., Mustafin, A. G., Tolstikov, G. A., Spirikhin, L. V. & Khalikov, L. M. Claisen rearrangement of sterically hindered N-alkenylindolines. *Bull. Acad. Sci. USSR Div. Chem. Sci.* **36**, 561–565 (1987).

125. Cooper, M. A., Lucas, M. A., Taylor, J. M., Ward, A. D. & Williamson, N. M. A Convenient Method for the Aromatic Amino-Claisen Rearrangement of N-(1,1-Disubstituted-allyl)anilines. *Synthesis (Stuttg).* **2001**, 0621–0625 (2001).

126. Liang, D. & Wang, Y. The first synthesis of 7-prenylisatin. *Mendeleev Commun.* **29**, 172–173 (2019).

127. Danishefsky, S. J. & Phillips, G. B. A rapid route to ergot precursors via aza-Claisen rearrangement. *Tetrahedron Lett.* **25**, 3159–3162 (1984).

128. Roe, J. M., Webster, R. A. B. & Ganesan, A. Total synthesis of (+)-okaramine J featuring an exceptionally facile N-reverse-prenyl to C-prenyl aza-Claisen rearrangement. *Org. Lett.* **5**, 2825–2827 (2003).

129. Maity, P., Pemberton, R. P., Tantillo, D. J. & Tambar, U. K. Brønsted acid catalyzed enantioselective indole aza-Claisen rearrangement mediated by an arene CH-O interaction. *J. Am. Chem. Soc.* **135**, 16380–16383 (2013).

130. Hurd, C. D. & Jenkins, W. W. Decomposition of Allylanilines in the Presence of Zinc Chloride. *J. Org. Chem.* **22**, 1418–1423 (1957).

131. Schmid, M., Hansen, H.-J. & Schmid, H. Zinkchloridkatalysierte, thermische Umlagerungen von N-Allyl in C-Allyl-aniline; ladungsinduzierte, aromatische Amino-Claisen-Umlagerungen. *Helv. Chim. Acta* **56**, 105–124 (1973).

132. Beholz, L. G. & Stille, J. R. Lewis acid-promoted 3-aza-Cope rearrangement of N-alkyl-N-allylanilines. *J. Org. Chem.* **58**, 5095–5100 (1993).

133. González, I., Bellas, I., Souto, A., Rodríguez, R. & Cruces, J. Microwave-assisted aza-Cope rearrangement of N-allylanilines. *Tetrahedron Lett.* **49**, 2002–2004 (2008).

134. Yadav, J. S., Reddy, B. V. S., Rasheed, M. A. & Kumar, H. M. S. Zn^{2+} Montmorillonite Catalyzed 3-Aza-Cope Rearrangement under Microwave Irradiation. *Synlett* **2000**, 487–488 (2000).

135. Sreekumar, R. & Padmakumar, R. Aromatic 3-aza-Cope rearrangement over zeolites. *Tetrahedron Lett.* **37**, 5281–5282 (1996).

136. Kupai, K., Banoczi, G., Hornyanszky, G., Kolonits, P. & Novak, L. Facile synthesis of cycloalkanoindole derivatives by aza-Claisen rearrangement. *Monatshefte für Chemie - Chem. Mon.* **143**, 1663–1669 (2012).

137. Wu, W-L., Burnett, D.A., Spring, R., Greenlee, W.J., Smith, M., Favreau, L., Fawzi, A., Zhang, H. & Lachowicz, J.E. Dopamine D1/D5 receptor antagonists with improved pharmacokinetics: Design, synthesis, and biological evaluation of phenol bioisosteric analogues of benzazepine D1/D5 antagonists. *J. Med. Chem.* **48**, 680–693 (2005).

138. Ghosh, D., Thander, L., Ghosh, S. & Chattopadhyay, S. Sequential Aza-Claisen Rearrangement and Ring-Closing Metathesis as a Route to 1-Benzazepine Derivatives. *Synlett* **2008**, 3011–3015 (2008).

139. Tuccinardi, T., Bertini, S., Martinelli, A., Minutolo, F., Ortore, G., Placanica, G., Prota, G., Rapposelli, S., Carlson, K.E., Katzenellenbogen, J.A. & Macchia, M. Synthesis of anthranylaldoxime derivatives as estrogen receptor ligands and computational prediction of binding modes. *J. Med. Chem.,* **49**, 5001–5012 (2006).

140. Lai, G. & Anderson, W.K. A concise synthesis of a benzimidazole analogue of

mycophenolic acid using a BF_3-Et_2O catalyzed amino-claisen rearrangement. *Tetrahedron Lett.,* **34**, 6849–6852 (1993).

141. Anderson, W. K. & Lai, G. Boron Trifluoride-Diethyl Ether Complex Catalyzed Aromatic Amino-Claisen Rearrangements. *Synthesis (Stuttg).* **1995**, 1287–1290 (1995).

142. Li, X. W., Si, T. X., Liu, Y. P., Wang, M. Z. & Chan, A. S. C. Divergent syntheses of okaramines C, J, L, and S-U. *Org. Biomol. Chem.* **18**, 3848–3852 (2020).

143. Irie, K., Koizumi, F., Iwata, Y., Ishii, T., Yanai, Y., Nakamura, Y., Ohigashi, H. & Wender, P.A. Synthesis and biological activities of new conformationally restricted analogues of (-)-indolactam-V: Elucidation of the biologically active conformation of the tumor-promoting teleocidins. *J. Am. Chem. Soc.,* **118**, 10733–10743 (1996).

144. Badamshin, A. G., Spirikhin, L. V., Salikov, R. F., Dokichev, V. A. & Tomilov, Y. V. Lewis acid-catalyzed reactions of N-allylanilines with diazo compounds involving aza-Claisen rearrangement. *Mendeleev Commun.* **25**, 438–439 (2015).

145. Kumar, M. S. L., Manna, S. K., Maji, S. & Panda, G. Indium triflate catalysed 3-aza-Cope rearrangement of amino acid derived α,β-unsaturated esters to alkylidene oxindoles. *Org. Biomol. Chem.* **15**, 1762–1766 (2017).

146. Alcaide, B., Almendros, P., Cembellín, S., Martínez del Campo, T. & Muñoz, A. Iron-catalyzed domino indole fluorination/allenic aza-Claisen rearrangement. *Chem. Commun.* **52**, 6813–6816 (2016).

147. Weston, M. H., Nakajima, K. & Back, T. G. Tandem Conjugate Additions and 3-Aza-Cope Rearrangements of Tertiary Allyl Amines and Cyclic α-Vinylamines with Acetylenic Sulfones. Applications to Simple and Iterative Ring Expansions Leading to Medium and Large-Ring Nitrogen Heterocycles. *J. Org. Chem.* **73**, 4630–4637 (2008).

148. Weston, M. H., Nakajima, K., Parvez, M. & Back, T. G. Ring-expansion of tertiary cyclic α-vinylamines by tandem conjugate addition to (p-toluenesulfonyl)ethyne and formal 3-aza-Cope rearrangement. *Chem. Commun.* 3903 (2006) doi:10.1039/b607713g.

149. Weston, M. H., Parvez, M. & Back, T. G. Conjugate Additions, Aza-Cope, and Dissociative Rearrangements and Unexpected Electrocyclic Ring Closures in the Reactions of 2-(2-Pyrrolidinyl)-Substituted Heteroaromatic Systems with Acetylenic Sulfones. *J. Org. Chem.* **75**, 5402–5405 (2010).

150. Schwan, A. L. & Warkentin, J. The reactions of simple dimethylallylamines with dimethyl acetylenedicarboxylate. Formation of 1-dimethylamino-2-allylmaleates via formal allyl transfer. *Can. J. Chem.* **66**, 1686–1694 (1988).

151. Vedejs, E. & Gingras, M. Aza-Claisen Rearrangements Initiated by Acid-Catalyzed Michael Addition. *J. Am. Chem. Soc.* **116**, 579–588 (1994).

152. Weng, J., Chen, Y., Yue, B., Xu, M. & Jin, H. Synthesis of Polysubstituted Pyrroles from Activated Alkynes and N -Propargylamines through Base-Catalyzed Cascade Reaction. *European J. Org. Chem.* **2015**, 3164–3170 (2015).

153. Diederich, M. & Nubbemeyer, U. Diastereoselective Zwitterionic Aza-Claisen Rearrangement: Synthesis of Nine-Membered Ring Lactams and Transannular Ring Contraction. *Chem. – A Eur. J.* **2**, 894–900 (1996).

154. Nubbemeyer, U. Diastereoselective Zwitterionic Aza-Claisen Rearrangement: The Synthesis of Bicyclic Tetrahydrofurans and a Total Synthesis of (+)-Dihydrocanadensolide. *J. Org. Chem.* **61**, 3677–3686 (1996).

155. Lambert, T. H. & MacMillan, D. W. C. Development of a new lewis acid-catalyzed [3,3]-

sigmatropic rearrangement: The allenoate-Claisen rearrangement. *J. Am. Chem. Soc.* **124**, 13646–13647 (2002).

156. Dai, R.-H., Wang, Q., Chen, Z.-X. & Tian, S.-K. Asymmetric Aza-Claisen Rearrangement between Enantioenriched α-Chiral Allylamines and Allenones. *J. Org. Chem.* **86**, 3065–3073 (2021).

157. Chen, X., Fan, H., Zhang, S., Yu, C. & Wang, W. Facile Installation of 2-Reverse Prenyl Functionality into Indoles by a Tandem N-Alkylation–Aza-Cope Rearrangement Reaction and Its Application in Synthesis. *Chem. – A Eur. J.* **22**, 716–723 (2016).

158. Cant, A. A., Bertrand, G. H. V., Henderson, J. L., Roberts, L. & Greaney, M. F. The benzyne aza-claisen reaction. *Angew. Chemie - Int. Ed.* **48**, 5199–5202 (2009).

159. Rao Mangina, N. S. V. M., Guduru, R. & Karunakar, G. V. Synthesis of medium-sized aryl-fused nitrogenous heterocycles via sequential aryne aza-Claisen rearrangement/ring-closing metathesis. *Org. Biomol. Chem.* **16**, 2134–2142 (2018).

160. Kaldas, S. J., Kran, E., Mück-Lichtenfeld, C., Yudin, A. K. & Studer, A. Reaction of Vinyl Aziridines with Arynes: Synthesis of Benzazepines and Branched Allyl Fluorides. *Chem. – A Eur. J.* **26**, 1501–1505 (2020).

161. Shimizu, T., Koya, S., Yamasaki, R., Mutoh, Y., Isao Azumaya, I., Katagiri, K. & Saito, S. Acid-mediated ring-expansion reaction of N-aryl-2-vinylazetidines: Synthesis and unanticipated reactivity of tetrahydrobenzazocines. *J. Org. Chem.,* **79**, 4367–4377 (2014).

162. Aoki, T., Koya, S., Yamasaki, R. & Saito, S. Cycloaddition reaction of 2-vinylazetidines with benzyne: A facile access to 1-benzazocine derivatives. *Org. Lett.* **14**, 4506–4509 (2012).

163. Han, L., Li, S., Zhang, X. & Tian, S. Aromatic Aza-Claisen Rearrangement of Arylpropargylammonium Salts Generated in situ from Arynes and Tertiary Propargylamines. *Chem. – A Eur. J.* **27**, 3091–3097 (2021).

164. Katayama, H. Amino-Claisen rearrangement. I. *Chem. Pharm. Bull.* **26**, 2027–2035 (1978).

165. Katayama, H. & Takatsu, N. Amino-claisen rearrangement. II. Quaternary amino-Claisen rearrangement of anilinium compounds with ortho substituents. *Chem. Pharm. Bull.* **29**, 2465–2477 (1981).

166. Katayama, H., Tachikawa, Y., Takatsu, N. & Kato, A. Amino-Claisen rearrangement. III. The effects of alkyl substituents on the allyl group upon the rearrangement. *Chem. Pharm. Bull.* **31**, 2220–2233 (1983).

167. Takamatsu, N., Inoue, S. & Kishi, Y. Synthetic study on echinulin and related compounds. Part I. acid-catalyzed amino claisen rearrangement of allyl- and 3,3-dimethylallyl-aniline derivatives. *Tetrahedron Lett.* **12**, 4661–4664 (1971).

168. McComsey, D. F. & Maryanoff, B. E. 3-Aza-Cope Rearrangement of Quaternary N -Allyl Enammonium Salts. Stereospecific 1,3 Allyl Migration from Nitrogen to Carbon on a Tricyclic Template. *J. Org. Chem.* **65**, 4938–4943 (2000).

169. Kwaśniewska, D., Chen, Y. L. & Wieczorek, D. Biological activity of quaternary ammonium salts and their derivatives. *Pathogens* **9**, 459–471 (2020).

170. Zee-Cheng, K. Y. & Cheng, C. C. Practical preparation of coralyne chloride. *J. Pharm. Sci.* **61**, 969–971 (1972).

171. Shen, Y., Shang, Z. & Yang, Y. Structurally Rigid 9-Amino-Benzo[c]cinnoliniums (aBCLs) are a Class of Compact and Large Stokes-Shift Fluorescent Dyes for Cell-Based Imaging Applications. *J. Org. Chem.* **80**, 5906–5911 (2015).

172. Manna, R. K., Jaisankar, P. & Giri, V. S. Synthesis of Indole Alkaloids and Alkaloidal Precursors: an Improved Synthesis of Flavopereirine. *J. Chem. Res.* 350–351 (1999) doi:10.1039/A900979E.

173. Prakash, S., Muralirajan, K. & Cheng, C. H. Cobalt-Catalyzed Oxidative Annulation of Nitrogen-Containing Arenes with Alkynes: An Atom-Economical Route to Heterocyclic Quaternary Ammonium Salts. *Angew. Chemie - Int. Ed.* **55**, 1844–1848 (2016).

174. Mayakrishnan, S., Tamizmani, M., Balachandran, C., Aoki, S. & Maheswari, N. U. Rh(III)-Catalysed synthesis of cinnolinium and fluoranthenium salts using C-H activation/annulation reactions: organelle specific mitochondrial staining applications. *Org. Biomol. Chem.* **19**, 5413–5425 (2021).

175. Denmark, S. E. & Chi, H. M. Synthesis of 2-Alkenyl-Tethered Anilines. *Synth.* **49**, 2873–2888 (2017).

176. Walsh, M. Rearrangements at Nitrogen Centres: photocatalytic Polonovski reaction and charged Aza-Claisen rearrangements. First Year Postgraduate Report. (Durham, 2017).

177. Kulchat, S. & Lehn, J.-M. Dynamic Covalent Chemistry of Nucleophilic Substitution Component Exchange of Quaternary Ammonium Salts. *Chem. Asian J.* **10**, 2484–2496 (2015).

178. Wilken, S., Treskow, M., Scheers, J., Johansson, P. & Jacobsson, P. Initial stages of thermal decomposition of LiPF6-based lithium ion battery electrolytes by detailed Raman and NMR spectroscopy. *RSC Adv.* **3**, 16359 (2013).

179. Stich, M., Göttlinger, M., Kurniawan, M., Schmidt, U. & Bund, A. Hydrolysis of LiPF6 in Carbonate-Based Electrolytes for Lithium-Ion Batteries and in Aqueous Media. *J. Phys. Chem. C* **122**, 8836–8842 (2018).

180. Wiemers-Meyer, S., Winter, M. & Nowak, S. Mechanistic insights into lithium ion battery electrolyte degradation – a quantitative NMR study. *Phys. Chem. Chem. Phys.* **18**, 26595–26601 (2016).

181. Tanaka, S., Suzuki, Y., Saburi, H. & Kitamura, M. Soft ruthenium and hard Brønsted acid combined catalyst for efficient cleavage of allyloxy bonds. Application to protecting group chemistry. *Tetrahedron* **71**, 6559–6568 (2015).

182. Gong, Y.J., Pyo, S., Kim, H., Cho, J., Yun, H., Kim, H., Ryu, S., Yooc, J. & Kim, Y.S. Advanced Li metal anode by fluorinated metathesis on conjugated carbon networks. *Energy Environ. Sci.,* **14**, 940–954 (2021).

183. Schlummer, B. & Hartwig, J. F. Brønsted Acid-Catalyzed Intramolecular Hydroamination of Protected Alkenylamines. Synthesis of Pyrrolidines and Piperidines. *Org. Lett.* **4**, 1471–1474 (2002).

184. Giumanini, A. G., Chiavari, G., Musiani, M. M. & Rossi, P. N -Permethylation of Primary and Secondary Aromatic Amines. *Synthesis (Stuttg).* **1980**, 743–746 (1980).

185. Giumanini, A. G., Chiavari, G. & Scarponi, F. L. N-Permethylation of polyamines for gas chromatographic and mass spectrometric analyses. *Anal. Chem.* **48**, 484–489 (1976).

186. Voss, T., Chen, C., Kehr, G., Nauha, E., Erker, G. & Stephan, D.W. Cyclizations via Frustrated Lewis Pairs: Lewis Acid Induced Intramolecular Additions of Amines to

Olefins and Alkynes. *Chem. Eur. J.,* **16**, 3005–3008 (2010).

187. van der Schaaf, P.A., Sutter, J-P., Grellier, M., van Mier, G.P.M., Spek, A.L., van Koten, G. & Pfeffer, M. Palladium-Mediated Intramolecular C-N Bond Formation between Tertiary Amines and Alkenes. *J. Am. Chem. Soc.,* **116**, 5134–5144 (1994).

188. Grellier, M. & Pfeffer, M. Allyl versus C-H activation mediated by palladium acetate. *J. Organomet. Chem.* **548**, 301–304 (1997).

189. Eberhart, A. J., Imbriglio, J. E. & Procter, D. J. Nucleophilic Ortho Allylation of Aryl and Heteroaryl Sulfoxides. *Org. Lett.* **13**, 5882–5885 (2011).

190. Li, C., Li, M., Zhong, W., Jin, Y., Li, J., Wu, W. & Jiang, H. Palladium-Catalyzed Oxidative Allylation of Sulfoxonium Ylides: Regioselective Synthesis of Conjugated Dienones. *Org. Lett.,* **21**, 872–875 (2019).

191. Mfuh, A. M., Doyle, J. D., Chhetri, B., Arman, H. D. & Larionov, O. V. Scalable, Metal- and Additive-Free, Photoinduced Borylation of Haloarenes and Quaternary Arylammonium Salts. *J. Am. Chem. Soc.* **138**, 2985–2988 (2016).

192. Drouillat, B., d'Aboville, E., Bourdreux, F. & François Couty, F. Synthesis of 2-Phenyl- and 2,2-Diarylpyrrolidines through Stevens Rearrangement Performed on Azetidinium Ions. Eur. J. Org. Chem., **2014**, 1103–1109 (2014).

193. Tayama, E., Takedachi, K., Iwamoto, H. & Hasegawa, E. Remarkable enhancement effect of potassium tert -butoxide / THF solution in base-induced Sommelet e Hauser rearrangements. *Tetrahedron* **66**, 9389–9395 (2010).

194. Paras, N. A., Simmons, B. & Macmillan, D. W. C. A process for the rapid removal of dialkylamino-substituents from aromatic rings . Application to the expedient synthesis of (R)-tolterodine. *Tetrahedron* **65**, 3232–3238 (2009).

195. Still, W. C., Kahn, M. & Mitra, A. Rapid chromatographic technique for preparative separations with moderate resolution. *J. Org. Chem.* **43**, 2923–2925 (1978).

196. Fulmer, G.R., Miller, A.J.M., Sherden, N.H., Gottlieb, E.H., Nudelman, A., Stoltz, B.M., Bercaw, J.E. & Goldberg, K.I. NMR chemical shifts of trace impurities: Common laboratory solvents, organics, and gases in deuterated solvents relevant to the organometallic chemist. *Organometallics,* **29**, 2176–2179 (2010).

197. Dolomanov, O. V., Bourhis, L. J., Gildea, R. J., Howard, J. A. K. & Puschmann, H. OLEX2: A complete structure solution, refinement and analysis program. *J. Appl. Crystallogr.* **42**, 339–341 (2009).

198. Sheldrick, G. M. SHELXT – Integrated space-group and crystal-structure determination. *Acta Crystallogr. Sect. A Found. Adv.* **71**, 3–8 (2015).

199. Hübschle, C. B., Sheldrick, G. M. & Dittrich, B. ShelXle : a Qt graphical user interface for SHELXL. *J. Appl. Crystallogr.* **44**, 1281–1284 (2011).

200. Yang, Z., Yu, B., Zhang, H., Zhao, Y., Ji, G., Ma, Z. & Liu, Z. $B(C_6F_5)_3$-catalyzed methylation of amines using CO_2 as a C1 building block. *Green Chem.,* **17**, 4189–4193 (2015).

201. Lee, B. K., Biscoe, M. R. & Buchwald, S. L. Simple, efficient protocols for the Pd-catalyzed cross-coupling reaction of aryl chlorides and dimethylamine. *Tetrahedron Lett.* **50**, 3672–3674 (2009).

202. Bush, T. S., Yap, G. P. A. & Chain, W. J. Transformation of N,N-Dimethylaniline N-Oxides into Diverse Tetrahydroquinoline Scaffolds via Formal Povarov Reactions. *Org. Lett.* **20**, 5406–5409 (2018).

203. Matsumoto, K., Takeda, S., Hirokane, T. & Yoshida, M. A Highly Selective Palladium-Catalyzed Aerobic Oxidative Aniline−Aniline Cross-Coupling Reaction. *Org. Lett.* **21**, 7279–7283 (2019).

204. Barker, T. J. & Jarvo, E. R. Umpolung Amination: Nickel-Catalyzed Coupling Reactions of N,N-Dialkyl-N-chloroamines with Diorganozinc Reagents. *J. Am. Chem. Soc.* **131**, 15598–15599 (2009).

205. Zhu, L., Wang, L.-S., Li, B., Li, W., & Fu, B. Methylation of Aromatic Amines and Imines Using Formic Acid over Heterogeneous Pt/C Catalyst. *Catal. Sci. Technol.* **6**, 6172–6176 (2016).

206. Chen, Z., Hu, Y. & Zheng, Q. [bmim]Br_3 as a New Reagent for Regioselective Monobromination of Aryl-amines under Solvent-Free Conditions. *Synthesis,* **17**, 2809–2812 (2004).

207. Higgs, D. E., Nelen, M. I. & Detty, M. R. Iodination of Organic Substrates with Halide Salts and H2O2 Using an Organotelluride Catalyst. *Org. Lett.* **3**, 349–352 (2001).

208. Jeon, K.O., Jun, J.H., Yu, J.S. & Lee, C.K. Infrared and Nuclear Magnetic Resonance Properties of Benzoyl Derivatives of Five-membered Monoheterocycles and Determination of Aromaticity Indices. *J. Het. Chem.,* **40**, 763–771 (2003).

209. Toyooka, G., Tuji, A. & Fujita, K. I. Efficient and versatile catalytic systems for the n-methylation of primary amines with methanol catalyzed by N-heterocyclic carbene complexes of iridium. *Synth.* **50**, 4617–4626 (2018).

210. Sunthankar, S. V. & Gilman, H. Silicon Containing Azo Dyes. *J. Org. Chem.* **15**, 1200–1210 (1950).

211. Reed, H., Paul, T. R. & Chain, W. J. Synthesis of Halogenated Anilines by Treatment of N, N-Dialkylaniline N-Oxides with Thionyl Halides. *J. Org. Chem.* **83**, 11359–11368 (2018).

212. Finkelstein, M., Petersen, R. C. & Ross, S. D. The Electrochemical Degradation of Quaternary Ammonium Salts. *J. Am. Chem. Soc.* **81**, 2361–2364 (1959).

213. Torbeev, V.Y., Lyssenko, K.A., Kharybin, O.N., Antipin, M.Y. & Kostyanovsky, R.G. Lamellar racemic twinning as an obstacle for the resolution of enantiomers by crystallization: The case of Me(All)$N^+(CH_2Ph)$Ph X^- (X = Br, I) salts. *J. Phys. Chem. B,* **107**, 13523–13531 (2003)